Planck explanatory supplement

First release v1.04 (29 April 2013)

PDF generated using the open source mwlib toolkit. See http://code.pediapress.com/ for more information.
PDF generated at: Tue, 30 Apr 2013 14:20:45 CET

Warning for readers of the pdf version

The pdf version of the Planck explanatory supplement still has a few problems:

- The bibliography is not displayed in the pdf version. Due to an incompatibility between the extension that formats the bibliography and the pdf generation software, instead of the bibliography you will only see the mediwiki tags that generate the bibliography entries in the online version;
- Some of the figures in the online version are not correctly displayed in the pdf version;
- Some of the equations are not correctly displayed in the pdf version. Instead you see the LaTex code that produces the equations.

Changelog (pdf)

Changes in v1.04

- Fixed link to SREM files in the SREM files page.
- In the LFI data processing Map-making page, fixed:
  - Link to the Noise Monte Carlo Simulations page, end of 2.2.1;
  - A typo in the title of 3.2.3;
  - The title of 5. "References" (previously "The Bibliography") for consistency with the rest of the ES.
  - Added three missing references to References2;

Changes in v1.03

- Cosmological Parameters page:
  - Important information was added to the caveats section;
  - Improved formatting.
- CMB and astrophysical component maps page:
  - Added comments on inpainting for SMICA and NILC maps;
  - Updated product descriptions to take into account the inpainting data contained in the SMICA and NILC maps;
  - Updated links to SMICA and NILC maps.
- Fixed incorrect links in Sky temperature maps page.

The Planck mission

The Planck mission

Introduction

Planck is a space telescope of the European Space Agency designed to answer key cosmological questions. Its main goal is to determine the geometry and content of the Universe, and which theories describing the birth and evolution of the Universe are correct. To achieve this ambitious objective, it observed the Cosmic Microwave Background radiation (CMB), emitted about 14 billion years ago, just over 300,000 years after the Big Bang. Today the CMB permeates the Universe and is observed to have an average temperature of 2.7 K. Small deviations from this average value (the so-called anisotropies), observable at angular scales larger than ~5 arcminutes, encode a wealth of information on the properties of the Universe in its infancy. The objective of Planck is to measure these properties with an unprecedented accuracy and level of detail.

The Planck collaboration institutes.

As with all ESA scientific missions, Planck was developed in a partnership with the European scientific community. Two consortia of scientific institutes, each led by a Principal Investigator, developed and delivered to ESA two instruments designed specifically for Planck. Each of these instruments targets a specific number of wavelength bands within the range in which the CMB is observable. Together, the two instruments are capable of collecting data of a quality adequate to measure the CMB signal and distinguish it from other confusing sources. A large telescope collects the light from the sky and deliver it to the instruments for measurement and analysis. The reflectors of the Planck telescope were developed and delivered to ESA by a Danish consortium of institutes. ESA retains overall management of the project, develops and procures the spacecraft, integrates the instruments into the spacecraft, and launches and operates it. Planck was launched on May 14th 2009 on an Ariane 5 rocket together with the Herschel Space Observatory. After launch, they were both placed into orbits around the L2 Lagrange of the Sun-Earth system, located about 1.5 million km from the Earth. From that far vantage point, Planck sweeped the sky regularly in large swaths, and covered it fully about six times. Each of the two instrument consortia operated their respective instrument and processed all the data into usable scientific products. At the end of the mission the consortia delivered the final products to ESA, which archives them and distributes them to the community.

Early operations and transfer to orbit

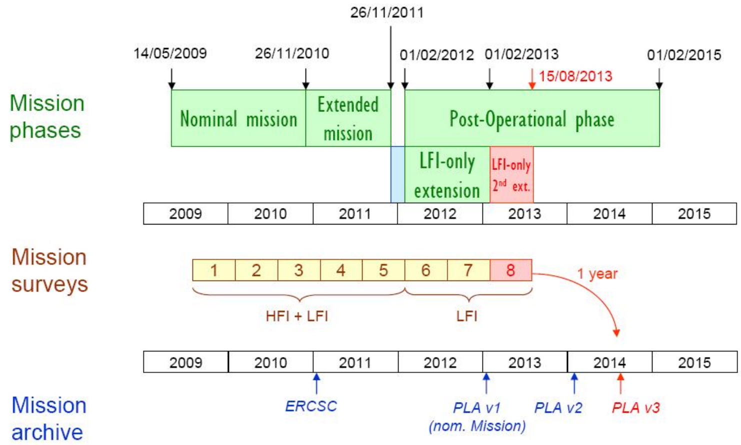
26/11/2011
14/05/2009
26/11/2010
01/02/2012
01/02/2013
01/02/2015
15/08/2013
Mission phases
Nominal mission
Extended mission
Post-Operational phase
LFI-only extension
LFI-only 2nd ext.
2009
2010
2011
2012
2013
2014
2015
Mission surveys
1
2
3
4
5
6
7
8
1 year
HFI + LFI
LFI
2009
2010
2011
2012
2013
2014
2015
Mission archive
ERCSC
PLA v1 (nom. Mission)
PLA v2
PLA v3

A timeline of the Planck operations and archiving.

Planck was launched from the Centre Spatial Guyanais in Kourou (French Guyana) on 14 May 2009 at its nominal lift-off time of 13:12 UT, on an Ariane 5 ECA rocket of Arianespace2. ESA’s Herschel observatory was launched on the same rocket. At 13:37:55 UT, Herschel was released from the rocket at an altitude of 1200 km; Planck followed suit at 13:40:25UT. The separation attitudes of both satellites were within 0.1 deg. of prediction. The Ariane rocket placed Planck with excellent accuracy (semimajor axis within 1.6 % of prediction), on a trajectory towards the second Lagrangian point of the Earth-Sun system (L2) . The orbit describes a Lissajous trajectory around L2 with a ~6 month period that avoids crossing the Earth penumbra for at least 4 years.

The Herschel and Planck spacecrafts in the launch vehicle configuration.

After release from the rocket, three large manoeuvres were carried out to place Planck in its intended final orbit. Once in its final orbit, very small manoeuvres are required at approximately monthly intervals (1 ms−1 per year) to keep Planck from drifting away from its intended path around L2. The attitude manoeuvres required to followthe scanning strategy require about 2.6 ms−1 per year. Overall, the excellent performance of launch and orbit manoeuvres will lead to a large amount (~160 kg, or ~40% of initial tank loading) of fuel remaining on board at end of mission operations.

Planck started cooling down radiatively shortly after launch. Heaters were activated to hold the focal plane at 250 K, which was reached around 5 h after launch. The valve opening the exhaust piping of the dilution cooler was activated at 03:30 UT, and the 4He-JT cooler compressors were turned on at low stroke at 05:20 UT. After these essential operations were completed, on the second day after launch, the focal plane temperature was allowed to descend to 170 K for out-gassing and decontamination of the telescope and focal plane.

Commissioning and initial science operations

Commissioning

The Herschel and Planck launch by an Ariane 5 ECA rocket.

The first period of operations focussed on commissioning activities, i.e., functional check-out procedures of all sub-systems and instruments of the Planck spacecraft in preparation for running science operations related to calibration and performance verification of the payload. Planning for commissioning operations was driven by the telescope decontamination period of 2 weeks and the subsequent cryogenic cool-down of the payload and instruments. The overall duration of the cool-down was approximately 2 months, including the decontamination period. The commissioning activities were executed very smoothly and all sub-systems were found to be in good health. The commissioning activities were formally completed at the time when the HFI bolometer stage reached its target temperature of 100 mK, on 3 July 2009 at 01:00 UT. At this time all the critical resource budgets (power, fuel, lifetime, etc.) were found to contain very significant margins with respect to the original specification.

Calibration and performance verification

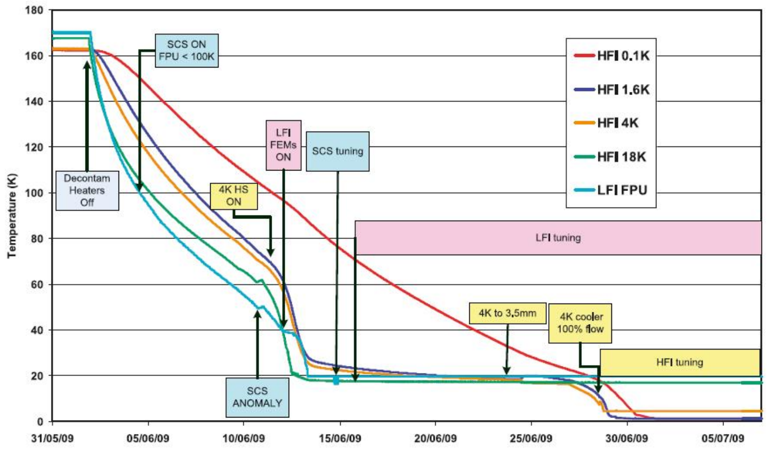

Schematics of the cool-down sequence, from Planck Coll. 2011, A&A 536, A1.

Calibration and performance verification (CPV) activities started during the cool-down period and continued until the end of August 2009. On completion of all the planned activities, it was concluded that the two instruments were fully tuned and ready for routine operations. No further parameter tuning was expected to be needed, except for the sorption cooler, which requires a weekly change in operational parameters. The scientific performance parameters of both instruments was in most respects as had been measured on the ground before launch. The only significant exception was that, due to the high level of Galactic cosmic rays, the bolometers of HFI were detecting a higher number of glitches than expected, causing a modest (~10%) level of systematic effects on their noise properties. The satellite did not introduce any major systematic effects into the science data. In particular, the telemetry transponder did not result in radio-frequency interference, which implies that the data acquired during visibility periods is useable for science.

First-Light Survey

The First Light Survey (FLS) was the last major activity planned before the start of routine surveying of the sky. It was conceived as a two-week period during which Planck would be fully tuned up and operated as if it was in its routine phase. This stable period could have resulted in the identification of further tuning activities required to optimise the performance of Planck in the long-duration surveys to come. The FLS was conducted between 13 and 27 August, and in fact led to the conclusion that the Planck payload was operating stably and optimally, and required no further tuning of its instruments. Therefore the period of the FLS was accepted as a valid part of the first Planck survey.

Routine operations phase

The routine operations phase of Planck is characterised by continuous and stable scanning of the sky and data acquisition by LFI and HFI. It started with the FLS on 13 August of 2009, at 14:15 UT.

The Planck satellite generates (and stores on-board) data continuously at the following typical rates: 21 kilobit s−1 (kbps) of house-keeping (HK) data from all on-board sources, 44 kbps of LFI science data and 72 kbps of HFI science data. The data are brought to ground in a daily pass of approximately 3 h duration. Besides the data downloads, the passes also acquire realtime HK and a 20 min period of real-time science (used to monitor instrument performance during the pass). Planck utilises the two ESA deep-space ground stations in New Norcia (Australia) and Cebreros (Spain), usually the former. Scheduling of the daily telecommunication period is quite stable, with small perturbations due to the need to coordinate the use of the antenna with other ESA satellites (in particular Herschel). At the ground station the telemetry is received by redundant chains of front-end/back-end equipment. The data flows to the mission operations control centre (MOC) located at ESOC in Darmstadt (Germany), where it is processed by redundant mission control software (MCS) installations and made available to the science ground segment. To reduce bandwidth requirements between the station and ESOC only one set of science telemetry is usually transferred. Software is run post-pass to check the completeness of the data. This software check is also used to build a catalogue of data completeness, which is used by the science ground segment to control its own data transfer process. Where gaps are detected, attempts to fill them are made as an offline activity (normally next working day), the first step being to attempt to reflow the relevant data from station. Early in the mission these gaps were more frequent, with some hundreds of packets affected per week (impact on data return of order 50 ppm) due principally to a combination of software problems with the data ingestion and distribution in the MCS, and imperfect behaviour of the software gap check. Software updates implemented during the mission have improved the situation such that gaps are much rarer, with a total impact on data return well below 1 ppm. Redump of data from the spacecraft is attempted when there have been losses in the space link. This has only been necessary on three occasions. In each case the spacecraft redump has successfully recovered all the data.

All the data downloaded from the satellite, and processed products such as filtered attitude information, are made available each day for retrieval from the MOC by the LFI and HFI Data Processing Centres (DPCs).

The scanning strategy is the following: the spin axis follows a cycloidal path on the sky by step-wise displacements of 2 arcmin approximately every 50 min. The dwell time (i.e., the duration of stable data acquisition at each pointing) has varied sinusoidally by a factor of ~2. Planck's scanning strategy results in significantly inhomogeneous depth of integration time across the sky; the areas near the ecliptic poles are observed with greater depth than all others.

The scanning strategy for the second year of Routine Operations (i.e., Surveys 3 and 4) is exactly the same as for the first year, except that all pointings are shifted by 1 arcmin along the cross-scanning direction, in order to provide finer sky sampling for the highest frequency detectors when combining two years of observations.

Orbit maintenance manoeuvres were carried out at approximately monthly intervals6. Although the manoeuvres only required a few minutes, preparations, post-manoeuvre massproperty calibration, and re-entry into scientific slewing mode increased the overhead to several hours. The manoeuvres were carried out without disturbing the path of the spin axis from its nominal scanning law. The dwell times of pointings before and after the execution of the manoeuvre were reduced to allow all pre-planned pointings to be carried out.

While the Planck detectors are scanning the sky, they also naturally observe celestial calibrators. The main objects used for this purpose are the Crab Nebula, and the bright planets Mars, Jupiter and Saturn.

Payload performance

The main achievements in terms of payload performance are the following:

- the angular resolution measured on planets is within a few per cent of that predicted on the ground
- the instantaneous sensitivity of the Planck LFI and HFI channels is estimated to be approximately 10% larger than that measured on the ground and extrapolated to launch conditions
- the photometric calibration uncertainty quoted is conservatively based on the current knowledge of systematic effects and data processing pipelines. There is no reason to believe that the mission goals (1% in CMB channels and 3% at the highest frequencies) will not be reached for all Planck channels in due time.

For more information

A complete overview of the Planck mission and its science programme can be found in the so-called Blue Book : http://www.sciops.esa.int/SA/PLANCK/docs/Bluebook-ESA-SCI%282005%291_V2.pdf

More details on the Planck mission performance can be found in #planck2011-1-1, Planck early paper I [1].

A complete list of Planck publications can be found here [2].

References

<biblio force=false>

1. References

</biblio>

References

[1] http://www.rssd.esa.int/doc_fetch.php?id=3135854&page=1
[2] http://www.sciops.esa.int/index.php?project=PLANCK&page=Planck_Published_Papers

The satellite

The satellite

Overview

The Planck satellite was designed, built and tested around two major modules:

- **The payload module** containing an off-axis telescope with a projected diameter of 1.5m, focussing radiation from the sky onto a focal plane shared by detectors of the LFI and HFI, operating at 20K and 0.1K respectively; a telescope baffle that simultaneously provides stray-light shielding and radiative cooling; and three conical “V-groove” baffles that provide thermal and radiative insulation between the warm service module and the cold telescope and instruments.
- **The service module** containing all the warm electronics servicing instruments and satellite; and the solar panel providing electrical power. It also contains the cryocoolers, the main on-board computer, the telecommand receivers and telemetry transmitters, and the attitude control system with its sensors and actuators. The most relevant technical characteristics of the Planck spacecraft are detailed in the Table bellow.

Table. Planck satellite characteristics.

Diameter	4.2 m	Defined by the solar array
Height	4.2 m	
Total mass at launch	1912 kg	Fuel mass = 385 kg at launch; He mass = 7.7 kg
Electrical power demand (avg)	1300 W	Instrument part: 685 W (Begining of Life), 780 W (End of Life)
Minimum operational lifetime	18 months	Planck operated for 32 months with both instruments; the LFI continues surveying the sky
Spin rate	1 rpm	± 0.6 arcmin/sec (changes due to manoeuvers); stability during inertial pointing $\sim 6.5 \times 10^{-5}$rpm/h
Max angle of spin axis to Sun	10 deg	To maintain the payload in the shade; default angle is 7.5 deg
Max angle of spin axis to Earth	15 deg	To allow communication to Earth
Angle between spin axis and telescope boresight	85 deg	Max extent of FOV~ 8 deg
On-board data storage capacity	32 Gbit	Two redundant units (only one is operational at any time)
Data transmission rate to ground (max)	1.5 Mbps	Within 15 deg of Earth, using a 35 m ground antenna
Daily contact period	3 h	The effective real-time science data acquisition bandwidth is 130 kbps

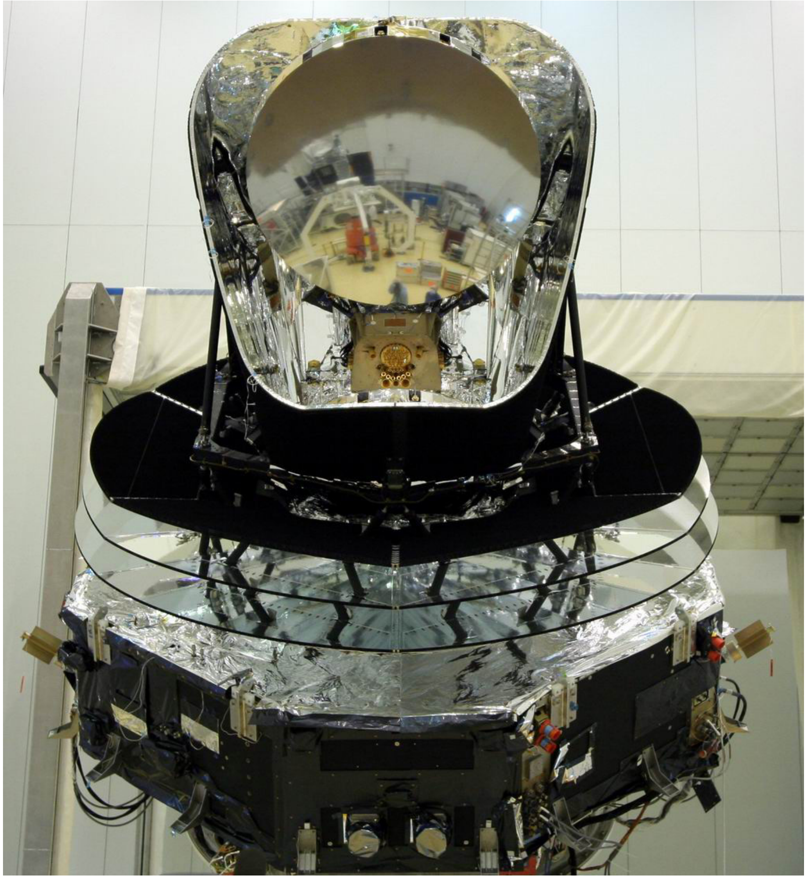

The fully assembled Planck satellite a few days before integration into the Ariane 5 rocket. Herschel is visible by reflection on the primary reflector.

For more information, see #planck2011-1-1.

The service module

The service module provides the various equipment and instruments housed in it with suitable mechanical and thermal environments during launch and orbit. It is formed by an octagonal box, built around a conical tube, which supports the following subsystems intervening in flight operations:

- Command and data management.
- Attitude control and measurement.
- Power control.
- Reaction control.
- Telemetry, tracking and command.
- Thermal control.

The service module contains all the warm satellite and payload electronic units, with the only exception of the box containing JFETs for impedance-matching to the HFI bolometers, which is mounted on the primary reflector support panel, to allow the operation of the JFETs at an optimal temperature of ~130 K. The service module holds:

- Main computer
- Attitude control computer
- Data processing units
- Star trackers
- LFI electronics
- Dilution control unit

- HFI readout electronics
- 4K compressors
- Helium tanks: 36000 litres of ^{4}He, and 12000 litres of ^{3}He gas are stored in four high-pressure tanks.
- Sorption cooler radiator
- Sorption cooler electronics
- Sorption compressors (2 redundant units)
- Hydrazine tanks
- Medium-gain antenna
- Telemetry subsystem.

For more information, see #tauber2010a.

Thermal design

The performance of the Planck instruments in space is enabled by their low operating temperatures, 20 K for LFI and 0.1 K for HFI, achieved through a combination of passive radiative cooling and three active coolers. The scientific requirement for very broad frequency coverage led to two detector technologies with widely different temperature and cooling needs. Active coolers could satisfy these needs; a helium cryostat, as used by previous cryogenic space missions (IRAS, COBE, ISO, Spitzer, AKARI), could not. Radiative cooling is provided by three V-groove radiators and a large telescope baffle. The active coolers are a hydrogen sorption cooler (<20 K), a ^{4}He Joule-Thomson cooler (4.7 K), and a ^{3}He- ^{4}He dilution cooler (1.4 K and 0.1 K). The flight system was at ambient temperature at launch and cooled in space to operating conditions. The HFI bolometer plate reached 93 mK on 3 July 2009, 50 days after launch. The solar panel always faces the Sun, shadowing the rest of Planck, and operates at a mean temperature of 384 K. At the other end of the spacecraft, the telescope baffle operates at 42.3 K and the telescope primary mirror operates at 35.9 K. The temperatures of key parts of the instruments are stabilized by both active and passive methods. Temperature fluctuations are driven by changes in the distance from the Sun, sorption cooler cycling and fluctuations in gas-liquid flow, and fluctuations in cosmic ray flux on the dilution and bolometer plates. These fluctuations do not compromise the science data.

The contrast between the high power dissipation in the warm service module ($\sim$1000 W at 300 K) and that at the coldest spot in the satellite ($\sim$100 nW at 0.1 K) are testimony to the extraordinary efficiency of the complex thermal system which has to achieve such disparate ends simultaneously while preserving a very high level of stability at the cold end. More details on the thermal design of the Planck satellite can be found in the Planck early paper II [1].

The Standard Radiation Environment Monitor

The standard radiation environment monitor (SREM)#SREM is a particle detector developed for satellite applications. It measures high-energy electrons and protons of the space environment with a $\pm 20\,^{\circ}$angular resolution, spectral information and provides the host spacecraft with radiation information. SREM was developed and manufactured by Contraves Space in cooperation with Paul Scherrer Institute under a development contract of the European Space Agency. SREM is the second generation of instruments in a programme, which was established by ESA's European Research and Technology Centre (ESTEC) to:

1. Provide minimum intrusive radiation detectors for space applications;
2. Provide radiation hazard alarm function to instruments on board spacecraft;
3. Assist in investigation activities related to possible radiation related anomalies observed on spacecraft;
4. Assist in in-flight Technology Demonstration Activities.

The design goals are low weight, small dimensions, low power consumption, combined with the ability to provide particle species and spectral information.

In the case of Planck, the use of the SREM was entirely within the scope of bullets 1 and 3 above as due to the nature of operations no real time alarms where possible

The SREM consists of three detectors (D1, D2, and D3) in two detector heads configurations. One system is a single silicon diode detector (D3). The main entrance window is covered with 0.7 mm aluminum, which defines the lower energy threshold for electrons to ∼0.5 MeV and for protons to ∼10MeV. The other system uses two silicon diodes (detectors D1/D2) arranged in a telescope configuration. The main entrance of this detector is covered with 2 mm aluminum giving a proton and electron threshold of 20 and 1.5 MeV, respectively.A 1.7-mm-thick aluminum and 0.7–mm-thick tantalum layer separate the two diodes of the telescope configuration.

The telescope detector allows measurement of the high-energy proton fluxes with enhanced energy resolution. In addition, the shielding between the two diodes in the telescope prevents the passage of electrons. However, protons with energies greater than ∼30 MeV go through. Thus, using the two diodes in coincidence gives pure proton count rates allowing subtraction of the proton contribution from the electron channels. A total of 15 discriminator levels (see table below) are available to bin the energy of the detected events.

SREM counters

Name	Logic	Particle	Energy (Mev)
TC1	D1	protons	>20
S12	D1	protons	20 - 550
S13	D1	protons	20 - 120
S14	D1	protons	20 - 27
S15	D1	protons	20 - 34
TC2	D2	protons	>39
S25	D2	ions	150 - 185
C1	D1 *D2	coinc. protons	40 - 50
C2	D1 *D2	coinc. protons	50 - 70
C3	D1 *D2	coinc. protons	70 - 120
C4	D1 *D2	coinc. protons	>130
TC3	D3	electrons	>0.5
S32	D3	electrons	0.55 - 2.3
S33	D3	protons	11 - 90
S34	D3	protons	11 - 30
PL1	D1	Dead Time	NA
PL2	D2	Dead Time	NA
PL3	D3	Dead Time	NA

Any two of the levels can be used to raise an alarm flag when the count rates exceed a programmable threshold. This alarm signal can then be used to control the operation of the spacecraft and its instruments. The detector electronics is capable of processing a detection rate of 100 kHz with dead-time correction below 20%. The SREM is contained in a single box of 20 × 12 × 10 and weighs 2.6 kg. The box contains the detector systems with the analog and digital front-end electronics, a power supply, and a TTC-B-01 telemetry and Telecommand interface protocol. By virtue of a modular buildup, the interface can be adapted to any spacecraft system. The power consumption is approximately 2.5 W. An essential input for the interpretation of the detection rates, in terms of particle fluxes, are the energy dependent

The SREM data are provided in the Planck Legacy Archive in the form of individual FITS files per calendar day. The SREM data is described here

The Fiber Optic Gyro unit

The Fiber-Optic Gyro unit (FOG) is an extra payload on-board Planck which is not used as part of the attitude control system. The FOG functioning is based on the physical phenomenon called *Sagnac effect*::

"*a solid-state optical interferometer enclosing a surface located on a rotating support will detect a phase difference of the optical signal, which is proportional to the angular rate and to the surface enclosed by the optical path*".

The FOG features the following architecture:

- An optical path enclosing a maximal surface: this is realized through the 1 km long fibre optic, winded many time round, in order to make a reasonable sized interferometer (< 120 mm in diameter).
- A source, to deliver the light to the interferometer.
- A multifunction Integrated Optical Circuit, which closes the interferometer, to share the light between the two extremities of the fiber optic coil, to filter undesirable polarization.
- A coupler to extract the optical signal coming back from the ring interferometer, which is the signal carrying the Sagnac inertial information, and to direct it towards an optical detector.
- A detection module to convert this light signal into an electrical signal.
- A closed-loop signal processing to increase the dynamic range and remove the effect of fluctuations of the optical power and of the gain of the detection chain, allowing an easy auto-calibration of the system and excellent scale factor stability and linearity.
- A biasing modulation allowing the measurement of very low rotation rates as well as the sign of those rotations.

Redundancy is offered by providing four skewed gyro channels, allowing the Attitude Control and Measurement Subsystem to use any triplet among the four axes to determine the spacecraft three axes rates. Nominally the four channels are activated, in case of failure or thermal criticalities a subset of channels could be used.

There is no dangerous FOG flight command. The FOG is designed to operate five years ON in orbit, withstanding 1000 ON/OFF cycles, and its performance is guaranteed under rotations of ± 10deg/second, and at the temperature range of 253 K up to 333 K. Power dissipations are in the range of 5.5 up to 6.7 W/channel.

The telescope

The telescope is an off-axis aplanatic design with two elliptical reflectors and a 1.5 m projected diameter and an overall emissivity $\lesssim 1\%$. The optical system was optimized for a set of representative detectors (eight HFI and eight LFI). The performance of the aplanatic configuration is not quite as good on the optical axis as the so-called Dragone-Mizuguchi Gregorian configuration, which eliminates astigmatism on the optical axis, but is significantly better over the large focal surface required by the many HFI and LFI feeds.

The Planck telescope consists of:

1. **The primary and secondary reflectors** (PR and SR), designed and manufactured by Astrium (Friedrichshafen, Germany);

2. **The support structure**, designed and manufactured by Oerlikon Space (Zurich, Switzerland).

For more information, see #tauber2010b.

The instruments

A complete technical description of the teo Planck instruments can be found here: HFI, LFI.

References

<biblio force=false>

1. References

</biblio>

References

[1] http://www.rssd.esa.int/doc_fetch.php?id=3135855&page=1

HFI design, qualification and performance

HFI design, qualification, and performance

This section is intended to provide an overview of the instrument and of its different sub-systems. Two papers that include and detail this information are available: #lamarre2010 Planck pre-launch paper 9 [1] and #planck2011-1-5 Planck early paper IV [2]. Additional detailed information potentially useful for the use of the HFI data is included into this section or annexed to it.

The HFI instrument is designed around 52 bolometers. Twenty of the bolometers (spider-web bolometers or SWBs) are sensitive to total power, and the remaining 32 units are arranged in pairs of orthogonally-oriented polarisation-sensitive bolometers (PSBs). All bolometers are operated at a temperature of ~0.1 K by mean of a space qualified dilution cooler coupled with a high precision temperature control system. A 4He-JT provides an active cooling for 4 K stages using vibration controlled mechanical compressors to prevent excessive warming of the 100 mK stage and minimize microphonic effects in the bolometers. Bolometers and sensitive thermometers are read using AC-bias scheme through JFET amplifiers operated at ~130 K that provide high sensitivity and low frequency stability. The HFI covers six bands centered at 100, 143, 217, 353, 545 and 857 GHz, thanks to a thermo-optical design consisting of three corrugated horns and a set of compact reflective filters and lenses at cryogenic temperatures.

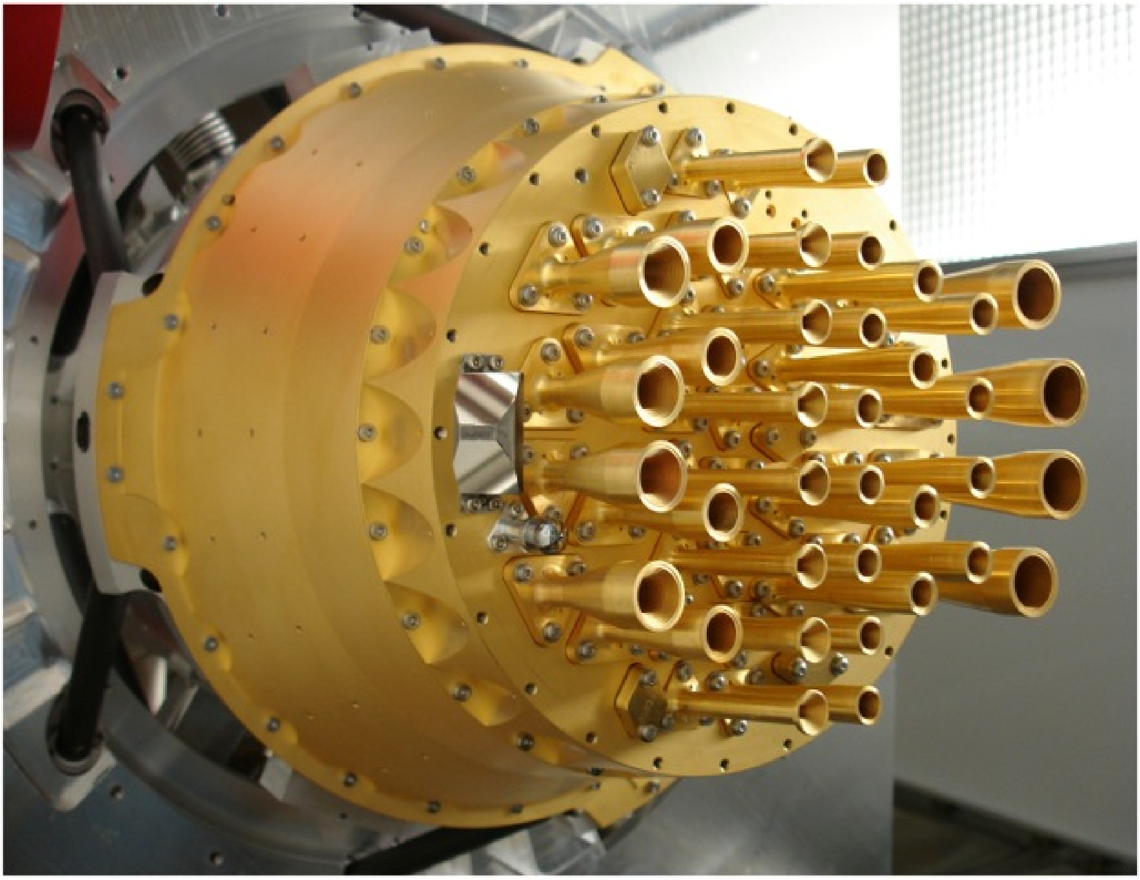

The HFI focal plane optics and 4K thermo-mechanical stage

The whole satellite is organized to provide thermal transitions between its warm part exposed to the sun and earth radiation, and the focal plane instruments that include the cold receivers (Sections HFI_cold_optics and HFI_detection_chain). The various parts of the HFI are distributed among three different stages of the satellite in order to provide each sub-system an optimal operating temperature. The "warm" parts, including nearly all the electronics and the sources of fluids of the 4K and 0.1K coolers, are attached and thermally linked to the service module of the satellite. The first stage of the preamplifiers is attached to the back of the passively cooled telescope structure. The focal plane unit is attached to the 20K stage cooled by the sorption cooler. This is detailed in Section HFI_detection_chain.

The telescope and horns select the geometrical origin of photons. They provide a high transmission efficiency to photons inside the main beam, while photons coming from the intermediate and far-side lobes have very low probability of being detected. This essential characteristics is known by a complex process mixing ground measurements of components (horns, reflectors), modeling the shape of the far side lobes, and measuring in-flight bright sources, especially planets.

The filters and bolometers define the spectral responses and absolute optical efficiency, that are known mostly from ground based measurements performed at component, sub-system and system levels reported in this document. The relations between spectral response and geometrical response are also addressed.

Photons absorbed by a bolometer include the thermal radiation emitted by the various optical devices: telescope, horns and filters. They are transformed in heat that propagates to the bolometer thermometer and influence its temperature which is itself measured by the readout electronics. Temperatures of all these items must be stable enough not to contaminate the scientific signal delivered by the bolometers. How this stability is reached is described in Section HFI_cryogenics.

The bolometer temperature depends also on the temperature of the bolometer plate, on the intensity of the biasing current and on any spurious inputs, such as cosmic rays and mechanical vibrations. Such systematics are included in a list discussed in Section HFI-Validation.

Since the bolometer thermometer is part of an active circuitry that also heats it, the response of this system is complex and has to be considered as a whole. In addition, due to the modulation of the bias current and to the sampling of the data, the response signal of the instrument when scanning a point source is still more complex. Item in Sub-Section Time_response and Annex HFI_time_response_model dedicated to the description of this time response.

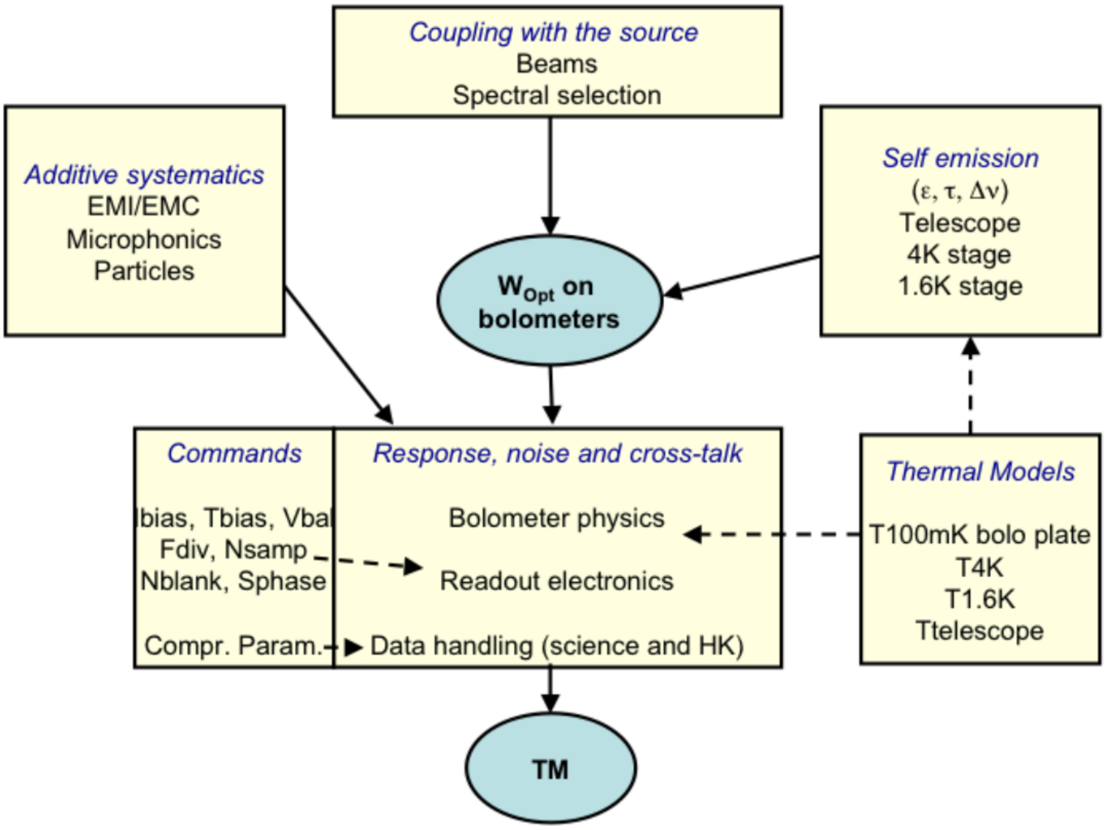
Coupling with the source
Beams
Spectral selection
Additive systematics
EMI/EMC
Microphonics
Particles
W$_{Opt}$ on bolometers
Self emission
(ε, τ, Δν)
Telescope
4K stage
1.6K stage
Commands
Ibias, Tbias, Vbal
Fdiv, Nsamp
Nblank, Sphase
Compr. Param.
Response, noise and cross-talk
Bolometer physics
Readout electronics
Data handling (science and HK)
Thermal Models
T100mK bolo plate
T4K
T1.6K
Ttelescope
TM

HFI signal formation

Logic of the formation of the signal in HFI. This is an idealized description of the physics that takes place in the instrument. The optical power that is absorbed by the bolometers comes from the observed sky and from the instrument itself. The bolometers and readout electronics, acting as a single and complex chain, transform this optical power in data that is compressed and transmitted for science data reduction.

References

<biblio force=false>

1. References
2. References2

</biblio>

References

[1] http://www.rssd.esa.int/doc_fetch.php?id=3135954&page=1
[2] http://www.rssd.esa.int/doc_fetch.php?id=3135857&page=1

HFI cryogenics

The dilution cooler

The HFI dilution cooler cools the bolometers down to 0.1 K through the dilution of ^{3}He into ^{4}He and the intermediate optical plate to 1.4 K through Joule-Thomson expansion of the ^{3}He and ^{4}He mixture. Two stages of PID regulation are included on the 0.1K stage. The first one (PID1) is at the dilution cold end itself and provides stability on long timescales. When no thermal perturbation is applied to the bolometer plate, the PID1 alone provides the required stability. A passive thermal filter is mounted between the dilution cold end and the bolometer optical plate. It gives a thermal time constant of several hours between these stages. A second regulation system (PID2) is on the bolometer plate, with a similar time constant. The dilution cooler is described in detail in section 2.3.3 of #planck2011-1-3 Planck early paper II [1].

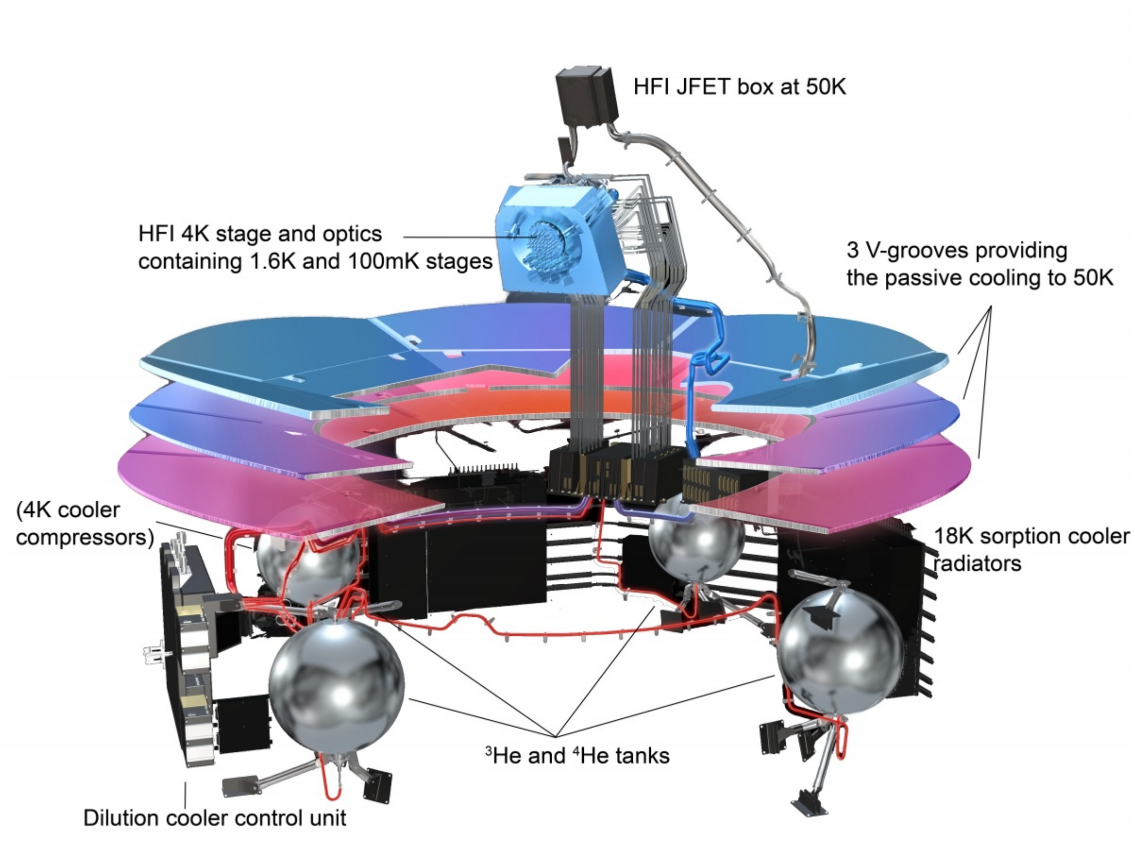
HFI JFET box at 50K
HFI 4K stage and optics containing 1.6K and 100mK stages
3 V-grooves providing the passive cooling to 50K
(4K cooler compressors)
18K sorption cooler radiators
³He and ⁴He tanks
Dilution cooler control unit

Thermal architecture of Planck/HFI

The dilution was operated with flows set to the minimum available values, providing a total lifetime of 30.5 months exceeding the nominal lifetime of 16 months by 14.5 months. The dilution stage was stabilized by the PID1 at a temperature close to 101 mK using 20 to 30 nW of power. The bolometer plate was stabilized by the PID2 at 102.8 mK with about 5 nW. The cooling power values were in very good agreement with those obtained during the ground tests and calibration.

However, the cosmic particles interactions with the 0.1K stage induced both temperature fluctuations of the 0.1K plates and glitches on the thermometer measurements.

At very low frequency, below 1 mHz, the temperature fluctuations are very well correlated with the hit rate of high energy particles, as measured by the on-board Standard Radiation Environment Monitor (SREM). At frequencies in the 10 mHz to 1 Hz range, single events inducing a global or partial temperature change of the bolometer plate are observed. Decorrelation of the bolometer signal from the thermal fluctuations is described in the TOI processing section.

The 1.4K stage is very stable and given the very low coupling coefficients between the 1.4K optical components and the detectors no effect can be measured on the signal. Detailed thermal analysis of the in-flight stability of the dilution cooler can be found in section 5.4 of #planck2011-1-3 Planck early paper II [2].

The 4K J-T cooler

The HFI 4K Joule-Thomson (J-T) cooler produces a temperature of 4K for the HFI 4K stage and optics and the precooling of the dilution gases. Full description of the 4K cooler can be found in section 2.3.2 of #planck2011-1-3 Planck early paper II [1].

The two mechanical compressors produce micro-vibrations and also induce electromagnetic interference affecting the science signals of bolometers. The risks associated with these effects were taken into account early in the design of the HFI by phase-locking the sample frequency of the data to a harmonic of the compressor frequency. The removal of these interferences is addressed in the 4K cooler lines variability section.

Operation of the 4K J-T cooler was flawless during the whole mission, but for an unexpected shutdown during the CPV on August 6th 2009, caused by an SEU on the precharge regulator. It never occured again, and the 4K J-T cooler was then operated without interruption during all the survey phase of the mission. It is still in operation as it also provides the cooling of the optical reference loads of the LFI.

The 4K J-T cooler compressor amplitude was set to 3450 micrometers during the CPV, and was maintained to this value during all the mission. Its cooling power is very stable and gives enough margin to cancel out the fluctuations and drifts induced by the sorption cooler fluctuations and adjustments. The PID stabilizing the temperature of the HFI optics is regulated at 4.81K using a power around 1.8mW.

Details on the in-flight performance of the 4K J-T cooler can be found in in section 5.3 of #planck2011-1-3 Planck early paper II [3].

References

<biblio force=false>

1. References
2. References2

</biblio>

References

[1] http://www.rssd.esa.int/doc_fetch.php?id=3135855&page=7
[2] http://www.rssd.esa.int/doc_fetch.php?id=3135855&page=23
[3] http://www.rssd.esa.int/doc_fetch.php?id=3135855&page=21

HFI cold optics

Horns, lenses and filters

The cold optics is described in #ade2010 Planck pre-launch paper 11 [1].

In order to meet with straylight, beam shapes and filtering requirements, a design using feedhorn coupled detectors has been chosen, with a triple horn configuration (see figure below). A detailed description of the HFI optical design and beam performances is given in #maffei2010 Planck pre-launch paper 12 [2].

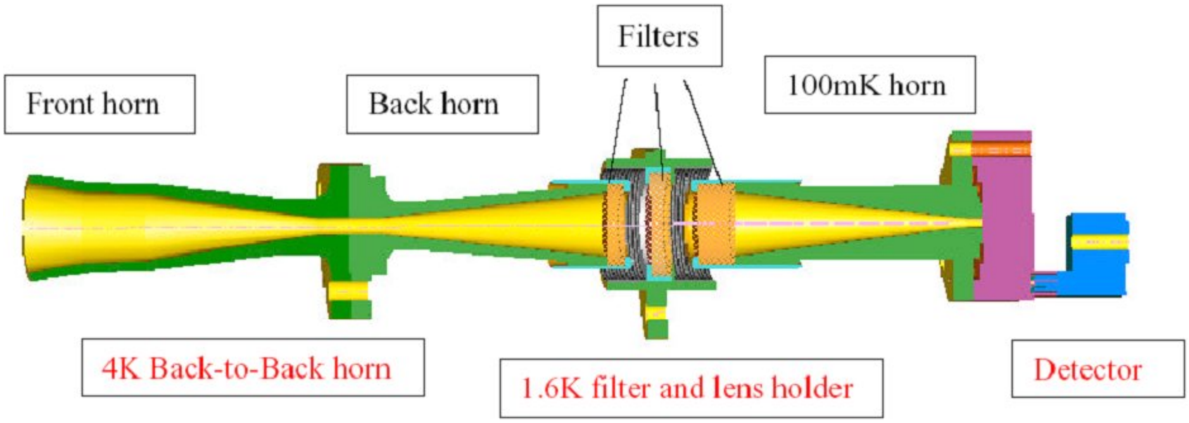

Optics of the HFI focal plane unit. The back-to-back horn (front and back horns) is coupling the incoming radiation from the telescope to a detector horn which is then coupling the radiation to the bolometer. The filters determining the spectral bands are located in between the two horn assemblies. A lens is refocussing the radiation from the back horn to the detector.

Horn design and patterns

The cosmological channels (100 GHz, 143 GHz, 217 GHz, 353 GHz) have been designed to detect a single mode mode with one or two polarizations, for Polarization Sensitive Bolometers or Spider Web Bolometers respectively. The spectral and geometrical properties of the horns have been characterized individually. A typical example for a single-moded horn is given in the figure below.

The fit is excellent down to very low levels, which validates, at least for single-moded horns, the logics that prevailed for ctheir development: Modelling and optimizing the horns before implementation and then validating the model with a complete measurement of the beam intensity patterns. For the single-moded horns, a method has been developed to use the measured intensities, together with the phase information from modeling to derive “worst-case” horn beam patterns that can be used in GRASP simulations of the telescope beams (phase information is mandatory). Worst-case beam patterns have been computed for all single-moded HFI horn types in order to estimate an upper limit of the spill over. As an example, in the figure below, we show the difference in encircled powers at isolevel intervals for the HFI 143_1a channel main beam using both the model and worst-case horns.

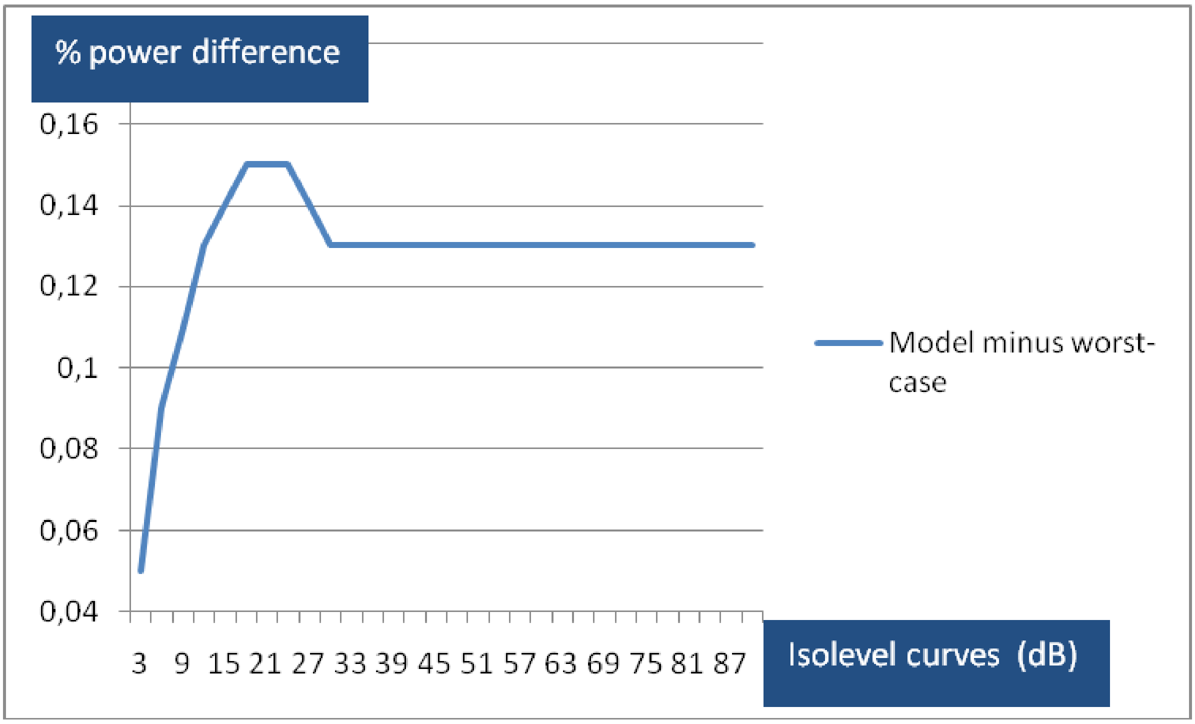

Difference in power encircled within 3 dB curves from peak value. Main beam encloses at least 99.5 % (model) and 99.4% (worst-case) of power.

In the high frequency 545 GHz and 857 GHz Planck pixels both the back-to-back (BTB) horns and the detector horn have overmoded waveguide filters (“Shaped Corrugated horns for Cosmic Microwave Background Anisotropy Measurements” B. Maffei, P.A.R. Ade, C.E. Tucker, E. Wakui, R.J. Wylde, J.A. Murphy, R.M. Colgan, Int Jour Infrared & Millimeter waves, 21, (12) 2023-2033, December 2000). The far-field patterns of the horns (which illuminate the Planck mirrors) have been simulated and are shown in the two figures below for a few spot frequencies across the 857 GHz band. Note that the edge taper is approx -30 dB at 25 degrees as required at the centre of the band. Superimposed is the broadband measurement which clearly looks narrower than the majority of the spot frequency measurements and requires explanation. The measured far field beam patterns across the band are narrower than the predicted far field beams right across the band. The simulated beams are too wide suggesting missing higher order modes, either due to attenuation between the cavity and the BTB, or to the experimental setup.

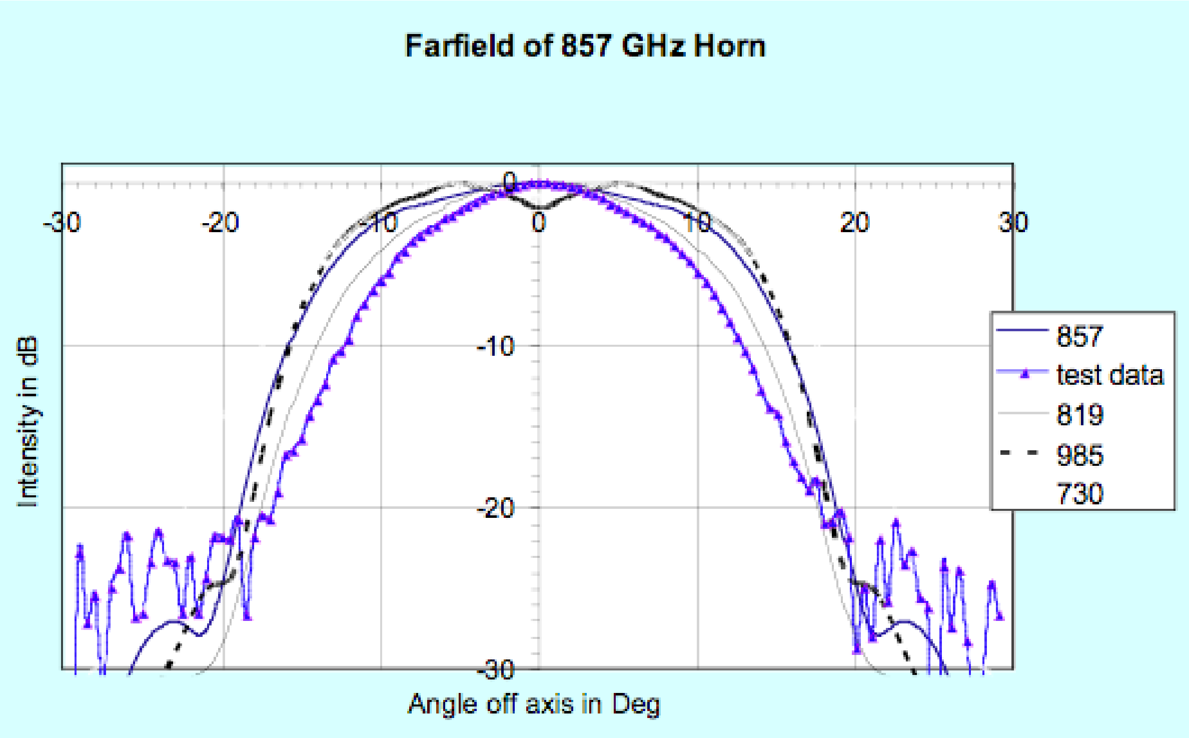

Model / Measurement comparison for the Far field pattern of the 857 GHz_Horn ; model at spot frequencies, superimposed with the broadband test data.

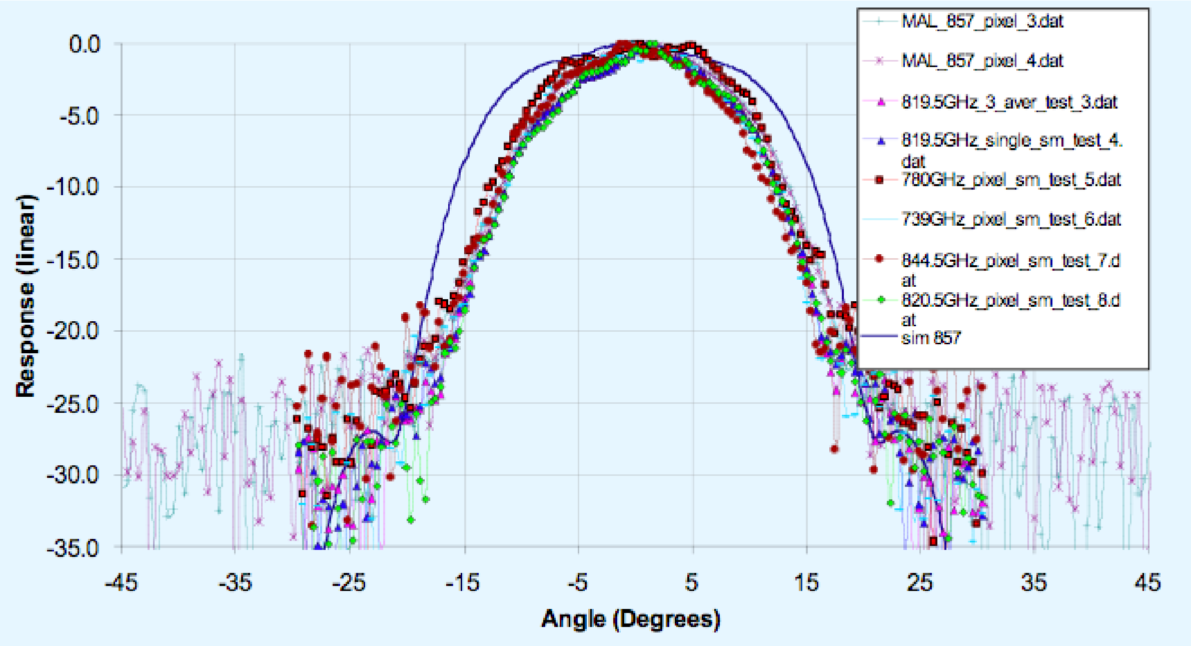

Model / Measurement comparison for the Far field pattern of the 857 GHz_Horn ; measurements for broadband and spot frequencies with the BTB horn both outside and inside the test dewar window (the inside case being more representative of the true Planck pixel).

Spectral response

The measurement of the spectral response of HFI is fully described in #planck2013-p03d Planck-2013-IX [3]. The experimental setup, data collection, and related data processing are described. The official version of the HFI detector spectral transmission profiles is available within the HFI instrument model and the RIMO files in the Planck Legacy archive. This data is comprised of broadband Fourier transform spectrometer (FTS) measurements conducted with the HFI focal plane assembly in a ground-based test cryostat, and includes a waveguide model for the low frequency spectral region, and component-level filter spectra for the remaining out of band spectral regions. Specific attention is given to in-band and near-band spectral regions surrounding CO rotational transitions in order to support the CO extraction component separation effort #planck2013-p03a,#planck2013-p06. The spectral transmission profiles are evaluated with parameters such as cut-on, cut-off, centre frequency, effective frequency (including spectral index), and band-width, all provided in this analysis. Further evaluation yields band-average spectra and unit conversion / colour correction coefficients ,#planck2013-p03d and software routines to generate additional unit conversion and colour correction coefficients (i.e., the Unit conversion and Color correction (UcCC) routines).

The main goal of the spectral transmission tests of the HFI instrument is to measure the spectral response of all HFI detectors to a known source of EM radiation individually. This was determined by measuring the interferometric output of all detection channels for radiation propagated through a continuously scanned polarising Fourier transform spectrometer (FTS). The required accuracy to which the spectral transmission is to be recovered is 1 $\%$. It is important to note that the absolute spectral calibration cannot be achieved solely from the analysis of the FTS data because of uncertainties in the coupling efficiency of the FTS source through the FTS, input optics, and integrating sphere. The relative FTS measurements must be combined with the optical efficiency tests which used internal black-body sources (see section HFI_optical_efficiency). A reference bolometer located in an intermediate integrating sphere (accepting 2πsr of incident radiation) within the FTS test setup was used to ratio the HFI detector spectra against to determine the throughput-normalized relative transmission spectra for each HFI detector. Data were collected over a series of pre-flight test campaigns, and processed/analyzed using standard Fourier data processing techniques.

Additional experiments

Two significant additional tests were used in the derivation of the HFI detector spectral transmission profiles beyond the scope of the integrated HFI FTS measurements. Additional filter measurements were recorded at component level during filter stack production. These measurements are used to extend the integrated HFI FTS spectral measurements beyond the HFI spectral passband. The other experiments, herein the EFF tests, are used to obtain optical efficiency parameters for each detector, and thus an estimate of the absolute spectral transmission. These parameters, when combined with the respective normalized spectral transmission profiles, provide an estimate of the absolute spectral transmission. The EFF tests are discussed in greater detail in #Catalano2008Thesis. The filter measurements and the optical efficiency experiments are described below.

Filter measurements

Prior to the integrated HFI measurements with the integrated HFI detectors and filter stacks, FTS measurements of the individual filters comprising the filter stacks for each band were conducted. As will be discussed in #Out-of-band spectral transmission content, the independent measure of the filter stack transmission is used for a portion of the HFI detector spectral transmission for regions of the spectrum where it is deemed to be of better quality than the integrated HFI FTS measurements (i.e. for frequencies outside of the band edge filter cut-off(s)). The filter stacks for each of the frequency bands are comprised of 5 filters. There is an additional low frequency cut-on filter for the 545 and 857 GHz bands as the waveguide cut-on is too low for these multi-moded channels. The figures below show the individual filter transmission measurements as well as the combined filter stack product.

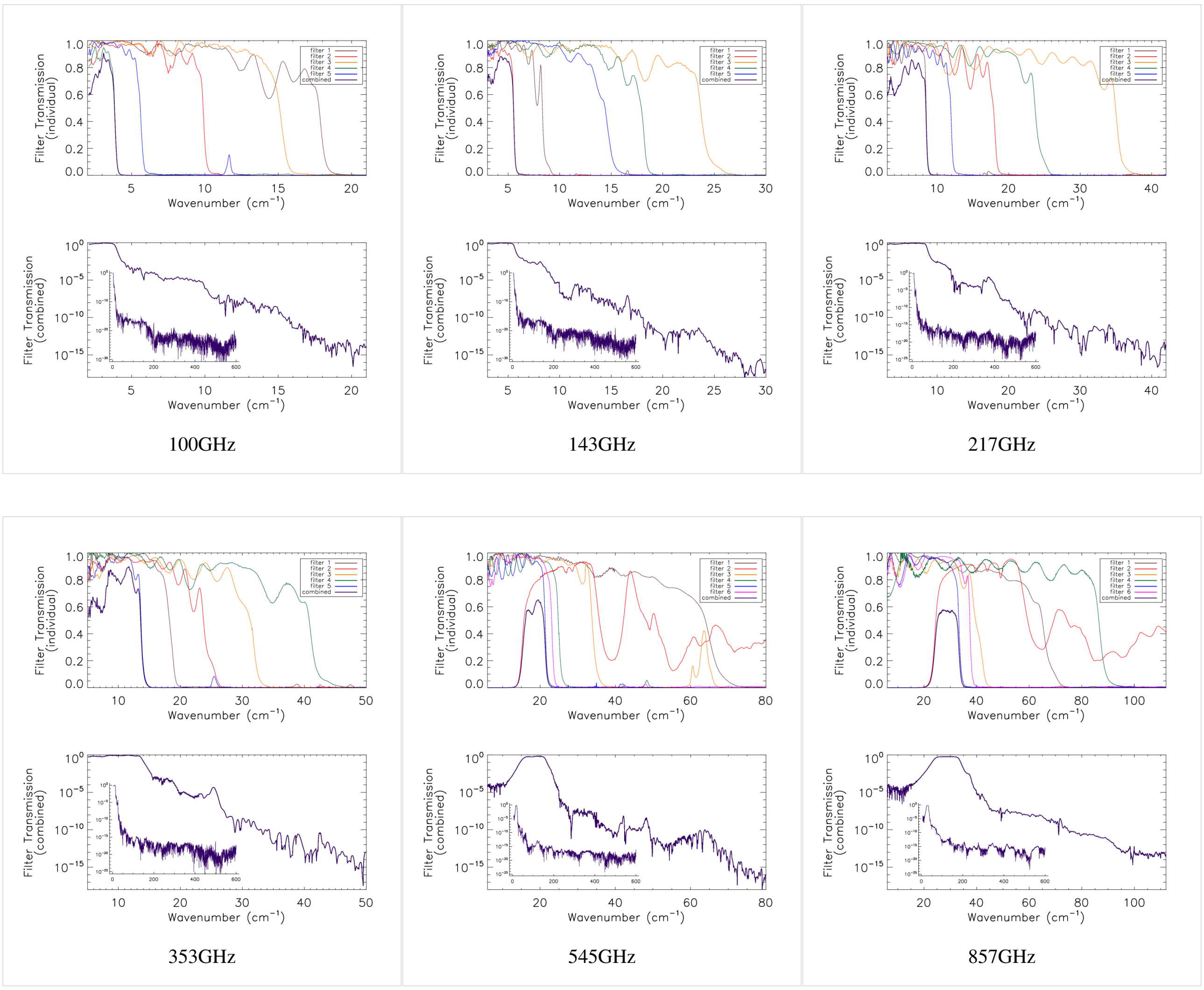

100GHz

143GHz

217GHz

353GHz

545GHz

857GHz

"Combined (bottom) and individual (top) filter transmission measurements for the 5 filters within the HFI band filter stacks (6 for 545 and 857 GHz)."

The uncertainty on the combined filter transmission measurement is determined as follows. Let $f_i(\sigma)$represent the individual filter transmission. The standard deviation of all values of $f_i(\sigma)$below a threshold of $0.001$is used as an approximate uncertainty for each individual filter measurement, i.e. ς_i. The individual uncertainty estimates are combined to provide an estimate of the combined filter transmission spectral uncertainty through standard error propagation. For the combined filter transmission represented as $F(\sigma)$, the associated uncertainty estimate is given as

As described below, the composite filter spectra illustrated above form part of the official HFI detector spectral response, specifically for a portion of the out-of-band spectral region. The band-average spectra, containing this data as a constituent, is provided in the RIMO files (see here). The RIMO files will also include the detector level spectra for future Planck data releases.

Optical efficiency

The optical efficiency tests, hereafter the EFF tests, were conducted to allow an estimate of the overall optical efficiency of the HFI detectors. These tests involved exposing the HFI detectors to a known blackbody source and observing the response, and comparing this to a theoretical model in combination with the detector spectral response data. The optical efficiency parameter derived for each detector is meant as a multiplicative factor to be combined with the normalized transmission spectra (spectra whose maxima are set to one). This product is an estimate of the absolute spectral transmission of a given HFI detector. The detector optical efficiency parameters are included within the header of the detector spectra in the RIMO files (here).

Further details regarding the derivation of the optical efficiencies are provided here.

Data processing and Fourier transformation

Having identified the data sections that are of interest, here follows the data processing sequence used to obtain the resulting spectra. The processing steps taken are as follows:

1. Selection and extraction of time sampled data sets
2. Conversion of time sampled data to arrays of Optical Path Difference (OPD) sampled interferogram data sets
3. Fourier transformation and averaging of interferogram data sets
4. Discrimination of poor quality spectra by standard deviation comparison (see HFI_spectral_response_data_processing)
5. Division of detector spectra by reference bolometer spectra to obtain normalized spectral transmission profiles
6. Combination of relative transmission spectra with filter measurements and waveguide models
7. Determination of optical efficiency through evaluation of normalized spectral transmission in the context of the EFF experiments
8. Addition of over-sampled data into spectrum for the CO transition regions (see HFI_CO_response)
9. Identification of common frequency sampling per channel and interpolation of spectra onto the common sampling

Further details regarding the interferogram processing are provided here.

Reference bolometer spectra

The reference bolometer is assumed to be spectrally flat across each HFI band to within 1%. Its spectra are obtained in a fashion similar to that used for the HFI detectors. Wherever possible, the same data processing is applied to the reference bolometer data as was applied to the HFI detector data, including optical filtering, scan speed, scan length, source intensity, apodization, phase correction, etc. The table included in HFI_reference_bolometer contains the reference bolometer data set properties corresponding to those listed for the HFI detectors in the table included in HFI_spectral_response_data_processing. Figures in HFI_reference_bolometer illustrate the resultant spectra and S/N from the reference bolometer data sets and compare the approximate S/N of the average spectrum for each detector against the reference bolometer average spectrum S/N over the same spectral region.

Further details are found in HFI_reference_bolometer.

Out-of-band spectral transmission content

The HFI detector spectral transmission profiles have been extended beyond the optical pass-band of the detectors. This is done by using a combination of a waveguide model and external filter measurements for the out-of-band regions of the detector spectral response. An uncertainty estimate for these additional spectral regions is also provided, however, it should be noted that the spectral uncertainty for the waveguide and filter spectra are determined indirectly (as described above/below). There is a transition from integrated HFI FTS data to filter data for every band edge which is defined by an optical filter. For the 100, 143, 217, and 353 GHz bands this is the high frequency cut-off band edge. For the 545 and 857 GHz bands a separate filter is used to define each of the high and low frequency band edges. For the spectral regions outside of the HFI detector optical bands, first the integrated HFI FTS data is used to qualitatively verify that there are no spectral leaks or features, and then the external filter measurements are grafted into the ratioed spectra where they better represent the relative spectral transmission.

The normalized ratioed (HFI detector spectrum divided by the reference bolometer spectrum) spectrum and filter are both scaled by the optical efficiency (see HFI_optical_efficiency). For the 100 - 353 bands, the filter spectrum is also scaled by λ^2 to account for single-moded throughput normalization. This frequency scaling results in a more accurate in- and near-band match between the two sets of spectra, at the cost of less accuracy at much higher frequencies where any transmission will not be single-moded. As ransmission at higher frequencies is significantly reduced, this trade-off is acceptable. The 545 and 857 GHz bands have their filter spectra without the additional frequency scaling as this is not correct for multi-moded propagation. Both lower and upper frequency thresholds, ν_l, and ν_u, are defined for each band, below and above which the integrated HFI FTS spectra and/or the composite filter spectra must be used, respectively. This is done to avoid introducing any detector nonlinearity residuals into the final spectral transmission data products. The region between these two points is defined as the transition region; within this region the amplitudes and slopes of the integrated HFI and filter spectra are used to determine the spectral cross-over/transition point. Additional checks are performed to ensure that non-physical data processing artefacts are not introduced into the spectral transition region. Additionally, a similar technique is used, with decreasing frequency instead of increasing, for the 545 and 857 GHz bands with a filter-induced frequency cut-on. The figure illustrates an example of both the FTS and filter spectra used in extending the transmission profiles beyond the HFI optical bands.

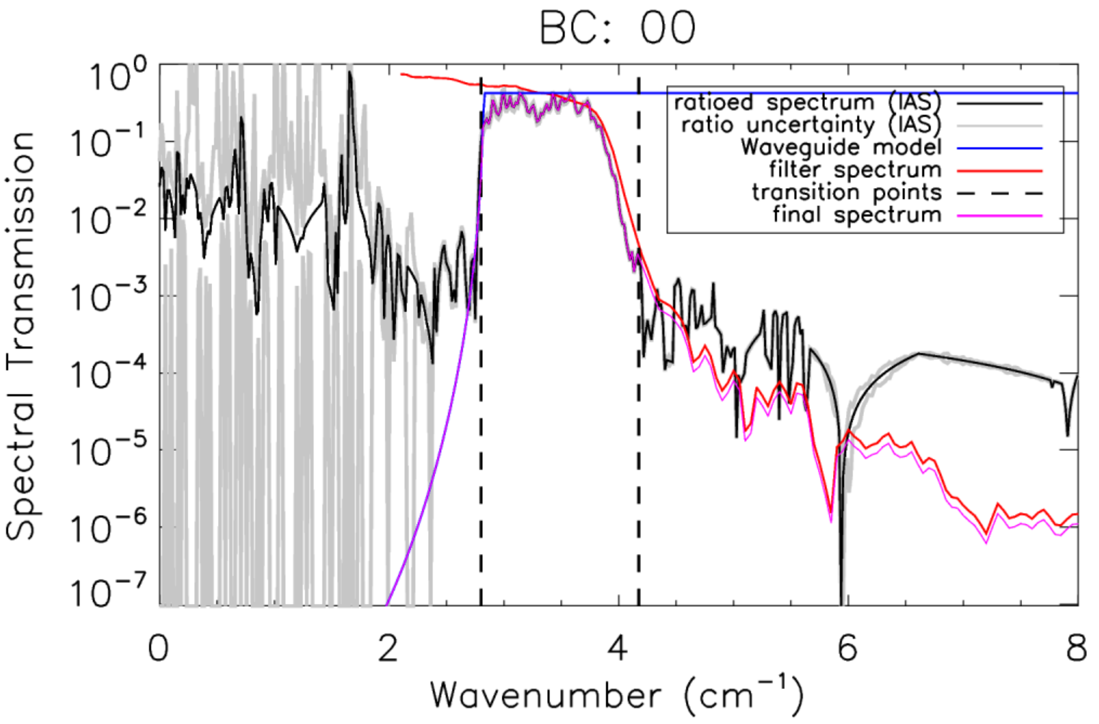

Demonstration of the combination of the waveguide model spectrum (left), the HFI measured spectrum (centre), and the combined filter spectra (right) for a given HFI detector.

Waveguide model

A waveguide model is used to provide the data for the lowest frequency portion of the HFI detector spectral transmission. For the 100, 143, 217, and 353 GHz bands the waveguide model is transitioned (with increasing frequency) to the FTS ratioed spectra directly. There is an intermediate transition to the filter data, and then the ratioed spectra for the 545 and 857 GHz bands. For each detector, the waveguide transmission, $W(\sigma)$, is given by the following relation

where σ is the frequency in cm $^{-1}$, r_w is the waveguide radius in cm, l_w is the waveguide length in cm, and c_{nm} is a waveguide specific constant; 1.841 for the TE $_{11}$/TM $_{11}$(HE $_{11}$) hybrid mode in this case . The table in HFI_detector_feedhorn_model_parameters lists the waveguide radii and lengths resultant from the waveguide model fit to the ratioed spectra. As all of the feedhorns for a given band are meant to be identical (i.e. within mechanical manufacturing tolerances) the uncertainty of the waveguide transmission is estimated statistically using all of the waveguide models for each band. I.e. for n bands, the uncertainty at each spectral data point is determined by the standard deviation of n transmission values at that frequency. As a result of each detector in a given band having a unique cut-on frequency, this method begins to over-estimate the uncertainty for frequencies approaching the cut-on; for regions very near the waveguide cut-on, the uncertainty is extrapolated from the ratioed spectrum as a more accurate representation.

CO interpolation

The integrated HFI FTS/Saturne data taken with the HFI detectors is limited to a spectral resolution of $\sim 0.017\ \mathrm{cm}^{-1}$ $(\sim 0.5\ \mathrm{GHz})$ by the mechanical travel of the FTS translation stage. This corresponds to an unapodized FTS Instrument Line Shape(ILS) FWHM of $\sim 0.020\ \mathrm{cm}^{-1}$ $(\sim 0.61\ \mathrm{GHz})$.

In order to provide an improved estimate of the spectral transmission near the CO features, an interpolation of the spectra by a factor of ~10 has been performed. This over-sampling was accomplished by zero-padding the FTS interferograms prior to Fourier transformation , and subsequently incorporated into the Nyquist-sampled spectral data near the CO transitions (see the CO table). Although the data are presented at higher resolution, the resolution of independent data points is not improved, i.e. the ILS line-width remains the same. A flag column has been added to the spectral transmission profile data files to indicate whether a given data point originates from the actual data, or is a result of the ILS-based interpolation. The region of the over-sampled, interpolated, data has been extended to also include other CO isotopes; the COJ1-0 – J9-8 transitions should be oversampled for CO, ^{13}CO, C ^{17}O, and C ^{18}O. The original data points within the over-sampled region have been preserved (i.e. every tenth data point – the data point that is not an interpolated one – is flagged with a zero rather than a one), as is indicated by the data flag, so a flag filter on the data will restore the independent data points easily. The figure below illustrates the regions where the over-sampling has been incorporated into the spectral transmission profiles.

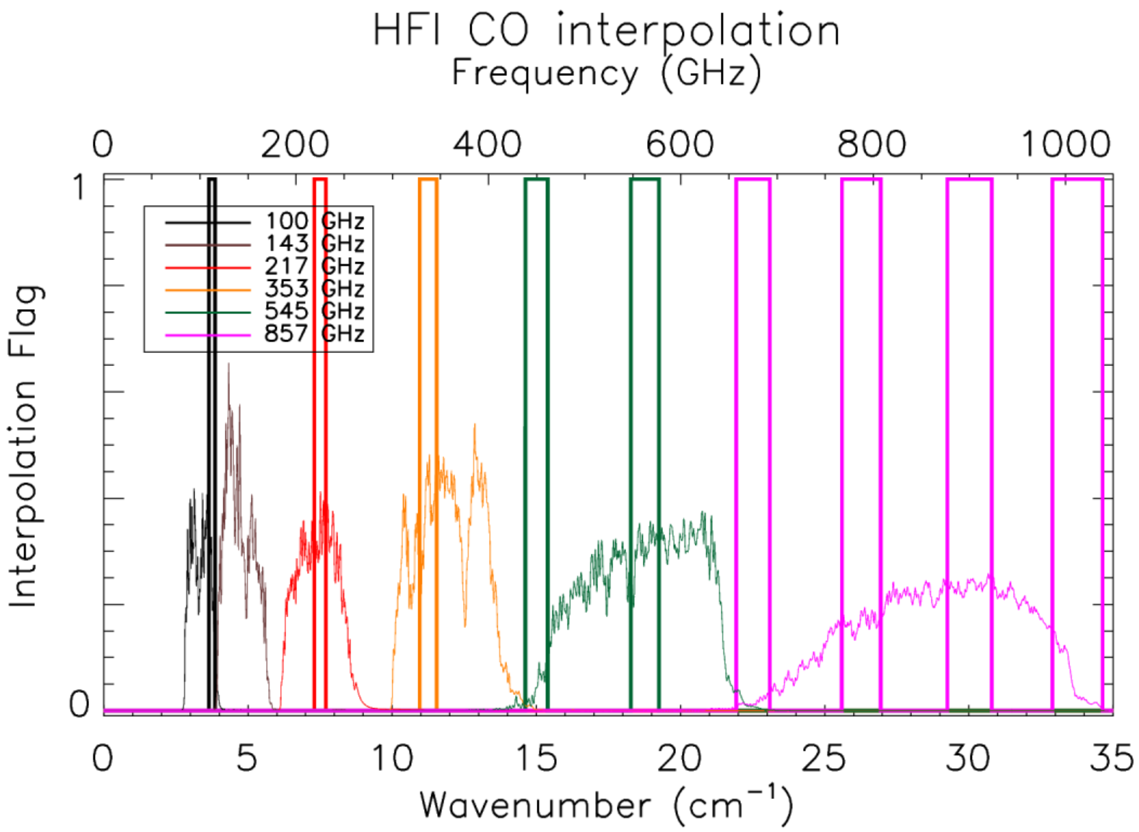

The CO regions over which the spectral transmission was interpolated using the FTS instrument line shape.

An example of the over-sampled spectra is shown in the figure below for the 100 GHz detectors.

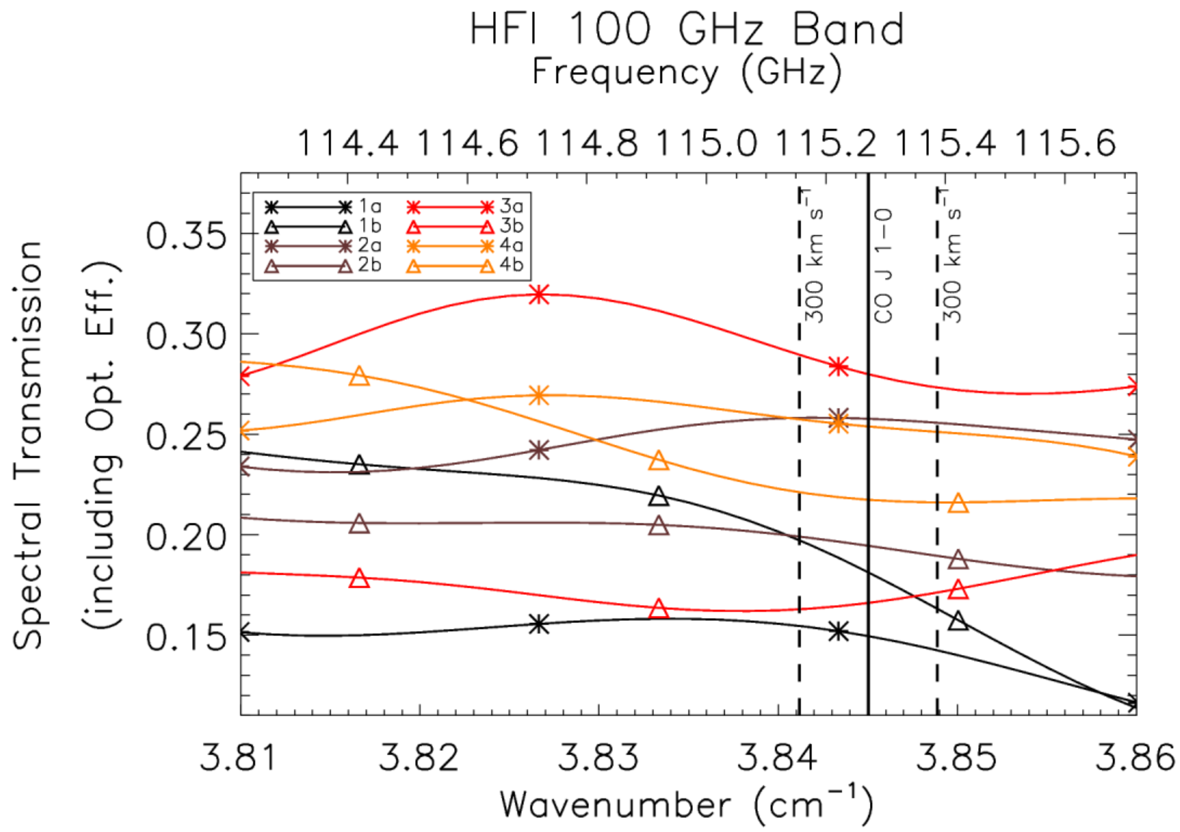

An example of the spectral transmission within 100 GHz detectors about the COJ1-0 rotational transition.

Examples for the other detector bands are shown in the §here.

Details of the HFI CO data products are available in the CO emission maps section.

Band (GHz)	CO transition (J_{Upper}- J_{Lower})	ν_o(GHz)	over-sampled region (GHz)
100	1 – 0	115.2712018	109.67 – 115.39
143	1 – 0	115.2712018	109.67 – 115.39
143	2 – 1	230.5380000	219.34 – 230.77
217	2 – 1	230.5380000	219.34 – 230.77
353	3 – 2	345.7959899	329.00 – 346.15
545	4 – 3	461.0407682	438.64 – 461.51
545	5 – 4	576.2679305	548.28 – 576.85
857	6 – 5	691.4730763	657.89 – 692.17
857	7 – 6	806.6518060	767.48 – 807.46
857	8 – 7	921.7997000	877.04 – 922.73
857	9 – 8	1036.9123930	986.57 – 1037.95

Regions of HFI spectral transmission profiles near CO transitions.

Spectral response conclusions and conformity with requirements

The two defining requirements indicated in the HFI calibration plan are the acquisition of the spectral transmission of the single pixels with a prescribed accuracy and spectral resolution. The desired accuracy is 3% for the low frequency channels (CMB – 100, 143, and 217 GHz) and 1% for the high frequency channels (353, 545, 857 GHz). The spectral resolution requirement is for a resolution superior to 0.1 cm $^{-1}$.

The spectral resolution requirement has been exceeded by more than a factor of five. It is also possible to degrade the spectral resolution to the 0.1 cm $^{-1}$requirement to gain an improvement in the S/N.

No quantitative number is present on the document regarding the blocking of high frequency (near IR, visible, UV) radiation outside the range of the instrument. Checks in order to quantify the rejection have been performed at subsystem level and estimates of the out-of-band transmission profiles have been incorporated into the data products. The high level of out-of-band signal attenuation is verified by in-flight observations as demonstrated in #planck2013-p03d Planck-2013-IX [3].

Considering statistical fluctuations in the determination of the spectra, these goals have been achieved. There are, however, caveats regarding the nature of error bars when dealing with frequency space. The nature of uncertainties in spectra determination is less obvious than when dealing with timestream data. Systematic effects produced from instrumental setup, but also by data reduction can in some cases exceed the actual statistical oscillation in the determination of the final spectra. This is the case for the high-frequency data for instance where the statistical fluctuation of the different determinations of the spectra in some case are better than 1 part in 10^3.

A second caveat regards the method of data analysis of the calibration test data, for which the ratio with the reference bolometer data (of which the relative error is a function of frequency) introduces an error that increase with wavelength. With the spectral resolution of the data provided being much higher than the stated 0.1 cm $^{-1}$, the transmission accuracy requirement is not met for the 100 GHz detectors. It is possible to degrade the spectral resolution to the 0.1cm $^{-1}$level to allow the accuracy to achieve the required level, but the higher spectral resolution data has been provided to better assist with the CO contamination removal from the 100 GHz signal.

Figures containing the full spectral response of each HFI detector, and band-average spectra, are provided in the Appendix [ref.]. Details of the generation of band-average spectra, unit conversion coefficients, and colour correction coefficients are provided in the Data Processing sections of the Explanatory Supplement. IDL scripts have been provided alongside the PLA to allow users to generate unit conversion and colour correction coefficients; these are described in this Unit_conversion_and_Color_correction section.

Further details regarding the use of the spectral response of the HFI detectors are found in the spectral response section.

References

<biblio force=false>

1. References
2. References2

</biblio>

References

[1] http://www.rssd.esa.int/doc_fetch.php?id=3135948&page=1
[2] http://www.rssd.esa.int/doc_fetch.php?id=3135950&page=1
[3] http://www.rssd.esa.int/doc_fetch.php?id=3167992&page=1

HFI detection chain

Bolometers

The heart of the HFI - the detectors - are bolometers, solid-state devices in which the incoming radiation dissipates its energy as heat that increases the temperature of a thermometer. The instrument Flight Model total number of bolometers is 52, split into 6 channels at central frequencies of 100, 143, 217, 353, 545, and 857 GHz. Two extra bolometers not optically coupled to the telescope are added to the focal plane to monitor thermal noise (dark bolometers).

The bolometers consist of

- an absorber that transforms the in-coming radiation into heat,
- a semi-conducting NTD thermistor that is thermally linked to the absorber and measures the temperature changes,
- and a weak thermal link to a thermal sink, to which the bolometer is attached.

There are two kinds of detector modules: Polarization Sensitive Bolometers (PSB) and Spider Web Bolometers (SWB).

Spider Web Bolometers #Bock1995, #Mauskopf1997

In these bolometers, the absorber consists of a metallic grid deposited on a Si3 N4 substrate in the shape of a spider web. The mesh design and the impedance of the metallic layer are adjusted to match vacuum impedance and maximize the absorption of millimeter waves, while minimizing the cross section to particles. The absorber is designed to offer equal impedance to any linearly polarised radiation. Nevertheless, the thermometer and its electrical leads define a privileged orientation that makes the SWBs slightly sensitive to polarisation, as detailed in #rosset2010 Planck pre-launch paper 13 [1]. The thermometers are made of neutron transmuted doped (NTD) germanium #Haller1996 chosen to have an impedance of about 10 MΩ at their operating temperature.

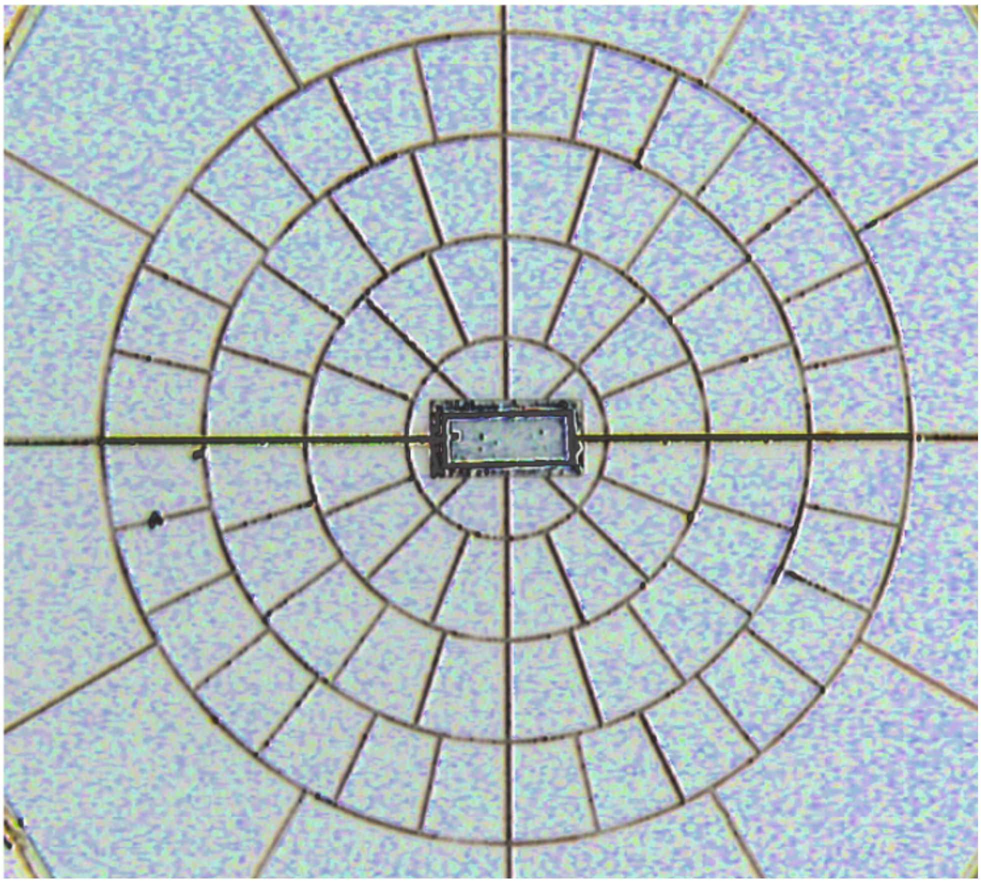

Picture of a Spider Web Bolometer. This a 143 GHz module, The temperature sensor is at the center of the absorbing grid.

Polarization Sensitive Bolometers

The absorber of PSBs is a rectangular grid with metallization in one direction #Jones2003. Electrical fields parallel to this direction develop currents and then deposit some energy in the grid, while perpendicular electrical fields propagate through the grid without significant interaction. A second PSB perpendicular to the first one absorbs the other polarisation. Such a PSB pair measures two polarisations of radiation collected by the same horns and filtered by the same devices, which minimises the systematic effects: differences between polarised beams collected by a given horn are typically less than −30 dB of the peak. The differences in the spectral responses of a PSB pair also proved to be a few percent in the worst case. Each pair of PSBs sharing the same horn is able to measure the intensity Stokes parameter and the Q parameter associated with its local frame. An associated pair of PSBs rotated by 45 ◦ scans exactly the same line (if the geometrical alignment is perfect), providing the U Stokes parameter.

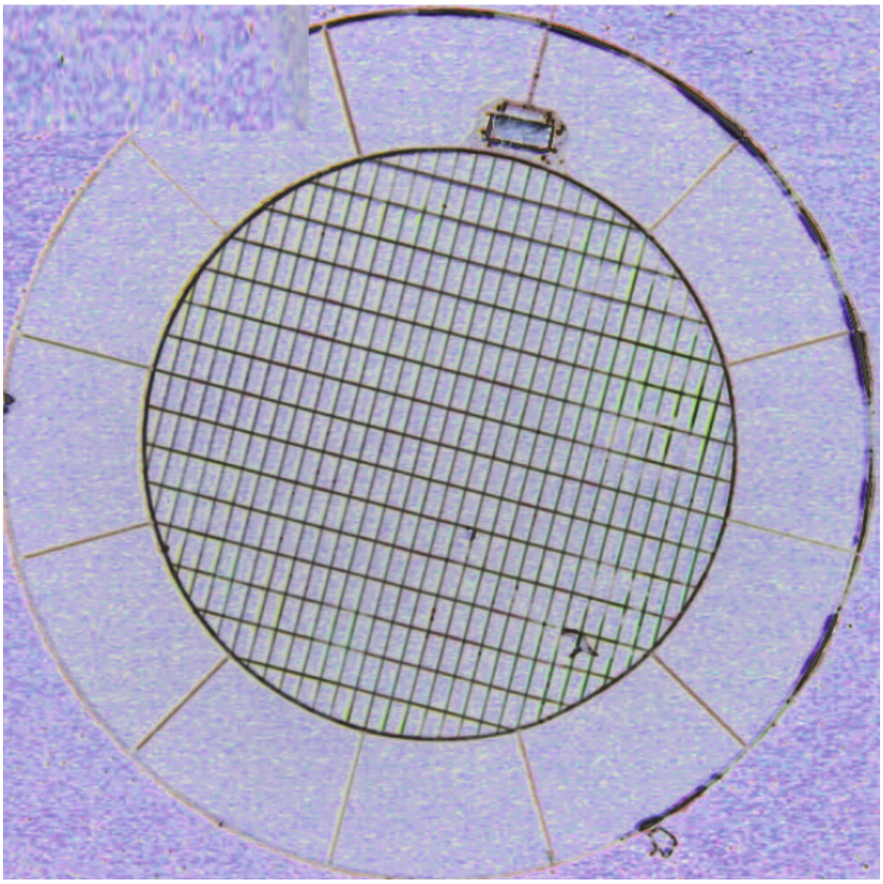

Picture of a Polarization Sensitive Bolometer. This is a 217 GHz module, The temperature sensor is located at an edge of the absorbing grid.

The detectors operate at a temperature close to 100 mK, while the filters are distributed on the 100 mK, 1.6 K, and 4 K stages in such a way that the heat load on the coldest stages is minimized to limit the heat load on the detectors and to decrease the heat lift requirement and thus enhance the mission lifetime. The self-emission of the 4K stage is minimised to limit the photon noise contribution on the detectors from the instrument. The HFI Focal Plane Unit accommodates sub-millimiter absorbing material in order to decrease the scattering inside it.

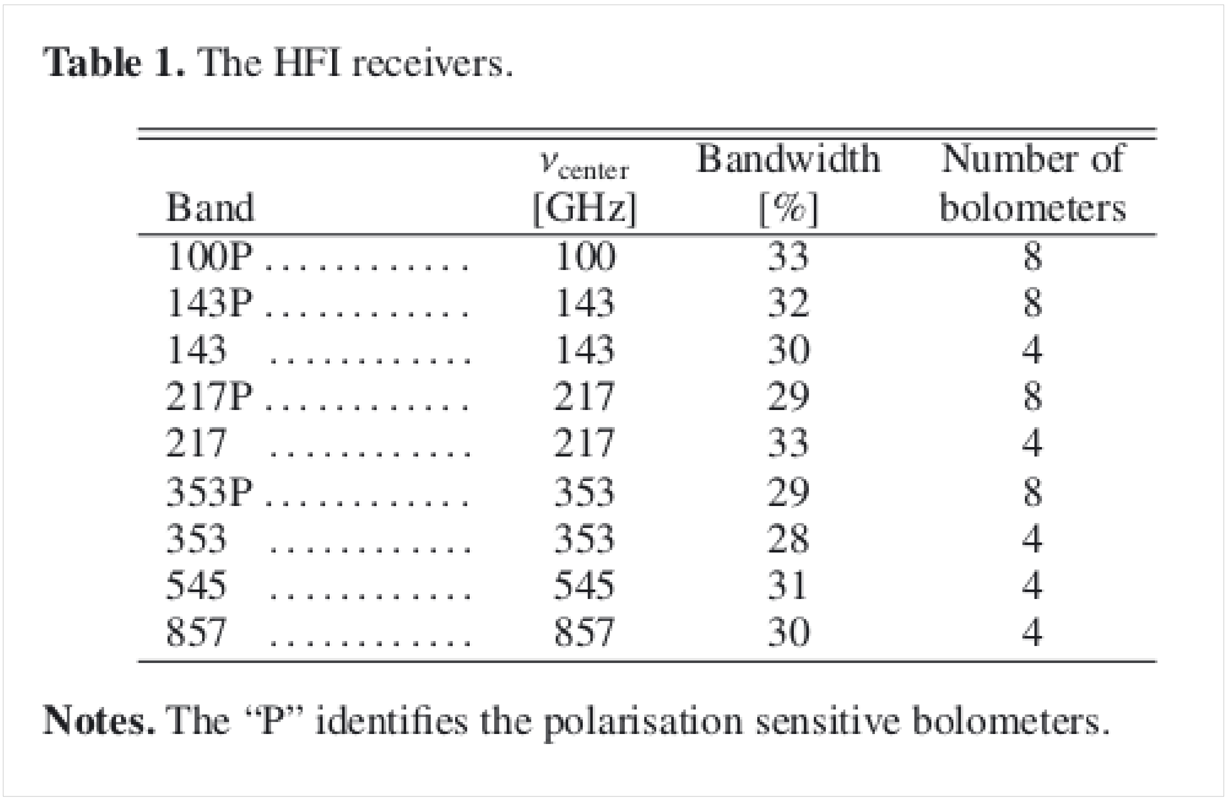

Table 1. The HFI receivers.

Band	ν_{center} [GHz]	Bandwidth [%]	Number of bolometers
100P	100	33	8
143P	143	32	8
143	143	30	4
217P	217	29	8
217	217	33	4
353P	353	29	8
353	353	28	4
545	545	31	4
857	857	30	4

Notes. The "P" identifies the polarisation sensitive bolometers.

Focal plane layout

The layout of the detectors in the focal plane is defined in relation to the scanning strategy. The HFI horns are positioned at the centre of the focal plane, where the optical quality is good enough for the high frequencies. The curvature of rows compensates for the distortion of images by the telescope. A pair of identical SWB will scan the same circle on the sky to provide redundancy. Similar horns feeding PSBs are also aligned so that two PSBs rotated by 45 ◦ with respect to each other scan the same line. This will provide the Q and U Stokes parameters with minimal correction for the pointing #rosset2010 Planck pre-launch paper 13 [1]). Residual systematics will come from the differences between the beam shapes of the two horns. In all cases except for the 100 GHz horns, a measurement is also done by a pair of similar channels shifted by 1.25 arcminutes in the cross-scan direction, to ensure adequate sampling. In the figures focal plane layout is reported.

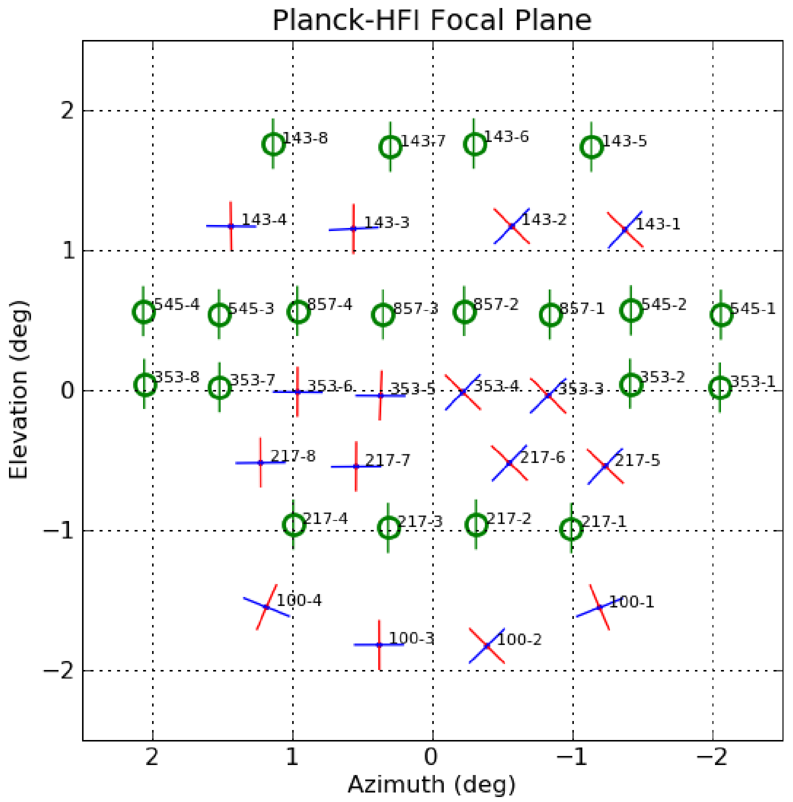

Focal plane layout as seen from outside the celestial sphere. In this case PSB orientations are indicated. Red rod is for "a" elements of PSBs, blue rod is for "b" elements. The scan direction is from left to right.

Readout

The AC bias readout electronics of the HFI instrument #Gaertner1997 includes the following features

- the cold load resistors were replaced by capacitors because they have no Johnson noise;
- the detectors are biased by applying a triangular voltage to the load capacitors which produces a square current (Ibias) in the capacitors, and a square voltage (T bias) that compensates for the stray capacitance of the wiring (producing a nearly square bias current into the bolometer;
- a square offset com-pensation signal is subtracted to the bolometric signal to minimise the amplitude of the signal that has to be amplified and digitized;
- the electronic scheme is symmetrical and uses a differential amplification scheme to optimize the immunity to electromagnetic interferences;
- and finally every parameter of the REU can be set by commands, which is made possible by using digital-to-analog and analog-to-digital converters extensively.

The readout electronics consists of 72 channels designed to perform low noise measurements of the impedance of 52 bolometers, two blind bolometers, 16 accurate low-temperature thermometers, all in the 10 MΩ range, one resistor of 10 MΩ and one capacitor of 100 pF. The semiconductor bolometers and thermometers of Planck-HFI operate at cryogenic temperature around 100 mK on the focal plane, with impedance of about 10 MΩ when biased at the optimal current. The readout electronics on the contrary has to operate at “room” temperature (300 K). The distance between the two extremities of the readout chain is about 10 m and could bring about an extreme susceptibility to electromagnetic interference. The readout electronic chain was split into three boxes. These are the JFET box, located on the 50 K stage of the satellite at 2.2 m from the focal plane, the pre-amplifier unit (PAU), located 1.8 m further at 300 K, and the REU, located on the opposite side of the satellite, 5 m away. Each of the three boxes (JFET, PAU and REU) consists of 12 belts of six channels. The first nine belts are dedicated to the bolometers, and the three last ones to the accurate thermometers, the resistor and the capacitor.

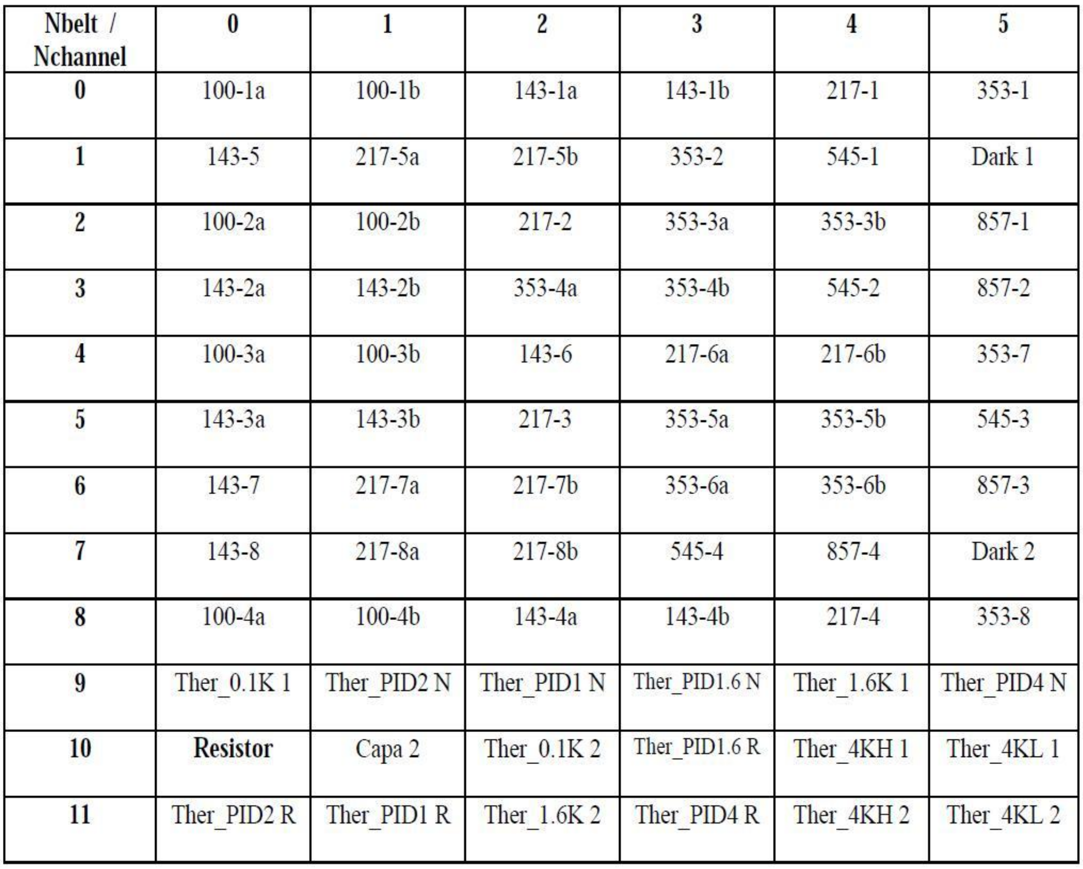

Nbelt / Nchannel	0	1	2	3	4	5
0	100-1a	100-1b	143-1a	143-1b	217-1	353-1
1	143-5	217-5a	217-5b	353-2	545-1	Dark 1
2	100-2a	100-2b	217-2	353-3a	353-3b	857-1
3	143-2a	143-2b	353-4a	353-4b	545-2	857-2
4	100-3a	100-3b	143-6	217-6a	217-6b	353-7
5	143-3a	143-3b	217-3	353-5a	353-5b	545-3
6	143-7	217-7a	217-7b	353-6a	353-6b	857-3
7	143-8	217-8a	217-8b	545-4	857-4	Dark 2
8	100-4a	100-4b	143-4a	143-4b	217-4	353-8
9	Ther_0.1K 1	Ther_PID2 N	Ther_PID1 N	Ther_PID1.6 N	Ther_1.6K 1	Ther_PID4 N
10	**Resistor**	Capa 2	Ther_0.1K 2	Ther_PID1.6 R	Ther_4KH 1	Ther_4KL 1
11	Ther_PID2 R	Ther_PID1 R	Ther_1.6K 2	Ther_PID4 R	Ther_4KH 2	Ther_4KL 2

Organization of the HFI readout. Each row represents a belt. Each belt has six channels.

Principles of the readout electronics

The bolometer is biased by a square wave AC current obtained by the differentiation of a triangular voltage through a load capacitance, in a completely differential architecture. The presence of the stray capacitance due to losses of charge in the wiring requires a correction of the shape of the square bias current by a transient voltage. Thus the bias voltage generation is controlled by the two parameters I-bias and T-bias that express the amplitude of the triangular and transient voltage. The compensation voltage added to the bolometric signal to optimize the dynamic of the chain is controlled by the V-bal parameter.

The following parameters of the Readout Unit can be set to optimize the detector performance:

- fmod, the modulation frequency of the square bias current, was set to 90.18685,
- Nsample, which defines the number of samples per half period of modulated signal was set to 40.

Each channel has its own settings for the following parameters:

- I-bias, amplitude of the triangular bias voltage,
- T-bias, amplitude of the transient bias voltage,
- V-bal, amplitude of the square compensation voltage,
- G-amp, value of the programmable gain of the REU [1/3, 1, 3, 7.6],
- N-blank, number of blanked samples at the beginning of halfperiod not taken into account during integration of the signal,
- S-phase, phase shift when computing the integrated signal.

All these parameters influence the effective response of the detection chains, and were optimized during the calibration campaigns and confirmed during the calibration and performance verification phase following the launch of Planck. The scientific signal is provided by the integral of the signal on each half-period, between limits fixed by the S-phase and N-blank parameters.

The interaction of modulated readout electronics with semiconductor bolometers is rather different from that of a classical DC bias readout #Jones1953. The differences were seen during the calibration of the HFI, although the readout electronics was designed to mimic the operation of a DC biased bolometric system as far as possible. With the AC readout the maximum of responsivity is lower and is obtained for higher bias current in the bolometer with respect to the DC model. This is caused by the stray capacitance in the wiring which has negligible effects for a DC bias and a major effect for an AC bias. In our case, a stray capacitance of 150 pF induces increases of NEP ranging from 4% (857 GHz bolometers) to 10% (100 GHz bolometers) and also affects the HFI time response. Details of the effect of the HFI AC bias system into the time response of the detectors are discussed in the time response section.

JFETs

Given the high impedance of the bolometers and the length of the connecting cables, it is essential that the impedance of the signal is lowered as close as possible to the detectors. In our system this is accomplished by means of JFET source followers, located in boxes connected to the 50 K stage #Brienza2006. There are two JFETs per channel, since the readout is fully differential, and they provide a current amplification of the signal while keeping the voltage amplification very close to unity.

Inside the box, the JFETs are mounted on a thermally insulated plate with an active temperature control to keep them at the optimal temperature of 110 K. With a dissipated power lower than 240 mW, mainly produced by the JFETs and the source resistors, we obtained a noise power spectral density of less than 3 nV Hz1/2 for the frequency range of interest. This increases the total noise of all bolometer channels by less than 5%.

Time response

The HFI bolometers and readout electronics have a finite response-time to changes of the incident optical power modeled as a Fourier domain transfer function (called the LFER4 model). LFER4 has two factors. The first one represents the bolometer thermal response, driven by its heat capacity, the thermal link to the bolometer plate at 100 mK, and by the thermo-electrical feed-back #catalano2010 resulting from the heat deposited in the bolometer by the readout electronics. This factor is empirically obtained from the observation of sources. The second factor is simply the time response of the part of the readout electronics that amplifies and digitizes the signal. It is obtained by modelling the electronics with only very few free parameters.

The time response of the HFI bolometers and readout electronics is modeled as a Fourier domain transfer function (called the LFER4 model) consisting of the product of a bolometer thermal response $F(\omega)$and an electronics response $H'(\omega)$.

Due to Planck's nearly constant scan rate, the time response is degenerate with the optical beam. However, because of the long time scale effects present in the time response, the time response is deconvolved from the data in the processing of the HFI data (see TOI processing). $F(\omega)$is tuned to optimize the "compactness" of the beams reconstructed with the deconvolved signal from planets.

Details about the time response model are to be found in this annex.

Data compression

The output of the readout electronics unit (REU) consists of one value for each of the 72 science channels (bolometers and thermometers) for each modulation half-period. This number, S_{REU}, is the sum of the 40 16-bit ADC signal values measured within the given half-period. The data processor unit (DPU) performs a lossy quantization of S_{REU}.

Details about the data compression scheme, performance of the data compression during the mission, setting the quantization step in flight, impact of the data compression on science are given in this annex.

References

<biblio force=false>

1. References
2. References2

</biblio>

References

[1] http://www.rssd.esa.int/doc_fetch.php?id=3135952&page=1

HFI operations

All satellite operations including the HFI instrument ones are under ESA MOC responsibilty for obvious safety reasons. The HFI instrument operations are nevertheless delegated to the HFI Instrument Operations Team (IOT) built from the HFI consortium and under the HFI Principal Investigator responsibility. Instrument management, operations and parameter monitoring are thus prepared and controlled by the IOT and serviced by MOC either in near real time during the DTCP or uploaded in the satellite mission timeline for defered execution. The HFI instrument health and science data quality has been monitored daily by the IOT from launch till the end of the HFI extension mission phase. Apart from ground based tests, different operations phases did occur:

- 14/05/2009-18/05/2009 **Launch Early Operational Phase**
- 18/05/2009-09/07/2009 **Commissioning Phase**. The operations during this phase were under ESA's Planck Project responsibilty. The main HFI activities have been functional tests of the instrument and its cooldown till 100 mK. Given the performance, the helium flow has been set to the minimal one giving an End Of Life estimation second half of January 2012.
- 10/07/2009-12/08/2009 **Calibration and Performance Verification Phase**. The operations during this phase were under ESA's Planck Science Office responsibilty. The main HFI operations have been performance tests and activities to mesure the effects of several systematics. The only instrument failure happened the 6th of August were the electronic part of the 4K cooler has been switched off probably due to a major cosmic particle. It has to be noted that no tuning of the HFI parameters have been executed in flight till the end of the full HFI mission, excepted in December 2009 for an adjustment of the on-board numerical compression parameters.
- 12/08/2009-28/11/2010 **HFI Nominal mission**
- 28/11/2010-13/01/2012 **HFI Extended mission**
- 13/01/2012-(to be continued) **LFI "only" extension phase**

The detailled operation timeline for HFI is given in this annex.

HFI performance summary

The HFI has been operating flawlessly for 30 months, the maximum autonomy expected for the helium of the dilution cooler. The telescope pointing was achieved with an accuracy better than expected and reconstructed to a few seconds of arc. Fifty of the fifty-two bolometers have collected data in very stable conditions during the whole mission, and practically all of the data was correctly recorded.

The essential characteristics of the HFI are gathered in the table below. The extreme sensitivity provided by the 100 mK bolometers and the HFI architecture has provided a new view of the submillimetre and millimetre sky with a noise not far from the fundamental limits set by the photon noise of the observed source. Expected and unexpected systematic effects were evidenced. The most noticeable of them are the spikes in the signal produced by cosmic rays hitting the bolometers and their immediate surrounding. The sensitivity is obtained from the half difference of the half rings. The overall sensitivity is finally around that announced as the goal in the "bluebook" #planck2005-bluebook http://www.sciops.esa.int/SA/PLANCK/docs/Bluebook-ESA-SCI(2005)1_V2.pdf, i.e. twice better than the required sensitivity. One can expect to improve these numbers by about root two when the whole mission data is available.

Beam size and sensitivity of maps for the nominal mission (15 months)

Frequency	100 GHz	143 GHz	217 GHz	353 GHz	545 GHz	857 GHz
Beam size (FWHM, arcmin)	9.66	7.27	5.01	4.86	4.84	4.63
Sensitivity per fiducial pixel	3.95 μK/K	2.35 μK/K	4.58 μK/K	15.17 μK/K	0.013 MJy/sr (*)	0.013 MJy/sr (*)
Goal sensitivity	2.5 μK/K	2.2 μK/K	4.8 μK/K	14.7 μK/K	0.023 MJy/sr	0.041 MJy/sr

(*) These sensitivities are only valid for high galactic latitude.

references

<biblio force=false>

1. References

</biblio>

HFI instrument annexes

This page lists all annexes about the HFI instrument section.

- Cold optics:
  - HFI spectral response optical efficiency measurements
  - HFI spectral response reference bolometer measurements
  - HFI spectral response data processing and Fourier transformation
  - HFI detector feedhorn waveguide model parameters
  - HFI spectral response over the CO rotational transition regions
- Detection chain:
  - HFI time response model
  - HFI data compression
- Operations:
  - HFI operations timeline

HFI optical efficiency

The HFI optical efficiency tests involved exposing the HFI detectors to a known blackbody source and observing the response. Sufficient details for the HFI detector spectral transmission profiles are provided here while full details of the experiments and results are provided in a separate technical report . A blackbody source internal to the Saturne cryostat was set to a variety of temperatures ($\sim 1-6$ K) and the bolometer detector response was recorded. A bolometer model was applied to the recorded response in order to obtain the radiative optical power absorbed by the detector, in units of W, i.e. $P_{\mathrm{abs}}(T_i)$where $T_i$represents the blackbody source temperature. Using the measured source temperature, the theoretical radiative optical power incident on the detector is also calculated using the Planck function. The ratio of the received power and the theoretical power provides the optical efficiency term. To remove any offsets in the measurement, a ratio of differences between unique temperature settings is used. The measured absorbed optical power difference is given by

where $T_j$and $T_i$represent two unique source temperature settings. The theoretical incident power is determined using the HFI detector spectral transmission profiles. Let $\tau(\nu)$represent the normalized detector transmission spectrum (i.e. it has been ratioed and had the waveguide model and filter data appropriately grafted). The spectral transmission is scaled for λ^2throughput and then re-normalized as follows

where $\mathrm{Norm}\,(f(x))$is the division of $f(x)$by its maximum value, and $c$is the speed of light. The normalized spectral transmission is then used with the Planck function at the temperature setting to determine the theoretical power, $P_{\mathrm{th}}(T_i)$, as follows

where $h$is the Planck constant, $k$is the Boltzmann constant, the integration limits are given by $\nu_1$and ν_2, and $n_m$is the expected mode content of the frequency band. Table [tab:modes] lists the $n_m$values used for each band. In this case the integration is performed over the range $\nu \in [67\ \mathrm{GHz}, 1142\ \mathrm{GHz}]$. The difference between the theoretical power loading is given by

which allows the optical efficiency term to be determined as follows

Thus, if $\epsilon\tau'(\nu)$were used in Equation [eq:EFFPth] in place of $\tau'(\nu)$, the resultant optical efficiency would be unity, indicating that the transmission losses have already been taken into account.

The uncertainty estimate of the optical efficiency is statistically based on the results from the multiple temperature settings used in the optical efficiency test sequences.

Mode content for the HFI detector bands.

Band (GHz)	100	143	217	353	545	857
n_m	1	1	1	1	3.4	8.3

HFI reference bolometer

Properties of reference bolometer spectra

Band (GHz)	# Ifgm.	# Spec.	MPD (cm)	ILS FWHM(cm $^{-1}$)	avg. S/N
100	164	164	29.644698	0.020357772	11.478057
143	164	164	29.644698	0.020357772	37.361317
217	164	164	29.644698	0.020357772	126.14280
353	24	24	29.652306	0.020352549	136.06159
545	24	24	29.652306	0.020352549	314.58093
857	24	24	29.652306	0.020352549	388.23050

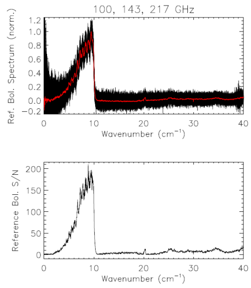

100 - 217 GHz

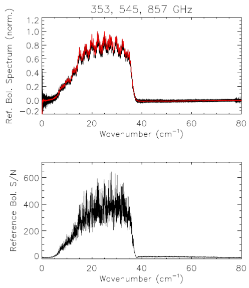

353 - 857 GHz

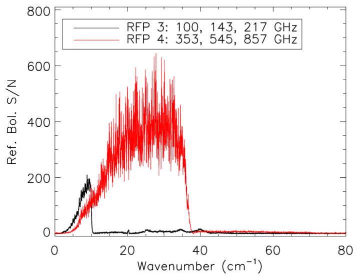

all bands

Reference bolometer spectra and S/N.

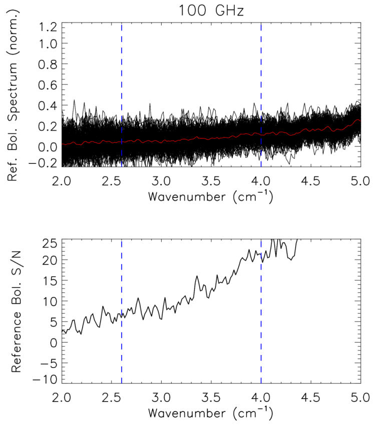

100GHz

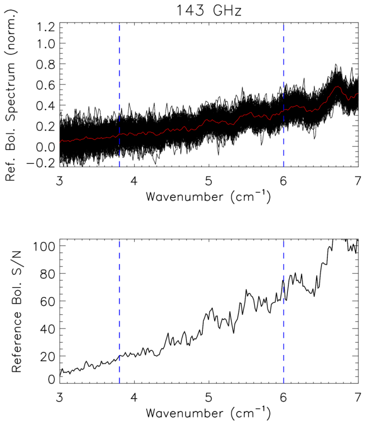

143GHz

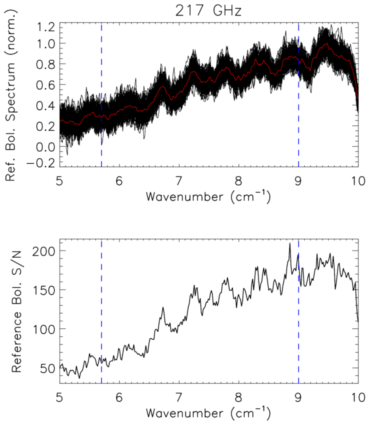

217GHz

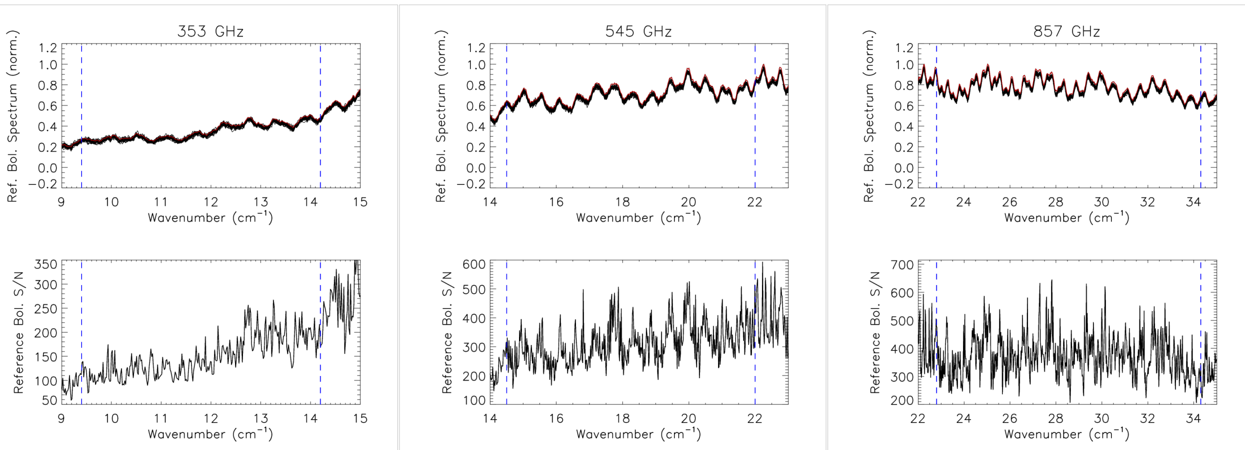

353GHz

545GHz

857GHz

Reference bolometer spectra (top) and S/N (bottom) for each of the HFI bands (vertical bars represent band edges).

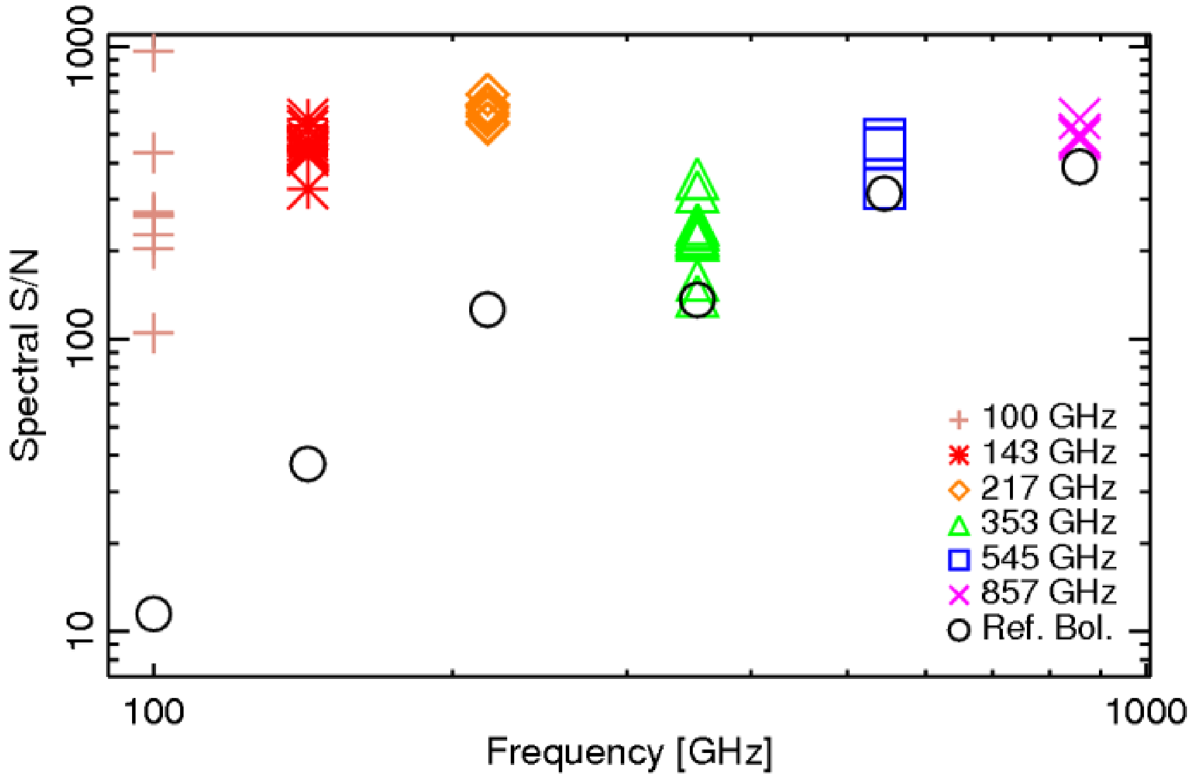

Approximate S/N ratio for the individual HFI detector spectra and the reference bolometer spectra.

HFI detector feedhorn model parameters

This section provides a table of the waveguide parameters used in modelling the low frequency cut-on for the various HFI detectors as described in equation (2) given in section waveguide model.

Waveguide model parameters for the HFI detectors.

Band (GHz)	bc	Det.	r^{W}(mm)	l^{W}(mm)
100	00	1a	1.039705	12.1000
100	01	1b	1.038040	12.5813
100	20	2a	1.038375	14.3000
100	21	2b	1.041035	12.3750
100	40	3a	1.042370	12.9250
100	41	3b	1.042370	12.5125
100	80	4a	1.033050	13.2000
100	81	4b	1.033050	12.6500
143	02	1a	0.740345	9.4500
143	03	1b	0.737550	9.5625
143	10	5	0.736155	9.4500
143	30	2a	0.740345	9.4500
143	31	2b	0.739880	9.2250
143	42	6	0.741275	9.4500
143	50	3a	0.741275	9.4500
143	51	3b	0.741275	9.4500
143	60	7	0.729635	9.7875
143	70	8	0.739415	9.4500
143	82	4a	0.739415	9.4500
143	83	4b	0.738480	9.4500
217	04	1	0.4740750	7.8000
217	11	5a	0.4814250	7.8000
217	12	5b	0.4817310	8.0000
217	22	2	0.4749935	7.8000
217	43	6a	0.4832625	8.0000
217	44	6b	0.4832625	8.0000
217	52	3	0.4753000	8.0000
217	61	7a	0.4820375	8.0000
217	62	7b	0.4820375	8.0000
217	71	8a	0.4838750	8.0000
217	72	8b	0.4838750	8.1000
217	84	4	0.4740750	7.6000
353	05	1	0.2921850	6.47500

353	13	2	0.2914300	7.00000
353	23	3a	0.2891650	7.70000
353	24	3b	0.2893535	7.52500
353	32	4a	0.2869000	7.35000
353	33	4b	0.2870890	7.39375
353	45	7	0.2876550	6.12500
353	53	5a	0.2936950	7.35000
353	54	5b	0.2936950	7.61250
353	63	6a	0.2929400	6.73750
353	64	6b	0.2925625	6.62500
353	85	8	0.2889765	6.73750
545	14	1	0.3861000	3.600
545	34	2	0.3865875	3.525
545	55	3	0.3800065	3.525
545	73	4	0.3787875	3.525
857	25	1	0.2985	2.4
857	35	2	0.2985	2.4
857	65	3	0.2985	2.4
857	74	4	0.2985	2.4

HFI CO response

Below is a table of the spectral transmission over the CO rotational transition/emission regions.

Spectral transmission for CO transitions for HFI detectors.

Band	BC	Det.	CO transition ($J_{\text{upper}} - J_{\text{lower}}$)	Transmission
100	00	1a	1 – 0	0.1495 ±0.0054
100	01	1b	1 – 0	0.1812 ±0.0052
100	20	2a	1 – 0	0.2577 ±0.0119
100	21	2b	1 – 0	0.1944 ±0.0086
100	40	3a	1 – 0	0.2798 ±0.0133
100	41	3b	1 – 0	0.1660 ±0.0093
100	80	4a	1 – 0	0.2538 ±0.0114
100	81	4b	1 – 0	2173 ±0.0105
217	04	1	2 – 1	0.3781 ±0.0026
217	11	5a	2 – 1	0.4530 ±0.0029
217	12	5b	2 – 1	0.4174 ±0.0030
217	22	2	2 – 1	0.3773 ±0.0026
217	43	6a	2 – 1	0.3149 ±0.0023

217	44	6b	2 − 1	0.3609 ±0.0030
217	52	3	2 − 1	0.3924 ±0.0025
217	61	7a	2 − 1	0.3428 ±0.0022
217	62	7b	2 − 1	0.2770 ±0.0017
217	71	8a	2 − 1	0.4623 ±0.0031
217	72	8b	2 − 1	0.4340 ±0.0031
217	84	4	2 − 1	0.3506 ±0.0025
353	05	1	3 − 2	0.4487 ±0.0036
353	13	2	3 − 2	0.5461 ±0.0044
353	23	3a	3 − 2	0.3443 ±0.0030
353	24	3b	3 − 2	0.4706 ±0.0037
353	32	4a	3 − 2	0.3099 ±0.0024
353	33	4b	3 − 2	0.2801 ±0.0027
353	45	7	3 − 2	0.2923 ±0.0022
353	53	5a	3 − 2	0.3150 ±0.0024
353	54	5b	3 − 2	0.3181 ±0.0023
353	63	6a	3 − 2	0.2059 ±0.0014
353	64	6b	3 − 2	0.2113 ±0.0017
353	85	8	3 − 2	0.3509 ±0.0028
545	14	1	4 − 3	0.0747 ±0.0003
545	34	2	4 − 3	0.0731 ±0.0003
545	55	3	4 − 3	0.0521 ±0.0002
545	73	4	4 − 3	0.0473 ±0.0002
545	14	1	5 − 4	0.3306 ±0.0012
545	34	2	5 − 4	0.3183 ±0.0011
545	55	3	5 − 4	0.2428 ±0.0009
545	73	4	5 − 4	0.2597 ±0.0009
857	25	1	6 − 5	0.0280 ±0.0001
857	35	2	6 − 5	0.0241 ±0.0001
857	65	3	6 − 5	0.0292 ±0.0001
857	74	4	6 − 5	0.0159 ±0.0001
857	25	1	7 − 6	0.1636 ±0.0005
857	35	2	7 − 6	0.1427 ±0.0004
857	65	3	7 − 6	2176 ±0.0007
857	74	4	7 − 6	0.1168 ±0.0003
857	25	1	8 − 7	0.2554 ±0.0009
857	35	2	8 − 7	0.2218 ±0.0007
857	65	3	8 − 7	0.2744 ±0.0009
857	74	4	8 − 7	0.1119 ±0.0004

857	25	1	9 – 8	0.0053 ±0.0000
857	35	2	9 – 8	0.0060 ±0.0000
857	65	3	9 – 8	0.0085 ±0.0000
857	74	4	9 – 8	0.0001 ±0.0000

HFI time response model

LFER4 model

If we write the input signal (power) on a bolometer as the bolometer physical impedance can be written as: where ω is the angular frequency of the signal and $F(\omega)$is the complex intrinsic bolometer transfer function. For HFI the bolometer transfer function is modelled as the sum of 4 single pole low pass filters: The modulation of the signal is done with a square wave, written here as a composition of sine waves of decreasing amplitude: where we have used the Euler relation $\sin x = (e^{ix} - e^{-ix})/2i$and $\omega_r$is the angular frequency of the square wave. The modulation frequency is $f_{mod} = \omega_r/2\pi$and was set to $f_{mod} = 90.18759$Hz in flight. This signal is then filtered by the complex electronic transfer function $H(\omega)$. Setting: $\omega_k^+ = \omega + (2k+1)\omega_r$ $\omega_k^- = \omega - (2k+1)\omega_r$we have: This signal is then sampled at high frequency ($2 f_{mod} NS$). $NS$is one of the parameters of the HFI electronics and corresponds to the number of high frequency samples in each modulation semi-period. In order to obtain an output signal sampled every π/ω_rseconds, we must integrate on a semiperiod, as done in the HFI readout. To also include a time shift Δt, the integral is calculated between $n\pi/\omega_r + \Delta t$and $(n+1)\pi/\omega_r + \Delta t$(with $T = 2\pi/\omega_r$ period of the modulation). The time shift $\Delta t$is encoded in the HFI electronics by the parameter S_{phase}, with the relation $\Delta t = S_{phase}/NS/f_{mod}$.

After integration, the n-sample of a bolometer can be written as where

The output signal in equation eqn:output can be demodulated (thus removing the $(-1)^n$) and compared to the input signal in equation bol_in. The overall transfer function is composed of the bolometer transfer function and the effective electronics transfer function, $H'(\omega)$: $TF(\omega) = F(\omega)H'(\omega)$

The shape of $H(\omega)$is obtained combining low and high-pass filters with Sallen Key topologies (with their respective time constants) and accounting also for the stray capacitance low pass filter given by the bolometer impedance combined with the stray capacitance of the cables. The sequence of filters that define the electronic band-pass function $H(\omega) = h_0 * h_1 * h_2 * h_3 * h_4 * h_5$are listed in the following table.

HFI electronics filter sequence. We define $s = i \omega$

Filter	**Parameters**	**Function**
0. Stray capacitance low pass filter	$\tau_{stray} = R_{bolo} C_{stray}$	$h_0 = \dfrac{1}{1.0 + \tau_{stray} * s}$
1. Low pass filter	$R_1 = 1_{\text{k}}\,\Omega$ $C_1 = 100_{\text{nF}}$	$h_1 = \dfrac{2.0 + R_1 * C_1 * s}{2.0 * (1.0 + R_1 * C_1 * s)}$
2. Sallen Key high pass filter	$R_2 = 51_{\text{k}}\,\Omega$ $C_2 = 1\mu$	$h_2 = \dfrac{(R_2 * C_2 * s)^2}{(1.0 + R_2 * C_2 * s)^2}$3
3. Sign reverse with gain		$h_3 = -5.1$

4. Single pole low pass filter with gain	$R_4 = 10_{\text{k}}\,\Omega$ $C_4 = 10_{\text{nF}}$	$h_4 = \dfrac{1.5}{1.0 + R_4 * C_4 * s}$
5. Single pole high pass filter coupled to a Sallen Key low pass filter	$R_9 = 18.7_{\text{k}}\,\Omega$ $R_{12} = 37.4_{\text{k}}\,\Omega$ $C = 10.0_{\text{nF}}$ $R_{78} = 510_{\text{k}}\,\Omega$ $C_{18} = 1.0\mu_{\text{F}}$ $K_3 = R_9^2 * R_{78} * R_{12}^2 * C^2 * C_{18}$ $K_2 = R_9 * R_{12}^2 * R_{78} * C^2 + R_9^2 * R_{12}^2 * C^2 + R_9 * R_{12}^2 * R_{78} * C_{18} * C$ $K_1 = R_9 * R_{12}^2 * C + R_{12} * R_{78} * R_9 * C_{18}$	$h_5 = \dfrac{2.0 * R_{12} * R_9 * R_{78} * C_{18} * s}{s^3 * K_3 + s^2 * K_2 + s * K_1 + R_{12} * R_9}$

Parameters of LFER4 model

The LFER4 model has are a total of 10 parameters(A_1, A_2, A_3, A_4, τ_1, τ_2, τ_3, τ_4, S_{phase}, τ_{stray}) 9 of which are independent, for each bolometer. The free parameters of the LFER4 model are determined using in-flight data in the following ways:

- $S_{phase}$is fixed at the value of the REU setting.
- $\tau_{stray}$is measured during the QEC test during CPV.
- A_1, τ_1, A_2, $\tau_2$are fit forcing the compactness of the scanning beam.
- A_3, τ_3, A_4 $\tau_4$are fit by forcing agreement of survey 2 and survey 1 maps.
- The overall normalization of the LFER4 model is forced to be 1.0 at the signal frequency of the dipole.

The details of determining the model parameters are given in (reference P03c paper) and the best-fit parameters listed below.

LFER4 model parameters.

Bolometer	A_1	τ_1(s)	A_2	τ_2(s)	A_3	τ_3(s)	A_4	τ_4(s)	τ_{stray}(s)	S_{phase}(s)
100-1a	0.392	0.01	0.534	0.0209	0.0656	0.0513	0.00833	0.572	0.00159	0.00139
100-1b	0.484	0.0103	0.463	0.0192	0.0451	0.0714	0.00808	0.594	0.00149	0.00139
100-2a	0.474	0.00684	0.421	0.0136	0.0942	0.0376	0.0106	0.346	0.00132	0.00125
100-2b	0.126	0.00584	0.717	0.0151	0.142	0.0351	0.0145	0.293	0.00138	0.00125
100-3a	0.744	0.00539	0.223	0.0147	0.0262	0.0586	0.00636	0.907	0.00142	0.00125
100-3b	0.608	0.00548	0.352	0.0155	0.0321	0.0636	0.00821	0.504	0.00166	0.00125
100-4a	0.411	0.0082	0.514	0.0178	0.0581	0.0579	0.0168	0.37	0.00125	0.00125
100-4b	0.687	0.0113	0.282	0.0243	0.0218	0.062	0.00875	0.431	0.00138	0.00139
143-1a	0.817	0.00447	0.144	0.0121	0.0293	0.0387	0.0101	0.472	0.00142	0.00125
143-1b	0.49	0.00472	0.333	0.0156	0.134	0.0481	0.0435	0.27	0.00149	0.00125
143-2a	0.909	0.0047	0.0763	0.017	0.00634	0.1	0.00871	0.363	0.00148	0.00125
143-2b	0.912	0.00524	0.0509	0.0167	0.0244	0.0265	0.0123	0.295	0.00146	0.00125
143-3a	0.681	0.00419	0.273	0.00956	0.0345	0.0348	0.0115	0.317	0.00145	0.00125
143-3b	0.82	0.00448	0.131	0.0132	0.0354	0.0351	0.0133	0.283	0.00161	0.000832
143-4a	0.914	0.00569	0.072	0.0189	0.00602	0.0482	0.00756	0.225	0.00159	0.00125
143-4b	0.428	0.00606	0.508	0.00606	0.0554	0.0227	0.00882	0.084	0.00182	0.00125
143-5	0.491	0.00664	0.397	0.00664	0.0962	0.0264	0.0156	0.336	0.00202	0.00139

143-6	0.518	0.00551	0.409	0.00551	0.0614	0.0266	0.0116	0.314	0.00153	0.00111
143-7	0.414	0.00543	0.562	0.00543	0.0185	0.0449	0.00545	0.314	0.00186	0.00139
217-5a	0.905	0.00669	0.0797	0.0216	0.00585	0.0658	0.00986	0.342	0.00157	0.00111
217-5b	0.925	0.00576	0.061	0.018	0.00513	0.0656	0.0094	0.287	0.00187	0.00125
217-6a	0.844	0.00645	0.0675	0.0197	0.0737	0.0316	0.0147	0.297	0.00154	0.00125
217-6b	0.284	0.00623	0.666	0.00623	0.0384	0.024	0.0117	0.15	0.00146	0.00111
217-7a	0.343	0.00548	0.574	0.00548	0.0717	0.023	0.0107	0.32	0.00152	0.00139
217-7b	0.846	0.00507	0.127	0.0144	0.0131	0.0479	0.0133	0.311	0.00151	0.00139
217-8a	0.496	0.00722	0.439	0.00722	0.0521	0.0325	0.0128	0.382	0.00179	0.00111
217-8b	0.512	0.00703	0.41	0.00703	0.0639	0.0272	0.0139	0.232	0.00173	0.00125
217-1	0.0136	0.00346	0.956	0.00346	0.0271	0.0233	0.00359	1.98	0.00159	0.00111
217-2	0.978	0.00352	0.014	0.0261	0.00614	0.042	0.00194	0.686	0.0016	0.00125
217-3	0.932	0.00355	0.0336	0.00355	0.0292	0.0324	0.00491	0.279	0.00174	0.00125
217-4	0.658	0.00135	0.32	0.00555	0.0174	0.0268	0.00424	0.473	0.00171	0.00111
353-3a	0.554	0.00704	0.36	0.00704	0.0699	0.0305	0.0163	0.344	0.0017	0.00125
353-3b	0.219	0.00268	0.671	0.00695	0.0977	0.0238	0.0119	0.289	0.00157	0.00111
353-4a	0.768	0.00473	0.198	0.00993	0.0283	0.0505	0.00628	0.536	0.00181	0.00125
353-4b	0.684	0.00454	0.224	0.0108	0.0774	0.08	0.0149	0.267	0.00166	0.00111
353-5a	0.767	0.00596	0.159	0.0124	0.0628	0.0303	0.0109	0.357	0.00156	0.00111
353-5b	0.832	0.00619	0.126	0.0111	0.0324	0.035	0.0096	0.397	0.00166	0.00111
353-6a	0.0487	0.00176	0.855	0.006	0.0856	0.0216	0.0105	0.222	0.00199	0.00125
353-6b	0.829	0.00561	0.127	0.00561	0.0373	0.0252	0.00696	0.36	0.00228	0.00111
353-1	0.41	0.000743	0.502	0.00422	0.0811	0.0177	0.0063	0.329	0.00132	0.00097
353-2	0.747	0.00309	0.225	0.00726	0.0252	0.0447	0.00267	0.513	0.00154	0.00097
353-7	0.448	0.0009	0.537	0.0041	0.0122	0.0273	0.00346	0.433	0.00178	0.00125
353-8	0.718	0.00223	0.261	0.00608	0.0165	0.038	0.00408	0.268	0.00177	0.00111
545-1	0.991	0.00293	0.00743	0.026	0.00139	2.6	0	0	0.00216	0.00111
545-2	0.985	0.00277	0.0128	0.024	0.00246	2.8	0	0	0.00187	0.00097
545-4	0.972	0.003	0.0277	0.025	0.000777	2.5	0	0	0.00222	0.00111
857-1	0.974	0.00338	0.0229	0.025	0.00349	2.2	0	0	0.00176	0.00111
857-2	0.84	0.00148	0.158	0.00656	0.00249	3.2	0	0	0.0022	0.00125
857-3	0.36	4.22e-05	0.627	0.0024	0.0111	0.017	0.002	1.9	0.00152	0.00126
857-4	0.278	0.0004	0.719	0.00392	0.00162	0.09	0.00152	0.8	0.00149	0.000558

HFI data compression

Data compression

Data compression scheme

The output of the readout electronics unit (REU) consists of one value for each of the 72 science channels (bolometers and thermometers) for each modulation half-period. This number, S_{REU}, is the sum of the 40 16-bit ADC signal values measured within the given half-period. The data processor unit (DPU) performs a lossy quantization of S_{REU}.

We define a compression slice of 254 S_{REU}values, corresponding to about 1.4 s of observation for each detector and to a strip on the sky about 8 degrees long. The mean $\langle S_{REU} \rangle$of the data within each compression slice is computed, and data are demodulated using this mean:

$$S_{demod,i} = (S_{REU,i} - \langle S_{REU} \rangle) * (-1)^i$$

where $1 < i < 254$is the running index within the compression slice.

The mean $\langle S_{demod} \rangle$of the demodulated data $S_{demod,i}$is computed and subtracted, and the resulting slice data is quantized according to a step size Q that is fixed per detector:

$$S_{DPU,i} = \mathrm{round}\left[(S_{demod,i} - \langle S_{demod} \rangle)/Q\right]$$

This is the lossy part of the algorithm: the required compression factor, obtained through the tuning of the quantization step Q, adds a noise of variance $\simeq 2\%$to the data. This will be discussed below.

The two means $\langle S_{REU} \rangle$and $\langle S_{demod} \rangle$are computed as 32-bit words and sent through the telemetry, together with the $S_{DPU,i}$values. Variable-length encoding of the $S_{DPU,i}$values is performed on board, and the inverse decoding is applied on ground.

Performance of the data compression during the mission

Optimal use of the bandpass available for the downlink was obtained initially by using a value of Q = σ/2.5 for all bolometer signals. After the 12th of December 2009, and only for the 857 GHz detectors, the value was reset to Q = σ/2.0 to avoid data loss due to exceeding the limit of the downlink rate. With these settings the load during the mission never exceeded the allowed band-pass width as is seen on the next figure.

Setting the quantization step in flight

The only parameter that enters the PLANCK-HFI compression algorithm is the size of the quantization step, in units of σ, the white noise standard deviation for each channel. It has been adjusted during the mission by studying the mean frequency of the central quantization bin [-Q/2,Q/2], $p_0$within each compression slice (254 samples). For a pure Gaussian noise, this frequency is related to the step size (in units of σ) by $\hat{Q} = 2\sqrt{2}\mathrm{Erf}^{-1}(p_0) \simeq 2.5 p_0$ where the approximation is valid up to $p_0 < 0.4$. In PLANCK however the channel signal is not a pure Gaussian, since glitches and the periodic crossing of the Galactic plane add some strong outliers to the distribution. By using the frequency of these outliers, p_{out}, above 5σ, simulations show that the following formula gives a valid estimate:

$$\hat{Q}_{\mathrm{cor}} = 2.5 \frac{p_0}{1 - p_{\mathrm{out}}}$$

The following figure shows an example of the $\hat{Q}$and $\hat{Q}_{\mathrm{cor}}$timelines that were used to monitor and adjust the quantization setting.

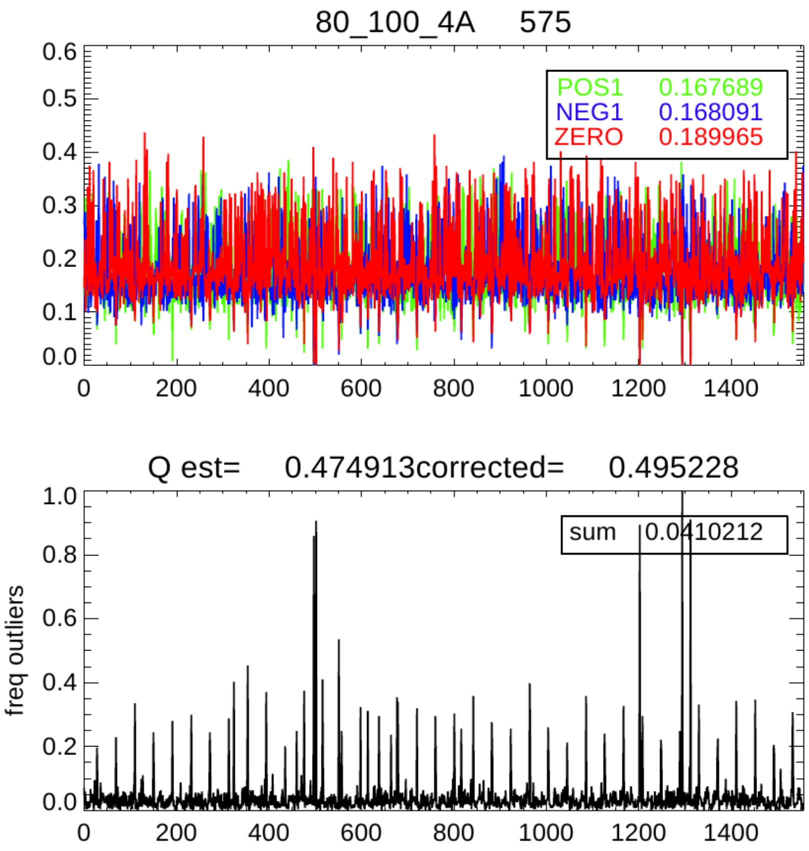

Example of the "bin0" frequency timeline (1 point per compression slice) p_0 (labeled "ZERO") for one of the channels. The -1 ("NEG1") and +1 ("POS1") bin frequencies are also shown. The lower plot shows the frequency timeline of outliers, where the glitches and periodic crossing of the Galaxy are visible. The estimated raw step size \hat Q=0.47 and corrected value \hat Q_\text{cor}=0.49 are automatically computed and the step size can be adjusted according to these control plots.

Impact of the data compression on science

The effect of a pure quantization process of step Q(in units of σ) on the statistical moments of a signal is well known (#widrow) When the step is typically below the noise level (which is largely the PLANCK case) one can apply the Quantization Theorem which states that the process is equivalent to the addition of a uniform random noise in the $[-Q/2, Q/2]$range. The net effect of quantization is therefore to add quadratically to the signal a $Q^2/12$ variance. For $Q \simeq 0.5$this corresponds to a 2%noise level increase. The spectral effect of the non-linear quantization process is theoretically much more complicated and depends on the signal and noise details. As a rule of thumb, a pure quantization adds some auto-correlation function that is suppressed by a $\exp[-4\pi^2(\frac{\sigma}{Q})^2]$factor #banta. Note however that PLANCK does not perform a pure quantization process. A baseline which depends on the data (mean of each compression slice value), is subtracted. Furthermore, for the science data, circles on the sky are coadded. Coaddition is again performed when projecting the rings onto the sky (map-making). To study the full effect of the PLANCK-HFI data compression algorithm on our main science products, we have simulated a realistic data timeline corresponding to the observation of a pure CMB sky. The compressed/decompressed signal was then back-projected onto the sky using the PLANCK scanning strategy. The two maps were analyzed using the \texttt{anafast} Healpix procedure and both reconstructed $C_\ell$were compared. The result is shown for a quantization step $Q = 0.5$.

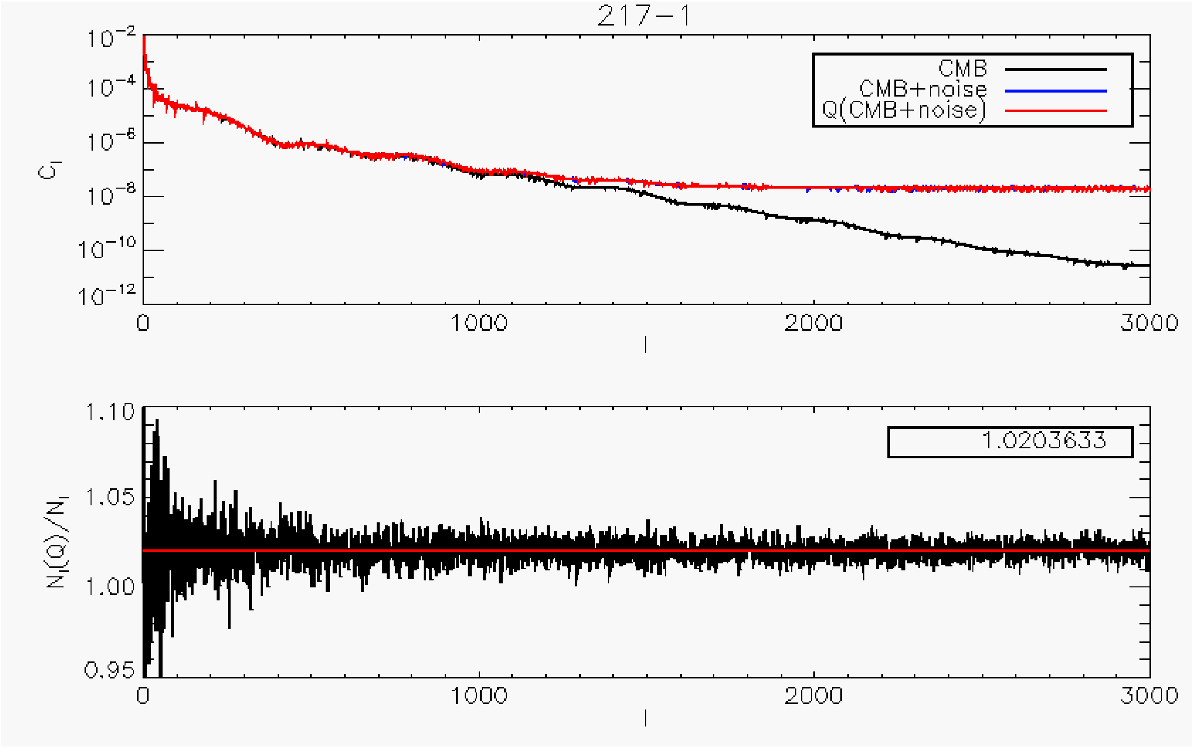

Effect of the PLANCK compression algorithm on the reconstructed power spectrum (C_ℓ) after data projection and map-making, according to the simulation. The upper plot shows the input reconstructed CMB power spectrum (black), the CMB+noise spectrum for this channel (blue, barely visible) and the reconstructed C_ℓ) when including the data compression in the chain (red). The lower plot shows these last two ratios and confirms the white nature of the final added noise at a level that can still be computed by the Quantization Theorem ($2\%$for $Q = 0.5$used here).

It is remarkable that the full procedure of baseline-subtraction+quantization+ring-making+map-making still leads to the 2%increase of the variance that is predicted by the simple timeline quantization (for $Q/\sigma = 2$). Furthermore we check that the noise added by the compression algorithm is white.

It is not expected that the compression brings any non-gaussianity, since the pure quantization process does not add any skewness and less than 0.001 kurtosis, and coaddition of circles and then rings erases any non-gaussian contribution according to the Central Limit Theorem.

<biblio force=false>

1. References

</biblio>

HFI operations timeline

The following list gives some known events and activities that have affected or might have affected the HFI data. The time information is the start time of the event in On Board Time. The label contains few keywords:

- **dtcp** : (for Daily Tele-Communication Period) refers to extended pass
- **HFI** : refers to HFI instrument operations (when during the Commissioning of the Calibration and Performance Verification phases, labels are usually followed bu the activity label)
- **period**: refers to the different phases of the mission
- **test** : refers to End Of Life tests executed on the HFI
- **therm** : refers to satellite events that might have a thermal impact on the HFI
- **sat** : refers to operations on the satellite SerVice Module that might have an impact on the HFI data
- **slew** : refers to thruster activity
- **solar flare** : refers to all solar events as detected by a thermal fluctuation on the HFI bolometer plate

```
14/05/2009 13:12:00      EPC Vulcain Engine ignition
14/05/2009 16:58:36      HFI: LCLs nominal switch on
14/05/2009 17:30:59      HFI: go from startup to standby
14/05/2009 17:36:08      HFI: choose DPU FDIR mode Desynchro
14/05/2009 17:39:39      HFI: open dilution cooler valves
14/05/2009 18:48:52      HFI: setup REU Ns (40 Hz) and Fdiv (124) parameters
14/05/2009 18:52:33      HFI: set 4K cooler internal frequency at 40Hz
14/05/2009 19:05:45      HFI: activate the 6 nominal cernox thermometers
14/05/2009 19:08:51      HFI: synchronise the 4K cooler clock (External)
14/05/2009 19:23:47      HFI: set the 4K cooler amplitude demand at 2000 microns
14/05/2009 19:28:42      HFI: power on the nominal 4K getter heater
14/05/2009 19:35:31      HFI: start the 4K cooler compressors
15/05/2009 12:00:00      therm: stop the Focal Plane Unit 250K heating
15/05/2009 19:17:06      slew: OCM LEOP (MAN-01a)
16/05/2009 12:06:55      HFI: switch on all REU analog belts
16/05/2009 12:17:23      HFI: REU FPGA reset
16/05/2009 12:26:40      HFI: start the 4K cooler compressors
16/05/2009 12:31:16      HFI: set the JFET PID heaters at 110K
16/05/2009 12:49:26      HFI: set the channel compression parameters
16/05/2009 12:54:37      HFI: raw signal cycle on channels
16/05/2009 14:20:15      HFI: science data production starts
16/05/2009 14:48:30      HFI: channel setup [all channels]
16/05/2009 15:41:23      HFI: VI measurement [bolos, thermos, resistor]
16/05/2009 16:00:00      HFI: test end of slew
16/05/2009 17:51:43      HFI: set Cernox thermistor [4K-1.6K switch, 4K, 1.6K at 100K-200K]
17/05/2009 12:28:32      HFI: set Cernox thermistor [0.1K nominal at 100K-200K]
18/05/2009 00:00:00      period: end of LEOP / start of Commissioning phase
01/06/2009 21:36:00      therm: end of reflectors anticontamination
02/06/2009 16:40:20      HFI: set the JFET PID heaters at 130K
02/06/2009 17:00:06      HFI: REU hardware test
02/06/2009 17:20:06      HFI: start the 4K cooler compressors
02/06/2009 17:39:56      HFI: save REU configuration in EEPROM
03/06/2009 17:24:00      therm: SCS active cooldown starts
```

```
05/06/2009 17:28:18      slew: OCM-z (MAN-02a)
06/06/2009 18:19:21      HFI: set Cernox thermistor [4K-1.6K switch, 4K, 1.6K at 40K-100K]
09/06/2009 16:29:33      HFI: activate the 18K-4K heat switch nominal (repeated every day till 24/06)
09/06/2009 22:28:02      HFI: Single Event Upset
11/06/2009 21:15:00      HFI: set Cernox thermistor [0.1K nominal at 40K-100K]
12/06/2009 03:00:00      HFI: QEC1 at 100K
12/06/2009 05:08:20      HFI: QEC1 at 100K [end]
12/06/2009 15:26:07      HFI: set Cernox thermistor [4K-1.6K switch, 4K, 1.6K at 19K-40K]
12/06/2009 15:32:10      HFI: PID setup [4K-1.6K switch PID activated at max power]
12/06/2009 15:33:31      HFI: PID setup [4K PID nominal at max power]
15/06/2009 03:00:00      HFI: LFER_A_test
15/06/2009 04:54:52      HFI: LFER_A_test [end]
17/06/2009 16:46:58      slew: OCM-z touch-up (MAN-02b)
18/06/2009 18:29:57      HFI: LFER_A
19/06/2009 13:12:53      HFI: LFER_A [end]
22/06/2009 10:11:08      HFI: set Cernox thermistor [0.1K nominal at 19K-40K]
23/06/2009 11:00:34      HFI: set Cernox thermistor [4K-1.6K switch, 4K, 1.6K at 9K-19K]
24/06/2009 10:40:15      HFI: PID setup [4K-1.6K switch PID desactivated]
24/06/2009 10:40:35      HFI: PID setup [4K PID nominal]
24/06/2009 10:44:36      HFI: activate the 18K-4K heat switch nominal for LFI test [1st attempt]
24/06/2009 10:49:01      HFI: set the 4K cooler amplitude demand at 3500 microns
24/06/2009 10:52:48      HFI: set the dilution cooler flow to FNOM2
24/06/2009 11:18:58      HFI: activate the 18K-4K heat switch nominal for LFI test [5th and last attempt]
26/06/2009 23:00:00      HFI: desactivate the 18K-4K heat switch nominal
27/06/2009 13:34:34      HFI: set Cernox thermistor [0.1K, 1.6K, 4K and 4K-1.6K switch at <9K]
28/06/2009 12:22:14      HFI: channel setup [R & C]
28/06/2009 12:53:22      HFI: 4K cooler amplitude tuning 1/2
29/06/2009 09:38:15      HFI: 4K cooler amplitude tuning 2/2
29/06/2009 11:58:41      HFI: channel setup [all 1.6K thermometers]
29/06/2009 12:08:27      HFI: VI measurement [1.6K thermometers]
29/06/2009 12:21:10      HFI: set the channel compression parameters [4K thermometers]
29/06/2009 12:29:51      HFI: channel setup [all 4K thermometers]
29/06/2009 12:38:30      HFI: VI measurement [4K thermometers]
29/06/2009 13:28:40      HFI: channel setup [4K PID nominal thermometer]
29/06/2009 13:31:24      HFI: PID setup [4K PID nominal]
29/06/2009 13:41:00      HFI: channel setup [4K PID nominal thermometer]
29/06/2009 14:56:15      HFI: channel setup [1.6K PID nominal thermometer]
29/06/2009 14:58:58      HFI: PID setup [1.6K PID nominal]
29/06/2009 15:07:42      HFI: set Cernox thermistor [0.1K nominal at 3.5K-9K]
29/06/2009 15:45:02      HFI: PID setup [4K PID nominal] (8 times hourly)
29/06/2009 21:59:57      HFI: LFER-B
30/06/2009 04:16:13      HFI: LFER-B [end]
30/06/2009 09:35:52      HFI: set Cernox thermistor [0.1K nominal at 2.2K-3.5K]
30/06/2009 10:41:53      HFI: channel setup [1.6K PID nominal thermometer]
30/06/2009 10:43:58      HFI: PID setup [1.6K PID nominal]
30/06/2009 10:57:31      HFI: channel setup [0.1K thermometers]
30/06/2009 12:35:07      HFI: set Cernox thermistor [0.1K nominal at 1.4K-2.2K]
```

```
30/06/2009 13:42:12      HFI: PID setup [1.6K PID nominal]
30/06/2009 14:20:51      HFI: VI measurement []
30/06/2009 18:09:59      HFI: set Cernox thermistor [0.1K nominal at <1.4 K]
30/06/2009 18:20:51      HFI: VI measurement []
30/06/2009 19:10:01      HFI: QEC2 at 1K
30/06/2009 21:18:31      HFI: QEC2 at 1K [end]
01/07/2009 00:20:51      HFI: VI measurement
01/07/2009 04:20:51      HFI: VI measurement
01/07/2009 12:10:01      HFI: QEC3 at 300mK
01/07/2009 14:18:21      HFI: QEC3 at 300mK [end]
01/07/2009 14:18:31      HFI: channel setup [bolometers at 200mk]
01/07/2009 15:20:51      HFI: VI measurement []
01/07/2009 19:20:51      HFI: VI measurement []
01/07/2009 23:20:51      HFI: VI measurement []
02/07/2009 04:20:51      HFI: VI measurement []
02/07/2009 08:20:51      HFI: VI measurement []
02/07/2009 09:24:41      HFI: channel setup [0.1K thermometers]
02/07/2009 10:35:26      HFI: channel setup [1.6K PID nominal thermometer]
02/07/2009 10:36:58      HFI: PID setup [1.6K PID nominal]
02/07/2009 11:15:46      slew: OCM Insertion (MAN-03a)
02/07/2009 12:34:36      HFI: set the dilution cooler flow to FNOM1
02/07/2009 13:58:16      HFI: set the channel compression parameters
03/07/2009 09:37:20      HFI: VI measurement [100mK bolometers]
03/07/2009 10:10:01      HFI: channel setup [bolometers at 100mk]
03/07/2009 10:17:56      HFI: set the dilution cooler flow to FMIN2
03/07/2009 12:50:00      HFI: PID setup [bolo PID activated]
03/07/2009 13:09:45      HFI: channel setup [thermo PID1R]
03/07/2009 13:10:58      HFI: PID setup [dilu PID activated]
03/07/2009 13:26:04      HFI: channel setup [1.6K PID nominal thermometer to 1.39 K]
03/07/2009 13:52:29      HFI: channel setup [1.6K PID nominal thermometer to 1.41 K]
03/07/2009 14:03:43      HFI: set the channel compression parameters
03/07/2009 16:15:01      HFI: QEC4 at 100mK
03/07/2009 18:23:21      HFI: QEC4 at 100mK [end]
03/07/2009 19:05:51      HFI: VI measurement []
03/07/2009 20:05:26      HFI: PID setup [1.6K PID nominal]
03/07/2009 22:00:02      HFI:  pre-RAW72
03/07/2009 23:13:08      HFI:  pre-RAW72 [end]
04/07/2009 02:00:00      therm: aphelion
04/07/2009 09:43:13      HFI: channel setup [1.6K PID nominal thermometer to 1.39 K]
04/07/2009 09:45:27      HFI: PID setup [1.6K PID nominal]
04/07/2009 20:26:32      HFI: channel setup [1.6K PID nominal thermometer]
04/07/2009 22:30:01      HFI: CPVA_01
05/07/2009 01:55:49      HFI: CPVA_01 [end]
05/07/2009 10:47:08      HFI: channel setup [1.6K PID nominal thermometer to 1.35 K]
05/07/2009 11:28:57      HFI: channel setup [1.6K PID nominal thermometer to 1.34 K]
05/07/2009 13:25:03      HFI: IBTU_01
06/07/2009 09:47:49      HFI: IBTU_01 [end]
```

```
06/07/2009 09:58:51      HFI: channel setup [1.6K PID nominal thermometer to 1.33 K]
06/07/2009 12:38:33      HFI: channel setup [1.6K PID nominal thermometer to 1.35 K]
06/07/2009 13:15:21      HFI: channel setup [100mK PID redundant to 98.5 mK]
07/07/2009 11:30:14      HFI: VI measurement [resistor, bolometers]
07/07/2009 13:24:37      HFI: set the channel compression parameters
07/07/2009 14:20:03      HFI: IBTU_02
08/07/2009 10:42:49      HFI: IBTU_02 [end]
08/07/2009 11:04:39      HFI: channel setup [1.6K PID nominal thermometer to 1.39 K]
08/07/2009 11:16:02      HFI: PID setup [1.6K PID redundant at 200 microW]
08/07/2009 11:24:40      HFI: channel setup [100mK PID redundant to 100.0 mK]
08/07/2009 23:00:01      HFI: LFER-B
09/07/2009 17:39:59      HFI: LFER-B [end]
09/07/2009 19:30:01      HFI: IBTU_03
10/07/2009 00:00:00      Start of CPV phase
10/07/2009 15:08:03      HFI: IBTU_03 [end]
10/07/2009 16:00:01      HFI: PHTU_01
11/07/2009 00:01:47      HFI: PHTU_01 [end]
11/07/2009 10:24:00      HFI: channel setup [4K PID nominal thermometer at 4.73 K]
11/07/2009 10:26:00      HFI: PID setup [desactivation of 4K PID redundant]
11/07/2009 10:50:16      HFI: 4KFT (bis)
11/07/2009 12:49:50      HFI: 4KFT (bis) [end]
11/07/2009 12:59:35      HFI: channel setup [1.6K PID nominal thermometer to 1.37 K]
11/07/2009 13:05:25      HFI: PID setup [1.6K PID redundant desactivated]
11/07/2009 14:10:01      HFI: XTLK_01
12/07/2009 00:34:38      HFI: Single Event Upset
12/07/2009 00:42:05      HFI: XTLK_01 [end]
12/07/2009 01:00:02      HFI:  RAW72_02
12/07/2009 07:00:10      HFI:  RAW72_02 [end]
12/07/2009 11:53:22      HFI: DPU soft reboot
12/07/2009 12:18:13      HFI: back to nominal
12/07/2009 13:02:33      HFI: channel setup [capacitor]
12/07/2009 13:22:13      HFI: set the channel compression parameters
12/07/2009 13:31:21      HFI: 01TO_01
13/07/2009 01:30:01      HFI: 01TO_01 [end]
13/07/2009 11:12:32      HFI: channel setup [4K PID nominal thermometer at 4.80 K]
13/07/2009 13:03:50      HFI: channel setup [4K PID nominal thermometer at 4.66 K]
13/07/2009 13:26:23      HFI: channel setup [4K PID nominal thermometer at 4.64 K]
14/07/2009 09:50:15      HFI: PID setup [1.6K PID redundant to 200 microW]
14/07/2009 13:12:01      HFI: PID setup [1.6K PID redundant to 260 microW]
14/07/2009 13:14:22      HFI: channel setup [1.6K PID nominal thermometer to 1.38 K]
15/07/2009 09:16:02      slew: OCM Insertion touch-up (MAN-03b)
15/07/2009 09:46:54      HFI: channel setup [4K PID nominal thermometer at 4.66 K]
16/07/2009 09:21:29      HFI: PID setup [4K PID redundant to 0.8 mW]
16/07/2009 09:23:30      HFI: channel setup [4K PID nominal thermometer at 4.68 K]
17/07/2009 09:26:56      HFI: PID setup [4K PID redundant to 1.2 mW]
17/07/2009 09:30:08      HFI: channel setup [4K PID nominal thermometer at 4.70 K]
17/07/2009 11:12:09      HFI: channel setup [1.6K PID nominal thermometer to 1.39 K]
```

```
17/07/2009 11:23:02      HFI: channel setup [thermometers]
17/07/2009 14:00:01      HFI: LFER_02
18/07/2009 08:40:59      HFI: LFER_02 [end]
18/07/2009 09:51:16      HFI: channel setup [1.6K PID nominal thermometer to 1.40 K]
18/07/2009 19:10:19      therm: elephant
19/07/2009 11:09:09      HFI: channel setup [100mK PID redundant to 100.5 mK]
20/07/2009 10:59:16      HFI: PID setup [1.6K PID redundant desactivated]
20/07/2009 12:53:40      HFI: channel setup [1.6K PID nominal thermometer to 1.37 K]
21/07/2009 10:05:59      HFI: channel setup [4K PID nominal thermometer at 4.72 K]
21/07/2009 13:02:01      HFI: channel setup [bolo PID at 102.3 mK]
21/07/2009 13:11:48      HFI: PID setup [bolo PID]
22/07/2009 10:21:20      HFI: channel setup [1.6K PID nominal thermometer to 1.38 K]
22/07/2009 10:26:49      HFI: PID setup [bolo PID]
23/07/2009 09:23:42      HFI: decrease the 4K cooler amplitude demand to 3450 microns
23/07/2009 09:47:32      HFI: PID setup [4K PID redundant at max power]
23/07/2009 09:54:04      HFI: channel setup [4K PID nominal thermometer at 4.77 K]
23/07/2009 10:53:39      HFI: channel setup [4K PID nominal thermometer at 4.80 K]
24/07/2009 10:44:08      HFI: PID setup [bolo PID]
24/07/2009 22:30:00      HFI: 4KTO
25/07/2009 08:30:00      HFI: 4KTO [end]
27/07/2009 01:56:42      HFI: Single Event Upset
27/07/2009 09:21:28      HFI: PID setup [4K PID redundant to 0,84 mW]
27/07/2009 09:27:54      HFI: 4K memory HCT dump
27/07/2009 09:56:06      HFI: channel setup [bolo PID at 103.0 mK]
27/07/2009 13:01:32      HFI: set the channel compression parameters (increase of the HFI telemetry rate)
28/07/2009 09:31:34      HFI: channel setup [nominal bolo PID]
28/07/2009 09:38:16      HFI: channel setup [100mK PID redundant to 101.0 mK]
28/07/2009 12:30:34      HFI: channel setup [nominal bolo PID]
28/07/2009 12:46:13      HFI: channel setup [nominal bolo PID]
31/07/2009 16:00:00      HFI: SUNI_1_1
01/08/2009 00:00:00      HFI: SUNI_1_2
01/08/2009 10:55:00      HFI: SPIN day 1 : RPM@1.05
02/08/2009 12:20:00      HFI: SPIN day 2 : RPM@0.95
03/08/2009 11:53:37      HFI: SPIN day 3 : RPM@1.00
03/08/2009 11:53:37      HFI: SPIN day 4 : RPM@1.00
05/08/2009 09:36:01      slew: 1.7' slews test
06/08/2009 10:00:00      HFI: SUNI_2_1
06/08/2009 17:31:31      HFI: 4K Charge Regulator Unit anomalous shutdown
06/08/2009 18:00:00      HFI: SUNI_2_2
07/08/2009 12:20:01      HFI: set Cernox thermistor [4K-1.6K switch, 4K, 1.6K]
07/08/2009 13:40:43      HFI: 4K CDE software reset
07/08/2009 13:45:43      HFI: activate the 4K VCS
07/08/2009 13:46:23      HFI: select the harmonic forces
07/08/2009 13:47:56      HFI: set the 4K cooler amplitude demand at 2000 microns
07/08/2009 13:49:28      HFI: start the 4K cooler compressors
07/08/2009 13:53:23      HFI: set the 4K cooler amplitude demand at 2500 microns
07/08/2009 13:55:16      HFI: set the 4K cooler amplitude demand at 3000 microns
```

```
07/08/2009 13:58:50      HFI: 4K getter on
07/08/2009 17:54:56      HFI: stop the 4K cooler compressors
07/08/2009 17:57:22      HFI: desactivate the 4K VCS
07/08/2009 17:58:17      HFI: set the 4K cooler amplitude demand at 3500 microns
07/08/2009 17:59:41      HFI: start the 4K cooler compressors
07/08/2009 18:41:27      HFI: PID setup [4K PID redundant]
08/08/2009 10:05:25      HFI: stop the 4K cooler compressors
08/08/2009 10:07:41      HFI: activate the 4K VCS
08/08/2009 10:08:09      HFI: select the harmonic forces
08/08/2009 10:08:52      HFI: set the 4K cooler amplitude demand at 3450 microns
08/08/2009 10:10:26      HFI: start the 4K cooler compressors
08/08/2009 10:48:56      HFI: set Cernox thermistor [4K-1.6K switch, 4K, 1.6K]
08/08/2009 11:48:33      HFI: PID setup [dilu PID activated]
08/08/2009 11:55:25      HFI: PID setup [4K PID redundant to 0,84 mW]
08/08/2009 14:05:36      period: first light survey
09/08/2009 03:58:53      star tracker switchover #1
11/08/2009 09:44:16      HFI: channel setup [100mK thermometers]
12/08/2009 10:24:46      HFI: channel setup [100mK PID redundant]
12/08/2009 10:29:52      HFI: PID setup [dilu PID]
12/08/2009 14:13:45      <span style="background:#00FF00">period: DPC survey#1 (ring#240)</span>
14/08/2009 12:30:10      slew: orbit maintenance manoeuvre #1
18/08/2009 11:43:42      long ring #440 for CDMU patch day 1
18/08/2009 12:39:09      sat: CDMU patch (day 1)
18/08/2009 12:39:20      sat: CDMU patch (end of day 1)
19/08/2009 11:49:40      long ring #474 for CDMU patch day 2
19/08/2009 12:45:31      sat: CDMU patch (day 2)
19/08/2009 12:45:34      sat: CDMU patch (end of day 2)
20/08/2009 11:53:46      long ring #509 for CDMU patch day 3
20/08/2009 12:45:32      sat: CDMU patch (day 3)
20/08/2009 12:45:36      sat: CDMU patch (end of day 3)
21/08/2009 11:56:03      long ring #544 for CDMU patch
21/08/2009 14:18:48      HFI: clock resynchronisation
22/08/2009 09:36:51      dtcp: transition to 3 h DTCP duration
31/08/2009 12:09:14      long ring #897 to allow the execution of the ACMS warm reset
31/08/2009 13:40:00      thrusters catbed heaters are switched off by error
31/08/2009 13:40:01      sat: FOG telemetry is disabled by error
31/08/2009 13:41:05      long ring #898 to allow the execution of the ACMS warm reset
04/09/2009 15:01:00      thurster under/over performed
11/09/2009 21:00:41      slew: orbit maintenance manoeuvre #2
16/09/2009 20:31:41      thrusters catbed heaters are switched back on
18/09/2009 19:06:15      planet: HFI Crab scan#1
20/09/2009 19:36:00      dtcp: extra pass CEB
20/10/2009 23:44:24      therm: HFI elephant LONG deltaT>10uK
22/10/2009 19:34:56      planet: HFI Mars scan#1
24/10/2009 11:01:39      therm: HFI elephant LONG deltaT>10uK
25/10/2009 15:30:49      planet: HFI Jupiter scan#1
28/10/2009 23:06:00      thurster under/over performed
```

```
01/11/2009 00:41:04      planet: HFI Neptune scan# 1
20/11/2009 18:52:25      long ring #3589 (29 hours) : no slew due to MTL uplink problem
21/11/2009 23:39:54      slew : resumption of SL after the MTL problem
22/11/2009 19:48:41      slew to SGR position
23/11/2009 08:47:54      slew to catchup
23/11/2009 19:48:10      SGR (end): back to nominal scanning law
25/11/2009 05:56:00      HFI: 1.6K stage event
26/11/2009 14:32:00      thurster under/over performed
04/12/2009 17:49:29      slew: orbit maintenance manoeuvre #3
05/12/2009 09:43:53      planet: HFI Uranus scan# 1
16/12/2009 20:42:11      sat: FOG telemetry is enabled back
21/12/2009 19:59:54      HFI: set the channel compression parameters
22/12/2009 11:46:18      dtcp: extra pass
03/01/2010 00:00:00      therm: perihelia
04/01/2010 00:25:49      planet: HFI Saturn scan#1
11/01/2010 19:16:32      star tracker switchover #2
15/01/2010 21:57:45      slew: orbit maintenance manoeuvre #4
25/01/2010 21:16:41      sat: transponder always on
08/02/2010 20:51:32      <span style="background:#00FF00">period: DPC survey#2 (ring#5721)</span>
26/02/2010 12:43:37      star tracker switchover #3
26/02/2010 23:02:49      slew: orbit maintenance manoeuvre #5
06/03/2010 05:04:43      planet: HFI Crab scan#2
01/04/2010 06:41:00      thurster under/over performed
02/04/2010 13:48:21      therm: major elephant
05/04/2010 10:00:00      solar flare: geomagnetic storm
10/04/2010 10:36:35      planet: HFI Mars scan#2
26/04/2010 17:55:37      slew: orbit maintenance manoeuvre #6
29/04/2010 17:34:58      therm: SCS TSA setpoint increase
06/05/2010 17:02:08      therm: SCS TSA setpoint increase
13/05/2010 16:30:13      therm: SCS TSA setpoint increase
17/05/2010 17:51:09      planet: HFI Neptune scan# 2
12/06/2010 01:00:00      solar flare
12/06/2010 01:57:16      planet: HFI Saturn scan#2
24/06/2010 18:31:09      therm: SCS TSA setpoint increase
30/06/2010 19:00:53      planet: HFI Uranus scan#2
03/07/2010 20:01:43      planet: HFI Jupiter scan#2
06/07/2010 11:00:00      therm: aphelion
14/07/2010 20:45:50      dtcp: extra pass
15/07/2010 18:13:43      therm: SCS TSA setpoint increase
18/07/2010 04:28:00      thurster under/over performed
21/07/2010 21:08:44      therm: moon transit
22/07/2010 00:42:59      therm: moon transit (end)
24/07/2010 16:36:11      therm: HFI elephant LONG deltaT>10uK
29/07/2010 17:45:52      therm: SCS TSA setpoint increase
03/08/2010 19:00:00      solar flare: possible geomagnetic storm
11/08/2010 10:14:37      long ring #11149 for SCS switchover
11/08/2010 11:00:00      therm: SCS switchover
```

```
11/08/2010 11:00:30      HFI: PID setup [1.6K PID nominal and 4K PIDs desactivated]
11/08/2010 17:17:50      HFI: deselect all 4K harmonics for VCS
11/08/2010 18:50:15      HFI: select all 4K harmonics for VCS
11/08/2010 18:52:44      HFI: PID setup [1.6K PID nominal and 4K PIDs reactivated]
11/08/2010 21:34:10      dtcp: extra pass CEB
12/08/2010 00:06:59      HFI: PID setup [4K PID redundant set to 1.14 mW]
12/08/2010 19:27:28      <span style="background:#00FF00">period: DPC survey#3 (ring#11195)</span>
13/08/2010 23:59:21      slew to interleaved pointings for survey#3
14/08/2010 11:00:00      solar flare
16/08/2010 18:00:09      slew: orbit maintenance manoeuvre #7
18/08/2010 08:35:00      solar flare
25/08/2010 17:51:58      HFI: 4K memory HCT dump
18/09/2010 18:28:04      planet: HFI Crab scan#3
04/10/2010 04:25:00      HFI: 1.6K stage event
04/10/2010 04:57:05      therm: HFI elephant SHORT deltaT>10uK
06/10/2010 19:00:46      dtcp: extra pass CEB
11/10/2010 13:26:47      long ring  #13333: manoeuvre failed
03/11/2010 08:11:34      planet: HFI Neptune scan#3
04/11/2010 13:20:14      therm: change of the DPU2 thermal control
04/11/2010 19:19:00      dtcp: extra pass NNO
11/11/2010 12:45:00      therm: SCS TSA setpoint increase
21/11/2010 03:02:51      therm: HFI elephant LONG deltaT>10uK
24/11/2010 11:23:01      long ring  #14627 for star tracker tests
24/11/2010 12:29:29      star tracker switchover for intercalibration test (STR1->STR2)
24/11/2010 20:23:53      slew back
25/11/2010 17:02:45      long ring  #14653 for star tracker tests
25/11/2010 17:59:37      star tracker switchover STR2->STR1
26/11/2010 01:55:21      slew back to nominal scanning strategy
27/11/2010 20:20:00      solar flare
02/12/2010 13:21:13      slew: orbit maintenance manoeuvre #8
06/12/2010 20:38:00      planet: HFI Jupiter scan#3
10/12/2010 14:55:44      planet: HFI Uranus scan#3
15/12/2010 08:19:00      thurster under/over performed
15/12/2010 10:30:00      thurster under/over performed
22/12/2010 16:33:14      HFI: Single Event Upset
23/12/2010 15:44:53      therm: SCS TSA setpoint increase
03/01/2011 19:00:00      therm: perihelia
18/01/2011 05:25:24      planet: HFI Saturn scan#3
24/01/2011 13:20:09      therm: SCS warm radiator warming
24/01/2011 17:28:00      dtcp: extra pass CEB
28/01/2011 02:00:00      solar flare
31/01/2011 14:06:49      slew: orbit maintenance manoeuvre #9
01/02/2011 13:31:33      therm: SCS TSA setpoint increase
08/02/2011 20:55:48      <span style="background:#00FF00">period: DPC survey#4 (ring#16692)</span>
10/02/2011 02:48:02      HFI: 1.6K stage event
15/02/2011 06:00:00      solar flare: X ray solar flare
18/02/2011 00:00:00      solar flare: X ray solar flare
```

```
24/02/2011 14:05:28      therm: SCS TSA setpoint increase
28/02/2011 23:20:41      slew: acceleration for Crab scan
06/03/2011 04:12:44      planet: HFI Crab scan#4
07/03/2011 21:00:00      solar flare: coronal mass ejection
10/03/2011 19:44:00      dtcp: extra pass CEB
15/03/2011 17:42:31      therm: SCS desorption power gap jump
15/03/2011 20:35:00      dtcp: extra pass
18/03/2011 15:15:00      dtcp: long pass (5h30mn)
21/03/2011 03:30:00      solar flare: radiation event
21/03/2011 21:10:17      slew: orbit maintenance manoeuvre #10
31/03/2011 21:02:52      therm: SCS TSA setpoint increase
07/04/2011 20:38:16      therm: SCS TSA setpoint increase
14/04/2011 21:03:33      therm: SCS TSA setpoint increase
21/04/2011 20:33:20      therm: SCS TSA setpoint increase
10/05/2011 16:48:13      therm: SCS TSA setpoint increase
20/05/2011 14:18:21      planet: HFI Neptune scan#4
04/06/2011 22:00:00      solar flare: geomagnetic storm
07/06/2011 07:00:00      solar flare: solar proton enhancement
23/06/2011 04:55:03      thurster under/over performed
29/06/2011 17:03:39      planet: HFI Saturn scan#4
04/07/2011 15:00:00      therm: aphelion
05/07/2011 22:00:17      planet: HFI Uranus scan#4
25/07/2011 17:38:00      slew: orbit maintenance manoeuvre #11
27/07/2011 16:51:00      on board mass properties update
29/07/2011 17:13:00      slew to survey#5
29/07/2011 17:43:32      <span style="background:#00FF00">period: DPC survey#5 (ring#21721)</span>
02/08/2011 07:00:00      solar flare: M1 class
03/08/2011 21:09:40      planet: HFI Jupiter scan#4
04/08/2011 04:30:00      solar flare
04/08/2011 15:55:38      therm: SCS TSA setpoint increase
08/08/2011 16:53:00      SGR: scanning law is interrupted
08/08/2011 17:32:00      slew back
08/08/2011 18:00:00      solar flare: X7 class
08/08/2011 18:44:00      planet: HFI Jupiter scan#4 (bis)
09/08/2011 01:54:00      slew to the catchup position
09/08/2011 08:00:00      solar flare
09/08/2011 17:23:00      SGR (end): back to nominal scanning law
06/09/2011 02:20:00      solar flare: M5.3
06/09/2011 23:00:00      solar flare: X2.1
13/09/2011 09:34:22      planet: HFI Crab scan#5
17/09/2011 08:00:00      solar flare: magnetic storm
20/09/2011 09:43:00      slew setting-up the second crab scan
20/09/2011 10:41:38      planet: HFI Crab scan#5 (bis)
21/09/2011 16:43:41      planet: HFI Crab scan#6
21/09/2011 18:33:00      dtcp: extra pass
22/09/2011 12:00:00      solar flare: complexe event
24/09/2011 00:42:34      slew back to survey 5 scanning strategy
```

```
26/09/2011 12:29:45      slew : station keeping manoeuvre half failed
04/10/2011 12:35:07      slew: orbit maintenance manoeuvre #12 bis
11/10/2011 12:35:13      HFI:  temperature steps on bolometer PID
12/10/2011 10:30:00      HFI:  EOL-Fast VI at 100mK
22/10/2011 14:00:00      solar flare: small event
27/10/2011 12:38:38      therm: SCS TSA setpoint increase
04/11/2011 00:00:00      solar flare: X2 class
07/11/2011 09:00:00      HFI : pre-EOL-LFER-1
07/11/2011 11:06:54      HFI : pre-EOL-LFER-1 [end]
08/11/2011 10:42:00      HFI:  EOL-IBTU
08/11/2011 16:10:03      HFI:  EOL-IBTU [end]
14/11/2011 09:00:00      HFI:  2nd pre-EOL-LFER-1
14/11/2011 11:08:42      HFI:  2nd pre-EOL-LFER-1 [end]
14/11/2011 23:58:33      slew: beginning of dwell duration compression phase
18/11/2011 00:00:00      HFI:  EOL-LFER-1
20/11/2011 14:33:42      HFI:  EOL-LFER-1 [end]
26/11/2011 07:00:00      solar flare: Radiation storm and Coronal Mass Ejection
28/11/2011 17:10:00      dtcp: extra pass
07/12/2011 17:00:00      spinup test at 1.4RPM
08/12/2011 10:00:00      planet: HFI Mars scan @ 1.4 RPM
09/12/2011 16:43:00      star tracker unhealthy
16/12/2011 18:35:00      slew: back to scanning law
17/12/2011 18:00:00      planet: HFI Mars scan#3
23/12/2011 15:10:06      HFI: He3 flow rate 0 -> 1
25/12/2011 14:45:16      HFI:  HFI: PID setup [1.6K PID redundant add 153.4 uW]
25/12/2011 20:00:00      solar flare: C-class
27/12/2011 11:42:10      HFI:  temperature steps on the bolometer plate II
27/12/2011 13:48:45      HFI:  temperature steps on the bolometer plate II [end]
29/12/2011 14:24:29      HFI: He3 flow rate 1 -> 2
02/01/2012 13:58:00      HFI: He3 flow rate 2 -> 3
03/01/2012 14:20:19      HFI:  temperature steps on bolo plate III (1st part)
04/01/2012 13:52:00      HFI: He3 flow rate 3 -> 4
04/01/2012 16:00:00      HFI:  temperature steps on bolo plate III (2nd part)
06/01/2012 00:00:00      HFI:  temperature steps on bolo plate III (2nd part) [end]
07/01/2012 14:10:52      HFI: He3 flow rate 4 -> 5
08/01/2012 07:20:00      slew to Jupiter deep annuli scan
09/01/2012 14:23:36      HFI: He3 flow rate 5 -> 6
10/01/2012 04:20:00      planet: HFI Jupiter scan
11/01/2012 14:48:04      HFI: He3 flow rate 6 -> 7
13/01/2012 15:04:33      HFI:  HFI: PID setup [1.6K PID and dilu PID desactivated]
14/01/2012 16:00:00      <span style="background:#00FF00">period: end of HFI nominal operations</span>
16/01/2012 15:00:00      HFI channel setup [100mK thermometers]
16/01/2012 15:00:12      HFI: bolo plate at 110mK
16/01/2012 15:45:09      HFI: bolo plate at 300mK
17/01/2012 14:13:54      HFI: set Cernox thermistor [0.1K nominal at 1.4K]
18/01/2012 15:20:10      HFI: set the channel compression parameters
18/01/2012 16:15:11      HFI:  EOL-Fast VI at 300 mK
```

```
19/01/2012 14:30:52      HFI: channel setup [bolometers]
20/01/2012 19:58:08      HFI:  EOL-RAW54 at 300mK
21/01/2012 13:29:58      HFI:  EOL-RAW54 at 300mK [end]
22/01/2012 00:18:00      therm: loss of satellite thermal control
22/01/2012 15:00:00      CDMU PM-A reset
22/01/2012 22:59:58      HFI: DPU soft reboot
23/01/2012 05:00:00      solar flare: major one
25/01/2012 14:45:00      HFI: set the channel compression parameters
27/01/2012 19:00:00      solar flare
30/01/2012 21:53:00      period: slew to survey#6
07/02/2012 00:00:00      slew: large orbit correction manœuvre
10/02/2012 16:30:00      HFI:  EOL-Fast VI at 600 mK
14/02/2012 14:20:00      therm: CDMU PM-A switch over
20/02/2012 10:00:00      HFI: set the channel compression parameters (EOL#0)
20/02/2012 14:57:00      slew: touchup manœuvre
21/02/2012 15:00:00      HFI: set the channel compression parameters (EOL#1)
21/02/2012 15:16:00      HFI: set the channel compression parameters (EOL#2)
22/02/2012 16:50:00      HFI: set the channel compression parameters (EOL#3)
23/02/2012 15:20:00      HFI: set the channel compression parameters (EOL#4)
```

LFI Design, qualification and performance

LFI design, qualification and performance

The Planck-LFI instrument is an array of 11 radiometric receivers in the Ka, Q and V bands, with centre frequencies close to 30, 44 and 70 GHz. The exact centre frequencies for each receiver are reported in #planck2011-1-4 Planck early paper III [1]; for simplicity, here we will refer to the three channels using their nominal centre frequency. A detailed description of the LFI instrument is given in #bersanelli2010 Planck pre-launch paper 4 [2], and references therein.

The heart of the LFI instrument is a compact, multi-frequency array of differential receivers with ultra-low-noise amplifiers based on cryogenic indium phosphide (InP) high-electron-mobility transistors (HEMTs). To minimise power dissipation in the focal plane unit, which is cooled to 20 K, the radiometers are split into two subassemblies connected by a set of waveguides, as shown in Fig. 1, left panel.

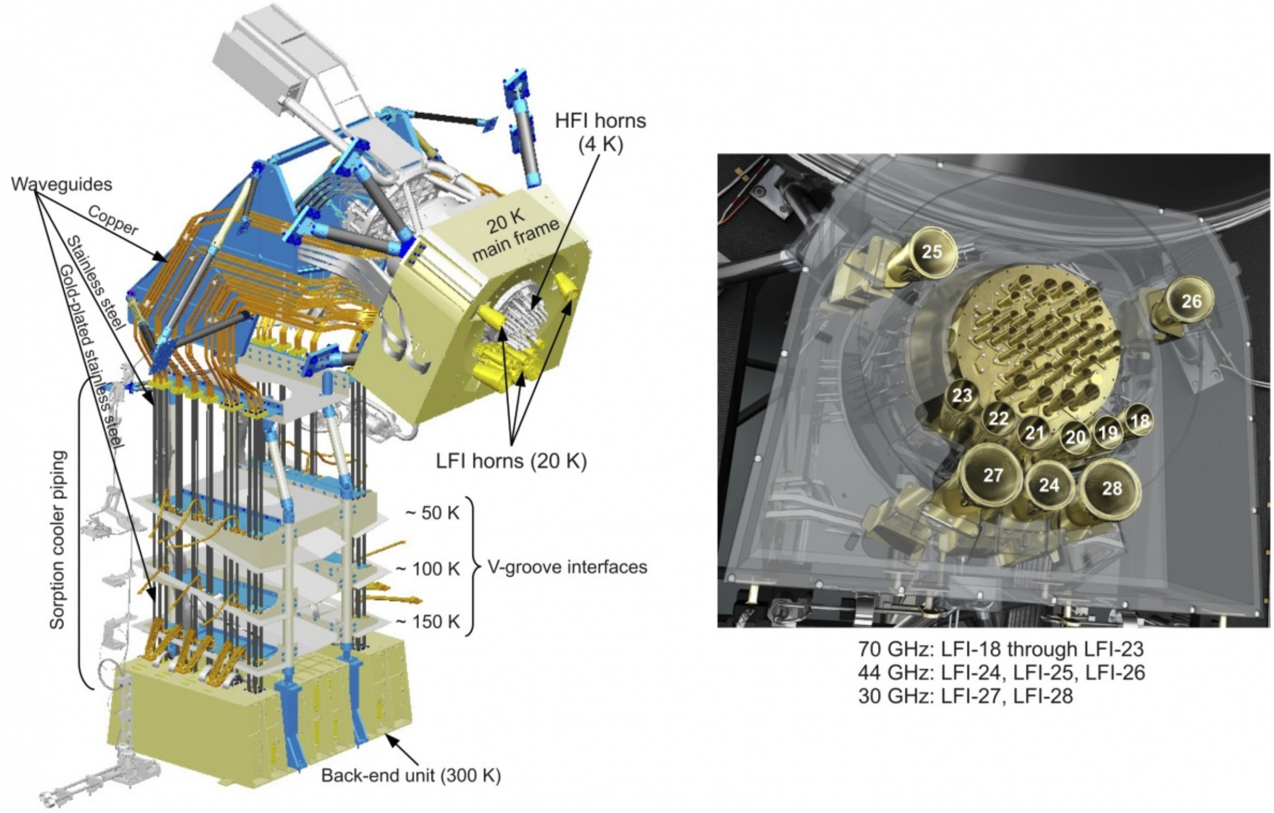
HFI horns
(4 K)
Waveguides
Copper
Stainless steel
Gold-plated stainless steel
20 K
main frame
Sorption cooler piping
LFI horns (20 K)
~ 50 K
~ 100 K
~ 150 K
V-groove interfaces
Back-end unit (300 K)
25
26
23
22
21
20
19
18
27
24
28
70 GHz: LFI-18 through LFI-23
44 GHz: LFI-24, LFI-25, LFI-26
30 GHz: LFI-27, LFI-28

Figure 1. Left Panel: the LFI instrument with main thermal stages, focal plane, waveguides and sorption cooler piping highlighted. Right Panel: Labelling of feed horns on the LFI focal plane.

The LFI horns are situated in a ring around the HFI, see Fig. 1 – right panel. Each horn collects radiation from the telescope and feeds it to one or more detectors. The radiometer design is driven by the need to suppress 1/f-type noise induced by gain and noise temperature fluctuations in the amplifiers, which would be unacceptably high for a simple total power system. A differential pseudo-correlation scheme is adopted, in which signals from the sky and from a black-body reference load are combined by a hybrid coupler, amplified in two independent amplifier chains, and separated out by a second hybrid (Fig. 2). The sky and the reference load power can then be measured and differenced. Since the reference signal has been subject to the same gain variations in the two amplifier chains as the sky signal, the true sky power can be recovered. Insensitivity to fluctuations in the back-end amplifiers and detectors is realized by switching phase shifters at ~8 kHz synchronously in each amplifier chain. The rejection of 1/f noise as well as the immunity to other systematic effects is optimised if the two input signals are nearly equal. For this reason the reference loads are cooled to ~4 K by mounting them on the 4-K structure of the HFI. In addition, the effect of the residual offset (< 2 K in nominal conditions) is reduced by introducing a gain modulation factor in the on-board processing to balance the output signal #Seiffert2002. The differencing receiver greatly improves the stability of the measured signal.

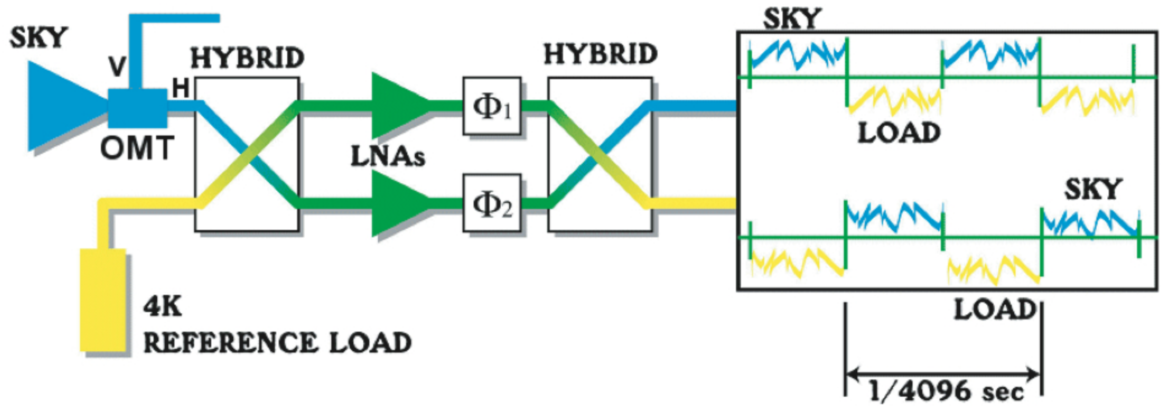

Figure 2. Schematic of the LFI front-end radiometer. The front-end unit is located at the focus of the Planck telescope, and comprises: dual profiled corrugated feed horns; low-loss (□0.2 dB), wide-band (> 20%) ortho-mode transducers; and radiometer front-end modules with hybrids, cryogenic low noise amplifiers, and phase switches.

References

<biblio force=false>

1. References

</biblio>

References

[1] http://www.rssd.esa.int/doc_fetch.php?id=3135856&page=1
[2] http://www.rssd.esa.int/doc_fetch.php?id=3135936&page=1

LFI design, qualification, and performance

Instrument description

The LFI instrument (see Fig. 1 in the LFI overview) consists of a 20 K focal plane unit hosting the corrugated feed horns, the orthomode transducers (OMTs) and the receiver front-end modules (FEMs). Forty four composite waveguides #darcangelo2009a are interfaced with three conical thermal shields and connect the front-end modules to the warm (~300 K) back-end unit (BEU) containing a further radio frequency amplification stage, detector diodes and all the electronics for data acquisition and bias supply.

Best LFI noise performance is obtained with receivers based on InP High Electron Mobility Transistor (HEMT) low noise amplifiers (LNAs) for minimal power dissipation and best performance. To further minimise power consumption in the focal plane, the radiometers are split into two sub-assemblies connected by waveguides, one located at the telescope focal area, the other on the 300 K portion of the Planck satellite. These design features allow the entire front-end LNAs dissipation to be <0.55 W, which enables the active cooling of the focal assembly. This is achieved with a vibration-less hydrogen sorption cooler, which also provides 18 K pre-cooling to the HFI helium J-T cooler. Two sorption cooler units are included in the flight hardware.

As shown schematically in Fig. 1 below, the LFI consists of the following subsystems:

- Radiometer Array Assembly (RAA)
- Sorption Cooler Subsystem (SCS)
- Radiometer Electronics Box Assembly (REBA)

The RAA includes the Front End Unit (FEU) and the Back End Unit (BEU), connected via waveguides. The FEU is located at the focus of the telescope, as one component of the joint LFI/HFI focal assembly (see sections below). The BEU is mounted on the top of the Planck service module (SVM). The REBA (Radiometer Electronics Box Assembly) and the warm parts of the Sorption Cooler System (SCS) are located on one of the lateral panels of the SVM. The FEU and the Sorption Cooler Compressor (SCC) are connected by concentric stainless steel tubes. The smaller tube carries hydrogen at ~60 atmospheres from the cooler compressors to the FEU, while the larger tube returns the hydrogen at ~0.3 atmospheres. These units are described in following sections and in the Annexes, the SCS is described in details in the Sorption Cooler section. All LFI units are linked together by the LFI harness, which also connects to the spacecraft interface.

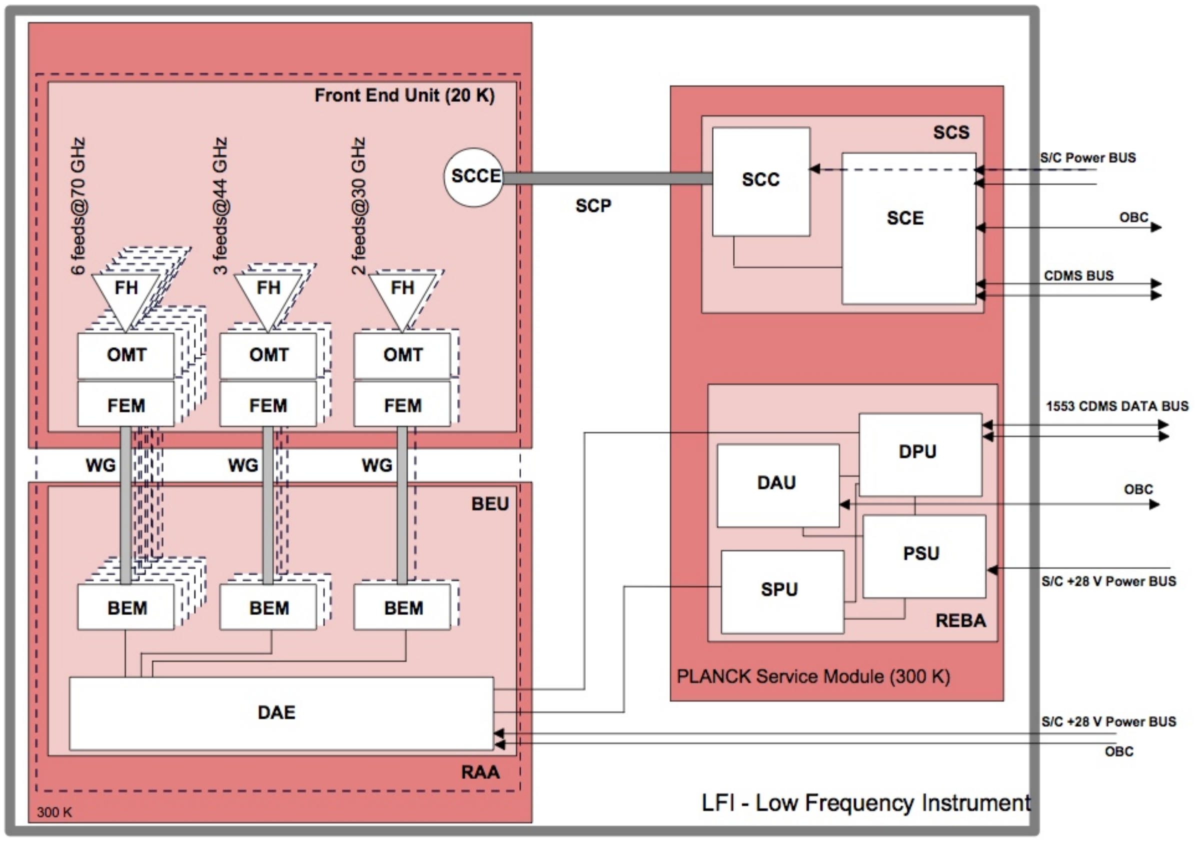
Front End Unit (20 K)
6 feeds@70 GHz
3 feeds@44 GHz
2 feeds@30 GHz
SCCE
FH
FH
FH
OMT
OMT
OMT
FEM
FEM
FEM
WG
WG
WG
BEU
BEM
BEM
BEM
DAE
RAA
300 K
SCP
SCS
SCC
SCE
S/C Power BUS
OBC
CDMS BUS
1553 CDMS DATA BUS
DPU
DAU
OBC
PSU
SPU
S/C +28 V Power BUS
REBA
PLANCK Service Module (300 K)
S/C +28 V Power BUS
OBC
LFI - Low Frequency Instrument

Figure 1. Block Diagram of LFI

Radiometer Array Assembly (RAA)

The Radiometer Array Assembly (RAA) consists of two main units (the front end unit, FPU and the Back End Unit, BEU), connected by a set of waveguides. The Focal Plane Unit (FPU) is the heart of the LFI instrument and it contains the feed array and associated orthomode transducers (OMTs) and FEMs, all cooled to 20 K by the sorption cooler. The FPU comprises a set of 11 modules, which are mounted on a mechanical support which meets the thermo-mechanical requirements of the instrument and adds thermal inertia. The BEU comprises the radiometer Back End Modules (BEM) and the Data Acquisition Electronics (DAE), which are connected by an internal harness. The HFI Unit is located inside the LFI FPU and supported by the LFI structure. The LFI structure gives the mechanical and thermal interface to the HFI unit with the proper stiffness and thermal de-coupling. The LFI structure also guarantees the proper alignment of the HFI detector with the telescope focal plane.

The time scale of the stability of the receiver is driven by the 1 rpm rotation speed of the spacecraft, which requires a very low 1/f-noise or gain variation of the low noise amplifiers and other components. The LFI uses a pseudo-correlation receiver concept (Fig. 2 below). This radiometer concept is chosen to maximise the stability of the instrument by reducing the effect of non-white noise generated in the radiometer itself. In this scheme, the difference between the inputs to each of the chains (the signal from the telescope and that from a reference black body respectively) is continuously being observed. To remove the effect of instability in the back-end amplifiers and detector diodes, it is necessary to switch the signal detected at the diodes at high rate. The signals from the sky and from a reference load are combined by a hybrid coupler, amplified in two independent amplifier chains, and separated out by another hybrid. The sky and the reference load power can then be measured and differenced. Since the reference signal has been subject to the same gain variations in the two amplifier chains as the sky signal, the true sky power can be recovered. The differencing receiver greatly improves the stability if the two input signals are almost equal, at a cost of a factor of $\sqrt{2}$in sensitivity compared to a perfectly stable total-power radiometer with the same noise temperature and bandwidth. This radiometer concept is capable of greatly reducing the knee frequency. We define as Radiometer Chain Assembly (RCA, see Fig. 2) each functional unit from the feed horn to the BEM. The RAA therefore includes a set of 11 RCAs and the Data Acquisition Electronics (see also Fig. 1 above), all mounted on a suitable mechanical structure. Although there are differences in the details of the radiometer chains at different frequencies, their overall configuration is similar, and a general description of its design is provided in this section. Planck LFI has 11 Radiometer Chain Assembly (RCA). Each RCA is constituted by feed horn and FEM in the FEU (at 20 K), BEM (at 300 K) in the BEU and four waveguides that connect each FEM-BEM couple. The frequency distribution of the RCA is the following:

- 2 RCAs at 30 GHz;
- 3 RCAs at 44 GHz;
- 6 RCAs at 70 GHz.

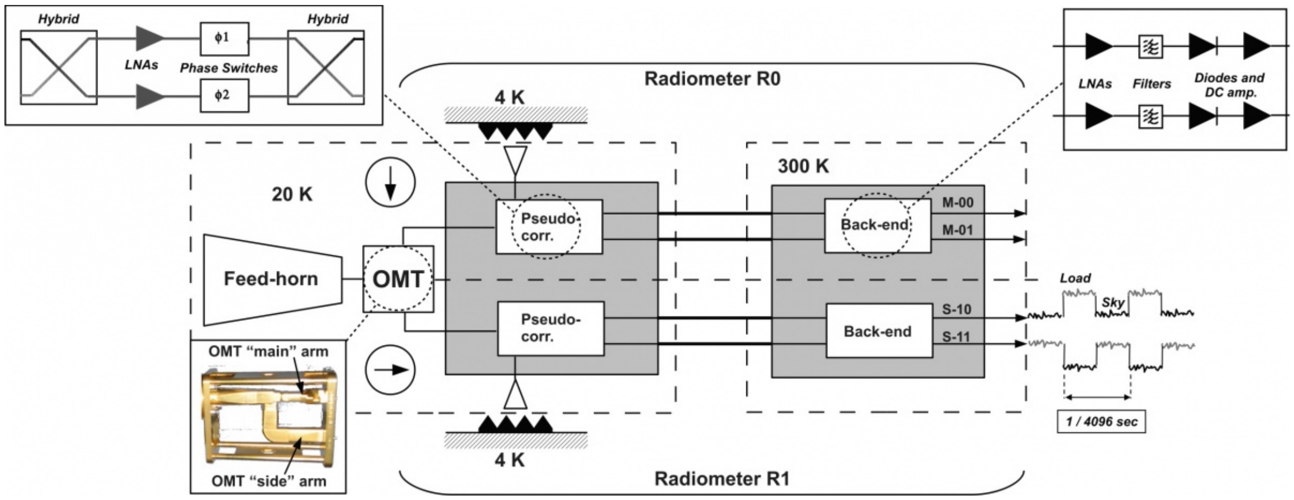

Figure 2. A complete RCA from feed-horn to analog voltage output. The insets show the OMT, the details of the 20 K pseudo-correlator and of the back-end radio-frequency amplification, low-pass filtering, detection and DC amplification.

Radiometer Chain Assembly (RCA)

Every RCA consists of two radiometers, each feeding two diode detectors (see Fig. 2 above), for a total of 44 detectors. The 11 RCAs are labelled by a numbers from 18 to 28 as outlined in Fig. 1 in LFI overview, right panel.

Fig. 2 provides a more detailed description of each radiometric receiver. In each RCA, the two perpendicular linear polarisation components split by the OMT propagate through two independent pseudo-correlation differential radiometers, labelled as *M* or *S* depending on the arm of the OMT they are connected to (*Main* or *Side*, see lower-left inset of Fig. 2).

In each radiometer the sky signal coming from the OMT output is continuously compared with a stable 4 K blackbody reference load mounted on the external shield of the HFI 4 K box #valenziano2009. After being summed by a first hybrid coupler, the two signals are amplified by ~30 dB, see upper-left inset of Fig. 2. The amplifiers were selected for best operation at low drain voltages and for gain and phase match between paired radiometer legs, which is crucial for good balance. Each amplifier is labelled with codes *1*, *2* so that the four outputs of the LNAs can be named with the sequence: *M1*, *M2* (radiometer *M*) and *S1*, *S2* (radiometer *S*). Tight mass and power constraints called for a simple design of the Data Acquisition Electronics (DAE) box so that power bias lines were divided into five common-grounded power groups with no bias voltage readouts; only the total drain current flowing through the front-end amplifiers is measured and is available to the house-keeping telemetry (this design has important implications for front-end bias tuning, which depends critically on the satellite electrical and thermal configuration and was repeated at all integration stages, during on-ground and in-flight satellite tests). A phase shift (or phase switch) alternating between 0° and 180° at the frequency of 4096 Hz is applied in one of the two amplification chains and then a second hybrid coupler separates back the sky and reference load components that are further amplified and detected in the warm BEU, with a voltage output ranging from -2.5 V to +2.5 V.

Each radiometer has two output diodes which are labelled with binary codes *00*, *01* (radiometer *M*) and *10*, *11* (radiometer *S*), so that the four outputs of each radiometric chain can be named with the sequence: *M-00*, *M-01*, *S-10*, *S-11*.

After detection, an analog circuit in the DAE box removes a programmable offset in order to obtain a nearly null DC output voltage and a programmable gain is applied to increase the signal dynamics and optimally exploit the ADC input range. After the ADC, data are digitally down-sampled, re-quantised and compressed in the REBA according to a scheme described in #herreros2009, maris2009, before preparing telemetry packets. On ground, telemetry packets are converted to sky and reference load time ordered data after calibrating the ADU samples into volt considering the applied offset and gain factors.

To first order, the mean differential power output for each of the four receiver diodes can be written as follows #seiffert2002, mennella2003, bersanelli2010 Planck early paper IV [2]:

where $G_{\rm tot}$ is the total gain, k is the Boltzmann constant, β the receiver bandwidth and a is the diode constant. $T_{\rm sky}$ and $T_{\rm ref}$ are the average sky and reference load antenna temperatures at the inputs of the first hybrid and $T_{\rm noise}$ is the receiver noise temperature.
The gain modulation factor #mennella2003, planck2011-1-6 Planck early paper V [1], r, is defined by:

and is used to balance (in software) the temperature offset between the sky and reference load signals and minimise the residual 1/f noise in the differential datastream. This parameter is calculated from the average uncalibrated total power data using the relationship:

where $< V_{\rm sky} >$ and $< V_{\rm ref} >$ are the average sky and reference voltages calculated in a defined time range. The white noise spectral density at the output of each diode is essentially independent from the reference-load absolute temperature and is given by:
If the front-end components are not perfectly balanced, then the separation of the sky and reference load signals after the second hybrid is not perfect and the outputs are mixed. First-order deviations in white noise sensitivity from the ideal behaviour are caused mainly by noise temperature and phase-switch amplitude mismatches. Following the notation used in #seiffert2002, we define ϵ_{Tn}, the imbalance in front end noise temperature, and ϵ_{A1} and ϵ_{A2}, the imbalance in signal attenuation in the two states of the phase switch. Equation above for the two diodes of a slightly imbalanced radiometer then becomes

which is identical for the two diodes apart from the sign of the term , representing the phase switch amplitude imbalance. This indicates that the isolation loss caused by this imbalance generates an anti-correlation between the white noise levels of the single-diode data streams. For this reason, the LFI scientific data streams are obtained by averaging the voltage outputs from the two diodes in each radiometer:

where w_1 and w_2 are inverse-variance weights calculated from the data as discussed in #planck2011-1-6. This way, the diode-diode anti-correlation is cancelled, and the radiometer white noise becomes

In Equations above, , while α is a term given by:

See Diode Combination section for the details of the diode combination procedure.

In Fig. 3 below we show a close-up of the two front end modules of an RCA with the four phase switches which are labelled with the four letters *A* and *B* (main arm), *C* and *D* (side arm). Each phase switch is characterised by two states: state 0 (no phase shift applied to the incoming wave) and state 1 (180° phase shift applied) and can either stay fixed in a state or switch at 4 kHz between the two states.

Phase switches are clocked and biased by the DAE and their configuration can be programmed via telecommand. In order to simplify the instrument electronics, phase switches are configured and operated in pairs: *A/C* and *B/D*. This means that if phase switches *A* and *C* are switching at 4 kHz then *B* and *D* are fixed both in the same state (either 0 or 1). This simplification, required during the design phase to comply with mass and power budgets, comes at the price of loosing some setup redundancy.

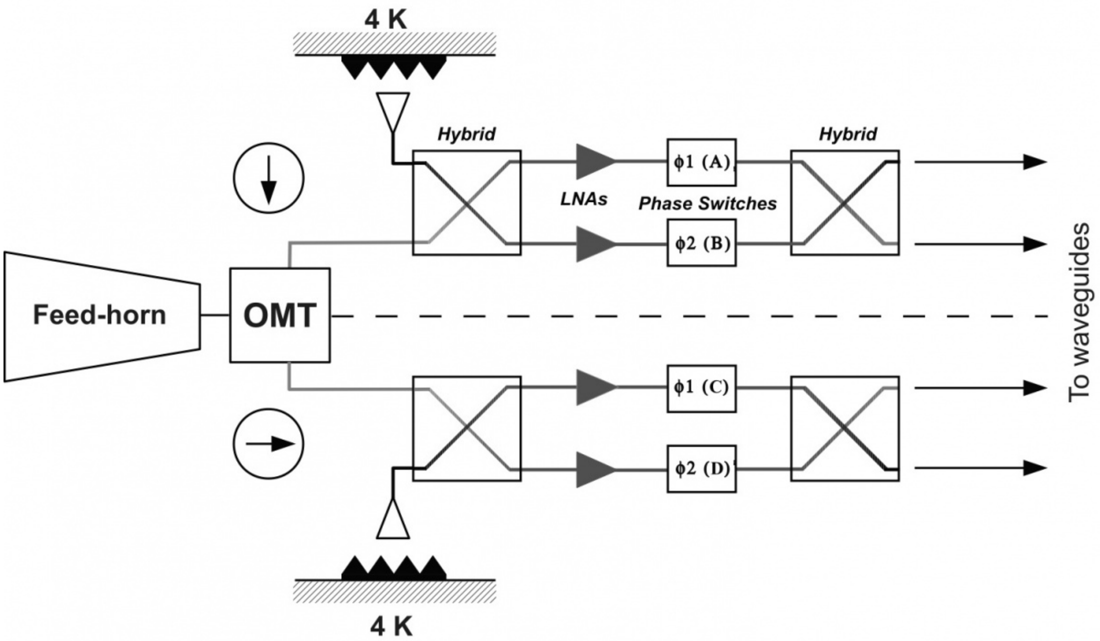

Figure 3. Close-up of the two front-end modules of an RCA. There are four phase switches, labelled A, B, C and D. Each switch can be fixed in one of its two positions (labelled as 0, 1) or switch at 4 kHz between 0 and 1. Phase switches are clocked and biased by the DAE in pairs: A/C and B/D.

Feed Horns (FH)

Dual profiled corrugated horns have been selected at all LFI frequencies as the best design in terms of shape of the main lobe, level of the side lobes, control of the phase centre, and compactness. Details of the design, flight model and tests of Planck-LFI feed horns can be found in #villa2009 and in the corresponding Annex section.

OrthoMode Transducers (OMT)

The Ortho–Mode Transducer (OMTs) separates the radiation collected by the feed horn in two orthogonal polarisation components. It consists of a circular to square waveguide transition (directly connected to the FH), a square waveguide section and two separate rectangular waveguide (the through and side arms, which separate and pick up the orthogonal polarisation, connected with the FEU). On the side arms is always present a 90 degrees bend, while a twist is also necessary on the main (30 and 44 GHz) and side (70 GHz) arm, in order to math the FEU polarisation.

The details of the flight models and measurements of the Planck LFI ortho-mode transducers can be found in #darcangelo2009b and in the corresponding Annex section.

Front End Modules (FEM)

Front End Modules are located in the FPU, just in cascade of the Feed Horn and the Ortho Mode Transducers. 70 GHz FEMs are mounted onto the inner wall of the mainframe (the wall facing HFI instrument) from the HFI side. 44 and 30 GHz FEMs are inserted into the mainframe from the WG side and fixed to the bottom plate. Screws to bottom plate are inserted from WG side. The LFI FEMs are the first active stage of amplification of the radiometer chain. Each FEM contains four amplification paths. Each path is composed by several cascaded LNAs followed by a phase switch. Two passive hybrids, at the input and output of the FEM, are used to mix couples of signals of the same radiometer (see Fig. 3). This makes the instabilities of each chain to be applied to both the sky and load signals.

The passive hybrid coupler (magic-tee) combines the signals from the sky and cold load with a fixed phase offset of either 90 deg or 180 deg between them. It has a 20% bandwidth, low loss, and amplitude balance needed at the output to ensure adequate signal isolation.

The details of the design, development and verification of the 70 GHz front-end modules for the Planck Low Frequency Instrument can be found in #varis2009 and in the corresponding Annex section.

Waveguides

The LFI Front End Unit (FEU) is connected to the Back End Unit (BEU) by 44 rectangular waveguides approximately 1.5-2.0 meter long. Each waveguide exhibits low voltage standing wave ratio, low thermal conductivity, low insertion loss, and low mass. In addition, the waveguide path shall permit the LFI/HFI integration and the electrical bonding between FPU and BEU. Because of the Focal Plane Unit arrangement, the waveguides are in general twisted and bended in different planes and with different angles, depending on the particular waveguide. From the thermal point of view the waveguides have to connect 2 systems (BEM and FEM) that are at very different temperatures. At BEM level the waveguides are at a temperature of 300K while at FEM level the temperature is 20K. The waveguides have to reduce the thermal flow from 300K to 20K. In Fig. 1 in LFI overview (left panel) a conceptual sketch of the LFI configuration is shown.

Details of the Planck-LFI flight model of the composite waveguides can be found in #darcangelo2009a and in the corresponding Annex section.

Back End Modules (BEM)

The BEMs are composed by four identical channels each made of Low Noise Amplifiers (LNA), RF Band Pass Filter, RF to DC diode detector and DC amplifiers. The FEM output signals are connected by waveguide from the Focal Plane Unit (FPU) assembly to the Back End Modules (BEM’s) housed adjacent to the Data Acquisition Electronics (DAE) assembly. To maintain compatibility with the FEM’s, each BEM accommodates four receiver channels from the four waveguide outputs of each FEM. The BEM internal signal routes are not cross coupled and can be regarded as four identical parallel circuits. Each BEM is constructed as two mirror halves. The two amplifier/detector assemblies each contain two amplifier/detector circuits. Each is supplied from one of a pair of printed circuit boards which also house two DC output amplifiers.

The details of the design, development and verification of the 30 and 44 GHz back-end modules for the Planck Low Frequency Instrument can be found in #artal2009. The details of the design, development and verification of the 70 GHz back-end modules for the Planck Low Frequency Instrument can be found in #varis2009. Details are reported also in the corresponding Annex section.

4K Load

The purpose of the 4 K reference load is to provide the radiometer with a stable reference signal. Reducing the input offset (the radiometric temperature difference between the sky and the reference load) reduces the minimum achievable radiometer 1/f noise knee frequency for a given amplifier fluctuation spectrum. A reference load temperature that matches the sky temperature (approximately 2.7 K) would be ideal.

Details of the design, characteristics and performance of the LFI 4K reference load units are given in #valenziano2009 and in the corresponding section of the Annexes.

Naming Convention

The naming of all the LFI elements is described in the previous sections but here is summarized again for clarity.

The 11 RCAs are labelled by a numbers from 18 to 28 as outlined in Fig. 1 in LFI overview, right panel. In each RCA, the two perpendicular linear polarisation components are labelled as *M* or *S* according to the arm of the OMT they are connected to (*Main* or *Side*, see lower-left inset of Fig. 2).

Each front-end amplifier (see upper-left inset of Fig. 2) is labelled with codes *1*, *2* so that the four outputs of the FEM LNAs can be named with the sequence: *M1*, *M2* (radiometer *M*) and *S1*, *S2* (radiometer *S*).

Each radiometer has two output diodes (see upper-right inset of Fig. 2) which are labelled with binary codes *00*, *01* (radiometer *M*) and *10*, *11* (radiometer *S*), so that the four outputs of each radiometric chain can be named with the sequence: *M-00*, *M-01*, *S-10*, *S-11*.

REBA

The Radiometer Electronics Box Assembly (REBA) is the electronic box in charge of processing the digitized scientific data and to manage the overall instrument. It is also in charge of the communication with the spacecraft. There are two REBA boxes, one nominal and one redundant. The redundancy concept is cold, which means that both boxes are never ON at the same time; the operation of each unit shall be managed by the spacecraft switching-on the corresponding unit. The REBA ASW (Application SoftWare) is the same in each REBA box.

A detailed description of the Planck LFI REBA can be found in #herreros2009 and in the corresponding section of the Annexes.

Instrument On-board Software

The REBA software is the on board software of LFI. It is installed in the two computing subunits of REBA: the DPU (Digital Processing Unit), responsible of the control and monitoring of the instrument and the interface with the spacecraft and; the SPU (Signal Processing Unit), responsible of the data reduction and compression.

Details can be found in the corresponding section of the Annexes.

Reduction and Compression of Science Data

To asses stability against 1/f noise, the Low Frequency Instrument (LFI) on-board the Planck mission will acquire data at a rate much higher than the data rate allowed by the science telemetry bandwidth of 35.5 kbps. The data are processed by an on-board pipeline, followed on-ground by a decoding and reconstruction step, to reduce the volume of data to a level compatible with the bandwidth while minimizing the loss of information. The on-board processing of the scientific data used by Planck/LFI to fit the allowed data-rate is an intrinsically lossy process which distorts the signal in a manner which depends on a set of five free parameters (N_{aver}, r_1, r_2, q, O) for each of the 44 LFI detectors. A brief description of the characteristics of this algorithm and the level of distortion introduced by the on-board processing as a function of these parameters can be found in the corresponding section of the Annexes, a full description of the Planck LFI on-board data handling system and the tuning and optimization method of the on-board processing chain in #maris2009.

The strategy adopted to fit into the bandwidth relies on three on-board processing steps: downsampling, pre-processing the data to ensure loss-less compression, and loss-less compression itself. To demonstrate these steps, a model of the input signal shall be used. It has to be noted that while the compression is loss-less, the pre-processing is not, due to the need to rescale the data and convert them in integers, (a process named data re-quantization). However, the whole strategy is designed to asses a strict control of the way in which lossy operations are done, of the amount of information loss in order to asses optimal compression rate with minimal information loss.

Instrument Operations

Operational Modes

The operations of the LFI are designed to be automatic and require little if any intervention from the ground. A small amount of commands is required for operating the instrument and eventually for diagnostic and reconfiguration purposes. Each sky survey is conducted by the LFI with the instrument in the Normal Operations Mode mode. No deployable elements, or mechanically moving parts are included in the instrument. The scanning of the sky is achieved by progressive repointing of the satellite spin axis, with the Sun direction always within a cone 10 degrees from the spin axis. Within the Normal Science Mode the instrument can be configured in order to fit with different science or diagnostic needs without changing the power consumption and thus the temperature in the FPU. Changes in power consumption in the FPU are minimised and should occur only in the case that failures in the radiometers that could create interference problems require an RCA to be switched off. Power adjustments on the first stage of the HEMT amplifiers which are contemplated, require extremely small power level variations.

A brief summary of the LFI Operational Modes and the transitions between them is given in the corresponding section of the Annexes.

Ground Tests

During its development, the LFI flight model was calibrated and tested at various integration levels from sub-systems #davis2009 to individual integrated receivers #villa2010 Planck pre-launch paper 6 [2] and the whole receiver array #mennella2010 Planck pre-launch paper 5 [3]. In every campaign we performed tests according to the following classification:

- *Functionality tests*, performed to verify the instrument functionality.
- *Tuning tests*, to tune radiometer parameters (biases, DC electronics gain and offset, digital quantisation and compression) for optimal performance in flight-like thermal conditions.
- *Basic calibration and noise performance tests*, to characterise instrument performance (photometric calibration, isolation, linearity, noise and stability) in tuned conditions.
- *Susceptibility tests*, to characterise instrument susceptibility to thermal and electrical variations.

Where possible, the same tests were repeated in several test campaigns, in order to ensure enough redundancy and confidence in the instrument behaviour repeatability. A matrix showing the instrument parameters measured in the various test campaigns is provided in Table 1 of #mennella2010 Planck pre-launch paper 5 [3].

The ground test campaign was developed in three main phases: cryogenic tests on the individual RCAs, cryogenic tests on the integrated receiver array (the so-called radiometer array assembly, RAA) and system-level tests after the integration of the LFI and HFI instruments onto the satellite. The first two phases were carried out at the Thales Alenia Space - Italia laboratories located in Vimodrone (Milano, Italy) (note that receiver tests on 70 GHz RCAs were carried out in Finlad, at Yilinen laboratories), system level tests (SLT) were conducted in a dedicated cryofacility at the Centre Spatiale de Liege (CSL) located in Liege (Belgium).

In Table 1 below we list the temperature of the main cold thermal stages during ground tests compared to in-flight nominal values. These values show that system-level tests were conducted in conditions that were as much as possible flight-representative, while results obtained during RCA and RAA tests needed to be extrapolated to flight conditions to allow comparison. Details about the RCA test campaign are discussed in #villa2010 Planck pre-launch paper 6 [2] while the RAA tests and the extrapolation methods are presented in #mennella2010 Planck pre-launch paper 5 [3].

Table 1. Temperatures of the main cold stages during the various ground test campaigns compared to in-flight nominal values

Temperature	Nominal	RCA tests	RAA tests	System-level
Sky	~ 3 K	≳ 8 K	≳ 18.5 K	~ 4 K
Ref. load	~ 4.5 K	≳ 8 K	≳ 18.5 K	~ 4.5 K
Front-end unit	~ 20 K	~ 20 K	~ 26 K	~ 20 K

During the various test campaigns the instrument was switched off and moved several times in a time period of about three years. A series of functional tests were always repeated at each location and also in flight, in order to verify the instrument functionality and the response repeatability. No failures or major problems have been identified due to transport and integration procedures.

The expected Planck LFI scientific performance, resulting mainly from cryogenic system level tests, are described in #mennella2010 Planck pre-launch paper 5 [3].

In-flight Calibration

The LFI Commissioning and Calibration and Performance Verification (CPV) phases started on June, 4th2009 and lasted until August, 12thwhen Planck started scanning the sky in nominal mode. At the onset of CPV, the active cooling started when the radiating surfaces on the payload module reached their working temperatures (~50 K on the 3rdV-groove, and ~40 K on the reflectors) by passive cooling. This was achieved during the transfer phase. Nominal temperatures were achieved on July, 3rd2009, when the dilution cooler temperature reached 0.1 K #planck2011-1-3, meinhold2009 Planck early paper II [1]. The cooldown of the HFI 4K stage (see Fig. 4 below), was key during CPV for the LFI as it provided a variable input signal that was exploited during bias tuning.

The LFI Commissioning and CPV was carried out in four phases:

- LFI switch on and basic functionality verification (Commissioning),
- Tuning of front-end biases and back-end electronics (CPV),
- Preliminary calibration tests (CPV),
- Thermal tests (CPV).

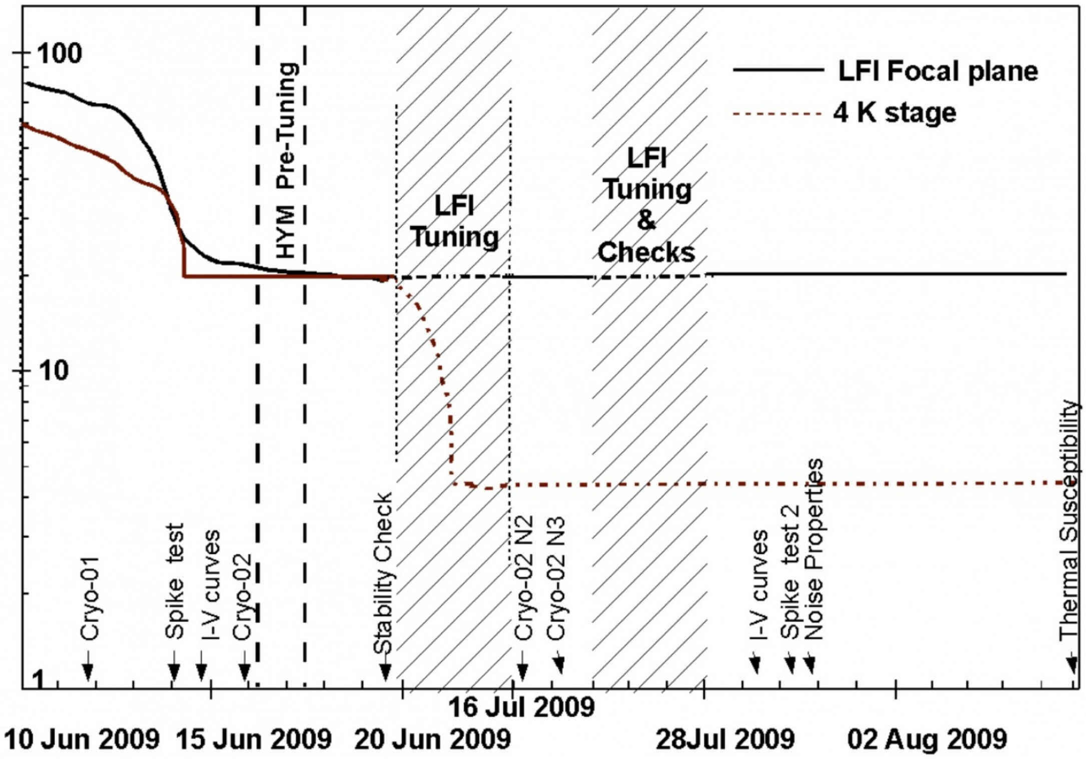

Figure 4. Functional tests performed during CPV against timeline. Curves from thermal sensors monitoring the 4K stage and the FPU temperature are superimposed.

Details of the LFI Commissioning and CPV test campaign are given in #gregorio2013.

Performance Summary

Instrument Scientific Performance

Optical Parameters

The most accurate measurements of the LFI main beams have been made with Jupiter, the most powerful unresolved (to Planck) celestial source in the LFI frequency range. Since the LFI feed horns point to different positions on the sky, they detect the signal at different times. To map the beam, each sample in the selected timelines was projected in the (u, v)-plane perpendicular to the nominal line-of-sight (LOS) of the telescope (and at 85° to the satellite spin axis). The $u$and $v$coordinates are defined in terms of the usual spherical coordinates :

To increase the signal-to-noise ratio, data were binned in an angular region of 2′ for the 70 GHz channels and 4′ for the 30 and 44 GHz channels. We recovered all beams down to −20 dB from the peak. An elliptical Gaussian was fit to each beam for both M and S radiometers. Differences between the M and S beams caused by optics and receiver non-idealities are inevitable at some level, but they appear to be well within the statistical uncertainties, and for the purposes of point-source extraction, the beams may be considered identical. For the details of the typical FWHM and ellipticity averaged over each frequency channel, refer to #planck2011-1-4 Planck early paper III [1]. Exhaustive details on all LFI beam parameters are presented in the LFI data processing section - Beams.

Photometric Calibration

Photometric calibration, i.e., conversion from voltage to antenna temperature, is performed for each radiometer after total power data have been cleaned of 1 Hz frequency spikes (see the LFI data processing section - Spikes Removal section and #planck2011-1-6 Planck early paper V [1]), and differenced. Here we report a brief overview of the photometric calibration, for the details see the LFI data processing section - Photometric Calibration.

Our calibrator is the well-known dipole signal induced by Earth and spacecraft motions with respect to the CMB rest frame. The largest calibration uncertainty comes from the presence of the Galaxy and of the CMB anisotropies in the measured signal. We therefore use an iterative calibration procedure in which the dipole is fitted and subtracted, producing a sky map that is then removed from the original data to enhance the dipole signal for the next iteration. Typically, convergence is obtained after a few tens of iterations.

In our current calibration model we use as calibration signal the sum of the solar dipole $\Delta T_{Sun}$and the orbital dipole ΔT_{orb}, which is the contribution from Planck's orbital velocity around the Sun,

where $\theta_{axis}$is the angle between the spacecraft axis and the overall dipole axis (solar + orbital). In this equation, the absolute calibration uncertainty is dominated by the uncertainty in T_{Sun}= 3.355 mK ± 0.008 mK hinshaw2009, which is known to about 0.2%. The modulation of the orbital dipole by the Earth motion around the Sun is known with an uncertainty almost three orders of magnitude smaller; however, at least one complete Planck orbit is needed for its measurement. The accuracy of our current calibration can be estimated by taking into account two components: 1) the statistical uncertainty in the regions of weak dipole; and 2) the systematic uncertainty caused by neglecting gain fluctuations that occur on periods shorter than the smoothing window. In our calibration procedure the gain is estimated for every pointing period: if we call $G_i$the gain estimate from the i_{th}pointing period we have that the associated uncertainty is

where $N$is the overall number of pointing and $< G >$is the average of the Ngains. We then approximate the effect of the smoothing filter as an average over Mconsecutive pointings, so that the overall uncertainty can be estimated as:

Noise Properties

The noise characteristics of the LFI datastreams are closely reproduced by a simple (white + $1/f$) noise model,

where $P(f)$is the power spectrum and . In this model, noise properties are characterised by three parameters, the white noise limit σ, the knee frequency f_{knee}, and the exponent of the $1/f$component α, also referred to as slope. Here we give noise performance estimates based on one year of operations, details of the analysis are given in LFI data processing section - Noise estimation and in #planck2011-1-6, planck2011-1-4 Planck early paper V [1], Planck early paper III [1].

Noise properties have been calculated following two different and complementary approaches: 1) fitting equation above to time-ordered data for each radiometer; and 2) building normalised noise maps by differencing data from the first half of the pointing period with data from the second half of the pointing period to remove the sky signal ("jackknife" data sets).

Typical uncertainties are ~0.5% for the white noise, between 5 and 10% for the slope, and between 10 and 20% for the knee frequency.

White Noise Sensitivity

Details of the white noise sensitivity can be found in #planck2011-1-4 Planck early paper III [1].

Table 2 summarizes the sensitivity numbers calculated during the first year of operations using methods and procedures described in detail in #planck2011-1-6 Planck early paper V [1], compared with scientific requirements. The measured sensitivity is in very good agreement with pre-launch expectations. While the white noise moderately exceeds the design specification, this performance is fully in line with the LFI science objectives.

Table 2. White noise sensitivity of the LFI frequency channels compared with requirements

Channel	Measurement [μK^{CMB}s$^{1/2}$]	Requirement [μK^{CMB}s$^{1/2}$]
70 GHz	152.5	119
44 GHz	173.1	119
30 GHz	146.8	119

Instrument Technical Performance

Spectral Response

The in-band receiver response has been thoroughly modelled and measured for all the LFI detectors during ground tests. The complete set of bandpass curves has been published in #zonca2009 where all the details of the LFI radiometer's spectral response are given. From each curve we have derived the effective centre frequency according to:

where is the receiver bandwidth and $g(\nu)$is the bandpass response. Details about colour corrections, $C(\alpha)$, needed to derive the brightness temperature of a source with a power-law spectral index α, are provided in #planck2011-1-6.
Some details are also given in the corresponding section of the Annexes.

Bandpass Estimation

As detailed in #zonca2009, our most accurate method to measure the LFI bandpasses is based on measurements of individual components integrated into the LFI Advanced RF Model (LARFM) to yield a synthesised radiometer bandpass. The LARFM is a software tool based on the open-source Quasi Universal Circuit Simulator (QUCS). The measured frequency responses of the various subsystems (feed-OMT, FEM, BEM) are considered as lumped S-parameter components. Measurements of single components are obtained with standard methods and provide highly reliable results, with precision of order 0.1-0.2 dB over the entire band. Waveguides are simulated with an analytical model, in order to reproduce the effect of their temperature gradient and the effect of standing waves caused by impedance mismatch at the interfaces between the FEM and BEM. This is because the 1.8-meter long waveguides were not measured at unit level in cryogenic conditions. The model provides accurate agreement with the measured waveguide response in the conditions of the test measurements (300 K). The composite bandpasses are estimated to have a precision of about 1.5 to 2 dB.

Some details are also given in the corresponding section of the Annexes.

Stability

Thanks to its differential scheme, the LFI is insensitive to many effects caused by 1/f noise, thermal fluctuations, or electrical instabilities. As detailed in #planck2011-1-4 Planck early paper III [1], one effect detected during the first survey was the daily temperature fluctuation in the back-end unit induced by the downlink transponder, which was powered on each day for downlinks during the first 258 days of the mission. As expected, the effect is highly correlated between the sky and reference load signals. In the difference, the variation is reduced by a factor , where r

is the gain modulation factor defined above (see eq. \ref{eq:erre1}).

A particular class of signal fluctuations occasionally observed during operations is due to electrical instabilities that appear as abrupt increases in the measured drain current of the front-end amplifiers, with a relaxation time variable from few seconds to some hundreds of seconds. Typically, these events cause a simultaneous change in the sky and reference load signals. Because they are essentially common-mode, their residual on the differenced data is negligible, and the data are suitable for science production. In a few cases the residual fluctuation in the differential output was large enough (a few millikelvin in calibrated antenna temperature units) to be flagged, and the data were not used. The total amount of discarded data for all LFI channels until Operational Day 389 was about 2000 s per detector, or 0.008%.

A further peculiar effect appeared in the 44 GHz detectors, where single isolated samples, either on the sky or the reference voltage output, were far from the rest. Over a reference period of four months, 15 occurrences of single-sample spikes (out of 24 total anomaly events) were discarded, an insignificant loss of data.

Thermal Susceptibility

As mentioned in section LFI In-flight Calibration above and detailed in #gregorio2013, during the CPV campaign, susceptibility tests were performed in order to characterise the LFI instrument susceptibility to thermal and electrical variations.

The effect of temperature fluctuations on the LFI radiometers is originated in the Planck cold end interface of the hydrogen sorption cooler to the instrument focal plane. The temperature is actively controlled through a dedicated stage, the Thermal Stabilization Assembly (TSA), providing a first reduction of the effect. The thermal mass of the focal plane strongly contribute to reduce residual fluctuations. The physical temperature fluctuations propagated at the front end modules cause a correlated fluctuation in the radiometer signal degrading the quality of scientific data. The accurate characterization of this effect is crucial for possibly removing it from raw data by exploiting the housekeeping information of thermal sensors.

The propagation of the temperature oscillations through the focal plane and the instrument response to thermal changes were characterized through two main tests:

- the thermal dynamic response aimed at measuring the dynamic thermal behaviour of the LFI Focal Plane;
- the radiometers thermal susceptibility.

Some details are also given in the corresponding section of the Annexes.

Instrument Budgets

LFI power, mass and telemetry budget are given in the corresponding section of the Annexes.

Systematic Effects

The LFI design was driven by the need to suppress systematic effects well below instrument white noise. The differential receiver scheme, with reference loads cooled to 4 K, greatly minimises the effect of 1/f noise and common-mode fluctuations, such as thermal perturbations in the 20K LFI focal plane. The use of a gain modulation factor (see Eq. \ref{eq:erre1} in RCA section above) largely compensates for spurious contributions from input offsets. Furthermore, diode averaging (Eq. \ref{eq:v1} in RCA section above) allows us to cancel second-order correlations such as those originating from phase switch imbalances.

We have developed an error budget for systematic effects (#planck2013-p02a, planck2011-1-4, bersanelli2010 Planck-2013-III [4], Planck early paper III [1], Planck pre-launch paper 4 [2]) as a reference for both instrument design and data analysis. Our goal is to ensure that each systematic effect is rejected to the specified level, either by design or by robust removal in software. At this stage, the following effects are relevant:

  - 1/f noise;

- 1 Hz frequency spikes;
- receivers non-linearities;
- thermal fluctuations in the back-end modules driven by temperature oscillations from the transponder during the first survey;
- thermal fluctuations in the 20 K focal plane;
- thermal fluctuations of the 4 K reference loads.

For each of these effects we used flight data and information from ground tests to build timelines, maps, and angular power spectra that represent our best knowledge of their impact on the scientific analysis. The details of the systematic effect analysis is given in section LFI data processing section - Systematic Effects uncertainties.

The Sorption Cooler

The Planck H2 Sorption Cooler is the first stage of the active cryogenic chain: its task is to maintain the LFI down to the operating temperature while providing a pre-cooling stage for the HFI refrigerators. The system performs a simple thermodynamic cycle based on hydrogen compression, gas pre-cooling by three passive radiators, further cooling due to the heat recovery by the cold low pressure gas stream, expansion through a J-T valve and evaporation at the cold stage #planck2011-1-3. A drawing of the Planck Sorption Cooler System (SCS) is shown in Fig. 5. The engine of the cryocooler is the compressor. It serves two main functions: to produce the high-pressure hydrogen gas flow and to maintain a stable gas recovery rate, which keeps the return pressure, hence the liquid temperature, constant. The high pressure gas flowing to the cold end is pre-cooled by exchanging heat with the three passive stages at the V-Grooves and with the evaporated cold gas returning back to the compressor. The gas then expands at the cold end through a J-T valve producing approximately 1 Watt of cooling power at a temperature of <20K: most of this heat lift is used at the LVHX2 (Liquid Vapour Heat eXchanger 2, see Fig. 5) interface to absorb the LFI heat load at a temperature around 20K. The remaining heat lift is used at the LVHX1 as a pre-cooling stage, at a temperature lower than 19 K, for the two HFI refrigerators. The cooler and its performance are described in detail in #morgante2009.

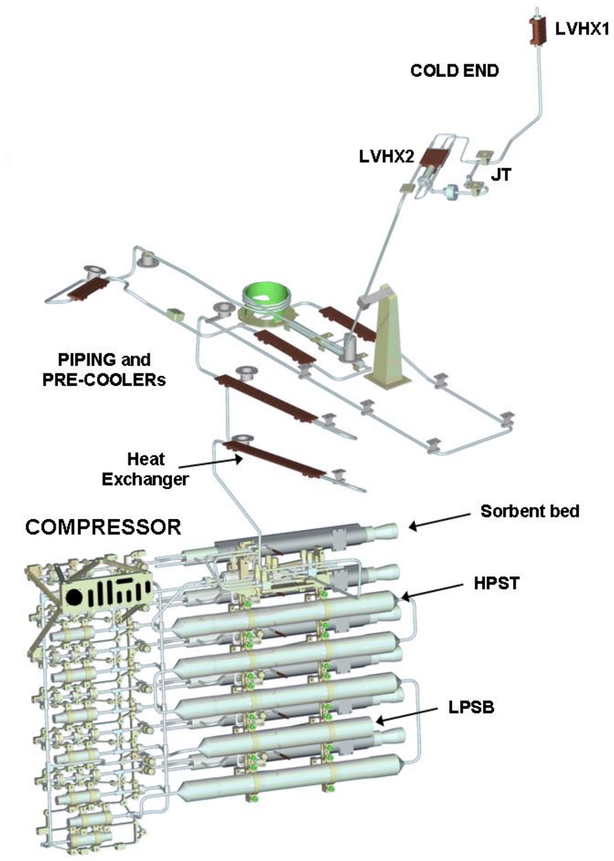

Figure 5. Planck Sorption Cooler CAD view with labels of the main sub-systems.

Both LVHX's provide a temperature around 18 K, with fluctuations driven by the cooler instabilities (compressor element variations, cycling, two phase flow dynamics etc.). Stabilization of the HFI interface (LVHX1) temperature is not necessary, as thermal control of the subsequent colder stages is more efficient and very effective. To reduce cold end fluctuations directly transmitted to the LFI radiometers, a copper block designated as the Temperature Stabilization Assembly (TSA), is inserted, as an intermediate stage, between LVHX2 and the LFI FocaL Plane Unit (FPU). The TSA comprises a temperature sensor and a heater controlled by a PID-type feedback loop working in combination with the passive thermal inertia. The set-point temperature of the TSA is an adjustable parameter of the sorption cooler system, chosen to provide dynamic range for control during mission: as the compressor elements age, the return gas pressure and thus the temperature of LVHX2 rise slowly. To keep the LFI T reference stable during operations the set point must be periodically adjusted to maintain the level of oscillations within the required range (Fig. 6).

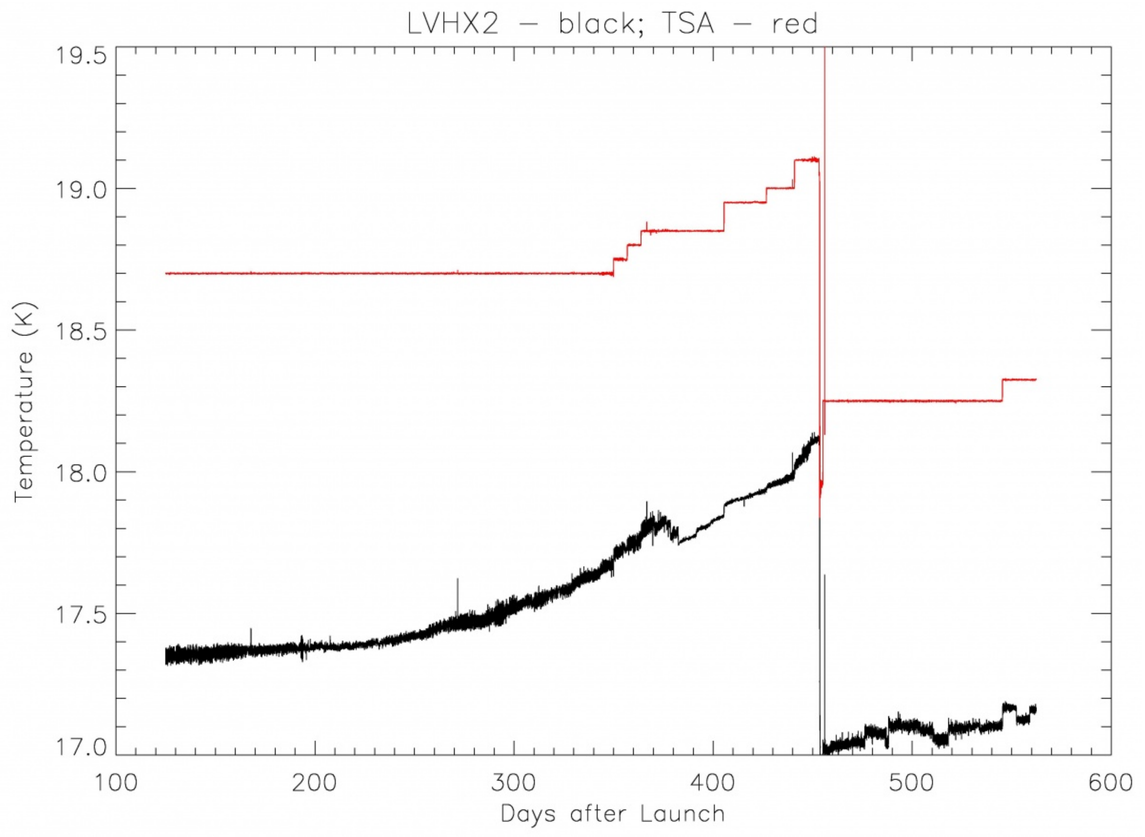

Figure 6.LVHX2 (black, HK parameter name SD029540) and TSA (red, HK parameter name SD030540) temperature profile from 125 to 563 days after launch.

Two sorption cooler units have been integrated on board the Planck spacecraft. Both units have been used to cover the mission lifetime: one cooler has been operated for the first two sky surveys. At the end of its lifetime a switchover operation, performed on August 11th 2010 (455 days after launch), has activated the second unit that has been running since then. The LVHX2 temperature change due to the new cooler start, and the subsequent re-adjustment of the LFI temperature stabilization stage, is clear in Fig. 6.

References

<biblio force=false>

1. References

</biblio>

References

[1] http://www.rssd.esa.int/doc_fetch.php?id=3135858&page=1
[2] http://www.rssd.esa.int/doc_fetch.php?id=3135846&page=1
[3] http://www.rssd.esa.int/doc_fetch.php?id=3135844&page=1
[4] http://www.rssd.esa.int/doc_fetch.php?id=3168400&page=1

LFI Annexes

Annexes: LFI Instrument

Here we report a more detailed definition of each component of the LFI instrument, briefly described in the main LFI instrument page.

Radiometer Array Assembly (RAA) Components

Feed Horns (FH)

Dual profiled corrugated horns have been selected at all LFI frequencies as the best design in terms of shape of the main lobe, level of the side lobes, control of the phase centre, and compactness. Dual profiled LFI horns are composed by a Sine Squared profiled section, and an exponential profile near the aperture plane. In order to optimise the optical matching of the feeds phase centres to the telescope focal surface, while preventing obscuration between horns, LFI has 6 different feed horn designs. For each frequency, the number of feeds and the number of different designs are reported in Table 1 below.

Table 1. Number of LFI feed horns and number of different feed horn designs

Frequency (GHz)	Number of Horns	Number of designs
30	2	1
44	3	2
70	6	3

LFI feed horn design specifications are reported in the table 2 below.

Table 2. LFI feed horn design specifications. The edge taper is the taper used to optimize the optical response; the return loss and the cross polarization are the maximum design values over the whole bandwidth; The phase center location is defined as the distance between the horn flange and the focal surface of the telescope.

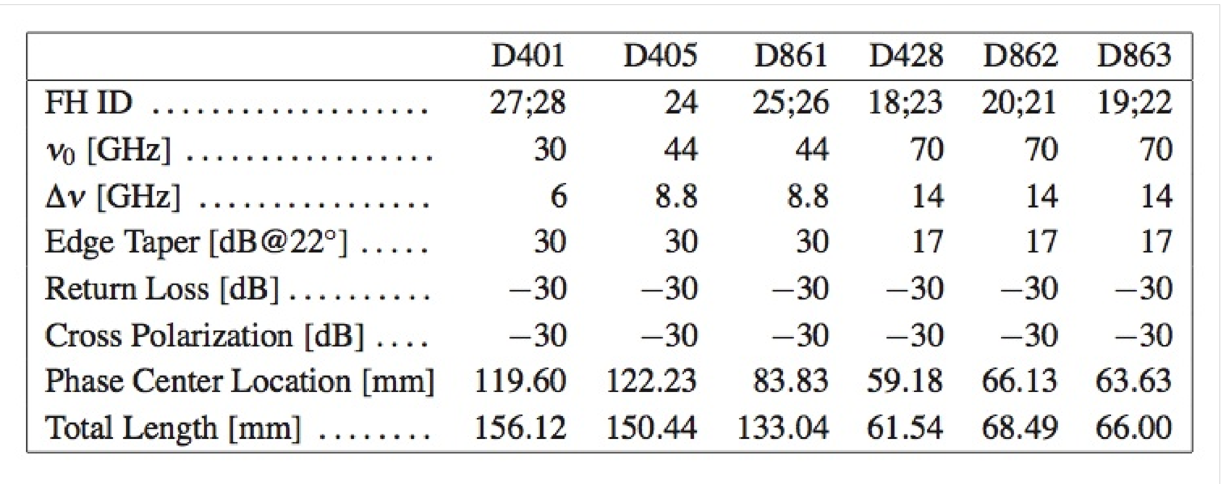

	D401	D405	D861	D428	D862	D863
FH ID	27;28	24	25;26	18;23	20;21	19;22
ν_0 [GHz]	30	44	44	70	70	70
$\Delta\nu$ [GHz]	6	8.8	8.8	14	14	14
Edge Taper [dB@22°]	30	30	30	17	17	17
Return Loss [dB]	−30	−30	−30	−30	−30	−30
Cross Polarization [dB]	−30	−30	−30	−30	−30	−30
Phase Center Location [mm]	119.60	122.23	83.83	59.18	66.13	63.63
Total Length [mm]	156.12	150.44	133.04	61.54	68.49	66.00

The design process led to a corrugation profile composed by a mixture of a sine-squared section, starting from the throat, and an exponential section near the aperture plane. The length of this last has a direct impact on the location of the phase center. The analytical expression of the corrugation profile, $R(z)$, is the following in the sine section, and

in the exponential region. Here, $R_{th}$is the throat radius, $R_s$is the sine squared region end radius (or exponential region initial radius), $R_{ap}$is the aperture radius, $L_s$is the sine squared region length and $L_e$is the exponential region length. The parameter modulates the first region profile between linear and pure sine squared type. The parameters $L_e/(L_e + L_s)$, $A$and $R_s$can be used to control, as far as possible, the position and frequency stability of the phase center and the compactness of the structure. The feed horn parameters are reported in table 3 below.

Table 3. LFI feed horn parameters.

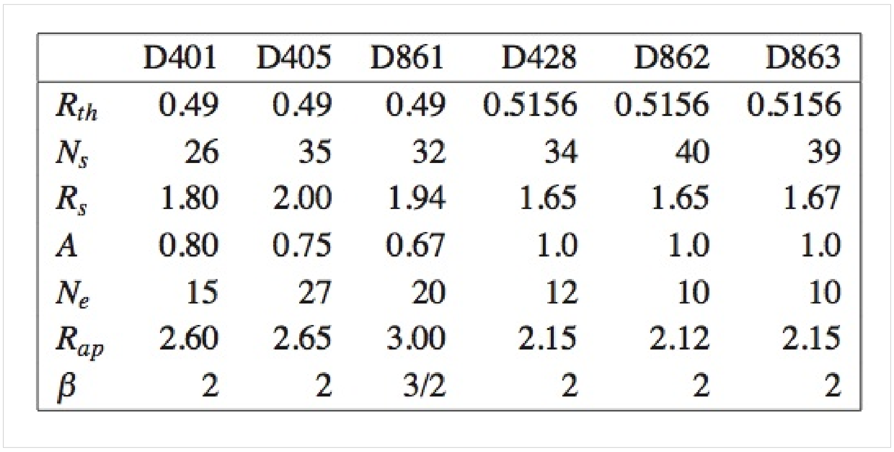

	D401	D405	D861	D428	D862	D863
R_{th}	0.49	0.49	0.49	0.5156	0.5156	0.5156
N_s	26	35	32	34	40	39
R_s	1.80	2.00	1.94	1.65	1.65	1.67
A	0.80	0.75	0.67	1.0	1.0	1.0
N_e	15	27	20	12	10	10
R_{ap}	2.60	2.65	3.00	2.15	2.12	2.15
β	2	2	3/2	2	2	2

The qualification campaign, mainly focused on RF return loss and pattern (amplitude and phase) measurements, was successfully concluded. The agreement between the pattern measurements and the expected performances (simulated using nominal corrugation profile) is excellent both in amplitude and in phase. Moreover reflection measurements show a good impedance match for all the horns, the return loss being better than -30 dB over the whole 20% of operational bandwidth.

Details of the design, flight model and tests of Planck-LFI feed horns can be found in #villa2009.

OrthoMode Transducers (OMT)

The Ortho–Mode Transducer (OMTs) separates the radiation collected by the feed horn in two orthogonal polarisation components. It consists of a circular to square waveguide transition (directly connected to the FH), a square waveguide section and two separate rectangular waveguide (the through and side arms, which separate and pick up the orthogonal polarisation, connected with the FEU). On the side arms is always present a 90 degrees bend, while a twist is also necessary on the main (30 and 44 GHz) and side (70GHz) arm, in order to math the FEU polarisation.

The required and measured performances for the LFI OMTs at all frequencies are reported in the following tables 4 and 5:

Table 4. Performance Characteristics of the LFI OMTs based on measurements. The values are the worst values over the entire 20% of bandwidth.

OMT ID	Bandwidth [GHz]	X–Pol [dB] (Main)	X–Pol [dB] (Side)	Return–Loss [dB] (Main)	Return–Loss [dB] (Side)
18	14	<29	<30	-15.0	-20.0
19	14	<26	<28	-15.0	-20.0
20	14	<32	<35	-15.0	-20.0
21	14	<32	<37	-15.0	-18.0
22	14	<26	<28	-15.0	-18.0
23	14	<26	<28	-15.0	-20.0
24	8.8	<38	<40	-13.0	-18.0
25	8.8	<31	<32	-13.0	-18.0
26	8.8	<27	<25	-13.0	-17.0
27	6	<38	<44	-16.0	-23.0
28	6	<36	<38	-16.0	-22.0

Table 5. Mean value of the IL over LFI bandwidth estimated at 20K and measured at room temperature.

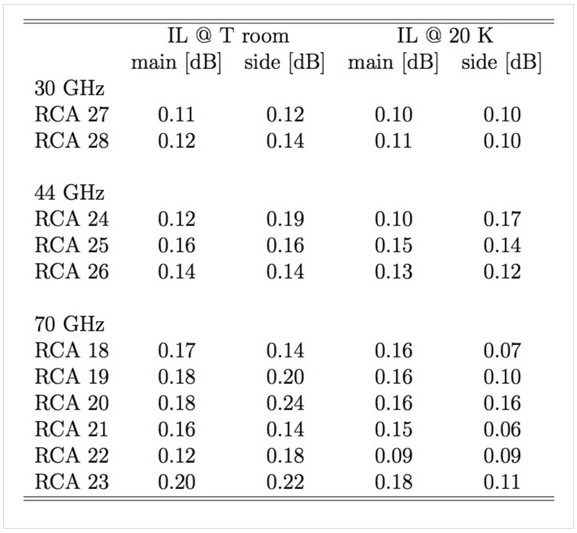

	IL @ T room		IL @ 20 K	
	main [dB]	side [dB]	main [dB]	side [dB]
30 GHz				
RCA 27	0.11	0.12	0.10	0.10
RCA 28	0.12	0.14	0.11	0.10
44 GHz				
RCA 24	0.12	0.19	0.10	0.17
RCA 25	0.16	0.16	0.15	0.14
RCA 26	0.14	0.14	0.13	0.12
70 GHz				
RCA 18	0.17	0.14	0.16	0.07
RCA 19	0.18	0.20	0.16	0.10
RCA 20	0.18	0.24	0.16	0.16
RCA 21	0.16	0.14	0.15	0.06
RCA 22	0.12	0.18	0.09	0.09
RCA 23	0.20	0.22	0.18	0.11

The details of the flight models and measurements of the Planck LFI ortho-mode transducers can be found in #darcangelo2009b.

Front End Modules (FEM)

Front End Modules are located in the FPU, just in cascade of the Feed Horn and the Ortho Mode Transducers. 70 GHz FEMs are mounted onto the inner wall of the mainframe (the wall facing HFI instrument) from the HFI side. 44 and 30 GHz FEMs are inserted into the mainframe from the WG side and fixed to the bottom plate. Screws to bottom plate are inserted from WG side. The LFI FEMs are the first active stage of amplification of the radiometer chain. Each FEM contains four amplification paths. Each path is composed by several cascaded LNAs followed by a phase switch. Two passive hybrids, at the input and output of the FEM, are used to mix couples of signals of the same radiometer (see Fig. 2 in RAA section). This makes the instabilities of each chain to be applied to both the sky and load signals.

The passive hybrid coupler (magic-tee) combines the signals from the sky and cold load with a fixed phase offset of either 90 deg or 180 deg between them. It has a 20% bandwidth, low loss, and amplitude balance needed at the output to ensure adequate signal isolation.

The FEM LNAs (InP MMIC) are biased providing 1 drain line per channel (that is 4 per FEM) and 2 gate lines per channel (that is 8 per FEM). The FEM Phase switches are biased providing 2 lines per channel (that is 8 per FEM) each capable of providing a direct bias current or a reverse bias voltage.

The LFI FEM parameters necessary to meet the science objectives at 30 and 44 GHz were given as requirements and goals and are summarised in table 6 below where they are compared with the values actually achieved. The FEM units meet the requirements, within the measurement errors, for most parameters and in particular the noise temperature. The units come close to the more stringent goals in several parameters. Of particular note are the noise temperatures achieved; these along with the wide bandwidths are critical for the high sensitivity required for the Planck mission. Some LNAs within the FEMs met the goals at 30 GHz and 44 GHz within the measurements errors and reached 3 and 5 times the theoretical quantum limit respectively at the band centres. Furthermore, a range of tests showed that LNAs and FEMs achieved the stability levels required to meet the observing strategy of Planck. In particular, the $1/f$ noise knee frequency ≤29 mHz, close to the goal, met the conditions imposed by the 60 second rotation period of the spacecraft. The linear polarization performance of the FEMs exceeded the requirements of the mission. The isolation between the E- and H- polarizations was measured to be between 51 and 58 dBs for the various FEMs. The LFI radiometers have very well determined position angle precision, being determined by the accuracy of the waveguide engineering. The 30 and 44 GHz geometry is accurate to ~ 0.1°; the corresponding precision is ~ 1° in the HFI polarimeters. The temperature stability requirement values are also given in the table 6 below.

Table 6. Summary of the FEM goals, requirements and mean achieved performances.

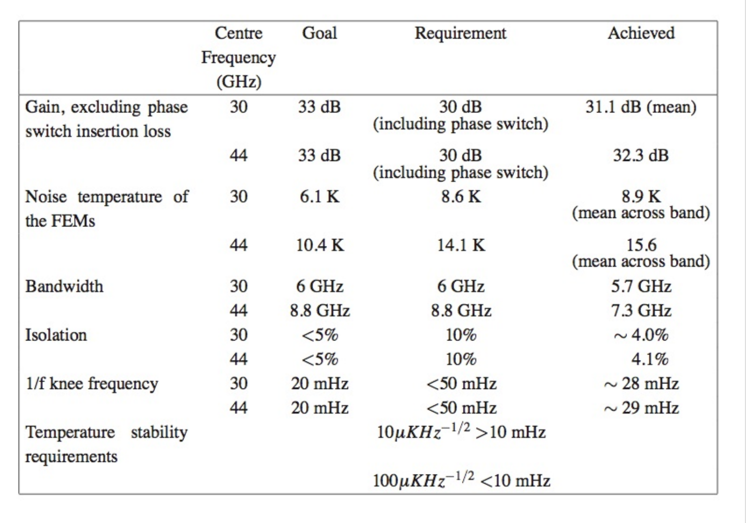

	Centre Frequency (GHz)	Goal	Requirement	Achieved
Gain, excluding phase switch insertion loss	30	33 dB	30 dB (including phase switch)	31.1 dB (mean)
	44	33 dB	30 dB (including phase switch)	32.3 dB
Noise temperature of the FEMs	30	6.1 K	8.6 K	8.9 K (mean across band)
	44	10.4 K	14.1 K	15.6 (mean across band)
Bandwidth	30	6 GHz	6 GHz	5.7 GHz
	44	8.8 GHz	8.8 GHz	7.3 GHz
Isolation	30	<5%	10%	~ 4.0%
	44	<5%	10%	4.1%
1/f knee frequency	30	20 mHz	<50 mHz	~ 28 mHz
	44	20 mHz	<50 mHz	~ 29 mHz
Temperature stability requirements			$10\mu KHz^{-1/2}$ >10 mHz	
			$100\mu KHz^{-1/2}$ <10 mHz	

The details of the design, development and verification of the 30 and 44 GHz front-end modules for the Planck Low Frequency Instrument can be found in #davis2009.

For what regards the 70 GHz channels, for the LNA selection of the FEMs, nine different wafers from various processing runs were evaluated, only the LNAs with the best performance were assembled as the first stage amplifiers in the FEM ACAs. For the phase switch selection, four different wafers were evaluated. When the signal is passed to an output, the gain is 35 dB or higher for almost the entire required range, and on average, the Planck requirement was fulfilled. In all FEMs, the average channel gains ranged from 34.0-40.0 dB (uncertainty ±0.1 dB).

When the signal is isolated from an output, the gain is 20 dB lower or more at all frequencies. This difference in gain is used as the measure for isolation. In all the six FEMs, the channel isolation values ranged from 11.3-22.1 dB (uncertainty ±0.1 dB).

Table 7 below summarises the best, the worst and the average values of the key performance parameters. The shown uncertainties are based on worst case estimates.

Table 7. Summary of the 70 GHz Protoflight Model radiometer performance.

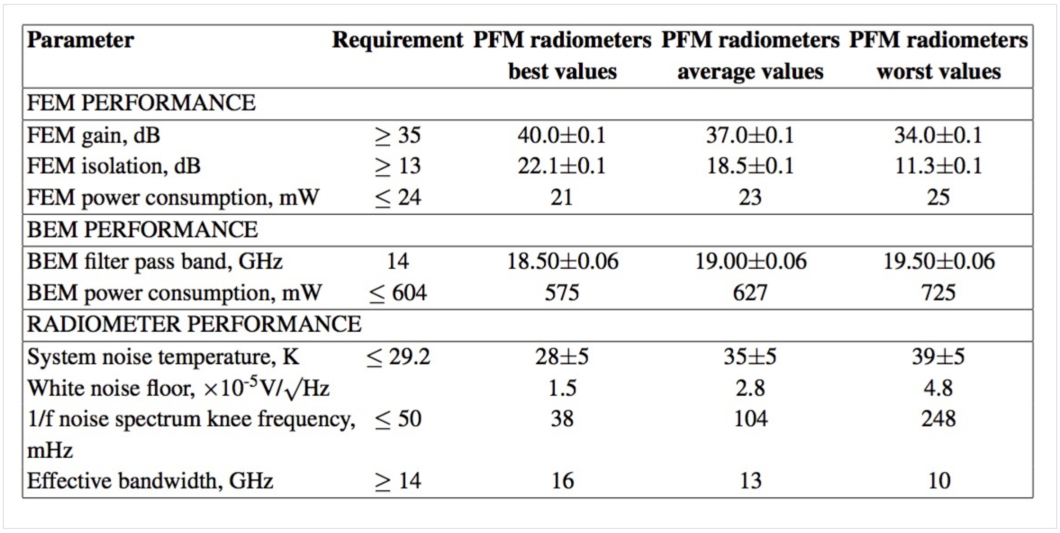

Parameter	Requirement	PFM radiometers best values	PFM radiometers average values	PFM radiometers worst values
FEM PERFORMANCE				
FEM gain, dB	≥ 35	40.0±0.1	37.0±0.1	34.0±0.1
FEM isolation, dB	≥ 13	22.1±0.1	18.5±0.1	11.3±0.1
FEM power consumption, mW	≤ 24	21	23	25
BEM PERFORMANCE				
BEM filter pass band, GHz	14	18.50±0.06	19.00±0.06	19.50±0.06
BEM power consumption, mW	≤ 604	575	627	725
RADIOMETER PERFORMANCE				
System noise temperature, K	≤ 29.2	28±5	35±5	39±5
White noise floor, $\times 10^{-5}$V/$\sqrt{}$Hz		1.5	2.8	4.8
1/f noise spectrum knee frequency, mHz	≤ 50	38	104	248
Effective bandwidth, GHz	≥ 14	16	13	10

The details of the design, development and verification of the 70 GHz front-end modules for the Planck Low Frequency Instrument can be found in #varis2009.

Waveguides

The LFI Front End Unit (FEU) is connected to the Back End Unit (BEU) by 44 rectangular waveguides approximately 1.5-2.0 meter long. Each waveguide exhibits low VSWR (Voltage Standing Wave Ratio), low thermal conductivity, low insertion loss, and low mass. In addition, the waveguide path shall permit the LFI/HFI integration and the electrical bonding between FPU and BEU. Because of the Focal Plane Unit arrangement, the waveguides are in general twisted and bended in different planes and with different angles, depending on the particular waveguide. From the thermal point of view the waveguides have to connect 2 systems (BEM and FEM) that are at very different temperatures. At BEM level the waveguides are at a temperature of 300K while at FEM level the temperature is 20K. The waveguides have to reduce the thermal flow from 300K to 20K. In Fig. 1 (left panel) of LFI overview section, a conceptual sketch of the LFI configuration is shown.

All the required characteristics cannot be realized with single material waveguide configuration; a composite waveguide configuration is needed. The WGs can be considered divided in three sections: 1. 400 mm of Stainless Steel (gold plated) straight waveguide section, attached to the BEU, ending after the 3rd V–groove; 2. 300 mm of non–plated Stainless Steel (SS). The SS-sections are identical for all the channels except for internal dimensions, depending on frequency. These guides are connected to all the V-grooves in order to dissipate the heat produced at BEU level. 3. bended and twisted 400 microns thin electroformed copper waveguide starting at the end of the SS–section and attached to the FEU, whose length varying from around 800 mm to 1300 mm, with 2 to 4 Cu-joints. The copper waveguides section is connected to a mechanical support structure in five points in order to increase the stiffness of the waveguide.

The performance for the LFI waveguides at all frequencies are reported in the following table 8:

Table 8. Number of LFI waveguides and performances. The Insertion Loss (IL), Return Loss (RL) and Electrical Resistance (R) values are the requirements. In between parenthesis the goal is reported also. Note that the RL value includes possible degradation due to presence of flanges.

Frequency	νband [GHz]	Number	IL [dB] @20 K	RL [dB]	Isolation [dB]	R [mΩ] @20 K	R [mΩ] @300 K
30	27-33	8	<2.5 (1.0)	<-25	<-30	11.8	27.3
44	39.6-48.4	12	<3.0 (1.5)	<-25	<-30	14.7	34.1
70	63-77	24	<5.0 (3.5)	<-25	<-30	26.2	60.5

From the thermal point of view the waveguides have to connect 2 systems (BEM and FEM) that are at different temperatures. At BEM level the waveguides are at a temperature of 300K while at FEM level the temperature is 20K. Along the Stainless Steel section the waveguides have to reduce the thermal flow from 300K to 20K. The Stainless Steel waveguide is connected to all the V-grooves in order to dissipate the heat produced at BEU level.

Details of the Planck-LFI flight model of the composite waveguides can be found in #darcangelo2009a.

Back End Modules (BEM)

The BEMs are composed by four identical channels each made of Low Noise Amplifiers (LNA), RF Band Pass Filter, RF to DC diode detector and DC amplifiers. The FEM output signals are connected by waveguide from the Focal Plane Unit (FPU) assembly to the Back End Modules (BEM's) housed adjacent to the Data Acquisition Electronics (DAE) assembly. To maintain compatibility with the FEM's, each BEM accommodates four receiver channels from the four waveguide outputs of each FEM. The BEM internal signal routes are not cross coupled and can be regarded as four identical parallel circuits. Each BEM is constructed as two mirror halves. The two amplifier/detector assemblies each contain two amplifier/detector circuits. Each is supplied from one of a pair of printed circuit boards which also house two DC output amplifiers.

In the 30 GHz BEM, each LNA consists of two cascaded MMIC amplifiers. The Band Pass Filter is based on microstrip coupled line structure. Its design is a three order Chebyshev response band pass filter. The detector is composed by a hybrid reactive/passive matching network, and a Schottky diode. A commercial Agilent beam-lead and zero-bias diode was selected. The detector diode is followed by a low noise operational amplifier that provides most of the DC amplification. A second stage is implemented using an operational amplifier to provide a balanced bipolar output.

In the 44 GHz BEM, each LNA consists of self designed MMIC amplifiers manufactured with the process ED02AH from OMMIC which employs a 0.2 μm gate length Pseudomorphic-High Mobility Transistor (P-HEMT) on GaAs. The topology chosen for the band-pass filter is a third order Chebyshef band pass filter made on a PTFE substrate, based on microstrip coupled line structure. The detector is composed by a hybrid reactive/passive matching network and a Schottky diode. A commercial Agilent beam-lead and zero-bias diode was selected. The detector diode is followed by a low noise operational amplifier that provides most of the DC amplification. A second stage is implemented using an operational amplifier to provide a balanced bipolar output.

Table 9 below shows the values of the equivalent noise temperature for each flight model BEM at three different temperatures in the range of possible operating temperature. The large variability of the equivalent noise temperature of 44 GHz BEM units was due to their large dependence on the input matching network result, which was observed to be a very critical parameter, not easy to control during the assembly process of MMIC.

Table 9. Equivalent noise temperature of the BEM Flight models in Kelvin. (One unit of each band is a Flight Spare). Estimated error: ± 20 K.

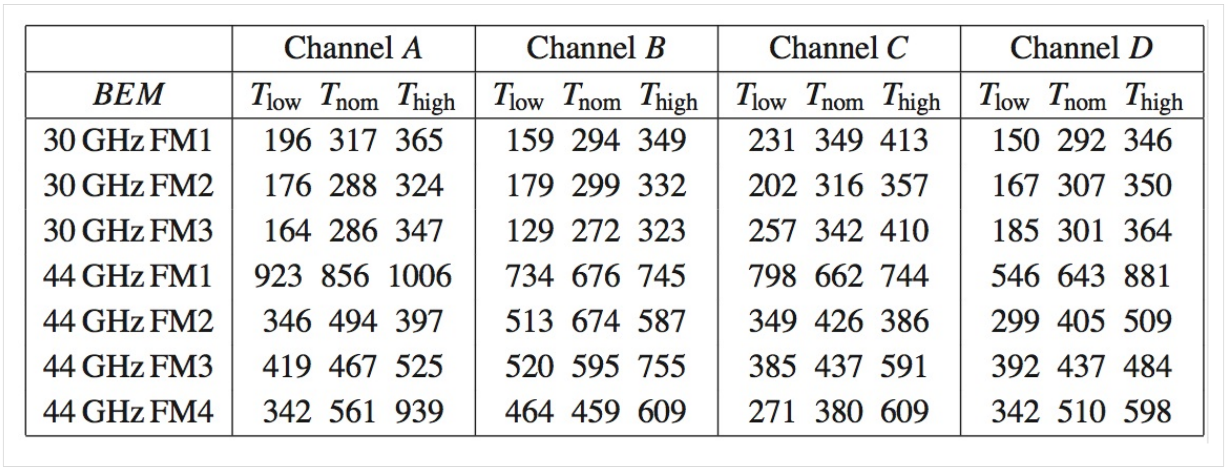

	Channel *A*			Channel *B*			Channel *C*			Channel *D*		
BEM	T_{low}	T_{nom}	T_{high}	T_{low}	T_{nom}	T_{high}	T_{low}	T_{nom}	T_{high}	T_{low}	T_{nom}	T_{high}
30 GHz FM1	196	317	365	159	294	349	231	349	413	150	292	346
30 GHz FM2	176	288	324	179	299	332	202	316	357	167	307	350
30 GHz FM3	164	286	347	129	272	323	257	342	410	185	301	364
44 GHz FM1	923	856	1006	734	676	745	798	662	744	546	643	881
44 GHz FM2	346	494	397	513	674	587	349	426	386	299	405	509
44 GHz FM3	419	467	525	520	595	755	385	437	591	392	437	484
44 GHz FM4	342	561	939	464	459	609	271	380	609	342	510	598

The raw measurements of the output spectrum are used for the determination of the $1/f$ knee frequency. The results for the four channels of a 30 GHz BEM unit are given in the table below.

Table 10.

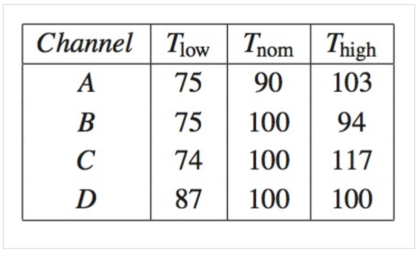

Channel	T_{low}	T_{nom}	T_{high}
A	75	90	103
B	75	100	94
C	74	100	117
D	87	100	100

The details of the design, development and verification of the 30 and 44 GHz back-end modules for the Planck Low Frequency Instrument can be found in #artal2009.

The 70 GHz BEM is constructed of machined aluminium with separate filter, amplifier/detector assemblies and an overall housing for other circuits and components. The BEM filter characteristics hold very accurately for every channel in the six BEMs. The -3 dB pass band, 62-81 GHz, was the same in every filter within 0.5 GHz. The BEM frequency response was measured as a function of input microwave power. Also, the pass bands roll at almost exactly 63 GHz and 77 GHz. The linearity of the channel is very good as well, especially from -57 dBm upwards. The dynamic range was at least 15 dB from -57 dBm to -42 dBm. In three cases, the BEMs fulfilled the power consumption requirement, while the limit was exceeded for the other three. For the total six BEMs, the limit, 3.6 W, was exceeded by approximately 140 mW. Table 7 above summarises the best, the worst and the average values of the key performance parameters. The shown uncertainties are based on worst case estimates.

The details of the design, development and verification of the 70 GHz back-end modules for the Planck Low Frequency Instrument can be found in #varis2009.

4K Load

The purpose of the 4 K reference load is to provide the radiometer with a stable reference signal. Reducing the input offset (the radiometric temperature difference between the sky and the reference load) reduces the minimum achievable radiometer $1/f$noise knee frequency for a given amplifier fluctuation spectrum. A reference load temperature that matches the sky temperature (approximately 2.7 K) would be ideal. In the 4KRL design, the reference temperature is provided by the HFI outer radiation shield, at a temperature around 4K. The 4KRL performance are reported in Table 11 below.

Table 11. RF measured performance for the 4KRL: RH (+WaveGuide) Insertion Loss, RH (+WG) RL, RH (+WG) + RT Return Loss. 70 GHz performance have been measured using a representative Reference Horn and waveguide, since RHs are internal to FEMs: this value is reported in the table. RCAs 24-26 are the LFI 44 GHz channels, 27 and 28 the 30 GHz ones. M and S refer to Main and Side OMT arm, respectively.

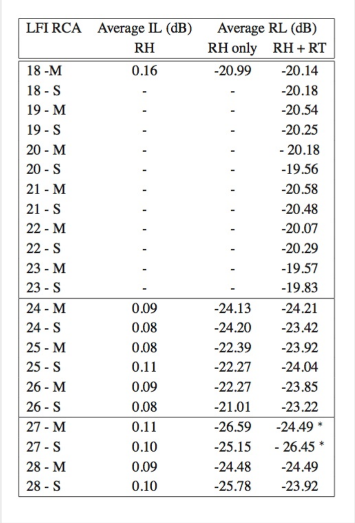

LFI RCA	Average IL (dB)	Average RL (dB)	
	RH	RH only	RH + RT
18 -M	0.16	-20.99	-20.14
18 - S	-	-	-20.18
19 - M	-	-	-20.54
19 - S	-	-	-20.25
20 - M	-	-	- 20.18
20 - S	-	-	-19.56
21 - M	-	-	-20.58
21 - S	-	-	-20.48
22 - M	-	-	-20.07
22 - S	-	-	-20.29
23 - M	-	-	-19.57
23 - S	-	-	-19.83
24 - M	0.09	-24.13	-24.21
24 - S	0.08	-24.20	-23.42
25 - M	0.08	-22.39	-23.92
25 - S	0.11	-22.27	-24.04
26 - M	0.09	-22.27	-23.85
26 - S	0.08	-21.01	-23.22
27 - M	0.11	-26.59	-24.49 *
27 - S	0.10	-25.15	- 26.45 *
28 - M	0.09	-24.48	-24.49
28 - S	0.10	-25.78	-23.92

The 4K reference load unit is formed by single targets, one for each radiometer (two for each FEM). The horns used to couple to the 4 K reference load targets need to be relatively small because the targets themselves are small. An optimisation process produced a different horn design for each LFI band: their dimensions increase with reducing frequency. Due to the LFI Focal Plane design, where higher frequency radiometers (70 GHz) are placed around the HFI cryostat and the lower frequency radiometers (30 and 44 GHz) in a second row, the target mounting structure is separated in two parts, see Fig. 1 below. The upper one is located around the conical part of the HFI outer shield. Reference targets are mounted on a supporting structure, thermally and mechanically connected to the HFI outer shield. Each target faces a reference horn, two for each FEM. This ensemble is fixed to a support structure on the HFI 4K shield. Thermal link between the mounting structure and the HFI is obtained via fixation point only. Thermal washers are interposed to damp temperature fluctuations on targets induced by the HFI outer shield temperature oscillations. The lower part is fixed in the cylindrical part. It is made with the same target geometry of the upper part, and it is fixed on the HFI shield. The reference horns face the loads and are connected to the FEMs through WGs. Reference WGs and RH (Reference Horns) are either included in the FEM (70 GHz) or external to FEM (30 and 44 GHz).

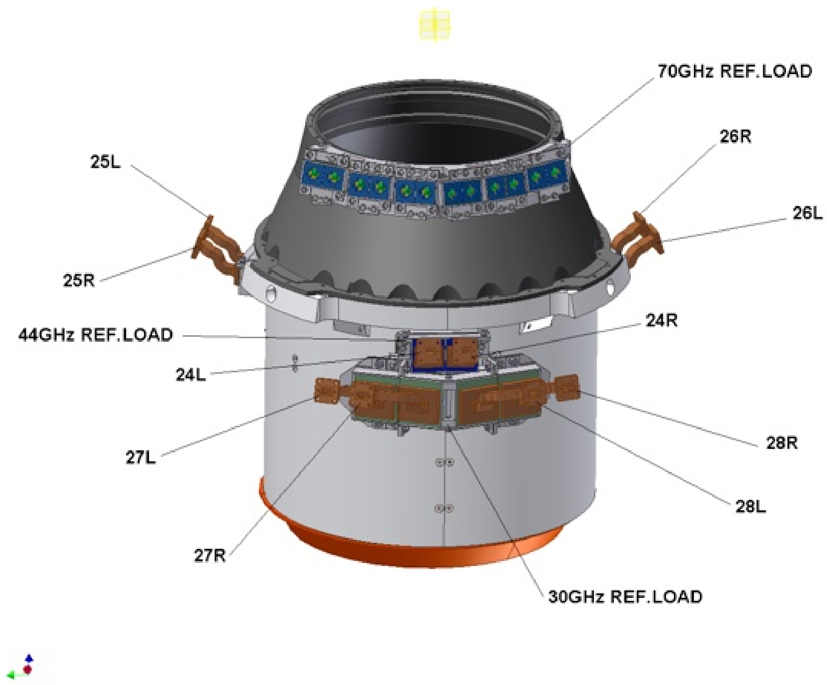

Figure 1. 4K reference load targets mounted on the HFI 4K shield.

Targets are formed of a back section, made of ECCOSORB CR117, which shows higher RF absorption but also high reflectivity. To reduce the target global reflectivity, a front section, assembled with an ECCOSORB specific cement to the back one, faces the radiometer Reference Horn. This last is casted from ECCOSORB CR110, whose RF reflectivity is lower than that of CR117. Target design is optimised to further reduce both reflectivity and leakage. Each target is metal backed and it is mounted in a metal enclosure.

Thermal tests were performed in the IASF-Bo 4K cryo facility, equipped with a GM cooler, with an heat lift up to 1.5 W at 4K. The setup simulated the real environment in the payload, where targets are mounted on the HFI 4K shield in front of the quasi-cylindrical LFI main frame at about 20 K. It was also used to test the susceptibility to fluctuations of the LFI.

The thermo-mechanical damping was evaluated from the transient test, inducing sinusoidal temperature fluctuation with periods of 60, 600, 667 (typical Sorption Cooler period) and 1000 seconds at the level of the attachment point of the loads on the support structures. The fluctuation at the level of the targets is then acquired and the transfer function (amplitude and phase) are estimated by the ratio of the amplitudes. The final results are summarized in the table 12.

Table 12. Thermal fluctuation damping measured for the reference loads at different frequencies.

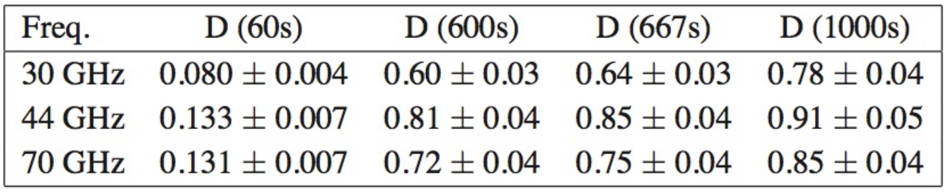

Freq.	D (60s)	D (600s)	D (667s)	D (1000s)
30 GHz	0.080 ± 0.004	0.60 ± 0.03	0.64 ± 0.03	0.78 ± 0.04
44 GHz	0.133 ± 0.007	0.81 ± 0.04	0.85 ± 0.04	0.91 ± 0.05
70 GHz	0.131 ± 0.007	0.72 ± 0.04	0.75 ± 0.04	0.85 ± 0.04

Details of the design and performance of the LFI 4K reference load units are given in #valenziano2009.

REBA

The Radiometer Electronics Box Assembly (REBA) is the electronic box in charge of processing the digitized scientific data and to manage the overall instrument. It is also in charge of the communication with the spacecraft. There are two REBA boxes, one nominal and one redundant. The redundancy concept is cold, which means that both boxes are never ON at the same time; the operation of each unit shall be managed by the spacecraft switching-on the corresponding unit. The REBA ASW (Application SoftWare) is the same in each REBA box.

Each REBA consists of the following subunits:

- The Power Supply Unit (PSU) which feeds the REBA unit. It consists of a DC/DC converter that converts the primary power received from the spacecraft PDU to the secondary regulated voltages required only by the REBA and provides galvanic isolation towards the spacecraft side of the interface. The PSU DC/DC converter also receives the On-Board Clock (OBC) from the CDMS that is used to increment the internal On Board Time register. There is no software interface with the REBA ASW.
- The Data Acquisition Unit (DAU) performs the analogue to digital conversion of the analogue housekeeping data of the REBA itself (temperatures and voltages). The REBA ASW collects from the DAU the HK data.
- The Signal Processing Unit (SPU) is a computing subunit in charge of the reduction and compression of the science data and implements part of the REBA ASW, the SPU ASW (stored in the EEPROM located in the DPU board and transferred to the SPU by the DPU ASW). It receives the science data from the DAE through a IEEE 1355 link implemented in a SMCS chip. A second IEEE 1355 link is used to control by link the remote DAE SMCS chip. The third IEEE 1355 link communicates with the DPU. A “Data Ready” electrical signal is connected between DAE and the SPU, this signal produces an interruption in the SPU when the DAE is ready to transfer data.
- The Digital Processing Unit (DPU) is a computing subunit and implements part of the REBA ASW, the DPU ASW. The DPU is in charge of the control and monitoring of the instrument as well as the communication with the spacecraft (CDMS). It contains another SMCS chip with 3 IEEE 1355 links that communicate with the SPU, and the DAE. A MIL-STD 1553B link is used to communicate with the CDMS. One IEEE 1355 link is used by the DPU ASW to communicate with the DAE to control by link the SMCS chip of DAE, the second one is used to communicate with the DAE to transfer commands and HK and the third one is used by DPU ASW to communicate with the SPU (commands and TM). Two Reset electrical lines are provided by the DPU to reset each of the two SMCS chips of DAE. The DPU ASW is stored in the EEPROM.

A detailed description of the Planck LFI REBA can be found in #herreros2009.

Instrument On-board Software

The REBA software is the on board software of LFI. It is installed in the two computing subunits of REBA: the DPU, responsible of the control and monitoring of the instrument and the interface with the spacecraft and; the SPU, responsible of the data reduction and compression. The REBA software can be classified (see Fig. 2) into:

1. the REBA Start-up Software (SUSW), installed in the PROM memories, which is the bootstrap code to switch on both the subunits;

2. the Application Software (ASW), which performs the nominal operations of the REBA;

3. the REBA Low Level Software Drivers (LLSWDRV) which are functions provided to the ASW to access the hardware capabilities.

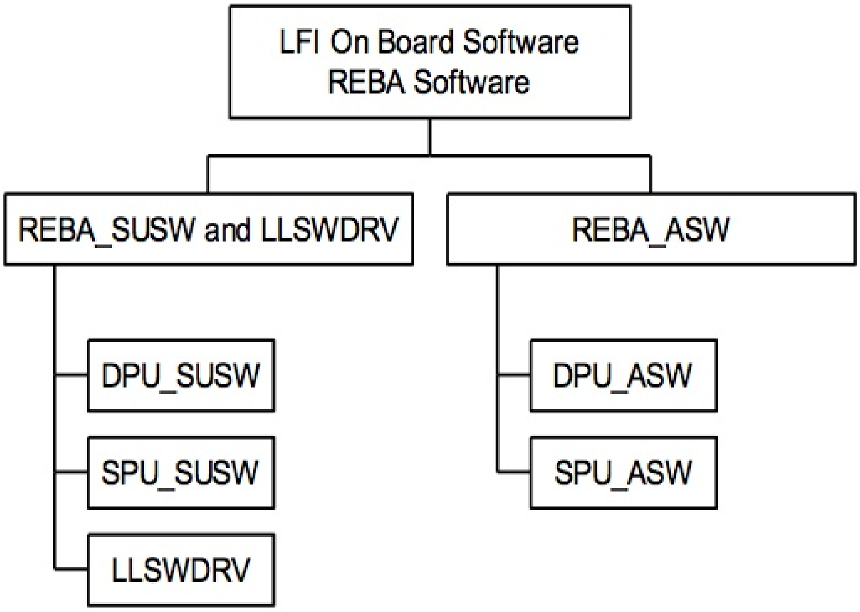

Figure 2. REBA Software, high level product tree.

The SPU SUSW and DPU SUSW, located in the PROM memories of SPU and DPU, respectively, are in charge of the booting of the subunits.

The REBA ASW performs the following main functions:

- SPU ASW reduction and compression of the scientific data;
- DPU ASW: control and monitoring of the instrument, interface with the spacecraft to transfer data and receive commands to/from ground, communication with the SPU SUSW during the start-up procedure to load the SPU ASW.

The REBA ASW checks periodically the following parameters:

– Science TM rate produced on board in order to control the filling of the spacecraft mass memory;

– CPU load of the SPU;

– Focal Plane temperature sensors;

– The communication links between REBA and DAE.

In case of deviations from nominal values, the REBA ASW activates autonomy functions that put the instrument in a safe state or recover from non-nominal situations. Autonomy functions allows to:

- Re-enable, in some cases, previously disabled science processing;
- Switch-off the Front End Unit by sending Disable RCA DC/DC commands to the DAE;
- Try to resume the communication between REBA and DAE or ask the CDMS to switch off the RAA.

The DPU ASW reports the activation of any autonomous function by sending to the CDMS an event report. The REBA monitors some LFI HK parameters in order to manage to some extent the safety of the instrument.

Reduction and Compression of Science Data

To asses stability against $1/f$noise, the Low Frequency Instrument (LFI) on-board the Planck mission will acquire data at a rate much higher than the data rate allowed by the science telemetry bandwidth of 35.5 kbps. The data are processed by an on-board pipeline, followed on-ground by a decoding and reconstruction step, to reduce the volume of data to a level compatible with the bandwidth while minimizing the loss of information. The on-board processing of the scientific data used by Planck/LFI to fit the allowed data-rate is an intrinsically lossy process which distorts the signal in a manner which depends on a set of five free parameters (N_{aver}, r_1, r_2, q, O) for each of the 44 LFI detectors. Her briefly describe the characteristics of this algorithm and the level of distortion introduced by the on-board processing as a function of these parameters. A full description of the Planck LFI on-board data handling system and the tuning and optimization method of the on-board processing chain can be found in #maris2009.

The strategy adopted to fit into the bandwidth relies on three on-board processing steps: downsampling, pre-processing the data to ensure loss-less compression, and loss-less compression itself. To demonstrate these steps, a model of the input signal shall be used. It has to be noted that while the compression is loss-less, the pre-processing is not, due to the need to rescale the data and convert them in integers, (a process named data re-quantization). However, the whole strategy is designed to asses a strict control of the way in which lossy operations are done, of the amount of information loss in order to asses optimal compression rate with minimal information loss.

A schematic representation of the sequence in which these steps are applied on-board and whenever possible reversed on-ground is given in Fig. 3 below.

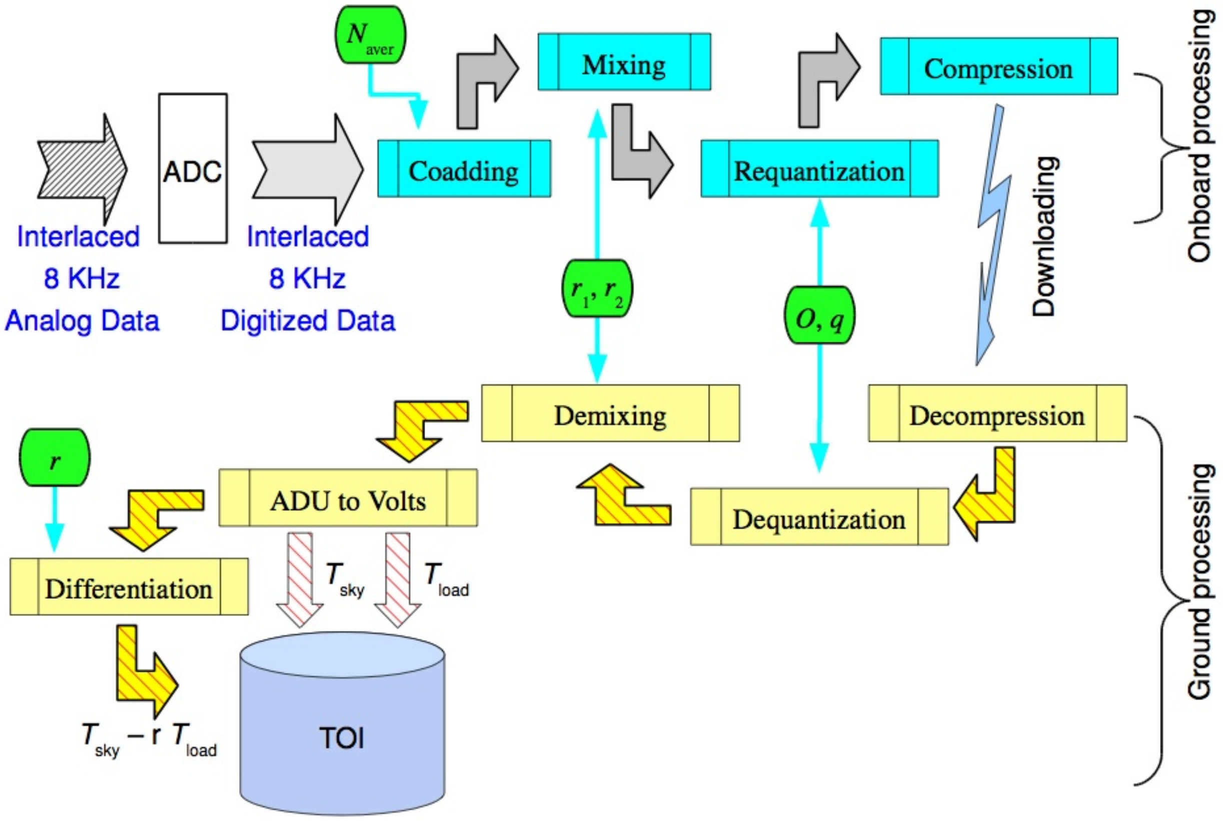

Figure 3. Schematic representation of the scientific onboard and ground processing for the Planck/LFI. Cyan boxes represent REBA operations, yellow boxes ground operations. Green pads specify the parameters needed by each operation. TOI could be produced both in undifferentiated form (T_{sky}, T_{load}stored separately) or in differentiated form.

The figure refers to a single radiometer chain and is ideally splitted into two parts: the upper part depicts the on-board processing with cyan boxes denoting the main steps. The corresponding on-ground processing is depicted in the lower part with the main steps colored in yellow. Green pads represents the processing parameters. The first four of them are referred to as REBA parameters, and they are applied both on-board and on-ground. The parameters are: the number of ADC raw samples to be coadded to form an instrumental sample, N_{aver}, the two mixing parameters r_1, r_2, the offset $O$to be added to data after mixing and prior to re-quantization, and the re-quantization step q. It is important to note that the on-board parameters are set by telecommands and are stamped in each scientific packet. The gain modulation factor, r(see Eq. (2) in RCA section above), is a parameter of the ground processing and is computed from the total power data received on ground. The final products in the form of Time

Ordered Data (TOI) either in total power or differentiated are stored in an archive represented by the light-blue cylinder.

All the needed optimization steps are performed by an automated software tool, the Onboard Computing Analysis (OCA), which simulates the on-board processing, explores the space of possible combinations of parameters, and produces a set of statistical indicators, among them: the compression rate $C_r$and the processing noise ϵ_Q. For Planck/LFI it is required that $C_r = 2.4$while, as for other systematics, $\epsilon_Q$would have to be less than 10% of rms of the instrumental white noise. An analytical model is developed that is able to extract most of the relevant information on the processing errors and the compression rate as a function of the signal statistics and the processing parameters to be tuned. This model is of interest for the instrument data analysis to asses the level of signal distortion introduced in the data by the on-board processing.

Once the instrument is completed tuned and stable, a tuning process is applied in order to optimize the REBA parameters. The procedure foresees to acquire chunks of about 15 minutes of *averaged data* to be analyzed by OCA. After setting the (optimized) REBA parameters, another session of 15 minutes of acquisition is applied, this time with the nominal processing.

The values for the optimal REBA parameters are mainly determined by the frequency of the radiometric channel with some dispersion from detector to detector. Table 13 below gives representative median values for r_1, r_2, q from on ground System Level tests (CSL) as well as for the quantities in Fig. 4 below and the resulting data rate. O is omitted since it is the most variable parameter and it has no significant impact on $\epsilon_q$and C_r. Table 13 below reports also the number of detectors for each frequency channel, the N_{aver}values which are kept constant, the compressed data rate per detector, per frequency channel and for the instrument as a whole. Quantities are reported in the form where δxrepresents the standard deviation taken as a measure of the internal dispersion of $x$within the given subset of detectors, this number must not be interpreted as an error and it must not be propagated.

The performance has been verified against the requirements with the result that the required data rate of 35.5 kbps has been achieved while keeping the processing error at a level of 3.8% of the instrumental white noise and well below the target 10% level.

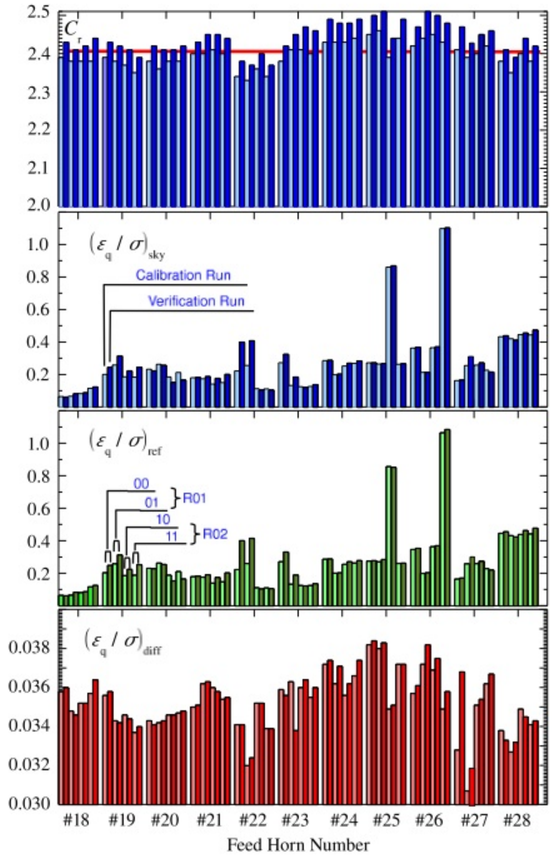

Figure 4. Results for a typical session of REBA parameters tuning during the CSL test campaign. From top to bottom the figure reports for each detector the mean $C_r,\ \epsilon_{q,sky}/\sigma_{sky},\ \epsilon_{q,load}/\sigma_{load},\ \epsilon_{q,diff}/\sigma_{diff}$ where σ_{diff} is the r.m.s. of the differentiated data. The red line in background of the top frame denotes the target $C_r^{Tgt} = 2.4$. Values are represented by bars. Light-bars are the results from the calibration phase, where raw data from the instrument are processed by OCA. Dark-bars are results from the verification phase, where processing is performed on-board. The second frame from Top gives an example for detector 00 of Feed-Horn #19. Feed-horns are numbered according to the internal Planck/LFI convention assigning at Planck/LFI the Feed-Horns numbers from #18 to #28. Detectors belonging to the same Feed-Horn are grouped together as shown in the third frame from top.

Table 13. Representative REBA Parameters, the measured

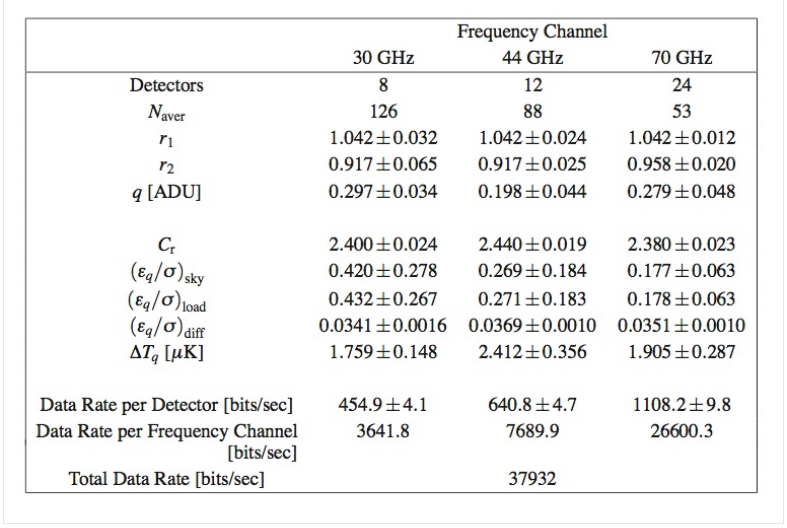

	Frequency Channel		
	30 GHz	44 GHz	70 GHz
Detectors	8	12	24
N_{aver}	126	88	53
r_1	1.042 ± 0.032	1.042 ± 0.024	1.042 ± 0.012
r_2	0.917 ± 0.065	0.917 ± 0.025	0.958 ± 0.020
q [ADU]	0.297 ± 0.034	0.198 ± 0.044	0.279 ± 0.048
C_r	2.400 ± 0.024	2.440 ± 0.019	2.380 ± 0.023
$(\varepsilon_q/\sigma)_{\text{sky}}$	0.420 ± 0.278	0.269 ± 0.184	0.177 ± 0.063
$(\varepsilon_q/\sigma)_{\text{load}}$	0.432 ± 0.267	0.271 ± 0.183	0.178 ± 0.063
$(\varepsilon_q/\sigma)_{\text{diff}}$	0.0341 ± 0.0016	0.0369 ± 0.0010	0.0351 ± 0.0010
ΔT_q [μK]	1.759 ± 0.148	2.412 ± 0.356	1.905 ± 0.287
Data Rate per Detector [bits/sec]	454.9 ± 4.1	640.8 ± 4.7	1108.2 ± 9.8
Data Rate per Frequency Channel [bits/sec]	3641.8	7689.9	26600.3
Total Data Rate [bits/sec]		37932	

In flight the procedure is to acquire continuously data by using the nominal processing. Short chunks of unprocessed data is daily acquired in turn from each detector. The comparison of unprocessed with processed data allows to monitor of the processing error. In addition the REBA tuning might be repeated daily on the chunk of unprocessed data in order to test whether some REBA parameters on-board the satellite should be changed or not.

Instrument Operations

LFI Operational Modes

The operations of the LFI are designed to be automatic and require little if any intervention from the ground. A small amount of commands is required for operating the instrument and eventually for diagnostic and reconfiguration purposes. Each sky survey is conducted by the LFI with the instrument in the Normal Operations Mode mode. No deployable elements, or mechanically moving parts are included in the instrument. The scanning of the sky is achieved by progressive repointing of the satellite spin axis, with the Sun direction always within a cone 10 degrees from the spin axis. Within the Normal Science Mode the instrument can be configured in order to fit with different science or diagnostic needs without changing the power consumption and thus the temperature in the FPU. Changes in power consumption in the FPU are minimised and should occur only in the case that failures in the radiometers that could create interference problems require an RCA to be switched off. Power adjustments on the first stage of the HEMT amplifiers which are contemplated, require extremely small power level variations.

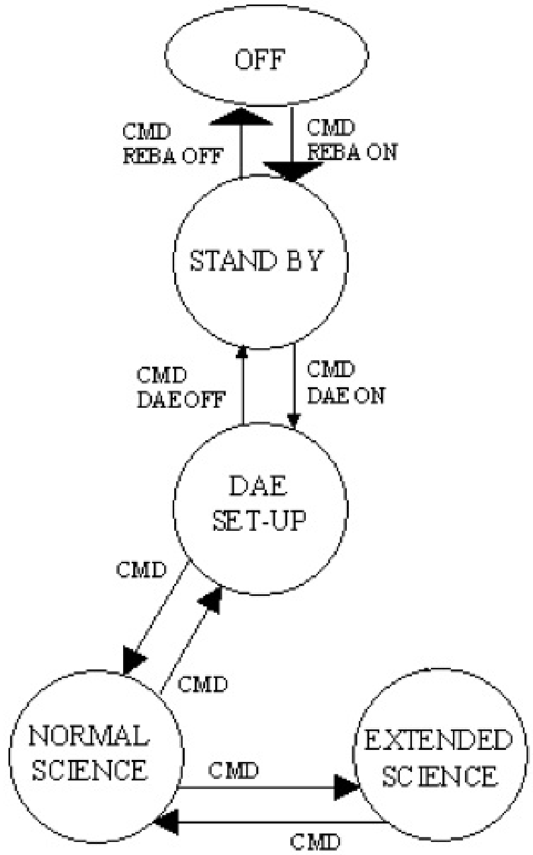

Figure 5. LFI Operating Modes and their nominal transitions.

A scheme of the nominal transitions between the LFI Operation Modes are shown in Fig. 5, a brief summary is given below.

1. OFF MODE: During this operating mode the instrument is completely off for example during the launch.
2. STAND-BY: During this mode only the REBA can be operated. It is the first interface to the instrument whenever the LFI is switched on. When the instrument is in this mode the RAA must be OFF because no data can be received and no control is possible on the radiometer chains.
3. DAE SET-UP: During this mode the REBA and the DAE are ON, but no radiometer chains are active. Nevertheless science data can be generated and contain only the background noise of the instrument.
4. NORMAL SCIENCE: During this mode the RAA is seen by the REBA as a set of 44 independent instruments. This means that each instrument can be operated, by the same SW, in different modes without affecting the LFI modes. Science data from the DAE are continuously acquired by the REBA that decides, on the basis of the activation table, which packets (either science or diagnostic) have to be produced. The whole set of HK is continuously acquired and sent to ground. This mode is the nominal for the LFI observation operations.
5. EXTENDED SCIENCE: This mode is similar to the previous except that for the total amount of telemetry sent to the ground. In fact this mode shall be used when, in particular cases, (e.g. calibration…) a larger telemetry rate is needed and made available by an agreement with HFI and the CDMS.

During launch, for contingency situations and/or to allow diagnostics of other spacecraft subsystems (e.g. HFI or others) LFI is in the OFF mode. When, upon a command from ground the REBA is powered on, the instrument is in its STAND-BY mode. A step-by-step bootstrap procedure commanded from ground documented by HK is initialized to turn the DAE on. This sets-up the internal communications, and allows the LFI subsystems to collect and deliver a full set of HK. The instrument is in DAE SET-UP mode. The following step is to upload from ground the DAE settings and processing parameters; then, to switch on the RCA on ground command. At this stage, on ground command, the acquisition of science data can start. A further step is needed to move to NORMAL SCIENCE, namely start processing and compressing the science raw data. When this is accomplished, science packets can be sent to ground.

Instrument Technical Performance

Spectral Response

The in-band receiver response has been thoroughly modelled and measured for all the LFI detectors during ground tests. The complete set of bandpass curves has been published in #zonca2009 where all the details of the LFI radiometer's spectral response are given. From each curve we have derived the effective centre frequency according to:

where is the receiver bandwidth and $g(\nu)$is the bandpass response. Table 14 below gives the centre frequencies of the 22 LFI radiometers. For each radiometer, $g(\nu)$is calculated by weight-averaging the bandpass response of the two individual diodes with the same weights used to average detector timestreams. For simplicity and for historical reasons, we will continue to refer to the three channels as the 30, 44, and 70 GHz channels.

Table 14. LFI centre frequencies.

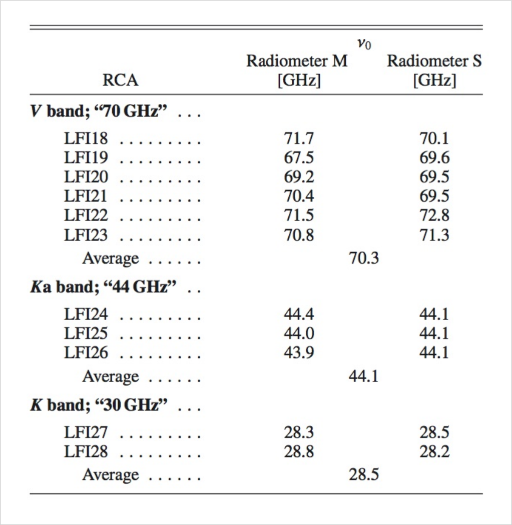

RCA	ν_0 Radiometer M [GHz]	Radiometer S [GHz]
***V* band; "70 GHz"** . . .		
LFI18	71.7	70.1
LFI19	67.5	69.6
LFI20	69.2	69.5
LFI21	70.4	69.5
LFI22	71.5	72.8
LFI23	70.8	71.3
Average	70.3	
***Ka* band; "44 GHz"** . .		
LFI24	44.4	44.1
LFI25	44.0	44.1
LFI26	43.9	44.1
Average	44.1	
***K* band; "30 GHz"** . . .		
LFI27	28.3	28.5
LFI28	28.8	28.2
Average	28.5	

Colour corrections, $C(\alpha)$, needed to derive the brightness temperature of a source with a power-law spectral index α, are given in the table 15 below. The values are averaged for the 11 RCAs and for the three frequency channels. Details about the definition of colour corrections are provided in #planck2011-1-6.

Table 15. Colour corrections for the 11 LFI RCAs individually and averaged by frequency.

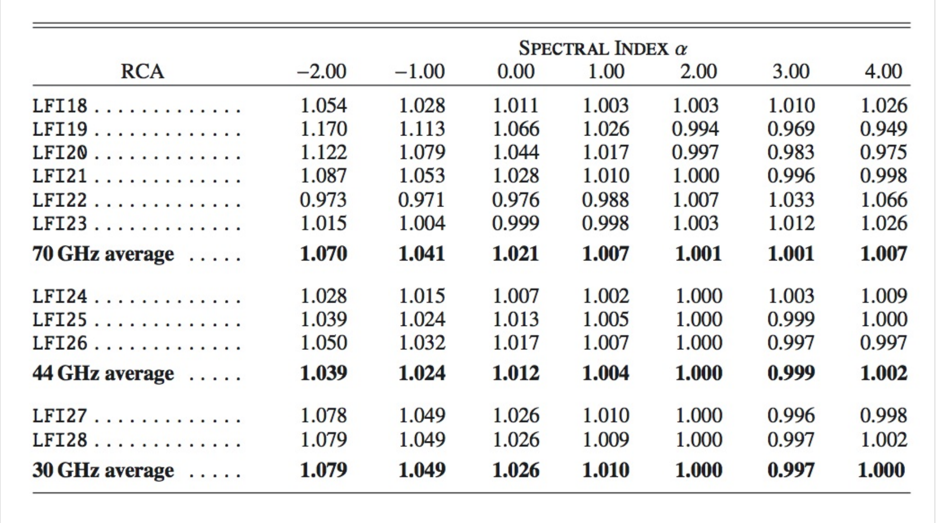

RCA	Spectral Index α −2.00	−1.00	0.00	1.00	2.00	3.00	4.00
LFI18	1.054	1.028	1.011	1.003	1.003	1.010	1.026
LFI19	1.170	1.113	1.066	1.026	0.994	0.969	0.949
LFI20	1.122	1.079	1.044	1.017	0.997	0.983	0.975
LFI21	1.087	1.053	1.028	1.010	1.000	0.996	0.998
LFI22	0.973	0.971	0.976	0.988	1.007	1.033	1.066
LFI23	1.015	1.004	0.999	0.998	1.003	1.012	1.026
70 GHz average	**1.070**	**1.041**	**1.021**	**1.007**	**1.001**	**1.001**	**1.007**
LFI24	1.028	1.015	1.007	1.002	1.000	1.003	1.009
LFI25	1.039	1.024	1.013	1.005	1.000	0.999	1.000
LFI26	1.050	1.032	1.017	1.007	1.000	0.997	0.997
44 GHz average	**1.039**	**1.024**	**1.012**	**1.004**	**1.000**	**0.999**	**1.002**
LFI27	1.078	1.049	1.026	1.010	1.000	0.996	0.998
LFI28	1.079	1.049	1.026	1.009	1.000	0.997	1.002
30 GHz average	**1.079**	**1.049**	**1.026**	**1.010**	**1.000**	**0.997**	**1.000**

Bandpass Estimation

As detailed in #zonca2009, our most accurate method to measure the LFI bandpasses is based on measurements of individual components integrated into the LFI Advanced RF Model (LARFM) to yield a synthesised radiometer bandpass. The LARFM is a software tool based on the open-source Quasi Universal Circuit Simulator (QUCS). The measured frequency responses of the various subsystems (feed-OMT, FEM, BEM) are considered as lumped S-parameter components. Measurements of single components are obtained with standard methods and provide highly reliable results, with precision of order 0.1-0.2 dB over the entire band. Waveguides are simulated with an analytical model, in order to reproduce the effect of their temperature gradient and the effect of standing waves caused by impedance mismatch at the interfaces between the FEM and BEM. This is because the 1.8-meter long waveguides were not measured at unit level in cryogenic conditions. The model provides accurate agreement with the measured waveguide response in the conditions of the test measurements (300 K). The composite bandpasses are estimated to have a precision of about 1.5 to 2 dB.

We also attempted an end-to-end measurement of the RCA spectral response in the cryo-facility as an independent check. Unfortunately, these measurements suffered some subtle systematic effects in the test setup (standing waves at 70 GHz; polarisation mismatch and narrow frequency coverage at 30 and 44 GHz), preventing an accurate cross-check. However, the comparison shows a general agreement within limits of the test reliability and repeatability.

Figg. 6 and 7 below show all the LFI bandpasses obtained by the frequency response data of each radiometer unit assembled by the LARFM. The 70 GHz channels show a low bandpass ripple, of about 10 dB, which is within scientific requirements. The spike between 60 and 61 GHz, below the low frequency cut-off, is due to a systematic effect present in all the BEM gain measurements and caused by the test setup. We removed this range from the bandpasses made available at the Data Processing Center in order to avoid possible spurious effects and therefore the frequency coverage is 61-80 GHz. The high frequency cut-off is not well defined in most of the channels. The 30 and 44 GHz bandpasses show a more complex shape, driven by the BEM spectral response, but still within ± 10dB. The low frequency cut-off is always well defined, while the high frequency cut-off is not well defined in RCA 24 and 26. However, comparing with the high frequency cut-off of RCA 25, it is expected that the additional bandwidth is very low. Frequency coverage is 25-50 GHz for the 44 GHz channels and 21.3-40 GHz for the 30 GHz channels.

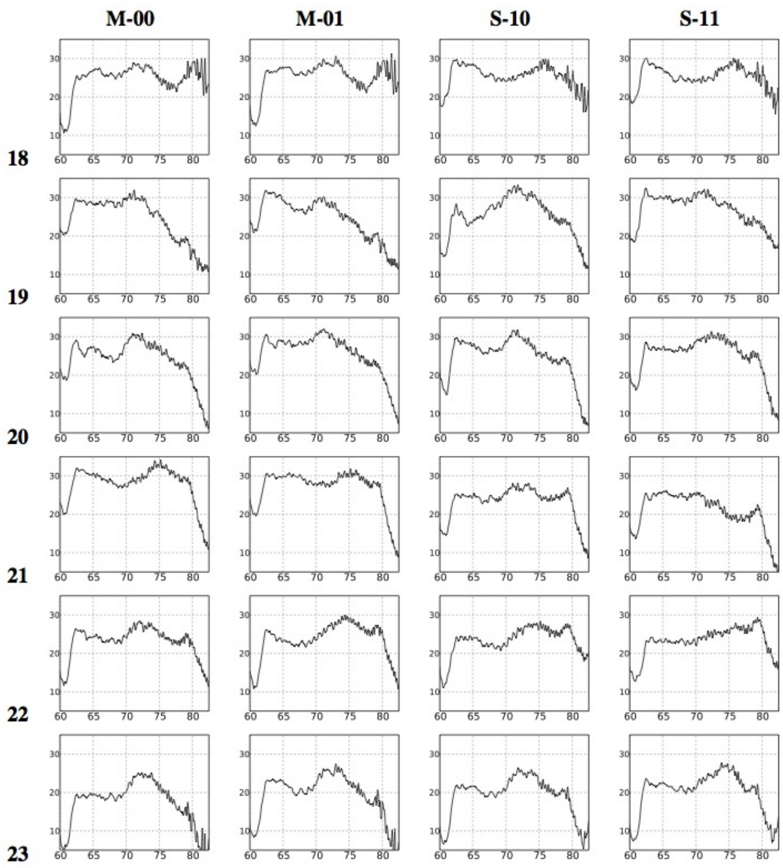

Figure 6. LFI 70 GHz channels' bandpasses. Each row shows the 4 bandpasses of a RCA ordered as M-00, M-01, S-10 and S-11. Units are [dB] $10\log(\frac{V_{out}}{V_{in}})$ plotted against frequency [GHz].

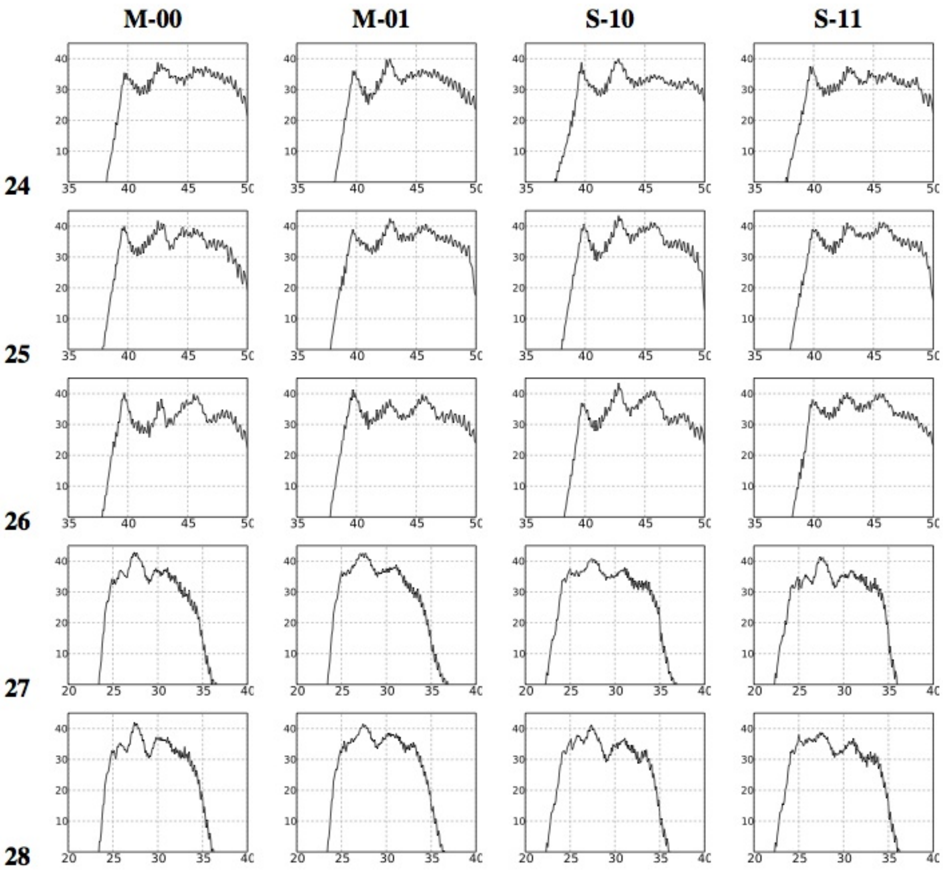

Figure 7. LFI30 and 44 GHz channels' bandpasses. Each row shows the 4 bandpasses of a RCA ordered as M-00, M-01, S-10 and S-11. Units are [dB] $10\log(\frac{V_{out}}{V_{in}})$ plotted against frequency [GHz].

Stability

Thanks to its differential scheme, the LFI is insensitive to many effects caused by $1/f$ noise, thermal fluctuations, or electrical instabilities. As detailed in #planck2011-1-4 [Planck early paper III [1]], one effect detected during the first survey was the daily temperature fluctuation in the back-end unit induced by the downlink transponder, which was powered on each day for downlinks during the first 258 days of the mission. As expected, the effect is highly correlated between the sky and reference load signals. In the difference, the variation is reduced by a factor , where r is the gain modulation factor defined in Eq. (2) in the RCA section.

A particular class of signal fluctuations occasionally observed during operations is due to electrical instabilities that appear as abrupt increases in the measured drain current of the front-end amplifiers, with a relaxation time variable from few seconds to some hundreds of seconds. Typically, these events cause a simultaneous change in the sky and reference load signals. Because they are essentially common-mode, their residual on the differenced data is negligible (Fig. 8), and the data are suitable for science production. In a few cases the residual fluctuation in the differential output was large enough (a few millikelvin in calibrated antenna temperature units) to be flagged, and the data were not used. The total amount of discarded data for all LFI channels until Operational Day 389 was about 2000 s per detector, or 0.008%.

A further peculiar effect appeared in the 44 GHz detectors, where single isolated samples, either on the sky or the reference voltage output, were far from the rest. Over a reference period of four months, 15 occurrences of single-sample spikes (out of 24 total anomaly events) were discarded, an insignificant loss of data.

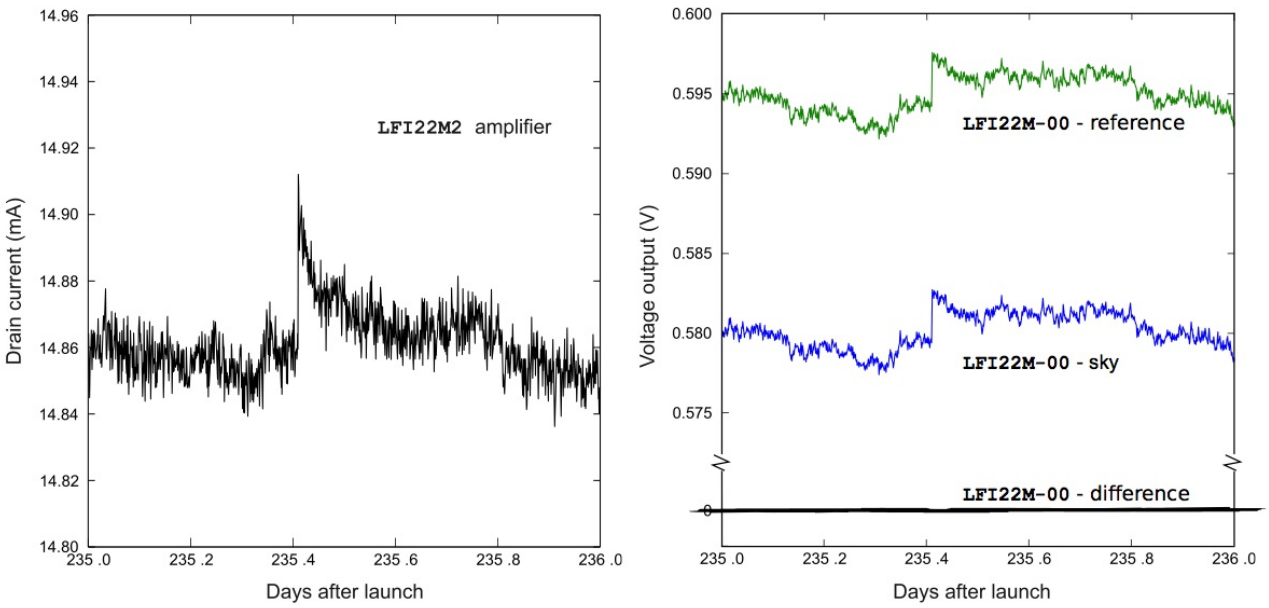

Figure 8. Short spikes in the drain current (left) affect total power signals (right). The jumps are strongly correlated in sky and reference signals, so that in the difference data the effect essentially disappears.

Thermal Susceptibility

As already mentioned in In-flight Calibration section and detailed in #gregorio2013, during the CPV campaign, susceptibility tests were performed in order to characterise the LFI instrument susceptibility to thermal and electrical variations.

The effect of temperature fluctuations on the LFI radiometers is originated in the Planck cold end interface of the hydrogen sorption cooler to the instrument focal plane. The temperature is actively controlled through a dedicated stage, the Thermal Stabilization Assembly (TSA), providing a first reduction of the effect. The thermal mass of the focal plane strongly contribute to reduce residual fluctuations. The physical temperature fluctuations propagated at the front end modules cause a correlated fluctuation in the radiometer signal degrading the quality of scientific data. The accurate characterization of this effect is crucial for possibly removing it from raw data by exploiting the housekeeping information of thermal sensors.

The propagation of the temperature oscillations through the focal plane and the instrument response to thermal changes were characterized through two main tests:

- the thermal dynamic response aimed at measuring the dynamic thermal behaviour of the LFI Focal Plane;
- the radiometers thermal susceptibility.

Thermal Dynamic Response

In order to amplify the effect and to get a more accurate measurement, the active control from the TSA was switched off. The resulting increased fluctuations, propagating at the cooler frequencies, were used to evaluate transfer functions between the TSA stage and the FPU sensors (see Fig. 9 below). The analysis produced damping factors of 2–5 at about 1 mHz. The source of fluctuations was characterized by two typical periods of the sorption cooler during the final CPV phase: (i) the single bed cycle time, 940 s, (ii) the complete cooler period, six times larger, 5640 s.

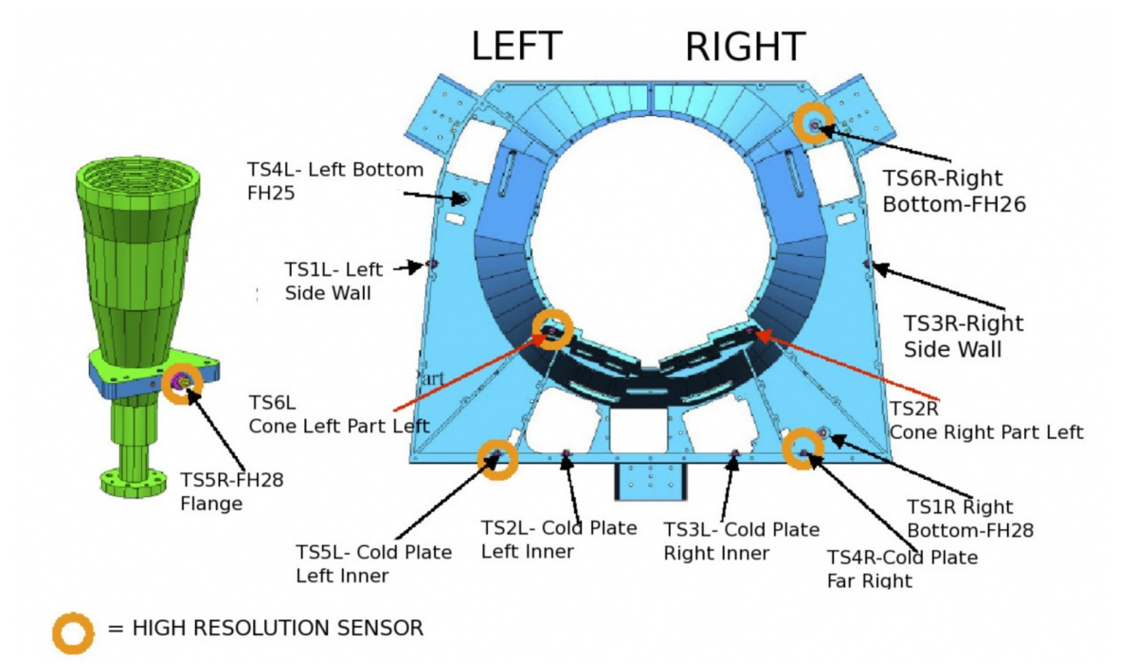
LEFT
RIGHT
TS4L- Left Bottom FH25
TS1L- Left Side Wall
TS6L Cone Left Part Left
TS5R-FH28 Flange
TS5L- Cold Plate Left Inner
TS2L- Cold Plate Left Inner
TS3L- Cold Plate Right Inner
TS6R-Right Bottom-FH26
TS3R-Right Side Wall
TS2R Cone Right Part Left
TS1R Right Bottom-FH28
TS4R-Cold Plate Far Right
= HIGH RESOLUTION SENSOR

Figure 9. Schema of the focal plane thermal sensor locations.

Results are shown in Table 16. Sorting the sensors by the transfer function amplitudes in descending order (second column of the table), the route of the propagation of temperature fluctuations through the focal plane sensors (shown in Fig. 9) was reproduced as expected: the largest amplitudes are in the sensor closest to the right bottom corner interface with the working cooler and they decrease in the direction left upwards. The measured values in flight showing a good agreement with what measured during the CSL ground test.

Table 16. Transmission amplitudes and phases of fluctuations at the two main cooler frequencies during the transient test. Typical fit parameters uncertainties are at 1% level.

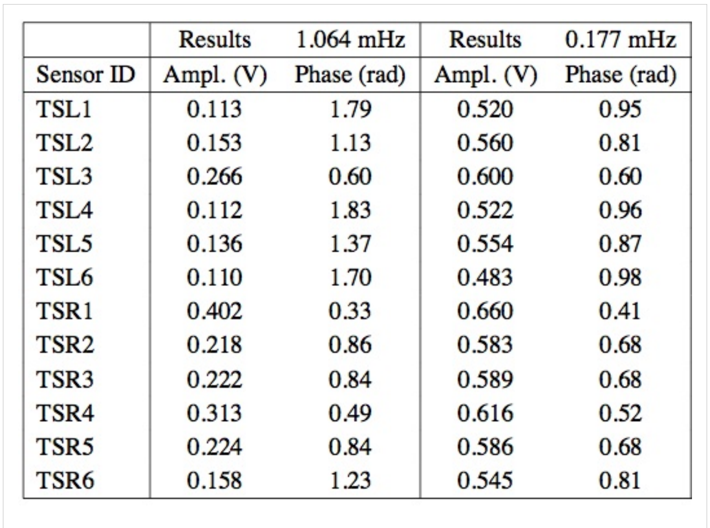

	Results	1.064 mHz	Results	0.177 mHz
Sensor ID	Ampl. (V)	Phase (rad)	Ampl. (V)	Phase (rad)
TSL1	0.113	1.79	0.520	0.95
TSL2	0.153	1.13	0.560	0.81
TSL3	0.266	0.60	0.600	0.60
TSL4	0.112	1.83	0.522	0.96
TSL5	0.136	1.37	0.554	0.87
TSL6	0.110	1.70	0.483	0.98
TSR1	0.402	0.33	0.660	0.41
TSR2	0.218	0.86	0.583	0.68
TSR3	0.222	0.84	0.589	0.68
TSR4	0.313	0.49	0.616	0.52
TSR5	0.224	0.84	0.586	0.68
TSR6	0.158	1.23	0.545	0.81

Radiometer Thermal Susceptibility

Fluctuations of the focal plane temperature would cause variations of important parameters (mainly the low noise amplifier gains and noise temperatures), impacting the radiometer output signal. The response of the LFI radiometers to thermal fluctuations was estimated by inducing discrete temperature steps on the focal plane through TSA set-point changes. The set-point was changed over four values (Fig. 47, left) and after a stabilization of at least two hours, the measured receivers output was characterized as a function of each temperature variation of about 0.3 K.

The slope of the resulting $T_{\mathbf{ant}}$vs $T_{\mathbf{phys}}$plot is the measured response of the receivers to a change in the temperature. Results, reported in the Table 17, confirmed that physical temperature fluctuations in the main frame are furtherly reduced when convolved with the radiometer thermal susceptibility coefficients: the derived output fluctuations, measured in antenna temperature, were actually reduced by an extra factor of 10 to 200 (according to the channel considered), of the same order of ground test results. This corresponds to reduce the mean peak-to-peak amplitudes of fluctuations measured by high resolution sensors, of the order of 4 mK in steady condition, of at least one order of magnitude in the output timestream.

Table 17. Results of thermal susceptibility test. Units are

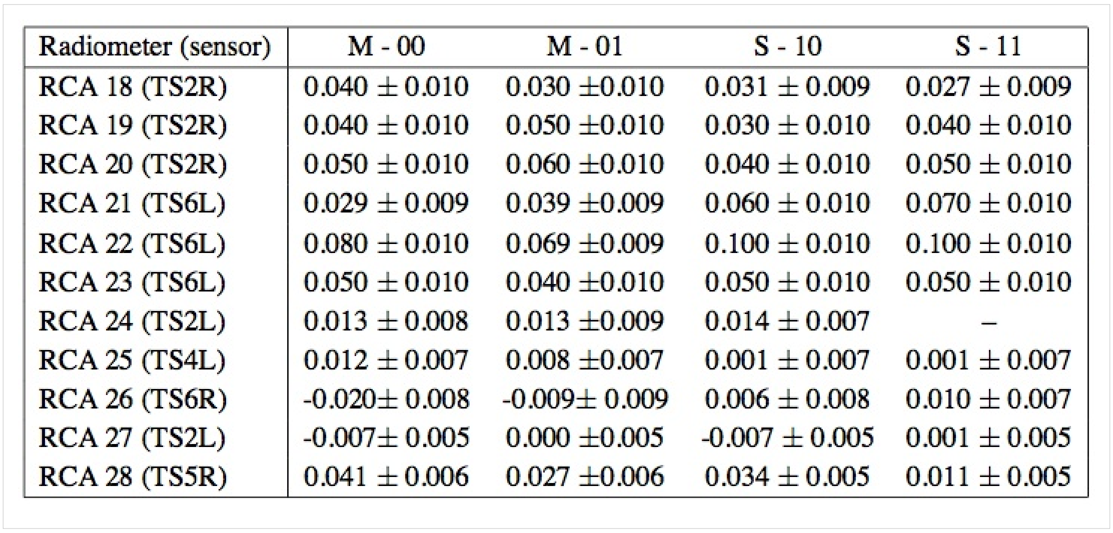

Radiometer (sensor)	M - 00	M - 01	S - 10	S - 11
RCA 18 (TS2R)	0.040 ± 0.010	0.030 ±0.010	0.031 ± 0.009	0.027 ± 0.009
RCA 19 (TS2R)	0.040 ± 0.010	0.050 ±0.010	0.030 ± 0.010	0.040 ± 0.010
RCA 20 (TS2R)	0.050 ± 0.010	0.060 ±0.010	0.040 ± 0.010	0.050 ± 0.010
RCA 21 (TS6L)	0.029 ± 0.009	0.039 ±0.009	0.060 ± 0.010	0.070 ± 0.010
RCA 22 (TS6L)	0.080 ± 0.010	0.069 ±0.009	0.100 ± 0.010	0.100 ± 0.010
RCA 23 (TS6L)	0.050 ± 0.010	0.040 ±0.010	0.050 ± 0.010	0.050 ± 0.010
RCA 24 (TS2L)	0.013 ± 0.008	0.013 ±0.009	0.014 ± 0.007	–
RCA 25 (TS4L)	0.012 ± 0.007	0.008 ±0.007	0.001 ± 0.007	0.001 ± 0.007
RCA 26 (TS6R)	-0.020± 0.008	-0.009± 0.009	0.006 ± 0.008	0.010 ± 0.007
RCA 27 (TS2L)	-0.007± 0.005	0.000 ±0.005	-0.007 ± 0.005	0.001 ± 0.005
RCA 28 (TS5R)	0.041 ± 0.006	0.027 ±0.006	0.034 ± 0.005	0.011 ± 0.005

Instrument Budgets

Power Budget

Table 18. LFI sub-system power budget.

Subsystem	Unit	Assembly	Sub-Assembly	Budget [W]
RAA				45.599
	FEU			0.329
		FE structure		N/A
		Feed Horns		N/A
		OMTs		N/A
		FEMs		0.329
			30 GHz	0.056
			44 GHz	0.121

			70 GHz	0.152
	BEU			45.270
		DAE		31.986
		BEMs		13.284
			30 GHz	4.914
			44 GHz	4.633
			70 GHz	3.737
		Waveguides		N/A
		RAA harness		N/A
	4K Load			N/A
REBA				22.700
System Harness				N/A
Total				68.299

Mass Budget

The maximum allocated mass for the Planck Instruments is 445 kg, 89 kg are allocated for the LFI instrument. The distribution of the instrument and cooler mass to the different interfaces in the system is as given in table 19 below.

Table 19. LFI sub-system mass budget.

Subsystem	Unit	Assembly	Sub-Assembly	Budget [kg]
RAA				77.900
	FEU			22.935
		FE structure		17.680
		Feed Horns+OMTs		2.825
			30 GHz	0.680
			44 GHz	0.732
			70 GHz	1.413
		FEMs		2.430
			30 GHz	0.810
			44 GHz	1.110
			70 GHz	0.510
	BEU			25.542
		DAE		23.130
		BEMs		2.412
			30 GHz	0.624
			44 GHz	0.864
			70 GHz	0.924
	Waveguides			23.005
		WG structure		15.940
		WGs		7.065

	RAA harness			5.491
		BEU internal harness		4.489
		DAE-FEU cryo-harness		1.002
	4K Load			0.927
REBA (2 units)				8.480
System Harness				3.495
Total				89.875

Telemetry Budget

All the science data flow coming from the foreseen on-board data processing can be summarised in the following table 20.

Table 20. Data processing and compression results.

	30 GHz	**44 GHz**	**70 GHz**	**Total**
Total samples	65	94	154	
Compression factor	2.4	2.4	2.4	
Compressed samples	27	39	64	
Science data available (word)	490	490	490	
Time per packet (s)	18.035	12.570	7.651	
Corresponding sky arc (°)	108	75	46	
Packet frequency (Hz)	0.444	0.955	3.317	
Net Data Volume (word/s)	217.352	467.778	1536.986	2222.116
Net Data Volume (kbps)	3.478	7.484	24.592	35.554

This result refers to the net science telemetry rate that LFI sends to ground. If we add the overhead due to the packet header (protocol) and the tertiary header we obtain a gross science telemetry rate of 37.150 kbps. This number should be added to the data coming from the calibration channel (uncompressed data used to verify the correct functionalities of the on-board compression algorithm, see Reduction and Compression of Science Data section) sent to ground in parallel. This channel has a worst case gross data production of 5.140 kbps for a total science data of 42.290 kbps.

The gross housekeeping telemetry budget is 2.425 kbps for a total budget of 44.715 kbps. The total data budget allocated to the LFI is 53.5 kbps well above the LFI total telemetry budget.

References

<biblio force=false>

1. References

</biblio>

Ground segment and operations

Ground Segment and Operations

Geographical distribution of the Planck Ground Segment

The Planck Ground Segment is made of four geographically distributed centres:

The Mission Operations Centre

The mission operations centre (MOC), located at ESA's operations centre in Darmstadt (Germany), is responsible for all aspects of flight control and of the health and safety of the Planck satellite, including both instruments. It plans and executes all necessary satellite activities, including instrument commanding requests by the instrument operations centres.

MOC communicates with the satellite using ESA's 35-m antenna located in New Norcia (Australia), or that in Cebreros (Spain), over a daily 3-h period, during which it uplinks a scheduled activity timeline which is autonomously executed by the satellite, and downlinks the science and housekeeping (HK) data acquired by the satellite during the past 24 h. The downlinked data are transferred from the antenna to the MOC over a period of typically 8 h; at MOC they are put onto a data server from where they are retrieved by the two Data Processing Centres.

The European Space Operations Centre in Darmstadt, Germany, home of the Planck Mission Operations Centre.

The Planck Science Office

The Planck Science Office (PSO)is located at ESA's European Space Astronomy Centre in Villanueva de la Cañada surroundings (Madrid, Spain).

Its main responsibilities include:

- coordinating scientific operations of the Planck instruments
- designing, planning and executing the Planck observation strategy.

It provides to MOC a detailed pointing plan with a periodicity of about one month.

- creating and updating the specifications of the Planck Legacy Archive developed by the Science Archives Team at ESAC
- testing and operating the PLA

The European Space Astronomy Centre in Villanueva de la Cañada, Madrid, Spain, see of the Planck Science Office.

The LFI instrument operations and data-processing centre

The LFI instrument operations and data processing centre, located at the Osservatorio Astronomico di Trieste (Italy), is notably responsible for:

- the optimal operation of the LFI instrument
- the processing of the data acquired by LFI into the final scientific products of the mission.

The HFI instrument operations and data-processing centre

The HFI instrument operations and data processing centres, located respectively at the Institut d'Astrophysique Spatiale in Orsay (France) and at the Institut d'Astrophysique de Paris (France), are similarly responsible for the optimal operation of the HFI instrument, and (with several other institutes in France and the UK) for the processing of the data acquired by HFI into the final scientific products of the mission.

The data flow in the Planck Ground Segment

The Planck Science Office (PSO), located at ESAC, Spain, sends the pointing lists (Pre-Programmed Pointing Lists) to the Mission Operations Centre at ESOC in Darmstadt, Germany. The Flight Dynamics team at ESOC adapts them into Augmented Pre-Programmed Pointing Lists (APPL) taking into account ground station scheduling, Operational Day (OD) boundaries and other issues.

MOC sends pointing and instrument commands to the spacecraft, and receives the house-keeping telemetry and science data through the ground stations (for Planck, mostly the New Norcia and Cebreros ones).

Science data is then transferred to both Data Processing Centres (DPC) which process the data and send quality reports to PSO.

Science products (timelines, maps, etc) are exchanged between DPCs in order to help calibration and other scientific issues.

More information about the Planck Ground Segment may be found in #tauber2010a.

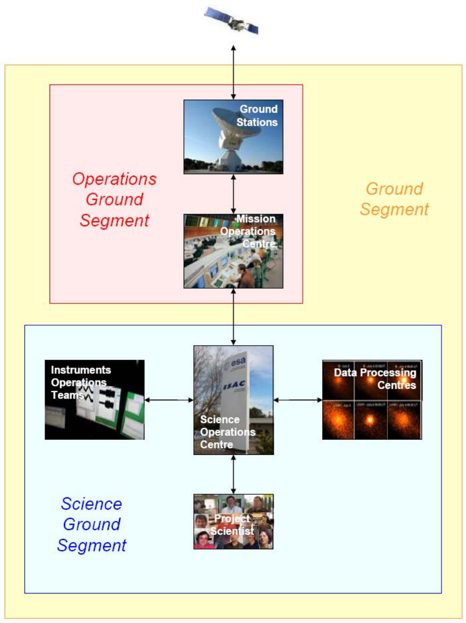
Ground Stations
Operations Ground Segment
Ground Segment
Mission Operations Centre
Instruments Operations Teams
Data Processing Centres
Science Operations Centre
Science Ground Segment
Project Scientist

General schematics of European Space Agency Science Ground Segments. This picture exhibits the way ESA Ground Segments are generally organized.

Contingencies

The main unplanned events included the following:

- Very minor deviations from the scanning law include occasional (on the average about once every two months) under-performance of the 1-N thrusters used for regular manoeuvres, which implied the corresponding pointings were not at the intended locations. These deviations had typical amplitudes of 30 arcsec, and have no significant impact on the coverage map.
- The thruster heaters were unintentionally turned off between 31 August and 16 September 2009 (the so-called "catbed" event).
- An operator error in the upload of the on-board command timeline led to an interruption of the normal sequence of manoeuvres and therefore to Planck pointing to the same

location on the sky for a period of 29 h between 20 and 21 November 2009 (“the day Planck stood still”). Observations of the nominal scanning pattern resumed on 22 November, and on 23 November a recovery operation was applied to survey the previously missed area. During the recovery period the duration of pointing was decreased to allow the nominal law to be caught up with. As a side effect, the RF transmitter was left on for longer than 24 h, which had a significant thermal impact on the warm part of the satellite.

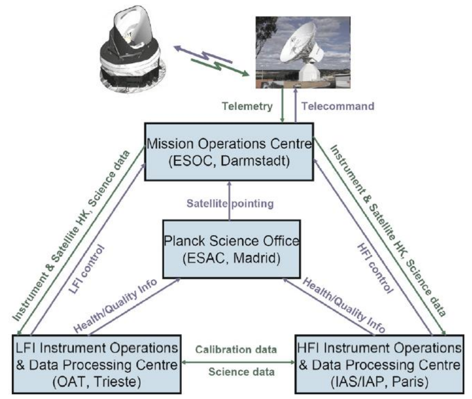
Telemetry
Telecommand
Mission Operations Centre
(ESOC, Darmstadt)
Instrument & Satellite HK, Science data
Instrument & Satellite HK, Science data
Satellite pointing
Planck Science Office
(ESAC, Madrid)
LFI control
HFI control
Health/Quality Info
Health/Quality Info
LFI Instrument Operations
& Data Processing Centre
(OAT, Trieste)
Calibration data
Science data
HFI Instrument Operations
& Data Processing Centre
(IAS/IAP, Paris)

Specific schematics of the Planck Science Ground Segment. This picture exhibits the way the specific Planck Science Ground Segment works.

- As planned, the RF transmitter was initially turned on and off every day in synchrony with the daily visibility window, in order to reduce potential interference by the transmitter on the scientific data. The induced daily temperature variation had a measurable effect throughout the satellite. An important effect was on the temperature of the 4He-JT cooler compressors, which caused variations of the levels of the interference lines that they induce on the bolometer data (Planck HFI Core Team 2011a). Therefore the RF transmitter was left permanently on starting from 25 January 2010 (257 days after launch), which made a noticeable improvement on the daily temperature variations.
- During the coverage period, the operational star tracker switched autonomously to the redundant unit on two occasions (11 January 2010 and 26 February 2010); the nominal star tracker was restored a short period later (3.37 and 12.75 h, respectively) by manual power-cycling. Although the science data taken during this period have normal quality, they have not been used because the redundant star tracker’s performance is not fully characterised.

For more information, see #planck2011-1-1.

References

<biblio force=false>

1. References

</biblio>

Operational history

(Note: Adapted from Planck Collaboration 2011, A&A 536, A1)

Provide a description of the product Planck Operational State History.

The major operational phases and milestones are:

Launch and transfer to orbit: (provide date, and summary overview)

Planck was launched from the Centre Spatial Guyanais in Kourou (French Guyana) on 14 May 2009 at its nominal lift-off time of 13:12 UT, on an Ariane 5 ECA rocket of Arianespace2. ESA's Herschel observatory was launched on the same rocket. At 13:37:55 UT, Herschel was released from the rocket at an altitude of 1200 km; Planck followed suit at 13:40:25UT. The separation attitudes of both satellites were within 0.1 deg of prediction. The Ariane rocket placed Planck with excellent accuracy (semimajor axis within 1.6% of prediction), on a trajectory towards the second Lagrangian point of the Earth-Sun system (L2). After release from the rocket, three large manoeuvres were carried out to place Planck in its intended final orbit. The first (14.35 ms−1), intended to correct for errors in the rocket injection, was executed on 15 May at 20:01:05 UT, with a slight overperformance of 0.9% and an error in direction of 1.3 deg (a touch-up manoeuvre was carried out on 16 May at 07:17:36 UT). The second and major (mid-course) manoeuvre (153.6ms−1) took place between 5 and 7 June, and a touch-up (11.8 ms−1) was executed on 17 June. The third and final manoeuvre (58.8ms−1), to inject Planck into its final orbit, was executed between 2 and 3 July. The total fuel consumption of these manoeuvres, which were carried out using Planck's coarse (20N) thrusters, was 205 kg. Once in its final orbit, very small manoeuvres are required at approximately monthly intervals (1 ms−1 per year) to keep Planck from drifting away from its intended path around L2. The attitude manoeuvres required to follow the scanning strategy require about 2.6 ms−1 per year. Overall, the excellent performance of launch and orbit manoeuvres will lead to a large amount (~160 kg, or ~40% of initial tank loading) of fuel remaining on board at end of mission operations.

Planck started cooling down radiatively shortly after launch. Heaters were activated to hold the focal plane at 250 K, which was reached around 5 h after launch. The valve opening the exhaust piping of the dilution cooler was activated at 03:30 UT, and the 4He-JT cooler compressors were turned on at low stroke at 05:20 UT. After these essential operations were completed, on the second day after launch, the focal plane temperature was allowed to descend to 170 K for out-gassing and decontamination of the telescope and focal plane.

Commissioning: (provide date, and summary overview)

The first period of operations focussed on commissioning activities, i.e., functional check-out procedures of all sub-systems and instruments of the Planck spacecraft in preparation for running science operations related to calibration and performance verification of the payload. Planning for commissioning operations was driven by the telescope decontamination period of 2 weeks and the subsequent cryogenic cool-down of the payload and instruments. The overall duration of the cool-down was approximately 2 months, including the decontamination period. The sequence of commissioning activities covered the following areas:

- on-board commanding and data management;
- attitude measurement and control;
- manoeuvreing ability and orbit control;
- telemetry and telecommand;
- power control;
- thermal control;
- payload basic functionality, including:
- the LFI;

- the HFI;
- the cryogenic chain;
- the Standard Radiation Environment Monitor;
- the Fibre-Optic Gyro unit (FOG), a piggy-back experiment which is not used as part of the attitude control system.

The commissioning activities were executed very smoothly and all sub-systems were found to be in good health. The most significant unexpected issues that had to be addressed during these early operational phases were the following.

- The X-band transponder showed an initialisation anomaly during switch-on which was fixed by a software patch.
- Large reorientations of the spin axis were imperfectly completed and required optimisation of the on-board parameters of the attitude control system.
- The data rate required to transmit all science data to the ground was larger than planned, due to the unexpectedly high level of Galactic cosmic rays, which led to a high glitch rate on the data stream of the HFI bolometers (Planck HFI Core Team 2011a); glitches increase the dynamic range and consequently the data rate. The total data rate was controlled by increasing the compression level of a few less critical thermometers.
- The level of thermal fluctuations in the 20-K stage was higher than originally expected. Optimisation of the sorption cooler operation led to an improvement, though they still remained ~25% higher than expected (Planck Collaboration 2011b).
- The 20-K sorption cooler turned itself off on 10 June 2009, an event which was traced to an incorrectly set safety threshold.
- A small number of sudden pressure changes were observed in the 4He-JT cooler during its first weeks of operation, and were most likely due to impurities present in the cooler gas (Planck Collaboration 2011b). The events disappeared after some weeks, as the impurities became trapped in the cooler system.
- The 4He-JT cooler suffered an anomalous switch to standby mode on 6 August 2009, following a current spike in the charge regulator unit which controls the current levels between the cooler electronics and the satellite power supply (Planck Collaboration 2011b). The cooler was restarted 20 h after the event, and the thermal stability of the 100-mK stage was recovered about 47 h later. The physical cause of this anomaly was not found, but the problem has not recurred.
- Instabilities were observed in the temperature of the 4He-JT stage, which were traced to interactions with lower temperature stages, similar in nature to instabilities observed during ground testing (Planck Collaboration 2011b). They were fixed by exploring and tuning the operating points of the multiple stages of the cryo-system.
- The length of the daily telecommunications period was increased from 180 to 195 min to improve the margin available and ensure completion of all daily activities.

The commissioning activities were formally completed at the time when the HFI bolometer stage reached its target temperature of 100 mK, on 3 July 2009 at 01:00 UT. At this time all the critical resource budgets (power, fuel, lifetime, etc.) were found to contain very significant margins with respect to the original specification

Calibration and Performance Verification: (provide date, and summary overview)

Calibration and performance verification (CPV) activities started during the cool-down period and continued until the end of August 2009. Their objectives were to:

- verify that the instruments were optimally tuned and their performance characterised and verified;
- perform all tests and characterisation activities which could not be performed during the routine phase;
- characterise the spacecraft and telescope characteristics of relevance for science;
- estimate the lifetime of the cryogenic chain.

CPV activities addressed the following areas:

- tuning and characterisation of the behaviour of the cryogenic chain;
- characterisation of the thermal behaviour of the spacecraft

and payload;

- for each of the two instruments: tuning; characterisation and/or verification of performance, calibration (including thermal, RF, noise and stability, optical response); and data compression properties;
- determination of the focal plane footprint on the sky;
- verification of scanning strategy parameters;
- characterisation of systematic effects induced by the spacecraft and the telescope, including:
- dependence on solar aspect angle;
- dependence on spin;
- interference from the RF transmitter;
- straylight rejection;
- pointing performance.

The schedule of CPV activities consumed about two weeks longer than initially planned, mainly due to:

- the anomalous switch to standby mode of the 4He-JT cooler on 6 August (costing 6 days until recovery);
- instabilities in the cryo-chain, which required the exploration of a larger parameter phase space to find an optimal setting point;
- additional measurements of the voltage bias space of the LFI radiometers, which were introduced to optimise its noise performance, and led to the requirement of artificially slowing the natural cool-down of the 4He-JT stage.

A more detailed description of the relevant parts of these tests can be found in Mennella et al. (2011) and Planck HFI Core Team (2011a). On completion of all the planned activities, it was concluded that:

- the two instruments were fully tuned and ready for routine operations. No further parameter tuning was expected to be needed, except for the sorption cooler, which requires a weekly change in operational parameters (Planck Collaboration 2011b);
- the scientific performance parameters of both instruments was in most respects as had been measured on the ground before launch. The only significant exception was that, due to the high level of Galactic cosmic rays, the bolometers of HFI were detecting a higher number of glitches than expected, causing a modest (~10%) level of systematic effects on their noise properties (see details in Planck HFI Core Team 2011a);
- the telescope survived launch and cool-down in orbit without any major distortions or changes in its alignment;
- the lifetime of the cryogenic chain was adequate to carry the mission to its foreseen end of operations in November 2010, with a margin of order one year;
- the pointing performance was better than expected, and no changes to the planned scanning strategy were required;
- the satellite did not introduce any major systematic effects into the science data. In particular, the telemetry transponder did not result in radio-frequency interference, which implies that the data acquired during visibility periods is useable for science.

Nominal Mission: (provide date, and summary overview)

The routine operations phase of Planck is characterised by continuous and stable scanning of the sky and data acquisition by LFI and HFI. It started with the First Light Survey (FLS) on 13 August of 2009, at 14:15 UT.

The FLS was the last major activity planned before the start of routine surveying of the sky. It was conceived as a two-week period during which Planck would be fully tuned up and operated as if it was in its routine phase. This stable period could have resulted in the identification of further tuning activities required to optimise the performance of Planck in the long-duration surveys to come. The FLS was conducted between 13 and 27 August, and in fact led to the conclusion that the Planck payload was operating stably and optimally, and required no further tuning of its instruments. Therefore the period of the FLS was accepted as a valid part of the first Planck survey.

Survey scanning and performance

The observation strategy

The Planck *observation strategy*, or *scanning strategy*, makes use of the characteristics of the Planck spacecraft #planck2011-1-1 and orbit in order to achieve the survey goals in terms of sky coverage and scanning directions.

The Planck focal plane scans the sky in the way explained in the figure below.

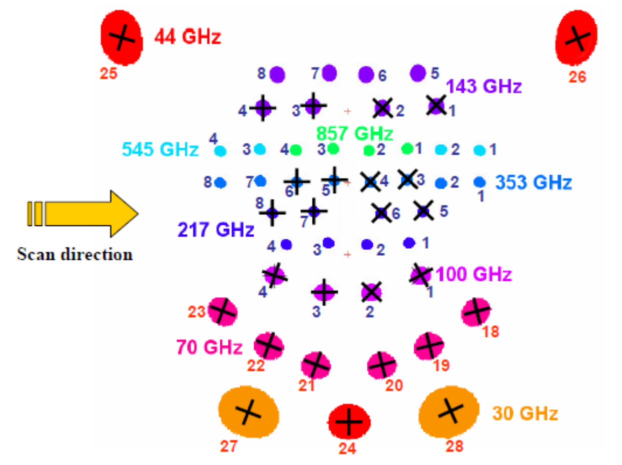

The Planck focal plane with the direction of scanning. Polarization-sensitive detectors are drawn with crosses indicating the polarization direction.

The 353 GHz row scans the sky in small circles with a 85 deg. bore-sight angle from the spin axis. 545 GHz, 857 GHz, 143 GHz bolometers as well as LFI 25-26 radiometers have a slightly smaller bore-sight angle, while the other part of the Planck focal plane have larger ones (up to ~ 89 deg.). The Planck spacecraft spins at a rate of 1 rpm.

Planck, being at L2, moves along the Ecliptic at ~ one degree per day, and needs to keep the Solar aspect angle below ~ 9 degrees at all times. In practice, during the surveys, the limit considered is 8 deg. Another celestial constraint is that the angle between the Planck spin axis and the anti-Earth direction cannot exceed 15 deg. (relaxed to 17 deg. from Survey 5 onward). These constraints have a very direct influence on the chosen scanning strategy.

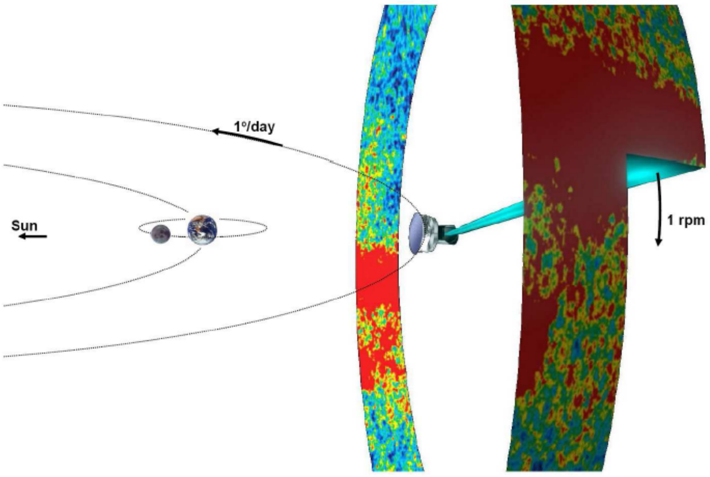

Simplified way to show the Planck scanning strategy, without additional motion of the spin axis

The path followed by the Planck spin axis is defined with respect to the Ecliptic plane. It corresponds to a motion in longitude which maintains an anti-Sun pointing (about one degree per day), to which is added a cycloidal motion (precession) of the spin axis around the anti-Sun position (fiducial point). The cycloidal path is defined by the following functions:

$\lambda = \theta \sin((-1)^n \omega (t-t_0)+\varphi)$ (eq. 1)

$\beta = -\theta \cos((-1)^n \omega(t-t_0) + \varphi)$ (eq. 2)

where λ is the angular distance from the fiducial point in Ecliptic longitude, β the angular distance from the fiducial point in Ecliptic latitude, θ the spin axis precession amplitude, ω the pulsation of the precession, φ its phase, n the parameter which controls the motion direction of the precession, t is the time, and t_0 is the first time during the Planck survey at which the fiducial point crosses the 0 Ecliptic longitude line.

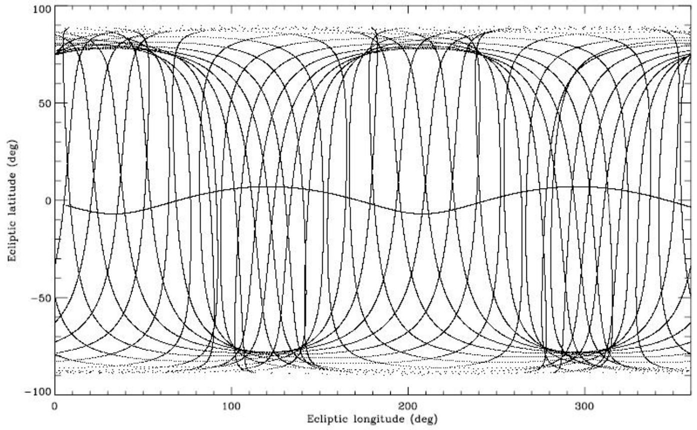

Spin axis path with a 7 degree amplitude cycloidal scanning, from #dupac2005

The reasons to decide to use such a precession of the spin axis are the following :

- An excursion of the spin axis from the anti-Sun direction is required to fully observe the whole sky (no excursion would leave a large area unobserved around the Ecliptic poles)
- The precession motion allows to keep the Sun aspect angle constant during the whole survey, therefore minimizing the thermal constraint variations on the spacecraft

The following precession parameters have been chosen for the BSS:

- amplitude $\theta = 7.5^o$ (this value is the lowest possible which allows to cover the whole sky with all detectors)
- n = 1 (anti-clockwise motion as seen from the Sun)
- pulsation ω = 2π / (half a year). Faster precession was considered, and has interesting advantages, but is not possible given the constraints if one wants to keep a 7.5 deg. amplitude (which is necessary to cover the whole sky).
- The phase of the precession was decided according to this set of criteria (in order of importance):

a) respecting the operational constraints,

b) allowing the largest possible angle between two scans on the Crab,

c) avoiding null dipole amplitude for the whole mission,

d) optimizing the position of the planets in the beginning of the survey and with respect to the feasibility of their recovery,

e) placing the two “deep fields” where Galactic foregrounds are minimum,

f) allowing a reasonable survey margin (i.e. the time allowed to recover lost pointings if a problem occurs)

The phase is 340 deg. for Surveys 1 to 4, and 250 deg. for Surveys 5 to 8.

The scanning strategy for the second year of Routine Operations (i.e. Surveys 3 and 4) is exactly the same as for the first year, except that all pointings are shifted by 1 arcmin along the cross-scanning direction, in order to provide finer sky sampling for the highest frequency detectors when combining two years of observations.

The change of phase between Survey 4 and Survey 5 occurred because it was found essential especially on the HFI side that scanning direction crossings are increased in the Planck survey. By choosing a phase 90 deg. away from the original one, one optimizes the scanning strategy in this respect.

The details of the justifications for these parameters can be found in PL-WG9-TN-001.

The scanning strategy parameters are input to the PSO Survey Planning and Performance Tool, which is the software which generates the series of pointing records to be sent out to MOC for implementation.

An approximate visualisation of the Planck scanning strategy can be found here [1] and there [2].

Spin axis manoeuvres and exact pointings

The motion of the spin axis is not continuous. Every change in the spin axis position is initiated by a manoeuvre which requires less than 5 minutes time to complete.

The duration between spin-axis manoeuvres is hereafter referred to as “dwelling times"; and the angular distance between manoeuvres along the spin axis path is hereafter referred to as “spacing”.

The dwelling times and spacings are defined as follows:

- The spacings are fixed to 2’ which roughly corresponds to Nyquist criterion for sampling the highest-frequency HFI detectors.
- The dwell times vary from 2360 s to 3904 s.

The exact series of coordinates and dwell times are set by equations 1 and 2 when one has fixed the spacings.

Data gap recoveries

Gaps in the data flow can occur because of various reasons:

- Anomalies may occur at spacecraft or instrument level, but also due to failures in the ground-to-spacecraft link or the ground segment itself. The adverse effects of such anomalies may be the loss of scientific data corresponding to one or several planned pointings, which have either not been acquired and/or stored in memory.
- Failure to acquire proper scientific data may occur to one or both instruments

In case a gap occurs, scientific criteria are applied to decide whether to recover the data through the Small-Gap Recovery procedure.

The Small-Gap Recovery (SGR) procedure can be applied by MOC or PSO:

- **MOC-triggered SGR**: Within its nominal scheduling procedure for an OD, the MOC searches the PPL for PREF corresponding to the OD being processed and any pointings which are subject of a Small Gap Recovery. As the PREF are sorted in chronological order according to their nominal start time, those corresponding to a small gap will naturally be the earliest. After checking attitude constraints, all observable pointings are listed and their dwell times reduced (initially) to the Minimum Dwell Time (MDT) as given in the PPL.

Having included all valid PREF the required slew times are calculated. With the required slew times and minimum dwell times for all pointings, the OD schedule may be under-populated; in this case the dwell times of all scheduled pointings will be increased equally to make use of all available time in the OD. If the resulting schedule is over-populated, even with MDT for all pointings, the recovery cannot be constrained to a single OD. The sequence of pointings for the ODs involved will be optimized in PREF scheduling and dwell times in order to effect the recovery and revert to the nominal timeline as quickly as possible.

- **PSO-triggered SGR**:

PSO declares a small gap when pointings that have been executed result in data of insufficient quality or inadequate frequency coverage. This assessment is based on data quality and instrument health information provided by the DPCs. The algorithm that is used by the PSO to check the scientific validity of a pointing is implemented within the SPPT software tool. The SPPT ingests on a weekly basis a Weekly Health Report (WHR) for the HFI and LFI containing information on the current working status of each detector and their expected condition over the next four weeks. On a daily basis, a Daily Quality Report (DQR) provided by the DPCs for both instruments, includes a set of parameters that describe the quality of the detection achieved by each individual detector for every pointing executed.

The scheme for declaring a Small-Gap Recovery from PSO is the following:

- If a pointing fails to meet the chosen requirement, it becomes an SGR candidate

- If there are at least 12 consecutive pointings which are declared SGR candidates, and the problem has been identified and solved, then an SGR is triggered Recoveries are only carried out if the recovery slewing out is guaranteed to be in OCM. MOC carries out this analysis and decides whether they perform the SGR accordingly.

- The start and end times of the gap and the list of the pointing numbers (or just the numbers of the first and last pointings to be recovered) are then sent to MOC by E-mail, with the notification to start a Small-Gap Recovery

- MOC implements the Small-Gap Recovery, provided the pointings can still be scheduled with respect to their latest start time, using the same scheme as described in the MOC-triggered SGR section

Throughout the Planck mission, data losses have been very rare. Small-Gap Recovery has been applied only a couple of times.

Special observations

The special observations are:

- normal scanning on Solar System objects for calibration purposes

This concerns the following objects (planets): Mars, Jupiter, Saturn, Uranus and Neptune whose thermal emission in the far-infrared and their point-source-like quality make them essential calibrators for spider-web bolometers and radiometers.

Mars is a particularly interesting calibrator for Planck because of its proper motion. However this proper motion makes it difficult to observe it many times during the mission.

Jupiter is the brightest source for (non-polarized) calibration. Saturn is also used a lot, and Uranus and Neptune are secondary calibrators.

- normal scanning on other (non-moving) sources for calibration purposes

This concerns mostly the Crab Nebula for polarizer calibration purposes. This supernova remnant is highly polarized and as such represents the main polarization calibrator for Planck.

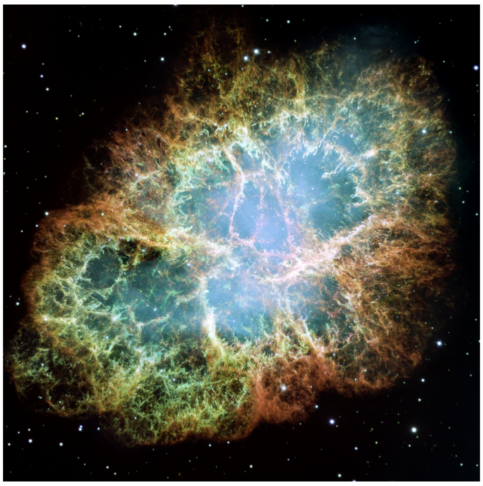

The Crab Nebula (Messier 1, NGC 1952, Taurus A), here seen by the Hubble Space Telescope

- special pointings during the calibration phase, not relative to celestial sources

- "deep rings" : these special observations are performed on each passage of Jupiter and the Crab Nebula, from January 2012 onward.

They consist of very deeply sampled observations (0.5') with the spin axis along the Ecliptic plane, during typically two to three weeks.

These observations benefit from special relaxing of the celestial constraints with Solar Aspect Angles < 9 deg. rather than < 8 deg. during cycloidal surveying.

- "drift scans" : these special observations are performed on Mars, making use of its proper motion

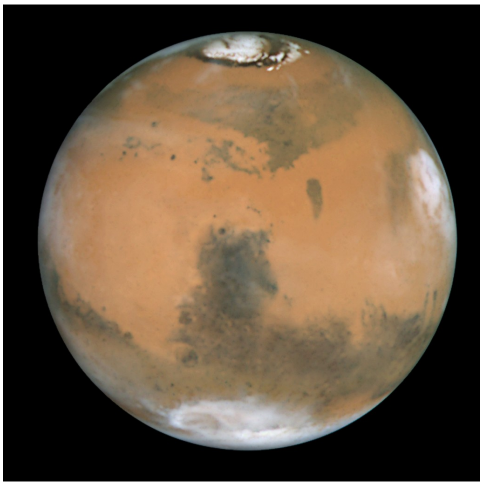

Mars as seen by the Hubble Space Telescope in 1999

Start and end of surveys

The completion of a given “survey” is declared when the logical AND of all frequency-coverage maps is greater than 95 %, OR the sky has been surveyed over a consecutive period of 7.5 months. Note that this definition is that of the Project Scientist and Planck Science Office. Data Processing Centres do not use the same concept of surveys to create "survey" maps.

In practice, since the gaps during the surveys have always been very small, it results in ~ six months per survey.

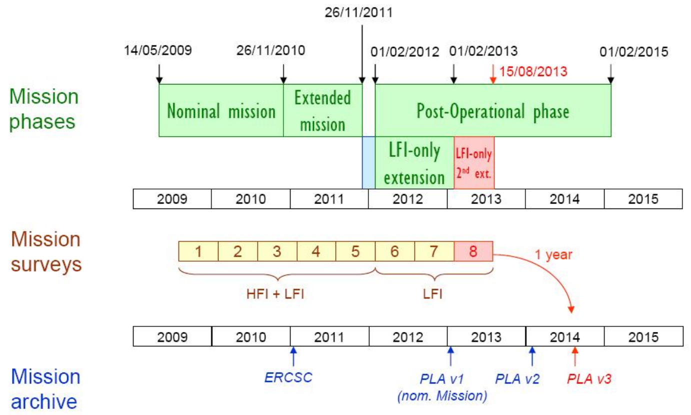
26/11/2011
14/05/2009
26/11/2010
01/02/2012
01/02/2013
15/08/2013
01/02/2015
Mission phases
Nominal mission
Extended mission
Post-Operational phase
LFI-only extension
LFI-only 2nd ext.
2009
2010
2011
2012
2013
2014
2015
Mission surveys
1
2
3
4
5
6
7
8
1 year
HFI + LFI
LFI
2009
2010
2011
2012
2013
2014
2015
Mission archive
ERCSC
PLA v1 (nom. Mission)
PLA v2
PLA v3

The Planck mission timeline with the distribution of the "sky surveys".

- **Survey 1**: starts August 13, 2009, ends Feb. 13, 2010
- **Survey 2**: starts Feb. 14, 2010, ends Aug. 13, 2010
- **Survey 3**: starts Aug. 14, 2010, ends Feb. 13, 2011
- **Survey 4**: starts Feb. 14, 2011, ends July 29th, 2011

This survey was shortened in ordered to start earlier with the new scanning strategy (see above).

- **Survey 5**: starts July 29th, 2011, ends January 30th, 2012
- **Survey 6** (LFI only): starts January 30th, 2012, ends July 31st, 2012
- **Survey 7** (LFI only): starts July 31st, 2012, ends January 31st, 2013
- **Survey 8** (LFI only): starts February 1st, 2013, ends August 1st, 2013

Completion of full sky coverage during Surveys 1-2

The picture gallery below exhibits the progress of sky coverage during the first months of survey (black color = unobserved areas).

The HFI 353 GHz integration time after N months of survey. Unit is seconds per square degree, normalized to one detector.

Main planet and Crab observations during Surveys 1-7

Solar System objects and the Crab Nebula have been observed many times during the Planck surveys. Here is a complete list of these observations. Note that the *deep rings* and *drift scans* (Mars only) are in **boldface**.

- Crab: Sept. 16-22, 2009
- Mars: Oct. 17-29, 2009
- Jupiter: Oct. 25 – Nov. 1, 2009
- Neptune: Nov. 1-8, 2009
- Uranus: Dec. 6-16, 2009
- Saturn: Jan. 2-8, 2010
- Crab: March 6-12, 2010
- Mars: April 9-18, 2010
- Neptune: May 15-23, 2010
- Saturn: June 13-22, 2010
- Uranus: June 27 – July 5, 2010
- Jupiter: July 1-9, 2010
- Crab: Sept. 15-21, 2010
- Neptune: Nov. 3-11, 2010
- Jupiter: Dec. 9-18, 2010
- Uranus: Dec. 12-21, 2010
- Saturn: Jan. 15-22, 2011
- Crab: March 7-12, 2011
- Neptune: May 18-26, 2011
- Saturn: June 30 - July 9, 2011
- Uranus: July 3-11, 2011
- Jupiter: Aug. 9-15, 2011
- Crab: Sept. 10-18, 2011

This Crab scan was performed with the 250 deg. phase cycloidal strategy.

- Crab: Sept. 20-23, 2011

This Crab scan was performed with the 340 deg. phase cycloidal strategy.

- **Mars**: Dec. 8-16, 2011 ("drift scan": Mars is let move through the Planck focal plane via its proper motion)
- Mars: Dec. 17-26, 2011 (normal scanning)
- **Jupiter**: Jan. 8-30, 2012 (deep ring)

- **Crab**: Feb. 26 - March 16, 2012 (deep ring)
- **Jupiter**: Sept. 1-14, 2012 (deep ring)
- **Crab**: Sept. 14 - Oct. 1, 2012 (deep ring)
- Neptune: Nov. 19-27, 2012
- Uranus: Dec. 24-30, 2012
- Saturn: Jan. 30 - Feb. 5, 2013
- **Jupiter**: Feb. 2013 (deep ring)

Resulting integration time distribution

The integration time after the end of HFI operations (January 2012) is shown in the following picture gallery.

Units are seconds per square degree, normalized to one detector, for all maps. The projection is full-sky Mollweide centered on the Galactic Centre.

Integration time after the end of HFI operations (January 2012). Units are seconds per square degree, normalized to one detector.

References

<biblio force=false>

1. References

</biblio>

References

[1] http://www.youtube.com/watch?v=WwFXuZ0B3B8
[2] http://www.youtube.com/watch?v=7Zu-aiEiDtY

Thermal environment

(Note: Adapted from Planck Collaboration 2011, A&A 536, A1)

The satellite design and its location at L2 provide an extremely stable thermal environment. The main temperature variation on long timescales is driven by the total radiative power absorbed by the solar panels, which varies depending on distance from the Sun and the solar aspect angle (i.e. the angle between the solar direction and the spin axis). On shorter timescales, temperature variations are driven by active thermal regulation cycles. Both seasonal and shorter-timescale variations are observed across the satellite's service module (SVM), but are heavily damped and almost unobservable within the payload module (PLM).

Specific operations and deviations from the scanning strategy have a thermal influence on the satellite and payload. Some significant effects are listed below.

– The thruster heaters were unintentionally turned off between 31 August and 16 September 2009 (the so-called “catbed” event).

– As planned, the RF transmitter was initially turned on and off every day in synchrony with the daily visibility window, in order to reduce potential interference by the transmitter on the scientific data. The induced daily temperature variation had a measurable effect throughout the satellite. An important effect was on the temperature of the 4He-JT cooler compressors, which caused variations of the levels of the interference lines that they induce on the bolometer data (Planck HFI Core Team 2011a). Therefore the RF transmitter was left permanently on starting from 25 January 2010 (257 days after launch), which made a noticeable improvement on the daily temperature variations.

– A significant thermal effect arises from the (approximately) weekly adjustments to the operation of the Sorption Cooler.

The thermal environment of the payload module is – by design – extremely well decoupled from that of the service module. As a consequence, in spite of the significant thermal perturbations originating in the SVM, the thermal variability affecting the detectors is essentially completely due to the operation of the cryogenic cooling chain (described in detail in Planck Collaboration 2011b), which ensures their cold environment.

Radiation environment

The Standard Radiation Environment Monitor on board Planck #SREM is a particle detector flown on several ESA satellites. The SREM consists of several detectors sensitive to different energy ranges, which can also be used in coincidence mode. In particular, the SREM measures count rates of high energy protons with E>20 MeV, electrons with E>0.5 MeV and Ions with 150 MeV < E < 185 MeV.

Particle fluxes measured by the SREM on board Planck are shown in the figures below. The radiation environment of Planck is characterised by a start near the minimum in the current solar cycle. As a consequence, the particle flux is dominated by Galactic cosmic rays, rather than by the solar wind.

The figure below shows the thermal and radiation environment around Planck during the nominal mission. Vertical lines indicate boundaries between surveys. The top panel shows the cosmic ray flux as measured by the onboard SREM; its decrease over time is due to the corresponding increase in solar activity, indicated by the sunspot number, from the Solar Influences Data Centre [1]. Solar flares show up as spikes in the proton flux. The second and third panels show the temperature variation at two representative locations in the room-temperature SVM, i.e., on one of the (HFI) Helium tanks and on one of the LFI back-end modules (BEM). The sine-wave modulation tracks the variation of distance from the Sun. The bottom panel shows the temperature evolution of VG3, the coldest of three so-called V-grooves, to which the sorption cooler is heat-sunk. The disturbances on the curve are due to adjustments of the operational parameters of this cooler.

The time evolution of the SREM measurements is well correlated with that of identical units flying simultaneously on other satellites (e.g., Herschel, Rosetta) and with indicators of Galactic cosmic rays, and is anti-correlated with solar flare events and with the solar cycle. More importantly for Planck, the SREM measurements are very well correlated with the heat deposition on the coldest stages of the HFI, and with glitch rates measured by the detectors of HFI. A more detailed interpretation of these data is provided in planck2011-1-5.

References

<biblio force=false>

1. References

</biblio>

References

[1] http://www.sidc.be/sunspot-data/

Pointing performance

The pointing performance of Planck can be measured by the difference between the executed pointings as described in the Attitude History Files (using the Star Trackers and the Fiber Optics Gyroscope), and the planned pointings by PSO in the Pre-Programmed Pointing Lists.

The MOC makes available to DPCs and PSO the reconstituted pointing information:

- the positions on the sky of the three axes bound to the ACMS system (ASTR) every second (quaternions or equivalent information).

The accuracy of this information complies with the requirements stated in the SRS document.

- For each circle (i.e. nominally a 60 second observation period), the spin axis position on the sky and spin velocity averaged over this circle plus the spin

phase.

- For each ring (i.e. nominally a ~ 1 hr observation period), the spin axis position on the sky, spin velocity and nutation parameters averaged over this ring.
- Any information the MOC has that might help the DPCs in assessing the quality of the above information.

The attitude history file contains high frequency data for slews, post slew and stable pointing periods at a maximum frequency of one record every 0.25 seconds. It also contains data averaged over a spin period and data averaged over an observation period. For the spin period and observation period, the information used to construct these data records is restricted to stable pointing periods.

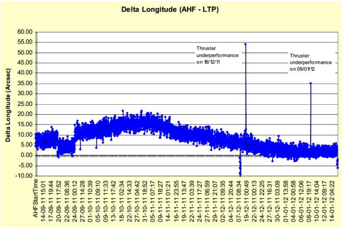

This plot exhibits the pointing errors in Ecliptic longitude for the period Sept. 2011 - Jan. 2012.

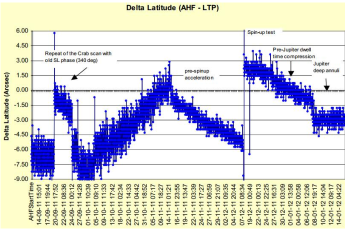

This plot exhibits the pointing errors in Ecliptic latitude for the period Sept. 2011 - Jan. 2012.

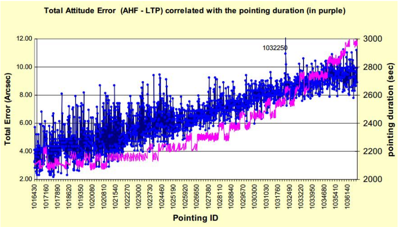

This plot exhibits a correlation between the periodic component of the pointing error and the duration of the pointing. This suggests a Solar drift origin to this component.

The pointing performance of Planck has been very good throughout operations, as the plots above show.

Data flow overview

The Planck satellite generates (and stores on-board) data continuously at the following typical rates: 21 kilobit s−1 (kbps) of house-keeping (HK) data from all on-board sources, 44 kbps of LFI science data and 72 kbps of HFI science data. The data are brought to ground in a daily pass of approximately 3 h duration. Besides the data downloads, the passes also acquire realtime HK and a 20 min period of real-time science (used to monitor instrument performance during the pass). Planck utilises the two ESA deep-space ground stations in New Norcia (Australia) and Cebreros (Spain), usually the former. Scheduling of the daily telecommunication period is quite stable, with small perturbations due to the need to coordinate the use of the antenna with other ESA satellites (in particular Herschel).

At the ground station the telemetry is received by redundant chains of front-end/back-end equipment. The data flows to the mission operations control centre (MOC) located at ESOC in Darmstadt (Germany), where it is processed by redundant mission control software (MCS) installations and made available to the science ground segment. To reduce bandwidth requirements between the station and ESOC only one set of science telemetry is usually transferred. Software is run post-pass to check the completeness of the data. This software check is also used to build a catalogue of data completeness, which is used by the science ground segment to control its own data transfer process. Where gaps are detected, attempts to fill them are made as an offline activity (normally next working day), the first step being to attempt to reflow the relevant data from station. Early in the mission these gaps were more frequent, with some hundreds of packets affected per week (impact on data return of order 50 ppm) due principally to a combination of software problems with the data ingestion and distribution in the MCS, and imperfect behaviour of the software gap check. Software updates implemented during the mission have improved the situation such that gaps are much rarer, with a total impact on data return well below 1 ppm.

Redump of data from the spacecraft is attempted when there have been losses in the space link. This has only been necessary on three occasions. In each case the spacecraft redump has successfully recovered all the data.

An operational principle of the mission is to avoid impact on the nominal science of a completely missed ground station pass. Commanding continuity is managed by keeping more than 24 h of commanding-timeline queued on-board. The telemetry resides on board the satellite in a ~60 h circular buffer in solidstate memory, and can be recovered subsequently using the margin in each pass, or more rapidly by seeking additional station coverage after an event. The lost-pass scenario has in fact occurred only once (on 21 December 2009), when snow on the dish at Cebreros led to the loss of the entire pass. A rapid recovery was made by using spare time available on the New Norcia station. Smaller impacts on the pass occur more often (e.g., the first ~10 min of a pass may be lost due to a station acquisition problem) and these can normally be recovered simply by restarting a software task or rebooting station equipment. Such delays are normally accommodated within the margin of the pass itself, or during the subsequent pass.

All the data downloaded from the satellite, and processed products such as filtered attitude information, are made available each day for retrieval from the MOC by the LFI and HFI Data Processing Centres (DPCs). Typically, the data arrive at the LFI (resp. HFI) DPC 2 (resp. 4) hours after the start of the daily acquisition window. Automated processing of the incoming telemetry is carried out each day by the LFI (resp. HFI) DPCs and yields a daily data quality report which is made available to the rest of the ground segment typically 22 (resp. 14) hours later. More sophisticated processing of the data in each of the two DPCs is described in Zacchei et al. (2011) and Planck HFI Core Team (2011b).

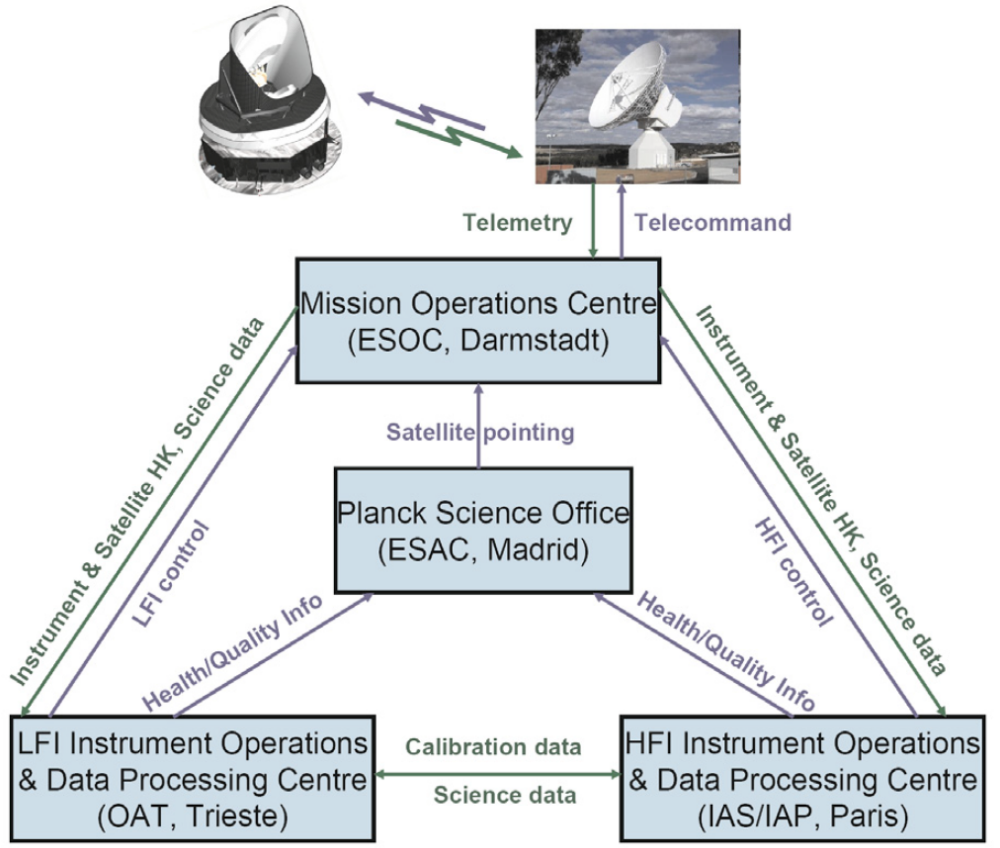
Telemetry
Telecommand
Mission Operations Centre (ESOC, Darmstadt)
Satellite pointing
Planck Science Office (ESAC, Madrid)
Instrument & Satellite HK, Science data
LFI control
Health/Quality Info
Instrument & Satellite HK, Science data
HFI control
Health/Quality Info
LFI Instrument Operations & Data Processing Centre (OAT, Trieste)
Calibration data
Science data
HFI Instrument Operations & Data Processing Centre (IAS/IAP, Paris)

A sketch of the centres involved in the Planck ground segment and the main data exchanges between them.

For more information, see #tauber2010a, #planck2011-1.1.

References

<biblio force=false>

1. References

</biblio>

MOC data transfer and storage

The Mission Operations Centre (MOC), located at ESA's operations centre in Darmstadt (Germany), is responsible for all aspects of flight control and of the health and safety of the Planck satellite, including both instruments. It plans and executes all necessary satellite activities, including instrument commanding requests by the instrument operations centres. MOC communicates with the satellite using two ESA deep-space ground stations in New Norcia (Australia) and Cebreros (Spain), usually the former, over a daily 3-h period, during which it uplinks a scheduled activity timeline which is autonomously executed by the satellite, and downlinks the science and housekeeping data acquired by the satellite during the past 24 h. The downlinked data are transferred from the ground station to the MOC over a period of typically 8 h; at MOC they are put onto a data server from where they are retrieved by the two Data Processing Centres.

There is no data processing done at MOC. Only transfer and storage of data is performed at this stage. MOC verifies the reception of all telemetry packets, which are transfered from the spacecraft via the ground station, as given by the Source Sequence Count related to each Virtual Channel and Application ID. All data are stored in the Long Term Archive as telemetry packets (duplicated in A and B archives), which present an archive of all data, both science and housekeeping, acquired through the whole mission.

HFI data processing

The HFI DPC

The first stage of HFI data processing is performed on-board in order to generate the telemetry as described in the Data compression section. On the ground, the HFI DPC has been organized into different "Levels": 1, 2, 3, 4 and "S". In brief, during operations, L1 feeds the database resulting in time-ordered information (TOI) objects. L2 is the core of the processing, which turns TOIs into clean calibrated sky maps. L3 transforms these maps at specific frequencies into more scientific products, like catalogues, maps and spectra of astrophysical components. L3 can rely on simulation provided by the LS, while L4 refers to delivering the DPC products to ESA. This processing relies on dedicated software and hardware infrastructures developed pre-launch.

The data processing applied for the *"Early Planck results"* series of publications was described in #planck2011-1-7 Planck early paper VI [1]. The #planck2013-p03 Planck-2013-VI [2] and its co-papers provide the reference for the processing done for the 2013 data release.

Level 1: building the reference database during flight operations

(L1): consists in receiving the telemetry and ancillary data files and ingesting them into the DPC database. This involves decompressing, in some cases changing data formats, computing the time of individual data samples from the time of the compression slices, but otherwise no processing proper. Other steps are:

- science, housekeeping and ancillary data ingestion
- timing and pointing interpolation

This is further described in the Pre-processing section.

Level 2: converting temporal information into clean calibrated maps

(L2): this is where the data are processed from timelines into maps. The main processing steps are

- Timeline (or Time-Ordered Information = TOI) processing, which includes conversion from ADUs to engineering units (volts), demodulation, deglitching, conversion from engineering to physical units (watts), removal of known systematic effects (non-linearities, 4K lines, Jumps, ring flagging), removal of the instrumental signature (time transfer function), temporal noise Estimation. See section TOI_processing.
- Pointing and beam of each detector. See sections Detector pointing and Beams.
- map-making & photometric calibration: projecting the TOIs onto all-sky maps, etc. See section Map-making.
- Characterisation/validation through angular power spectra. See section PowerSpectra.
- Overal HFI data validation, through difference tests, comparison to detailed simulations, etc., See section HFI-Validation
- The resulting data characteristics are given in section Summary.

Level 3: basic analyses of (Level 2) sky temperature maps

(L3): This is where the data in the form of frequency maps are converted to catalogues and full sky astrophysical component maps. Much of this is done in common with the LFI DPC, and is further described in the HFI/LFI common sections .

Level S : a common HFI/LFI simulation software

Level S is the so-called "Simulation Level" software suite common to both consortia, which, given a sky model (generated by the Planck sky model, `PSM`), detectors pointing and beams, generates the infalling power on each detector. It can also provide a simplified description of eg. the noise. It is further described in the HFI/LFI common section. HFI specific developments (configuration control & MC bench, specific effects like 4K lines, glitches, ADC non-linearity, etc.) are described in the HFI data validation section.

HFI DPC Infrastructures

The HFI Data Processing Centre can be thought of as a centralized backbone providing hardware and software infrastructures to a relatively large number of geographically distributed groups of developers and other R&D groups in the HFI and LFI core teams. An overview was given in #planck2011-1-7. In particular:

- Code and configuration management can be found at Planck early paper VI [3],
- Data management at Planck early paper VI [3],
- Instrument model (IMO) database at Planck early paper VI [4],
- Data flow management at Planck early paper VI [4],
- Hardware at Planck early paper VI [5].

References

<biblio force=false>

1. References

</biblio>

References

[1] http://www.rssd.esa.int/doc_fetch.php?id=3135867&page=1
[2] http://www.rssd.esa.int/doc_fetch.php?id=3168069&page=1
[3] http://www.rssd.esa.int/doc_fetch.php?id=3135867&page=34
[4] http://www.rssd.esa.int/doc_fetch.php?id=3135867&page=35
[5] http://www.rssd.esa.int/doc_fetch.php?id=3135867&page=36

Pre-processing

Overview

In terms of data processing, the HFI ground segment handles two types of data, both made available via the MOC:

- telemetry data transmitted from the satellite. These come from the different subsystems of the satellite service module, from the sorption cooler and from the two instruments.
- auxiliary data. These are data produced by MOC. The only 3 products used by the HFI DPC are the pointing data, the orbit data, and the time correlation data.

All data are retrieved by the HFI level 1 software and stored in the HFI database.

Telemetry data

The digitized data from the satellite are assembled on board in packets according to the ESA Packet Telemetry Standard and Packet Telecommand Standard, the CCSDS Packet Telemetry recommendations and the ESA Packet Utilization Standard. The packets are dumped to the ground during the Daily Tranmission Control Period, consolidated by and stored at MOC. Telemetry data contain the housekeeping data and the bolometer (ie science) data.

Housekeeping data

For several reasons (systems monitoring, potential impact of the environment, understanding of the bolometer data), the HFI level 1 software gathers and stores in its database the satellite subsystems housekeeping parameters:

- Command and Data Management System
- Attitude Control & Measurement Subsystem
- Thermal Control System
- Sorption Cooler System
- HFI housekeeping parameters

The structure and the frequency of the packets built by these subsystems and the format of the house keeping parameters are described in the Mission Information Bases. The HFI L1 software uses these MIBs to extract the house keeping parameters from the packets. Given the status of each subsystem, the parameters are gathered in the HFI database in groups. The HFI L1 software builds in each group a vector of time (usually named TIMESEC) and a single vector per housekeeping parameter.

Bolometer data

The HFI science data is retrieved and reconstructed as described in section 3.1 of #planck2011-1-7 Planck early paper VI [1].

The first stage of HFI data processing is performed on-board in order to generate the telemetry. This is described in the HFI_detection_chain#Data_compression section.

On board, the signal from the 72 HFI channels is sampled at 180.4Hz by the Read-out Electronic Unit. 254 samples per channel are grouped into a compression slice. The Data Processing Unit then builds a set of several telemetry packets containing the compression slice data and adds to the first packet the start time of the compression slice. When receiving this set of telemetry packets, the L1 software extracts the samples and computes the time of each sample based on the compression slice start time (digitized with $2^{-16}s = 15.26$µs quantization steps) and a mean sample time between samples. For the nominal instrument configuration, the sample integration time is measured to be Tsamp = 5.54404 ms

The two plots show the histogram of time differences between two successive samples for the full mission. 6 sample intervals (> 6 ms) correspond to 3 occurrences of packets lost on board when the on board sofwtare of the Command and Data Management Unit has been patched (18, 19 and 20th of August 2009). The right plot is a blow up of the left one. It shows the distribution around the mean value of 5,54 ms and the 15 µs quantization step.

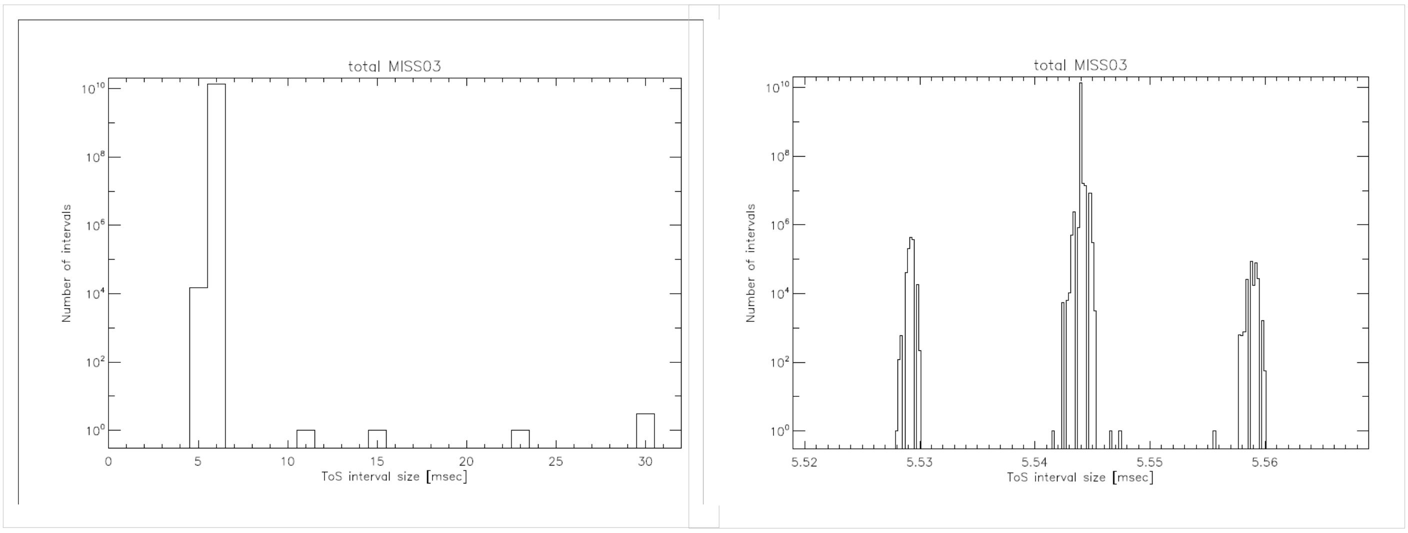

Transfer functions

In order to ease the reading data in the HFI database, so called transfer functions are created. They allow software items to read data on which functions are applied on the fly. A simple example of a transfer function is the conversion of a thermometer data in Analogic to Digital Units (ADU) to Kelvins. Here we show the 2 transfer functions applied on the bolometer samples in the data processing pipelines:

From raw signal to non demodulated signal in Volts (transf1_nodemod)

$$Signal\_ND\_V_{bc} = \frac{\frac{C_{bc}}{N_{sample} - Nblanck_{bc}} - offset_{bc}}{F1_{bc}} \times \frac{Gamp_{ETAL}}{Gamp_{bc}}$$

where:

- bc refers to a bolometer usually labelled by its electronic belt and channel. Eg. bc=00 refers to the *a* part of the first 100 GHz Polarized Sentivite Bolometer.
- C_{bc} is the bolometer sample in Analogic Digital Units (ADU)
- N_{sample} is the number of samples in half a modulation period. This parameter is common to all bolometer channels and - although kept fixed during the whole mission - is read from the housekeeping parameter. $N_{sample} = 40$
- $Nblanck_{bc}$ is the number of samples suppressed at the beginning oft each half modulation period. Although kept fixed during the whole mission, it is read from the housekeeping parameter. For bc=00, $Nblanck_{00} = 0$
- $F1_{bc}$ is a calibration factor. For bc=00, $F1_{00} \simeq 1.8 \times 10^7$.
- $offset_{bc}$ is close to 32768
- $Gamp_{ETAL}$ is the gain amplifier mesured during the calibration phase. For bc=00, $Gamp_{ETAL} = 1$
- $Gamp_{bc}$ is the current gain amplifier. Although kept fixed during the whole mission, it is read from the housekeeping parameter. For bc=00, $Gamp_{00} = 1$

From raw signal to demodulated signal in Volts (transf1)

The same formula as above is used but with the demodulation and a 3-point filter computed as:

$$Signal\_V_{bc}[n] = -\frac{1}{4}(-1)^{parity_{n-1}} Signal\_ND\_V_{bc}[n-1] + \frac{1}{2}(-1)^{parity_n} Signal\_ND\_V_{bc}[n] - \frac{1}{4}(-1)^{parity_{n+1}} Signal\_ND\_V_{bc}[n+1]$$

where:

- $n-1$, and $n+1$ refer to the samples before and after the given n sample to demodulate
- $parity$ is computed by the HFI L1 software

Statistics on the telemetry data

The table gives some statistics about the data handled at the pre-processing level:

-	**Nominal mission(1)**	**Full mission(1)**	**From launch to the end of full mission(1)**
Duration	473_{days}	884_{days}	974_{days}
Number of HFI packets generated onboard (HSK/science)(2)	19 668 436/ 376 294 615	37 762 493/ 704 852 262	41 689 4090/765 043 713
Number of HFI packets lost (3) (HSK/science)	2/20	2/20	2/20
ratio of HFI lost packets vs generated on board (HSK/science)	$1 \times 10^{-7}/5 \times 10^{-8}$	$5 \times 10^{-8}/3 \times 10^{-8}$	$5 \times 10^{-8}/3 \times 10^{-8}$
Number of different housekeeping parameters stored in the database (HFI/SCS/sat)	3174/708/12390		
Number of science samples stored in the database	530 632 594 653	991 929 524 565	1 090 125 748 960
Number of missing science samples	2 537 499	6 634 491(4)	7 521 758
Ratio of missing science samples vs samples stored	5×10^{-6}	7×10^{-6}	7×10^{-6}

- (1) : mission periods are defined in this page.
- (2) : science packets refer to the number of telemetry packets containing science data (ie: bolometer data and *fine thermometer* data) when the instrument is in observation mode (Application Program IDentifier = 1412). HSK packets refer to the number of HFI *non essential* housekeeping telemetry packets (Application Program IDentifier = 1410).
- (3) : all lost packets have been lost on board ; no HFI packet has been lost at ground segment level.
- (4) : this amount of lost science samples is distributed as
  - 0.3% are due to Single Event Unit
  - 18.5% have been lost during the 3 CDMU patch days and the consecutive clock resynchronisation
  - 29.1% have been lost because of compression errors
  - 52.1% have been lost due to the EndOfSlew buffer overflow being triggered by solar flare events

Pointing data

The pointing data are built by the MOC Flight Dynamics team. The pointing data are made available to the DPC via AHF files. See AHF description document [2] and AHF files repository [3]. All data contained in the AHF files are ingested in the HFI database. The present section describes the steps to produce the HFI pointing solution.

- During the stable pointing period (ie during the dwell), data sampling rate is given at 8 Hz while it is at 4 Hz during the satellite slews. Those data are thus interpolated to the bolometer sampling rate using a spherical linear interpolation as described in section 3.4 of of Planck early paper VI [4].
- The pointing solution is then amended from the wobble effect as delivered by MOC Flight Dynamics in the AHF files.
- A final correction is then applied based on the study of main planets and point sources seen by the bolometers.

Note: an **HFI ring** corresponds to each stable pointing period, when the spin axis is pointing towards an essentially fixed direction in the sky and the detectors repeatedly scan the same circle on the sky. More precisely the **HFI ring** start time is defined as the *time of the first thurster firing*. The end time of the HFI ring is the start time of the following ring.

The plot below shows the evolution of the ring duration along the whole mission. It mainly reflects the scanning strategy and few *long* rings due to operational constraints or tests.

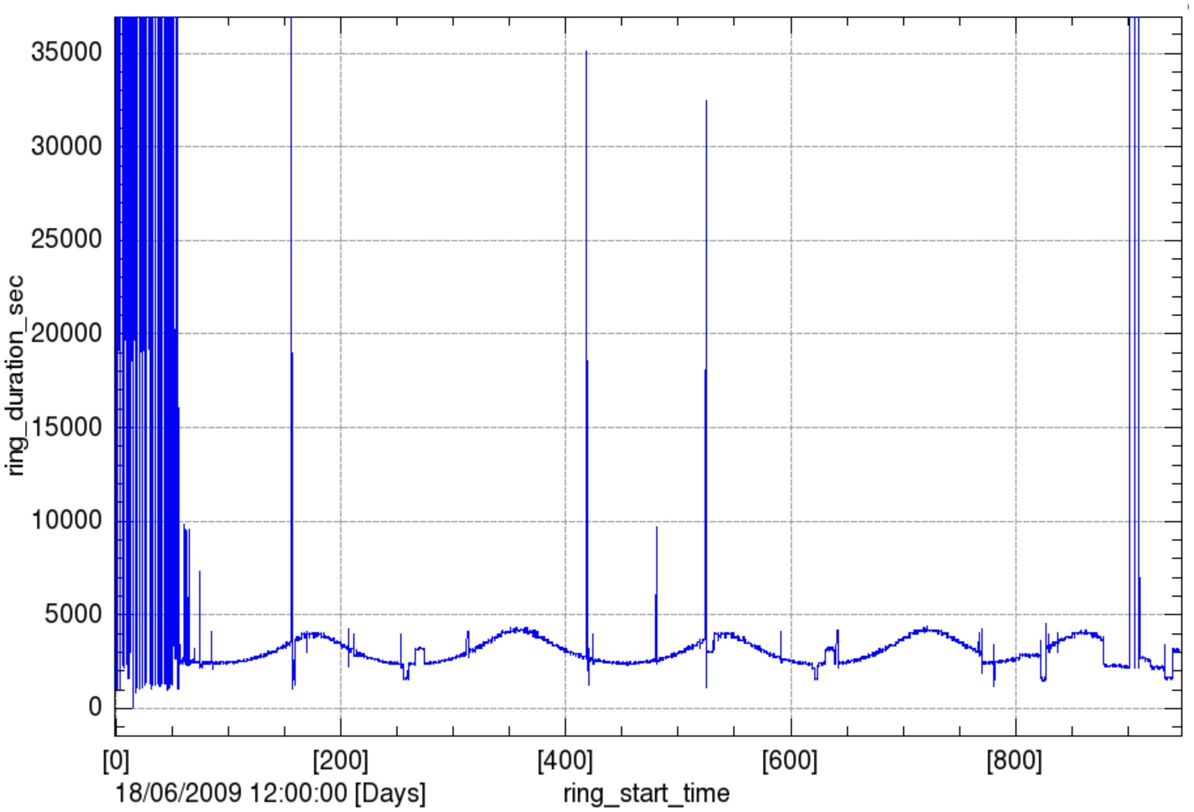

ring duration

Orbit data

Satellite orbit velocity is built by the MOC Flight Dynamics team and made available to the HFI DPC via orbit files. See Orbit description document [5] and orbit files repository [3]. As those orbit files contain both effective and predictive data, they are regularly ingested updated in the HFI database.

*Note: these same data are also ingested in parallel into the NASA JPL Horizons system (*http://ssd.jpl.nasa.gov/*) under ESA's responsibility.*

The satellite orbit data preprocessing is the following.

- The sampling of the MOC provided orbit velocity data is appromximately 1 every 5 mn. These data are interpolated to the time of the middle of the HFI rings.
- The reference frame of the orbit data is translated from the MOC given Earth Mean Equator and Equinox J2000 (EME2000) reference frame to the ecliptic reference frame in cartesian coordinates.
- The earth velocity provided by the NASA JPL Horizons system (http://ssd.jpl.nasa.gov/) is interpolated to the time of the middle of the HFI rings. It is then added to the satellite velocity data.

The use of the satellite orbit velocity is three-fold:

1. computation of the CMB orbital dipole (see calibration section),
2. computation of the positions of solar system objects (see data masking section),
3. computation of the abberation correction.

Time correlation data

The MOC is responsible for providing information about the relationship between the satellite On Board Time (OBT) and Coordinated Universal Time (UTC). This information comes via several measurements of OBT and UTC pairs each day, measured during the satellite ranging. See Time Correlation document [6].

The following plot shows the (OBT, UTC) data couples provided by MOC since Planck launch. The x axis is in number of days since the 17th of May 2009 while the y axis is the difference of OBT and UTC in seconds. The very slow drift is approximately 0.05 seconds per day. The small wiggles are due to the satellite global temperature trends due to its orbit and distance to the sun.

Note: The isolated point on the 1st of June 2010 (just above 400 in abscisse) is not significant and due to a misconfiguration of the ground station parameters.

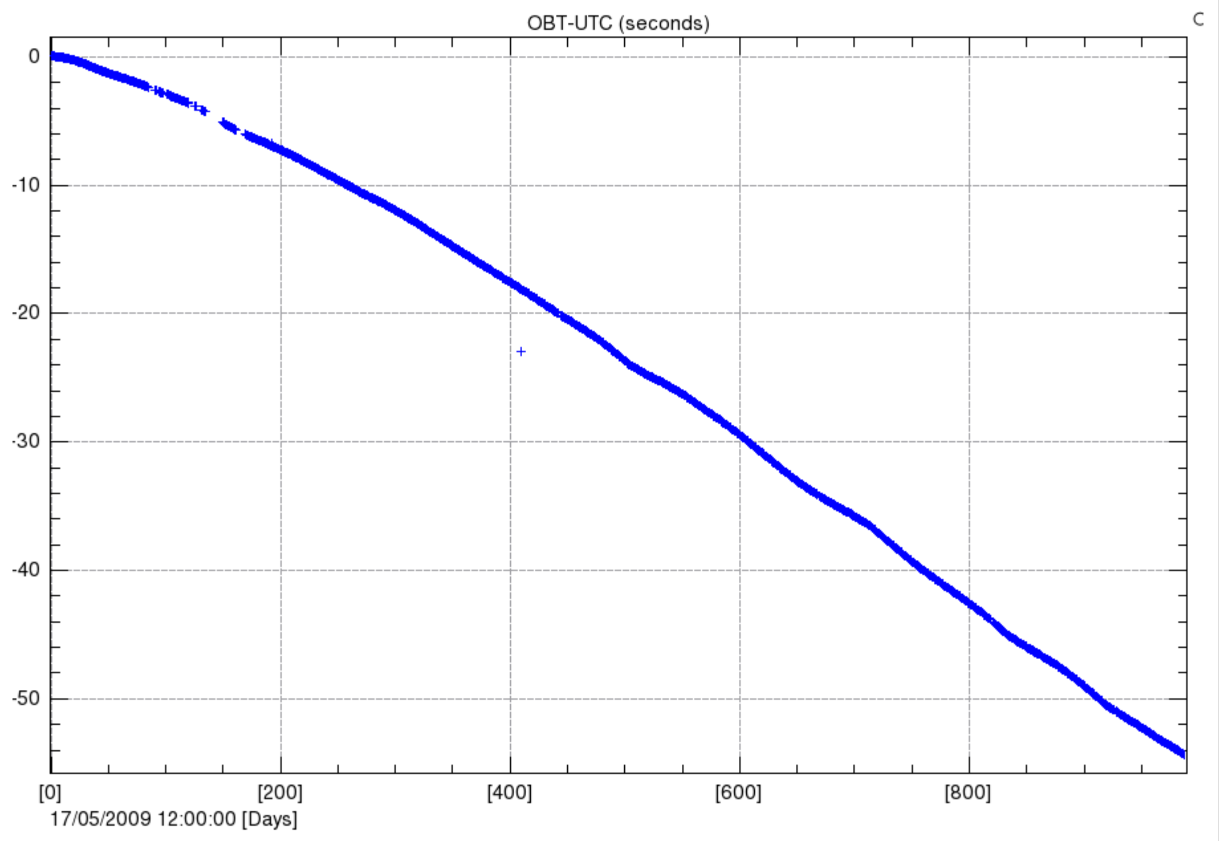

OBT-UTC correlation data

An order 3 polynomial is then fitted to the data. As the whole HFI data management and processing uses OBT, the OBT-UTC information is only used when importing orbit data from Horizons.

References

<biblio force=false>

1. References

</biblio>

References

[1] http://www.rssd.esa.int/doc_fetch.php?id=3135867&page=5
[2] http://www.rssd.esa.int/doc_fetch.php?id=3139505&page=1
[3] http://pla.esac.esa.int/pla/aio/metadata-action?PAGE_SIZE=1500&PAGE=1&RESOURCE_CLASS=OPERATIONAL_FILE&SELECTED_FIELDS=OPERATIONAL_FILE.FILE_ID,OPERATIONAL_FILE.SIZE&OPERATIONAL_FILE_TYPE.NAME=&RELEASE.NAME=PR1&RETURN_TYPE=HTML
[4] http://www.rssd.esa.int/doc_fetch.php?id=3135867&page=6
[5] http://www.rssd.esa.int/doc_fetch.php?id=3139509&page=1
[6] http://www.rssd.esa.int/doc_fetch.php?id=3139618&page=1

TOI processing

Overview

We describe here how the TOIs are processed in order to be used for map production. We do not repeat the general features of the pipeline which are given in the HFI Data Processing article #planck2013-p03 Planck-2013-VI [2]. Here we give complementary explanations on some details. The TOI of each bolometer is processed independently of the other bolometers, so as to keep the noise properties as uncorrelated as possible. The processing involves modifying the TOI itself for what concerns the conversion to absorbed power and the correction of glitch tails. It also adds a flag TOI that masks the TOI samples that are not to be projected on maps for various reasons.

Input TOI

The input TOI consists in the AC modulated voltage output of the readout of each bolometer. The input has previously been decompressed, and converted from internal digital units to voltage via a constant factor. The TOI has a regular sampling at the acquisition frequency of facq=180.373700+-0.000050 Hz. There are almost no missing data in the TOIs, except for few hundred samples of 545 and 857 GHz TOIs which were lost in the on-board compression due to saturation on the Galactic Center crossings.

General pipeline structure

The following figure shows how the initial TOI is transformed and how flags are produced:

Output TOIs and products

A TOI of clean calibrated samples and a combined flag TOI are the outputs of the processing. The clean calibrated TOI is calibrated so as to represent the instantaneous power absorbed by the detector up to a constant (which will be determined by the map-making destriper). It is worth mentioning how the clean calibrated TOI is changed with respect to the input TOI, beyond the harmless constant conversion factor from voltage to absorbed power. The demodulation stage allows one to get the demodulated bolometer voltage. The non-linearity correction is a second-order polynomial correction based on the physical but static bolometer model. In order to avoid too much masking after glitches, a glitch tail is subtracted after an occurrence of a glitch in the TOI. The 4K cooler lines are removed at a series of 9 single temporal frequencies. Finally, the temporal response of the bolometer is deconvolved.

This affects mostly the high-temporal frequency part of the TOI, although a small but significant low frequency (the long time response) tail is corrected too. Although flagged samples are not projected, their value influences the valid samples somehow. Hence interpolation procedures introduce some indirect modifications of the TOI. The flag TOI is a combination a dozen flags with an OR logic. Only unflagged data are projected. The exhaustive list of flags is given here: CompressionError, NoData, SSO, UnstablePointing, Glitch, BoloPlateFluctuation, RTS, Jump, PSBab. A complete qualification of the data is obtained at the ring level. If the TOI shows an anomalous behaviour on a given ring, this ring is discarded from projection. A special TOI is also produced as an input to the beam analysis with Mars, Jupiter and Saturn.

Examples of clean TOIs

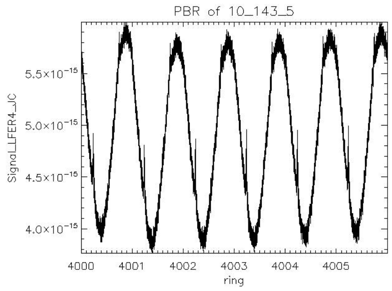

Phase-binned signal (PBR) for 6 consecutive rings from 4000 to 4005

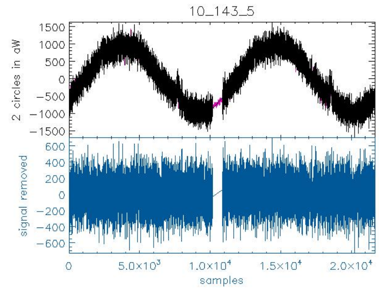

Valid signal (up) and noise (bottom) for 2 consecutive circles of the ring 4000

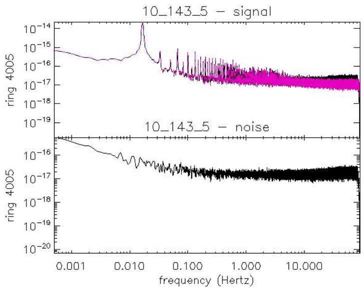

Fourier power spectral density of the first 30 minutes of the ring 4005 with signal before (pink) and after (black) deconvolution (top) and noise (bottom)

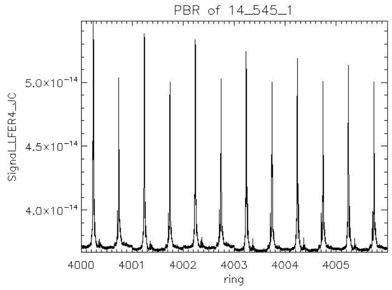

Phase-binned signal (PBR) for 6 consecutive rings from 4000 to 4005

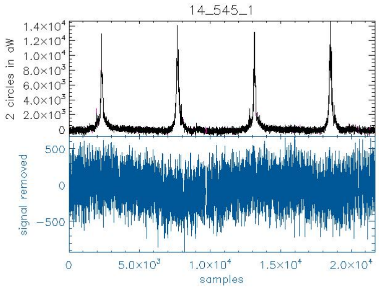

Valid signal (up) and noise (bottom) for 2 consecutive circles of the ring 4000

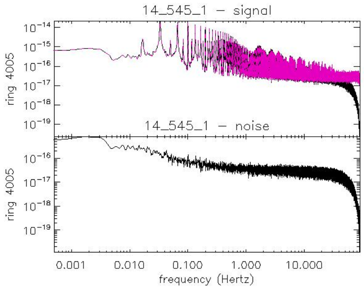

Fourier power spectral density of the first 30 minutes of the ring 4005 with signal before (pink) and after (black) deconvolution (top) and noise (bottom)

Samples of PBR, TOIs, and PSDs of all detectors are shown in this file.

Trends in the output processing variables

Here we intend to show the trend of the systematic effects that are dealt with in the TOI processing. The full impact of each of them is analyzed in the HFI-Validation section.

ADC baseline

The following figure shows the ADC baseline which is used prior to demodulation (a constant offset is removed for clarity). This baseline is obtained by smoothing on an hour block average the undemodulated TOI on unflagged samples.

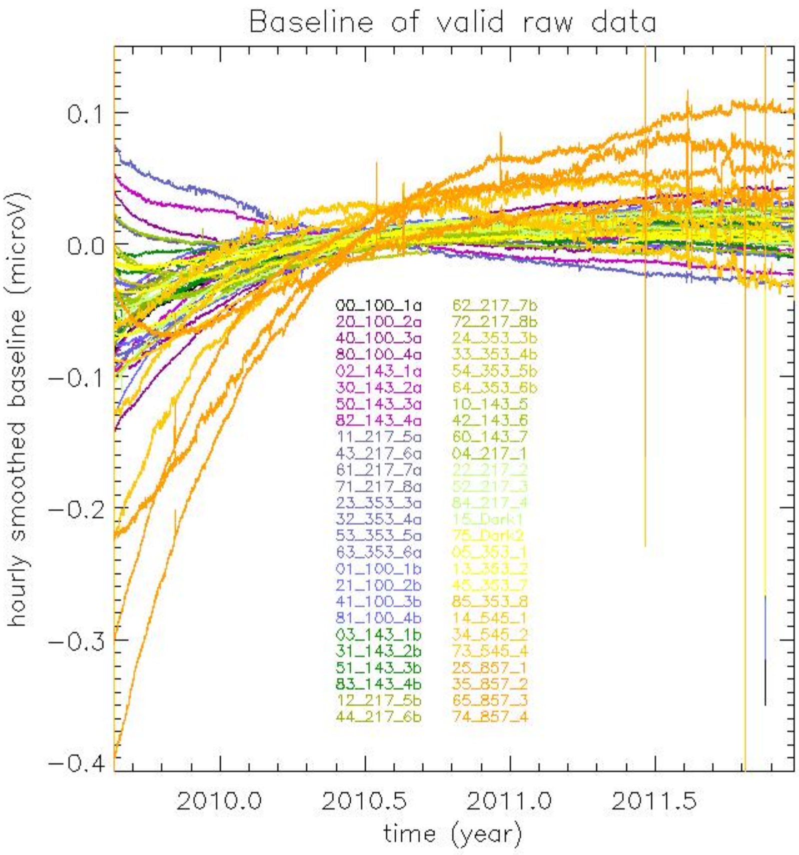

ADC baseline for all bolometers

Glitch statistics

The glitch rate per channel is shown in this figure. For details, see copap. #planck2013-p03e Planck-2013-X [1]

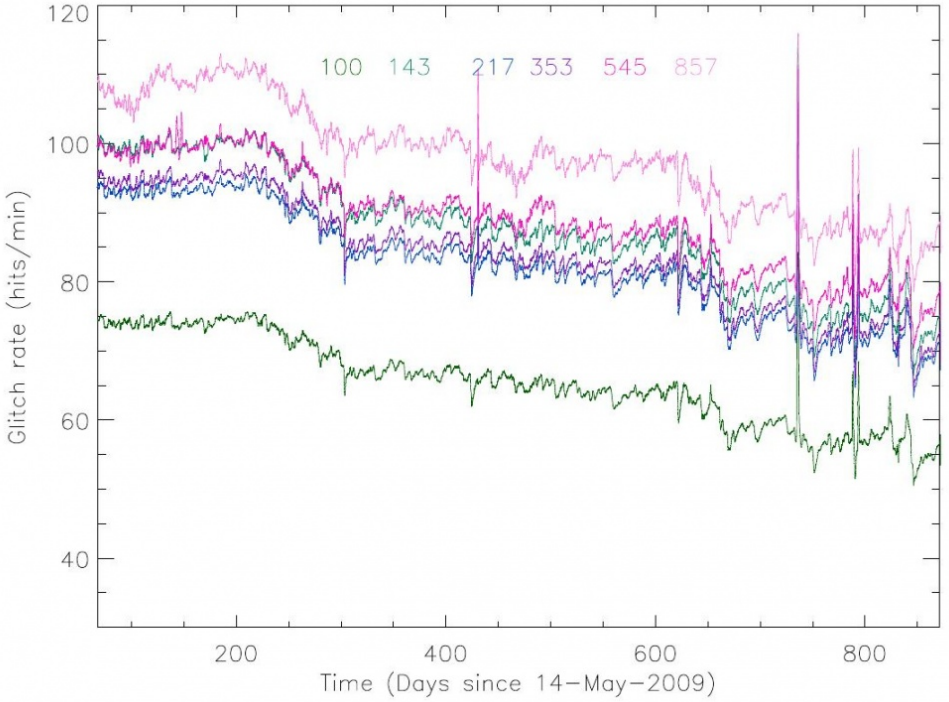

Glitch rate evolution

The percentage of flagged data (mostly due to Cosmic Rays) at the ring level is shown in these examples. No smoothing was applied. Only valid rings are shown.

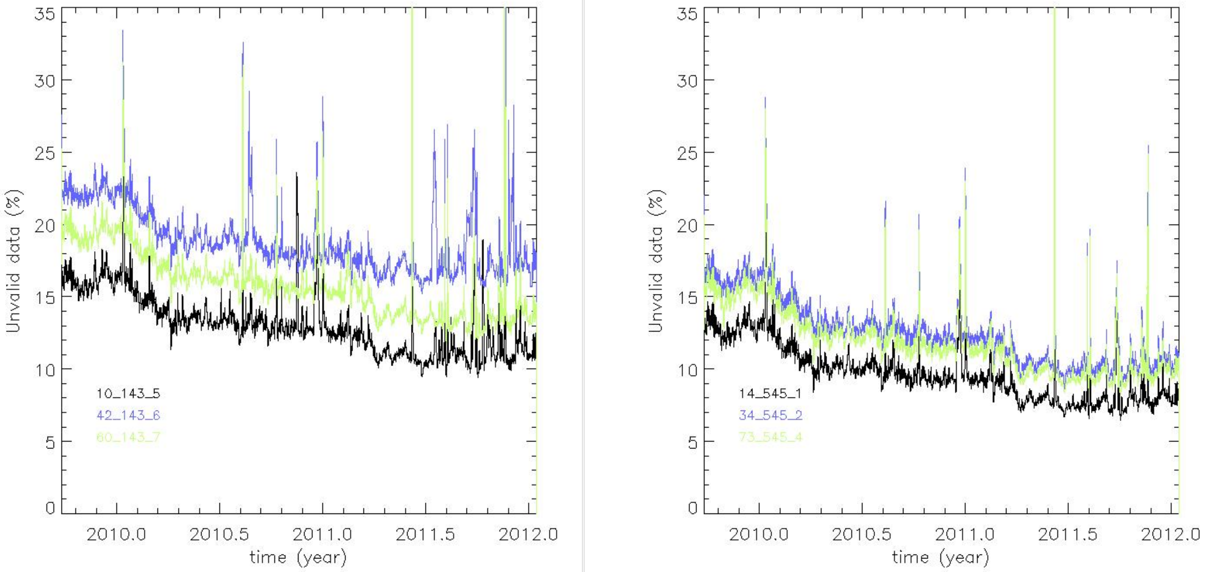

143 GHz bolometers

545 GHz bolometers

Percentage of flagged data

The complete set of plots is attached here.

Thermal template for decorrelation

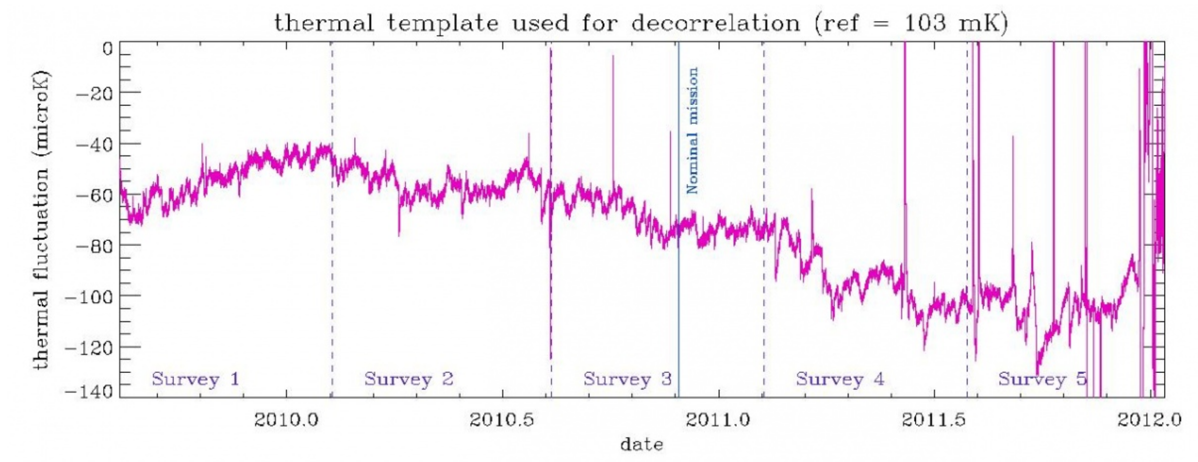

Thermal template used for the decorrelation from bolometer plate temperature fluctuations

A simple linear decorrelation is performed using the 2 dark bolometers as a proxy of the bolometer plate temperature. Coupling coefficients were measured during the CPV phase.

4K cooler lines variability

The amplitude of the nine 4K cooler lines in aW at 10, 20, 30, 40, 50, 60, 70, 80 and 17 Hz is shown for two bolometers in the following figures. The trend is smoothed over 31 ring values after having discarded measurements done at a ring which is discarded for all bolometers.

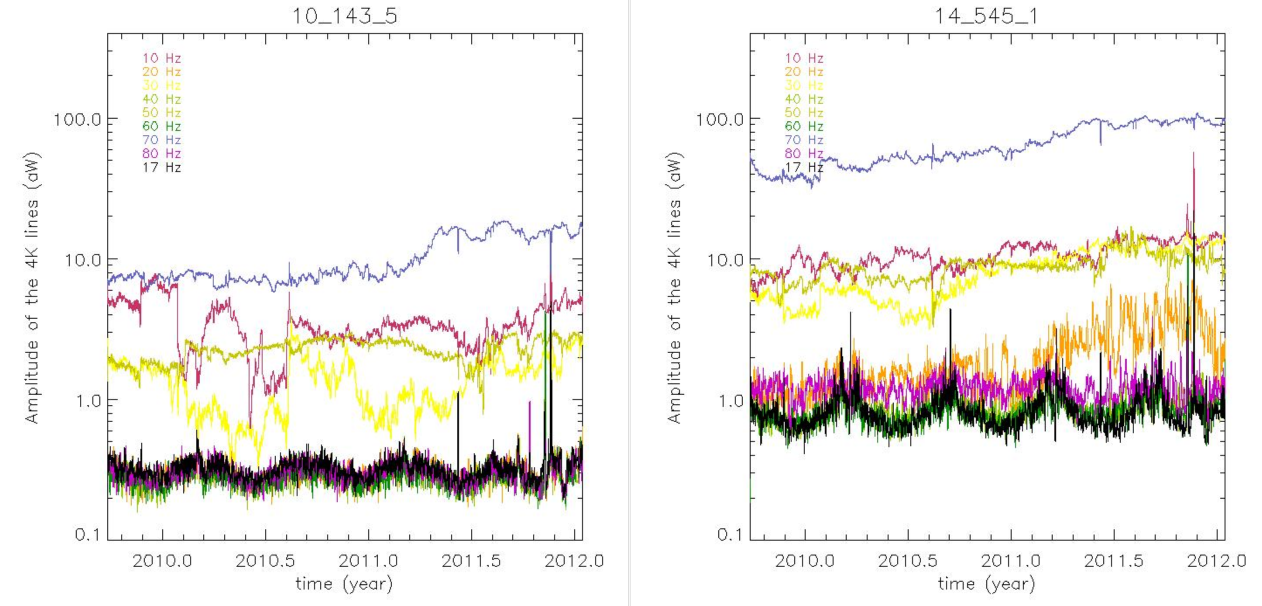

143_5 bolometer

545_1 bolometer

Amplitude of the nine 4K cooler lines

The 4K cooler line coefficients of all bolometers are shown in this file.

The 4K cooler lines project onto the maps only for a limited fraction of rings, the so-called resonant rings. This is graphically shown in the following figure. For each ring (stable pointing period), the spin rate is very stable at about 1 rpm. From one ring to another, the spin frequency (shown as diamonds) changes around that value. The sky signal is imprinted at the corresponding spin frequency and its 5400 (60x90) harmonics. If one of the nine 4K cooler lines happens to coincide with one of the spin frequency harmonics (a resonant ring), it will project a sine-wave systematic on the maps. The horizontal coloured bars show the zone of influence of a particular 4K line (labeled on the left side of the plot), when folded around 16.666 mHz. When the spin frequency hits one of these zones, we have a resonant ring. The 4K line coefficient is interpolated for this ring and an estimate of the systematic effect is subtracted from the TOI. Resonant rings are different for different 4K lines. Note the two-level oscillation pattern of the spin frequency is due to the satellite attitude control system.

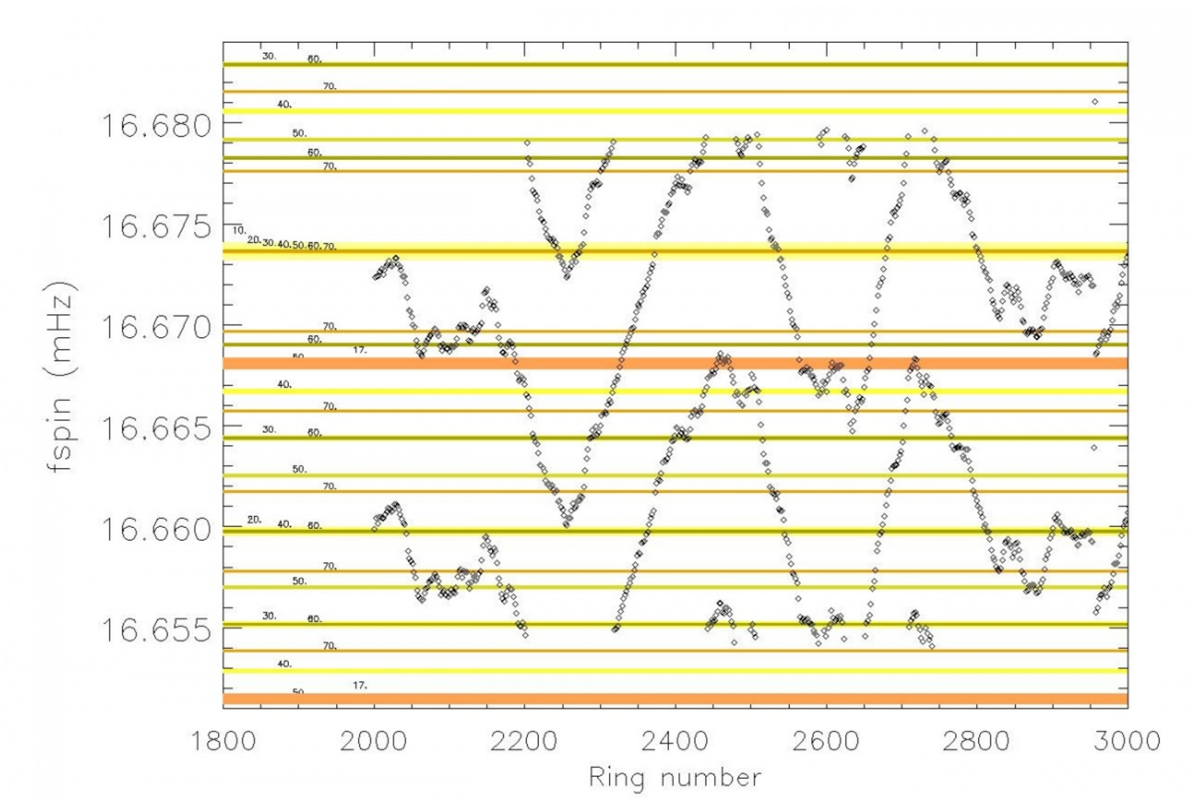

Spin frequency and 4K line zones of influence

Jump correction

A piecewise constant value is removed to the TOI if a jump is detected. See a jump example in this figure:

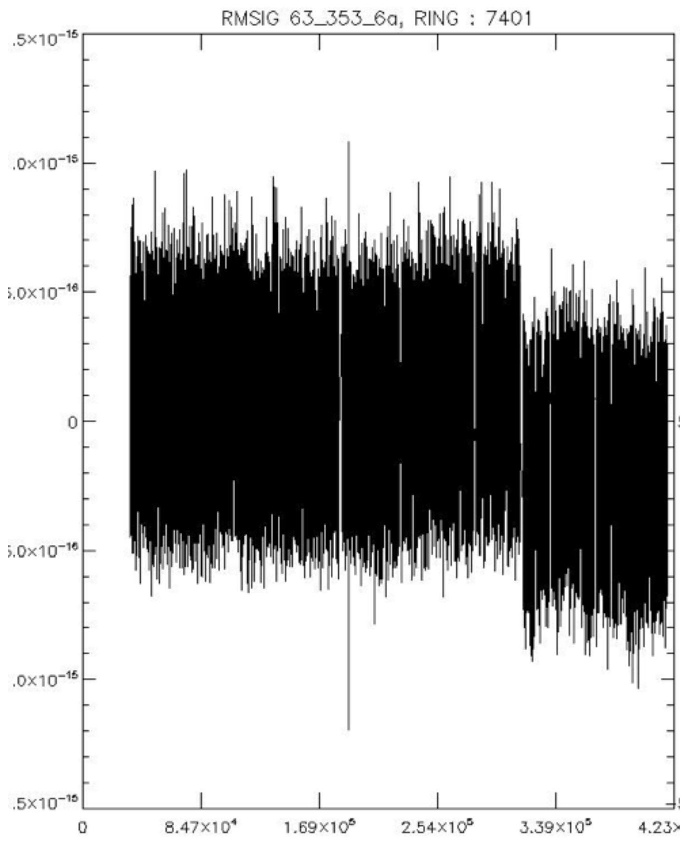

An example of a jump seen on the noise TOI

The number of jumps per day (all bolometers included) is shown in this figure:

The jumps are uncorrelated from bolometer to bolometer. The total number of jumps detected in the nominal and full mission is shown here:

Trends in noise and signal

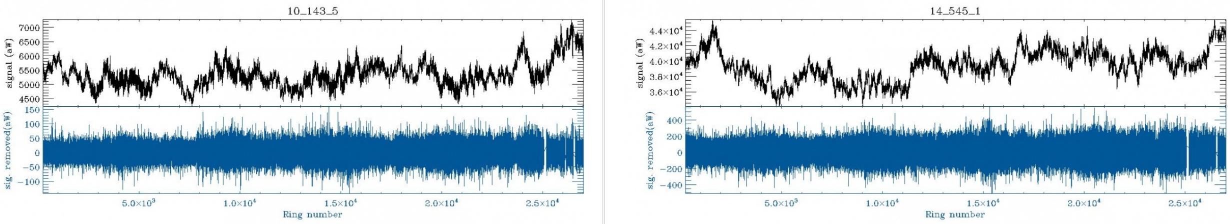

143_5 bolometer

545_1 bolometer

Signal (top) and noise (bottom) smoothed at 1 minute. All values falling in a discarded ring are not plotted.

The smooth TOIs of all detectors are shown in this file.

Noise stationarity

This is not the final version but gives a good idea of power spectra at the detector level of noise TOIs. All PSDs can be seen in this file.

The standard deviation per ring corrected by ring duration bias is given here, one per bolometer using only valid rings. No smoothing is applied (except a 31-point smoothing for the 545 and 857 GHz channels) but values for rings discarded for all bolometers (see below) are not used. The standard deviation is computed on samples valid for map-making which are also not affected by the Galaxy or the point-sources using the usual flags. Two examples are given here.

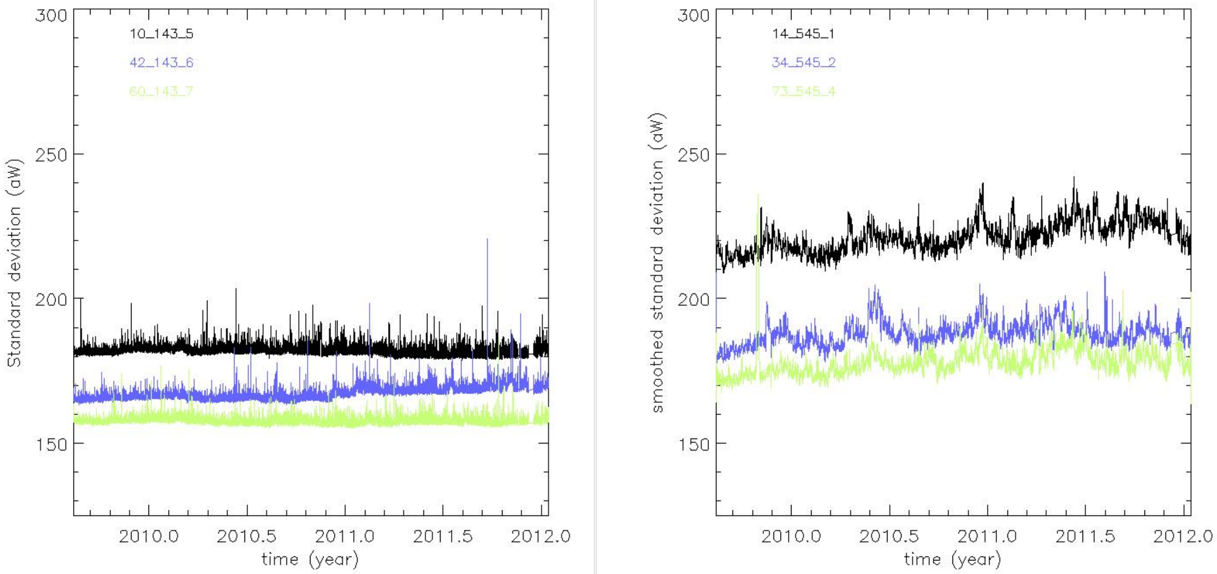

143_5 bolometer

545_1 bolometer

Standard deviation per ring

The full series of plots is here: Standard deviation of noise TOIs at the ring level

Note the presence for 3 bolometers of a two-level noise system. No correction can be done for that effect. See one example here:

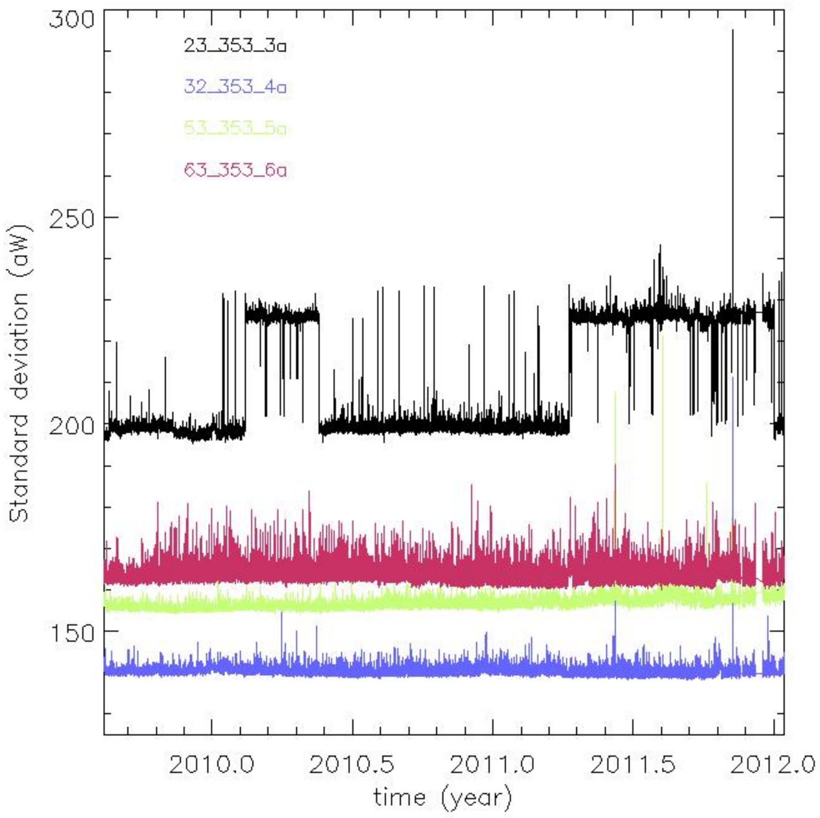

An example of two-level noise system is seen in bolometer 23_353_3a

An example of the higher order statistics which are used to unveil rings affected by RTS problems.

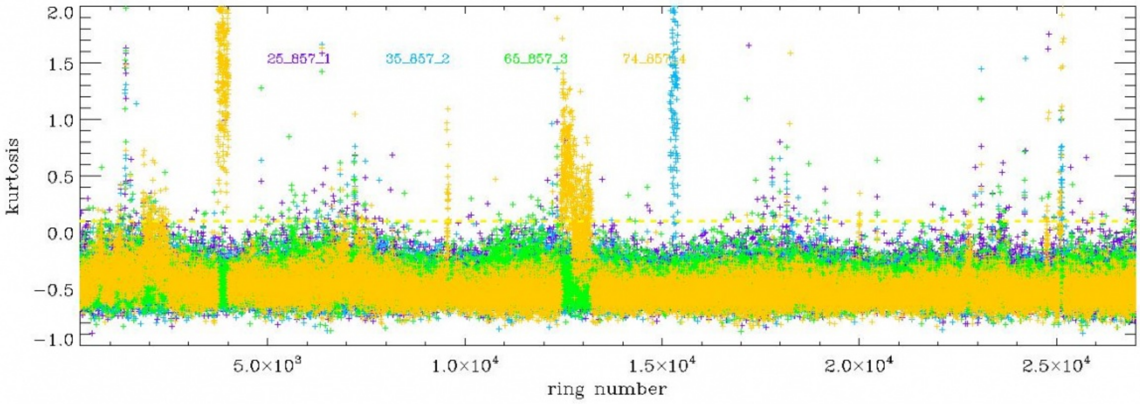

Discarded rings

Some rings are discarded (flagged) from further use (beam making, map making) by using ring statistics (see above and #planck2013-p03 Planck-2013-VI [2]). For each statistic, we compare each ring value to the ring values averaged (RVA) over a large selection of rings (between 3000 and 21700). We also define the modified standard deviation (MSD) of a ring quantity as the standard deviation of that quantity over the rings that deviate by less than five nominal standard deviations. This truncation is necessary to be robust against extreme deviant rings.

More specifically, a ring is discarded if it matches one of the following criteria:

- the | mean-median | deviates from the RVA by more than fifteen times the MSD.
- the standard deviation deviates from the RVA by more than -5 times the MSD (all cases corresponding to almost empty rings) or +15 times the MSD.
- the Kolmogorov-Smirnov test deviates from the RVA by more than 15 times the MSD.
- the ring duration is more than 90 min.
- the ring is contaminated by RTS with an amplitude of more than one standard deviation of the noise. It concerns a few hundreds of rings for 3 bolometers (44_217_6b, 71_217_8a, 74_857_4). Notice that two bolometers are completely discarded for maps: 55_545_3 and 70_143_8, which present RTS at all time.

For the three first criteria, a visual inspection of the noise TOI at each of the incriminated rings has shown that all these anomalous rings are due to either a drift, a small jump in the TOI trend or a sudden change of noise level, the origin of which is unknown at present.

Once the list of discarded rings per bolometer is produced, a common list of discarded rings can be extracted for all bolometers (by using discarded rings for at least half the bolometers). Such rings correspond to identified phenomena, as can be seen on the following table.

Furthermore, an isolated valid ring stuck between two common discarded rings becomes discarded as well.

Table of **common discarded rings** of the nominal mission (rings 240-14723).

Cause	ring number
manoeuvre	304 1312 3590 3611 3642 3922 4949 6379 8456 11328
Sorption Cooler switchover	11149 11150 11151 11152
rings too long	440 474 509 544 897 898 3589 13333 14627 14653
star tracker switchover	14628 14654
massive glitch event	7665
solar flare	11235

The following figure is a summary of the impact of the discarding process **for each bolometer** (the solid black line is the common discarded ring percentage). The outlier bolometers have some RTS problems as mentionned above.

Effective integration time

The following figure summarizes the effective integration time per bolometer. For that purpose the number of unflagged samples in non-discarded pointing periods have been used within the nominal mission. The average value is of about 335 days of effective integration time.

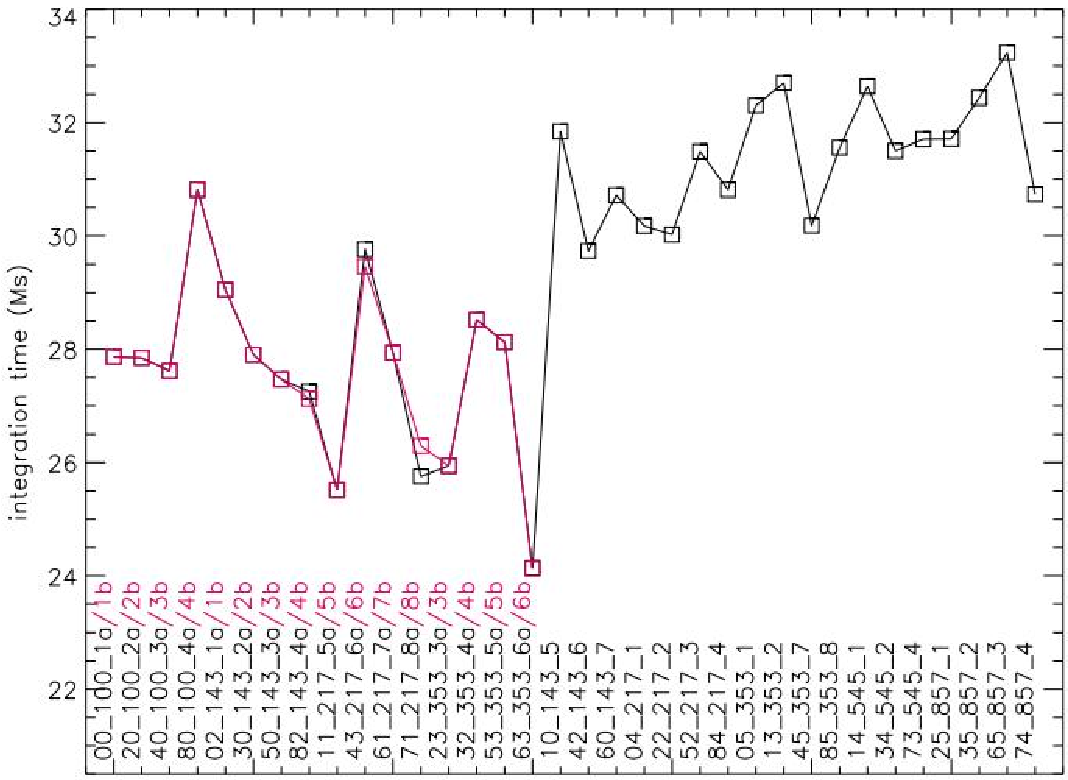

Effective integration time per bolometer

Flag description

Input flags

These flags are used as inputs to the TOI processing

The point-source flag (PSflag)

> An earlier version of HFI point-source catalog is read back into a flag TOIs, at a given frequency. In practice, 5 sigma sources are masked within a radius of 1.3 FWHM (9, 7, 5, 5, 5, 5 arcmin at 100,143,217,353,545,857 GHz) TBC.

the galactic flag (Galflag

> An earlier version of HFI maps is thresholded and apodized. The produced masks are read into flag TOIs. The retained threshold corresponds to a sky coverage of respectively 70, 70, 80, 90, 90, 90% at 100,143,217,353,545,857 GHz.

Solar System Object flag

> For the TOI flag, Mars, Jupiter, Saturn are flagged up to a radius of NbBeam= 2,3,3,4,4,4 times the fiducial SSO_FWHM with SSO_FWHM= 9, 7, 5, 5, 5, 5 arcmin at 100,143,217,353,545,857 GHz.
>
> As an input to planet mask for maps, Mars, Jupiter, Saturn are flagged with a radius computed as a coefficient depending on the planet (Factor_per_source) times NbBeam times SSO_FWHM, with Factor_per_source = 1.1, 2.25, 1.25 for Mars, Jupiter, Saturn respectively and NbBeam = 2.25, 4.25, 4.0, 5.0,.6.0, 8.0 at 100, 143,

217, 353, 545, 857 GHz. This flag is called SSOflag4map.

A small trailing tail is added to the mask to take into account the non-deconvolution of the planet signal which has been replaced by background values. The width of that tail is 10 % of the main flag diameter. The number of samples which are additionnaly flagged are the Factor_per_Source times AddSNafter with (trail) times (Factor_per_source)^3 samples where trail = 10, 30, 20, 20, 30, 40 at 100, 143, 217, 353, 545, 857 GHz.

Uranus and Neptune together with detected asteroids are masked by HFI. They are masked at the TOI level using an exclusion radius of 1.5 SSO_FWHM. At 857 GHz, 24 asteroids have been detected with HFI : 1Ceres, 2Pallas, 3Juno, 4Vesta, 7Iris, 8Flora, 9Metis, 10Hygiea, 11Parthenope, 12Victoria, 13Egeria, 14Irene, 15Eunomia, 16Psyche, 18Melpomene, 19Fortuna, 20Massalia, 29Amphitrite, 41Daphne, 45Eugenia, 52Europa, 88Thisbe, 704Interamnia, 324Bamberga.

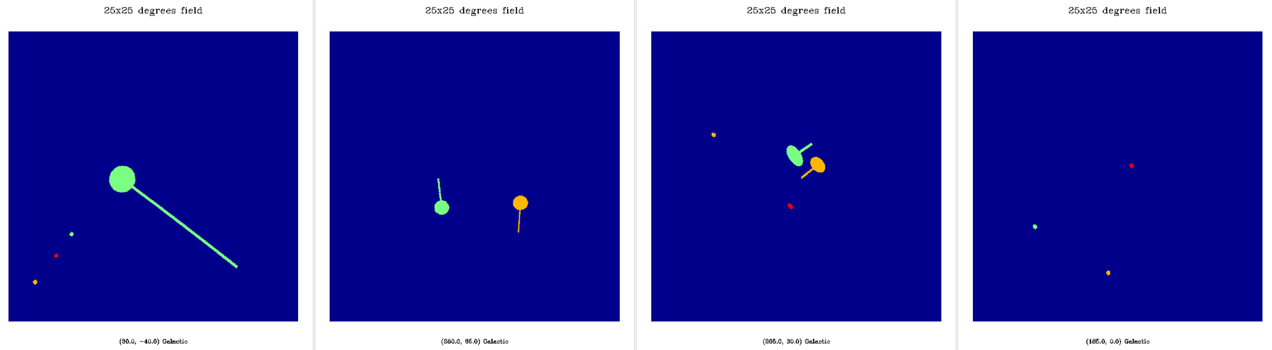
25x25 degrees field
25x25 degrees field
25x25 degrees field
25x25 degrees field
(30.0, −40.0) Galactic
(260.0, 65.0) Galactic
(305.0, 30.0) Galactic
(185.0, 0.0) Galactic

143 SWB row, around Jupiter 1st crossing

143 SWB row, around Saturn

143 SWB row, around Mars

143 SWB row, random field in the ecliptic plane

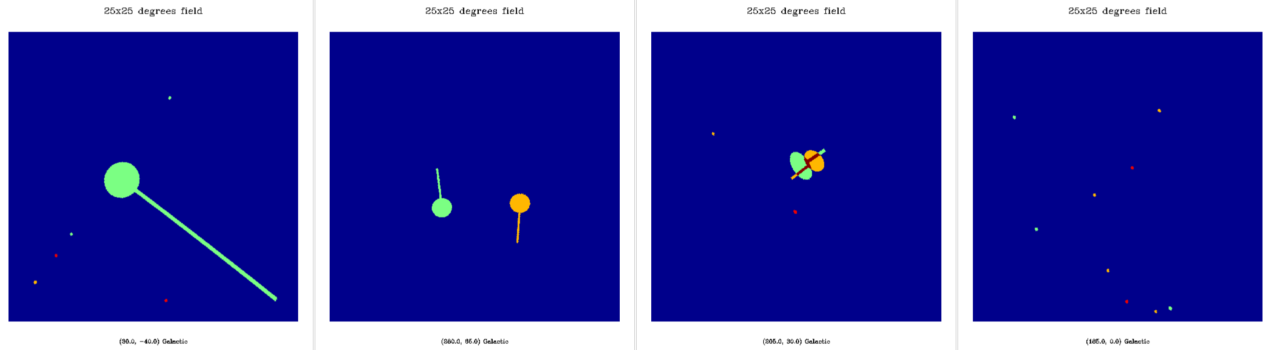
25x25 degrees field
25x25 degrees field
25x25 degrees field
25x25 degrees field
(30.0, −40.0) Galactic
(260.0, 65.0) Galactic
(305.0, 30.0) Galactic
(185.0, 0.0) Galactic

545/857 row, around Jupiter 1st crossing

545/857 row, around Saturn

545/857 row, around Mars

545/857 row, random field in the ecliptic plane

Local maps showing the SSO flag. The colors correspond to the surveys involved in the nominal mission (green = Survey I, yellow = Survey II, red = Survey III).

Output flags

A FlagTOIproc is produced by the TOIprocessing. It marks measurements which are not reliable for any of the following reasons:

- gap (no valid input data), enlarged by one sample on each side. It flags less than 0.00044% (resp. 0.00062%) of the nominal (resp. complete) mission. It is equivalent to less than 3 (resp. 8) minutes of data.
- "glitch" on dark bolometers: as the thermal template used for decorrelation is computed from these bolometer data, chunks of one minute-length data are discarded for all bolometers if at least 50\% of the data for at least one dark bolometer are flagged during this time. It is efficient to flag the data around the maximum of thermal events.
- "glitch" on individual bolometers : samples where the signal from a cosmic ray hit dominates the sky signal at more than 3 σ are discarded.
- jump as 100 samples are flagged around the computed position of the jump to take into account the error on this reconstructed position.

So the flag produced for the map making, called Total_flag, is defined by:

- Total_flag = UnstablePointing Flag OR FlagTOIproc OR SSOflag4map OR SSOflag seen

where FlagTOIproc = gap OR flag thermal template OR glitch OR jump and for PSB bolometers, FlagTOIproc_AB = FlagTOIproc_A OR FlagTOIproc_B. Note that the Total_flag is then identical for the A and B bolometers of a PSB pair.

At the destriping stage, a more restricted flag, called Total_flag_PS, is used. It is defined by Total_flag_PS = Total_flag OR PS_flag.

References

<biblio force=false>

1. References

</biblio>

References

[1] http://www.rssd.esa.int/doc_fetch.php?id=3168071&page=1

Detector pointing

Introduction and Summary

The overall geometry of the Planck focal plane is shown here:

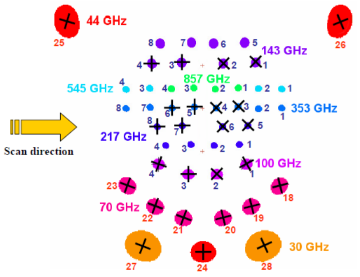

The Planck Focal Plane

In order to take full advantage of the HFI beams, we must know the individual detector positions to a precision of better than several arcseconds, over the course of the entire mission. Spacecraft pointing comes from the on-board star tracker at 4 Hz. This is translated via a series of three-dimensional rotations to a pointing for the centre of the focal plane and resampled to the HFI TOI data rate for convenience. We must then further translate this focal-plane boresight pointing to the individual detector locations. Because neither the rotations from the star tracker to the boresight nor those from the boresight to the individual detectors are known exactly a priori, we must calibrate using flight data. Specifically, measurements of HFI Detector pointing are based largely on observations of individual planets, with information from the much more frequent observation of lower-flux galactic and extragalactic high-frequency sources used to monitor and build a model of overall pointing drift. This long-term drift of the spacecraft attitude is due to changes in the moment of inertia and includes specific events which may induce sudden changes, essentially random as far as our ability to predict the effects thereof. Note that the resulting pointing model cannot easily be directly compared to a physical/optical model: in particular, it includes an unmeasured phase shift in the scan direction from the convolution and deconvolution of the detector transfer function, which is complex in the Fourier domain (Planck Collaboration P03c). Comparison with the initial optical model indicates that the in-scan change due to this phase shift is of the order of 1 arcminute. Note also that aberration is corrected in all observations. The final pointing model is measured to be better than 2 arcsecond rms in the co-scan and cross-scan directions averaged over ten-day periods.

Initial measurements: Mars 1 and other planets

The first observation of Mars, which occured around OD 80, is the baseline against which other objects are compared. Here, we show the relative pointing of Mars 1 to the pre-launch RFFM.

Focal plane drift: map-based measurement of detector positions

Prior to modeling of systematic changes in the Planck pointing, we find secular drifts of order one arcminute over the course of the nominal mission. We monitor this by making point-source catalogs based on single Planck surveys, only counting those objects which are observed over the course of less than seven days (this limits us to observations away from the ecliptic poles where Planck's observing strategy is highly cross-linked). We cross-match these catalog positions to the known IRAS point-source catalog (Wang and Rowan-Robinson 2008) and average the deviations in ten-day blocks (the individual measurements are shown as lighter points; error bars assume equal weighting for all points, but the results are not sensitive to any imposed S/N cutoff):

A similar analysis performed directly in the timestream gives similar results, below.

A model for Planck Pointing

These analyses allow us to build a model for the pointing drift.

The correction is based on the measurement of pointing offset directly from the timeline, on a small sample of known and bright radio sources and planets. First the beam shape of each detector is measured by stacking individual timeline observation of bright planets. This process is of course amperes by pointing error, but those are reduced by allowing each pass on the planet to be slightly displaced in order to correct for the observed location of the planet. This process yield a very clean estimate of the beam of each detector.

Then those beam are used to determine the offset of observed location of planets (Mars, Saturn & Jupiter) as well as a few (~10) bright radio sources.

This offset are estimated for all detectors for the planet, and only for 100Ghz to 217Ghz one for the radio sources.

From the planet observations, one can recover the alignment of each detector in the focal plane, as well as a first pointing correction at the time of planet observations. This pointing correction is obtained by fitting splines on the planet observation from each detector. We further allow this correction to have a sharp jump between the first and second survey (SCS switchover).

This first pointing correction is further refined using the point sources observations in order to fill the period between planet observations. The radio sources offsets require further treatment than the planet based offsets. First, the brightness of the sources being much smaller than planets, the offset on individual detector observation are very noisy, and we filter out the noise by building median offsets for each point source observation. Second, since the sources can be slightly extended we still observe systematic offset above and below the planet based pointing correction in a regular alternating pattern. This is due to the fact that we are observing those extended objects scanning in alternating directions, and our fit of those extended sources to our beam translate into this systematic alternating pattern. We thus allow for a small, arcsec correction of those offsets : i.e. each object is allowed a single offset displacement of order arc seconds in order to minimize the offset between different observations of the same object at different time.

The resulting list of point source offsets is then merged with the planet offsets. Again a spline based correction is built fitting all of this data, and allowing rupture of continuity at the time of the SCS switchover and other major onboard event (typically between each surveys).

Once we assume the full Planck pointing model and re-measure the position of Mars for this observation, we see sub-arcsecond deviations (as expected); this gives an indication of the purely numerical limitations of the method. Further planet observations show the small remaining uncorrected drift present in the pointing model (note that cross-scan positions are measured with considerably less data than in-scan positions due to the scan strategy): Redoing the single-survey map- and catalog-based computation with the corrected pointing shows that Planck has achieved the arcsecond-scale goal of pointing rms:

References

<biblio force=false>

1. References

</biblio>

Beams

Scanning Beams

The scanning beams describe the instrument's instantaneous beam profile. Due to the near constant spin rate of the spacecraft, time domain effects (including residual time response and lowpass filtering) are degenerate with the spatial response due to the optical system. The scanning beam reconstruction recovers both of these effects, aside from residual time domain effects on a longer time scale than can be captured with the extent of the scanning beam model.

In #planck2013-p03c we consider two models of the beam in order to better understand systematics in the reconstruction. Here we describe only the B-Spline beams which are used to compute the delivered effective beam (see next section).

B-Spline Beam construction

We use seasons 1 and 2 of the Mars observation to reconstruct the beam. The data are processed with the bigPlanets TOI processing. We use JPL Horizons ephemerides to determine the pointing of each detector relative to the planet. We subtract the astrophysical background in the time domain using a bicubic interpolation of the Planck maps.

The time ordered data are used to fit a two dimensional B-Spline surface using a least square minimization and a smoothing criterion to minimize the effects of high spatial frequency variations. We therefore assume the scanning beam to be smooth. The smoothing criterion as well as the locations of the nodes used to compute the B-Spline basis functions are set using GRASP physical optics simulations as inputs which are the best assumptions on the spatial frequency content of the in-flight beams.

The smoothing criterion is defined as follows:

And the global inversion criterion :

$$\zeta = \eta + p \times \delta$$

with δusual least square estimator and $p$coefficient giving the relative weight to $\delta$with respect to the smoothing criterion.

The B-Spline nodes are located on a regular spaced grid in the detector coordinate framset. At the edge of the reconstructed beam map area, 4 coincident nodes are added to avoid vanishing basis functions.

Let $B_{i,k+1}$, $k$degree B-Spline build using nodes { λ_i, ..., λ_{i+k+1}} (*De Boor & Cox*, 1972) :

$$B_{i,l+1}(x) = \frac{x - \lambda_i}{\lambda_{i+l} - \lambda_i} B_{i,l}(x) + \frac{\lambda_{i+l+1} - x}{\lambda_{i+l+1} - \lambda_{i+1}} B_{i+1,l}(x)$$
$$l = 1, \ldots, k$$

Simulations and errors

We estimate the reconstruction bias and noise in the measurements using an ensemble of simulated planet observations for each channel. Further details are discussed in #planck2013-p03c. Kept fixed in each simulation are:

- the input beam assumed: we use a supersampled version of the reconstructed B-Spline beam (or whatever comes out of the current ongoing tests!)
- Astrophyical background is the same as that subtracted from the real data.
- StarTracker pointing (using the ptcor6 pointing model).

The following are varied in each simulation:

- detector noise realizations obtained by filtering randomly generated white noise with the measured noise PSDs
- random pointing errors with 2 arcsecond rms, and a spectrum that replicates the real errors.

- simulated glitches and the deglitching procedure
- Mars brightness temperature variability

400 simulated timelines are generated for each bolometer and for each of the two seasons of Mars observations used in the beam reconstruction. The simulated timelines are made into beam maps, projecting onto the B-Spline basis in the same way as the real data.

The beam maps are propagated to effective beam window functions using the quickbeam approach (see effective beams below) and used to evaluate the reconstruction bias and to construct error eigenmodes in the effective beam window function.

Residuals

There are two known beam effects that are not included in the main beam model and are estimated as a separate bias in flux and angular power spectrum measurement: 1. long tails due to errors in low frequency time response deconvolution, and 2. near sidelobes.

We stack all five observations of Jupiter to estimate the long time scale residuals due to incomplete deconvolution of the long time scale response.

Effective Beams

The **effective beam** is the average of all scanning beams pointing at a certain direction within a given pixel of the sky map for a given scan strategy. It takes into account the coupling between azimuthal asymmetry of the beam and the uneven distribution of scanning angles across the sky. It captures the complete information about the difference between the true and observed image of the sky. They are, by definition, the objects whose convolution with the true CMB sky produce the observed sky map.

Several methods of effective beams determination have been developped and cross-validated.

The main products are produced using FEBeCoP and details of the processing are given in the Effective Beams products page. See also the equivalent page discussing the LFI beams

FEBeCoP

The full algebra for this method for the calculation of effective beams was presented in [Mitra, Rocha, Gorski et al. [1]] #mitra2010. Here we summarise the main results. The observed temperature sky $\widetilde{\mathbf{T}}$is a convolution of the true sky $\mathbf{T}$and the effective beam $\mathbf{B}$:

where

$t$is time samples, $A_{ti}$is 1if the pointing direction falls in pixel number i, else it is 0, $\mathbf{p}_t$represents the exact pointing direction (not approximated by the pixel centre location), and $\hat{\mathbf{r}}_j$is the centre of the pixel number j, where the scanbeam $b(\hat{\mathbf{r}}_j, \hat{\mathbf{p}}_t)$is being evaluated (if the pointing direction falls within the cut-off radius of $\sim 2.5\times$ FWHM.

The algebra is a bit more involved for polarised detectors. The observed stokes parameters at a pixel i, $(\widetilde{I}, \widetilde{Q}, \widetilde{U})_i$, are related to the true stokes parameters $(I, Q, U)_i$, by the following relation:
where the polarised effective beam matrix

and $\mathbf{w}_t$and $\mathbf{W}(\hat{\mathbf{r}}_j, \hat{\mathbf{p}}_t)$are the the polarisation weight vectors, as defined in \cite{mitra2010}.
The task is to compute $B_{ij}$for temperature only beams and the 3×3matrices $\mathbf{B}_{ij}$for each pixel i, at every neighbouring pixel $j$that fall within the cut-off radius around the the center of the i^{th}pixel.
The effective beam is computed by stacking within a small field around each pixel of the HEALPix sky map. Due to the particular features of Planck scanning strategy coupled to the beam asymmetries in the focal plane, and data

processing of the bolometer and radiometer TOIs, the resulting Planck effective beams vary over the sky.

FEBeCoP, given information on Planck scanning beams and detector pointing during a mission period of interest, provides the pixelized stamps of both the Effective Beam, EB, and the Point Spread Function, PSF, at all positions of the HEALPix-formatted map pixel centres.

FICSBell

For more details, see #planck2013-p03c.

Since the HFI beams are not azimuthally symmetric, the scanning strategy has to be taken into account in the effective beam response modelling. This is done using the FICSBell method (Hivon et al, in preparation), which generalizes to polarization and to include other sources of systematics the approach used for TT $C(l)$estimation in WMAP-3yr Hinshaw et al (2007) and by Smith et al (2007) in the detection of CMB lensing in WMAP maps. The different steps of the method used for this study can be summarized as follows:

1. The scanning related information (i.e., statistics of the orientation of each detector within each pixel) is computed first, and only once for a given observation campaign. Those orientation hit moments are only computed up to degree 4, for reasons described in point 2 below. At the same time, the first two moments of the distribution of samples within each pixel (ie, their center of mass and moments of inertia) are computed and stored on disc.
2. The scanning beam map or beam model of each detector $d$is analyzed into its Spherical Harmonics coefficients

where is the beam map centered on the North pole, and is the Spherical Harmonics basis function. Higher $s$indexes describes higher degrees of departure from azimuthal symmetry and, for HFI beams, the coefficients $b^d_{ls}$are decreasing functions of $s$at most $l$considered. It also appears that, for $l < 3000$, the coefficients with $|s| > 4$ account for 1%or less of the beam throughput. For this reason, only modes with $|s| \leq 4$are considered in the present analysis. Armitage-Caplan and Wandelt (2009) reached a similar conclusion in their deconvolution of Planck-LFI beams.

3. The b^d_{ls}coefficients computed above are used to generate s-spin weighted maps, as well as the first and second order derivatives, for a given CMB sky realization.
4. The spin weighted maps and orientation hit moments of the same order $s$are combined for all detectors involved, to provide an “observed” map. Similarly the local spatial derivatives are combined with the location hit moments to describe the effect of the non-ideal sampling of each pixel (see [sec:pixelization]). In this combination, the respective number of hits of each detector in each pixel is considered, as well as the weighting (generally proportional to the inverse noise variance) applied to each detector in order to minimize the final noise.
5. The power spectrum of this map can then be computed, and compared to the input CMB power spectrum to estimate the effective beam window function over the whole sky, or over a given region of the sky.

Monte-Carlo (MC) simulations in which the sky realisations are changed can be performed by repeating steps 3, 4 and 5. The impact of beam model uncertainties can be studied by including step 2 into the MC simulations.

QuickBeam

For more details, see #planck2013-p03c

Planck observes the sky after convolution with a “scanning beam”, which captures its effective response to the sky as a function of displacement from the nominal pointing direction. Decomposing the scanning beam into harmonic coefficients B_{lm}, each time-ordered data (TOD) sample can be modelled as (neglecting the contribution from instrumental noise, which is independent of beam asymmetry) where the TOD samples are indexed by i, and $\tilde{T}_{lm}$is the underlying sky signal. The spin spherical harmonic ${}_sY_{lm}$rotates the scanning beam to the pointing location (θ, ϕ), while the $e^{-is\alpha_i}$factor gives it the correct orientation. Eq. may be evaluated with the “TotalConvolver” algorithm of Wandelt and Gorski (2001), accelerated using the “conviqt” recursion relations Prezeau and Reinecke (2010) This approach is implemented in LevelS. </ref>, although because it involves working with a TOD-sized objected it is necessarily slow.

On the small angular scales comparable to the size of the beam, it is a good approximation to assume that the procedure of mapmaking from TOD samples is essentially a process of binning: where $H(p)$is the total number of hits in pixel $\hat{n}$.

Start with a normalized, rescaled harmonic transform of the beam B_{lm}, sky multipoles $\tilde{T}_{lm}$and a scan history object $w(\hat{n}, s)$given by $w(\hat{n}, s) = \sum_{j \in p} e^{is\alpha_j}/H(\hat{n})$where the sum is over all hits $j$of pixel $p$at location $\hat{n}_p$, and $\alpha_j$is the scan angle for observation j. The harmonic transform of this scan-strategy object is given by ${}_s w_{LM} = \int d^2\hat{n}_s Y^*_{LM}(\hat{n}) w(\hat{n}, s)$.The beam-convolved observation is then given by $\tilde{T}(\hat{n}) = \sum_{slm} w(\hat{n}, -s) B_{ls} T_{lm\,s} Y_{lm}(\hat{n})$.Taking the ensemble average of the pseudo-Cl power spectrum of these T_{lm}we find

where is a cross-power spectrum of scan history objects. Note that the w(n,s) which we have used here can also incorporate a position dependent weighting to optimize the pseudo-Cl estimate, such as inverse-noise or a mask– the equations are unchanged. Writing the pseudo-Cl in position space (a la Dvorkin and Smith (2009)) with Wigner-d matrices we have

This integral can be implemented exactly using Gauss-Legendre quadrature, with a cost of $\cal 0(l_{\rm max}^2 s_{\rm max}^2)$. For simplicity, we've written all the equations here for the auto-spectrum of a single detector, but the generalization to a map made by adding several detectors with different weighting is straightforward. The cost to compute all of the necessary terms exactly in that case becomes .

Are beams really so difficult? On the flat-sky beam convolution is easy: just multiplication in Fourier space by a beam rotated onto the scan direction. Multiple hits with different scan directions are incorporated by averaging (as the “scan history” objects above encapsulate). Does the sphere really require everything to be so complicated? For a scan strategy which is fairly smooth across the sky, we can pretend that we are observing many independent flat-sky patches at high-L with fairly good accuracy. There is in fact a fairly good approximation to the beam convolved pseudo-Cl power spectrum which is essentially a flat-sky approximation. In the limit that $L \gg l_1$, with $C_{l_2}$and B_{l_2} being slowly-varying function in $l_2$the pseudo-Cl sum above can be approximated as where the average $<>_p$is taken over the full sky. It's illustrative to consider three limits of this equation: for a “raster” scan strategy in which each pixel is observed with the same direction, we have and the predicted pseudo-Cl is just the power spectrum of the beam. For a "best-case" scan strategy, in which each pixel is observed many times with many different orientation angles, we have $< | w(, M) |^2 >_p = {}_{M0}$, and the transfer function is just the azimuthally symmetric part of the beam. Note that this is for a full-sky observation– in the presence of a mask, the average above produces an fsky factor, as expected. It just neglects the coupling between L multipoles (which can be calculated with the more complete equations above).

Effective beam window functions

The effective beam window functions $B(l)$ for HFI, computed using Quickbeam, are available in the RIMO. They do not contain the pixel window function.

Pixelization Artifacts

For more details, see #planck2013-p03c

- Several codes available to simulate effects of pixelization.
- Mixes the CMB gradient into a pixelization ``noise *with a level comparable to that of $2\mu Karcmin$ instrumental noise.*
- Quantitative estimate of effect should be included with each released map, but expect not to matter significantly for CMB analysis, as small compared to instrumental noise.

[sec:pixelization]

Planck maps are produced at resolution 11 $(N_{\mathrm{side}} = 2048)$, corresponding to pixels with a typical dimension of $1.7'$, comparable to the spacing between scanning rings . This results in an uneven distribution of hits within pixels, which introduces some complications in the analysis and interpretation of the maps. A sample of the hit distribution is illustrated in Fig. [fig:pixcoverage]. Below we discuss the simulation and modeling of this pixelization effect in more detail.
[fig:pixcoverage]

The collaboration has produced 3 codes which may be used to simulate the effect of pixelization on the observed sky, LevelS/TotalConvoler/Conviqt, FeBeCoP, and FICSBell references and further discussion of the three methods and how they each simulate the pixelization effect..

For the measurement of CMB fluctuations, it is also possible to gain intuition for the effects of pixelization analytically. On the small scales relevant to pixelization, the observed CMB is smooth, both due to physical damping as well as the convolution of the instrumental beam. Taylor expanding the CMB temperature about a pixel center to second order, the typical gradient amplitude is given by $\langle|\nabla T|^2\rangle = \frac{1}{4\pi}\sum_l l(l+1)(2l+1)C_l^T W_l \approx 1\times 10^9 \mu K^2/\mathrm{rad}^2$.where the approximate value is calculated for a ΛCDMcosmology with a $7'$fwhm Gaussian beam. The typical curvature of the observed temperature, on the other hand is given by $\langle|\nabla^2 T|^2\rangle = \frac{1}{4\pi}\sum_l [l(l+1)]^2(2l+1)C_l^T W_l \approx 7\times 10^{14} \mu K^2/\mathrm{rad}^4$.On the scales relevant to the maximum displacement from the center of a $1.7'$pixel, the maximum displacement is , and so the gradient term tends to dominate, although the curvature term is still non-negligible. For each observation of a pixel, we can denote the displacement from the center as $d = d_\theta + i d_\phi$. The average over all hits within a pixel gives an overall deflection vector which we will denote for a pixel center located at $\hat{n}$as $d(\hat{n})$. This represents the center of mass of the hit distribution; in Fig. [fig:pixcoverage] we have plotted these average deflections using black arrows. The deflection field $d(\hat{n})$may be decomposed into spin-1 spherical harmonics as $d_{lm} = \int_{4\pi} {}_1Y^*_{lm} d(\hat{n})$. With a second order Taylor expansion of the CMB temperature about each pixel center, it is then possible to calculate the average pseudo-Cl power spectrum of the pixelized sky. This is given by

where $R^d = \langle|d|^2\rangle/2$is half the mean-squared deflection magnitude (averaged over hits within a pixel, as well as over pixels). $C_l^{d+}$is the sum of the gradient and curl power spectra of d_{lm}, and $C_l^{d-}$is the gradient spectrum minus the curl spectrum. The R^dterm describes a smearing of the observed sky due to pixelization. For uniform pixel coverage of $N_{\mathrm{side}} = 2048$pixels $\sqrt{\langle|d|^2\rangle} = 0.725'$. For the hit distribution of Planck frequency maps, $R^d$is typically within xxx. calculate for final maps, looks like will be better than 10%percent of this value, and so this term is accurately described by the pixel window function, which is derived under the assumption of uniform pixel coverage.
The effect of pixelization is essentially degenerate with that of gravitational lensing of the CMB, with the difference that it (1) acts on the beam-convolved sky, rather than the actual sky and (2) produces a curl-mode deflection field as well as a gradient mode. This is discussed further in the [#planck2013-p12|Planck gravitational lensing] paper, where the subpixel deflection field constitutes a potential source of bias for the measured lensing potential. Indeed, Eq. [eqn:clt$_p$ixelized] is just a slightly modified version of the usual first order CMB lensing power spectrum (Hu (2000), Lewis and Challinor (2006)) to accommodate curl modes.

A useful approximation to Eq. which is derived in the unrealistic limit that the deflection vectors are uncorrelated between pixels, but in practice gives a good description of the power induced by the pixelization, is that the $d(\hat{n})$ couples the CMB gradient into a source of noise with an effective level given by

where the average is taken over all pixels and $R^T$is half the mean-squared power in the CMB gradient: $R^T = \frac{1}{8\pi}\sum_l l(l+1)(2l+1)\tilde{C}_l^T$.For frequency-combined maps, $\sqrt{\langle|d(\hat{n})|^2\rangle}$is typically on the order of $0.1'$

, and so the induced noise is at the level of $\sigma^N \sim 2\mu Karcmin$. This is small compared to the instrumental contribution, although not disappear when taking cross-spectra, depending on how coherent the hit distributions of the two maps in the cross-spectrum are.

References

<biblio force=false>

1. References

</biblio>

References

[1] http://arxiv.org/pdf/1005.1929|

Map-making and photometric calibration

Introduction

This page will give an overview of the map-making and photometric calibration procedures used by the HFI DPC to build detector and frequency maps. This processing and its performances are described in planck2013-p03 Planck-2013-VI [2] and planck2013-p03b Planck-2013-VIII [1].

To build HFI maps, we use the destriping approximation, in which noise is assumed to decompose into two components : white noise plus low frequency drifts. Using the sky redundancy, the low frequency drifts are modelled as one constant, or offset, per pointing period. To speed up the ulterior processing we first build intermediate products, by taking advantage of redundancies : we average signal and detector orientation on healpix pixels visited during each fixed pointing period, which we call hereafter 'ring'. Detector's pointing are corrected for slow drifts and aberration (displacement on the sky indouced by the satellite's motion). This intermediate product is called HPR for healpix pixel ring. They have been constructed using the same map resolution as the final HFI products (corresponding to nside=2048). This new dataset is used as input in the following steps.

Photometric calibration

Dipole calibration (100 to 353 GHz)

For the 2013 data release, the calibrator for the CMB frequency was the solar dipole, as measured by the WMAP team #hinshaw2009. We use a two components template fitting procedure, performed for each detector independently, to determine ring by ring an estimation of the dipole gain. The two fitted components are the Solar dipole and a sky template. We used the PSM for thermal dust emission at the detector's frequency as a first approximation of the sky template in pur early release. Using the HFI channel map as a template brings negligible change in the averaged gain, but reduces the systematic ring-to-ring dispersion of our estimation. We average these estimations over a subset of rings in the first survey (2000 to 6000) in which the dipole's amplitude is high enough with respect to that of the sky template, to get a single dipole gain per detector.

Several pieces of evidence led us to the conclusion that out bolometers presented apparent gain variation with time, after comparing the 3rd scan of the sky with the first one. This was later (mid-2012) explained by inequalities in the steps of the analog-to-digital converters (ADC) used in each bolometer's electronic chain. These devices had to be characterized using warm data after the end of the HFI observations. This process is still on-going (01/2012).

In the mean time we used an empiric correction, looking for a gain estimation and an offset per ring. This amounts to solve the non-linear equation :

where d is s the detector measurement, both S the sky signal, g the detector gain, O the offset (for ring no i) are the unknowns to be determined, and n the noise. We linearized this equation starting from the constant gain approximation, to get a measurement of the apparent time-varying gains for each bolometer independently. The limitations of this process are intrinsic signal variability from one observation to the other, like polarization or intra-pixel gradient. This procedure was thus only used for the 100 to 217 GHz detectors, for which the dipole signal is brighter and galactic signal (and polarization). A mask was used to removed the inner part of the Galactic plane.

Higher frequency calibration (545 and 857 GHz)

We therefore finally derived the sub-mm channels' calibration for the 2013 Planck data release from the comparison of measurements of the Neptune and Uranus fluxes (with aperture photometry) with their expectations from the Moreno et al model of their atmospheres' emission. This procedure is justified, since for both planets, at the lower frequencies (100-353 Ghz), the fluxes we recover are in agreement within ~ +/-5\% with what is expected from the planet spectral model, and the HFI detector's band-passes.

We determined zero-level for the released maps is selected regions of the sky where dust emissions are low and well correlated with HI. We may thus estimate and subtract dust emissions using the Hi template, and CMB from a Planck component separated template. The remaining astrophysical zero level is that of CIB. By imposing that the vele we find is equal to that of the CIB model of Bethermin et al, we may aset the sezo level of our maps.

Building of maps

Using the photometric calibration parameters, we build maps in two steps :

- we determine the destriping offsets using the full mission data
- we build the maps, using these offsets, by inverting the photometric equation :

where d is the destriped and calibrated signal at the HPR level. Detector's data are combined with an inverse noise weights derived from each detector's NEP. Q and U maps are build whenever possible. We propagate the white noise by building the 3x3 (or 1x1 if only I is reconstructed) covariance matrices in each pixel. At each frequency we build maps combining all detectors and independent detector sets. We use the offsets build for the full mission for building maps for each scan survey and for the nominal mission duration. We also build maps from the two independent halves of each rings. Altogether, more than 6000 maps are built at each release.

HPR and Maps are built in galactic coordinates.

Noise properties

Map noise properties can be evaluated using several methods, thanks to the high level of observation redundancies. We can use the maps built from the difference between the first and second half of each rings, or compare individual sky scans, of detector sets with each other.

Low resolution (nside = 8, 16, 32 ?) pixel-to-pixel noise covariance matrices are build using an analytic approach from the measured noise power spectra.

Zodiacal light correction

At the highest Planck frequencies, zodiacal light emission is visible in a survey difference map:

This map is a difference between the 857 GHz Survey 2 map and the 857 GHz Survey 1 map. This difference effectively removes Galactic and other emissions which originate far from Planck. As the Solar elongation is different for measurements of the same point on the sky for the two surveys, we see zodiacal light emission, while all emission from further sources is removed. The zodiacal light emission follows the Ecliptic plane, which starts at the lower left of the image, then crosses the center of the plot towards the upper right. Note that the "arcs" at the top and bottom of the image are images of the Galactic center in the Far Sidelobes, which are discussed in the section below. Similar plots for other HFI frequencies, for maps both before and after removal, are shown here.

Zodiacal light emission is removed from the 353, 545 and 857 GHz channels. It is described in planck2013-p03 Planck-2013-VI [2], but a synopsis of the procedure is as follows:

- During each survey, a large fraction of the sky has observations which all fall within a week of each other. That is, during a single survey, most pixels are observed during a short, well-defined period. The contribution from zodiacal light emission to the total brightness seen, then, is well defined.
- We use the the COBE model of the zodiacal light emission to make predictions for this zodiacal light emission for those pixels observed over a span of one week or less, and use GRASP models of the beams to predict the emission from the galaxy given our sidelobes. The templates from the COBE model are shown here.
- We fit the survey difference maps with these model templates to estimate the emissivity of each zodi component and sidelobe at the Planck wavelengths. The results of these fits at each frequency are shown here.
- We reconstruct each ring of the the full mission using the combination of the COBE geometric model with the emissivities determined above and the sidelobe models.
- We remove the reconstruction above from each ring of data.
- We then make maps as described previously in this section. Maps with and without, as well as the differences between the two, are shown here. The survey differences before and after this removal are shown with and without zodical light emission removal here. The power spectra of what is removed from each map is shown here.

Far SideLobes (FSL)

The far sidelobe correction for the highest frequency HFI channels is described in the section above. Note that this correction is not always used, as other, CMB-specific, component separation methods have been more effective at removing the zodiacal light emission, though as this is done along with dust and other component removal, it is difficult to characterize the zodiacal light emission in this fashion.

Fit values for specific horns and surveys are show here

We have made estimates of the contamination of the far sidelobes at 143 GHz by taking the 143 GHz map, adding the dipole, and passing it through our simulator, using a GRASP calculation of the far sidelobes for the 143-1a detector as the beam. The resulting maps is

While there is one small region that might reach 20 micro-K (this happens when the secondary spillover overlaps with the Galactic center), most of the map is quite quiet. This is evidenced by the power spectrum of the above map, which is quite small.

CO correction

The extraction of CO maps from HFI maps is described in detail in the planck2013-p03a Planck-2013-XIII [2]. The CO maps are produced by a combination of bolometer maps or frequency maps.

Map validation

Several validations of HFI maps are described in planck2013-p03 Planck-2013-VI [2], largely based on the analysis of the differences between half ring maps.

ADC non-linearities induce significant differences (of order 1 micro-K_cmb) at low ell (<25) that are well reproduced by simulations including this effect.

These checks showed that at higher multipole, half ring map differences give an estimation of the noise level in the total map that is biased low of ~0.5%. This bias is introduced by the deglitching algorithm which uses the same, eventually biased, signal estimation for the two halves of each rings.

Further checks are presented in the planck2013-p08 Planck-2013-XV [3] and in planck2013-p01a Planck-2013-XI [4].

References

<biblio force=false>

1. References

</biblio>

References

[1] http://www.rssd.esa.int/doc_fetch.php?id=3168401&page=1
[2] http://www.rssd.esa.int/doc_fetch.php?id=3168075&page=1
[3] http://www.rssd.esa.int/doc_fetch.php?id=3168544&page=1
[4] http://www.rssd.esa.int/doc_fetch.php?id=3168402&page=1

Spectral response

HFI Spectral Response

This section outlines the unit conversion and colour correction protocol for Planck/HFI. Tables of unit conversion and colour correction coefficients will be included (there is not room for these in the P03d Co-Paper). Some of the checks on the unit conversion and colour correction coefficients will be described here also. Planet colour correction coefficients will be provided here (or perhaps in the joint HFI/LFI section). There will be links to the UcCC subsection of the PLA section, but the numbers and details belong here. The PLA UcCC subsection is primarily to introduce the software tools.

The band-average HFI spectral response data are shown in the figure below, and provided in the RIMO file (here).

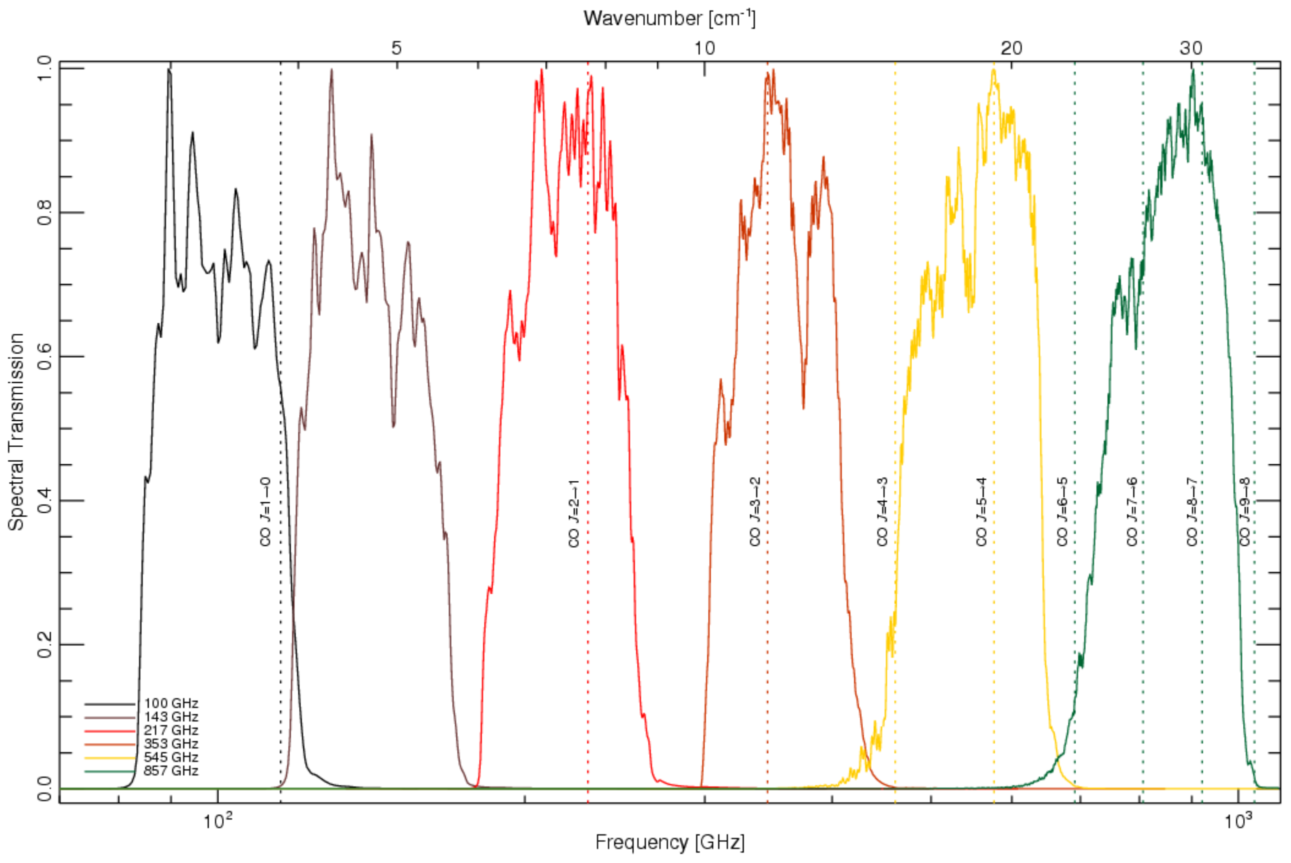

Band-average HFI transmission spectra. Vertical bars illustrate the CO rotational transition frequencies.

The integration ranges used in determining the unit conversion and colour correction coefficients are verified through an iterative approach starting at one extreme and reducing to the band-centre for both the low and high frequency edges. The figure below demonstrates the stability in the integral once a sufficient data range has been employed. The range used in the official coefficients is thus sufficient to ensure that it falls within the flat region of the demonstration figure below.

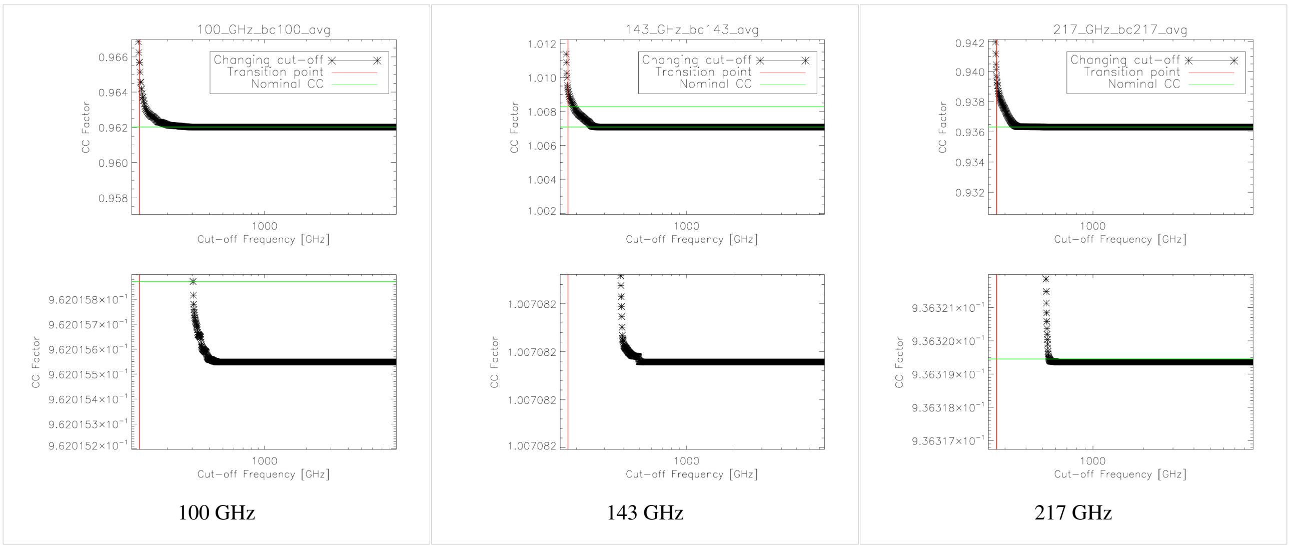

100 GHz 143 GHz 217 GHz

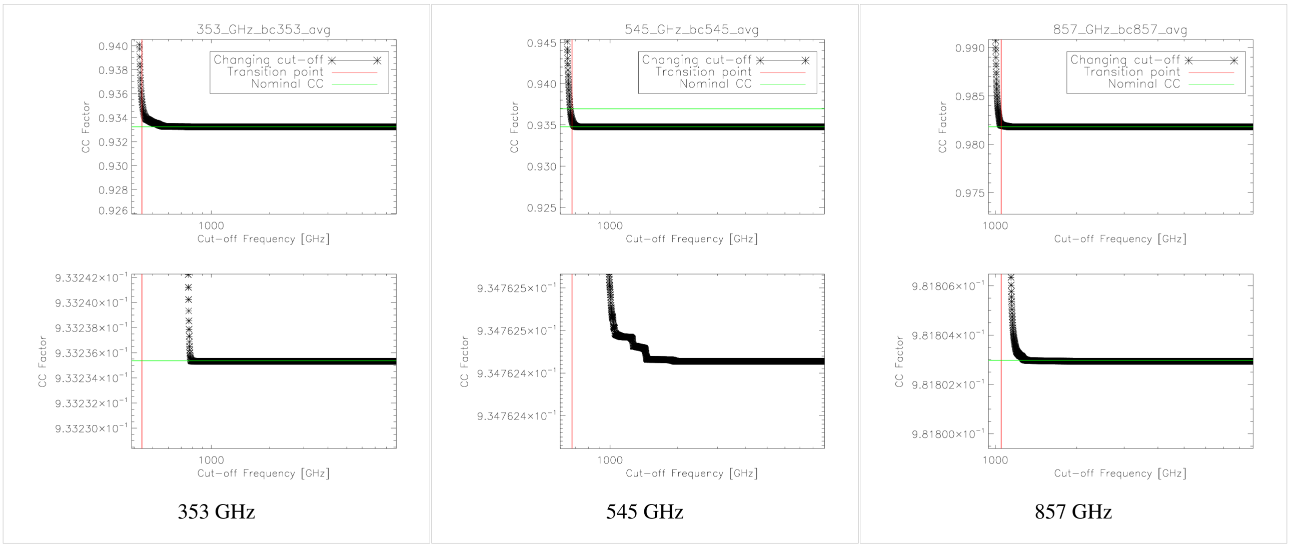

353 GHz 545 GHz 857 GHz

Colour Correction (alpha = -1 to +2) stability with integration cut-off variation. The horizontal bars illustrate the nominal colour correction values. Similar results are found for the integration cut-on.

The band-average spectrum for a given frequency band is derived using a hit-map normalized inverse-square noise weighted detector spectrum average. Thus, the effective band-average spectrum changes depending on the region of sky in question, really the Planck coverage of any sky region. The histograms below demonstrate the variation across the sky of the detector weight coefficients, and thus the validity of using a single band-average spectrum for the entire sky map. Future analysis with the full Planck dataset may require incorporating the variation of the relative detector weights across the sky into understanding the differential spectral transmission between complementary maps (e.g. detset -1 cf. detset-2 maps).

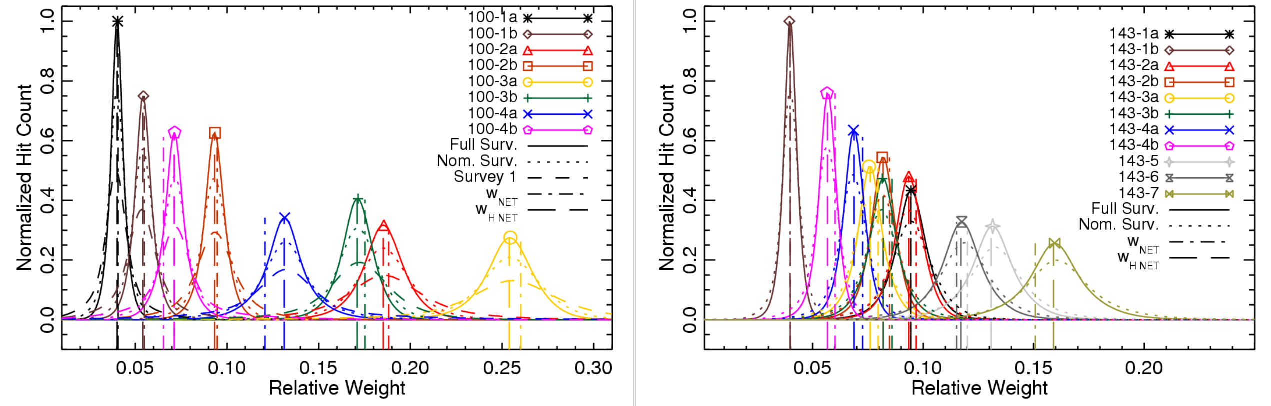

100 GHz

143 GHz

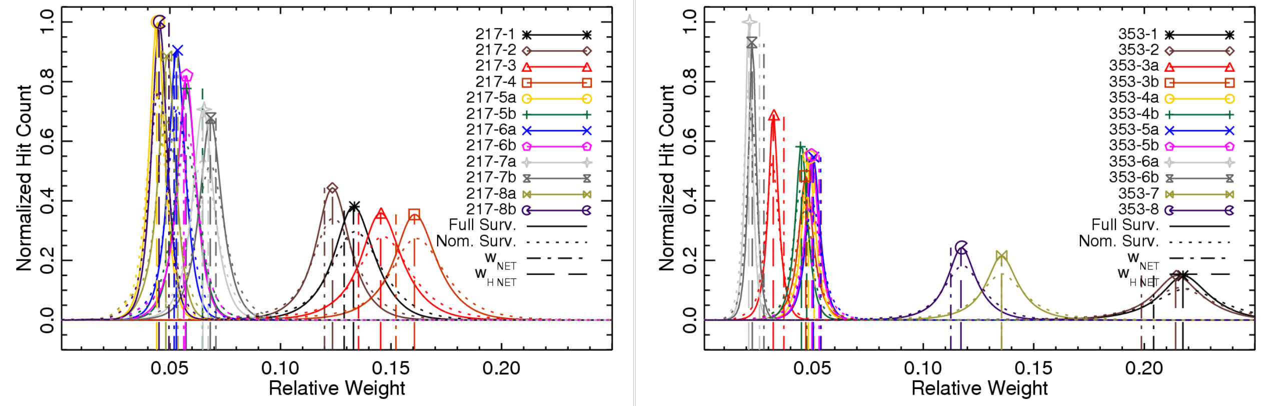

217 GHz

353 GHz

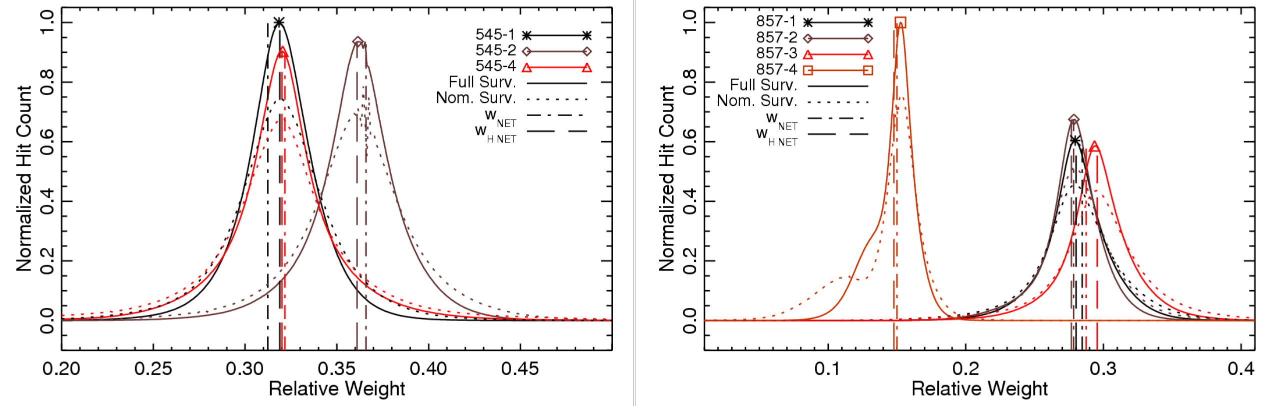

545 GHz

857 GHz

Colour Correction (alpha = -1 to +2) stability with integration cut-off variation. The horizontal bars illustrate the nominal colour correction values. Similar results are found for the integration cut-on.

The following table presents basic characteristics of the HFI detector spectral response, including optical efficiency, effective frequency, etc. Further details on the definition of these parameters are available in #planck2013-p03d.

Properties of HFI detector spectra

Band (GHz)	$\nu_{\text{cut-on}}$ [GHz]	$\nu_{\text{cut-off}}$ [GHz]	BW [GHz]	$\nu_{\text{cen.}}$ [GHz]	$\nu_{\text{eff.}}$ [GHz]	ε	$\epsilon_{\text{Int.}}$	ν_{-1} [GHz]	ν_{+2} [GHz]	ν_{+4} [GHz]
100-1a	84.8 ± 0.5	113.96 ± 0.16	29.1 ± 0.6	99.4 ± 0.3	100.28 ± 0.11	0.419 ± 0.008	0.310 ± 0.008	99.45 ± 0.12	101.93 ± 0.11	103.59 ± 0.10
100-1b	86.5 ± 1.0	115.32 ± 0.08	28.8 ± 1.0	100.9 ± 0.5	100.87 ± 0.11	0.563 ± 0.011	0.324 ± 0.011	100.06 ± 0.11	102.51 ± 0.10	104.18 ± 0.09
100-2a	86.0 ± 0.6	116.4 ± 0.4	30.4 ± 0.9	101.2 ± 0.3	101.34 ± 0.12	0.550 ± 0.012	0.372 ± 0.012	100.38 ± 0.12	103.34 ± 0.11	105.47 ± 0.10
100-2b	84.3 ± 0.5	115.5 ± 0.4	31.3 ± 0.7	99.9 ± 0.3	101.19 ± 0.11	0.634 ± 0.009	0.334 ± 0.009	100.23 ± 0.11	103.14 ± 0.10	105.16 ± 0.09
100-3a	84.21 ± 0.17	117.36 ± 0.06	33.14 ± 0.18	100.78 ± 0.09	101.64 ± 0.12	0.493 ± 0.005	0.331 ± 0.005	100.68 ± 0.12	103.60 ± 0.10	105.60 ± 0.09
100-3b	84.19 ± 0.19	116.81 ± 0.16	32.6 ± 0.2	100.50 ± 0.13	100.63 ± 0.12	0.426 ± 0.004	0.281 ± 0.004	99.74 ± 0.12	102.45 ± 0.11	104.35 ± 0.10
100-4a	84.74 ± 0.07	118.09 ± 0.09	33.34 ± 0.12	101.42 ± 0.05	101.77 ± 0.12	0.461 ± 0.003	0.255 ± 0.003	100.77 ± 0.13	103.82 ± 0.11	105.96 ± 0.10
100-4b	84.9 ± 0.3	118.30 ± 0.05	33.4 ± 0.3	101.58 ± 0.14	101.91 ± 0.13	0.396 ± 0.003	0.258 ± 0.003	100.92 ± 0.13	103.92 ± 0.12	105.98 ± 0.10
100-avg	84.4 ± 0.3	117.36 ± 0.05	32.9 ± 0.3	100.89 ± 0.13	101.31 ± 0.05	0.479 ± 0.003	0.304 ± 0.003	100.36 ± 0.05	103.24 ± 0.05	105.25 ± 0.04
100-detset1	84.77 ± 0.05	117.81 ± 0.06	33.03 ± 0.08	101.29 ± 0.04	101.43 ± 0.07	0.4199 ± 0.0020	0.2645 ± 0.0020	100.49 ± 0.07	103.35 ± 0.06	105.34 ± 0.06
100-detset2	84.3 ± 0.3	117.14 ± 0.05	32.8 ± 0.3	100.72 ± 0.13	101.25 ± 0.06	0.505 ± 0.003	0.321 ± 0.003	100.31 ± 0.06	103.19 ± 0.06	105.21 ± 0.05
143-1a	121.2 ± 0.4	162 ± 2	41 ± 2	141.5 ± 1.1	141.71 ± 0.04	0.66 ± 0.02	0.43 ± 0.02	140.37 ± 0.04	144.48 ± 0.04	147.35 ± 0.03
143-1b	119.99 ± 0.03	162.8 ± 0.7	42.8 ± 0.8	141.4 ± 0.4	142.29 ± 0.04	0.608 ± 0.007	0.347 ± 0.007	140.97 ± 0.04	145.02 ± 0.04	147.79 ± 0.04
143-2a	119.7 ± 0.2	162.76 ± 0.05	43.1 ± 0.2	141.21 ± 0.11	141.79 ± 0.04	0.626 ± 0.003	0.449 ± 0.003	140.42 ± 0.04	144.61 ± 0.04	147.51 ± 0.04
143-2b	119.2 ± 0.4	163.3 ± 0.5	44.1 ± 0.6	141.3 ± 0.3	142.50 ± 0.04	0.619 ± 0.007	0.443 ± 0.007	141.17 ± 0.05	145.21 ± 0.04	148.00 ± 0.04
143-3a	120.2 ± 0.3	158.8 ± 0.4	38.6 ± 0.5	139.5 ± 0.2	140.51 ± 0.05	0.970 ± 0.008	0.539 ± 0.008	139.17 ± 0.05	143.28 ± 0.05	146.09 ± 0.05
143-3b	119.88 ± 0.04	161.3 ± 1.0	41.4 ± 1.0	140.6 ± 0.5	141.63 ± 0.05	0.718 ± 0.012	0.457 ± 0.012	140.28 ± 0.05	144.41 ± 0.04	147.22 ± 0.04
143-4a	118.7 ± 0.2	168.21 ± 0.03	49.5 ± 0.2	143.47 ± 0.12	142.71 ± 0.04	0.532 ± 0.002	0.324 ± 0.002	141.29 ± 0.05	145.61 ± 0.04	148.56 ± 0.04
143-4b	119.0 ± 0.3	161.58 ± 0.04	42.6 ± 0.3	140.27 ± 0.14	142.19 ± 0.05	0.538 ± 0.003	0.339 ± 0.003	140.87 ± 0.05	144.87 ± 0.04	147.59 ± 0.04
143-5	119.9 ± 0.3	166.608 ± 0.016	46.7 ± 0.3	143.28 ± 0.16	144.24 ± 0.04	0.386 ± 0.002	0.305 ± 0.002	142.93 ± 0.04	146.86 ± 0.04	149.48 ± 0.03
143-6	119.97 ± 0.20	166.14 ± 0.04	46.2 ± 0.2	143.06 ± 0.10	143.00 ± 0.04	0.4531 ± 0.0016	0.3128 ± 0.0016	141.66 ± 0.05	145.72 ± 0.04	148.49 ± 0.04
143-7	120.39 ± 0.07	167.5 ± 0.3	47.1 ± 0.3	143.95 ± 0.15	144.46 ± 0.04	0.427 ± 0.002	0.308 ± 0.002	143.14 ± 0.05	147.09 ± 0.04	149.69 ± 0.04

143-8	120.7 ± 0.4	165.59 ± 0.06	44.8 ± 0.4	143.16 ± 0.18	143.55 ± 0.04	0.393 ± 0.002	0.277 ± 0.002	142.18 ± 0.05	146.30 ± 0.04	149.02 ± 0.04
143-avg	119.994 ± 0.018	165.76 ± 0.04	45.76 ± 0.05	142.876 ± 0.018	142.710 ± 0.012	0.5069 ± 0.0007	0.3669 ± 0.0007	141.363 ± 0.012	145.458 ± 0.011	148.235 ± 0.011
143-detset1	120.05 ± 0.03	160.18 ± 0.09	40.13 ± 0.10	140.12 ± 0.05	141.45 ± 0.02	0.7049 ± 0.0017	0.4614 ± 0.0017	140.11 ± 0.02	144.22 ± 0.02	147.05 ± 0.02
143-detset2	118.95 ± 0.08	164.9 ± 0.8	45.9 ± 0.8	141.9 ± 0.4	142.27 ± 0.02	0.507 ± 0.007	0.379 ± 0.007	140.91 ± 0.02	145.05 ± 0.02	147.902 ± 0.019
143-SWBs	120.17 ± 0.03	166.308 ± 0.018	46.14 ± 0.04	143.238 ± 0.017	143.96 ± 0.02	0.3967 ± 0.0006	0.3123 ± 0.0006	142.64 ± 0.02	146.63 ± 0.02	149.282 ± 0.020
217-1	189.0 ± 0.4	251.24 ± 0.05	62.2 ± 0.4	220.14 ± 0.20	222.817 ± 0.016	0.414 ± 0.002	0.322 ± 0.002	221.099 ± 0.016	226.274 ± 0.017	229.76 ± 0.02
217-2	188.66 ± 0.02	253.68 ± 0.02	65.03 ± 0.04	221.169 ± 0.017	223.231 ± 0.018	0.4575 ± 0.0004	0.3624 ± 0.0004	221.430 ± 0.018	226.814 ± 0.018	230.35 ± 0.02
217-3	190.49 ± 0.05	253.174 ± 0.018	62.68 ± 0.06	221.83 ± 0.03	223.116 ± 0.016	0.4125 ± 0.0004	0.3257 ± 0.0004	221.440 ± 0.017	226.458 ± 0.016	229.774 ± 0.019
217-4	190.8 ± 0.4	253.219 ± 0.017	62.4 ± 0.4	222.03 ± 0.18	222.717 ± 0.018	0.4043 ± 0.0018	0.3132 ± 0.0018	221.033 ± 0.018	226.116 ± 0.017	229.55 ± 0.02
217-5a	182.69 ± 0.07	253.2 ± 0.6	70.5 ± 0.6	217.9 ± 0.3	220.421 ± 0.017	0.548 ± 0.003	0.387 ± 0.003	218.489 ± 0.018	224.293 ± 0.017	228.15 ± 0.02
217-5b	182.75 ± 0.06	250.1 ± 0.4	67.3 ± 0.4	216.41 ± 0.19	220.655 ± 0.018	0.621 ± 0.002	0.377 ± 0.002	218.746 ± 0.018	224.465 ± 0.018	228.234 ± 0.020
217-6a	182.284 ± 0.020	253.70 ± 0.02	71.41 ± 0.03	217.991 ± 0.014	220.619 ± 0.018	0.4497 ± 0.0003	0.3019 ± 0.0003	218.705 ± 0.018	224.441 ± 0.018	228.24 ± 0.02
217-6b	182.85 ± 0.04	253.373 ± 0.015	70.52 ± 0.04	218.113 ± 0.019	220.619 ± 0.017	0.5274 ± 0.0004	0.3349 ± 0.0004	218.707 ± 0.017	224.408 ± 0.016	228.109 ± 0.017
217-7a	188.217 ± 0.019	253.88 ± 0.02	65.66 ± 0.03	221.049 ± 0.012	220.766 ± 0.016	0.4299 ± 0.0003	0.3065 ± 0.0003	218.925 ± 0.016	224.458 ± 0.016	228.122 ± 0.018
217-7b	189.22 ± 0.03	250.88 ± 0.02	61.66 ± 0.04	220.054 ± 0.018	220.332 ± 0.018	0.4371 ± 0.0003	0.2776 ± 0.0003	218.468 ± 0.018	224.055 ± 0.018	227.718 ± 0.019
217-8a	181.98 ± 0.02	253.722 ± 0.018	71.74 ± 0.03	217.852 ± 0.013	220.510 ± 0.018	0.5282 ± 0.0003	0.3768 ± 0.0003	218.544 ± 0.019	224.432 ± 0.018	228.32 ± 0.02
217-8b	181.875 ± 0.013	252.99 ± 0.04	71.12 ± 0.04	217.433 ± 0.018	220.712 ± 0.017	0.6265 ± 0.0004	0.3872 ± 0.0004	218.837 ± 0.018	224.440 ± 0.017	228.127 ± 0.020
217-avg	188.892 ± 0.012	253.419 ± 0.007	64.527 ± 0.014	221.156 ± 0.006	221.915 ± 0.005	0.39900 ± 0.00013	0.33846 ± 0.00013	220.113 ± 0.005	225.517 ± 0.005	229.097 ± 0.006
217-detset1	183.32 ± 0.15	253.61 ± 0.02	70.29 ± 0.15	218.46 ± 0.07	220.548 ± 0.009	0.4577 ± 0.0007	0.3053 ± 0.0007	218.666 ± 0.010	224.312 ± 0.009	228.038 ± 0.010
217-detset2	182.159 ± 0.012	253.592 ± 0.008	71.433 ± 0.015	217.875 ± 0.007	220.614 ± 0.009	0.47458 ± 0.00016	0.34838 ± 0.00016	218.697 ± 0.009	224.429 ± 0.009	228.200 ± 0.010
217-SWBs	189.02 ± 0.06	253.247 ± 0.014	64.22 ± 0.06	221.14 ± 0.03	222.957 ± 0.008	0.4072 ± 0.0003	0.3226 ± 0.0003	221.241 ± 0.008	226.395 ± 0.008	229.834 ± 0.010
353-1	306.3 ± 0.5	406.8 ± 0.4	100.5 ± 0.7	356.5 ± 0.3	360.289 ± 0.018	0.540 ± 0.003	0.390 ± 0.003	357.546 ± 0.018	365.762 ± 0.019	371.15 ± 0.02
353-2	305.82 ± 0.16	409.697 ± 0.020	103.88 ± 0.16	357.76 ± 0.08	360.866 ± 0.019	0.5947 ± 0.0008	0.4515 ± 0.0008	358.005 ± 0.019	366.615 ± 0.020	372.29 ± 0.02

353-3a	308.5 ± 0.3	404.77 ± 0.03	96.3 ± 0.3	356.63 ± 0.13	359.59 ± 0.02	0.4106 ± 0.0008	0.2862 ± 0.0008	357.16 ± 0.02	364.49 ± 0.02	369.37 ± 0.02
353-3b	308.3 ± 0.4	406.230 ± 0.015	98.0 ± 0.4	357.24 ± 0.19	359.65 ± 0.02	0.4689 ± 0.0014	0.3546 ± 0.0014	357.02 ± 0.02	365.01 ± 0.02	370.41 ± 0.02
353-4a	321.275 ± 0.018	407.94 ± 0.11	86.66 ± 0.11	364.61 ± 0.06	362.224 ± 0.018	0.4334 ± 0.0004	0.3119 ± 0.0004	359.944 ± 0.017	366.853 ± 0.019	371.52 ± 0.02
353-4b	311.71 ± 0.05	407.71 ± 0.03	96.00 ± 0.06	359.71 ± 0.02	362.212 ± 0.019	0.4152 ± 0.0003	0.3123 ± 0.0003	359.739 ± 0.019	367.22 ± 0.02	372.23 ± 0.02
353-5a	302.25 ± 0.04	406.41 ± 0.15	104.17 ± 0.16	354.33 ± 0.08	358.73 ± 0.02	0.3991 ± 0.0005	0.2965 ± 0.0005	355.88 ± 0.02	364.42 ± 0.02	370.01 ± 0.02
353-5b	301.37 ± 0.05	416.77 ± 0.05	115.40 ± 0.07	359.07 ± 0.03	358.84 ± 0.02	0.3626 ± 0.0002	0.2542 ± 0.0002	355.80 ± 0.02	364.98 ± 0.02	371.11 ± 0.03
353-6a	302.4 ± 0.4	407.99 ± 0.03	105.6 ± 0.4	355.19 ± 0.19	359.91 ± 0.03	0.3036 ± 0.0007	0.1946 ± 0.0007	357.09 ± 0.03	365.58 ± 0.03	371.18 ± 0.03
353-6b	314.08 ± 0.03	398.19 ± 0.04	84.11 ± 0.05	356.13 ± 0.02	356.06 ± 0.02	0.2990 ± 0.0002	0.2193 ± 0.0002	353.67 ± 0.02	360.93 ± 0.02	365.83 ± 0.03
353-7	323.2 ± 1.6	406.0 ± 0.9	83 ± 2	364.6 ± 0.7	363.35 ± 0.03	0.313 ± 0.006	0.272 ± 0.006	360.84 ± 0.03	368.40 ± 0.02	373.41 ± 0.03
353-8	309 ± 3	408.20 ± 0.08	99 ± 3	358.5 ± 1.7	365.10 ± 0.02	0.374 ± 0.011	0.294 ± 0.011	362.25 ± 0.02	370.82 ± 0.02	376.53 ± 0.04
353-avg	306.8 ± 0.6	408.22 ± 0.02	101.4 ± 0.6	357.5 ± 0.3	361.290 ± 0.008	0.4057 ± 0.0019	0.3353 ± 0.0019	358.564 ± 0.008	366.764 ± 0.009	372.193 ± 0.010
353-detset1	303.582 ± 0.016	406.333 ± 0.018	102.75 ± 0.03	354.957 ± 0.011	359.156 ± 0.011	0.39123 ± 0.00015	0.29902 ± 0.00015	356.386 ± 0.011	364.744 ± 0.011	370.302 ± 0.012
353-detset2	318.885 ± 0.015	407.86 ± 0.02	88.97 ± 0.03	363.372 ± 0.013	360.870 ± 0.013	0.35915 ± 0.00014	0.28730 ± 0.00014	358.409 ± 0.013	365.850 ± 0.013	370.837 ± 0.013
353-SWBs	306.3 ± 0.4	408.81 ± 0.03	102.5 ± 0.4	357.56 ± 0.18	361.921 ± 0.013	0.4381 ± 0.0013	0.3575 ± 0.0013	359.158 ± 0.013	367.455 ± 0.013	372.930 ± 0.015
545-1	466.41 ± 0.03	642.58 ± 0.05	176.17 ± 0.06	554.50 ± 0.03	559.83 ± 0.05	0.37600 ± 0.00018	0.29576 ± 0.00018	554.44 ± 0.07	570.00 ± 0.03	579.24 ± 0.02
545-2	466.78 ± 0.03	641.44 ± 0.07	174.66 ± 0.08	554.11 ± 0.04	556.05 ± 0.05	0.31937 ± 0.00019	0.26874 ± 0.00019	550.61 ± 0.07	566.37 ± 0.03	575.78 ± 0.03
545-3	470.6 ± 0.9	637.44 ± 0.05	166.9 ± 0.9	554.0 ± 0.4	557.40 ± 0.08	0.2536 ± 0.0011	0.2127 ± 0.0011	552.26 ± 0.13	567.14 ± 0.04	576.05 ± 0.03
545-4	470.9 ± 0.3	638.52 ± 0.10	167.6 ± 0.3	554.73 ± 0.16	556.85 ± 0.05	0.2630 ± 0.0004	0.2143 ± 0.0004	551.76 ± 0.08	566.48 ± 0.03	575.32 ± 0.02
545-avg	469.5 ± 0.6	640.81 ± 0.03	171.3 ± 0.6	555.2 ± 0.3	557.53 ± 0.03	0.3036 ± 0.0008	0.2612 ± 0.0008	552.22 ± 0.04	567.596 ± 0.016	576.778 ± 0.014
545-detset1	466.44 ± 0.02	642.36 ± 0.04	175.91 ± 0.05	554.40 ± 0.02	557.86 ± 0.03	0.32548 ± 0.00013	0.28031 ± 0.00013	552.43 ± 0.05	568.118 ± 0.020	577.458 ± 0.018
545-detset2	470.9 ± 0.3	638.52 ± 0.09	167.6 ± 0.3	554.73 ± 0.18	556.85 ± 0.05	0.2631 ± 0.0004	0.2143 ± 0.0004	551.76 ± 0.08	566.48 ± 0.03	575.32 ± 0.02
857-1	748.7 ± 0.9	992.5 ± 0.3	243.8 ± 1.0	870.6 ± 0.5	866.05 ± 0.10	0.2595 ± 0.0010	0.2283 ± 0.0010	858.1 ± 0.3	880.89 ± 0.03	894.38 ± 0.03
857-2	726.3 ± 0.4	989.09 ± 0.13	262.8 ± 0.4	857.7 ± 0.2	860.55 ± 0.08	0.2435 ± 0.0003	0.1973 ± 0.0003	852.28 ± 0.19	876.22 ± 0.03	890.59 ± 0.03

857-3	742.0 ± 0.5	991.7 ± 1.4	249.7 ± 1.5	866.8 ± 0.7	864.92 ± 0.09	0.2888 ± 0.0015	0.2573 ± 0.0015	857.0 ± 0.2	879.90 ± 0.03	893.53 ± 0.03
857-4	731.4 ± 0.4	979.9 ± 0.2	248.4 ± 0.4	855.7 ± 0.2	854.75 ± 0.09	0.1414 ± 0.0002	0.1189 ± 0.0002	847.2 ± 0.2	868.94 ± 0.03	881.94 ± 0.03
857-avg	743.9 ± 0.5	989.78 ± 0.08	245.9 ± 0.5	866.8 ± 0.3	862.68 ± 0.05	0.2412 ± 0.0005	0.2165 ± 0.0005	854.69 ± 0.11	877.724 ± 0.017	891.462 ± 0.014
857-detset1	736.9 ± 0.3	990.38 ± 0.06	253.4 ± 0.3	863.65 ± 0.13	863.42 ± 0.07	0.2446 ± 0.0002	0.2121 ± 0.0002	855.33 ± 0.16	878.67 ± 0.02	892.59 ± 0.02
857-detset2	741.79 ± 0.14	987.01 ± 0.09	245.22 ± 0.18	864.40 ± 0.08	861.74 ± 0.08	0.23780 ± 0.00017	0.21419 ± 0.00017	853.89 ± 0.18	876.53 ± 0.03	890.03 ± 0.03

References

<biblio force=false>

1. References

</biblio>

Internal overall validation

The HFI validation is mostly modular. That is, each part of the pipeline, be it timeline processing, map-making, or any other, validates the results of its work at each step of the processing, looking specifically for known issues. In addition, we do additional validation with an eye towards overall system integrity by looking at generic differences between sets of maps, in which most problems will become apparent, whether known or not. Both these are described below.

Expected systematics and tests (bottom-up approach)

Like all experiments, Planck/HFI had a number of "issues" which it needed to track and verify were not compromising the data. While these are discussed in appropriate sections, here we gather them together to give brief summaries of the issues and refer the reader to the appropriate section for more details.

- Cosmic Rays - Unprotected by the atmosphere and more sensitive than previous bolometric experiment, HFI was subjected to many more cosmic ray hits than previous experiments. These were detected, the worst parts of the data flagged as unusable, and "tails" were modeled and removed. This is described in the section on glitch statistics and in the section on cosmic rays, as well as in

the 2013 HFI Cosmic Ray Removal paper [1]#planck2013-p03e.

- Elephants - Cosmic rays also hit the 100 mK stage and cause the temperature to vary, inducing small temperature and thus noise variations in the detectors. These are effectively removed with the rest of the thermal fluctuations, described directly below.
- Thermal Fluctuations - HFI is an extremely stable instrument, but there are small thermal fluctuations. These are discussed in the timeline processing section on thermal decorrelation and in the section on 1.6 K and 4 K thermal fluctuations.
- Popcorn Noise - Some channels were occasionally affected by what seems to be a "split-level" noise, which has been variously called popcorn noise or random telegraphic signal. These data are usually flagged. This is described in the section on noise stationarity and the section on Random Telegraphic Signal Noise
- Jumps - Similar to but distinct from popcorn noise, small jumps were occasionally found in the data streams. These data are usually corrected. This is described in the section on jump corrections.

- 4 K Cooler-Induced EM Noise - The 4 K cooler induced noise in the detectors with very specific frequency signatures, which is filtered. This is described in

the 2013 HFI DPC Paper [2] #planck2013-p03, the section below on 4K line residuals, and their stability is discussed in the section on 4K cooler line stability.

- Compression - Onboard compression is used to overcome our telemetry bandwidth limitations. This is explained in #planck2011-1-5.
- Noise Correlations - Correlations in noise between detectors seems to be negligble but for two polarization sensitive detectors in the same horn. This is discussed in

the 2013 HFI Cosmic Ray Removal paper [2] #planck2013-p03e.

- Pointing - The final pointing reconstruction for Planck is near the arcsecond level. This is discussed in

the 2013 HFI DPC paper [2] #planck2013-p03.

- Focal Plane Geometry - The relative positions of different horns in the focal plane is reconstructed using planets. This is also discussed in

the 2013 HFI DPC paper [2] #planck2013-p03.

- Main Beam - The main beams for HFI are discussed in the 2013 Beams and Transfer function paper #planck2013-p03d.
- Ruze Envelope - Random imperfections or dust on the mirrors can increase the size of the beam a bit. This is discussed in

the 2013 Beams and Transfer function paper [3] #planck2013-p03d.

- Dimpling - The mirror support structure causes a pattern of small imperfections in the beams, which cause small sidelobe responses outside the main beam. This is discussed in

the 2013 Beams and Transfer function paper [3] #planck2013-p03d

- Far Sidelobes - Small amounts of light can sometimes hit the detectors from just above the primary or secondary mirrors, or even from reflecting off the baffles. While small, when the Galactic center is in the right position, this can be detected in the highest frequency channels, so this is removed from the data. This is discussed in

the 2013 Beams and Transfer function paper [3] #planck2013-p03d and, non-intuitively, the 2013 Zodiacal emission paper [1] #planck2013-pip88.

- Planet Fluxes - Comparing the known fluxes of planets with the calibration on the CMB dipole is a useful check of calibration for the CMB channels, and is the primary calibration source for the submillimeter channels. This is done in

the 2013 Map-Making and Calibration Paper [1] #planck2013-p03b.

- Point Source Fluxes - As with planet fluxes, we also compare fluxes of known, bright point sources with the CMB dipole calibration. This is done in

the 2013 Map-Making and Calibration paper [1] #planck2013-p03c.

- Time Constants - The HFI bolometers do not react instantaneously to light; there are small time constants, discussed in

the 2013 Beams and Transfer function paper [3] #planck2013-p03d.

- ADC Correction - The HFI Analog-to-Digital Converters are not perfect, and are not used perfectly. While this is an on-going effort, their effects on the calibration are discussed in

the 2013 Map-Making and Calibration paper [1] #planck2013-p03c.

- Gain changes with Temperature Changes
- Optical Cross-Talk - This is negligible, as noted in the optical cross-talk note.
- Bandpass - The transmission curves, or "bandpass" has shown up in a number of places. This is discussed in

the spectral response paper [3] #planck2013-p03d.

- Saturation - While this is mostly an issue only for Jupiter observations, it should be remembered that the HFI detectors cannot observe arbitrarily bright objects. This is discussed in the section below on saturation.

Generic approach to systematics

While we track and try to limit the individual effects listed above, and we do not believe there are other large effects which might compromise the data, we test this using a suite of general difference tests. As an example, the first and second years of Planck observations used almost exactly the same scanning pattern (they differed by one arc-minute at the Ecliptic plane). By differencing them, the fixed sky signal is almost completely removed, and we are left with only time variable signals, such as any gain variations and, of course, the statistical noise.

In addition, while Planck scans the sky twice a year, during the first six months (or survey) and the second six months (the second survey), the orientations of the scans and optics are actually different. Thus, by forming a difference between these two surveys, in addition to similar sensitivity to the time-variable signals seen in the yearly test, the survey difference also tests our understanding and sensitivity to scan-dependent noise such as time constant and beam asymmetries.

These tests use the `Yardstick` simulations below and culminate in the "Probabilities to Exceed" tests just after.

HFI simulations

The '`Yardstick`' simulations allows gauging various effects to see whether they need be included in monte-carlo to describe data. It also allows gauging the significance of validation tests on data (e.g. can the value obtained in a difference test can be accounted for by the model?). They are completed by dedicated '`Desire`' simulations (`Desire` stands for DEtector SImulated REsponse), as well as Monte-Carlo simulations of the Beams determination to determine their uncertainty.

`Yardstick` simulations

The `Yardstick` V3.0 characterizes the DX9 data which is the basis of the nominal mission data release. It goes through the following steps:

1. The input maps are computed using the Planck Sky Model, taking the RIMO bandpasses as input.
2. The `LevelS` is used to project input maps on timeline using the RIMO (B-Spline) scanning beam and the DX9 pointing. The real pointing is affected by aberration that is corrected by map-making. The `Yardstick` does not simulate aberration. Finally, the difference between the projected pointing from simulation and from the nominal mission is equal to the aberration.
3. The simulated noise timelines, that are added to the projected signal, have the same spectrum (low and high frequency) as the nominal mission noise. For the`yardstick` V3.0 Althoough detectable, no correlation in time or between detectors have been simulated.
4. The simulation map making step use the nominal mission sample flags.
5. For the low frequencies (100, 143, 217, 353), the `yardstick` output are calibrated using the same mechanism (e.g. dipole fitting) as the nominal data reduction. This calibration step is not perfromed for higher frequency (545, 857) which use a differnt principle
6. The Official map making is run on those timelines using the same parameters than for real data.

A `yardstick` production is composed of

- all survey map (1,2 and nominal),
- all detector Detsets (from individual detectors to full channel maps).

The `Yardstick` V3.0 is based on 5 noise iterations for each map realization.

NB1: the `Yardstick` product is also the validating set for other implementations which are not using the HFI DPC production codes, an exemple of which are the so-called `FFP` simulations, where FFP stands for Full Focal Plane and are done in common by HFI & LFI. This is further described in HL-sims

NB2: A dedicated version has been used for Monte-Carlo simulations of the beams determination, or `MCB`. See Beams#Simulations_and_errors

`Desire` simulations

Complementary to the `Yardstick` simulations, the `Desire` simulations are used in conjunction with the actual TOI processing, in order to investigate the impact of some systematics. The `Desire` pipeline allows to simulate the response of the HFI-instrument, including the non-linearity of the bolometers, the time transfer-function of the readout electronic chain, the conversion from power of the sky to ADU signal and the compression of the science data. It also includes various components of the noise like the glitches, the white and colored noise, the one-over-f noise and the RTS noise. Associated to the Planck Sky Model and LevelS tools, the Desire pipeline allows to perform extremely realistic simulations, compatible with the format of the output Planck HFI-data, including Science and House Keeping data. It goes through the following steps (see Fig. `Desire` End-to-End Simulations) :

1. The input maps are computed using the Planck Sky Model, taking the RIMO bandpasses as input;
2. The LevelS is used to project input maps into Time ordered Inputs TOIs, as described for the Yardstick simulations;
3. The TOIs of the simulated sky are injected into the Desire pipeline to produce TOIs in ADU, after adding instrument systematics and noise components;
4. The official TOI processing is applied on simulated data as done on real Planck-HFI TOIs;
5. The official map-making is run on those processed timelines using the same parameters as for real data;

This Desire simulation pipeline allows to explore systematics such as 4K lines or Glitches residual after correction by the official TOI processing, as described below.

Simulations versus data

The significance of various difference tests perfromed on data can be assessed in particular by comparing them with `Yardstick` realisations.

`Yardstick` production contains sky (generated with `LevelS` starting from `PSM` V1.77) and noise timeline realisations proceeded with the official map making. The final production was regenerated with the same code as the nominal mission in order to get rid of possible differences that might appear for not running the official pipeline in the same conditions.

We compare statistical properties of the cross spectra of null test maps for the 100, 143, 217, 353 GHz channels. Null test maps can either be survey null test or half focal plane null test, each of which having a specific goal :

- survey1-survey2 (S1-S2) aim at isolating transfer function or pointing issues, while
- half focal plane null tests enable to focus on beam issues.

Comparing cross spectra we isolate systematic effects from the noise, and we can check whether they are properly simulated. Spectra are computed with `spice` masking either nominal mission point sources or simulated point sources, and masking the galactic plane with several mask width, the sky fraction from which spectra are computed are around 30%, 60% and 80%.

The nominal mission data and the Y3.0 realisations are binned. For each bin we compute the statistical parameters (mean and variance) of the `Yardstick` distribution. The following figure is a typical example of a consistency test, it shows the differences between the Y3.0 mean and the nominal mission, considering the standard deviation of the yardstick. We also indicate chi square values, which are computed within larger bin : [0,20], [20,400], [400,1000][1000,2000], [2000, 3000], using the ratio between (Nominal-Y3.0 mean)^2 and Y3.0 variance within each bin. This binned chi-square is only indicative: it may not be always significant, since data variations sometimes disappear as we average them in a bin, the mean is then at the same scale as the yardstick one.

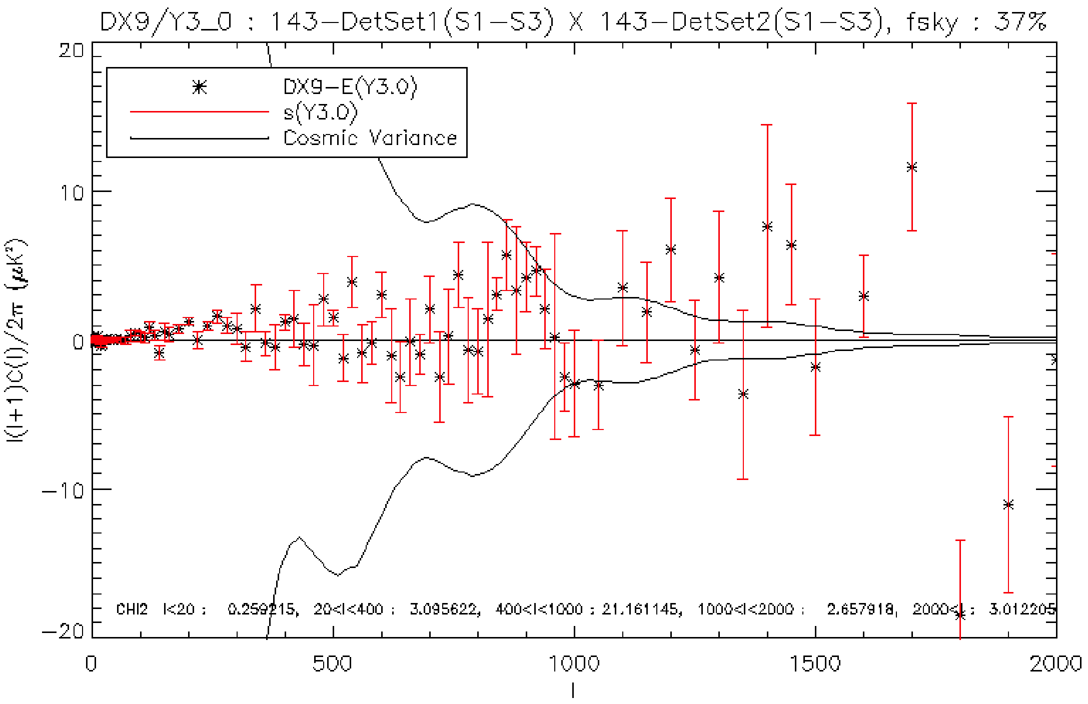

Example of consistency test for 143 survey null test maps.

Here will be a linlk to a (big) pdf file with all those plots, and/or a visualisation page.

Systematics impact estimates

Cosmic rays

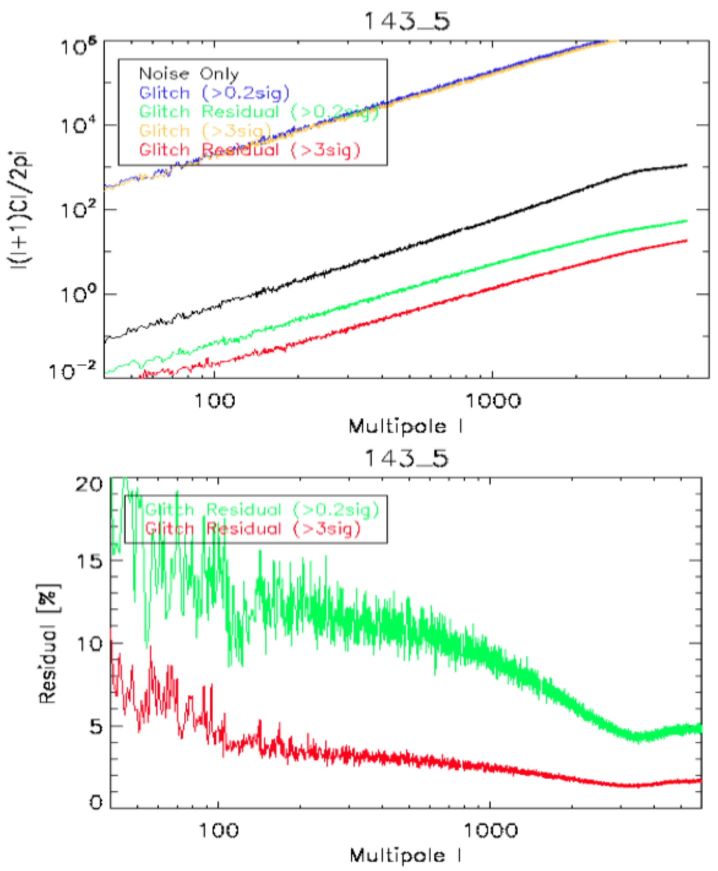

Comparison of Power SPectra with and without Glitch and Glitch corection

We have used `Desire` simulations to investigate the impact of glitch residuals at 143GHz. We remind that TOIs are highly affected by the impact of cosmic rays inducing glitches on the timelines. While the peak of the glitch signal is flagged and removed from the data, the glitch tail is removed from the signal during the TOI processing. We have quantified the efficiency and the impact of the official TOI processing when removing glitch tails on the scientific signal.

The Glitch model used in this set of simulations has been built using the real data extraction, in order to reproduce the 3 families observed (i.e. long, short and snail) and their relative distribution. This modelling has been validated on 143GHz channels, by comparing the glitch statistics of simulated timelines with real ones. Two types of models have been introduced for these simulations: the first only includes detectable glitches, with a glitch amplitude at the level of at least 3 times the noise level ; the second model also includes undetectable glitches until a level of 0.3 times the noise level.

The input sky used for these end-to-end simulations includes the CMB signal, our Galaxy, the compact sources and the planets. Not any other kind of systematics has been introduced, except the glitches associated with a white and colored noise to reproduce realistic data. For each bolometer three sets of simulated TOIs have been produced: (i) white plus colored noise only, (ii) noise plus "detectable glitches model" and (iii) noise plus "undetectable glitches model". On the simulated TOIs with glitches, two options of the TOI-processing have been used: with or without correction of the glitches (Despike Module), leading to a set of 5 processed TOIs. Maps and power spectra can be built on these sets of data.

It appears that in the case of the "detectable glitch model", the glitch tail residual represents less than 10% of the noise for ell<100 and less than 5% for ell>100. In the case of the "undetectable glitch model", these numbers goes to 20% for ell<100 and 15% for ell>100. Nevertheless the number of undetectable glitches remains largely unknown, and can only be extrapolated from power laws. Hence the results obtained for model 2 including undetectable glitches have to be taken as upper limits of the impact of glitch residuals on the power spectrum. These simulations also show that the glitch tail residuals do not produce any kind of 1/f supplementary noise.

1.6K and 4K stage fluctuations

The 4K and 1.6K stages are thermally regulated. The level of (controlled) fluctuations is less than 20uK/sqrt(Hz) above the spin frequency (and below 0.2 Hz) for the 4K stage and 10uK/sqrt(Hz) for the the 1.6K stage. Using a typical coupling coefficient of 150 fW/K_4K, this translates into a noise of 3 aW/sqrt(Hz). This is 4% of the bolometer noise variance (with a NEP of typically 15aW/sqrt(Hz)), and is thus negligible.

RTS noise

The Random Telegraphic Signal (RTS) noise, also called Popcorn Noise, appears as 2-levels jumps added on the baseline signal. Three bolometers are known to be affected by a high-RTS noise: 143-8, 545-3 and 857-4. While the 143-8 and 545-3 detectors are currently excluded from use in any products, other bolometers may show small amounts of small RTS.

We have investigated the probable impact of RTS noise present below the detection limit, i.e. 0.2 times the standard deviation noise of the signal. The `Desire` simulations with and without RTS noise have been produce on 143GHz bolometers. The analysis performed on the TOIS has shown that the impact measured is in perfect agreement with the expectation derived from the pre-launch RTS report. Residual RTS appears to be strongly limited, with a negligible impact on TOI noise – does not dominate over the 1/f noise at low frequencies (0.01Hz or below), and it would disappear rapidly above 1 Hz, very probably irrelevant at map level.

Baseline jumps

Similar to but distinct from popcorn noise, small baseline jumps were occasionally found in the data streams. They differ from the RTS noise by a much longer duration of the plateau. These data are usually corrected by subtracting a constant baseline before and after the jumps. About 320 jumps are found per bolometers, this represents 16 jumps per day for hFI, i.e. 12800 over the mission lifetime. While the detection efficiency of the biggest jumps is extremely high, the question of the impact of the jumps with amplitudes lower than 0.5% of the standard deviation of signal is still open. `Desire` simulations are about to be produced to answer this.

Split-level noise

The Split-Level noise is the major component of the non-stationnary noise. It appears as a strong increase of the noise level during one or a few rings, and is characterized by the addition of anoher 1/f noise component. The impact of such a systematics effect is under investigation using dedicated `Desire` simulations at 143GHz.

Pointing-change microphonics

The "Thruster signal" is not present for all bolometer for 100, 143, 217 GHz. After the peak "Thruster signal", the relaxing time "normal noise" is about the same for all bolometers over channels, i.e. 12 seconds, but amplitude is different. Thus the effect of the manouver has decayed away long before the end of the "unstable" period, which would be minutes after the first thrust.

This effect can be neglected, and does not need to be included in the simulation runs.

Electrical cross-talk

The Electrical Cross-Talk consists in the electrical contamination received by a given channel and coming from the other channels of the focal plane. This is mainly driven by the locations of the channels inside the electronic devices of the readout chain, and not by their locations in the focal plane.

This effect has been first measured during the ground calibration phase, and then during the inflight 'Calibration, Performance and Validation' phase (CPV Phase) after launch. These two sets of measurements agree to show that the level of electrical cross-talk is smaller than 0.01% for SWBs and 0.1% for PSBs. These estimates have been confirmed by the analysis of the glitches. While the thousands of detected glitches have been flagged for a given channel, the signal of the neighbor channels have been stacked at the same dates of the glitch flags to reveal the amount of electrical contamination coming from the glitched signal. Strong glitches have also been used in the same scope in a second study. These two analysis based on glitches give the same estimates of electrical cross-talk as measured during calibration phases.

Hence the electrical cross-talk has a negligible impact on science data, except probably for PSBs on which further `Desire` simulations will be carried out.

Optical cross-talk

It has been shown using planets crossing that the optical cross-talk is negligible, with an upper limit of 0.01%. This effect can be neglected in the total budget error, without any end-to-end simulation.

Time constant

The impact of the uncertainty of the time response has been studied using a set of 50 `Yardstick` simulations with CMB only on 8 143GHz bolometers. The set of 50 Time Transfer Function (TF)realizations have been chosen with a Low Frequency Excess Response (LFER) varying within 1.5% around its nominal value. While the same CMB sky map has been convolved through the optical beam, projected into TOIs and convolved with each of the 50 TF realizations, it has then been deconvolved by the nominal TF, leading to the deconvolved TOIs. Maps and power spectra have then been produced using these TOIs and compared to each others.

These simulations have shown that an uncertainty of 1.5% of the LFER yields 1% of error on the power spectrum at all scales, and even less at large scales.

4K line residuals

The 4K lines are the 4 K cooler induced noise in the detectors with very specific frequency signatures. They are filtered and corrected during the TOI-processing. The efficiency of this correction has been studied using two types of simulations at 143GHz: `Yardstick` and `Desire` simulations.

The `Yardstick` simulations have explored the impact of 4K lines residuals on CMB signal only, by adding a 4K lines pattern on the CMB TOIs, and by applying the same module of correction as used in the TOI-processing. The impact on the CMB power spectrum has been estimated by comparing the spectra obtained on data without 4K lines and data with corrected 4K lines.

The end-to-end `Desire` simulations include a complete sky (i.e. CMB, Galaxy and point sources) and the complete TOI-processing on the simulated data. The analysis and comparison is then performed on the maps directly and on the power spectra. It has been checked that the 4K lines modeling inputs used in the two sets of simulation are in agreement between them and with in-flight data. Those simulations have been performed on the full 143GHz channel, i.e. 12 detectors, and the full nominal mission range.

Both analysis converge to show that the 4K lines residual represent 2% to 2.5% maximum of the noise level at particular ell values affected by the 4K lines (such as ell=1800). These residuals are well below the one-sigma discrepancy of the noise itself at the same particular ell values.

Hence the 4K lines residuals are negligible. Nevertheless, the correlation between the 4K lines and the ADC correction discussed in #planck2013-p03 Planck-2013-VI [2] may have an impact on the gain variation estimates at the end of the processing. This has still to be quantified.

Saturation

The Planck-HFI signal is converted into digital signal (Raw-Signal) by a 16 bit ADC. This signal is expressed in ADU, from 1 to 65535, and centered around 32768. A full saturation of the ADC corresponds to the value of 1310680 ADU, corresponding to the number of samples per half period times, N_sample, times 2^15. Nevertheless, the saturation of the ADC starts to appear when a fraction of the raw signal hits the 32767 (2^15) value.

We have used the SEB tool (standing for Simulation of Electronics and Bolometer) to simulate the response of the Readout Electronics Chain at a very high sampling, to mimic the high frequency behavior of the chain and investigate sub-period effects. It has been shown by this kind of simulations that the saturation of the ADC starts to appear if the signal is more then 7*10^5 - 8*10^5 ADU. Hence the variation of the gain, due to the saturation of the ADC, has an impact only when crossing Jupiter for SWB353GHz and SWB857GHz bolometers. This effect can be neglected.

References

<biblio force=false>

1. References

</biblio>

References

[1] http://www.rssd.esa.int/doc_fetch.php?id=3168403&page=1

Power spectra

This page describes the HFI based power spectra.

We call intra-frequency checks those performed between detectors (or sets of detectors) in the same frequency bands, which thus respond similarly to the sky emission. Interfrequency-checks on the other hand correspond to checks between detector in different frequency bands, imposing further reliance on a sky model to perform the test.

Intra-frequency checks

These compare the power spectra between various detector sets operating within the same frequency channel. They see the same sky, and should therefore give consistent results, up to the noise level, and up to color corrections due to their somewhat different spectral band passes. These corrections are rather small if one restricts the comparison to specific portions of the sky, for instance dominated by extra-Galactic components, like it is done for extracting the CMB power spectrum in the likelihood analysis where $f_{sky} \sim 0.4$.

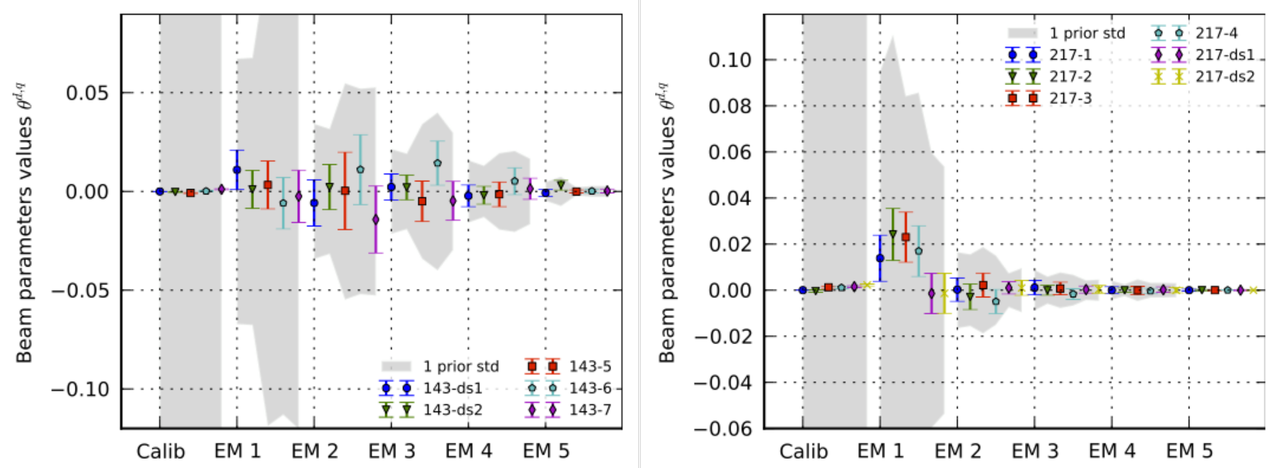

143 GHz detector sets

217 GHz detector sets

Consistency checks

The pictures shows in grey the prior deduced from the beam parameters uncertainty analysis. At 217 GHz, the distance between PSB and SWB suggests an accounted for effect (fortunately small enough for the likelihood analysis). The relative calibration appear to be at the 0.1% level.

This shows that whatever systematic effect might remain, it has to be common to all detectors within a frequency band to a very high level of accuracy.

Summary of HFI data characteristics

This page will contains the information from the summary section of the HFI DPC paper (#planck2013-p03), which describes the most important characteristics of the HFI instrument and data.

Note that some of these parameters are available in the RIMO, which is described in detail in the RIMO section.

The LFI DPC

Overview

The LFI DPC processing is organized into different "Levels": 1,2,3,4 and S. In brief the Level-1 has the scope to analyze the data in a daily base, transform the telemetry packets in to timelines containing engineering values and feed it in the DPC database. Level-2 use the output of the Level-1 transforming raw TOI in to calibrated timelines with all the know systematic sources removed, those timelines are then used in the mapmaking process to create all the possible maps combinations. Level-3 use the Level-2 output of both DPC to derive astrophysical results like Catalogue, CMB map, foreground etc…. Level-S is the common simulation pipeline used to validate the results and any algorithm before its introduction into the official pipeline. Finally the Level-4 just act as a collector pointing used to reformat, document and deliver the products to the final archive.

From packets to TOI

Level 1 takes input from the MOC’s Data Distribution System (DDS), decompresses the raw data, and outputs Time Ordered Information for Level 2. This will be done by using software. The input to Level 1 are the telemetry (TM) and auxiliary data as they are released by the MOC (Mission Operation Centre). Level 1 will use TM data for performing a routine analysis (RTA) of the S/C and P/L with the aim of monitoring the overall health of the payload and detecting possible anomalies, and performing a quick-look data analysis of the science TM to monitor the operation of the observation plan and to verify the behavior of the instrument. Additional tasks of Level 1 relate to its role of instrument control and as the DPC interface with the MOC. Level-1 processing is described in detail in the Pre-processing section.

Level 2: From TOI to Maps

The DPC Level 2 has many tasks. The first one is the creation of differenced data. Level 1 stores data from both Sky and Load. These two have to be properly combined to produce differenced data therefore reducing the impact of 1/f noise. This is done via the computation of the so-called gain modulation factor “R” which is derived taking the ratio of the mean signals from both Sky and Load. After differenced data are produced, the next step are the removal of know systematic effects and then the photometric calibration where calibrated means essentially that TOD are in physical units instead of engineering units; the following major task is the production of frequency maps calibrated and free from systematic effects (which is a complex task and involves several sub-pipelines). Level-2 processing is described in detail in the TOI processing section.

Level 3: From Maps to Component

The aim of Level 3 is to transform the frequency maps produced by both instruments into preliminary maps of the underlying astrophysical components by means of pipeline processing and to provide other data sets including description of astrophysical sources (final catalogue of point sources, extended source maps and catalogues, description of global or statistical properties etc …). Data from both HFI and LFI are analyzed jointly to reach the final expected result. Level-3 processing is described in detail in the Power Spectra and HFI/LFI joint data processing section.

Level S : A common HFI/LFI simulation software

Level S is the so-called "Simulation Level" software suite common to both consortia, which, given a sky model (generated by the Planck sky model, `PSM`), detectors pointing and beams, generates the infalling power on each detector. It can also provide a simplified description of eg. the noise. It is further described in the HFI/LFI joint data processing.

LFI DPC Infrastructures

The LFI DPC provide a centralized hardware and software infrastructure to a large number of geographically distributed institution participating to the Planck mission. In few word the data are interfaced to a database where only meta-information are stored. This allow very high flexibility to eventually modify the product to be delivered.

Published Paper

The description of the pipeline applied to the *Early Planck results* can be found at the following link Planck early paper V [1], and instrument performances are reported in Planck early paper III [1].

LFI data processing

Pre-processing

Overview

The first processing level of the LFI DPC is the so called Level 1. The source data of the Level 1 software includes:

- raw housekeeping telemetry packets retrieved from different satellite subsystems: the LFI instrument, the Sorption cooler, the HFI instrument and the Central Data Management Unit (CDMU).
- the LFI raw scientific telemetry
- Additional auxiliary data provided by the MOC and the Flight dynamics:
  - The Attitude History File (AHF)
  - Time correlation data (time correlation coefficients and time couples)
  - Command History data
  - The Sorption cooler out of limit data

Only a subset of the raw housekeeping telemetry packets is daily processed and converted into TOIs, i.e. those relevant to the LFI Daily Quality Report production and the estimation of the LFI instrument systematic effects.

Scientific telemetry

Each LFI radiometer provides two analog outputs, one for each amplifier chain. In a nominal configuration, each output yields a sequence of alternating V_{sky}, V_{load}signals at the frequency of the phase switch. By changing the phase switches configuration, the output can be a sequence of either V_{sky}or V_{load}signals.

The conversion from analog to digital form of each radiometer output is performed by a 14 bits Analog-to-Digital Converter (ADC) in the Data Acquisition Electronics unit (DAE). The DAE transforms the signal in the range [-2.5 V, +2.5 V]: first it applies a tunable *offset*, O_{DAE}, then it amplifies the signal with a tunable *gain*, G_{DAE}, in order to make full use of the resolution of the ADC, and finally the signal is integrated. To eliminate phase switch raise transients, the integration takes into account a *blanking time*, i.e. a blind time in the integrator where data are not considered. The default value of the blanking time is 7.5 μs. Both the O_{DAE}, the $G_{DAE}$and the blanking time are parameters set through the LFI on-board software. The equation applied to transform a given input signal V_{in}into an output $V_{out}$is:

$$V_{out} = G_{DAE}(V_{in} + O_{DAE}) + Z_{DAE}$$

with $G_{DAE} = 1, 2, 3, 4, 6, 8, 12, 16, 24, 48$, $O_{DAE}$is one of 255 possible offset steps from +0 up to +2.5 V and where $Z_{DAE}$is a small offset introduced by the DAE when applying a selected gain. The values of $G_{DAE}$and $O_{DAE}$are set by sending, through specific telecommands, the DAE Gain Index (DGI) and the DAE Offset Index (DOI) associated to the desired values.

The ADC quantizes the V_{out}uniformly in the range $-2.5V \leq V_{adc} \leq +2.5V$, so that the quantization step is $q_{ADC} = 5.0/2^{14} = 0.30518$mV. The quantization formula is

$$S = \text{round}\left(\frac{V_{out} + 2.5}{q_{ADC}}\right),$$

and the output is stored as an unsigned integer of 16 bits.

The digitized scientific data is then processed by the Radiometer Electronics Box Assembly (REBA) which runs the LFI on-board software. For each LFI detector, the REBA processes the data in the form of time series which are split into telemetry packets. To satisfy the LFI assigned telemetry budget limit of 53.5 Kbps, the REBA implements 7 acquisition modes (processing types) which reduce the scientific data rate by applying a number of processing steps. The following figure illustrates the main steps of the on-board processing and the corresponding processing types (PTypes).

PType 0

in this mode the REBA just packs the raw data of the selected channel without any processing.

PType 1

consecutive S_{sky}or S_{load}samples are coadded and stored as unsigned integers of 32 bits. The number of consecutive samples to be coadded is specified by the N_{aver}parameter.

PType 2

in this mode, two main processing steps are applied. First, pairs of averaged $S_{sky}$and S_{load}samples, respectively $\overline{S}_{sky}$and $\overline{S}_{load}$, are mixed by applying two different gain modulation factors, GMF1 and GMF2: The operations are performed as floating point operations. Then the two values obtained are requantized, converting them into two 16-bit signed integers:

PType 3

with respect to PType 2, in this mode only a single gain modulation factor is used, GMF1, obtaining:

$$P = \overline{S}_{sky} - \mathrm{GMF1} \cdot \overline{S}_{load}$$

and analogously to PType 2, the value is requantized obtaining a 16-bit signed integer.

PTypes 4, 5, 6

with the processing types PType 4, PType 5 and PType 6, the REBA performs a loss-less adaptive arithmetic compression of the data obtained respectively with the processing types PType 0, PType 2 and PType 3. The compressor takes couples of 16 bit numbers and stores them in the output stream up to the complete filling of the data segment for the packet in process.

A set of REBA processing parameters — N_{aver}, GMF1, GMF2, q and Offset — is selected for each of the 44 LFI channels.They are also included in a teartiary header of each scientific telemetry packet sent to ground. The REBA can acquire data from a channel in two modes at the same time. This capability is used to verify the effect of a certain processing type on the data quality. So, in nominal conditions, the LFI instrument uses PType 5 for all its 44 detectors and every 15 minutes a single detector, in turn, is also processed with PType 1, in order to periodically check the gain modulation factors and the second quantization parameters. The other processing types are mainly used for diagnostic, testing or contingency purposes.

Packets generated by the REBA follow the ESA Packet Telemetry Standard and Packet Telecommand Standard, the CCSDS Packet Telemetry recommendations and the ESA Packet Utilization Standard (PUS). The packet structure for an LFI scientific telemetry packet is shown in the following figure.

From packets to raw TOIs

On a daily basis, the LFI Level 1 software pipeline retrieves the housekeeping and scientific telemetry packets dumped from the satellite on-board memory through the MOC Data Disposition System (DDS). The Level 1 software has to recover most accurately the values of the original (averaged) sky and load samples acquired on-board. Data acquired with PTypes 4, 5 and 6 is first uncompressed. The loss-less compression applied on-board is simply inverted and the number of samples obtained is checked with the value stored in the tertiary header.

The digitized data, processed by the REBA, are not in physical units but in ADU (Analog to Digital Unit). Conversion of $S_{sky}$and S_{load}in Volt requires the Data Source Address (DSA), i.e. the radiometer and detector from which the data are generated, the blanking time (indicized by the Blancking Time Index, BTI), the DGI and the DOI. The DSA and BTI values are recovered from the packet tertiary header, while the DGI and DOI values are recovered from the LFI HK telemetry. Hence, the value in Volt is obtained as:

$$V_i = \frac{S_i \cdot q_{ADC} - Z_{DAE} - 2.5}{G_{DAE}} - O_{DAE} \approx \frac{S_i - \tilde{Z}_{DAE}(\mathrm{DSA}, \mathrm{BTI}, \mathrm{DGI})}{\tilde{G}_{DAE}(\mathrm{DSA}, \mathrm{BTI}, \mathrm{DGI})} - \tilde{O}_{DAE}(\mathrm{DSA}, \mathrm{BTI}, \mathrm{DOI})$$

where $\tilde{G}_{DAE}(\mathrm{DSA}, \mathrm{BTI}, \mathrm{DGI})$, $\tilde{O}_{DAE}(\mathrm{DSA}, \mathrm{BTI}, \mathrm{DOI})$and $\tilde{Z}_{DAE}(\mathrm{DSA}, \mathrm{BTI}, \mathrm{DGI})$are look-up tables estimated during the LFI ground calibration campaign with:

- $\tilde{G}_{DAE}(\mathrm{DSA}, \mathrm{BTI}, \mathrm{DGI}) \approx \frac{G_{DAE}}{q_{ADC}}$,
- $\tilde{O}_{DAE}(\mathrm{DSA}, \mathrm{BTI}, \mathrm{DOI}) \approx O_{DAE}$,
- $\tilde{Z}_{DAE}(\mathrm{DSA}, \mathrm{BTI}, \mathrm{DGI}) \approx \frac{Z_{DAE} + 2.5}{q_{ADC}}$.

This conversion is the only processing required by PTypes 0 and 3 and it is the last step in the processing of all the other processing types. Since PType 1 data is just coadded on-board, the division by $N_{aver}$is performed by the Level 1 software. PType 2 and 5 data have to be dequantized by:

$$P_i = \frac{Q_i}{q} - \mathrm{Offset}$$

and then demixed to obtain $\overline{S}_{sky}$and $\overline{S}_{load}$:

On-board time reconstruction

The On-Board Time (OBT) reconstruction for scientific data has to take into account the phase switch status and the processing type applied on-board. If the phase switch is off, it means that the packet contains consecutive values of either sky or load samples, and the sampling frequency, $f_{sampling}$, is 8192 Hz. Denoting with $i \geq 0$the sample index within the packet, for PType 0 and 4 we have that:

$$t_i^{obt} = t_0^{obt} + i \frac{1}{f_{sampling}},$$

where $t_0^{obt}$is the on-board time of the packet (t_{pkt}^{obt}) and $i = 0$denotes the first sample in the packet. If the switching status is on, either consecutive pairs of (sky, load) samples or (load, sky) samples are stored in the packets. Hence, consecutive couples of samples have the same time stamp and $f_{sampling}$= 4096 Hz.

For averaged data (PTypes 1, 2, 3, 5, 6), the first sample of a scientific packet is the sum (mean) of N_{aver}samples, and the packet time, t_{pkt}^{obt}, is the time of the first of the N_{aver}samples. In this case, $t_0^{obt}$is computed as:

$$t_0^{obt} = t_{pkt}^{obt} + \frac{N_{aver} - 1}{2} \frac{1}{f_{sampling}}$$

and

$$t_i^{obt} = t_0^{obt} + i \frac{N_{aver}}{f_{sampling}}, \mathrm{for} \quad i \geq 1$$

Housekeeping telemetry handling

The structure of telecommand and housekeeping telemetry packets of the entire satellite is defined by the Mission Information Base (MIB), a database formed by a set of ASCII tables formatted according to the ESA Mission Control System interface control documents. The MIB information includes the type and structure of the telemetry packets, the location, type and format of the monitoring parameters within the packets, the calibration curves to convert each parameter raw value into an engineering value, the out of limit values to be checked for each parameter.

The Level1 software uses the MIB information to group the housekeeping packets according to their type (PUS service type, sub-sytem, periodicity). A subset of the housekeeping packets that are relevant for the daily instrument quality verification and the scientific data analysis are further processed: samples of each parameter are extracted, grouped into timelines and saved as TOIs. Each TOI contains, for each parameter sample, the on-board time, the UTC time, the parameter raw and engineering value, flags reporting some quality measures (time quality, out of limit checking result).

Auxiliary data handling

The MOC Flight Dynamics team daily provides the Attitude History information as an ASCII file (AHF), automatically delivered through the Planck File Transfer System. For stable pointing periods, the AHF provides quaternions describing, at given on-board times, the orientation of the Planck body reference frame with respect to the Ecliptic inertial reference system, and additional information such as wobble angles, spin phase angle and rate. An AHF file contains also different type of records: high frequency data records containing the raw attitude data; spin period frequency records, that are derived from the high frequency records by averaging data over a complete spin period; observation frequency records, where data is averaged over a complete observation period. The Level1 software simply reformat all data contained in the AHF, ingesting it in the LFI Level1 data management system.

The MOC is also responsible of computing the correlation between the On-Board Time (OBT) and the ground Coordinated Universal Time (UTC) and providing the UTC time of each telemetry packet. Time couples (OBT, UTC), generated by processing the Standard Time Source packets received from spacecraft, and the Time Correlation Coefficients, computed by a linear fit of the time couples, are also provided by MOC as auxiliary data. The Level1 software uses the time correlation coefficients to check the UTC time provided by MOC. Moreover, the time couples are used to recompute the UTC time of each packet with a variation of the MOC fitting procedure, in order to reduce the time correlation variance.

TOI processing

Overview

The LFI Level2 Pipeline analyzes each horn of the instrument separately, one pointing period at time, and store results in object the length of an OD. Each diode of the horn is corrected from systematic, differentiated and then combined with its complementary diode in the same radiometer. The horn is then calibrated and the photometric calibration is applied.

Pre-processing

Before the run of the Level2 pipeline and to improve the analysis the Mission information and data sampling divisions are stored in the database.

The Mission information is a set of objects, one for each Operational Day (OD, as defined in the glossary), in which are stored Pointing Period data: DPC pointing ID (where 1 is the first pointing of the nominal mission), PSO pointing ID, start OBT of the pointing maneuver, start OBT of the stable pointing, end OBT of the pointing, spin axis ecliptic longitude and latitude.

The sampling information is a set of objects, one for each LFI frequency, in which are stored for each pointing ID: start OBT of the pointing maneuver, start OBT of the stable pointing, end OBT of the pointing, number of samples of the pointing, number of stable samples of the pointing, start sample of the stable pointing and sample number from the start of the nominal mission. Valid samples and OBTs are defined where any of the radiometers from that frequency cohort contain valid data.

ADC Correction

During analysis it appeared that white noise and calibration seemed affected by something in common. It turn out to be a non linearity in the Analogic/Digital Converter on board. More on #planck2013-p02, planck2013-p02a Planck-2013-II [1], Planck-2013-III [4].

Evaluation

The mathematical model represents the digital ADC output as:

$$X = (V - \Delta)\gamma + x_0$$

where V is the voltage input, γ is the DAE gain, Δ is the DAE offset and x_0 is the DAE T_{zero}.

We can model the non-linearity as a function of the input voltage $R(V)$. So we have the apparent inferred voltage V' and we can link it to the actual input voltage with:

$$((V - \Delta)\gamma + x_0)R(V) = X = ((V' - \Delta)\gamma + x_0$$

so that:

$$R(V) = \frac{(V' - \Delta)\gamma + x_0}{(V - \Delta)\gamma + x_0}$$

Since $V >> \Delta$ and $V\gamma >> x_0$ we can use the much simpler relation:

$$R(V) = \frac{V'}{V}$$

and we expect it to be very near to unity for all V.

To find the response curve we have only the apparent voltage to work with, so we had to use the inverse response function $R'(V')$ and replace the real input voltage with T_{sys} times the time varying gain factor $G(t)$.

$$V = V'R'(V') = G(t)T_{sys}$$

If we introduce a small signal on top of T_{sys} which leads to increased detected voltage and corresponding apparent voltage increment:

$$V + \delta V = (V' + \delta V') = (V' + \delta V')R'(V' + \delta V') = G(t)(T_{sys} + \delta T)$$

so carrying out the differentiation respect to V' to the relation between true and apparent signal voltage leads to:

$$\delta V = \left(V'\frac{dR'(V')}{dV' + R'(V')}\right)\delta V' = G(t)\delta T$$

We now assume T_{sys} and δT are fixed and that the variations are due to slow drifts in the gain. So we can isolate the terms:

$$V' = \frac{G(t)T_{sys}}{R'(V')}$$

$$\delta V' = \frac{G(t)\delta T}{V'\frac{dR'(V')}{dV} + R'(V')}$$

Combining the equations through the gain factor to remove it:

$$\frac{V'R'(V')}{T_{sys}} = \frac{\delta V'\frac{dR'(V')}{dV'} + R'(V')}{\delta T}$$

Rearranging and putting $a = \dfrac{\delta T}{T_{sys}}$

$$\frac{dR'(V')}{dV'} = \left(\frac{a}{dV'} - \frac{1}{V'}\right)R'(V')$$

So there is the expected direct proportionality of $\delta V'$ to V' due to the assumption that the variations in voltage are due to overall gain drift, so the amplitude of voltage and signal will vary together. Then there is the additional differential term which will pull signal amplitude away from the linear relationship. So if we plot measured white noise or dipole gain factor against recovered voltage we should see this linear curve with variations due to local slope changes at particular voltages. The linear part can be taken out and the differential part fitted. This was numerically integrated up to get the inverse response curve, what we need to convert the measured voltages to corrected voltages.

Application

For each of the 44 LFI diodes there is the corresponding object in the Database. Each object contains 4 columns: the input voltages coming from the sky channel and the corresponding linearized output, the input voltages coming from the reference channel and the corresponding linearized output.

Data loaded by the module are used to initialize two different interpolators using CSPLINE and the functions from gsl (GNU Scientific Libraries [2]) libraries. The interpolators are then used to correct each sample.

Spikes Removal

Some of the LFI receivers exhibit a small artifact with exactly 1 second repetition, which visible in the power spectra. The effect is a set of spikes at 1 Hz and harmonics. The spurious signal is very well modeled and is removed from the timelines. More information can be found in #planck2013-p02, planck2013-p02a Planck-2013-II [1], Planck-2013-III [4].

Modeling

The cause of the spikes at 1 Hz and harmonics is a tiny 1 second square wave embedded in affected channels. The method to estimate the 1 Hz signal is to build a template in time domain synchronized with the spurious signal. The first step is dividing each second of data into time bins using OBT. The number of bins is computed using:

$$nbins = fsamp * template\_resolution$$

where fsamp is the sampling frequency and is 136 at 70 GHz, 80 at 44 GHz and 56 at 30 GHz. Then the bins vector is initialized with time intervals. To avoid aliasing effects template resolution is $\sqrt{3}$. We can write the process adding an index to the time sample: lower index denotes the particular time sample, while the upper index labels the bin into which the sample falls. The linear filter can be written as:

$$s(t_i^j) = a_j\left(1 - \Delta x(t_i^j)\right) + a_{j+1}\Delta x(t_i^j)$$

Here $\Delta x(t_i^j)$ is the filter weight which is determined by where within the bin sample lies. If we use t^j with only an upper index to denote the start of each bin, then we can write the filter weight as follows:

$$\Delta x(t_i^j) = \frac{t_i^j - t^j}{t^{j+1} - t^j}$$

In other words, the filter weight is the time sample value minus the start of the bin divided by the width of the bin.

We must estimate the parameters a_j from the data. With the assumption that the instrument has stable noise properties, we can use a least square algorithm to estimate the bin values:

This can be represented in matrix equation:

$$M_{jk}a_k = b_j$$

with the following definitions:

$$M_{k,k-1} = \sum_i (1 - \Delta x(t_i^{k-1}))\Delta x(t_i^{k-1})$$

$$M_{k,k} = \sum_i (1 - \Delta x(t_i^k))^2 \Delta x(t_i^{k-1})^2$$
$$M_{k,k+1} = \sum_i (1 - \Delta x(t_i^k)) \Delta x(t_i^k)$$
$$M_{k,k+n}(|n| > 1) = 0$$
$$b_j = \sum_i d_i^k (1 - \Delta x(t_k^i)) + d_i^{k-1} \Delta x(t_i^{k-1})$$

With these definitions we have to make use of periodic boundary conditions to obtain the correct results, such that if $k = 0, k - 1 = n - 1$ and $k = n - 1, k + 1 = 0$. Once this is done, we have a symmetric tridiagonal matrix with additional values at the upper right and lower left corners of the matrix. The matrix is solved with LU decomposition. In order to be certain of the numerical accuracy of the result, we can perform a simple iteration. The solving of the linear system and the iterative improvement of the solution are implemented as suggested in Numerical Recipes.

Application

For each of the 44 LFI diodes there is the corresponding object in the Database. Because of the amplitude of the spikes we choose to apply the correction only on the 44 GHz radiometers. Each object contains 3 columns: the bins start time vector, the sky amplitudes and the reference amplitudes.

For each sample the value to be subtracted is computed using:

$$V = skyAmp_k(1 - \Delta x(t_k)) + skyAmp_{k+1} \Delta x(t_k)$$

where k is the index of the bins at a given time.

Gaps Filling

During the mission some of the data packets were lost (see #planck2013-p02) Planck-2013-II [1]. Moreover in two different and very peculiar situations LFI was shutdown and restarted, giving inconsistencies in data sampling. All of those data aren't used for scientific purpose but to avoid discrepancies in data analysis all of the radiometers at the same frequency must have the same samples.

To accomplish this the length of the data stream to be reduced in a specific pointing period is compared with the data stored in the sample information object. If the length is not the same the OBT vector is filled with missing sample times, the data vector is filled with zeros and in the flag column the bit for gap is raised.

Gain Modulation Factor

The pseudo-correlation design of the LFI radiometers allows a dramatic reduction of $1/f$ noise when the V_{sky} and V_{load} outputs are differenced (see LFI instrument description). The two streams are slightly unbalanced, as one looks at the 2.7 K sky and the other looks at the ~4.5 K reference load. To force the mean of the difference to zero, the load signal is multiplied by the Gain Modulation Factor (R). For each pointing period this factor is computed using (see eq. (3) in LFI description):

$$R = \frac{< V_{sky} >}{< V_{load} >}$$

Then the data are differenced using:

This value for R minimizes the 1/f and the white noise in the difference timestream. The i index represents the diode and can be 0 or 1.

At this point the maneuver flag bit is set to identify which samples have missing data, using the information stored in the sampling information object. This identifies which data to ignore in the next step of the Pipeline.

The R values are stored in the database. At the same time the mean values of $V_{sky}$and $V_{load}$are stored in order to be used in other steps of the analysis.

Diode Combination

The two complementary diodes of each radiometer are combined. The relative weights of the diodes in the combination are chosen for optimal noise. We assign relative weights to the uncalibrated diode streams based on their first order calibrated noise.

Evaluation

From first order calibration we compute an absolute gain $G_0$and G_1, subtract an estimated sky signal and calculate the calibrated white noise $\sigma_0$and σ_1, for the pair of diodes (see eq. (6) in LFI description):. The weights for the two diodes (i= 0 or 1) are:

$$W_i = \frac{\sigma_i^2}{G_{01}} \frac{1}{\sigma_0^2 + \sigma_1^2}$$

where the weighted calibration constant is given by:

$$G_{01} = \frac{1}{\sigma_0^2 + \sigma_1^2} [G_0 \sigma_1^2 + G_1 \sigma_0^2]$$

The weights are fixed to a single value per diode for the entire dataset. Small variations in the relative noise of the diodes would in principle suggest recalculating the weights on shorter timescales, however, we decided a time varying weight could possibly induce more significant subtle systematics, so chose a single best estimate for the weights for each diode pair.

Horn	Weight M-00	Weight M-01	Weight S-10	Weight S-11
18	0.567304963	0.432695037	0.387168785	0.612831215
19	0.502457723	0.497542277	0.55143474	0.44856526
20	0.523020094	0.476979906	0.476730576	0.523269424
21	0.500324722	0.499675278	0.563712153	0.436287847
22	0.536283158	0.463716842	0.553913461	0.446086539
23	0.508036034	0.491963966	0.36160661	0.63839339
24	0.602269189	0.397730811	0.456037835	0.543962165
25	0.482050606	0.517949394	0.369618239	0.630381761
26	0.593126369	0.406873631	0.424268188	0.575731812
27	0.519877701	0.480122299	0.484831449	0.515168551
28	0.553227696	0.446772304	0.467677355	0.532322645

Application

The weights in the table above are used in the formula:

$$TOI_{diff} = w_0 TOI_{diff0} + w_1 TOI_{diff1}$$

Planet Flagging

Extraction Method

The planets Temperature have been estimated from chunk of samples affected, plus a surrounding region, projected onto a grid (microstripes), by assuming an elliptical Gaussian beam using parameters from instrument database.

Microstripes are a way to extract and store relevant samples for planets detection. Relevant samples are samples affected by the planet plus samples in the neighbor. The search radius to select samples as relevant is 5 deg around the planet position, computed at the pointing period mid time. For each sample we store SCET (Spacecraft Event Time), pointing directions and calibrated temperature. Destriping is applied during application.

Random errors are estimated by taking the variance of samples entering each micromap pixel. This is fast and the major problems (near a bright source the noise gives a larger value and it is difficult to extract the correlation matrix) causes the noise to be overestimated by a factor of two that in this situation is not a major drawback.

The apparent position of Planets as seen from Planck at a given time is derived from JPL Horizon [3]. Position are sampled in tables at steps of 15 minutes and then linearly interpolated at the sampling frequency of each detector. JPL Horizons tables allow also to derive other quantities such as the Planet-Planck distance and the Planet-Sun distance nad the planet angular diameter affecting the apparent brightness of the planet.

The antenna temperature is a function of the dilution factor, according to:

$$T_{ant,obs} = 4log2T_{ant,1}\left(\frac{\theta}{b_{fwhm}}\right)^2$$

where $T_{ant,obs}$and $T_{ant,1}$are the observed and reduced T_{ant}, $\theta$the instantaneous planets angular diameter and $b_{fwhm}$the beam full width half maximum.

With the above definition $T_{ant,1}$could be considered as the $T_{ant}$for a planet with $b_{fwhm} = \theta$, but a more convenient view is to take a Reference Dilution factor D_0, as the dilution factor for a standardized planet angular diameter and beam fwhm b_{fwhm}, θ_0, to have:

$$D_0 = \left(\frac{\theta_0}{b_0}\right)^2$$

leading to the following definition of a standardized T_{ant}:

$$T_{ant,obs} = 4log2T_{ant,0}\left(\frac{b_{fwhm,0}}{b_{fwhm}}\frac{\theta}{\theta_0}\right)^2$$

with the advantage of removing variations among different detectors and transits while keeping the value of T_{ant} similar to that seen by the instrument and then allowing a prompt comparison of signals and sensitivities.

Application

The OBT vector found by the search are saved in a set of object, one for each horn. In Level2 Pipeline those OBTs are compared with the OBT vector of the data to raise planet bit flag where needed.

Photometric Calibration

Photometric calibration is the procedure used to convert data from volts to kelvin. The source of the calibration is the well known CMB dipole, caused by the motion of the Solar System with respect to the CMB reference frame. To this signal we add the modulation induced by the orbital motion of Planck around the Sun. The resulting signal is then convoluted with the horn beam to get the observed Dipole.

Beam Convolved Dipole

In computing the beam convolved dipole we used an elegant algorithm to save time and computing power. In computing the cosmological dipole signal it is common to assume a pencil-like beam acting as a Dirac delta function. In this case a dipole timeline is defined as:

$$\Delta T_{D,\delta}(t) = \mathbf{P}_E(t) \cdot \mathbf{D}_E$$

where $\mathbf{P}_E(t)$is the pointing direction, in the observer reference frame and $\mathbf{D}_E$is the dipole axis scaled by the dipole amplitude again in the same reference frame.
In general the true signal would have to be convolved with the beam pattern of the given radiometer, usually described as a fixed map in the beam reference frame or as a time dependent map in the observer reference frame. In this case it is easiest to describe the convolution in the beam reference frame, since the function to be convolved is described by a single vector.

Denoting with $\mathcal{U}(t)$the matrix converting from the observer to the beam reference frame, so that:

$$\mathcal{U}(t)\mathbf{P}_E(t) = \mathbf{e}_z$$

the instantaneous dipole direction in the beam reference frame is:

$$\mathbf{D}(t) = \mathcal{U}(t)\mathbf{D}_E$$

By denoting with $\mathbf{P}$a pointing direction in the beam reference frame then:

$$\Delta T_D(t) = N \int_{4\pi} B(\mathbf{P})\mathbf{P} \cdot \mathbf{D}(t) d^3\mathbf{P}$$

where $\mathbf{N}$is a normalization costant.

$$N^{-1} = \int_{4\pi} B(\mathbf{P}) d^3\mathbf{P}$$

Denoting with $\mathbf{P}_x$, $\mathbf{P}_y$, $\mathbf{P}_z$the three cartesian components of the $\mathbf{P}$the integral of the dot product can be decomposed into three independent integrals:

$$S_x = N \int_{4\pi} B(\mathbf{P}) P_x d^3\mathbf{P}$$

$$S_y = N \int_{4\pi} B(\mathbf{P}) P_y d^3\mathbf{P}$$

$$S_z = N \int_{4\pi} B(\mathbf{P}) P_z d^3\mathbf{P}$$

those integrals define a time independent vector characteristic of each radiometer and constant over the mission.

Detector ID	S_x	S_y	S_z
LFI18S	1.4105692317321994e-03	-3.7689062388084022e-04	9.9999893412338192e-01
LFI18M	1.1200251268914613e-03	-3.2838598619563524e-04	9.9999931885294768e-01
LFI19S	1.7861136968831050e-03	-4.4036975450455066e-04	9.9999830793473898e-01
LFI19M	1.4292780457919835e-03	-4.7454175238335579e-04	9.9999886598655352e-01
LFI20S	1.7008692096818349e-03	-6.1036624911600191e-04	9.9999836724715374e-01
LFI20M	1.5548897911626446e-03	-5.9289001736737262e-04	9.9999861539862389e-01
LFI21S	1.6975720932854463e-03	6.0961185087824777e-04	9.9999837330986663e-01
LFI21M	1.5486274949897787e-03	5.9228926426513112e-04	9.9999862547220986e-01
LFI22S	1.7861136968831245e-03	4.4036975450366470e-04	9.9999830793473898e-01
LFI22M	1.4292780457920242e-03	4.7454175238250377e-04	9.9999886598655352e-01
LFI23S	1.4105692317321714e-03	3.7689062387997129e-04	9.9999893412338203e-01
LFI23M	1.1200251268914476e-03	3.2838598619481239e-04	9.9999931885294757e-01
LFI24S	3.4636411743209074e-04	-2.8530917087092225e-07	9.9999994001590664e-01
LFI24M	4.3939553230170735e-04	-2.9414231975370517e-07	9.9999990346573508e-01
LFI25S	-1.0428719495964051e-04	1.9328051933678115e-04	9.9999997588341061e-01
LFI25M	-1.1004766833423990e-04	2.7656488668259429e-04	9.9999995570068612e-01
LFI26S	-1.0428719495970346e-04	-1.9328051933760877e-04	9.9999997588341061e-01
LFI26M	-1.1004766833430009e-04	-2.7656488668343130e-04	9.9999995570068612e-01
LFI27S	1.6613273546973915e-03	6.6518363019636186e-04	9.9999839875979735e-01
LFI27M	1.5583345016298123e-03	6.4183510236962536e-04	9.9999857981963269e-01
LFI28S	1.6633788116048607e-03	-6.6629002345089925e-04	9.9999839461297824e-01
LFI28M	1.5571200481047094e-03	-6.4144198187461837e-04	9.9999858196366442e-01

By using this characteristic vector the calculation of the convolved dipole is simply defined by a dot product of the vector $\mathbf{S}$by the dipole axis rotated in the beam reference frame.

$$\Delta T(t) = \mathbf{S}^T \mathcal{U}(t) \mathbf{D}_E$$

Binning

In order to simplify the computation and to reduce the amount of data used in the calibration procedure the data are phase binned in map with Nside 256. During phase binning all the data with flagged for maneuvers, planets, gaps and the ones flagged in Level1 analysis as not recoverable are discharged.

Fit

The first order calibration values are given by a Least Square Fit between the signal and the dipole. For each pointing a gain (g_k) and an offset (b_k) values are computed minimizing:

$$\chi^2 = \sum_{i \in k} \frac{[\Delta V(t_i) - \Delta V_m(t_i | g_k, b_k)]^2}{rms_i^2}$$

The sum includes samples outside a Galactic mask.

Mademoiselle

The largest source of error in the fit arises from unmodeled sky signal $\Delta T_a$from CMB anisotropy. To correct this we iteratively project the calibrated data (without the dipole) onto a map, scan this map to produce a new TOD with astrophysical signal removed, and finally run a simple destriping algorithm to find the corrections to the gain and offset factors.

To reduce the impact of the noise during the iterative procedure the sky estimation is built using data from both radiometers of the same horn.

Smoothing

To improve accuracy given by the iterative algorithm and remove noise from the solution a smoothing algorithm must be performed. We used two different algorithms: OSG for the 44 and 70 GHz radiometers, and DV/V Fix for the 30 GHz. The reasons behind this choice can be found in #planck2013-p02b Planck-2013-V [4].

OSG

OSG is a python code that performs smoothing with a 3 step algorithm.

The first step is a Moving Average Window: the gain and offset factors are streams containing one value for each pointing period, that we call dipole fit raw streams. The optimized window has a length of 600 pointing periods.

The second step is a wavelet algorithm, using pywt (Discrete Wavelet Transform in Python [5]) libraries. Both dipole fit raw streams and averaged streams are denoised using wavelets of the Daubechies family extending the signals using symmetric-padding.

The third step is the combination of dipole fit raw and averaged denoised signal using knowledge about the instrument performance during the mission.

4 K total-power and Fix

For the 30 GHz channels we used 4K total-power to track gain changes. The theory and explanation of the choice can be found in #planck2013-p02b Planck-2013-V [4].

The algorithm uses V_{load}mean values computed during differentiation and raw gains as they are after iterative calibration, performing a linear weighted fit between the two streams using as weight the dipole variance in single pointing periods. The fit is a single parameter fit, so the offsets are put to zero in this smoothing method. It uses the gsl libraries.

In addition to the smoothing, to better follow sudden gain changes due to instrument configuration changes, a fix algorithm is implemented. The first step is the application of the 4k total-power smoothed gains to the data and the production of single radiometer maps in the periods between events. The resulting maps are then fit with dipole maps covering the same period of time producing two factor for each radiometer: $corrM$is the result of the fit using the main radiometer and $corrS$the one coming from the side radiometer. The correction to be applied to the gain values is then computed as:

$$corr = \frac{1}{1 + \frac{corrM + corrS}{2}}$$

Gain Application

The last step in TOI processing is the creation of the calibrated stream. For each sample we have:

where t is the time and k is the pointing period. $convDip$is the CMB Dipole convolved with the beam.

Noise

This pipeline step aims at the reconstruction of the noise parameters from calibrated flight TOI. The goal is two-folds: one the one side we need to know the actual noise properties of our instrument in order to properly take them into account especially during the following processing and analysis steps like map-making and power spectrum estimation. On the other side evaluation of noise properties along the instrument life-time is a way to track down possible variations, anomalies and general deviations from the expected behaviour.

Operations

Noise estimation is performed on calibrated data and since we would like to track possible noise variations along mission life-time, we select data in chunks of 5 ODs (Operational Days). These data are processed by the ROMA Iterative Generalized Least Square (IGLS) map-making algorithm which includes a noise estimation tool. In general an IGLS map-making is a quite consuming in terms of time and resources required. However the length of the data is such that running on the DPC cluster in very short time (~1-2 minutes).

The method implemented can be summerized as follows. We model the calibrated TOI as

$\mathbf{\Delta T} = \mathbf{P} \mathbf{m} + \mathbf{n}$

where $\mathbf{n}$ is the noise vector and $\mathbf{P}$ is the pointing matrix that links a pixel in the map $\mathbf{m}$ with a sample in the TOI $\mathbf{d}$. The zero-th order estimation of the signal is obtained simply rebinning TOI into a map. Then an iterative approach follows in which both signal and noise are estimated according to

$\mathbf{\hat{n}_i} = \mathbf{\Delta T} - \mathbf{P\hat{m}_i}$

$\mathbf{\hat{m}_{i+1}} = \mathbf{(P^T\hat{N}_i^{-1}P)^{-1}P^T\hat{N}_i^{-1}\Delta T}$

where $\mathbf{\hat{N}_i}$ is the noise covariance matrix in time domain out from iteration $i$. After three iterations convergence is achieved.

We then perform an FFT (Fast Fourier Transform) on the noise time stream out from the iterative approach and then fit the resulting spectrum.

Fitting Pipeline

In the very first release of Planck data, once noise spectra were extracted a simply log-periodogram fitting approach was applied to derive the most important noise parameters (white noise level, knee-frequency and slope of the low-frequency noise component). However during mission life-time there were some specific events (e.g. the switch over of the sorption coolers) that we expect were able to cause variation in instrument behaviour and hence in its noise properties. In this respect we have improved our fitting pipeline adding a Monte Carlo Markov Chain approach to estimate noise parameters.

MCMC approach

This new approach allows us to improve our noise model. Indeed this can be parametrized by the usual combination of white plus $1/f$noise

$$P(f) = \sigma^2 \left[1 + \left(\frac{f}{f_k}\right)^{\beta}\right]$$

with three basic noise parameters. However it is also possible to work with a functional form with two more parameters as

$$P(f) = \sigma^2 \left[1 + \left(\frac{f}{f_{k1}}\right)^{\beta_1} + \left(\frac{f}{f_{k2}}\right)^{\beta_2}\right]$$

This latter could be useful when there are clearly two different behaviour in the low-frequency part of the spectrum where, beside usual radiometric $1/f$noise, appears signature of thermal fluctuations induced noise.

As for the white noise part, this is, as before, computed making a simple average of noise spectrum on the last 10% of frequency bins. This percentage works well for almost all radiometers at 44 and 70 GHz but it is indeed quite delicate for the 30 GHz radiometers which show typical values of knee-frequency around 100 mHz and, therefore, require a smaller number to get an un-biased white noise estimation. Once white noise is computed, the code creates Markov Chains for the other parameters. Discarding the burn-in period of the chains we can directly get from the chain samples distribution, the expected value and variance of each noise parameters sampled.

The left panel of the following Figure shows a typical spectrum at 70 GHz with superimposed the simple log-periodogram fit (purple line) and the new MCMC derived spectrum (blue line). The right panel instead shows distribution for knee-frequency and slope derived from the example spectrum.

The final noise parameters

As already reported we know that during the nominal operations there was a quite dramatic change in LFI induced by the switch over of the two sorption coolers and particularly we expect to see the effect of degradation of the performance of the first sorption cooler and the onset of the redundant one.

In the following figure we report a set of noise frequency spectra for three LFI radiometers (LFI28M, LFI24S and LFI18M) from the beginning of the operation till the time of the current data release. Some comments are in order. First of all the white noise level is extremely stable in all the three cases (but this is also true for all the LFI radiometer). Also knee-frequency and low-frequency slope are quite stable till OD 326. After that period spectra show a noise increase and two slopes for the low-frequency part which become more evident for spectra around OD 366 and OD 466 where the first cooler starts to be less effective and produces low-frequency thermal noise. After the switch-over to the redundant cooler data still present (the very last spectrum) thermal noise at very low-frequency. This behaviour is almost present in all radiometers with different trends ranging from the small effect shown by LFI24S to more prominent effect as shown by LFI28M and LFI18M.

References

<biblio force=false>

1. References

</biblio>

References

[1] http://www.rssd.esa.int/doc_fetch.php?id=3167991&page=1

[2] http://www.gnu.org/software/gsl/

[3] http://ssd.jpl.nasa.gov/?horizons

[4] http://www.rssd.esa.int/doc_fetch.php?id=3168068&page=1

[5] http://www.pybytes.com/pywavelets/

Detector pointing

Detector Pointing

Detector pointing reconstruction requires knowledge of the spacecraft attitude and the location of the horns in the focal plane. The AHF (Attitude History File, see Pointing performance) gives the orientation of the spacecraft spin axis in quaternions sampled at 8 Hz, as well as the beginning and the end times for each pointing period.

The computation needs to initialize the horn and beam information: it reads the θ, $\phi$and ψposition and rotation angles from the instrument database and builds the rotation matrix from the spin axis to the focal plane ($ax2det$). At the same time the major corrections are initialized.

Wobble Angle

Wobble angles are the angles which defines the relationship between the Principal Axis Reference Frame of Planck and the Body Reference Frame of Planck, both of which have their origin in the Planck Baricenter (ACMS, AHF-ICD).

Pointings are determined by a set of rotations converting coordinates in the STR reference frame to ecliptical reference frame, i.e. defining the rotation matrix $R_{ecl,str}$. The matrix can be decomposend in a sequence of matrix mutiplications:

$$R_{ecl,str} = R_{ecl,A} R_{A,B} R_{B,str}$$

here we used $R_{rfb,rfa}$to denote transformation from Rerference Frame RFA to Reference Frame RFB, and $R_{rfa,rfb} = R^{-1}_{rfb,rfa}$.

The $R_{B,str}$converts from STR coordinates to Body Reference Frame coordinates, it is a constant matrix.

$$\begin{bmatrix} \cos\beta & 0 & -\sin\beta \\ 0 & 1 & 0 \\ \sin\beta & 0 & \cos\beta \end{bmatrix}$$

where $\beta = 85\,\mathrm{deg}$is the STR boresight angle assumed to be constant and aligned with the telescope LOS, but this is not the case. The STR is located on the SVM, at about 1.5 m from the origin of the Body reference frame, a change in its position of 0.15 mm will result in a change of its orientation of about 10^{-4}radiants about 20 arcsec.

There is no way to measure directly those changes. So the effect is that to have an apparent change in the ψ_1, ψ_2 (tilt angles as defined in the AHF) and ψ_3(azimuth angle as defined in the AHF) angles: the reason is apparent immediately when looking at the way a perturbation in STR reference frame orientation propagates.

AHF provides wobble angle measures at 1 minute (ψ_1, ψ_2) and one OD (ψ_3) rate. Indeed $\psi_3$is provided at each pointing period but measures within each given OD are constant.

Assuming to have quaternions represented by rotation matrix $R_{ecl,B}(t)$at a time t, and assuming to have representative values of true wobble angles $\psi_{1,0}$, $\psi_{2,0}$, $\psi_{3,0}$and a way to estimate the apparent $\delta\psi_1(t)$, $\delta\psi_2(t)$, $\delta\psi_3(t)$it is possible to remove the apparent effect.

With the available information it can be done for $\psi_1$and ψ_2.

The correction algorithm initializes two rotation matrices as references using $\psi_1$and $\psi_2$from the first pointing period of the nominal mission:

$$R_{psi1} = \begin{bmatrix} \cos\psi_{1,ref} & \sin\psi_{1,ref} & 0 \\ -\sin\psi_{1,ref} & \cos\psi_{1,ref} & 0 \\ 0 & 0 & 1 \end{bmatrix}$$

$$R_{psi2} = \begin{bmatrix} \cos\psi_{2,ref} & 0 & -\sin\psi_{2,ref} \\ 0 & 1 & 0 \\ \sin\psi_{2,ref} & 0 & \cos\psi_{2,ref} \end{bmatrix}$$

Then, for each pointing period, builds two correction matrices using $\psi_1$and $\psi_2$as provided by the AHF in the Observation section:

$$R^T_{psi1} = \begin{bmatrix} \cos\psi_1 & -\sin\psi_1 & 0 \\ \sin\psi_1 & \cos\psi_1 & 0 \\ 0 & 0 & 1 \end{bmatrix}$$

$$R^T_{psi2} = \begin{bmatrix} \cos\psi_2 & 0 & \sin\psi_2 \\ 0 & 1 & 0 \\ -\sin\psi_2 & 0 & \cos\psi_2 \end{bmatrix}$$

From these matrices the correction matrix is build:

$$R = R^T_{psi1} R^T_{psi2} R_{psi2} R_{psi1}$$

Each quaternion of the AHF is finally corrected using R.

Stellar Aberration

The corrected quaternions are interpolated using Spherical Linear Interpolation algorithm and transformed in cartesian vector, which we call DPT. For each sample the stellar aberration correction is applied:

$$DPT = DPT - \frac{v_{sat}}{c}$$

where $v_{sat}$is the satellite velocity and $c$is the speed of light. After this operation the vector is normalized.

Finally the cartesian vetor is converted in Ecliptic Coordinates, the detector pointing.

Beam Rotation

The rotation of the beam with respect the north direction is the ψangle and is computed rotating the corrected quaternions Qusing:

$$R = R_\theta R_\phi Qax2det$$

The resulting rotation matrix represents the rotation of the beam, the \psi angle is then:

$$\psi = -\arctan(R[0][1], R[0][0])$$

Beams

Overview

LFI is observing the sky with 11 pairs of beams associated with the 22 pseudo-correlation radiometers. Each beam of the radiometer pair (Radiometer Chain Assembly - RCA) is named as LFIXXM or LFIXXS. XX is the RCA number ranging from 18 to 28; M and S are the two polarization namely main-arm and side-arm of the Orthomode transducers #darcangelo2009b (see also LFI naming convention).

Main Beams and Focal Plane calibration

As the focal plane calibration we refer to the determination of the beam pointing parameters in the nominal Line of Sight (LOS) frame through main beam measurments using Jupiter transits. the parametes that characterise the beam pointing are the following:

- THETA_UV (θ_{uv})
- PHI_UV (ϕ_{uv})

They are calculated starting from u,v coordinates derived form the beam reconstruction algorithm as

$\theta_{uv} = \arcsin(u^2+v^2)$

$\phi_{uv} = \arctan(v/u)$

Two additional angles are used to characterize the beams in the RIMO:

- PSI_UV (ψ_{uv})
- PSI_POL (ψ_{pol})

ψ_{uv} and ψ_{pol} are **not** derived from measurements but they are extimated form **optical simulations**. They are the quantities that represent the polarization direction of each beam, in the following approximation: **the M- and S- beams of the same RCA point at the same direction on the sky**.

The main beams are characterised by 2 method:

- elliptical (or bivariate) gaussian fit as in #[planck2011-1-6] with modification explained in #[planck2013-p02d]

Planck-2013-IV [1]. This method is used to determine

  - the beam centre
  - the average full width half maximum defined as $\sqrt{FWHM_{max}\cdot FWHM_{min}}$
  - the beam ellipticity defined as $FWHM_{max}\over{FWHM_{min}}$
  - the beam tilting, ψ_{ell}, with respect the u-axis.
- Electromagnetic simulation (using GRASP Physical Optics code) by appropriately tuning the Radio Frequency Flight Model (RFFM) #tauber2010b. The Radio Frequency Tuned Model, called RFTM, was implemented to fit the beam data with electromagnetic model. It is derived as follow:
  - the Focal plane unit electromagnetic model has shifted by 3.5mm toward the secondary mirror;
  - All the simulated beams where monochromatic, i.e calculated at a single frequency called Optical Center Frequency (OCF). For the RFTM model the OCF has been chosen at 28.0, 44.0, 70.0. In fact the optical and radiometer bandshapes as reported in #zonca2009 demonstrates that for the 30 GHz channel, the radiometer responses are better described by a central frequency closer to 28 GHz with respect to the nominal one, whereas for the other two frequency channels the OCF is close to the nominal one.
  - each feed horn phase centre has been moved alogn horn axis to optimize the match between simulations and data. The optimization was obtained by minimizing the variance according to the following definition: If $B_s[u,v]$ is the peak-normalized scanning beam matrix (for semplicity we use here (u,v) coordinates also

as indexes of the beam matrix) and $B_o[u,v]$ is the smeared peak-normalized simulated GRASP beam, the variance, $\sigma$, can be evaluated for each beam:

\begin{eqnarray} \label{eqsigma} \sigma &=& {\sum_{u,v}{(f[u,v] - \overline{f})^2}}\cdot {1\over N} \\ f[u,v]&=&w[u,v] \cdot (B^{dB}_s(u,v)- B^{dB}_o(u,v)) \\ w[u,v]&=&\sqrt{T[u,v]} \end{eqnarray} where also $T[u,v]$ is the temperature or the scanning beam not normalized to peak, and $N$ is the number of points considered in the comparison so that the number of point in the (u,v) plane. The parameter $\sigma$, as already said, is the variance of the difference between two beams weighted by the measured beam itself. For each beam the variance has computed computed down to $-15$dB from beam peak to avoid bias due to noise and background. The comparison between the simulated RFTM beams and the data are reported in #planck2013-p02d Planck-2013-IV [1].

Effective beams

The **effective beam** is the average of all scanning beams pointing at a certain direction within a given pixel of the sky map for a given scan strategy. It takes into account the coupling between azimuthal asymmetry of the beam and the uneven distribution of scanning angles across the sky. It captures the complete information about the difference between the true and observed image of the sky. They are, by definition, the objects whose convolution with the true CMB sky produce the observed sky map.

The full algebra involving the effective beams for temperature and polarisation was presented in [Mitra, Rocha, Gorski et al. [1]] #mitra2010. Here we summarise the main results. The observed temperature sky $\widetilde{\mathbf{T}}$is a convolution of the true sky $\mathbf{T}$and the effective beam $\mathbf{B}$:

where

$t$is time samples, $A_{ti}$is 1if the pointing direction falls in pixel number i, else it is 0, $\mathbf{p}_t$represents the exact pointing direction (not approximated by the pixel centre location), and $\hat{\mathbf{r}}_j$is the centre of the pixel number j, where the scanbeam $b(\hat{\mathbf{r}}_j, \hat{\mathbf{p}}_t)$is being evaluated (if the pointing direction falls within the cut-off radius of $\sim 2.5\times$ FWHM.

The algebra is a bit more involved for polarised detectors. The observed stokes parameters at a pixel i, $(\widetilde{I}, \widetilde{Q}, \widetilde{U})_i$, are related to the true stokes parameters $(I, Q, U)_i$, by the following relation:
where the polarised effective beam matrix

and $\mathbf{w}_t$and $\mathbf{W}(\hat{\mathbf{r}}_j, \hat{\mathbf{p}}_t)$are the the polarisation weight vectors, as defined in \cite{mitra2010}.
The task is to compute $B_{ij}$for temperature only beams and the 3×3matrices $\mathbf{B}_{ij}$for each pixel i, at every neighbouring pixel $j$that fall within the cut-off radius around the the center of the $i^{\rm th}$pixel.
The effective beam is computed by stacking within a small field around each pixel of the HEALPix sky map. Due to the particular features of Planck scanning strategy coupled to the beam asymmetries in the focal plane, and data processing of the bolometer and radiometer TOIs, the resulting Planck effective beams vary over the sky.

FEBeCoP, given information on Planck scanning beams and detector pointing during a mission period of interest, provides the pixelized stamps of both the Effective Beam, EB, and the Point Spread Function, PSF, at all positions of the HEALPix-formatted map pixel centres.

Production process

The methodology for computing effective beams for a scanning CMB experiment like Planck was presented in [Mitra, Rocha, Gorski et al. [1]].

FEBeCoP, or Fast Effective Beam Convolution in Pixel space, is an approach to representing and computing effective beams (including both intrinsic beam shapes and the effects of scanning) that comprises the following steps:

- identify the individual detectors' instantaneous optical response function (presently we use elliptical Gaussian fits of Planck beams from observations of planets; eventually, an arbitrary mathematical representation of the beam can be used on input)
- follow exactly the Planck scanning, and project the intrinsic beam on the sky at each actual sampling position
- project instantaneous beams onto the pixelized map over a small region (typically <2.5 FWHM diameter)
- add up all beams that cross the same pixel and its vicinity over the observing period of interest
- create a data object of all beams pointed at all N'_pix_' directions of pixels in the map at a resolution at which this precomputation was executed (dimension N'_pix_' x a few hundred)
- use the resulting beam object for very fast convolution of all sky signals with the effective optical response of the observing mission

Computation of the effective beams at each pixel for every detector is a challenging task for high resolution experiments. FEBeCoP is an efficient algorithm and implementation which enabled us to compute the pixel based effective beams using moderate computational resources. The algorithm used different mathematical and computational techniques to bring down the computation cost to a practical level, whereby several estimations of the effective beams were possible for all Planck detectors for different scanbeam models and different lengths of datasets.

Pixel Ordered Detector Angles (PODA)

The main challenge in computing the effective beams is to go through the trillion samples, which gets severely limited by I/O. In the first stage, for a given dataset, ordered lists of pointing angles for each pixels---the Pixel Ordered Detector Angles (PODA) are made. This is an one-time process for each dataset. We used computers with large memory and used tedious memory management bookkeeping to make this step efficient.

effBeam

The effBeam part makes use of the precomputed PODA and unsynchronized reading from the disk to compute the beam. Here we tried to made sure that no repetition occurs in evaluating a trigonometric quantity.

One important reason for separating the two steps is that they use different schemes of parallel computing. The PODA part requires parallelisation over time-order-data samples, while the effBeam part requires distribution of pixels among different computers.

Computational Cost

The whole computation of the effective beams has been performed at the NERSC Supercomputing Center. In the table below it isn displayed the computation cost on NERSC for nominal mission both in terms of CPU hrs and in Human time.

Computational cost for PODA, Effective Beam and single map convolution.The cost in Human time is computed using an arbitrary number of nodes/core on Carver or Hopper NERSC Supercomputers

Channel	030	044	070
PODA/Detector Computation time (CPU hrs)	85	100	250
PODA/Detector Computation time (Human minutes)	7	10	20
Beam/Channel Computation time (CPU hrs)	900	2000	2300
Beam/Channel Computation time (Human hrs)	0.5	0.8	1
Convolution Computation time (CPU hr)	1	1.2	1.3
Convolution Computation time (Human sec)	1	1	1
Effective Beam Size (GB)	173	123	28

The computation cost, especially for PODA and Convolution, is heavily limited by the I/O capacity of the disc and so it depends on the overall usage of the cluster done by other users.

Inputs

In order to fix the convention of presentation of the scanning and effective beams, we show the classic view of the Planck focal plane as seen by the incoming CMB photon. The scan direction is marked, and the toward the center of the focal plane is at the 85 deg angle w.r.t spin axis pointing upward in the picture.

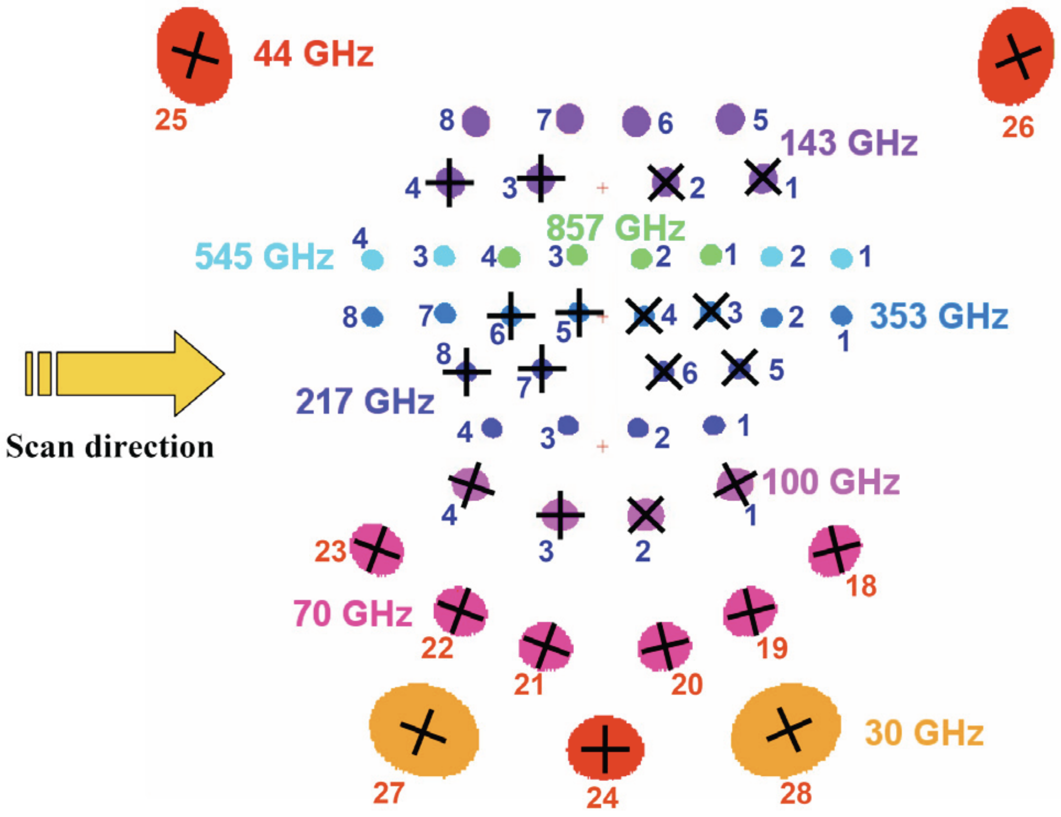
44 GHz
25
26
8
7
6
5
143 GHz
4
3
2
1
857 GHz
545 GHz
4
3
4
3
2
1
2
1
8
7
6
5
4
3
2
1
353 GHz
8
7
6
5
217 GHz
Scan direction
4
3
2
1
100 GHz
4
3
2
1
23
18
70 GHz
22
19
21
20
30 GHz
27
24
28

Planck Focal Plane

The Focal Plane DataBase (FPDB)

The FPDB contains information on each detector, e.g., the orientation of the polarisation axis, different weight factors, (see the instrument RIMOs):

- The LFI RIMO [2]

The scanning strategy

The scanning strategy, the three pointing angle for each detector for each sample: Detector pointings for the nominal mission covers about 15 months of observation from Operational Day (OD) 91 to OD 563 covering 3 surveys and half.

The scanbeam

The scanbeam modeled for each detector through the observation of planets. Which was assumed to be constant over the whole mission, though FEBeCoP could be used for a few sets of scanbeams too.

- LFI: GRASP scanning beam - the scanning beams used are based on Radio Frequency Tuned Model (RFTM) smeared to simulate the in-flight optical response.

(see the instrument RIMOs)

- The LFI RIMO [2]

Beam cutoff radii

- N times the geometric mean of FWHM of all detectors in a channel, where N=2.5 for all LFI frequency channels.

Map resolution for the derived beam data object

- $N_{side} = 1024$for all LFI frequency channels.

Comparison of the images of compact sources observed by Planck with FEBeCoP products

We show here a comparison of the FEBeCoP derived effective beams, and associated point spread functions,PSF (the transpose of the beam matrix), to the actual images of a few compact sources observed by Planck, for 30GHz frequency channel, as an example. We show below a few panels of source images organized as follows:

- Row #1- DX9 images of four ERCSC objects with their galactic (l,b) coordinates shown under the color bar
- Row #2- linear scale FEBeCoP PSFs computed using input scanning beams, Grasp Beams, GB, for LFI and B-Spline beams,BS, Mars12 apodized for the CMB channels and the BS Mars12 for the sub-mm channels, for HFI (see section Inputs below).
- Row #3- log scale of #2; PSF iso-contours shown in solid line, elliptical Gaussian fit iso-contours shown in broken line

Histograms of the effective beam parameters

Here we present histograms of the three fit parameters - beam FWHM, ellipticity, and orientation with respect to the local meridian and of the beam solid angle. The shy is sampled (pretty sparsely) at 768 directions which were chosen as HEALpix nside=8 pixel centers for LFI to uniformly sample the sky.

Where beam solid angle is estimated according to the definition: **4pi* sum(effbeam)/max(effbeam)** ie $4\pi \sum(B_{ij})/max(B_{ij})$

Sky variation of effective beams solid angle and ellipticity of the best-fit Gaussian

- The discontinuities at the Healpix domain edges in the maps are a visual artifact due to the interplay of the discretized effective beam and the Healpix pixel grid.

Statistics of the effective beams computed using FEBeCoP

We tabulate the simple statistics of FWHM, ellipticity (e), orientation (ψ) and beam solid angle, (Ω), for a sample of 768 directions on the sky for LFI data. Statistics shown in the Table are derived from the histograms shown above.

- The derived beam parameters are representative of the DPC NSIDE 1024 healpix maps (they include the pixel window function).
- The reported FWHM_eff are derived from the beam solid angles, under a Gaussian approximation. These are best used for flux determination while the the Gaussian fits to the effective beam maps are more suited for source identification.

Statistics of the FEBeCoP Effective Beams Computed with the BS Mars12 apodized for the CMB channels and oversampled

frequency	**mean(fwhm) [arcmin]**	**sd(fwhm) [arcmin]**	**mean(e)**	**sd(e)**	**mean(ψ) [degree]**	**sd(ψ) [degree]**	**mean(Ω) [arcmin ^{2}]**	**sd(Ω) [arcmin ^{2}]**	**FWHM_eff [arcmin]**
030	32.239	0.013	1.320	0.031	-0.304	55.349	1189.513	0.842	32.34
044	27.005	0.552	1.034	0.033	0.059	53.767	832.946	31.774	27.12
070	13.252	0.033	1.223	0.026	0.587	55.066	200.742	1.027	13.31

Beam solid angles for the PCCS

- Ω_{eff}- is the mean beam solid angle of the effective beam, where beam solid angle is estimated according to the definition: $4\pi * sum(effective_{beam})/max(effective_{beam})$, i.e. as an integral over the full extent of the effective beam, i.e. $4\pi \sum(B_{ij})/max(B_{ij})$.
- from Ω_{eff}we estimate the $fwhm_{eff}$, under a Gaussian approximation - these are tabulated above
  - $\Omega^{(1)}_{eff}$is the beam solid angle estimated up to a radius equal to one $fwhm_{eff}$and $\Omega^{(2)}_{eff}$up to a radius equal to twice the $fwhm_{eff}$.
    - These were estimated according to the procedure followed in the aperture photometry code for the PCCS: if the pixel centre does not lie within the given radius it is not included (so inclusive=0 in query disc).

Band averaged beam solid angles

Band	Ω_{eff}[arcmin ^{2}]	**spatial variation** [arcmin ^{2}]	$\Omega^{(1)}_{eff}$[arcmin ^{2}]	**spatial variation-1** [arcmin ^{2}]	$\Omega^{(2)}_{eff}$[arcmin ^{2}]	**spatial variation-2** [arcmin ^{2}]
30	1189.513	0.842	1116.494	2.274	1188.945	0.847
44	832.946	31.774	758.684	29.701	832.168	31.811
70	200.742	1.027	186.260	2.300	200.591	1.027

Monte Carlo simulations

FEBeCoP software enables fast, full-sky convolutions of the sky signals with the Effective beams in pixel domain. Hence, a large number of Monte Carlo simulations of the sky signal maps map convolved with realistically rendered, spatially varying, asymmetric Planck beams can be easily generated. We performed the following steps:

- generate the effective beams with FEBeCoP for all frequencies for Nominal Mission data
- generate 100 realizations of maps from a fiducial CMB power spectrum
- convolve each one of these maps with the effective beams using FEBeCoP
- estimate the average of the Power Spectrum of each convolved realization, C_ℓ^{out}, and 1 sigma errors

As FEBeCoP enables fast convolutions of the input signal sky with the effective beam, thousands of simulations are generated. These Monte Carlo simulations of the signal (might it be CMB or a foreground (e.g. dust)) sky along with LevelS+Madam noise simulations were used widely for the analysis of Planck data. A suite of simulations were rendered during the mission tagged as Full Focalplane simulations.

Window Functions

The **Transfer Function** or the **Beam Window Function** $W_\ell$relates the true angular power spectra $C_\ell$with the observed angular power spectra $\widetilde{C}_\ell$:

Note that, the window function can contain a pixel window function (depending on the definition) and it is {\em not the angular power spectra of the scanbeams}, though, in principle, one may be able to connect them though fairly complicated algebra.

The window functions are estimated by performing Monte-Carlo simulations. We generate several random realisations of the CMB sky starting from a given fiducial C_ℓ, convolve the maps with the pre-computed effective beams, compute the convolved power spectra $C_\ell^{\mathbf{conv}}$, divide by the power spectra of the unconvolved map $C_\ell^{\mathbf{in}}$and average over their ratio. Thus, the estimated window function

For subtle reasons, we perform a more rigorous estimation of the window function by comparing $C_\ell^{conv}$with convolved power spectra of the input maps convolved with a symmetric Gaussian beam of comparable (but need not be exact) size and then scaling the estimated window function accordingly.

Beam window functions are provided in the RIMO.

Beam Window functions, Wl, for LFI channels

Sidelobes

There is no direct measurements of sidelobes for LFI. The sidelobe pattern for LFI was been simulated using GRASP9 Multi-reflector GTD. We used the RFTM electromagnetic model. Seven beams for each radiometer have been computed in spherical polar cuts with a step of 0.5 degrees both in theta and phi. The beams have been computed in the same frames used for the main beams. The intermediate beam region (theta < 5 degrees) has been replaced with null values.

- In the computation we considered:
  - the direct field from the feed
  - the 1st order contributions: Bd, Br, Pd, Pr, Sd, Sr, Fr
  - the 2nd order contributions SrPd and SdPd

where B=buffle', P=primary reflector, S=secondary reflector, F=Focal Plane Unit Box. and where d=diffraction, r=reflection. For example Br, means that we considered in the calculation the reflection on the telescope baffle system.

A refinement of the sidelobes model will be considered in a future release, taking into account more contributions together with Physical Optics models.

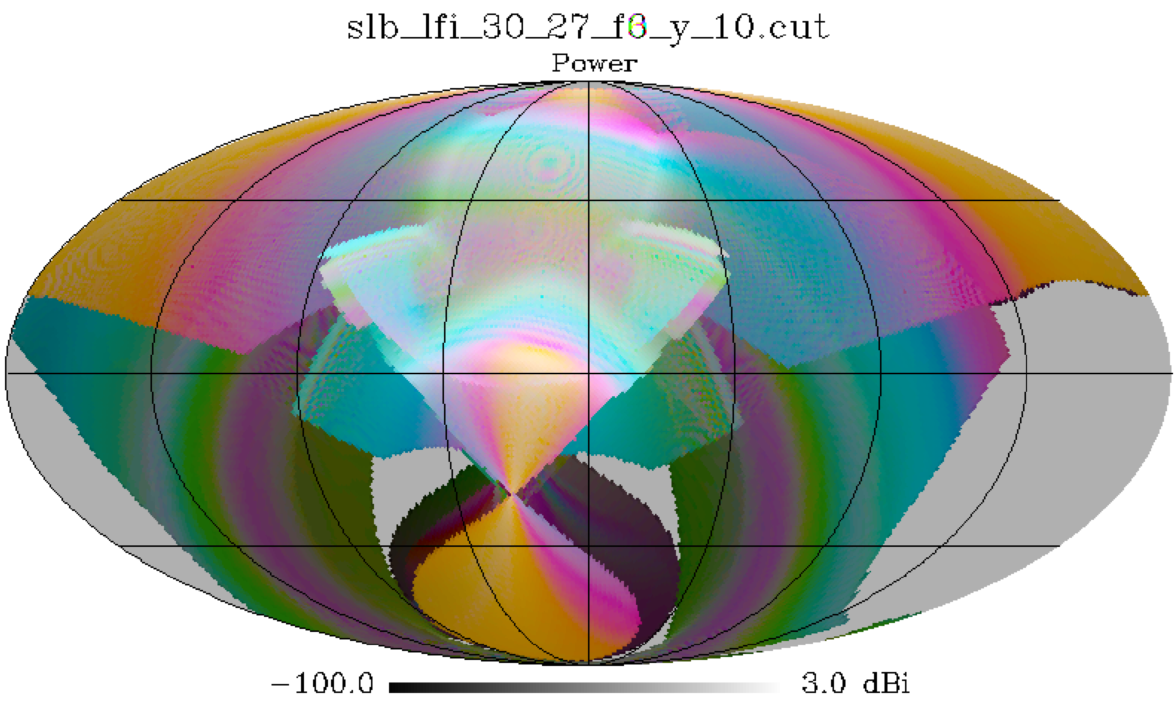

The image of the LFI27-M sidelobes is created as RGB picture where the red channel is the 27 GHz (f0), the green channel is the 30 GHz (f3), and the blue channel is the 33 GHz (f6). Because of the combined map does not show any wide white region, the sidelobe pattern change with frequency, as expected.

References

<biblio force=false>

1. References

</biblio>

References

[1] http://www.rssd.esa.int/doc_fetch.php?id=3168067&page=1
[2] http://pla.esac.esa.int/pla/aio/product-action?DOCUMENT.DOCUMENT_ID=LFI_RIMO_R1.12.fits

Map-making LFI

Map-making

The input of the map-making step consists of the calibrated timelines, along with the corresponding pointing information. The main output consists of temperature and polarization maps. An important part of the map-making step is the removal of correlated 1/f noise.

LFI maps were constructed with the Madam map-making code, version 3.7.4. The code is based on generalized destriping technique, where the correlated noise component is modeled as a sequence of constant offset, "baselines". The baseline solution is constrained by a noise filter. As auxiliary information the code produces a hit count map and a white noise covariance matrix. No beam information is used, but the signal is assigned to the pixel where the center of the beam falls.

In the first release the chosen baseline length was one second. This gives a good noise removal, without being computationally heavy. The noise filter was built according to the noise parameters listed in Table 1.

Flagged samples were excluded from the analysis. The galaxy region was masked out in the destriping phase, to reduce error arising from strong signal gradients. Radiometers were combined according to the horn-uniform weighting scheme to minimize systematics. The polarization component was included in the analysis, although only the temperature maps are released. A detailed description of the map-making procedure is given in planck2013-p02 Planck-2013-II [1]. See also section Frequency Maps.

The maps are in Healpix format, at resolution $N_{\rm side}$=1024, in nested pixeling scheme. Unobserved pixels are marked by a special value.

The released maps are in galactic coordinates. The conversion from ecliptic to galactic coordinate system is described by rotation matrix $

```
\newcommand{\Re}{\mathrm{Re}\,}
\newcommand{\pFq}[5](p) =  [ \mathbf{j_1}(p) - \mathbf{j_2}(p)] \ / \ \mathbf{w_{\rm hit}}(p)\,,$
```

with weights

$\mathbf{w_{hit}}(p) = \sqrt{ \mathbf{hit_{full}}(p) \left[\frac{1}{\mathbf{hit_1}(p)} +

```
      \frac{1}{\mathbf{hit_2}(p)} \right]}\,$.
```

Here $\mathbf{hit_{full}}(p) = \mathbf{hit_1}(p) + \mathbf{hit_2}(p)$ is the hit count at pixel p in the full map $\mathbf{m}$, while $\mathbf{hit_1}$ and $\mathbf{hit_2}$ are the hit counts of $\mathbf{j_1}$ and $\mathbf{j_2}$, respectively. The weight factor $\mathbf{w_{hit}}(p)$ is equal to 2 only in those pixels where $\mathbf{hit_1}(p) = \mathbf{hit_2}(p)$. In a typical pixel, $\mathbf{hit_1}(p)$ will differ slightly from $\mathbf{hit_2}(p)$ and hence the weight factor is $\mathbf{w_{hit}}(p) > 2$.

The half-ring difference maps $\mathbf{n_{m}}$ are the most direct measure of the noise in the actual maps. The other noise estimates (NCVM and noise Monte Carlo) rely on specific modelling of the noise and this modelling can be validated by comparing to the half-ring difference maps. However, the half-ring difference maps can only capture the noise that varies faster than half of the duration of the pointing period, i.e., the noise whose frequency is $f \gtrsim 1/20\,\mbox{min} = 0.85\,$mHz.

We calculated the noise maps $\mathbf{n_{m}}$, from half-ring jackknife maps for temperature (I) and polarization (Q and U) and as a first quality check of the maps (and as one of the tests of the whole data processing pipeline up to the maps) tested both numerically and visually that these noise maps divided pixel-by-pixel by square root of the white noise covariance maps were approximately Gaussian with variance near to unity. Temperature noise maps for the nominal survey and for the first and second sky surveys are shown in the next subsection. Further we calculated from the noise maps the temperature and polarization (E and B mode) auto-correlation and cross-correlation noise angular power spectra by anafast and compared to these the results from the white noise covariance matrices and from the noise Monte Carlo simulations. A similar comparison was made between downgraded half-ring noise maps, downgraded noise Monte Carlo maps and the low resolution noise covariance maps. Detailed results are presented in the Systematic Effects paper.

Examples of Half-ring Difference Maps and Noise Angular Power Spectra

Hit Count Weighted Half-ring Difference Maps

Here we show some hitcount weighted half-ring difference maps, i.e., noise maps for temperature. The columns are for different LFI frequencies: 30, 44, and 70 GHz. The rows are the nominal survey (a bit more than 1 year of observations), survey 1 (the first sky survey, approx first half a year of observations) and survey 2 (the second sky survey, approx the second half a year of observations). Some features are visible in particular in the galactic plane. These are due to "gradient leakage". (In regions where the gradient in the sky signal is very large even a tiny difference in the pointing of the first and second half of each pointing period causes the signal to "leak" to the half-ring difference map. In practice this is not a problem for noise estimation, since these regions - the galaxy, orion, crab nebula, etc - will be masked in the cosmology analysis.

Half-ring difference maps calculated at the native nside 1024 resolution. Columns: frequency (30, 44, 70 GHz), rows: sky survey (nominal, survey_1, survey_2).

Half-ring difference maps (the same as above, but) **smoothed** with 60 arcmin fwhm Gaussian. Columns: frequency (30, 44, 70 GHz), rows: sky survey (nominal, survey_1, survey_2).

Hit Count Weighted Half-ring Difference Maps Normalized by sqrt of white noise variance at each pixel

Now we show the same as above, but divided by the square root of the estimate of white noise variance in each pixel. These normalized noise maps should be approximately Gaussian with a unit variance (at the native resolution), apart from some stripes that are due to correlated (non-Gaussian) $1/f$noise. The large-scale $1/f$noise is more apparent in the smoothed version of the figure that follows after the native resolution version.

Normalized Half-ring difference maps calculated at the native nside 1024 resolution. Columns: frequency (30, 44, 70 GHz), rows: sky survey (nominal, survey_1, survey_2).

Normalized Half-ring difference maps (the same as above, but) **smoothed** with 60 arcmin fwhm Gaussian. Columns: frequency (30, 44, 70 GHz), rows: sky survey (nominal, survey_1, survey_2).

Noise Angular Power Spectra from Half-ring Difference Maps

The noise angular power spectra calculated by anafast from half-ring difference temperature maps and normalized by the sky coverage to estimate the noise level if there was a full sky coverage in order to make a comparison of different surveys easier. Columns: frequency (30, 44, 70 GHz). Colors: black = nominal, red = survey_1, blue = survey_2.

Comparison of Noise Calculated from Half-ring Difference and from Other Noise Estimates

Here we compare noise angular power spectra estimated from half-ring difference maps (RED) to the estimate from white noise covariance maps (BLUE) and the full noise Monte Carlo simulations (BLACK, top curve 16% quantile, middle curve 50% quantile, i.e., median, and bottom curve 84% quantile) - see the next section for the details of noise Monte Carlo.

High-ell average ($\ell = 1150..1800$) noise relative to the white noise estimate

The same as previous figures, but the noise comparison made from the high ell tails off the angular power spectra where the white noise dominates. We have taken the average of C_ℓ from the multipoles between 1150 and 1800, and subtracted the white noise estimate. Half-ring difference noise estimate is RED, the full noise Monte Carlo estimate is BLACK, and the white noise estimate from noise Monte Carlo is GREEN. The white noise estimate from the white noise covariance map (WNC), BLUE, has been subtracted from all the results.

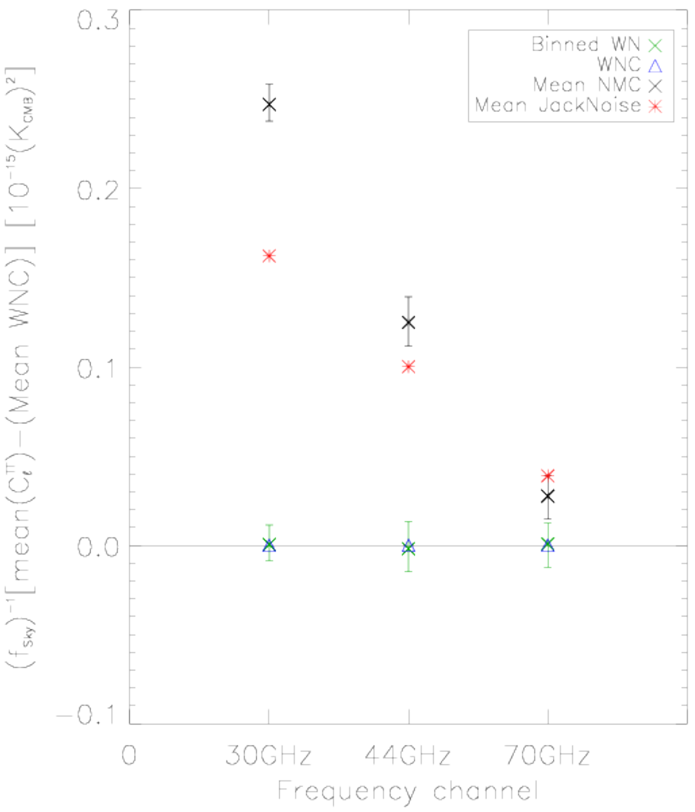

Nominal survey

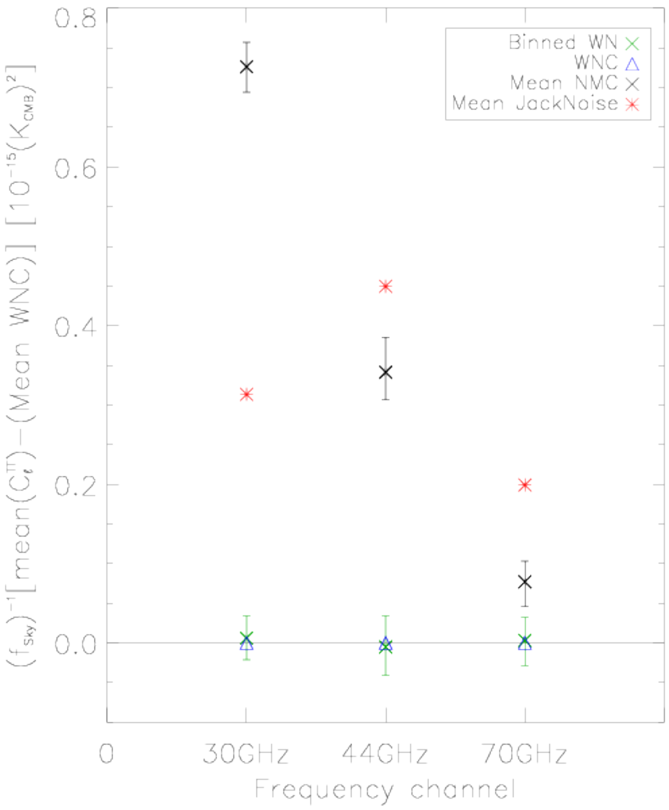
Binned WN
WNC
Mean NMC
Mean JackNoise
0.8
0.6
0.4
0.2
0.0
0
30GHz
44GHz
70GHz
Frequency channel
$(f_{sky})^{-1}[\mathrm{mean}(C_\ell^{TT})-(\mathrm{Mean\ WNC})]\ [10^{-15}(K_{CMB})^2]$

Survey_1

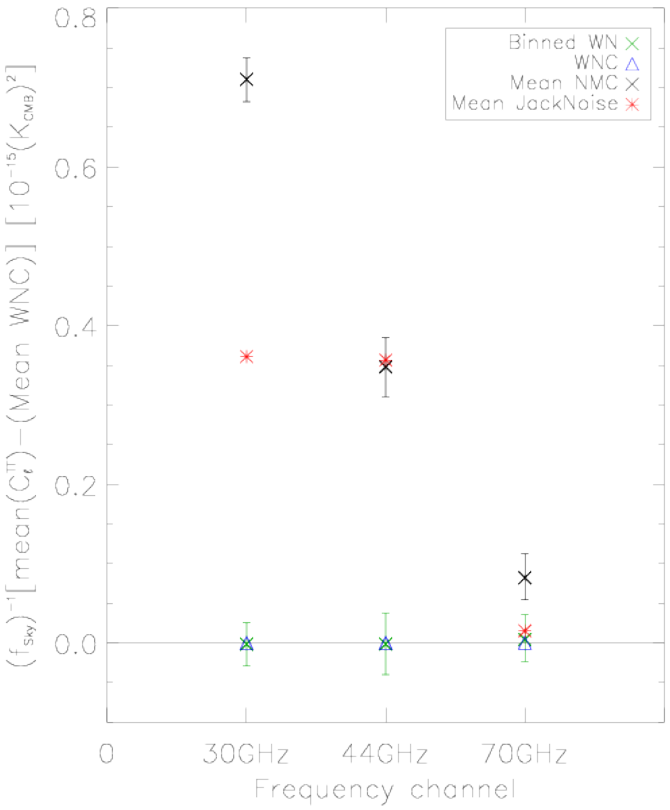

Survey_2

Noise Monte Carlo Simulation

Overview

Calculating and handling full pixel-to-pixel noise covariance matrices for Planck maps if feasible only at low resolution. To support the analysis of high-resolution maps, a Monte Carlo set of noise maps were produced. These maps were produced from noise timelines using the same map-making procedure as for the flight data. In the noise Monte Carlo it was possible to follow exactly the map-making procedure used for the flight maps, whereas for the calculation of noise covariance matrices some approximations had to be made. Such noise Monte Carlos were produced at two levels of the analysis: 1) LFI Monte Carlo (MC) as part of the LFI data processing, and 2) Full Focal Plane (FFP) Monte Carlo as part of the joint HFI/LFI data processing. This page describes the LFI noise MC. For the FFP MC, see HL-sims and Simulation data.

Inputs

The noise MC uses a three-parameter (white noise level (σ), slope, and knee frequency (f_knee)) noise model, where the noise consists of white noise and correlated ($1/f$) noise and the latter has a power spectrum

$$ P(f) = \frac{2\sigma^2}{f_\mathrm{sample}}\left(\frac{f}{f_\mathrm{knee}}\right)^\mathrm{slope} .$$

Here f_sample is the sampling frequency of the instrument. The noise parameters were determined separately for each radiometer as described in Noise, assuming they stayed constant over the mission.

The detector pointing was reconstructed from satellite pointing, focal-plane geometry, pointing correction (tilt angle), and sample timing, using Level-S simulation software. The same pointing solution (two focal planes) was used as for the LFI flight maps. Due to numerical accuracy, the detector pointing in the noise MC was not exactly the same as for the flight maps, but some data samples (of the order of one in a thousand) whose pointing was near the pixel boundary ended up assigned to the neighboring pixel. During the map-making from the flight data, a gap file was produced to represent the samples that were omitted from map-making due to various flags. This gap file was used in the noise MC instead of the full set of flags. The flight map-making used a destriping mask to exclude regions of strong signal gradients from contributing to the noise baseline solution. These same destriping masks (one for each frequency channel) were used for the noise MC.

Production

The noise was generated internally in the Madam map-making code using a Stochastic Differential Equation (SDE) method, to avoid time-consuming writing and reading noise timelines to/from disk. Noise for each pointing period was generated separately, using a double-precision random number seed constructed from the realization number, radiometer number, and the pointing period number; to allow regeneration of the same noise realization when needed. White noise and $1/f$ noise were generated separately.

The same map-making code (Madam) with the same parameter settings was used for the noise MC as for the flight maps. In addition to the destriped maps from the full noise (output maps), also binned maps from just the white noise (binned white noise maps) were produced; they represent the white noise part of the output maps. The difference between these two maps represent the residual correlated noise in the output map. The maps were made at Healpix resolution $N_\mathrm{side} = 1024$. For low-resolution analysis, these maps were downgraded (and the temperature part was smoothed) to $N_\mathrm{side} = 32$ and $N_\mathrm{side} = 16$.

In addition to frequency maps for the nominal survey, also single-survey and 70 GHz horn-pair maps were produced in the noise MC. For each case 102--1026 realizations were produced.

Usage

These noise Monte Carlo maps were used for a number of things in LFI data analysis. They were compared to the low-resolution noise covariance matrices, generated for the same noise model to see the impact of the approximations in the noise covariance matrix calculation. They were compared to the half-ring noise maps to see how well the noise model matches the noise in the flight maps (noting, however, that the half-ring noise maps misrepresent the lowest noise frequencies in the flight maps, and contain some effects from the sky signal). They were also used in power spectrum estimation and non-Gaussianity estimation.

Examples

As an example, we show below images of the first realization of the 70 GHz frequency map noise for the nominal survey. The images are in order: destriped full noise, binned white noise, residual correlated noise. Note that it is difficult to see any difference between the first too images, since the residual correlated noise is more than an order of magnitude below the white noise level. The units are CMB K.

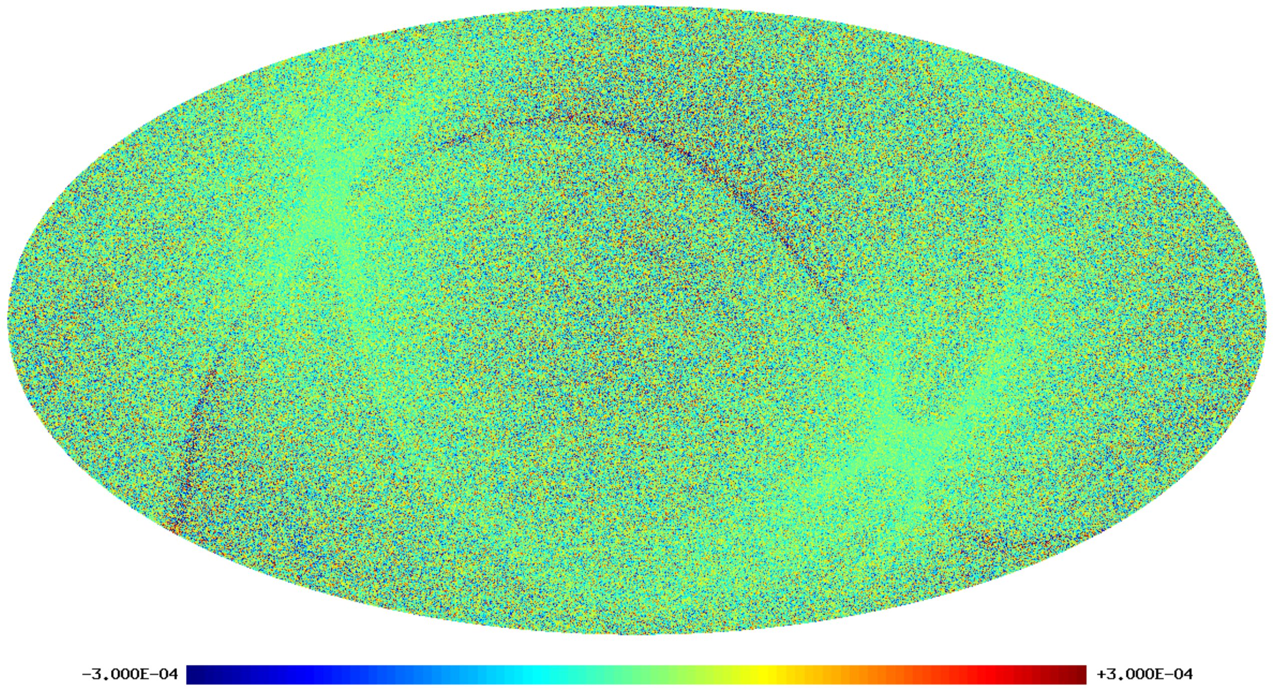

destriped full noise

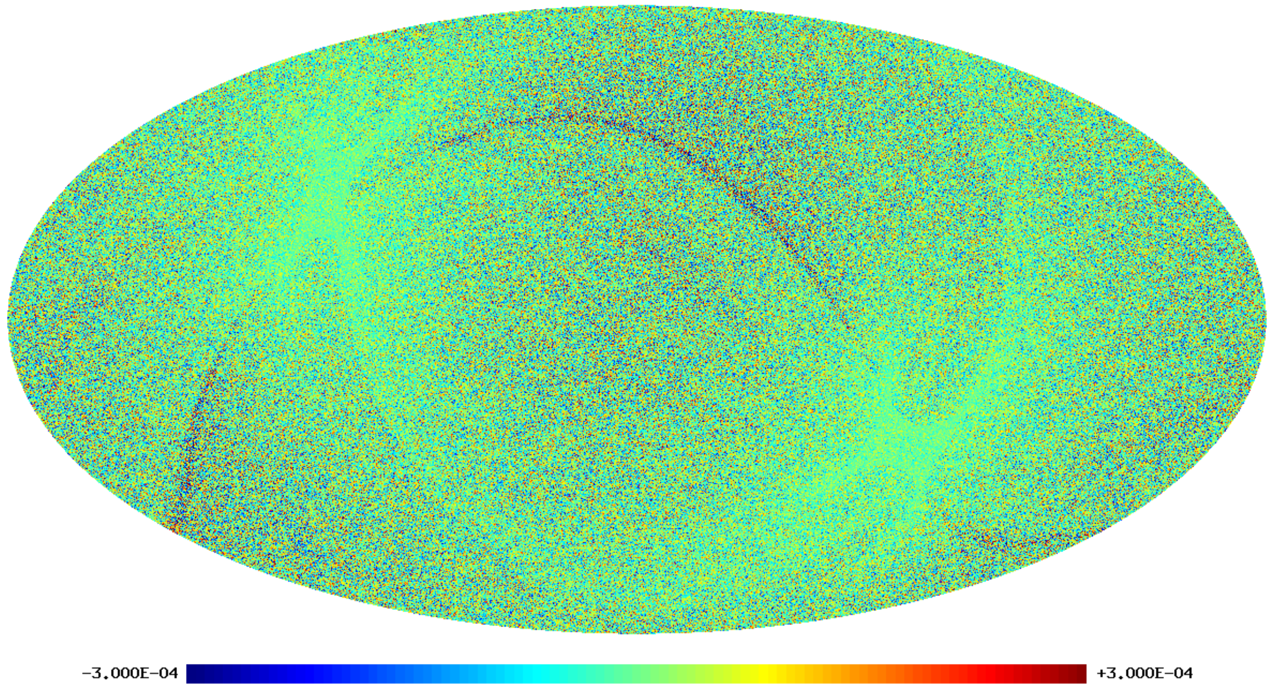

binned white noise

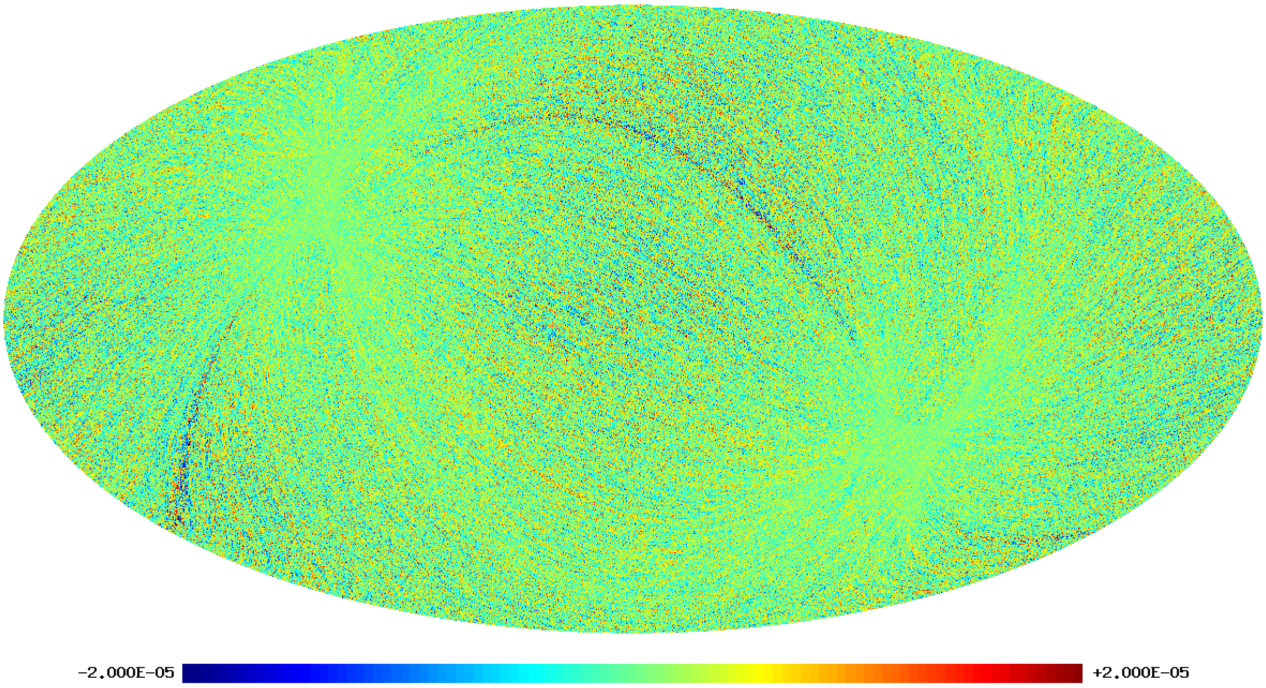

residual correlated noise

The following two images show the statistics of the angular power spectra of 101 realizations of the 70 GHz frequency map noise for the nominal survey. The thick black line shows the median C_ℓ, and the green line the mean C_ℓ. Thin black lines show the minimum, 16% quantile, 84% quantile, and the maximum C_ℓ. The red line is the 102nd realization. The first plot is for the full noise in the output map, the second plot is for the residual correlated noise.

References

<biblio force=false>

1. References

</biblio>

Systematic effect uncertainties

Overview

Known systematic effects in the Planck-LFI data can be divided into two broad categories: effects independent of the sky signal, which can be considered as additive or multiplicative spurious contributions to the measured timelines, and effects which are dependent on the sky and that cannot be considered independently from the observation strategy.

Here we report a brief summary of these effects, all the details can be found in #planck2013-p02a Planck-2013-III [4].

Summary of uncertainties due to systematic effects

In this section we provide a top-level overview of the uncertainties due to systematic effects in the Planck-LFI CMB temperature maps and power spectra. Table 1 provides a list of these effects with short indications of their cause, strategies for removal and references to sections and/or papers where more information is found.

Table 1. List of known instrumental systematic effects in Planck LFI.

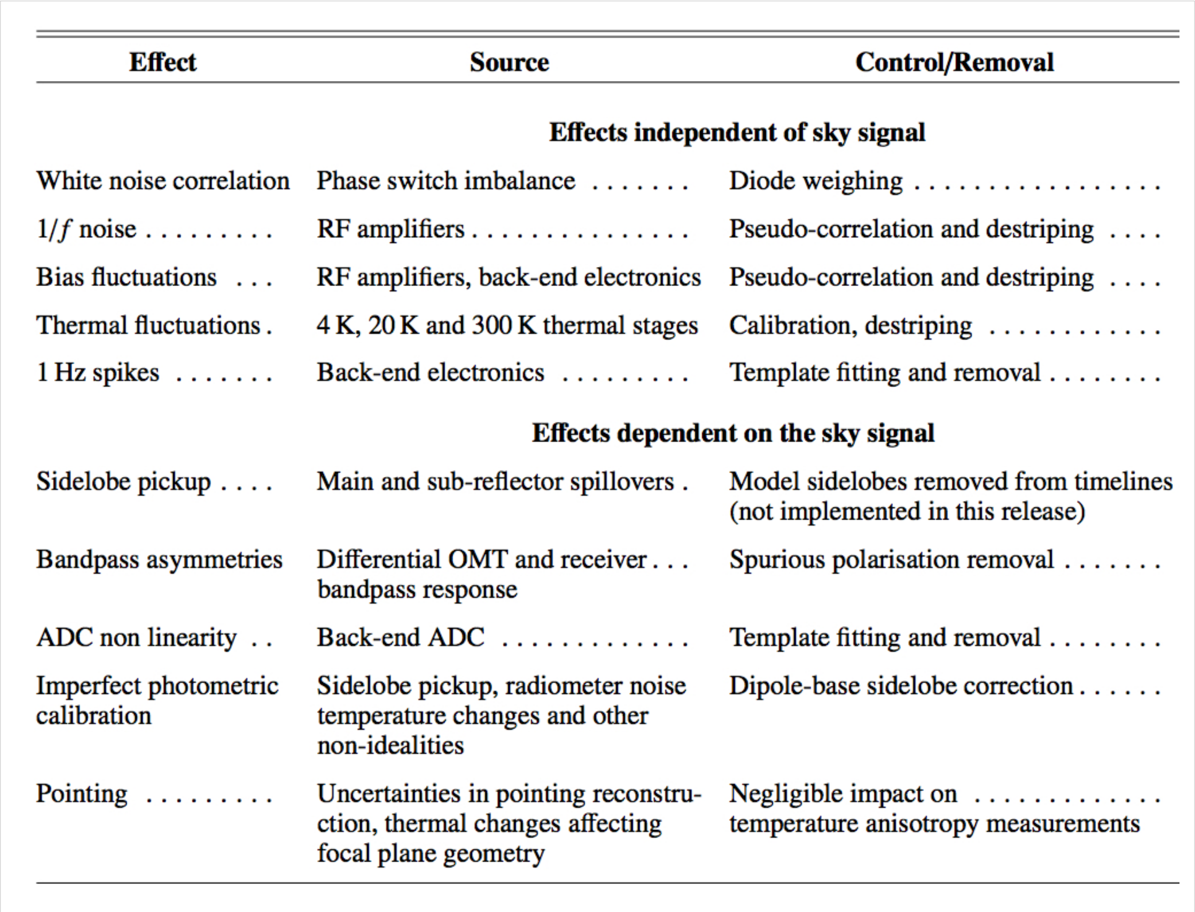

Effect	Source	Control/Removal
		Effects independent of sky signal
White noise correlation	Phase switch imbalance	Diode weighing
$1/f$ noise	RF amplifiers	Pseudo-correlation and destriping
Bias fluctuations	RF amplifiers, back-end electronics	Pseudo-correlation and destriping
Thermal fluctuations	4 K, 20 K and 300 K thermal stages	Calibration, destriping
1 Hz spikes	Back-end electronics	Template fitting and removal
		Effects dependent on the sky signal
Sidelobe pickup	Main and sub-reflector spillovers	Model sidelobes removed from timelines (not implemented in this release)
Bandpass asymmetries	Differential OMT and receiver bandpass response	Spurious polarisation removal
ADC non linearity	Back-end ADC	Template fitting and removal
Imperfect photometric calibration	Sidelobe pickup, radiometer noise temperature changes and other non-idealities	Dipole-base sidelobe correction
Pointing	Uncertainties in pointing reconstruction, thermal changes affecting focal plane geometry	Negligible impact on temperature anisotropy measurements

The impact of 1/f noise has been assessed using half-ring noise maps normalised to the white noise estimate at each pixel obtained from the white noise covariance matrix, so that a perfectly white noise map would be Gaussian and isotropic with unit variance. Deviations from unity trace the contribution of residual 1/f noise in the final maps, which ranges from 0.06% at 70 GHz to 2% at 30 GHz. Pixel uncertainties due to other systematic effects have been calculated on simulated maps degraded at N_{side} = 128 at 30 and 44 GHz and N_{side} = 256 at 70 GHz in order to approximate the optical beam size. This downgrading has been applied in all cases a systematic effect has been evaluated at map level.

In Table 2 we list the r.m.s. and the difference between the 99% and the 1% quantities in the pixel value distributions. For simplicity we refer to this difference as peak-to-peak (p-p) difference although it neglects outliers but effectively approximates the peak-to-peak variation of the effect on the map. The last row in Table 2 reports the r.m.s. value of survey difference maps (first – second survey, after a correction which takes into account the white noise. These values thus represent the level of r.m.s. uncertainty per pixel due to known and unknown systematic effects.

Table 2. Summary of systematic effects uncertainties on maps in μK_{CMB}.

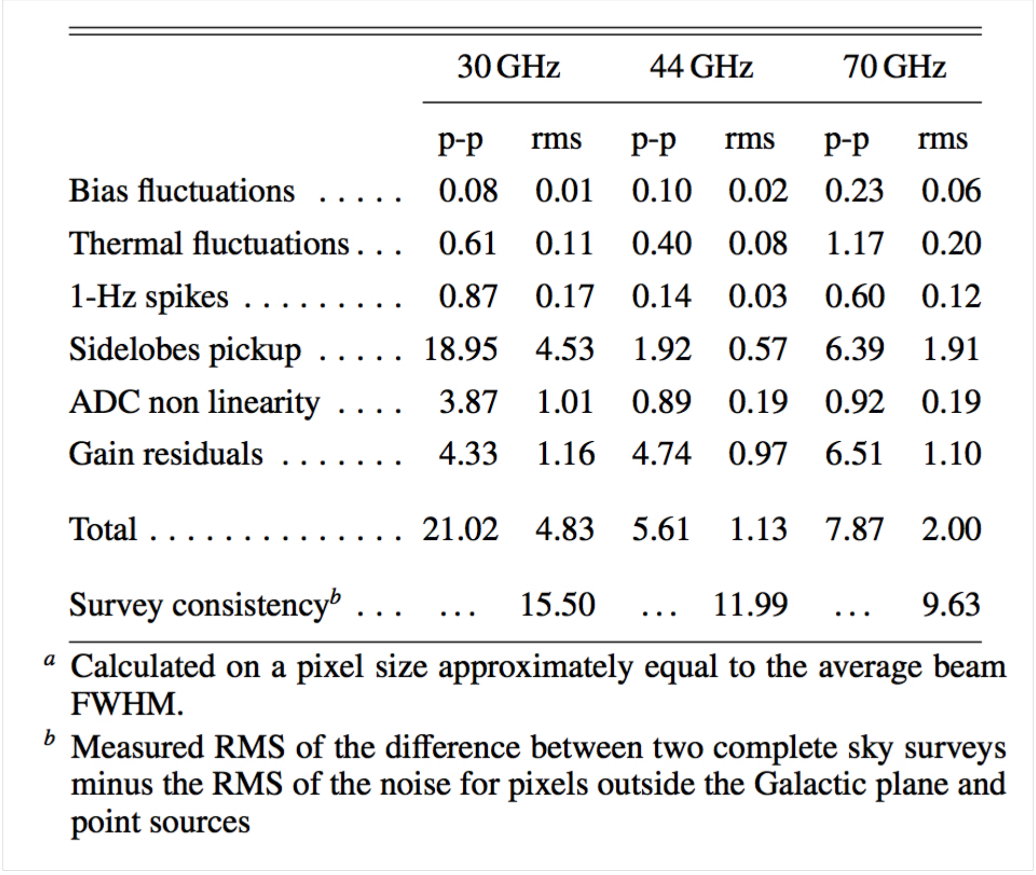

	30 GHz		44 GHz		70 GHz	
	p-p	rms	p-p	rms	p-p	rms
Bias fluctuations	0.08	0.01	0.10	0.02	0.23	0.06
Thermal fluctuations . . .	0.61	0.11	0.40	0.08	1.17	0.20
1-Hz spikes	0.87	0.17	0.14	0.03	0.60	0.12
Sidelobes pickup	18.95	4.53	1.92	0.57	6.39	1.91
ADC non linearity	3.87	1.01	0.89	0.19	0.92	0.19
Gain residuals	4.33	1.16	4.74	0.97	6.51	1.10
Total	21.02	4.83	5.61	1.13	7.87	2.00
Survey consistency[b] . . .	. . .	15.50	. . .	11.99	. . .	9.63

[a] Calculated on a pixel size approximately equal to the average beam FWHM.

[b] Measured RMS of the difference between two complete sky surveys minus the RMS of the noise for pixels outside the Galactic plane and point sources

Angular power spectra have been obtained from full resolution (N_{side} = 1024) systematic effect maps at each frequency using HEALPix Anafast #gorski2005. We have then evaluated the propagation of the various effects in the final CMB map by assuming a simple ILC component separation. In Fig. 1 we show how the power spectrum of the various effects compared with the Planck temperature spectrum, with the noise level coming from the half-ring difference maps and with the residual map obtained from a difference map between survey 1 and survey 2. The large plot in the top panel shows the power spectra obtained from frequency-independent maps resulting from the weighted-average of frequency maps. Spectra in the three small plots in the lower panel, instead, show contributions of systematic effects from individual frequency maps.

Our assessment shows that the global impact of systematic effects uncertainties is at least two order of magnitudes less than the CMB power spectrum and demonstrates the robustness of Planck-LFI temperature anisotropy measurements. Comparison between the total simulated systematic effects and residual signal obtained by differencing survey 1 and survey 2 maps highlights an excess signal in the multipole range that is not completely accounted for in our simulations. This excess comes mainly from the 30 GHz channel and is likely to be caused by galactic emissions picked up by beam sidelobes. Understanding this excess and further reducing the level of residual systematic uncertainties is the primary goal of our current analysis to obtain polarization measurements with a level of purity comparable to what has been achieved with temperature anisotropies.

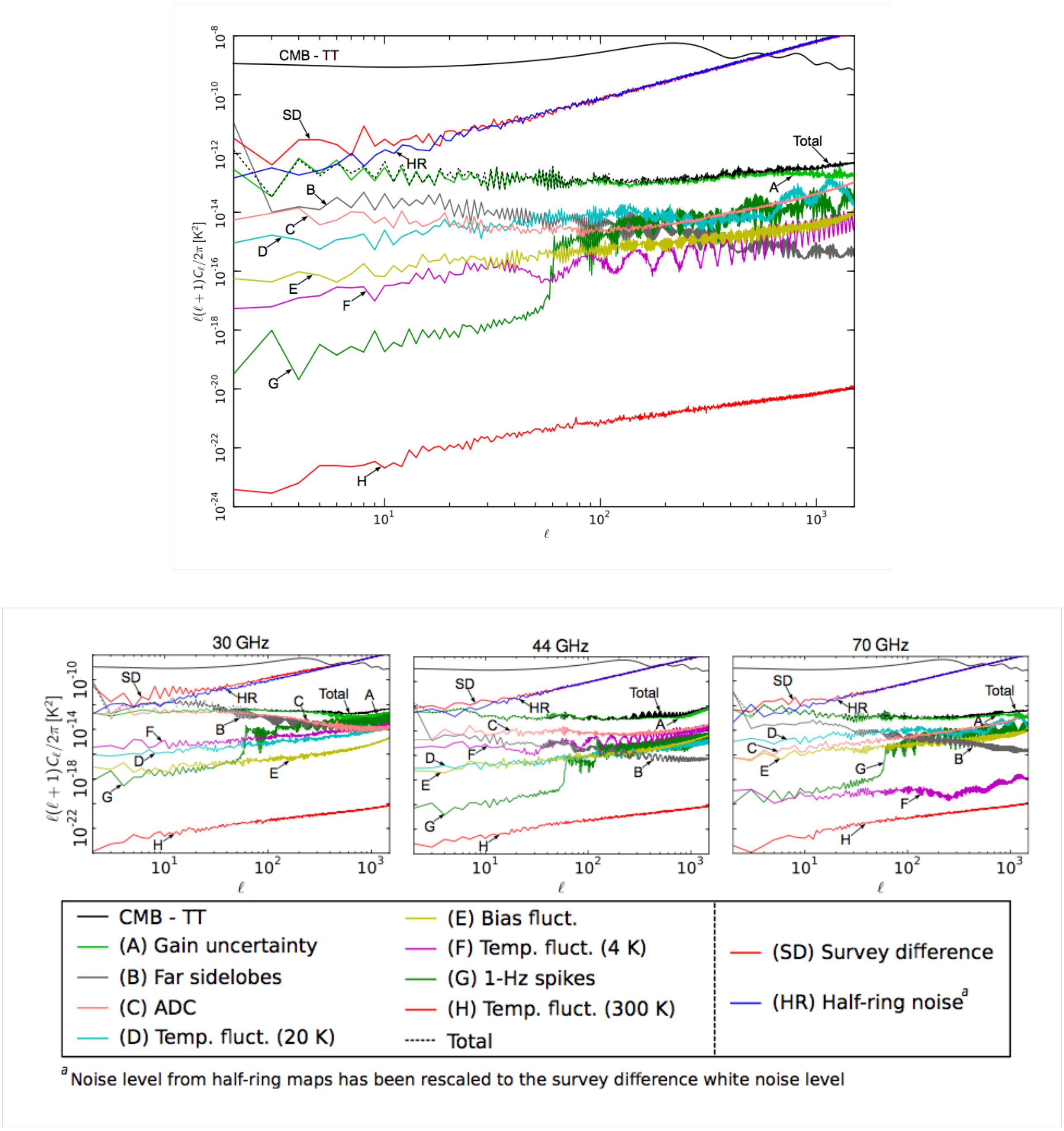

Figure 1. The angular power spectrum of the various systematic effects compared to the Planck temperature spectrum. The black curve, representing the total contribution, has been derived from a map where all the systematic effects have been summed. Top panel: power spectra obtained from frequency independent maps resulting from the weighted-average of individual systematic effects frequency maps. Bottom panel: contributions of systematic effects from individual frequency maps. The CMB curve corresponds to the Planck best-fit model presented in #planck2013-p08 Planck-2013-XV [3].

Effects independent of sky signal

Noise correlations and 1/f noise

As described in #seiffert2002, planck2011-1-4 imperfect matching of components generates isolation between the complementary diodes of a receiver between −10 and −15 dB. This imperfect isolation leads to a small anti correlated component in the white noise that is cancelled by a weighted average of the time ordered data from the two diodes of each receiver as the first step of analysis. This avoids the complication of tracking the anti correlated white noise throughout the analysis. We treat the combined diode data as the raw data, and calibration, noise estimation, map making etc. are performed on these combined data. The weights were determined from some initial estimates of the calibrated noise for each detector, and are kept fixed for the entire mission.

We estimate the signal subtracted noise power spectrum of each receiver on 5-day time periods. Except for specific, mostly well understood events, shorter time scale noise estimation does not produce any evident trends. For nearly all the radiometers our noise model is a very good approximation of the power spectrum.

Over the course of the nominal mission, the noise is well fit by the model, with the exception of the early parts of sky survey 3. During this time, thermal instabilities brought on by the switchover from the nominal to the redundant sorption cooler cause poor fits and some changes in the parameters.

Thermal effects

The LFI is susceptible to temperature fluctuations in the 300 K back-end modules, in the 4 K reference loads and in the 20 K focal plane.

Temperature of 70 GHz reference loads is actively con- trolled by a proportional-integral-derivative (PID) system and is very stable (δT_{rms} ~ 0.13 mK). Reference loads of 30 and 44 GHz channels, instead, do not benefit from active thermal control. Their temperature is consequently more unstable and susceptible to major system-level events like, for example, the switchover to the redundant sorption cooler.

The 20 K LFI focal plane temperature is measured by a sensor placed on the feed horn flange of the LFI28 receiver. The temperature during the first sky survey was very stable. Towards the end of the first year of operations the sorption cooler performance started to degrade and its stability was maintained with a series of controlled temperature changes. The switchover to the redundant cooler left a clear signature on all the main LFI temperatures. After this operation the level of temperature fluctuations on the focal plane increased unexpectedly, and this was later understood to be the effect of liquid hydrogen that was still present in the cold-end of the nominal cooler because the degraded compressor system was not able to absorb all the hydrogen that was present in the cooler line. Although this effect was later mitigated by a series of dedicated operations, most of the third sky survey suffered from a higher-than-nominal level of temperature variations.

The temperature of the 300 K electronics box is measured by one of its temperature sensors. During the first sky survey the back-end temperature suffered from a 24-hour fluctuation caused by the satellite transponder that was switched on daily during contact with the ground station. After day 258 the system was left continuously on and the 24-hour modulation disappeared. This operation caused an increase of the absolute temperature level. The second temperature change occurred in correspondence to the sorption cooler switch over operation. A yearly temperature modulation due to the satellite rotation around the sun and a temperature spike need also to be considered. This was caused by an operational anomaly that caused the satellite to fail repointing for an entire day with a corresponding temperature increase of the warm units.

Details about the thermal stability performance of Planck can be found in #planck2011-1-3, while the susceptibility of the LFI to temperature variations is discussed in #terenzi2009b.

Bias fluctuations

The signal detected by the radiometers can vary because of fluctuations in the front-end and back-end amplifiers bias voltages. In the LFI these fluctuations occurred according to two time scales:

- slow electric drifts, due to thermal changes in the power supply, in the RF amplifiers and in the detector diodes;
- fast and sudden electric instabilities, arising in the warm electronics or from electromagnetic interference effects, and affecting both the cold amplifiers and the warm detector diodes.

The effect of slow drifts is suppressed by the pseudo-correlation architecture of the differential radiometers. Fast electric changes produce quasi-random fluctuations and abrupt steep drops or jumps in the signal. If jumps are caused by instabilities in the front-end bias voltage then the effect involves the output voltage of both diodes in the radiometer. When the jumps occur in the back-end detector diodes (so-called "pop-corn noise") they impact only the output voltage of the corresponding diode and affect sky and reference load samples. In both cases the differenced signal is largely immune from these effects.

1-Hz spikes

This effect is caused by pickup from the housekeeping electronics clock that occurs after the detector diodes and before the ADC converters #meinhold2009, mennella2010, mennella2011. This spurious signal is detected in the radiometer time-domain outputs as a one second square wave with a rising edge near 0.5 s and a falling edge near 0.75 s in on-board time. In the frequency domain it appears at multiples of 1 Hz. Frequency spikes are present at some level in the output from all detectors, but affect the 44 GHz data most strongly because of the low voltage output and high post-detection gain values in that channel. For this reason spikes are removed from the 44 GHz time-ordered data via template fitting, as described in #planck2013-p02 Planck-2013-II [1].

Effects dependent on sky signal

Sidelobe pick-up

Straylight contamination arise from the spurious signal pickup from the telescope far sidelobes. Main sources of straylight contamination are the Galaxy, especially at 30 GHz, and the cosmological dipole, mainly detected in the directions of the main and sub reflectors spillover. In principle we should also include the straylight contribution from the orbital dipole, but its effect is of a factor ten lower than the cosmic dipole so that it can safely be neglected in this framework (but it has been considered in the calibration pipeline). Further details about the Planck optical system are reported in #tauber2010 and the LFI beam properties are provided in #sandri2010.

Straylight impacts the measured signal essentially in two ways: (i) through direct contamination and coupling with the main beam sky signal and (ii) in the photometric calibration of the radiometer detected signal. The impact on calibration and the adopted mitigation strategies are described in #planck2013-p02b Planck-2013-V [4]. Because of the beam orientation, the straylight fingerprint is different in odd surveys compared to even surveys. The Galaxy, for example, is detected by the sub spillover in the odd surveys and by the main spillover in the even surveys. Because the sub spillover points approximately in the main beam direction, the Galaxy straylight pattern is close to the galactic plane. The main spillover, instead, points at about 85 degrees from the main beam so that the Galaxy is re-imaged onto a ring.

ADC non linearity

The linearity of analogue-to-digital converters (ADC) requires that the voltage step sizes between successive binary outputs are constant over the entire input dynamic range. If these steps are not constant we have a non linearity in the ADC response that leads to calibration errors.

The typical fingerprint of ADC non linearity is a variation of the detector voltage output white noise not paired by a detectable variation in the voltage level. This effect was observed in the LFI radiometer data for the first time in flight, where drops of few percent were observed in the voltage white noise but not in the output level over periods of few weeks. The typical amplitude of the region where the non linearity occurs is of the order of 1 mV, corresponding to about three bits in the ADC. The ADC effect is strongest (3 to 6%) in the 44 GHz channels, because of their lower detector voltages. The ADC non linearity effect has been characterised from flight data and removed from the TOIs according to the procedure described in the main LFI data processing paper #planck2013-p02 Planck-2013-II [1].

Imperfect photometric calibration

An important set of systematic effects are those related with the photometric calibration of the radiometers. Such effects are discussed at length by #planck2013-p05 Planck-2013-XXVIII [1]. There are three different kinds of systematic effects that can affect the calibration.

- Incorrect assumptions regarding the calibration signal.In the case of LFI, the signal used for the calibration is the dipolar field caused by the motion of the Solar System with respect to the CMB rest frame and by the motion of the spacecraft around the Sun. We model the former using the values quoted by #hinshaw2009 and the latter using the spacecraft's attitude information. Any error in the numbers would directly lead to an error in the calibration of Planck-LFI data.
- Incorrect treatment of the calibration signal. To actually use any previous knowledge of the CMB dipole, we need to convolve the signal with the beam response of LFI radiometer. Any error in this step would produce a systematic effect in the map not only because of the wrong shape expected for the calibration signal, but also because of the removal of the (wrong) dipole from the calibrated maps done by the Planck-LFI pipeline #planck2013-p02

Planck-2013-II [1]. Possible types of errors include: systematic errors in WMAP's dipole estimate, wrong convolution of the expected dipole with the radiometer beams, uncorrect masking of the Galaxy when fitting the observed signal with the dipole, etc.

- Incorrect reconstruction of gain fluctuations. Some of the algorithms we used in calibrating LFI data for this release use the radiometer equation and the recorded variations of the radiometers total-power output to track gain changes. In principle, any deviation in the behaviour of the radiometer from the ideal case (e.g., ADC non linearities) can therefore induce systematic effects in the gain curves.

Pointing effects

Pointing uncertainties are translated into uncertainties in pixel temperature measurements. If pointing uncertainties are not constant in time then the statistics of the sky anisotropy measurements is not preserved with a consequent impact on power spectrum and cosmological parameters. In Planck-LFI pointing uncertainties arise from:

- Satellite pointing determination. The Planck Attitude Control Movement System guarantees a pointing accuracy of ~ 2″ #planck2013-p01

Planck-2013-I [2], which is well within scientific requirements. However, small non idealities in the system and errors in the attitude reconstruction caused, for example, by thermoelastic effects, can affect the data.

- Uncertainties in the focal plane geometry reconstruction. The measurement of Planck-LFI focal plane geometry is based on the determination of the beam pointing with respect to the nominal line of sight exploiting Jupiter observation. The peak of each beam has been determined by fitting data with a bivariate gaussian function which may be not representative of the real beam centre.

References

<biblio force=false>

1. References

</biblio>

References

[1] http://www.rssd.esa.int/doc_fetch.php?id=3168553&page=1

[2] http://www.rssd.esa.int/doc_fetch.php?id=3168066&page=1

Internal overall validation

Overview

Data validation is a step of paramount importance in the complex process of data analysis and the extraction of the final scientific goals of an experiment. The LFI approach to data validation is based upon null-tests approach and here we present the rationale behind envisaged/performed null-tests and the actual results for the present data release. Also we will provide results of the same kind of tests performed on previous release to show the overall improvements in the data quality.

Null-tests approach

In general null-tests are performed in order to highlight possible issues in the data related to instrumental systematic effect not properly accounted for within the processing pipeline and related to known events of the operational conditions (e.g. switch-over of the sorption coolers) or to intrinsic instrument properties coupled with sky signal like stray-light contamination.

Such null-tests are expected to be performed considering data on different time scales ranging from 1-minute to one year of observations, at different unit level (radiometer, horn, horn-pair, within frequency and cross-frequency both in total intensity and, when applicable, to polarisation.

This is quite demanding in terms of all possible combinations. In addition some tools are already available and can be properly used for this kind of analysis. However it may be possible that on some specific time-scale, detailed tools have to be developed in order to produce the desired null-test results. In this respect the actual half-ring jack-knives are suitable to track any effects on pointing period times scales. On time-scales between half-ring and survey there are lot of possibilities. It has to be verified if the actual code producing half-ring jack-knives (madam) can handle data producing jack-knives of larger (e.g. 1 hour) times scales.

It is fundamental that such test have to be performed on DPC data product with clear and identified properties (e.g. single \$R\$, \$DV/V\$ single fit, etc.) in order to avoid any possible mis-understanding due to usage of non homogeneous data sets.

Many of the null-tests proposed are done at map level with sometime compression of their statistical information into an angular power spectrum. However together with full-sky maps it is interesting to have a closer look on some specific sources. I would be important to compare fluxes from both polarized and un-polarized point sources with different radiometers in order to asses possible calibration mis-match and/or polarization leakage issues. Such comparison will also possibly indicate problems related to channel central frequencies. The proposed set of sources would be: M42, Tau A, Cas A and Cyg A. However other $H\,II$regions like Perseus are valuable. One can compare directly their fluxes from different sky surveys and/or the flux of the difference map and how this is consistent with instrumental noise.

Which kind of effect is probed with a null-test on a specific time scale? Here it is a simple list. At survey time scale it is possible to underlying any side-lobes effects, while on time scales of full-mission, it is possible to have an indication of calibration problems when observing the sky with the same S/C orientation. Differences at this time scale between horns at the same frequency may also reveal central frequency and beam issues.

Total Intensity Null Tests

In order to highlight different issues, several time scales and data combinations are considered. The following table is a sort of null-test matrix to be filled with test results. It should be important to try to set a sort of pass/fail criteria for each of the tests and to be prepared to detailed actions in order to avoid and correct any failure of the tests. To assess the results an idea could be to proceed as in the nominal pipeline $i.e.$ to compare the angular power spectra of null test maps with a fiducial angular power spectrum of a white noise map. This could be made automatic and, in case the test does not pass then a more thorough investigation could be performed. This will provide an overall indication of the residuals. However structures in the residual are important as well as the overall average level and visual inspection of the data is therefore fundamental.

Concerning null-tests on various time scales a comment is in order. At large time scales (i.e. of the order of a survey or more) it is clear that the basic data set will be made of the single survey maps at radiometer/horn/frequency level that will be properly combined to obtain the null-test under consideration. For example at 6 months time scale we will analysis maps of the difference between different surveys for the radiometer/horn/frequency under test. On the other hand at 12 months time scale we will combine surveys 1 and 2 together to be compared with the same combination for surveys 3 and 4. At full-mission time scale, the analysis it is not always possible e.g. at radiometer level we have only one full-mission data set. However it would be interesting to combine odd surveys together and compare them with even surveys again combined together. On shorter time scales (i.e. less than a survey) the data products to be considered are different and will be the output of the jack-knives code when different time scales are considered: the usual half-ring JK on pointing period time scale and the new, if possible, jack-knives on 1 minute time scale. Therefore null-tests will use both surveys/full-mission maps as well as tailored jack-knives maps.

The following table reports our total intensity null-tests matrix with a $\checkmark$ where tests are possible.

Data Set	1minute	1 hour	Survey	Full Mission
Radiometer (M/S)	$\checkmark$	$\checkmark$	$\checkmark$	$\checkmark$
Horn (M+S)	$\checkmark$	$\checkmark$	$\checkmark$	$\checkmark$
Horn Pair^1			$\checkmark$	$\checkmark$
Frequency	$\checkmark$	$\checkmark$	$\checkmark$	$\checkmark$
Cross-Frequency			$\checkmark$	$\checkmark$

^{1} this is (M+S)/2 and differences are between couple of horns (e.g. (28M+28S)/2- (27M+27S)/2)

Polarisation Null Tests

The same arguments applies also for polarization analysis with only some differences regarding the possible combination producing polarized data. Radiometer will not be available, instead of sum between M and S radiometer we will consider their difference.

Data Set	1minute	1 hour	Survey	Full Mission
Horn (M-S)	$\checkmark$	$\checkmark$	$\checkmark$	$\checkmark$
Horn Pair^1			$\checkmark$	$\checkmark$
Frequency	$\checkmark$	$\checkmark$	$\checkmark$	$\checkmark$
Cross-Frequency			$\checkmark$	$\checkmark$

^{1} this is difference between couple of horns (e.g. (28M-28S)/2- (27M-27S)/2)

Practical Considerations

For practical purposed and visual inspection of the null-tests results it would be useful to produce results smoothed at 3° (and at 10° for highlight larger angular scales) for all the total intensity maps. For polarization, as we already did several times when comparing to $WMAP$ data, a downgrade of the product at $N_{\rm side}=128$ would be useful to highlight large scale residuals. These considerations are free to evolve according to our needs.

Due to large possibilities and number of data sets to be considered, it would be desirable to have sort of automatic tools that ingest two, or more, inputs maps and produce difference map(s) and corresponding angular power spectrum(spectra). This has been implemented using Python language and interacting directly with FITS files of a specific data release. The code is parallel and can run both at NERSC and at DPC producing consistent results. In addition for each null-tests performed a JSON DB file is produced in which main test informations are stored together with interesting computed quantities like mean, standard deviation of the residual maps. Beside JSON files also GIF images of the null-test are produced. Such JSON and GIF files are used to create (both with Python again and with Scheme) a report in form of an HTML page from the LFI Wiki.

Together with images, power spectra of the residual are also produced and compared with the expected level of white noise derived from the half-ring jack-knifes. With these quantities are combined to produce a sort of χ^2. This gives an indication of the deviation of the residuals with respect to the white noise level. Of course underlying signal does not posses a Gaussian statistic and therefore with non-Gaussian data, the χ^2 tests is less meaningful. However this gives an hint on the presence of residuals which in some cases are indeed expected: in fact making difference between odd and even survey at horn and frequency level, is a way to show the signature of the external stray-light which, although properly accounted for during the calibration procedure, has not been removed from the data.

Consistency checks

All the details can be found in #planck2013-p02 Planck-2013-II [1].

Intra frequency consistency check

We have tested the consistency between 30, 44, and 70 GHz maps by comparing the power spectra in the multipole range around the first acoustic peak. In order to do so, we have removed the estimated contribution from unresolved point source from the spectra. We have then built the scatter plots for the three frequency pairs, i.e. 70 vs 30 GHz, 70 vs 44 GHz, and 44 vs 30 GHz, and performed a linear fit accounting for errors on both axis. The results reported in Fig. 1 show that the three power spectra are consistent within the errors. Moreover, please note that current error budget does not account for foreground removal, calibration, and window function uncertainties. Hence, the resulting agreement between spectra at different frequencies can be fairly considered even more significant.

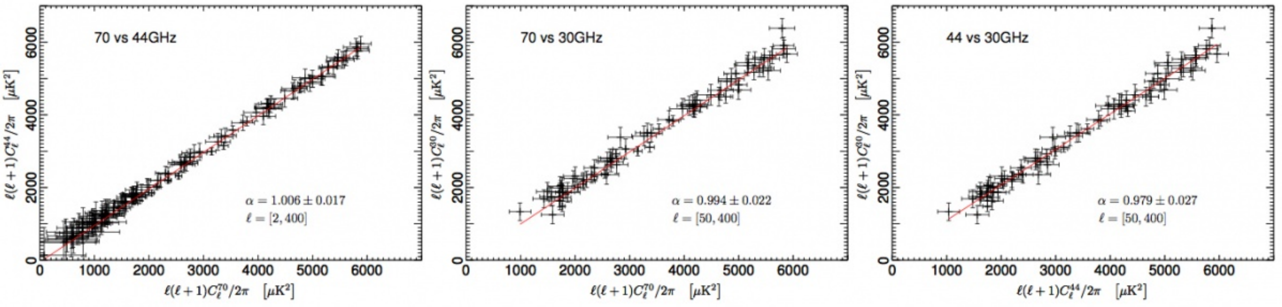

Figure 1. Consistency between spectral estimates at different frequencies. From left to right: 70 vs 44 GHz; 70 vs 30 GHz; 44 vs 30 GHz. Solid red lines are the best fit of the linear regressions, whose angular coefficients α are consistent with 1 within the errors.

70 GHz internal consistency check

We use the Hausman test #polenta_CrossSpectra to assess the consistency of auto and cross spectral estimates at 70 GHz. We define the statistic:

$$H_\ell = \left(\hat{C}_\ell - \tilde{C}_\ell\right) / \sqrt{Var\left\{\hat{C}_\ell - \tilde{C}_\ell\right\}}$$

where $\hat{C}_\ell$ and $\tilde{C}_\ell$ represent auto- and cross-spectra respectively. In order to combine information from different multipoles into a single quantity, we define the following quantity:

$$B_L(r) = \frac{1}{\sqrt{L}} \sum_{\ell=2}^{[Lr]} H_\ell, r \in [0,1]$$

where $[\cdot]$ denotes integer part. The distribution of $B_L(r)$ converges (in a functional sense) to a Brownian motion process, which can be studied through the statistics $s_1 = \sup_r B_L(r)$ $s_2 = \sup_r |B_L(r)|$ and $s_3 = \int_0^1 B_L^2(r) dr$. Using the *FFP6* simulations we derive the empirical distribution for all the three test statistics and we compare with results obtained from Planck data (see Fig. 2). Thus, the Hausman test shows no statistically significant inconsistencies between the two spectral estimates.

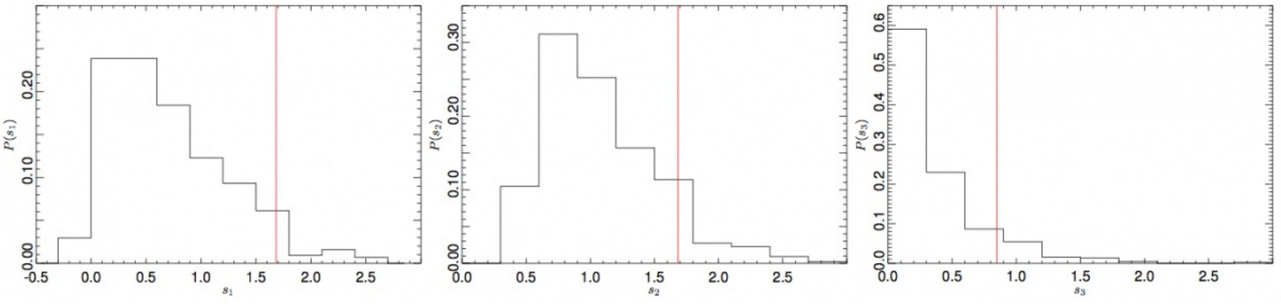

Figure 2. From left to right, the empirical distribution (estimated via *FFP6*) of the s_1, s_2, s_3 statistics (see text). The vertical line represents 70 GHz data.

As a further test, we have estimated the temperature power spectrum for each of three horn-pair map, and we have compared the results with the spectrum obtained from all the 12 radiometers shown above. In Fig. 3 we show the difference between the horn-pair and the combined power spectra. Again, The error bars have been estimated from the *FFP6* simulated dataset. A χ^2 analysis of the residual shows that they are compatible with the null hypothesis, confirming the strong consistency of the estimates.

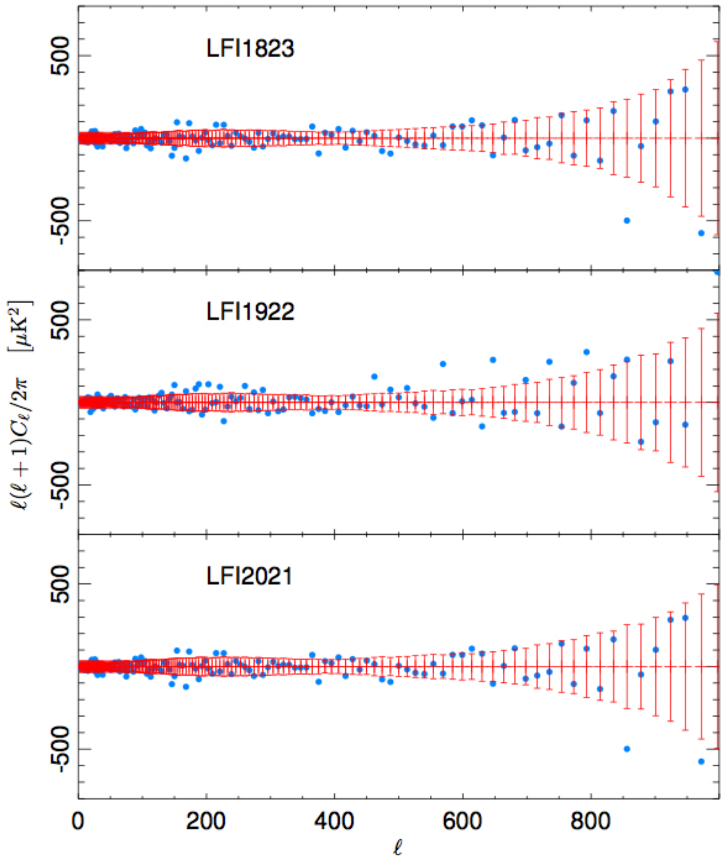

Figure 3. Residuals between the auto power spectra of the horn pair maps and the power spectrum of the full 70 GHz frequency map. Error bars are derived from *FFP6* simulations.

References

<biblio force=false>

1. References

</biblio>

Power spectra

Power Spectra

LFI temperature power spectra are computed from frequency maps using a cROMAster, a implementation of the pseudo- $C_\ell$method described in #master extended to derive both auto- and cross-power spectra (see #polenta_CrossSpectra) for a comparison between the two estimators). Noise bias and covariance matrix have been computed through the Full Focal Plane Simulations version 6 *FFP6*, that include 1000 realization of both signal and noise maps consistent with Planck data. The angular response of the instrument is accounted for by using the beam window functions presented in #planck2013-p02d Planck-2013-IV [1]. Coupling kernels to correct for uncompleted sky coverage are computed as described in Annex. B of #planck2013-p08 Planck-2013-XV [3]. We have masked Galactic plane and point sources using masks described in Sec. 3 of #planck2013-p06 Planck-2013-XII [1]. In particular, we have used the 70% Galactic mask for 44 and 70 GHz, while we have used the 60% Galactic mask for 30 GHz. We report in Fig. 1 the 30, 44, and 70 GHz temperature power spectra. These have been produced from frequency maps without performing component separation. Nevertheless, there is a clear agreement between the observed spectra and the Planck Likelihood Code bestfit #planck2013-p08 Planck-2013-XV [3] when adding a simple foreground component to account for unresolved point source residuals.

The details can be found in #planck2013-p02 Planck-2013-II [1].

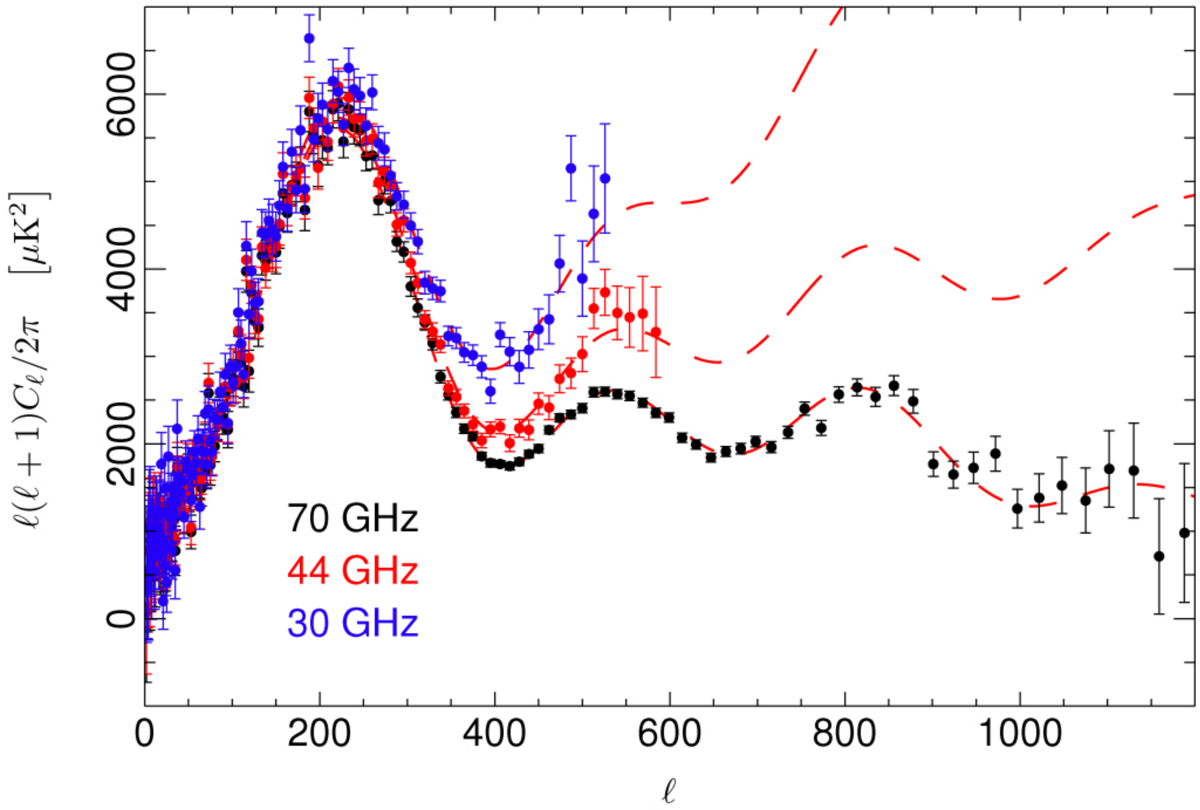

Figure 1. Temperature power spectra at 30, 44 and 70 GHz. Dashed lines correspond to the Planck Likelihood Code best-fit plus a foreground component to account for unresolved point sources.

References

<biblio force=false>

1. References

</biblio>

References

[1] http://www.rssd.esa.int/doc_fetch.php?id=3167993&page=1

Summary of LFI data characteristics

The LFI performance are summarized in Table 1 below. All the details can be found in the LFI data processing paper #planck2013-p02 Planck-2013-II [1].

Table 1. Summary of the LFI performance parameters

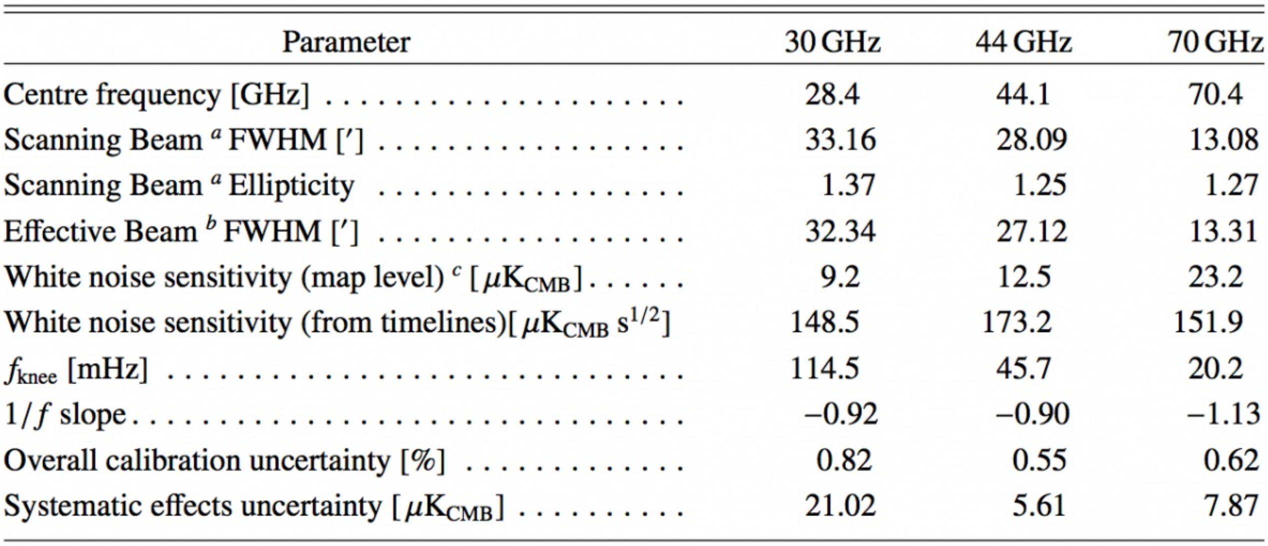

Parameter	30 GHz	44 GHz	70 GHz
Centre frequency [GHz]	28.4	44.1	70.4
Scanning Beam ^{a} FWHM [$'$]	33.16	28.09	13.08
Scanning Beam ^{a} Ellipticity	1.37	1.25	1.27
Effective Beam ^{b} FWHM [$'$]	32.34	27.12	13.31
White noise sensitivity (map level) ^{c} [μK$_{\mathrm{CMB}}$]	9.2	12.5	23.2
White noise sensitivity (from timelines)[μK$_{\mathrm{CMB}}$ s$^{1/2}$]	148.5	173.2	151.9
f_{knee} [mHz]	114.5	45.7	20.2
$1/f$ slope	−0.92	−0.90	−1.13
Overall calibration uncertainty [%]	0.82	0.55	0.62
Systematic effects uncertainty [μK$_{\mathrm{CMB}}$]	21.02	5.61	7.87

[a] FWHM and ellipticity from scanning beam evaluated fitting Jupiter directly in the timelines. [b] FWHM from effective beam estimated from the main beam solid angle of the effective beam. Those are the values used in the source extraction pipeline #planck2013-p05 Planck-2013-XXVIII [1]. [c] White noise per pixel computed from half-ring difference maps. Those values are within the 1% with the white noise sensitivity computed directly on the timelines, taking in account the actual mission time minus the manoeuvres and bad-science flagged data.

References

<biblio force=false>

1. References

</biblio>

HFI/LFI join data processing

HFI/LFI joint data processing

HFI/LFI common processing uses as basic input the maps at the nine frequencies covered by the two instruments.

The goal is to obtain various catalogues, identify the different astrophysical components whose superposition leads to the observed sky, and provides a statistical characterisation of the CMB, in particular through a likelihood code (of a particular theoretical $C(\ell)$given Planck data).

Compact Source catalogues

Planck Catalogue of Compact Sources

The Planck Catalogue of Compact Sources (PCCS) is a sample of reliable sources, both Galactic and extragalactic, extracted directly from the Planck nominal maps. The first public version of the PCCS is derived from the data acquired by Planck between August 13 2009 and November 26 2010. The PCCS consists of nine lists of sources, extracted independently from each of Planck's nine frequency channels. It is fully described in #planck2013-p05.

The whole PCCS can be downloaded here [1].

Detection procedure

The Mexican Hat Wavelet 2 (MHW2; Gonzalez-Nuevo et al., 2006) is the base algorithm used to produce the single channel catalogues of the PCCS. Although each DPC has is own implementation of this algorithm (IFCAMEX and HFI-MHW), the results are compatible at least at the statistical uncertainty level. Additional algorithms are also implemented, like the multi-frequency Matrix Multi-filters (MTXF; Herranz et al., 2009) and the Bayesian PowellSnake (Carvalho et al. 2009), but for the current version of the PCCS they are used just for the validation of the results obtained by the MHW2.

The full-sky maps are divided into a sufficient number of overlapping flat patches in such a way that 100% of the sky is covered. Each patch is then filtered by the MHW2 with a scale that is optimised to provide the maximum signal-to-noise ratio in the filtered maps. A sub-catalogue of objects is produced for each patch and then, at the end of the process, all the sub-catalogues are merged together, removing repetitions.

The driving goal of the ERCSC was reliability greater than 90 %. In order to increase completeness and explore possibly interesting new sources at fainter flux density levels, however, the initial overall reliability goal of the PCCS was reduced to 80 %. The S/N thresholds applied to each frequency channel have been determined, as far as possible, to meet this goal. The reliability of the catalogues has been assessed using the internal and external validation described below.

At 30, 44, and 70 GHz, the reliability goal alone would permit S/N thresholds below 4. A secondary goal of minimizing the upward bias on flux densities led to the imposition of an S/N threshold of 4.

At higher frequencies, where the confusion caused by the Galactic emission starts to become an issue, the sky has been divided into two zones, one Galactic (52 % of the sky) and one extragalactic (48 % of the sky). At 100, 143, and 217 GHz, the S/N threshold needed to achieve the target reliability is determined in the extragalactic zone, but applied uniformly on sky. At 353, 545, and 857 GHz, the need to control confusion from Galactic cirrus emission led to the adoption of different S/N thresholds in the two zones. The extragalactic zone has a lower threshold than the

Galactic zone. The S/N thresholds are given in Table 1.

Bandfilling is the process by which flux density estimates at specific bands are generated based on source positions defined in another band. For the current PCCS release we compute the flux density at 217, 353, and 545 GHz at the positions of each source detected at 857 GHz, using aperture photometry. Bandfilling is not attempted at other frequencies due to the variation in spatial resolution across the bands, which makes multifrequency associations challenging, especially in crowded regions such as the Galactic Plane.

Photometry

In addition of the native flux density estimation provided by the detection algorithm, three additional measurements are obtained for each of the source in the parent samples. These additional flux density estimations are based on aperture photometry, PSF fitting and Gaussian fitting (see #planck2013-p05 for a detailed description of these additional photometries). The native flux density estimation is the only one that is obtained directly from the filtered maps while for the others the flux density estimates has a local background subtracted. The flux density estimations have not been colour corrected. Colour corrections are available in Table 15 of LFI Appendix and HFI spectral response pages.

Validation process

The PCCS, its sources and the four different estimates of the flux density, have undergone an extensive internal and external validation process to ensure the quality of the catalogues. The validation of the non-thermal radio sources can be done with a large number of existing catalogues, whereas the validation of thermal sources is mostly done with simulations. These two approaches will be discussed below. Detections identified with known sources have been appropriately flagged in the catalogues.

Internal validation

The catalogues for the HFI channels have primarily been validated through an internal Monte-Carlo quality assessment process that uses large numbers of source injection and detection loops to characterize their properties. For each channel, we calculate statistical quantities describing the quality of detection, photometry and astrometry of the detection code. The detection is described by the completeness and reliability of the catalogue: completeness is a function of intrinsic flux, the selection threshold applied to detection (S/N) and location, while reliability is a function only of the detection S/N. The quality of photometry and astrometry is assessed through direct comparison of detected position and flux density parameters with the known inputs of matched sources. An input source is considered to be detected if a detection is made within one beam FWHM of the injected position.

External validation

At the three lowest frequencies of Planck, it is possible to validate the PCCS source identifications, completeness, reliability, positional accuracy and flux density accuracy using external data sets, particularly large-area radio surveys. Moreover, the external validation offers the opportunity for an absolute validation of the different photometries, directly related with the calibration and the knowledge of the beams.

At higher frequencies, surveys as the South-Pole Telescope (SPT), the Atacama Cosmology Telescope (ACT) and H-ATLAS or HERMES form Herschel will also be very important, although only for limited regions of the sky. In particular, the Herschel synergy is crucial to study the possible contamination of the catalogues caused by the Galactic cirrus at high frequencies.

Cautionary notes

We list here some cautionary notes for users of the PCCS.

- Variability: At radio frequencies, many of the extragalactic sources are highly variable. A small fraction of them vary even on time scales of a few hours based on the brightness of the same source as it passes through the different Planck horns #planck2013-p02,#planck2013-p03. Follow-up observations of these sources might show significant differences in flux density compared to the values in the data products. Although the maps used for the PCCS are based on 2.6 sky coverages, the PCCS provides only a single average flux density estimate over all Planck data samples that were included in the maps and does not contain any measure of the variability of the sources from survey to survey.
- Contamination from CO: At infrared/submillimetre frequencies (100 GHz and above), the Planck bandpasses straddle energetically significant CO lines (see #planck2013-p03a). The effect is the most significant at 100 GHz, where the line might contribute more than 50% of the measured flux density. Follow-up observations of these sources, especially those associated with Galactic star-forming regions, at a similar frequency but different bandpass, should correct for the potential contribution of line emission to the measured continuum flux density of the source.
- Photometry: Each source has multiple estimates of flux density, DETFLUX, APERFLUX, GAUFLUX and PSFFLUX, as defined above. The appropriate photometry to be used depends on the nature of the source. For sources which are unresolved at the spatial resolution of Planck, APERFLUX and DETFLUX are most appropriate. Even in this regime, PSF fits of faint sources fail and consequently these have a PSFFLUX value of NaN (‘Not a Number’). For bright resolved sources, GAUFLUX might be most appropriate although GAUFLUX appears to overestimate the flux density of the sources close to the Galactic plane due to an inability to fit for the contribution of the Galactic background at the spatial resolution of the data. For the 353–857 GHz channels, the complex native of the diffuse emission and the relative undersampling of the beam produces a bias in DETFLUX, so we recommend that APERFLUX is used instead.
- Colour correction: The flux density estimates have not been colour corrected. Colour corrections are described in #planck2013-p02 and #planck2013-p03.
- Cirrus/ISM: A significant fraction of the sources detected in the upper HFI bands could be associated with Galactic interstellar medium features or cirrus. The 857 GHz brightness proxy described in Sect. 3.4), can be used as indicator of cirrus contamination. Alternately, the value of CIRRUS N in the catalogue can be used to flag sources which might be clustered together and thereby associated with ISM structure. Candidate ISM features can also be selected by choosing objects with EXTENDED = 1 although nearby Galactic and extragalactic sources which are extended at Planck spatial resolution will meet this criterion too.

Planck Sunyaev-Zeldovich catalogue

The Planck SZ catalogue is a nearly full-sky list of SZ detections obtained from the Planck data. It is fully described in #planck2013-p05a. The catalogue is derived from the HFI frequency channel maps after masking and filling the bright point sources (SNR >= 10) from the PCCS catalogues in those channels. Three detection pipelines were used to construct the catalogue, two implementations of the matched multi-filter (MMF) algorithm and PowellSnakes (PwS), a Bayesian algorithm. All three pipelines use a circularly symmetric pressure profile, the non-standard universal profile from #arnaud2010, in the detection.

- MMF1 and MMF3 are full-sky implementations of the MMF algorithm. The matched filter optimizes the cluster detection using a linear combination of maps, which requires an estimate of the statistics of the contamination. It uses spatial filtering to suppress both foregrounds and noise, making use of the prior knowledge of the cluster pressure profile and thermal SZ spectrum.

- PwS differs from the MMF methods. It is a fast Bayesian multi-frequency detection algorithm designed to identify and characterize compact objects in a diffuse background. The detection process is based on a statistical model comparison test. Detections may be accepted or rejected based on a generalized likelihood ratio test or in full Bayesian mode. These two modes allow quantities measured by PwS to be consistently compared with those of the MMF algorithms.

A union catalogue is constructed from the detections by all three pipelines. A mask to remove Galactic dust, nearby galaxies and point sources (leaving 83.7% of the sky) is applied a posteriori to avoid detections in areas where foregrounds are likely to cause spurious detections.

Early Release Compact Source Catalogue

The ERCSC is a list of high reliability (>90%) sources, both Galactic and extragalactic, derived from the data acquired by Planck between August 13 2009 and June 6 2010. The ERCSC consists of:

- nine lists of sources, extracted independently from each of Planck's nine frequency channels
- two lists extracted using multi-channel criteria: the Early Cold Cores catalogue (ECC), consisting of Galactic dense and cold cores, selected mainly on the basis of their temperature ; and the Early Sunyaev-Zeldovich catalogue (ESZ), consisting of galaxy clusters selected by the spectral signature of the Sunyaev-Zeldovich effect.

The whole ERCSC can be downloaded here [2].

The ERCSC is also accessible via the NASA/IPAC Infrared Science Archive [3].

References

<biblio force=false>

1. References

</biblio>

References

[1] http://www.sciops.esa.int/index.php?project=planck&page=Planck_Legacy_Archive
[2] http://www.sciops.esa.int/index.php?project=PLANCK&page=Planck_Data_Products
[3] http://irsa.ipac.caltech.edu/Missions/planck.html

Astrophysical component separation

CMB and foreground separation

See the Component Separation paper #planck2013-p06 Planck-2013-XII [1] for details.

NILC

NILC is a linear method for combining the input channels. It implements an ILC with weighting coefficients varying over the sky and over the multipole range up to $\ell = 3200$and it does so using 'needlets' which are spherical wavelets. A special procedure is used for processing the coarsest needlet scale which contains the large scale multipoles.

SEVEM

The aim of Sevem is to produce clean CMB maps at one or several frequencies by using a procedure based on template fitting. The templates are internal, i.e., they are constructed from Planck data, avoiding the need for external data sets, which usually complicates the analyses and may introduce inconsistencies. The method has been successfully applied to Planck simulations Leach et al., 2008 and to WMAP polarisation data Fernandez-Cobos et al., 2012. In the cleaning process, no assumptions about the foregrounds or noise levels are needed, rendering the technique very robust.

The input maps used are all the Planck frequency channels. In particular, we have cleaned the 100, 143 GHz and 217 GHz maps using four templates constructed as the difference of the following Planck channels (smoothed to a common resolution): (30-44) GHz, (44-70) GHz, (545-353) GHz and (857-545)GHz.

The templates are constructed by subtracting two neighbouring Planck frequency channel maps, after first smoothing them to a common resolution to ensure that the CMB signal is properly removed. A linear combination of the templates is then subtracted from the Planck sky map at the frequency to be cleaned, in order to produce the clean CMB. The coefficients of the linear combination are obtained by minimising the variance of the clean map outside a given mask. Although we exclude very contaminated regions during the minimization, the subtraction is performed for all pixels and, therefore, the cleaned maps cover the full-sky (although we expect that foreground residuals are present in the excluded areas).

An additional level of flexibility can also be considered: the linear coefficients can be the same for all the sky, or several regions with different sets of coefficients can be considered. The regions are then combined in a smooth way, by weighting the pixels at the boundaries, to avoid discontinuities in the clean maps. In order to take into account the different spectral behaviour of the foregrounds at low and high galactic latitudes, we have chosen to use two regions: the region with the 3 per cent brightest Galactic emission, and the region with the remaining 97 per cent of the sky.

The final CMB map has then been constructed by combining the 143 and 217 GHz cleaned maps by weighting the maps in harmonic space taking into account the noise level, the resolution and a rough estimation of the foreground residuals of each map (obtained from realistic simulations). This final map has a resolution corresponding to a Gaussian beam of FWHM =5 arcminutes.

SMICA

A linear method, SMICA reconstructs a CMB map as a linear combination in the harmonic domain of N_{chan}input frequency maps with weights that depend on multipole ℓ. Given the vector $\mathbf{x}_{\ell m}$of spherical harmonic coefficients for the input maps, it computes coefficients $s_{\ell m}$for the CMB map as

where the vector $\mathbf{w}_{\ell}$which contains the multipole-dependent weights is built to offer unit gain to the CMB with minimum variance. This is achieved with

where vector $\mathbf{a}$is the emission spectrum of the CMB evaluated at each channel (allowing for possible inter-channel recalibration factors) and $\mathbf{R}_{\ell}$is the spectral covariance matrix of $\mathbf{x}_{\ell m}$. Taking $\mathbf{R}_{\ell}$in Eq. \ref{eq:smica:w} to be the sample spectral covariance matrix $\hat{\mathbf{R}}_{\ell}$of the observations:

would implement a simple harmonic-domain ILC. This is not what SMICA does. As discussed below, we instead use a model and determine the covariance matrix to be used in Eq. \ref{eq:smica:w} by fitting to $\hat{\mathbf{R}}_{\ell}$. This is done in the maximum likelihood sense for stationary Gaussian fields, yielding the best fit model parameters θ as

SMICA models the data is a superposition of CMB, noise and foregrounds. The latter are not parametrically modelled; instead, we represent the total foreground emission by $d$templates with arbitrary frequency spectra, angular spectra and correlations:

where $C_{\ell}$is the angular power spectrum of the CMB, $\mathbf{A}$is a matrix, $\mathbf{P}_{\ell}$is a positive matrix, and $\mathbf{N}_{\ell}$is a diagonal matrix representing the noise power spectrum. The parameter vector contains all or part of the quantities in Eq. (5).

The above equations summarize the founding principles of SMICA; its actual operation depends on a choice for the spectral model and on several implementation-specific details.

The actual implementation of SMICA includes the following steps:

Inputs

All nine Planck frequency channels from 30 to 857 GHz, harmonically transformed up to $\ell = 4000$.

Fit

In practice, the SMICA fit,i.e.,the minimization of Eq. (4), is conducted in three successive steps: We first estimate the CMB spectral law by fitting all model parameters over a clean fraction of sky in the range and retaining the best fit value for vector $\mathbf{a}$. In the second step, we estimate the foreground emissivity by fixing a to its value from the previous step and fitting all the other parameters over a large fraction of sky in the range and retaining the best fit values for the matrix $\mathbf{A}$. In the last step, we fit all power spectrum parameters; that is, we fix $\mathbf{a}$and $\mathbf{A}$to their previously found values and fit for each $C_{\ell}$and $\mathbf{P}_{\ell}$at each ℓ.

Beams

The discussion thus far assumes that all input maps have the same resolution and effective beam. Since the observed maps actually vary in resolution, we process the input maps in the following way. To the i-th input map with effective beam $b_i(\ell)$and sampled on an HEALPix grid with N^i_{side}, the CMB sky multipole $s_{\ell m}$ actually contributes $s_{\ell m} a_i b_i(\ell) p_i(\ell)$, where $p_i(\ell)$is the pixel window function for the grid at N^i_{side}. Seeking a final CMB map at 5-arcmin resolution, the highest resolution of Planck, we work with input spherical harmonics re-beamed to 5 arcmins, $\tilde{\mathbf{x}}_{\ell m}$; that is, SMICA operates on vectors with entries , where $b_5(\ell)$is a 5 arcmin Gaussian beam function. By construction, SMICA then produces an CMB map with an effective Gaussian beam of 5 arcmin (without the pixel window function).

Pre-processing

We start by fitting point sources with SNR > 5 in the PCCS catalogue in each input map. If the fit is successful, the fitted point source is removed from the map; otherwise it is masked and the hole in-painted. This is done at all frequencies but 545 and 857 GHz, where all point sources with SNR > 7.5 are masked and in-painted.

Masking and in-painting

In practice, SMICA uses a small Galactic mask leaving 97% of the sky. We deliver a full-sky CMB map in which the masked pixels (Galactic and point-source) are replaced by a constrained Gaussian realization.

Binning

In our implementation, we use binned spectra.

High ℓ

Since there is little point trying to model the spectral covariance at high multipoles, because the sample estimate is sufficient, SMICA implements a simple harmonic ILC at $\ell > 1500$; that is, it applies the filter (Eq. 2) with $\mathbf{R}_\ell = \hat{\mathbf{R}}_\ell$.

Viewed as a filter, SMICA can be summarized by the weights $\mathbf{w}_\ell$applied to each input map as a function of multipole. In this sense, SMICA is strictly equivalent to co-adding the input maps after convolution by specific axi-symmetric kernels directly related to the corresponding entry of $\mathbf{w}_\ell$. The SMICA weights used here are shown in figure below for input maps in units of K. They show, in particular, the (expected) progressive attenuation of the lowest resolution channels with increasing multipole.

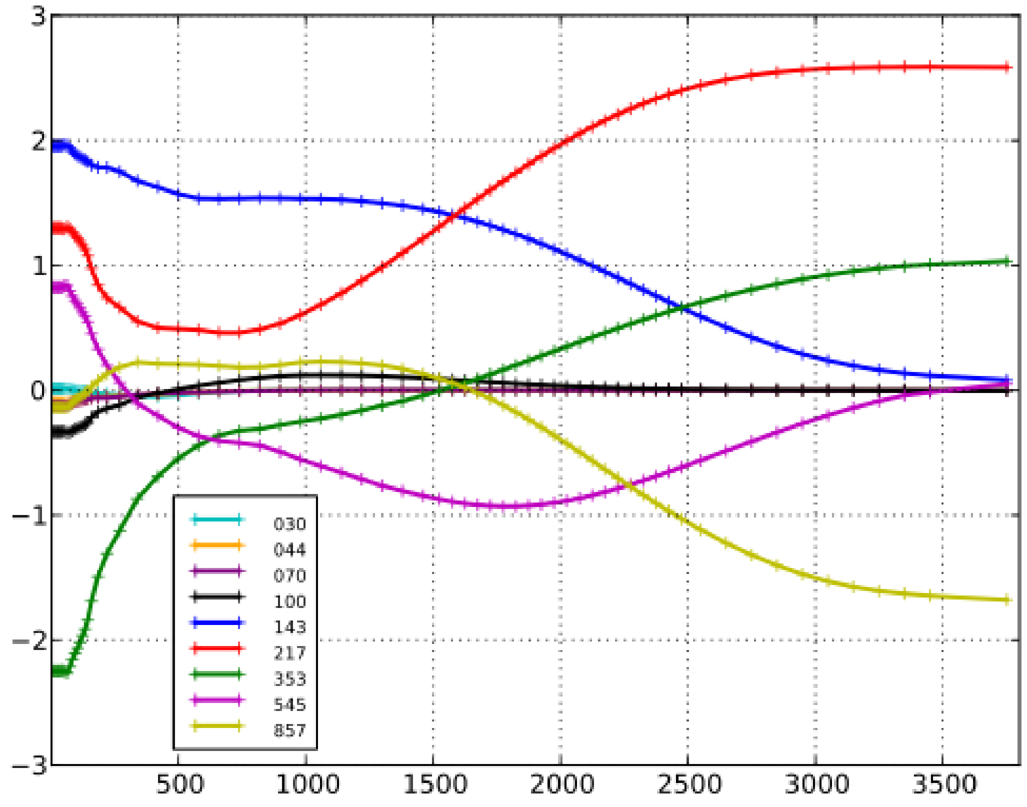

Weights $w_\ell$given by SMICA to the input maps, after they are re-beamed to 5 arcmin and expressed in K, as a function of multipole.

Commander-Ruler

The Commander-Ruler (C-R) approach implements Bayesian component separation in pixel space, fitting a parametric model to the data by sampling the posterior distribution for the model parameters. For computational reasons, the fit is performed in a two-step procedure: First, both foreground amplitudes and spectral parameters are found at low-resolution using MCMC/Gibbs sampling algorithms (Jewell et al. 2004; Wandelt et al. 2004; Eriksen et al. 2004, 2007, 2008). Second, the amplitudes are recalculated at high resolution by solving the generalized least squares system (GLSS) per pixel with the spectral parameters fixed to the their values from the low-resolution run.

For the CMB-oriented analysis presented in this paper, we only use the seven lowest Planck frequencies, i.e., from 30 to 353 GHz. We first downgrade each frequency map from its native angular resolution to a common resolution of 40 arcminutes and re-pixelize at HEALPix N = 256. Second, we set the monopoles and dipoles for each frequency band using a method that locally conserves spectral indices (Wehus et al. 2013, in preparation). We approximate the effective instrumental noise as white with an RMS per pixel given by the Planck scanning pattern and an amplitude calibrated by smoothing simulations of the instrumental noise including correlations to the same resolution. For the high-resolution analysis, the important pre-processing step is the upgrading of the effective low-resolution mixing matrices to full Planck resolution: this is done by repixelizing from N = 256 to 2048 in harmonic space, ensuring that potential pixelization effects from the low-resolution map do not introduce sharp boundaries in the high-resolution map.

References

<biblio force=false>

1. References

</biblio>

Mission products

Mission products

The products of the Planck mission that are made public at this time and described in this document consist of:

- different types of **sky maps**, i.e., maps of the unpolarized signal received from the sky, accompanied by;
- various **catalogues**: of point sources, one per frequency band, and of the SZ clusters (of which there are several compiled with different extraction methods);
- a set of **astrophysical component maps**, which attempt to separate the different astrophysical components, namely the CMB and several foregrounds;
- a **dust opacity map and model** derived from the dust component but using also external information;
- a set of **sky power spectra** obtained from selected combinations of detectors, which are for use in likelihood studies;
- a **CMB power spectrum**, the best the DPCs could produce at this time.

To support the interpretation of these data, these products are accompanied by:

- instrument-level data (beam properties, noise levels, bandpass profiles, and more) compiled into the **Reduced Instrument Model**, or **RIMO**, of which there is one per instrument.
- the **effective beams**

Two software packages are also included as Mission Products:

- the Likelihood code package, which is itself split into a software package and a data package,
- the Unit Conversion and Color Correction (UcCC) package, which is used together with the bandpass profiles in the RIMO.

There are no low-level science products in this release of Planck data, in particular no timeline data (detector signal, pointing, housekeeping), and in general no instrument data at the single detector level.

The data products are packaged into FITS files that contain a main product (e.g., a signal map) and one or more other products to characterize it (e.g., a variance map and a hit-count map). Depending on the details of the products, the data are written into a single *BINTABLE* or a few extensions, or an *IMAGE* extension. The RIMO is also packaged into a FITS file, but given the nature of its different elements it was necessary to use several hundred *BINTABLE* extensions.

The software is delivered as a tarball of code, and if necessary a second tarball of associated data is also delivered. The details depend on the code and are described elsewhere in this document.

This chapter is divided by type of product. Each section contain a brief description of how each type of product is obtained, while the details of the processing are given in the HFI Data Processing and LFI Data Processing chapters, and any known problems with the product. The list of product files is then given, and sample FITS headers are given and explained.

A very brief description of how to start using the PLA can be found in the PLA appendix. The PLA software provides a more extensive user guide.

Timelines

This section was intentionally left empty. It will be filled in future releases of the PLA to accompany the Timeline products.

Sky temperature maps

General description

Sky maps give the best estimate of the intensity of the signal from the sky after removal, as far as possible, of known systematic effects and of the dipole signals induced by the motion of the solar system in the CMB and of the Planck satellite in the solar system. Sky maps are provided for the nominal Planck mission and also, separately, for the first two single surveys, the third one being covered only for a small part during the nominal mission.The details of the start and end times of each are given in this table. As a secondary product, maps with estimates of the Zodiacal light and Far-Side-Lobes contribution removed are also provided.

For characterization purposes, are also provided maps covering the nominal survey but each one using only half of the available data. These are the *ringhalf_{1|2}* maps, which are built using the first and second half of the stable pointing part in each pointing period. These maps are used extensively to investigate the (high frequency) noise properties the maps themselves and of other products described elsewhere (see e.g., the data validation section).

To help in further processing, there are also masks of the Galactic Plane and of point sources, each provided for several different depths.

All sky maps are in Healpix format, with Nside of 2048 for HFI and of 1024 for LFI (note that the LFI 70 GHz has been delivered also at Nside of 2048 to be directly comparable with HFI maps), in Galactic coordinates, and Nested ordering. The signal is given in units of K_{cmb} for 30-353 GHz, and of MJy/sr (for a constant $\nu F_\nu$ energy distribution) for 545 and 857 GHz. Each sky map is packaged into a *BINTABLE* extension of a FITS file together with a hit-count map (or hit map, for short, giving the number of observation samples that are cumulated in a pixel, all detectors combined) and a variance map (determined from the half-ring maps), and additional information is given in the FITS file header. The structure of the FITS file is given in the FITS file structure section below.

Types of maps

Full channel maps

> Full channel maps are built using all the valid detectors of a frequency channel and cover the nominal mission. For HFI, the 143-8 and 545-3 bolometers are rejected entirely as they are seriously affected by RTS noise. The maps are displayed in the figures below. The range is the same from 30 - 143 GHz in order to show the CMB at the same level. At higher frequencies the range is increased in order to keep the Galactic Plane from invading the whole sky.

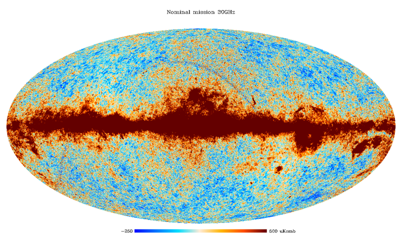
Nominal mission 30GHz
−250
500 uKcmb

Nominal mission, 30 GHz

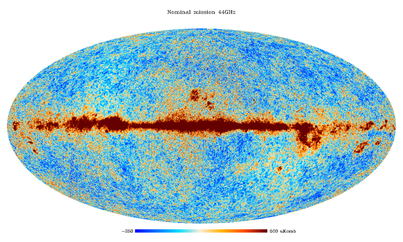
Nominal mission 44GHz
−250
500 uKcmb

Nominal mission, 44 GHz

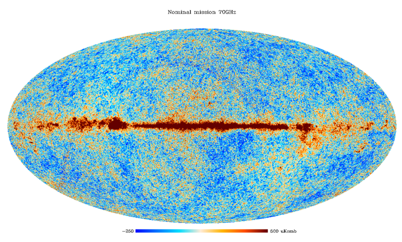
Nominal mission 70GHz
−250
500 uKcmb

Nominal mission, 70 GHz

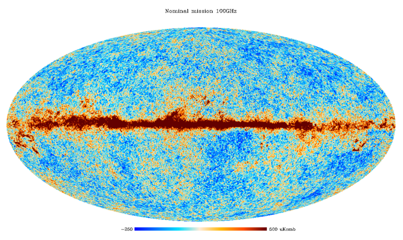
Nominal mission 100GHz
−250
500 uKcmb

Nominal mission, 100 GHz

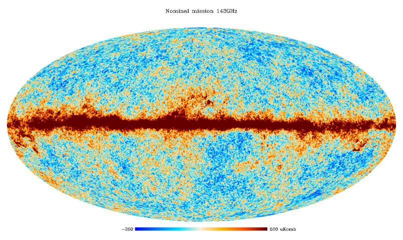
Nominal mission 143GHz
−250
500 uKcmb

Nominal mission, 143 GHz

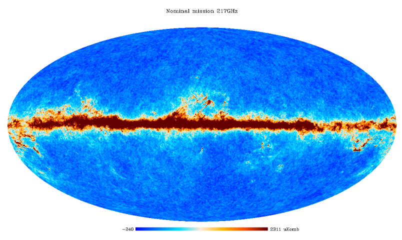
Nominal mission 217GHz
−240
2311 uKcmb

Nominal mission, 217 GHz

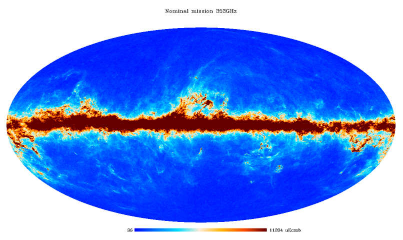
Nominal mission 353GHz
36
11204 uKcmb

Nominal mission, 353 GHz

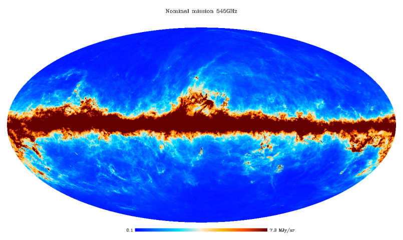
Nominal mission 545GHz
0.1
7.3 MJy/sr

Nominal mission, 545 GHz

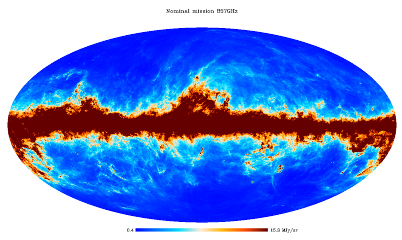
Nominal mission 857GHz
0.4
15.3 MJy/sr

Nominal mission, 857 GHz

Single survey maps

Single survey maps are built using all valid detectors of a frequency channel; they cover separately the different sky surveys. The surveys are defined as the times over which the satellite spin axis rotates but 180 degrees, which, due to the position of the detectors in the focal plane does not cover the full sky, but a fraction between ~80 and 90% depending on detector position.

Detector set or detector pairs maps

These are maps built from a subset of the detectors in a frequency channel, typically our of two PSB pairs (i.e., four poloarisation-sensitive bolometers with different orientation on the sky), for HFI in order to extract a single temperature map. While none of these maps are part of the first Planck data release, the concept of *detset* is used, and thus it is worth mentioning it here. In particular, information by detector set is available at the sky power spectrum level and in the RIMO.

Half-ring maps

Half-ring maps are built using only the first or the second half of the stable pointing period data. There are thus two half-ring maps per frequency channel named *ringhalf_1* and *ringhalf_2* respectively. These maps are built for characterization purposes in order to perform null tests. In particular, the difference between the two half-ring maps at a given frequency give a good estimate of the high frequency noise in the data (albeit biased low by ~0.5% for the HFI channels due to specifics of the TOI processing).

Masks

Masks are provided of the Galactic Plane and of the point sources. For the Galactic Plane, eight masks are given covering different fractions of the sky, and for the points sources two masks are given, at the 5 and 10 sigma level, for each Planck HFI frequency channel. These are generic masks, specific masks applicable to other products are delivered with the products themselves.

Caveats and known issues

The primary limitation of the HFI maps are

- the absence of correction of the ADC non-linearities,
- the far-side lobe contribution is not accounted for in the processing and in the calibration,
- the dipole removal is based on the non-relativistic approximation which leaves a weak quadrupole component in the map.

And thus the overall calibration accuracy is at the 0.2% level in 100-217 GHz channels

The LFI 70 GHz maps at Nside=2048 should be considered as additional product, the default are the LFI maps at Nside=1024. No effective beam at Nside=2048 is provided, only at Nside=1024, for this reason the use of the effective beam with maps at Nside 2048 is discouraged.

Map zero-level

For the 100 to 857 GHz maps, the zero levels are set to their optimal levels for Galactic and CIB studies. A procedure for adjusting them to astrophysical values is given in the HFI Calibration paper #planck2013-p03b Planck-2013-VIII [1].

For the 30, 44 and 70 GHz, maps are corrected for zero level monopole by applying an offset correction, see LFI Calibration paper #planck2013-p02b Planck-2013-V [4] section 3.4 "Setting the zero levels in the maps". Note that the offset applied is indicated in the header as a comment keyword.

The Zodiacal light and the Far-Side Lobes

The figures below show the modeled Zodiacal light and Far Side Lobes projected onto the maps; they are simply the difference between the *main product* and the *ZodiCorrected* maps for the nominal mission. The units are given in the figures. The *heat* color table has been used in place of the standard Planck for clarity reasons.

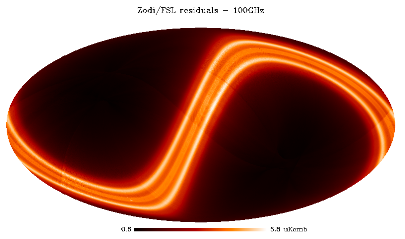

zodi/FSL rediduals - 100 GHz

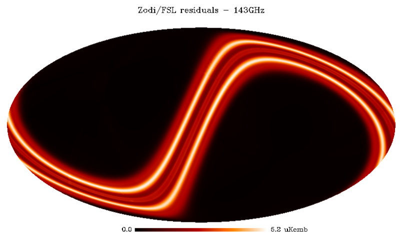

zodi/FSL rediduals - 143 GHz

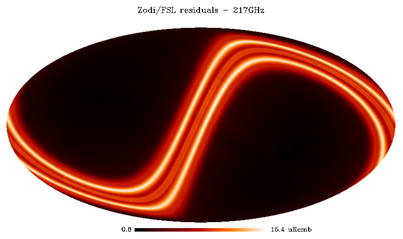

zodi/FSL rediduals - 217 GHz

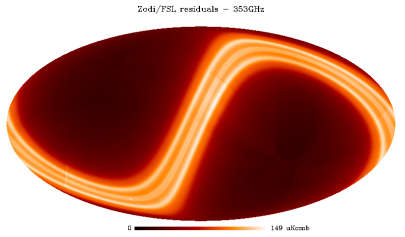

zodi/FSL rediduals - 353 GHz

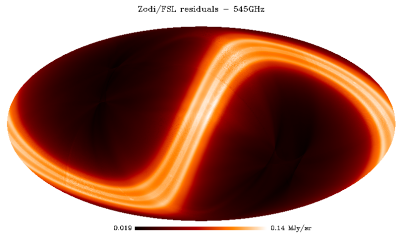

zodi/FSL rediduals - 545 GHz

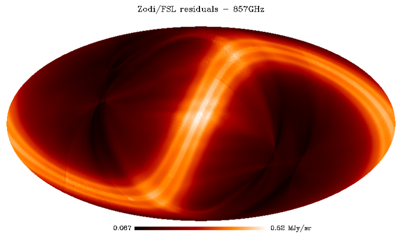

zodi/FSL rediduals - 857 GHz

The effects of the FSLs are seen most clearly at the highest frequencies, as structures roughly symmetric about the center of the image, which corresponds to the location of the Galactic Centre, which is in turn the source of most of the radiation that is scattered into the FSLs.

Artifacts near caustics of the scanning strategy

The scanning strategy is such that regions around the Ecliptic poles are surveyed very deeply and compared to the average, and the transition from the nominal depth to the high depth, as shows on hit-count maps is very rapid, namely a few pixels, for a contrast of ~30. These transitions, or caustics in the maps, occur at different positions on the sky for different detectors, as the positions depend on their location in the focal plane of the instrument. As a result, when data from different detectors are combined to build a full channel map, the the weights of different detectors in the mix changes rapidly across the caustic, and given the remaining errors in the relative calibration of the detectors, a visible effect can be introduced in the maps, especially when the SNR is very high, i.e. at the highest frequencies and near bright regions like the Galactic Plane. Some examples are shown below.

Production process

Sky maps are produced by combining appropriately the data of all working detectors in a frequency channel over some period of the mission. They give the best estimate of the signal from the sky (unpolarised) after removal, as far as possible, of known systematic effects and of the dipole signals induced by the motion of the solar system in the CMB and of the Planck satellite in the solar system. In particular, they include the Zodiacal light emission (Zodi for short) and also the scattering from the far-side lobes of the beams (FSL). More on this below.

HFI processing

The inputs to the mapmaking are TOIs of signal that have been cleaned (as far as possible) of instrumental effects and calibrated in absorbed watts. While the processing involved is described in detail in the TOI processing section, we give a very brief summary here for convenience. That pipeline performs the following operations:

demodulation

> this is performed around a variable level which is determined from the valid input data (a validity flag from a previous version of the processing is used for this purpose), and the data are converted to engineering units (V) using known conversion coefficients.

despiking

> using the demodulated data converted to V (by the transfer function) the glitches are identified and fitted with templates. A glitch flag is produced that identifies the strongest part of the glitches, and a timeline of glitch tails is produced from the template fits, and subtracted from the demodulated timeline from step 1. Finally, the flagged ranges are replaced with data from an average over the pointing period (TBC)

dark template removal

> the two dark bolometers are demodulated and despiked as above; the resulting timelines are then smoothed and used as an indicator of the overall temperature variations of the bolometer plate. Where the variations are consistent with each other, they are combined and removed from the bolometer signal timelines using appropriate coupling coefficients. The few percent of the data where they are not consistent are flagged on the timelines.

conversion to absorbed power

> the timeline is converted to watts of absorbed power using the bolometer function. This includes a non-linearity correction; removal of the 4K cooler lines: the electromagnetic interference of the 4K cooler with the bolometer readout wires induces some sharp lines in the signal power spectra at frequencies of the 4K

cooler's fundamental and its multiples, folded by the signal modulations. Fourier coefficients of the relevant lines are determined on a per-ring basis, and then removed from the data. The quality of the removal depends on the bolometer.

deconvolution by the time transfer function

this is done to correct for the non-instantaneous time response of the bolometers. The function itself is modeled using 4 parameters which are adjusted primarily on the planet data and also from comparisons of the northward and southward scans of the Galactic Plane. It is then removed using Fourier techniques, which has the side-effect of increasing the noise at high frequencies.

jump correction

removes some (relatively rare: 0.3 jumps per bolometer per pointing period, on average) jumps in the signal baseline. The jumps are detected characterized on smoothed TOIs, and corrected by adding a constant to part of the signal timeline. The origin of the jumps is not known.

The results of this processing are a timeline of signal (in absorbed watts) and a *valid data* flag timeline for each of the 50 valid bolometers processed; these timelines contain the full sky signal, i.e., including the solar and orbital dipoles, the Zodiacal light, and contributions from the Far-Side lobes. The dipoles are necessary for the flux calibration and are removed at the mapmaking stage. The remaining two bolometers (143-8 and 535-3) show semi-random jumps in the signal level, typically jumping over 2-5 different *pseudo-baseline* levels, a behavior known as *Random Telegraphic Signal*, so that these are commonly called the RTS bolometers. Finally, ring-level statistics of different types (mean, median, rms, kurtosis, etc.) are determined on a per-ring basis for all timelines, and a selection based on these statistics is used to discard anomalous rings, which are recorded in a ring-level flag for each valid bolometer timeline (see the Discarded rings section).

Throughout this processing, bright planets (Mars, Jupiter, Saturn, Uranus) and bright asteroids are masked in the timeline in order to avoid ringing effects in the processing. Since they move on the sky, the portion of the sky masked during one survey is observed during one, and no hole is left in the final map. In parallel, the planet data are processed in a similar way, but with different parameters for the despiking step, and without the final jump correction step. These results are processed separately to determine the beam shapes and the focal plane geometry.

The pointing is determined starting from the AHF produced by MOC, which gives the direction and orientation of the LOS of a fiducial position in the focal plane at frequencies of 8Hz during stable pointing and 4 Hz during maneuvers (TBC for details, reference). This is interpolated to the times of data observation (ref to method), corrected for the wobble and other time-dependent offsets determined from the observed positions of a large number of sources around the sky, and finally converted to the LOS of each detector using the quaternions in the IMO (which are determined from observations of bright planets - see the Detector_pointing section).

The mapmaking and calibration process is described in detail in the Map-making section, where detailed references are found. In brief it consists of:

binning the TOI data onto *rings*

Healpix rings (HPRs) are used here, each ring containing the combined data of one pointing period.

flux calibration

at 100-353 GHz, the flux calibration factors are determined for each pointing period (or ring) from the solar-motion dipole, using the WMAP dipole as the reference, and after removal of the dipole signal induced by the motion of the Planck satellite in the solar system. This gain by ring is smoothed with a window of width 50 rings, which reveals an apparent variation of ~1-2% on a scale of 100s to 1000s of rings for the 100-217 GHz channels, and is applied. At 353GHz, where the solar motion dipole is weaker compared to the signal, no gain variation is detected (within the uncertainties), and a single fixed gain is applied to all rings. At 545 and 857 GHz the gain is determined from the observation of Uranus and Neptune (but not Jupiter which is too bright) and comparison to recent models made explicitly for this mission. A single gain is applied to all rings at these frequencies.

destriping

in order to remove low-frequency noise, an offset per ring is determined by minimizing the differences between HPRs at their crossings, and removed.

projection onto the map

the offset-corrected and flux-calibrated HPRs are projected onto Healpix maps, with the data of each bolometer weighted by a factor of 1/NET of that bolometer, and accounting for the slight different band transmission profiles of the bolometers in each band.

These maps provide the main mission products. A second, reduced, set of maps, cleaned of the Zodiacal emission of the FSL leakage is also produced for the nominal mission and the two single surveys, but not for the half-rings (since the contribution would be the same for the two halves of each ring). For this purpose, the the Zodiacal emission and the FSL contamination, which are not fixed on the sky, are modeled separately at HPR-level, and subtracted from the signal HPR before projecting them onto the maps.

Together with signal maps, hit count and variance maps are also produced. The hit maps give the (integer) number of valid TOI-level samples that contribute to the signal of each pixel. All valid samples are counted in the same way, i.e., there is no weighting factor applied. The variance maps project the white noise estimate, provided by the NETs, in the sky domain.

LFI processing

LFI maps were constructed with the Madam map-making code, version 3.7.4. The code is based on generalized destriping technique, where the correlated noise component is modeled as a sequence of constant offset, called baselines. A noise filter was used to constrain the baseline solution allowing the use of 1 second baselines.

Radiometers were combined according to the horn-uniform weighting scheme to minimize systematics. The used weights are listed in Map-making. The flagged samples were excluded from the analysis by setting their weights to C_{w}^{-1} = 0. The galaxy region was masked out in the destriping phase, to reduce error arising from strong signal gradients. The polarization component was included in the analysis, although only the temperature maps are released.

A detailed description of the map-making procedure is given in #planck2013-p02 Planck-2013-II [1] and in section Map-making.

Inputs

HFI inputs

- The cleaned TOIs of signal of each detector, together with their flags, produced by the TOI processing pipeline
- The TOIs of pointing (quaternions), described in Detector_pointing
- Bolometer-level characterization data, from the DPC's internal IMO (not distributed)
- Planck orbit data used to compute and remove the earth dipole
- WMAP solar dipole information used to calibrate the CMB channels
- Planet models used to calibrate the Galactic channels.

LFI inputs

The Madam map-maker takes as an input:

- The calibrated timelines (for details see TOI Processing)
- The detector pointings (for details see Detector pointing)
- The noise information in the form of three-parameter (white noise level (σ), slope, and knee frequency (f_knee)) noise model (for details see RIMO)

Related products

Masks

Masks are provided of

the Galactic Plane

> 8 masks are provided giving 20, 40, 60, 70, 80, 90, 97, and 99% sky coverage in two different files, at Nside=2048. For the HFI they can be used as they are, for the LFI they need to be downgraded at Nside=1024 (note that if using the 70 GHZ at Nside=2048 no downgraded is needed)

the point sources

> 18 masks are provided, 2 per frequency channel, each masking at the 5 and 10σ level. For the HFI they can be used as they are, for the LFI they need to be downgraded at Nside=1024 (note that if using the 70 GHZ at Nside=2048 no downgraded is needed)

The masks are binary, in GALACTIC coordinates, and NESTED ordering. The table below give the filenames.

FITS filenames for masks

Galactic Plane masks	Point Sources masks
HFI_Mask_GalPlane_2048_R1.10.fits [1]	HFI_Mask_PointSrc_2048_R1.10.fits [2]

The masks are shows below in a single figure. While this is quite clear for the Galactic Plane masks, it is less so for the point source masks, but it does give a clear perspective on how the latter are distributed over the sky.

File names

The FITS filenames are of the form *{H|L}FI_SkyMap_fff_nnnn_R1.nn_{coverage}_{type}.fits*, where *fff* are three digits to indicate the Planck frequency band, and *nnnn* is the Healpix Nside of the map, *coverage* indicates which part of the mission is covered, and the optional *type* indicates the subset of input data used. A full list of products, with links to them in the Archive, is given in the tables below.

FITS filenames

Frequency	Full channel maps
30GHz	LFI_SkyMap_030_1024_R1.10_nominal.fits [3]
44GHz	LFI_SkyMap_044_1024_R1.10_nominal.fits [4]
70GHz	LFI_SkyMap_070_1024_R1.10_nominal.fits [5]
70GHz	LFI_SkyMap_070_2048_R1.10_nominal.fits [6]
100GHz	HFI_SkyMap_100_2048_R1.10_nominal.fits [7]
143GHz	HFI_SkyMap_143_2048_R1.10_nominal.fits [8]
217GHz	HFI_SkyMap_217_2048_R1.10_nominal.fits [9]
353GHz	HFI_SkyMap_353_2048_R1.10_nominal.fits [10]
545GHz	HFI_SkyMap_545_2048_R1.10_nominal.fits [11]
857GHz	HFI_SkyMap_857_2048_R1.10_nominal.fits [12]
Frequency	**Full channel, Zodi-corrected maps**
100GHz	HFI_SkyMap_100_2048_R1.10_nominal_ZodiCorrected.fits [13]
143GHz	HFI_SkyMap_143_2048_R1.10_nominal_ZodiCorrected.fits [14]
217GHz	HFI_SkyMap_217_2048_R1.10_nominal_ZodiCorrected.fits [15]
353GHz	HFI_SkyMap_353_2048_R1.10_nominal_ZodiCorrected.fits [16]
545GHz	HFI_SkyMap_545_2048_R1.10_nominal_ZodiCorrected.fits [17]
857GHz	HFI_SkyMap_857_2048_R1.10_nominal_ZodiCorrected.fits [18]

FITS filenames

Frequency	Survey 1 maps	Survey 2 maps
30GHz	LFI_SkyMap_030_1024_R1.10_survey_1.fits [19]	LFI_SkyMap_030_1024_R1.10_survey_2.fits [20]
44GHz	LFI_SkyMap_044_1024_R1.10_survey_1.fits [21]	LFI_SkyMap_044_1024_R1.10_survey_2.fits [22]
70GHz	LFI_SkyMap_070_1024_R1.10_survey_1.fits [23]	LFI_SkyMap_070_1024_R1.10_survey_2.fits [24]
70GHz	LFI_SkyMap_070_2048_R1.10_survey_1.fits [25]	LFI_SkyMap_070_2048_R1.10_survey_2.fits [26]
100GHz	HFI_SkyMap_100_2048_R1.10_survey_1.fits [27]	HFI_SkyMap_100_2048_R1.10_survey_2.fits [28]
143GHz	HFI_SkyMap_143_2048_R1.10_survey_1.fits [29]	HFI_SkyMap_143_2048_R1.10_survey_2.fits [30]
217GHz	HFI_SkyMap_217_2048_R1.10_survey_1.fits [31]	HFI_SkyMap_217_2048_R1.10_survey_2.fits [32]
353GHz	HFI_SkyMap_353_2048_R1.10_survey_1.fits [33]	HFI_SkyMap_353_2048_R1.10_survey_2.fits [34]
545GHz	HFI_SkyMap_545_2048_R1.10_survey_1.fits [35]	HFI_SkyMap_545_2048_R1.10_survey_2.fits [36]
857GHz	HFI_SkyMap_857_2048_R1.10_survey_1.fits [37]	HFI_SkyMap_857_2048_R1.10_survey_2.fits [38]

Frequency	Survey 1 Zodi-corrected maps	Survey 2 Zodi-corrected maps
100GHz	HFI_SkyMap_100_2048_R1.10_survey_1_ZodiCorrected.fits [39]	HFI_SkyMap_100_2048_R1.10_survey_2_ZodiCorrected.fits [40]
143GHz	HFI_SkyMap_143_2048_R1.10_survey_1_ZodiCorrected.fits [41]	HFI_SkyMap_143_2048_R1.10_survey_2_ZodiCorrected.fits [42]
217GHz	HFI_SkyMap_217_2048_R1.10_survey_1_ZodiCorrected.fits [43]	HFI_SkyMap_217_2048_R1.10_survey_2_ZodiCorrected.fits [44]
353GHz	HFI_SkyMap_353_2048_R1.10_survey_1_ZodiCorrected.fits [45]	HFI_SkyMap_353_2048_R1.10_survey_2_ZodiCorrected.fits [46]
545GHz	HFI_SkyMap_545_2048_R1.10_survey_1_ZodiCorrected.fits [47]	HFI_SkyMap_545_2048_R1.10_survey_2_ZodiCorrected.fits [48]
857GHz	HFI_SkyMap_857_2048_R1.10_survey_1_ZodiCorrected.fits [49]	HFI_SkyMap_857_2048_R1.10_survey_2_ZodiCorrected.fits [50]
Frequency	**Half-ring 1 maps**	**Half-ring 2 maps**
30GHz	LFI_SkyMap_030_1024_R1.10_nominal_ringhalf_1.fits [51]	LFI_SkyMap_030_1024_R1.10_nominal_ringhalf_2.fits [52]
44GHz	LFI_SkyMap_044_1024_R1.10_nominal_ringhalf_1.fits [53]	LFI_SkyMap_044_1024_R1.10_nominal_ringhalf_2.fits [54]
70GHz	LFI_SkyMap_070_1024_R1.10_nominal_ringhalf_1.fits [55]	LFI_SkyMap_070_1024_R1.10_nominal_ringhalf_2.fits [56]
70GHz	LFI_SkyMap_070_2048_R1.10_nominal_ringhalf_1.fits [57]	LFI_SkyMap_070_2048_R1.10_nominal_ringhalf_2.fits [58]
100GHz	HFI_SkyMap_100_2048_R1.10_nominal_ringhalf_1.fits [59]	HFI_SkyMap_100_2048_R1.10_nominal_ringhalf_2.fits [60]
143GHz	HFI_SkyMap_143_2048_R1.10_nominal_ringhalf_1.fits [61]	HFI_SkyMap_143_2048_R1.10_nominal_ringhalf_2.fits [62]
217GHz	HFI_SkyMap_217_2048_R1.10_nominal_ringhalf_1.fits [63]	HFI_SkyMap_217_2048_R1.10_nominal_ringhalf_2.fits [64]
353GHz	HFI_SkyMap_353_2048_R1.10_nominal_ringhalf_1.fits [65]	HFI_SkyMap_353_2048_R1.10_nominal_ringhalf_2.fits [66]
545GHz	HFI_SkyMap_545_2048_R1.10_nominal_ringhalf_1.fits [67]	HFI_SkyMap_545_2048_R1.10_nominal_ringhalf_2.fits [68]
857GHz	HFI_SkyMap_857_2048_R1.10_nominal_ringhalf_1.fits [69]	HFI_SkyMap_857_2048_R1.10_nominal_ringhalf_2.fits [70]

FITS file structure

The FITS files for the sky maps contain a minimal primary header with no data, and a *BINTABLE* extension (EXTENSION 1, EXTNAME = *FREQ-MAP*) containing the data. The structure is shows schematically in the figure at right.

The *FREQ-MAP* extension contains is a 3-column table that contain the signal, hit-count and variance maps, all in Healpix format, in columns 1, 2, and 3, respectively. The number of rows is 50331648 for HFI and LFI 70 GHz at Nside=2048 and 12582912 for LFI maps at Nside=1024 (N.B: Npix = 12 Nside^2). The three columns are *I_STOKES* for the intensity (or temperature) signal, *HIT* for the hit-count and *II_COV* for the variance. The exact order of the columns in the figure is indicative only, and the details can be found in the keywords.

Keywords indicate the coordinate system (GALACTIC), the Healpix ordering scheme (NESTED), the units (K_cmb or MJy/sr) of each column, and of course the frequency channel (FREQ). The COMMENT fields give a one-line summary of the product, and some other information useful for traceability within the DPCs. The original filename is also given in the *FILENAME* keyword as are the datasum and the md5 checksum for the extension. The *BAD_DATA* keyword gives the value used by Healpix to indicate pixels for which no signal is present (these will also have a hit-count value of 0). The COMMENT fields give further information including some traceability data for the DPC's. The main parameters are summarised below:

Sky map file data structure

1. EXTNAME = 'FREQ-MAP' : Data columns			
Column Name	**Data Type**	**Units**	**Description**
I_STOKES	Real*4	K_cmb or MJy/sr	The signal map
HITS	Int*4	none	The hit-count map
II_COV	Real*4	K_cmb^2 or (MJy/sr)^2	The variance map
Keyword	**Data Type**	**Value**	**Description**
PIXTYPE	string	HEALPIX	
COORDSYS	string	GALACTIC	Coordinate system
ORDERING	string	NESTED	Healpix ordering
NSIDE	Int	1024 or 2048	Healpix Nside
FIRSTPIX	Int*4	0	First pixel number
LASTPIX	Int*4	12582911 or 50331647	Last pixel number
FREQ	string	nnn	The frequency channel

The same structure applies to all *SkyMap* products, independent of whether they are full channel, survey of half-ring. The distinction between the types of maps is present in the FITS filename (and in the traceability comment fields).

References

<biblio force=false>

1. References

</biblio>

References

[1] http://pla.esac.esa.int/pla/aio/product-action?MAP.MAP_ID=HFI_Mask_GalPlane_2048_R1.10.fits
[2] http://pla.esac.esa.int/pla/aio/product-action?MAP.MAP_ID=HFI_Mask_PointSrc_2048_R1.10.fits
[3] http://pla.esac.esa.int/pla/aio/product-action?MAP.MAP_ID=LFI_SkyMap_030_1024_R1.10_nominal.fits
[4] http://pla.esac.esa.int/pla/aio/product-action?MAP.MAP_ID=LFI_SkyMap_044_1024_R1.10_nominal.fits
[5] http://pla.esac.esa.int/pla/aio/product-action?MAP.MAP_ID=LFI_SkyMap_070_1024_R1.10_nominal.fits
[6] http://pla.esac.esa.int/pla/aio/product-action?MAP.MAP_ID=LFI_SkyMap_070_2048_R1.10_nominal.fits
[7] http://pla.esac.esa.int/pla/aio/product-action?MAP.MAP_ID=HFI_SkyMap_100_2048_R1.10_nominal.fits
[8] http://pla.esac.esa.int/pla/aio/product-action?MAP.MAP_ID=HFI_SkyMap_143_2048_R1.10_nominal.fits
[9] http://pla.esac.esa.int/pla/aio/product-action?MAP.MAP_ID=HFI_SkyMap_217_2048_R1.10_nominal.fits
[10] http://pla.esac.esa.int/pla/aio/product-action?MAP.MAP_ID=HFI_SkyMap_353_2048_R1.10_nominal.fits
[11] http://pla.esac.esa.int/pla/aio/product-action?MAP.MAP_ID=HFI_SkyMap_545_2048_R1.10_nominal.fits
[12] http://pla.esac.esa.int/pla/aio/product-action?MAP.MAP_ID=HFI_SkyMap_857_2048_R1.10_nominal.fits
[13] http://pla.esac.esa.int/pla/aio/product-action?MAP.MAP_ID=HFI_SkyMap_100_2048_R1.10_nominal_ZodiCorrected.fits
[14] http://pla.esac.esa.int/pla/aio/product-action?MAP.MAP_ID=HFI_SkyMap_143_2048_R1.10_nominal_ZodiCorrected.fits
[15] http://pla.esac.esa.int/pla/aio/product-action?MAP.MAP_ID=HFI_SkyMap_217_2048_R1.10_nominal_ZodiCorrected.fits
[16] http://pla.esac.esa.int/pla/aio/product-action?MAP.MAP_ID=HFI_SkyMap_353_2048_R1.10_nominal_ZodiCorrected.fits
[17] http://pla.esac.esa.int/pla/aio/product-action?MAP.MAP_ID=HFI_SkyMap_545_2048_R1.10_nominal_ZodiCorrected.fits

[18] http://pla.esac.esa.int/pla/aio/product-action?MAP.MAP_ID=HFI_SkyMap_857_2048_R1.10_nominal_ZodiCorrected.fits
[19] http://pla.esac.esa.int/pla/aio/product-action?MAP.MAP_ID=LFI_SkyMap_030_1024_R1.10_survey_1.fits
[20] http://pla.esac.esa.int/pla/aio/product-action?MAP.MAP_ID=LFI_SkyMap_030_1024_R1.10_survey_2.fits
[21] http://pla.esac.esa.int/pla/aio/product-action?MAP.MAP_ID=LFI_SkyMap_044_1024_R1.10_survey_1.fits
[22] http://pla.esac.esa.int/pla/aio/product-action?MAP.MAP_ID=LFI_SkyMap_044_1024_R1.10_survey_2.fits
[23] http://pla.esac.esa.int/pla/aio/product-action?MAP.MAP_ID=LFI_SkyMap_070_1024_R1.10_survey_1.fits
[24] http://pla.esac.esa.int/pla/aio/product-action?MAP.MAP_ID=LFI_SkyMap_070_1024_R1.10_survey_2.fits
[25] http://pla.esac.esa.int/pla/aio/product-action?MAP.MAP_ID=LFI_SkyMap_070_2048_R1.10_survey_1.fits
[26] http://pla.esac.esa.int/pla/aio/product-action?MAP.MAP_ID=LFI_SkyMap_070_2048_R1.10_survey_2.fits
[27] http://pla.esac.esa.int/pla/aio/product-action?MAP.MAP_ID=HFI_SkyMap_100_2048_R1.10_survey_1.fits
[28] http://pla.esac.esa.int/pla/aio/product-action?MAP.MAP_ID=HFI_SkyMap_100_2048_R1.10_survey_2.fits
[29] http://pla.esac.esa.int/pla/aio/product-action?MAP.MAP_ID=HFI_SkyMap_143_2048_R1.10_survey_1.fits
[30] http://pla.esac.esa.int/pla/aio/product-action?MAP.MAP_ID=HFI_SkyMap_143_2048_R1.10_survey_2.fits
[31] http://pla.esac.esa.int/pla/aio/product-action?MAP.MAP_ID=HFI_SkyMap_217_2048_R1.10_survey_1.fits
[32] http://pla.esac.esa.int/pla/aio/product-action?MAP.MAP_ID=HFI_SkyMap_217_2048_R1.10_survey_2.fits
[33] http://pla.esac.esa.int/pla/aio/product-action?MAP.MAP_ID=HFI_SkyMap_353_2048_R1.10_survey_1.fits
[34] http://pla.esac.esa.int/pla/aio/product-action?MAP.MAP_ID=HFI_SkyMap_353_2048_R1.10_survey_2.fits
[35] http://pla.esac.esa.int/pla/aio/product-action?MAP.MAP_ID=HFI_SkyMap_545_2048_R1.10_survey_1.fits
[36] http://pla.esac.esa.int/pla/aio/product-action?MAP.MAP_ID=HFI_SkyMap_545_2048_R1.10_survey_2.fits
[37] http://pla.esac.esa.int/pla/aio/product-action?MAP.MAP_ID=HFI_SkyMap_857_2048_R1.10_survey_1.fits
[38] http://pla.esac.esa.int/pla/aio/product-action?MAP.MAP_ID=HFI_SkyMap_857_2048_R1.10_survey_2.fits
[39] http://pla.esac.esa.int/pla/aio/product-action?MAP.MAP_ID=HFI_SkyMap_100_2048_R1.10_survey_1_ZodiCorrected.fits
[40] http://pla.esac.esa.int/pla/aio/product-action?MAP.MAP_ID=HFI_SkyMap_100_2048_R1.10_survey_2_ZodiCorrected.fits
[41] http://pla.esac.esa.int/pla/aio/product-action?MAP.MAP_ID=HFI_SkyMap_143_2048_R1.10_survey_1_ZodiCorrected.fits
[42] http://pla.esac.esa.int/pla/aio/product-action?MAP.MAP_ID=HFI_SkyMap_143_2048_R1.10_survey_2_ZodiCorrected.fits
[43] http://pla.esac.esa.int/pla/aio/product-action?MAP.MAP_ID=HFI_SkyMap_217_2048_R1.10_survey_1_ZodiCorrected.fits
[44] http://pla.esac.esa.int/pla/aio/product-action?MAP.MAP_ID=HFI_SkyMap_217_2048_R1.10_survey_2_ZodiCorrected.fits
[45] http://pla.esac.esa.int/pla/aio/product-action?MAP.MAP_ID=HFI_SkyMap_353_2048_R1.10_survey_1_ZodiCorrected.fits
[46] http://pla.esac.esa.int/pla/aio/product-action?MAP.MAP_ID=HFI_SkyMap_353_2048_R1.10_survey_2_ZodiCorrected.fits
[47] http://pla.esac.esa.int/pla/aio/product-action?MAP.MAP_ID=HFI_SkyMap_545_2048_R1.10_survey_1_ZodiCorrected.fits
[48] http://pla.esac.esa.int/pla/aio/product-action?MAP.MAP_ID=HFI_SkyMap_545_2048_R1.10_survey_2_ZodiCorrected.fits
[49] http://pla.esac.esa.int/pla/aio/product-action?MAP.MAP_ID=HFI_SkyMap_857_2048_R1.10_survey_1_ZodiCorrected.fits
[50] http://pla.esac.esa.int/pla/aio/product-action?MAP.MAP_ID=HFI_SkyMap_857_2048_R1.10_survey_2_ZodiCorrected.fits
[51] http://pla.esac.esa.int/pla/aio/product-action?MAP.MAP_ID=LFI_SkyMap_030_1024_R1.10_nominal_ringhalf_1.fits
[52] http://pla.esac.esa.int/pla/aio/product-action?MAP.MAP_ID=LFI_SkyMap_030_1024_R1.10_nominal_ringhalf_2.fits
[53] http://pla.esac.esa.int/pla/aio/product-action?MAP.MAP_ID=LFI_SkyMap_044_1024_R1.10_nominal_ringhalf_1.fits
[54] http://pla.esac.esa.int/pla/aio/product-action?MAP.MAP_ID=LFI_SkyMap_044_1024_R1.10_nominal_ringhalf_2.fits
[55] http://pla.esac.esa.int/pla/aio/product-action?MAP.MAP_ID=LFI_SkyMap_070_1024_R1.10_nominal_ringhalf_1.fits
[56] http://pla.esac.esa.int/pla/aio/product-action?MAP.MAP_ID=LFI_SkyMap_070_1024_R1.10_nominal_ringhalf_2.fits
[57] http://pla.esac.esa.int/pla/aio/product-action?MAP.MAP_ID=LFI_SkyMap_070_2048_R1.10_nominal_ringhalf_1.fits
[58] http://pla.esac.esa.int/pla/aio/product-action?MAP.MAP_ID=LFI_SkyMap_070_2048_R1.10_nominal_ringhalf_2.fits
[59] http://pla.esac.esa.int/pla/aio/product-action?MAP.MAP_ID=HFI_SkyMap_100_2048_R1.10_nominal_ringhalf_1.fits
[60] http://pla.esac.esa.int/pla/aio/product-action?MAP.MAP_ID=HFI_SkyMap_100_2048_R1.10_nominal_ringhalf_2.fits
[61] http://pla.esac.esa.int/pla/aio/product-action?MAP.MAP_ID=HFI_SkyMap_143_2048_R1.10_nominal_ringhalf_1.fits
[62] http://pla.esac.esa.int/pla/aio/product-action?MAP.MAP_ID=HFI_SkyMap_143_2048_R1.10_nominal_ringhalf_2.fits
[63] http://pla.esac.esa.int/pla/aio/product-action?MAP.MAP_ID=HFI_SkyMap_217_2048_R1.10_nominal_ringhalf_1.fits
[64] http://pla.esac.esa.int/pla/aio/product-action?MAP.MAP_ID=HFI_SkyMap_217_2048_R1.10_nominal_ringhalf_2.fits
[65] http://pla.esac.esa.int/pla/aio/product-action?MAP.MAP_ID=HFI_SkyMap_353_2048_R1.10_nominal_ringhalf_1.fits
[66] http://pla.esac.esa.int/pla/aio/product-action?MAP.MAP_ID=HFI_SkyMap_353_2048_R1.10_nominal_ringhalf_2.fits
[67] http://pla.esac.esa.int/pla/aio/product-action?MAP.MAP_ID=HFI_SkyMap_545_2048_R1.10_nominal_ringhalf_1.fits
[68] http://pla.esac.esa.int/pla/aio/product-action?MAP.MAP_ID=HFI_SkyMap_545_2048_R1.10_nominal_ringhalf_2.fits
[69] http://pla.esac.esa.int/pla/aio/product-action?MAP.MAP_ID=HFI_SkyMap_857_2048_R1.10_nominal_ringhalf_1.fits
[70] http://pla.esac.esa.int/pla/aio/product-action?MAP.MAP_ID=HFI_SkyMap_857_2048_R1.10_nominal_ringhalf_2.fits

The instrument model

Overview

The RIMO, or *Reduced Instrument Model* is a FITS file containing selected instrument characteristics that are needed by users who work with the released data products. It is described in detail in *The HFI and LFI RIMO ICD* (ref). There will be two RIMOs, one for each instrument, which will follow the same overall structure, but will differ in the details. The type of data in the RIMO can be:

Parameter

namely scalars to give properties such as a noise level or a representative beam FWHM

Table

to give, e.g., filter transmission profiles or noise power spectra

Image

namely 2-D "flat" array, to give, e.g., the beam correlation matrices

The FITS file begins with primary header that contains some keywords that mainly for internal use and no data. The different types of data are written into different BINTABLE (for parameters and tables) or IMAGE (for 2-D arrays) extensions, as described below.

File Names

HFI

HFI_RIMO_R1.10.fits [1]

LFI

LFI_RIMO_R1.12.fits [2]

Map-level parameter data

The map-level data table contains the effective beam solid angle (total and out to different multiples of the beamFWHM) and noise information. It is written into a BINTABLE extension named *MAP_PARAMS* whose structure is different for HFI and LFI and is as follows. The noise description below is very simplified; a more accurate rendition can be obtained from the half-ring maps. Regarding the characterization of systematics, the user should use the survey differences.

HFI

FREQUENCY (String)

a 3-digit string giving the reference frequency in GHz, i.e., of the form *217*

OMEGA_F, *OMEGA_F_ERR* (Real*4)

the full beam solid angle and its uncertainty, in armin^2

OMEGA_1, *OMEGA_1_DISP* (Real*4)

the beam solid angle out to 1FWHM, and its dispersion, in arcmin^2

OMEGA_2, *OMEGA_2_DISP* (Real*4)

the beam solid angle out to 2FWHM, and its dispersion, in arcmin^2

FWHM (Real*4)

FWHM of a Gaussian beam having the same (total) solid angle, in armin^2. This is the best value for source flux determination

FWHMGAUS (Real*4)

FWHM derived from best Gaussian fit to beam maps, in armin^2. This is the best value for source identification

NOISE (Real*4)

This is the typical noise/valid observation sample as derived from the high-*l* spectra of the half-ring maps, in the units of the corresponding map

For the Omega columns, the 'DISP' (for *dispersion*) column gives an estimate of the spatial variation as a function of position on the sky. This is the variation induced by combining the scanning beam determined from the planet observations with the scanning strategy, as described in Beams.

LFI

FREQUENCY (String)

a 3-digit string giving the reference frequency in GHz, i.e., of the form *030, 044, 070*

FWHM (Real*8)

FWHM of a Gaussian beam having the same (total) solid angle, in arcmin

NOISE (Real*8)

This is the average noise in T ·s$^{1/2}$

CENTRALFREQ (Real*4)

This is the average central frequency in GHz

FWHM_EFF, *FWHM_EFF_SIGMA* (Real*4)

This is the average FWHM of the effective beam, in arcmin, and its dispersion

ELLIPTICITY_EFF, *ELLIPTICITY_EFF_SIGMA* (Real*4)

This is the average ellipticity and its dispersion

SOLID_ANGLE_EFF, *SOLID_ANGLE_EFF_SIGMA* (Real*4)

This is the average full beam solid angle, in arcmin^2, and its dispersion

Effective band transmission profiles

The effective filter bandpasses are given in different BINTABLE extensions. The extension is named *BANDPASS_{name}*, where *name* specified the frequency channel. In the case of the maps, the bandpasses are a weighted average of the bandpasses of the detectors that are used to build the map. For details see #planck2013-p03d. The bandpasses are given as 4-column tables containing:

HFI

WAVENUMBER (Real*4)

the wavenumber in cm-1, conversion to GHz is accomplished by multiplying by $10^{-7}c$[mks].

TRANSMISSION (Real*4)

the transmission (normalized to 1 at the max for HFI)

ERROR (Real*4)

the statistical 1σuncertainty for the transmission profile.

FLAG (Integer)

a flag indicating if the data point is an independent frequency data point (nominally the case), or an FTS instrument line shape (ILS)-interpolated data point. The frequency data has been over-sampled by a factor of ~10 to assist in CO component separation efforts #planck2013-p03a, #planck2013-p03d.

The number of rows will differ among the different extensions, but are the same, by construction, within each extension. Tables with the unit conversion coefficients and color correction factors for the HFI detectors (and LFI in some instances), including uncertainty estimates based on the uncertainty of the HFI detector spectral response are given in this appendix.

LFI

WAVENUMBER (Real*8)

the wavenumber in GHz.

TRANSMISSION (Real*8)

the transmission (normalized to have an integral of 1 for LFI)

UNCERTAINITY (Real*4)

the statistical 1σuncertainty for the transmission profile (not provided for LFI)

FLAG (Character)

a flag, not used by now by the LFI

The number of rows will differ among the different extensions, but are the same, by construction, within each extension.

Beam Window Functions

Beam window functions and associated error descriptions are written into a BINTABLE for each *detection unit*, where *detection unit* consists of an auto or a cross product (for HFI only) of one (or two) frequency maps or detset maps used in the likelihood. Here they are:

For the HFI

- the 6 HFI frequency channels, producing 21 extensions
  - 100, 143, 217, 353, 545, 857
- 26 detsets, producing 351 extensions; the detsets used are, by frequency channel:
  - 100-DS1, 100-DS2,
  - 143-DS1, 143-DS2, 143-5, 143-6, 143-7,
  - 217-DS1, 217-DS2, 217-1, 217-2, 217-3, 217-4,
  - 353-DS1, 353-DS2, 353-1, 353-2, 353-7, 353-8,
  - 545-1, 545-2, 545-4,
  - 857-1, 857-2, 857-3, 857-4

For the LFI

- the 3 LFI frequency channels, producing 3 extensions
  - 30, 44, 70

and the extension names are of the form *BEAMWF_U1XU2* where U1 and U2 are one (possibly the same) detection unit from one of the main groups above (i.e. there are no cross products between detsets and frequency channels, or between HFI and LFI). Each extension contains the columns:

NOMINAL (Real*4)

the beam window function proper,

EIGEN_n (Real*4, n=1-5 for the HFI, n=1-4 for the LFI)

the five/four corresponding error modes.

and the following keywords give further information, only for the HFI:

NMODES (Integer)

the number of EIGEN_* modes,

LMIN and *LMAX* (Integer)

the starting and ending (both included) multipoles of the vectors NOMINAL and EIGEN_*

LMIN_EM and *LMAX_EM* (Integer)

that give the range of the valid samples of the EIGEN_* vectors. Here *LMAX_EM* is always less than or equal to *LMAX*. On the range *LMAX_EM*+1 to *LMAX* the values of EIGEN_* are set to NaN, while the values of NOMINAL only are a Gaussian extrapolation of the lower multipole window function, only provided for convenience.

CORRMAT (string)

the name of the extension containing the corresponding beam correlation matrix

Beam Correlation Matrix

Two beam correlation matrices are given for the HFI, in two *IMAGE* extensions:

CORRBEAM_FREQ (Real*8)

for the frequency channels (21 units), 105x015 pixel matrix,

CORRBEAM_DSET (Real*8)

for the detsets (351 units), 1755x1755 pixel matrix

Each is a symmetric matrix with 1-valued diagonal, made of NBEAMS*NBEAMS blocks, each block being NMODES*NMODES in size. The nth row- (and column-) block entry relates to the B(l) model whose name is indicated in ROWn = BEAMWF_U1XU2 keywords, and the corresponding eigenmodes are stored in a HDU of the same name.

Each extension contains also the following keywords:

NDETS (Integer)

the number of detector units

NBEAMS (Integer)

the number of beams = NSETS * (NSETS+1) / 2

NMODES (Integer)

here 5

L_PLUS (Integer)

Eigenmode > 0 to break degeneracies

BLOCKn (string)

for n=1-NBEAMS, gives the name of the extension containing the beam WF and error eigenmodes for the nth block

and some other ones for internal data checking and traceability

No beam correlation matrices are produced by the LFI by now.

Appendices

- Unit correction and color correction tables

References

<biblio force=false>

1. References

</biblio>

References

[1] http://pla.esac.esa.int/pla/aio/product-action?DOCUMENT.DOCUMENT_ID=HFI_RIMO_R1.10.fits

Effective Beams

Product description

The **effective beam** is the average of all scanning beams pointing at a certain direction within a given pixel of the sky map for a given scan strategy. It takes into account the coupling between azimuthal asymmetry of the beam and the uneven distribution of scanning angles across the sky. It captures the complete information about the difference between the true and observed image of the sky. They are, by definition, the objects whose convolution with the true CMB sky produce the observed sky map.

Details of the beam processing are given in the respective pages for HFI and LFI.

The full algebra involving the effective beams for temperature and polarisation was presented in [Mitra, Rocha, Gorski et al. [1]] #mitra2010, and a discussion of its application to Planck data is given in the appropriate LFI #planck2013-p02d and HFI #planck2013-p03c papers. Relevant details of the processing steps are given in the Effective Beams section of this document.

Comparison of the images of compact sources observed by Planck with FEBeCoP products

We show here a comparison of the FEBeCoP derived effective beams, and associated point spread functions, PSF (the transpose of the beam matrix), to the actual images of a few compact sources observed by Planck, for all LFI and HFI frequency channels, as an example. We show below a few panels of source images organized as follows:

- Row #1- DX9 images of four ERCSC objects with their galactic (l,b) coordinates shown under the color bar
- Row #2- linear scale FEBeCoP PSFs computed using input scanning beams, Grasp Beams, GB, for LFI and B-Spline beams,BS, Mars12 apodized for the CMB channels and the BS Mars12 for the sub-mm channels, for HFI (see section Inputs below).
- Row #3- log scale of #2; PSF iso-contours shown in solid line, elliptical Gaussian fit iso-contours shown in broken line

Comparison images of compact sources and effective beams, PSFs

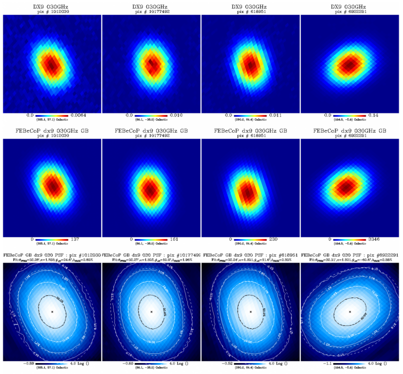

30GHz

Histograms of the effective beam parameters

Here we present histograms of the three fit parameters - beam FWHM, ellipticity, and orientation with respect to the local meridian and of the beam solid angle. The shy is sampled (pretty sparsely) at 3072 directions which were chosen as HEALpix nside=16 pixel centers for HFI and at 768 directions which were chosen as HEALpix nside=8 pixel centers for LFI to uniformly sample the sky.

Where beam solid angle is estimated according to the definition: $4\pi\sum$**(effbeam)/max(effbeam)** i.e., $4\pi\sum(B_{ij})/max(B_{ij})$

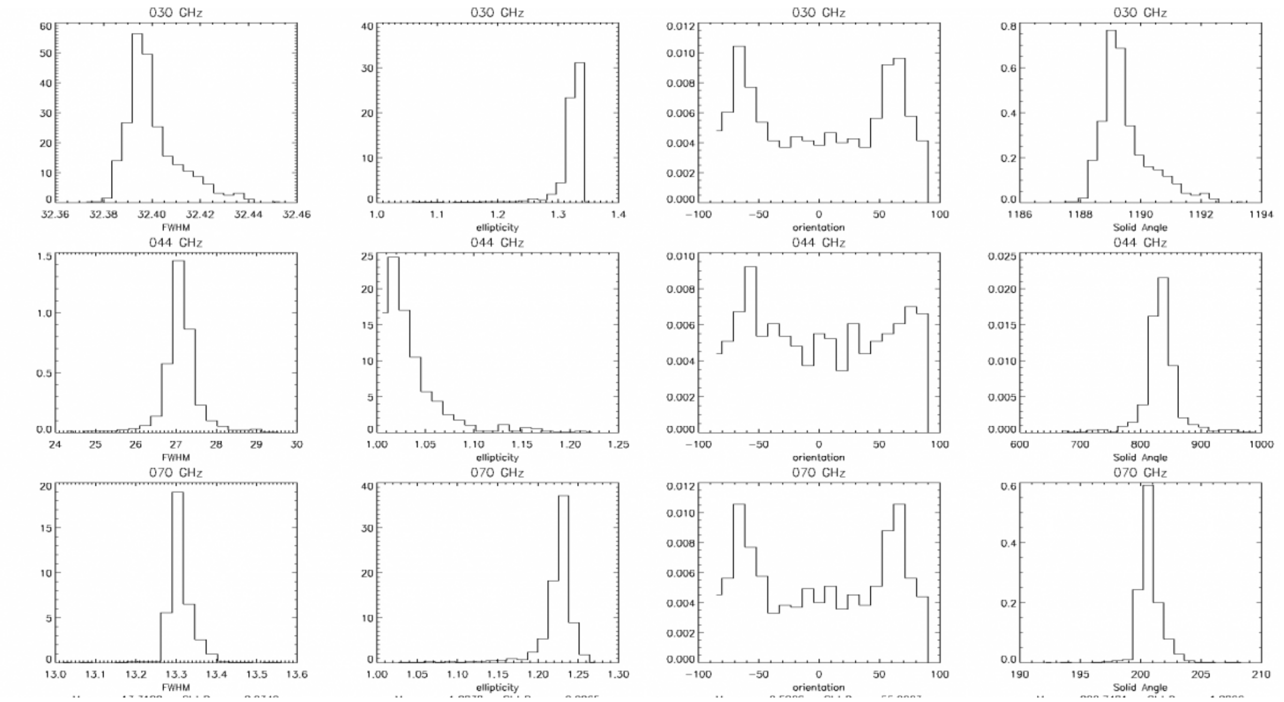

Histograms for LFI effective beam parameters

Sky variation of effective beams solid angle and ellipticity of the best-fit Gaussian

- The discontinuities at the Healpix domain edges in the maps are a visual artifact due to the interplay of the discretized effective beam and the Healpix pixel grid.

Sky variation of effective beams ellipticity of the best-fit Gaussian

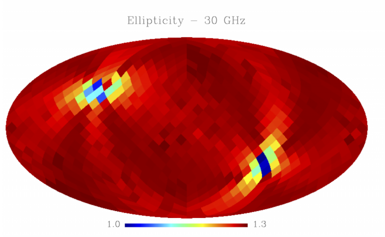

ellipticity - 30GHz

Sky (relative) variation of effective beams solid angle of the best-fit Gaussian

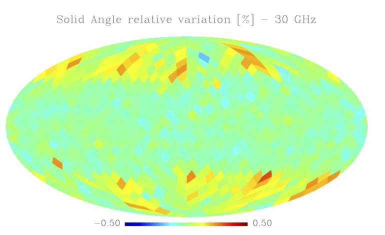

beam solid angle (relative) variations wrt scanning beam - 30GHz

Sky (relative) variation of effective beams fwhm of the best-fit Gaussian

Sky variation of effective beams ψ angle of the best-fit Gaussian

Statistics of the effective beams computed using FEBeCoP

We tabulate the simple statistics of FWHM, ellipticity (e), orientation (ψ) and beam solid angle, (Ω), for a sample of 3072 and 768 directions on the sky for HFI and LFI data respectively. Statistics shown in the Table are derived from the histograms shown above.

- The derived beam parameters are representative of the DPC NSIDE 1024 and 2048 healpix maps (they include the pixel window function).
- The reported FWHM_eff are derived from the beam solid angles, under a Gaussian approximation. These are best used for flux determination while the the Gaussian fits to the effective beam maps are more suited for source identification.

Statistics of the FEBeCoP Effective Beams Computed with the BS Mars12 apodized for the CMB channels and oversampled

frequency	mean(fwhm) [arcmin]	sd(fwhm) [arcmin]	mean(e)	sd(e)	mean(ψ) [degree]	sd(ψ) [degree]	mean(Ω) [arcmin ^{2}]	sd(Ω) [arcmin ^{2}]	FWHM_eff [arcmin]
030	32.239	0.013	1.320	0.031	-0.304	55.349	1189.513	0.842	32.34
044	27.005	0.552	1.034	0.033	0.059	53.767	832.946	31.774	27.12
070	13.252	0.033	1.223	0.026	0.587	55.066	200.742	1.027	13.31
100	9.651	0.014	1.186	0.023	-0.024	55.400	105.778	0.311	9.66
143	7.248	0.015	1.036	0.009	0.383	54.130	59.954	0.246	7.27
217	4.990	0.025	1.177	0.030	0.836	54.999	28.447	0.271	5.01
353	4.818	0.024	1.147	0.028	0.655	54.745	26.714	0.250	4.86
545	4.682	0.044	1.161	0.036	0.544	54.876	26.535	0.339	4.84
857	4.325	0.055	1.393	0.076	0.876	54.779	24.244	0.193	4.63

Beam solid angles for the PCCS

- Ω_{eff}- is the mean beam solid angle of the effective beam, where beam solid angle is estimated according to the definition: $4\pi\sum$**(effbeam)/max(effbeam)**, i.e. as an integral over the full extent of the effective beam, i.e. $4\pi\sum(B_{ij})/max(B_{ij})$.
- from Ω_{eff}we estimate the $fwhm_{eff}$, under a Gaussian approximation - these are tabulated above
  - $\Omega^{(1)}_{eff}$is the beam solid angle estimated up to a radius equal to one $fwhm_{eff}$and $\Omega^{(2)}_{eff}$up to a radius equal to twice the $fwhm_{eff}$.
    - These were estimated according to the procedure followed in the aperture photometry code for the PCCS: if the pixel centre does not lie within the given radius it is not included (so inclusive=0 in query disc).

Band averaged beam solid angles

Band	Ω_{eff}[arcmin ^{2}]	**spatial variation** [arcmin ^{2}]	$\Omega^{(1)}_{eff}$[arcmin ^{2}]	**spatial variation-1** [arcmin ^{2}]	$\Omega^{(2)}_{eff}$[arcmin ^{2}]	**spatial variation-2** [arcmin ^{2}]
30	1189.513	0.842	1116.494	2.274	1188.945	0.847
44	832.946	31.774	758.684	29.701	832.168	31.811
70	200.742	1.027	186.260	2.300	200.591	1.027
100	105.778	0.311	100.830	0.410	105.777	0.311
143	59.954	0.246	56.811	0.419	59.952	0.246
217	28.447	0.271	26.442	0.537	28.426	0.271
353	26.714	0.250	24.827	0.435	26.653	0.250
545	26.535	0.339	24.287	0.455	26.302	0.337
857	24.244	0.193	22.646	0.263	23.985	0.191

Production process

FEBeCoP, or Fast Effective Beam Convolution in Pixel space [Mitra, Rocha, Gorski et al. [1]], is an approach to representing and computing effective beams (including both intrinsic beam shapes and the effects of scanning) that comprises the following steps:

- identify the individual detectors' instantaneous optical response function (presently we use elliptical Gaussian fits of Planck beams from observations of planets; eventually, an arbitrary mathematical representation of the beam can be used on input)
- follow exactly the Planck scanning, and project the intrinsic beam on the sky at each actual sampling position
- project instantaneous beams onto the pixelized map over a small region (typically <2.5 FWHM diameter)
- add up all beams that cross the same pixel and its vicinity over the observing period of interest
- create a data object of all beams pointed at all N'_pix_' directions of pixels in the map at a resolution at which this precomputation was executed (dimension N'_pix_' x a few hundred)
- use the resulting beam object for very fast convolution of all sky signals with the effective optical response of the observing mission

Computation of the effective beams at each pixel for every detector is a challenging task for high resolution experiments. FEBeCoP is an efficient algorithm and implementation which enabled us to compute the pixel based effective beams using moderate computational resources. The algorithm used different mathematical and computational techniques to bring down the computation cost to a practical level, whereby several estimations of the effective beams were possible for all Planck detectors for different scanbeam models and different lengths of datasets.

Pixel Ordered Detector Angles (PODA)

The main challenge in computing the effective beams is to go through the trillion samples, which gets severely limited by I/O. In the first stage, for a given dataset, ordered lists of pointing angles for each pixels---the Pixel Ordered Detector Angles (PODA) are made. This is an one-time process for each dataset. We used computers with large memory and used tedious memory management bookkeeping to make this step efficient.

effBeam

The effBeam part makes use of the precomputed PODA and unsynchronized reading from the disk to compute the beam. Here we tried to made sure that no repetition occurs in evaluating a trigonometric quantity.

One important reason for separating the two steps is that they use different schemes of parallel computing. The PODA part requires parallelisation over time-order-data samples, while the effBeam part requires distribution of pixels among different computers.

Computational Cost

The computation of the effective beams has been performed at the NERSC Supercomputing Center. The table below shows the computation cost for FEBeCoP processing of the nominal mission.

Computational cost for PODA, Effective Beam and single map convolution. Wall-clock time is given as a guide, as found on the NERSC supercomputers.

Channel	030	044	070	100	143	217	353	545	857
PODA/Detector Computation time (CPU hrs)	85	100	250	500	500	500	500	500	500
PODA/Detector Computation time (wall clock hrs)	7	10	20	20	20	20	20	20	20
Beam/Channel Computation time (CPU hrs)	900	2000	2300	2800	3800	3200	3000	900	1100
Beam/Channel Computation time (wall clock hrs)	0.5	0.8	1	1.5	2	1.2	1	0.5	0.5
Convolution Computation time (CPU hr)	1	1.2	1.3	3.6	4.8	4.0	4.1	4.1	3.7
Convolution Computation time (wall clock sec)	1	1	1	4	4	4	4	4	4
Effective Beam Size (GB)	173	123	28	187	182	146	132	139	124

The computation cost, especially for PODA and Convolution, is heavily limited by the I/O capacity of the disc and so it depends on the overall usage of the cluster done by other users.

Inputs

In order to fix the convention of presentation of the scanning and effective beams, we show the classic view of the Planck focal plane as seen by the incoming CMB photon. The scan direction is marked, and the toward the center of the focal plane is at the 85 deg angle w.r.t spin axis pointing upward in the picture.

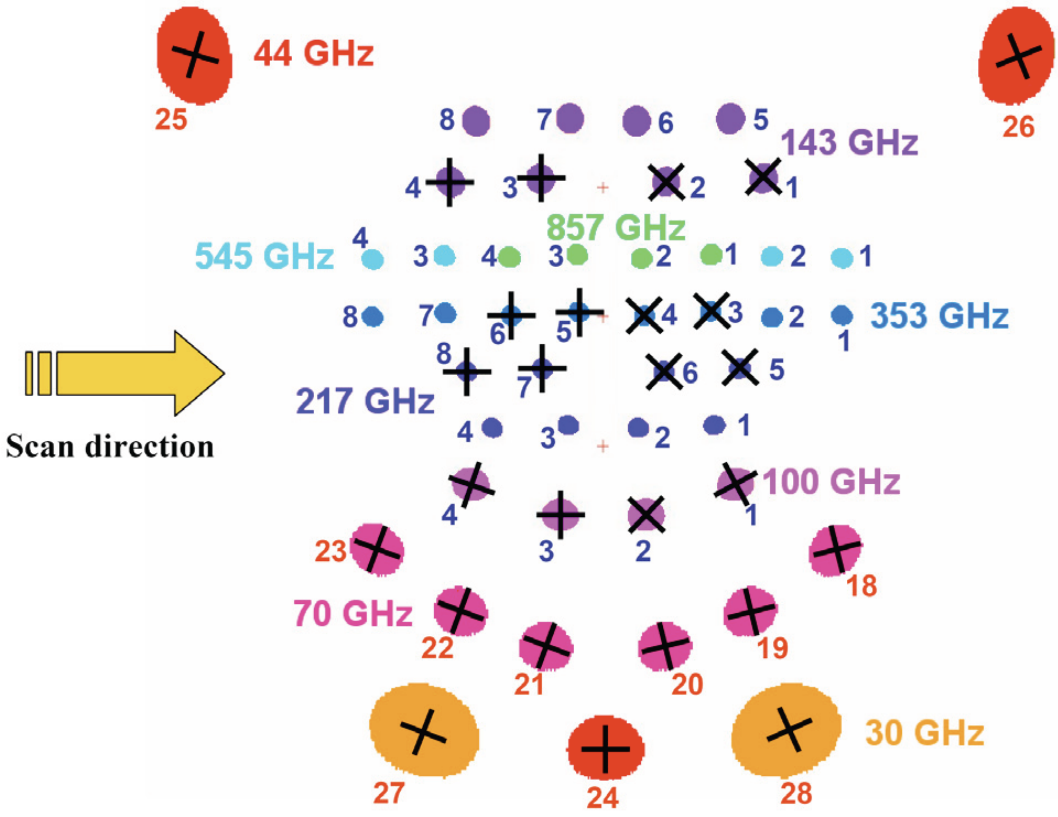

Planck Focal Plane

The Focal Plane DataBase (FPDB)

The FPDB contains information on each detector, e.g., the orientation of the polarisation axis, different weight factors, (see the instrument RIMOs):

- HFI - The HFI RIMO [1]
- LFI - The LFI RIMO [2]

The scanning strategy

The scanning strategy, the three pointing angle for each detector for each sample: Detector pointings for the nominal mission covers about 15 months of observation from Operational Day (OD) 91 to OD 563 covering 3 surveys and half.

The scanbeam

The scanbeam modeled for each detector through the observation of planets. Which was assumed to be constant over the whole mission, though FEBeCoP could be used for a few sets of scanbeams too.

- LFI: GRASP scanning beam - the scanning beams used are based on Radio Frequency Tuned Model (RFTM) smeared to simulate the in-flight optical response.
- HFI: B-Spline, BS based on 2 observations of Mars.

(see the instrument RIMOs).

Beam cutoff radii

N times geometric mean of FWHM of all detectors in a channel, where N

Beam cut off radius

channel	Cutoff Radii in units of fwhm	fwhm of full beam extent
30 - 44 - 70	2.5	
100	2.25	23.703699
143	3	21.057402
217-353	4	18.782754
sub-mm	4	18.327635(545GHz) ; 17.093706(857GHz)

Map resolution for the derived beam data object

- $N_{side} = 1024$for LFI frequency channels
- $N_{side} = 2048$for HFI frequency channels

Related products

Monte Carlo simulations

FEBeCoP software enables fast, full-sky convolutions of the sky signals with the Effective beams in pixel domain. Hence, a large number of Monte Carlo simulations of the sky signal maps map convolved with realistically rendered, spatially varying, asymmetric Planck beams can be easily generated. We performed the following steps:

- generate the effective beams with FEBeCoP for all frequencies for dDX9 data and Nominal Mission
- generate 100 realizations of maps from a fiducial CMB power spectrum

- convolve each one of these maps with the effective beams using FEBeCoP
- estimate the average of the Power Spectrum of each convolved realization, C'_\ell_'^out^'}, and 1 sigma errors

As FEBeCoP enables fast convolutions of the input signal sky with the effective beam, thousands of simulations are generated. These Monte Carlo simulations of the signal (might it be CMB or a foreground (e.g. dust)) sky along with LevelS+Madam noise simulations were used widely for the analysis of Planck data. A suite of simulations were rendered during the mission tagged as Full Focalplane simulations, FFP#. For example FFP6

Beam Window Functions

The **Transfer Function** or the **Beam Window Function** W_l relates the true angular power spectra C_l with the observed angular power spectra $\tilde{C}_l$:

Note that, the window function can contain a pixel window function (depending on the definition) and it is {\em not the angular power spectra of the scanbeams}, though, in principle, one may be able to connect them though fairly complicated algebra.

The window functions are estimated by performing Monte-Carlo simulations. We generate several random realisations of the CMB sky starting from a given fiducial C_l, convolve the maps with the pre-computed effective beams, compute the convolved power spectra $C_l^{\rm conv}$, divide by the power spectra of the unconvolved map $C_l^{\rm in}$ and average over their ratio. Thus, the estimated window function

For subtle reasons, we perform a more rigorous estimation of the window function by comparing C^{conv}_l with convolved power spectra of the input maps convolved with a symmetric Gaussian beam of comparable (but need not be exact) size and then scaling the estimated window function accordingly.

Beam window functions are provided in the RIMO.

Beam Window functions, Wl, for Planck mission

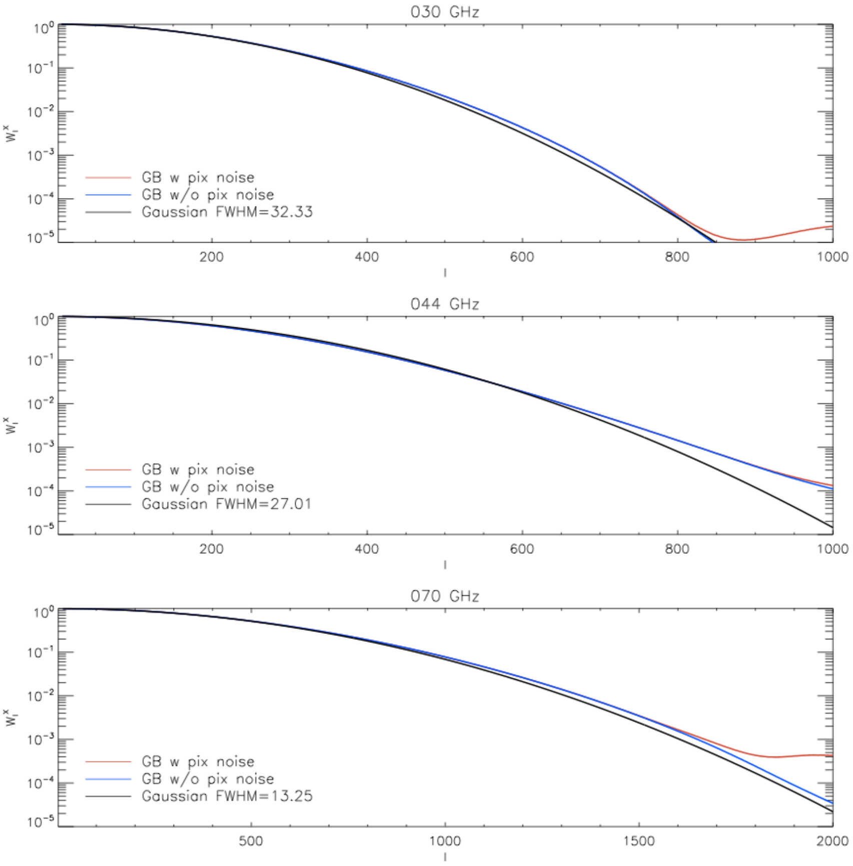

Beam Window functions, Wl, for LFI channels

File Names

The effective beams are stored as unformatted files in directories with the frequency channel's name, e.g., 100GHz, each subdirectory contains N unformatted files with names beams_###.unf, a beam_index.fits and a beams_run.log. For 100GHz and 143GHz: N=160, for 30, 44, 70 217 and 353GHz: N=128; for 545GHz: N=40; and 857GHz: N=32.

- beam_index.fits
- beams_run.log

Retrieval of effective beam information from the PLA interface

In order to retrieve the effective beam information, the user should first launch the Java interface from this page: http://www.sciops.esa.int/index.php?project=planck&page=Planck_Legacy_Archive

One should click on "Sky maps" and then open the "Effective beams" area. There is the possibility to either retrieve one beam nearest to the input source (name or coordinates), or to retrieve a set of beams in a grid defined by the Nside and the size of the region around a source (name or coordinates). The resolution of this grid is defined by the Nside parameter. The size of the region is defined by the "Radius of ROI" parameter.

Once the user proceeds with querying the beams, the PLA software retrieves the appropriate set of effective beams from the database and delivers it in a FITS file which can be directly downloaded.

Meta data

The data format of the effective beams is unformatted.

References

<biblio force=false>

1. References

</biblio>

References

[1] http://pla.esac.esa.int/pla/aio/product-action?DOCUMENT.DOCUMENT_ID=HFI_RIMO_R1.00.fits

Catalogues

The Catalogue of Compact Sources

Product description

The PCCS is a set of nine single-frequencies lists of sources extracted from the Planck nominal mission data. By definition its reliability is > 80% and a special effort was made to use simple selection procedures in order to facilitate statistical analyses. With a common detection method for all the channels and the additional three photometries, spectral analysis can also be done safely. The deeper completeness levels and, as a consequence, the higher number of sources compared with its predecessor the ERCSC, will allow the extension of previous studies to more sources and to fainter flux densities. The PCCS is the natural evolution of the ERCSC, but both lack polarization and multi-frequency information. Future releases will take advantage of the full mission data and they will contain information on properties of sources not available in this release, such as polarization, multi-frequency and variability.

Table 1: PCCS characteristics

Channel	**30**	**44**	**70**	**100**	**143**	**217**	**353**	**545**	**857**
Frequency [GHz]	28.4	44.1	70.4	100.0	143.0	217.0	353.0	545.0	857.0
Beam FWHM[1] [arcmin]	32.38	27.10	13.30	9.88	7.18	4.87	4.65	4.72	4.39
SNR threshold	4.0	4.0	4.0	4.6	4.7	4.8	4.9[2]/6.0[3]	4.7/7.0	4.9/7.0
# of detections	1256	731	939	3850	5675	16070	17689	26472	35719
# of detections for |b| > 30°)	572	258	332	845	1051	1901	2035	4164	7851
Flux density uncertainty [mJy]	109	198	149	61	38	35	74	132	189
Min flux density[4] [mJy]	461	825	566	266	169	149	298	479	671
90% completeness [mJ]	575	1047	776	300	190	180	330	570	680
Position uncertainty[5] [arcmin]	1.8	2.1	1.4	1.0	0.7	0.7	0.8	0.5	0.4

Notes

1. The Planck beams are described in #planck2013-p02d

Planck-2013-IV [1]; #planck2013-p03c Planck-2013-VII [1]. This table shows the values which were adopted for the PCCS (derived from the effective beams).

1. In the extragalactic zone (48% of the sky; see Fig. 2 in #planck2013-p05

Planck-2013-XXVIII [1]).

1. In the Galactic zone (52% of the sky; see Fig. 2 in #planck2013-p05

Planck-2013-XXVIII [1]).

1. Minimum flux density of the catalogue at |b| > 30° after excluding the 10% faintest sources.
2. Positional uncertainty derived by comparison with PACO sample (#PATCABright,#PATCAfaint,#PATCASpec) up to 353 GHz and with Herschel samples (HRS, KINGFISH, HeViCS, H-ATLAS) in the other channels.

Before using the PCCS, please read the Cautionary Notes in the PCCS general description section. For full details, see paper #planck2013-p05 Planck-2013-XXVIII [1].

Production process

For a description of the production and validation processes of the PCCS see the corresponding section.

Inputs

The data obtained from the Planck nominal mission between (2009 August 12 and 2010 November 27) have been processed into full-sky maps by the HFI and LFI Data Processing Centres (DPCs). A description of the processing can be found in #planck2013-p02,#planck2013-p03 Planck-2013-II [1] Planck-2013-VI [2]. The data consist of two complete sky surveys and 60% of the third survey. This implies that the flux densities of sources obtained from the nominal mission maps are the average of at least two observations. The nine Planck frequency channel maps are used as input to the source detection pipelines. The relevant properties of the frequency maps and main parameters used to generate the catalogues are summarized in Table 1.

The input data used to generate this product are the following:

- nominal survey, full channel sky maps
- RIMO
- effective beams

Related products

Other products that are related and share some commonalities with the product being described here are the other catalogues:

1. ERCSC
2. SZ catalogue

File names

COM_PCCS_030_R1.30.fits [2]
COM_PCCS_044_R1.30.fits [3]
COM_PCCS_070_R1.30.fits [4]
COM_PCCS_100_R1.10.fits [5]
COM_PCCS_143_R1.10.fits [6]
COM_PCCS_217_R1.10.fits [7]
COM_PCCS_353_R1.10.fits [8]

COM_PCCS_545_R1.10.fits [9]

COM_PCCS_857_R1.10.fits [10]

Meta Data

The PCCS source list in each frequency is structured as a FITS binary table having one row for each detected source. The details of the FITS file structure are below

FITS file structure

Extension 0: Primary header, no data			
FITS Keyword	**Data Type**	**Units**	**Description**
INSTRUME	String		LFI or HFI
VERSION	String		Version of PCCS
DATE	String		Date file created:yyyy-mm-dd
ORIGIN	String		Name of organization responsible for the data (LFI-DPC – HFI-DPC)
TELESCOP	String		PLANCK
CREATOR	String		Pipeline Version
DATE-OBS	String	days	Start-up time of the survey: yyyy-mm-dd
DATE-END	String	days	Ending time of the survey: yyyy-mm-dd
Extension 1: (BINTABLE)			
Column Name	**Data Type**	**Units**	**Description**
Identification			
NAME	String		Source name (Note 1)
Source Position			
GLON	Real*8	degrees	Galactic longitude based on extraction algorithm
GLAT	Real*8	degrees	Galactic latitude based on extraction algorithm
RA	Real*8	degrees	Right ascension (J2000) transformed from (GLON,GLAT)
DEC	Real*8	degrees	Declination (J2000) transformed from (GLON,GLAT)
Photometry			
DETFLUX	Real*4	mJy	Flux density of source as determined by detection method
DETFLUX_ERR	Real*4	mJy	Uncertainty (1 sigma) in derived flux density from detection method
APERFLUX	Real*4	mJy	Flux density of source as determined from the aperture photometry
APERFLUX_ERR	Real*4	mJy	Uncertainty (1 sigma) in derived flux density from the aperture photometry
PSFFLUX	Real*4	mJy	Flux density of source as determined from PSF fitting
PSFFLUX_ERR	Real*4	mJy	Uncertainty (1 sigma) in derived flux density from PSF fitting
GAUFLUX	Real*4	mJy	Flux density of source as determined from 2-D Gaussian fitting
GAUFLUX_ERR	Real*4	mJy	Uncertainty (1 sigma) in derived flux density from 2-D Gaussian fitting
GAU_SEMI1	Real*4	arcmin	Gaussian fit along axis 1 (FWHM; see Note 4 for axis definition)
GAU_SEMI1_ERR	Real*4	arcmin	Uncertainty (1 sigma) in derived Gaussian fit along axis 1
GAU_SEMI2	Real*4	arcmin	Gaussian fit along axis 2 (FWHM)
GAU_SEMI2_ERR	Real*4	arcmin	Uncertainty (1 sigma) in derived Gaussian fit along axis 2

GAU_THETA	Real*4	deg	Gaussian fit orientation angle (Note 4)
GAU_THETA_ERR	Real*4	deg	Uncertainty (1 sigma) in derived gaussian fit orientation angle
GAU_FWHM_EFF	Real*4	arcmin	Gaussian fit effective FWHM
Flags and validation			
EXTENDED	Integer*2		Extended source flag (Note 2)
CIRRUS_N	Integer*2		Number of sources detected at 857 GHz within 1 degree
EXT_VAL	Integer*2		External validation flag (Note 3)
ERCSC	String		Name of the ERCSC counterpart if any
ONLY 857 GHz Catalogue			
APERFLUX_217	Real*4	mJy	Estimated flux density at 217 GHz
APERFLUX_ERR_217	Real*4	mJy	Uncertainty in source flux density at 217 GHz
APERFLUX_353	Real*4	mJy	Estimated flux density at 353 GHz
APERFLUX_ERR_353	Real*4	mJy	Uncertainty in source flux density at 353 GHz
APERFLUX_545	Real*4	mJy	Estimated flux density at 545 GHz
APERFLUX_ERR_545	Real*4	mJy	Uncertainty in source flux density at 545 GHz

Notes

1. Source names consist of a prefix and a position. The prefix used is PCCS1 fff for the catalogue at fff GHz. The position is in Galactic coordinates and specified as "Glll.ll±bb.bb" where the (l,b) values are truncated to two decimal places. For example, a source detected at (l,b) = (120.237, 4.231) in the 545 GHz Planck map would be labelled PCCS1 545 G120.23±04.23.
2. The EXTENDED flag has the value of 0 if the source is compact and the value of 1 is it extended. The source size is determined by the geometric mean of the Gaussian fit FWHMs, with the criteria for extension being sqrt(GAU_FWHMMAJ * GAU_FWHMIN) > 1.5 times the beam FWHM.
3. The EXT_VAL flag takes the value of 0, 1, or 2, based on the following conditions:

   = 2: The source has a clear counterpart in one of the catalogues considered as ancillary data.

   = 1: The source has no clear counterpart in one of the ancillary catalogues but it has been detected by the internal multi-frequency method (LFI channels) or match with neighbouring frequencies, above or below (HFI channels).

   = 0: The source has no clear counterpart in one of the ancillary catalogues and it has not been detected by the internal multi-frequency method or neighbouring frequencies.
4. The x-axis is defined for each source as parallel to the line of constant colatitude, with the same direction as the longitude. Therefore the position angles are measured anticlockwise from the y-axis.

The SZ catalogues

The Planck SZ catalogue is constructed as described in SZ catalogue and in section 2 of #planck2013-p05a Planck-2013-XXIX [11].

Three pipelines are used to detect SZ clusters: two independent implementations of the Matched Multi-Filter (MMF1 and MMF3), and PowellSnakes (PwS). The main catalogue is constructed as the union of the catalogues from the three detection methods. The individual catalogues are provided for the expert user in order to assess the consistency of the pipelines. The completeness and reliability of the catalogues have been assessed through internal and external validation as described in sections 3-6 of #planck2013-p05a Planck-2013-XXIX [11].

The union catalogue contains the coordinates and the signal-to-noise ratio of the detections and a summary of the external validation information, including external identification of a cluster and its redshift if it is available.

The individual catalogues contain the coordinates and the signal-to-noise ratio of the detections, and information on the size and flux of the detections. The entries are cross-referenced to the detections in the union catalogue.

The size of a detection is given in terms of the scale size, θ_s, and the flux is given in terms of the total integrated Comptonization parameter, $Y = Y_{5r_{500}}$. The parameters of the GNFW profile assumed by the detection pipelines is written in the headers in the catalogues. For the sake of convenience, the conversion factor from Y to Y_{500} is also written in the header.

The full information on the degeneracy between θ_s and Y is included in the individual catalogues in the form of the two-dimensional probability distribution for each detection. It is computed on a well-sampled grid to produce a two-dimensional image for each detection. The degeneracy information is provided in this form so it can be combined with a model or external data to produce tighter constraints on the parameters.

Union Catalogue

The union catalogue is contained in a file called *COM_PCCS_SZ-union_Rx.xx.fits*, where *x.xx* is the release number.

Extension 0: Primary header, no data			
FITS Keyword	**Data Type**	**Units**	**Description**
INSTRUME	String		Instrument.
VERSION	String		Version of catalogue.
DATE	String		Date file created: yyyy-mm-dd.
ORIGIN	String		Name of organization responsible for the data.
TELESCOP	String		PLANCK.
CREATOR	String		Pipeline version.
DATE-OBS	String		Start time of the survey: yyyy-mm-dd.
DATE-END	String		End time of the survey: yyyy-mm-dd.
PROCVER	String		Data version.
PP_ALPHA	Real*4		GNFW pressure profile α parameter.
PP_BETA	Real*4		GNFW pressure profile β parameter.
PP_GAMMA	Real*4		GNFW pressure profile γ parameter.
PP_C500	Real*4		GNFW pressure profile c_{500} parameter.
PP_Y2YFH	Real*4		Conversion factor from Y to Y_{500}.
Extension 1: data extension (BINTABLE)			
Column Name	**Data Type**	**Units**	**Description**
INDEX	Int*4		Index. Used to cross-reference with individual catalogues.
NAME	String		Source name, (Note 1)
GLON	Real*8	degrees	Galactic longitude.
GLAT	Real*8	degrees	Galactic latitude.
RA	Real*8	degrees	Right ascension (J2000) transformed from (GLON,GLAT).
DEC	Real*8	degrees	Declination (J2000) transformed from (GLON,GLAT).
POS_ERR	Real*4	arcmin	Position uncertainty (95% confidence level).
SNR	Real*4		Signal-to-noise ratio of the detection.

PIPELINE	Int*4		Souce pipeline: 1= MMF1; 2 = MMF3; 3 = PwS.
PIPE_DET	Int*4		Pipelines which detect this object (note 2).
PCCS	Bool		Indicates whether detection matches any PCCS source.
VALIDATION	Int*4		External validation status (Note 3)
ID_EXT	String		External identifier of cluster.
REDSHIFT	Real*4		Redshift of cluster.
COSMO	Bool		Detection is in the cosmology sample.
COMMENT	Bool		Detection has a comment in the associated text file (Note 4).

Notes

1. format is *PSZ1 Glll.ll+mn;bb.b* where (l,b) are the Galactic and truncated to 2 decimal places.
2. The three least significant decimal digits are used to represent detection or non-detection by the pipelines. Order of the digits: hundreds = MMF1; tens = MMF3; units = PwS. If it is detected then the corresponding digit is set to 1, otherwise it is set to 0.
3. values are: 1 = candidate of class 1; 2 = candidate of class 2; 3 = candidate of class 3; 10 = Planck cluster confirmed by follow-up; 20 = known cluster.
4. The comments on the detections in the catalogue are contained in a text file called *COM_PCCS_SZ-union_comments_R1.11.txt*, which contains one line for each detection in the union catalogue with COMMENT = T. The line starts with the INDEX and NAME of the detection to facilitate cross-referencing. The remainder of the line is the comment on that detection.

Individual Catalogues

The individual pipeline catalogues are contained in FITS files called *COM_PCCS_SZ-{pipeline}_R1.11.fits*, where *{pipeline}* is the name of the pipeline (*MMF1*, *MMF3*, or *PwS*). The structure of the FITS files is as follows:

FITS file structure

Ext. 0: Primary header, no data			
FITS Keyword	**Data Type**	**Units**	**Description**
INSTRUME	String		Instrument.
VERSION	String		Version of catalogue.
DATE	String		Date file created: yyyy-mm-dd.
ORIGIN	String		Name of organization responsible for the data.
TELESCOP	String		PLANCK.
CREATOR	String		Pipeline version.
DATE-OBS	String		Start time of the survey: yyyy-mm-dd.
DATE-END	String		End time of the survey: yyyy-mm-dd.
PROCVER	String		Data version.
PP_ALPHA	Real*4		GNFW pressure profile α parameter.
PP_BETA	Real*4		GNFW pressure profile β parameter.
PP_GAMMA	Real*4		GNFW pressure profile γ parameter.
PP_C500	Real*4		GNFW pressure profile c_{500} parameter.
PP_Y2YFH	Real*4		Conversion factor from Y to Y_{500}.

Ext. 1: EXTNANE = *PSZ_INDIVIDUAL* (BINTABLE)			
Column Name	**Data Type**	**Units**	**Description**
INDEX	Int*4		Index from union catalogue.
NAME	String		Source name - see Note1
GLON	Real*8	degrees	Galactic longitude.
GLAT	Real*8	degrees	Galactic latitude.
RA	Real*8	degrees	Right ascension (J2000) transformed from (GLON,GLAT).
DEC	Real*8	degrees	Declination (J2000) transformed from (GLON,GLAT).
POS_ERR	Real*4	arcmin	Position uncertainty (95% confidence interval).
SNR	Real*4		Signal-to-noise ratio of the detection.
SNR_COMPAT	Real*4		SNR of the detection in compatibility mode (Note 2)
TS_MIN	Real*4		Minimum value of θ_s in grid in second extension HDU (see below).
TS_MAX	Real*4		Maximum value of θ_s in grid in second extension HDU (see below).
Y_MIN	Real*4		Minimum value of Y in grid in second extension HDU (see below).
Y_MIN	Real*4		Maximum value of Y in grid in second extension HDU (see below).
Keyword	**Data Type**	**Value**	**Description**
PIPELINE	String		Name of detection pipeline.
Ext. 2: EXTNAME = *PSZ_PROBABILITY* (IMAGE) - Note 3			
Keyword	**Data Type**	**Value**	**Description**
NAXIS1	Integer	256	Dim 1
NAXIS2	Integer	256	Dim 2
NAXIS3	Integer	Nsources	Dim 3 = Number of sources
Keyword	**Data Type**	**Value**	**Description**
PIPELINE	String		Name of detection pipeline.

Notes

1. Format *PSZ1 Glll.ll±bb.bb* where (l, b) are the Galactic coordinates truncated to 2 decimal places.
2. For PwS, this is the S/N evaluated in a manner compatible with the MMF pipelines. For MMF1 and MMF3, it is identical to SNR.
3. Ext. 2 contains a three-dimensional image with the two-dimensional probability distribution in θ_s and Y for each detection. The probability distributions are evaluated on a 256 × 256 linear grid between the limits specified in Ext. 1. The limits are determined independently for each detection. The dimension of the 3D image is 256 × 256 × n, where n is the number of detections. The first dimension is θ_s and the second dimension is Y.

Mask

The mask used to construct the catalogue is contained in a file called *COM_PCCS_SZ-unionMask_2048_R1.10.fits*. It is in GALACTIC coordinates, NESTED ordering, NSIDE=2048

The ERCSC

The Plank Early Release Compact Source Catalogue was the first Planck product to be publicly released in Jan 2011. It was produced with a very rapid turnaround to facilitate follow-up observations with existing c ryogenic observatories such as Herschel. It contained a list of all high reliability sources, both Galactic and extragalactic, that were derived from the first all sky coverage by Planck. i.e., using observations obtained from 12 August 2009 to 6 June 2010. Thus the full sky was covered once, and ~60% of the sky was covered twice. The goals were to achieve a photometric accuracy of 30% and a positional accuracy 1/5 of the beam FWHM in the RMS sense.

The ERCSC consisted of nine source lists, one at each of the nine Planck frequency channels. The number of sources in the lists range from 705 at 30 GHz to 8988 at 857 GHz. No attempt was made to cross-match the sources from the different frequencies due to the wide range of spatial resolutions (33 arcmin at 30 GHz to 4.3 arcmin at 857 GHz) spanned by Planck. Furthermore, a list of *Cold Cores* of interstellar molecular clouds within the Galaxy and a list of galaxy clusters detected through the Sunyaev- Zel'dovich effect (SZ), were also provided. These consisted of candidate sources that were detected using multifrequency algorithms that use the distinct spectral signature of such sources. The Cold Cores catalogue contained 915 sources while the SZ cluster catalogue consisted of 189 sources

In order to generate the ERCSC, four source detection algorithms were run as part of the ERCSC pipeline. A Monte-Carlo algorithm based on the injection and extraction of artificial sources into the Planck maps was implemented to select reliable sources among all extracted candidates such that the cumulative reliability of the catalogue is >90%. Reliability is defined as the fraction of sources in the catalog which have measured flux densities which are within 30% of their true flux density. There is no requirement on completeness for the ERCSC. As a result of the Monte-Carlo assessment of reliability of sources from the different techniques, an implementation of the PowellSnakes source extraction technique was used at the five frequencies between 30 and 143 GHz while the SExtractor technique was used between 217 and 857 GHz. The 10σ photometric flux density limit of the catalogue at $lbl > 30$ deg is 0.49, 1.0, 0.67, 0.5, 0.33, 0.28, 0.25, 0.47 and 0.82 Jy at each of the nine frequencies between 30 and 857GHz. Sources which are up to a factor of ~2 fainter than this limit, and which are present in "clean" regions of the Galaxy where the sky background due to emission from the interstellar medium is low, are included in the ERCSC if they meet the high reliability criterion. The sensitivity of the ERCSC is shown in the figure below. The ERCSC sources have known associations to stars with dust shells, stellar cores, radio galaxies, blazars, infrared luminous galaxies and Galactic interstellar medium features. A significant fraction of unclassified sources are also present in the catalogs.

The multifrequency information from Planck allows some basic classification of the sources to be undertaken. In the Galactic plane, at frequencies below 100 GHz, the majority of the sources are dominated by synchrotron or free-free emission. At the higher frequencies, the sources are almost exclusively dominated by thermal dust emission. At high Galactic latitudes however, the synchrotron sources dominate the source counts to 217 GHz with dusty sources being the primary source population at 353 GHz and higher. Recent attempts to classify a subset of the Planck 857 GHz sources at high latitudes based on cross-correlations with sources in other catalogs such as WISE and SDSS, found that almost half of them are associated with stars and low-redshift galaxies while a significant fraction (44%) might be interstellar medium features #Johnson2013.

Full details on the construction, contents and usage of the ERCSC, ECC and ESZ catalogues can be found in #planck2011-1-10 Planck early paper VII [12], #planck2011-5-1a Planck early paper VIII [13], #planck2011-7-7b Planck early paper XXIII [14].

The figure shows the ERCSC flux density limits, quanitfied as the faintest ERCSC source at |b|<10 deg (dashed black line) and at |b|>30 deg (solid black line), compared to those of other wide area surveys (#planck2011-1-10 Planck early paper VII [12]). Also shown are spectra of known sources of foreground emission as red lines. The ERCSC sensitivity is worse in the Galactic plane due to the strong contribution of ISM emission, especially at submillimeter wavelengths. At face value, the WMAP and Planck flux density limits appear to be comparable at the lowest frequencies, but the Planck ERCSC is much more complete as discussed in #planck2011-1-10 Planck early paper VII [12].

References

<biblio force=false>

1. References

</biblio>

References

[1] http://www.rssd.esa.int/doc_fetch.php?id=3168070&page=1
[2] http://pla.esac.esa.int/pla/aio/product-action?SOURCE_LIST.NAME=COM_PCCS_030_R1.30.fits
[3] http://pla.esac.esa.int/pla/aio/product-action?SOURCE_LIST.NAME=COM_PCCS_044_R1.30.fits
[4] http://pla.esac.esa.int/pla/aio/product-action?SOURCE_LIST.NAME=COM_PCCS_070_R1.30.fits
[5] http://pla.esac.esa.int/pla/aio/product-action?SOURCE_LIST.NAME=COM_PCCS_100_R1.10.fits
[6] http://pla.esac.esa.int/pla/aio/product-action?SOURCE_LIST.NAME=COM_PCCS_143_R1.10.fits
[7] http://pla.esac.esa.int/pla/aio/product-action?SOURCE_LIST.NAME=COM_PCCS_217_R1.10.fits
[8] http://pla.esac.esa.int/pla/aio/product-action?SOURCE_LIST.NAME=COM_PCCS_353_R1.10.fits
[9] http://pla.esac.esa.int/pla/aio/product-action?SOURCE_LIST.NAME=COM_PCCS_545_R1.10.fits
[10] http://pla.esac.esa.int/pla/aio/product-action?SOURCE_LIST.NAME=COM_PCCS_857_R1.10.fits
[11] http://www.rssd.esa.int/doc_fetch.php?id=3168419&page=1
[12] http://www.rssd.esa.int/doc_fetch.php?id=3135869&page=1
[13] http://www.rssd.esa.int/doc_fetch.php?id=3135871&page=1
[14] http://www.rssd.esa.int/doc_fetch.php?id=3135990&page=1

Sky temperature power spectra

HFI maps power spectra

Angular power spectra of cut sky CMB dominated maps are provided to allow independent cosmological analysis at high ℓ.

Product description

The auto and cross-spectra of the 13 detector set (detset) maps at 100, 143 and 217 GHz, all analyzed on the same 42.8% of the sky, are provided. The mask used is apodized to reduce the power leakage from large scale to small scale (see input section). Except for the removal of the most contaminated pixels through masking, no attempt at astrophysical components separation has been performed.

For each pair of detectors X and Y, are provided,

- the unbinned *estimated* power spectrum $\hat{C}^{XY}_\ell$ for all ℓ from 0 to 3508 (see Figure 1 below), as well as
- the unbinned symmetric covariance matrix

\begin{align}

```
\hat{M}^{XY}_{\ell \ell'} \equiv \langle\Delta \hat{C}^{XY}_\ell\Delta \hat{C}^{XY}_{\ell'}\rangle
\label{eq:covmatCl}
```

\end{align} for all ℓ on the same range. At the price of some extra hypotheses, that information can be used to build the likelihood of a given theoretical power spectrum C_{ℓ} given the data, and therefore determine the best cosmological models fitting the data. Several examples of such high-ℓ likelihoods are described, discussed and compared in #planck2013-p08 Planck-2013-VIII [1].

$ \newcommand{\bfE}{\boldsymbol{\mathrm{E}}} \newcommand{\bfM}{\boldsymbol{\mathrm{M}}} \newcommand{\bfx}{\boldsymbol{\mathrm{x}}} \newcommand{\lmax}{\ell_{\mathrm{max}}} $ Note that $\hat{\bfM}$ only describes the statistical covariance of the power spectrum induced by the signal and noise of the input map on the cut sky begin analyzed. Most sources of systematic effects (such as uncertainty on the beam modeling) as well as post-processing steps (such as foreground subtraction) will increase the covariance. In the particular case of the uncertainty on the beam window functions $B(l)$, the RIMO provides for each pair XY a set of eigen-vectors $E_{p}^{XY}(\ell)$ of the relative error on B^{XY}_{ℓ} (see "HFI time response and beams paper"planck2013-p03c Planck-2013-VII [1]), defined for p in $[1,5]$ and ℓ in $[0, \lmax]$ (with $\lmax$ being 2500, 3000 or 4000 when the lowest of the nominal frequencies of the detectors X and Y is respectively 100, 143 or 217GHz). The extra contribution to the covariance of C^{XY}_ℓ is then \begin{align}

```
\hat{M}^{XY, \mathrm{beam}}_{\ell_1 \ell_2} = 4 \hat{C}^{XY}_{\ell_1} \hat{C}^{XY}_{\ell_2} \sum_{p=1}^{5} E^{XY}_p(\ell_1) E^{XY}_p(\ell_2).
\label{eq:covmatBeam}
```

\end{align}

Auto and Cross Power Spectra

The spectra computed up to$l=3508$ using PolSpice[1] (Szapudi2001, Chon2004) are corrected from the effect of the cut sky, and from the nominal beam window function and average pixel function. The different steps of the calculation are

- computation of the Spherical Harmonics coefficients of the masked input maps $\Delta T^X(p)$ and of the input mask $w(p)$,

\begin{align}

```
\tilde{a}^X_{\ell m} = \sum_p \Omega_p\, \Delta T^X(p)\, w(p)\, Y^*_{\ell m}(p), \label{eq:almdef}
```

\end{align} \begin{align}

```
\tilde{w}^{(n)}_{\ell m} = \sum_p \Omega_p\ w^n(p)\, Y^*_{\ell m}(p); \label{eq:wlmdef}
```

\end{align} where the sum is done over all sky pixels p, Ω_p is the pixel area, and n is either 1 or 2;

- the sky (cross or auto) pseudo-power spectrum and mask power spectrum are computed from the $\tilde{a}_{\ell m}$ and $\tilde{w}_{\ell m}$,

\begin{align}

```
\tilde{C}^{XY}_\ell =  \sum_{\ell m} \tilde{a}^X_{ m} \tilde{a}^{Y^*}_{\ell m}   / (2 \ell + 1), \label{eq:alm2cl}
```

\end{align} \begin{align}

```
\tilde{W}^{(n)}_\ell =  \sum_{\ell m} \tilde{w}^{(n)}_{ m} {\tilde{w}^{(n)}}^*_{\ell m}   / (2 \ell + 1); \label{eq:wlm2wl}
```

\end{align}

- the sky and mask angular correlation function are computed from the respective power spectra,

\begin{align}

```
\tilde{\xi}(\theta) = \sum_\ell \frac{2\ell+1}{4\pi} \tilde{C}_{\ell} P_\ell(\theta),\label{eq:cl2xi}
```

\end{align} \begin{align}

```
\tilde{\xi}_W(\theta) = \sum_\ell \frac{2\ell+1}{4\pi} \tilde{W}^{(1)}_{\ell} P_\ell(\theta),
```

\end{align} where P_ℓ is the Legendre Polynomial of order ℓ;

- the ratio of the sky angular correlation by the mask correlation provides the cut sky corrected angular correlation,

\begin{align}

```
\xi(\theta) = \tilde{\xi}(\theta) / \tilde{\xi}_W(\theta); \label{eq:xi_deconv}
```

\end{align}

- the sky angular correlation function which is then turned into a angular power spectrum,

\begin{align}

```
 {C'}_\ell =  2\pi \sum_i w_i \xi(\theta_i) P_\ell(\theta_i), \label{eq:xi2cl}
```

\end{align} where w_i are the weights of the Gauss-Legendre quadrature, for θ in $[0, \pi]$;

- the resulting power spectrum is corrected from the nominal beam window function B_ℓ and average pixel window function $w_{\mathrm{pix}}(\ell)$, to provide the final Spice estimator $\hat{C}_\ell$,

\begin{align}

```
\hat{C}_\ell = {C'}_\ell / \left( B^2_\ell w^2_{\mathrm{pix}}(\ell) \right). \label{eq:clfinal}
```

\end{align}

Covariance Matrices

The covariance matrix for the pair XY is computed by PolSpice using the formalism described in Efstathiou2004, also sketched in the appendix of "CMB power spectra and likelihood paper"planck2013-p08, assuming the instrumental noise to be white and uniform.

$ \newcommand{\hC}{\hat C} $ One note that a good approximation of the covariance matrix $\tilde{M}$ of the pseudo $\tilde{C}_{\ell}$ is related to the underlying *estimated* auto- and cross-spectra $\hC_{\ell}$ through \begin{align} \tilde{M}_{\ell_1\ell_2} \equiv \langle\Delta \tilde{C}^{XY}_{\ell_1}\Delta \tilde{C}^{XY}_{\ell_2}\rangle = \left(\left(\hC^{XX}_{\ell_1} \hC^{YY}_{\ell_1} \hC^{XX}_{\ell_2} \hC^{YY}_{\ell_2}\right)^{1/2}

```
  + \hC^{XY}_{\ell_1} \hC^{XY}_{\ell_2} \right)
\sum_{\ell_3} \frac{2\ell_3+1}{4\pi} \tilde{W}^{(2)}_{\ell_3} \left(
  \begin{array}{ccc}
      \! \ell_1\! & \ell_2\!  & \ell_3\!  \\
      \! 0     \! & 0     \!  & 0     \!
    \end{array}
\right)^2,
```

\label{eq:covpseudo} \end{align} where $\tilde{W}^{(2)}_{\ell}$ is the power spectrum of the square of the pixel mask (Eqs. \ref{eq:wlmdef} and \ref{eq:wlm2wl} for $n=2$). The covariance matrix $\hat{M}$ of the Spice estimator is then computed by applying Eqs. \ref{eq:cl2xi}, \ref{eq:xi_deconv}, \ref{eq:xi2cl} and \ref{eq:clfinal} on each row and column of $\tilde{M}$.

Inputs

Maps

The input maps are the 13 HFI detset (see *Type of maps* section for details) maps available at 100, 143 and 217 GHz. These are the same as the ones used for high-ell part of the likelihood code, but that code applies different masks for each cross-spectra in order to minimize further the foreground contamination.

Sky mask

All maps were analyzed on the 42.8% of the sky defined by the apodized mask *HFI_PowerSpect_Mask_2048_R1.10.fits*, which masks out Galactic Plane and point sources (see planck2013-p08), and which is shown in Figure 2 below

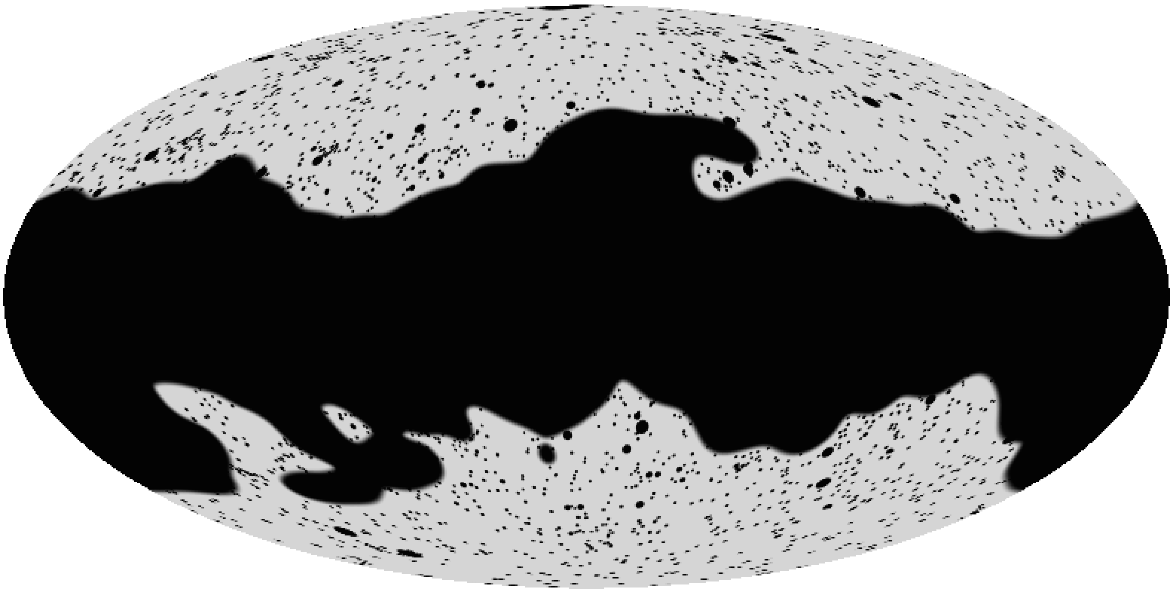

Figure 2: Apodized pixel mask used for HFI power spectrum estimation

Beam Window Function

> The beam window functions $B(l)$, and their uncertainties, are the ones used in the high-ell likelihood analysis, described in section 6.1 "Error Eigenmodes" of planck2013-p08 and provided in the HFI RIMO.

Related products

None

FITS file structure

Power spectra are provided for the auto and cross products built from the 13 detsets available at 100, 143 and 217 GHz, namely:

- 100-ds1, 100-ds2,
- 143-ds1, 143-ds2, 143-5, 143-6, 143-7,
- 217-ds1, 217-ds2, 217-1, 217-2, 217-3, 217-4

which makes 13*(13+1)/2 = 91 spectra. Filenames for the auto spectra are *HFI_PowerSPect_{detset}_Relnum.fits* and *HFI_PowerSPect_{detset1}x{detset2}_Relnum.fits* for the auto- and cross-spectra, respectively. The list of the 91 files is given below. Each files contains 2 BINTABLE extensions:

Power spectrum file data structure

1. EXTNAME = 'POW-SPEC' (BINTABLE)			
Column Name	**Data Type**	**Units**	**Description**
TEMP_CL	Real*4	$\mu$K$_{\mathrm{cmb}}^{2}$	the power spectrum
TEMP_CL_ERR	Real*4	$\mu$K$_{\mathrm{cmb}}^{2}$	estimate of the uncertainty in the power spectrum
Keyword	**Data Type**	**Value**	**Description**
LMIN	Integer	0	First monopole
LMAX	Integer	value	Last monopole
2. EXTNAME = 'PSCOVMAT' (IMAGE)			

COVMAT	Real*4	$\mu$K$_{cmb}^{4}$	the covariance matrix
Keyword	**Data Type**	**Value**	**Description**
NAXIS1	Integer	dim1	matrix first dimension
NAXIS2	Integer	dim2	matrix second dimension

where LMAX is the same for both vectors, and dim1 = dim2 = LMAX+1 by construction.

List of filenames

FITS filenames

Auto power spectra
HFI_PowerSpect_100-ds1_R1.10.fits
HFI_PowerSpect_100-ds2_R1.10.fits
HFI_PowerSpect_143-5_R1.10.fits
HFI_PowerSpect_143-6_R1.10.fits
HFI_PowerSpect_143-7_R1.10.fits
HFI_PowerSpect_143-ds1_R1.10.fits
HFI_PowerSpect_143-ds2_R1.10.fits
HFI_PowerSpect_217-1_R1.10.fits
HFI_PowerSpect_217-2_R1.10.fits
HFI_PowerSpect_217-3_R1.10.fits
HFI_PowerSpect_217-4_R1.10.fits
HFI_PowerSpect_217-ds1_R1.10.fits
HFI_PowerSpect_217-ds2_R1.10.fits
Cross power spectra
HFI_PowerSpect_100-ds1x100-ds2_R1.10.fits
HFI_PowerSpect_100-ds1x143-5_R1.10.fits
HFI_PowerSpect_100-ds1x143-6_R1.10.fits
HFI_PowerSpect_100-ds1x143-7_R1.10.fits
HFI_PowerSpect_100-ds1x143-ds1_R1.10.fits
HFI_PowerSpect_100-ds1x143-ds2_R1.10.fits
HFI_PowerSpect_100-ds1x217-1_R1.10.fits
HFI_PowerSpect_100-ds1x217-2_R1.10.fits
HFI_PowerSpect_100-ds1x217-3_R1.10.fits
HFI_PowerSpect_100-ds1x217-4_R1.10.fits
HFI_PowerSpect_100-ds1x217-ds1_R1.10.fits
HFI_PowerSpect_100-ds1x217-ds2_R1.10.fits
HFI_PowerSpect_100-ds2x143-5_R1.10.fits
HFI_PowerSpect_100-ds2x143-6_R1.10.fits
HFI_PowerSpect_100-ds2x143-7_R1.10.fits

HFI_PowerSpect_100-ds2x143-ds1_R1.10.fits
HFI_PowerSpect_100-ds2x143-ds2_R1.10.fits
HFI_PowerSpect_100-ds2x217-1_R1.10.fits
HFI_PowerSpect_100-ds2x217-2_R1.10.fits
HFI_PowerSpect_100-ds2x217-3_R1.10.fits
HFI_PowerSpect_100-ds2x217-4_R1.10.fits
HFI_PowerSpect_100-ds2x217-ds1_R1.10.fits
HFI_PowerSpect_100-ds2x217-ds2_R1.10.fits
HFI_PowerSpect_143-5x143-6_R1.10.fits
HFI_PowerSpect_143-5x143-7_R1.10.fits
HFI_PowerSpect_143-5x217-1_R1.10.fits
HFI_PowerSpect_143-5x217-2_R1.10.fits
HFI_PowerSpect_143-5x217-3_R1.10.fits
HFI_PowerSpect_143-5x217-4_R1.10.fits
HFI_PowerSpect_143-5x217-ds1_R1.10.fits
HFI_PowerSpect_143-5x217-ds2_R1.10.fits
HFI_PowerSpect_143-6x143-7_R1.10.fits
HFI_PowerSpect_143-6x217-1_R1.10.fits
HFI_PowerSpect_143-6x217-2_R1.10.fits
HFI_PowerSpect_143-6x217-3_R1.10.fits
HFI_PowerSpect_143-6x217-4_R1.10.fits
HFI_PowerSpect_143-6x217-ds1_R1.10.fits
HFI_PowerSpect_143-6x217-ds2_R1.10.fits
HFI_PowerSpect_143-7x217-1_R1.10.fits
HFI_PowerSpect_143-7x217-2_R1.10.fits
HFI_PowerSpect_143-7x217-3_R1.10.fits
HFI_PowerSpect_143-7x217-4_R1.10.fits
HFI_PowerSpect_143-7x217-ds1_R1.10.fits
HFI_PowerSpect_143-7x217-ds2_R1.10.fits
HFI_PowerSpect_143-ds1x143-5_R1.10.fits
HFI_PowerSpect_143-ds1x143-6_R1.10.fits
HFI_PowerSpect_143-ds1x143-7_R1.10.fits
HFI_PowerSpect_143-ds1x143-ds2_R1.10.fits
HFI_PowerSpect_143-ds1x217-1_R1.10.fits
HFI_PowerSpect_143-ds1x217-2_R1.10.fits
HFI_PowerSpect_143-ds1x217-3_R1.10.fits
HFI_PowerSpect_143-ds1x217-4_R1.10.fits
HFI_PowerSpect_143-ds1x217-ds1_R1.10.fits
HFI_PowerSpect_143-ds1x217-ds2_R1.10.fits

HFI_PowerSpect_143-ds2x143-5_R1.10.fits
HFI_PowerSpect_143-ds2x143-6_R1.10.fits
HFI_PowerSpect_143-ds2x143-7_R1.10.fits
HFI_PowerSpect_143-ds2x217-1_R1.10.fits
HFI_PowerSpect_143-ds2x217-2_R1.10.fits
HFI_PowerSpect_143-ds2x217-3_R1.10.fits
HFI_PowerSpect_143-ds2x217-4_R1.10.fits
HFI_PowerSpect_143-ds2x217-ds1_R1.10.fits
HFI_PowerSpect_143-ds2x217-ds2_R1.10.fits
HFI_PowerSpect_217-1x217-2_R1.10.fits
HFI_PowerSpect_217-1x217-3_R1.10.fits
HFI_PowerSpect_217-1x217-4_R1.10.fits
HFI_PowerSpect_217-1x217-ds1_R1.10.fits
HFI_PowerSpect_217-1x217-ds2_R1.10.fits
HFI_PowerSpect_217-2x217-3_R1.10.fits
HFI_PowerSpect_217-2x217-4_R1.10.fits
HFI_PowerSpect_217-2x217-ds1_R1.10.fits
HFI_PowerSpect_217-2x217-ds2_R1.10.fits
HFI_PowerSpect_217-3x217-4_R1.10.fits
HFI_PowerSpect_217-3x217-ds1_R1.10.fits
HFI_PowerSpect_217-3x217-ds2_R1.10.fits
HFI_PowerSpect_217-4x217-ds1_R1.10.fits
HFI_PowerSpect_217-4x217-ds2_R1.10.fits
HFI_PowerSpect_217-ds1x217-ds2_R1.10.fits
Sky mask
HFI_PowerSpect_Mask_2048_R1.10.fits [2]

The full list of HFI power spectra with links to the files in the PLA can be found here [3].

LFI maps power spectra

Product description

The angular power spectrum provides information about the distribution of power on the sky map at the various angular scales. It is especially important for CMB, because it is characterized by a number of features, most notably the acoustic peaks, that encode the dependence from cosmological parameters. Therefore, angular power spectra are the basic inputs for the Planck Likelihood Code, and for estimation of cosmological parameters in general.

For this release we have computed only temperature power spectra. Polarization is not included.

Please note that these spectra come from frequency maps. No component separation has been applied, and we have only masked Galactic Plane and detected point sources. Units are $\mu\mathrm{K}^2_{\mathrm{CMB}}$.

Production process

Spectra are computed using cROMAster, a implementation of the pseudo-Cl method described in #master. In addition to the original approach, our implementation allows for estimation of cross-power spectra from two or more maps (see #polenta_CrossSpectra for details). The software package uses HEALPix [4] modules for spherical harmonic transform and Cl calculation. The schematic of the estimation process is as follows:

- computing the a_lm coefficients from the input temperature map after masking Galactic Plane and point sources.
- computing the pseudo power spectrum from the alms.
- estimating the bias due to the noise power spectrum of the map from noise-only Monte Carlo simulations based on detector noise properties
- correcting for the effect of the adopted mask by computing the mode-mode coupling kernel corresponding to that mask
- deconvolving the effect due to the finite angular resolution of the telescope by using the beam window function
- deconvolving the effect due to the finite size of the pixel in the map by using a pixel window function
- binning the power spectrum from individual multipoles into bandpowers
- estimating error bars on bandpowers from signal plus noise Monte Carlo simulations, where signal simulations include only CMB anisotropies.

Inputs

The inputs are the following:

- LFI Frequency Maps
- Point source and galactic plane masks (the name being specified in the comment keyword in the header, see Note in *Meta Data* section below):

Point source masks
LFI_MASK_030-ps_2048_R1.00.fits [5]
LFI_MASK_044-ps_2048_R1.00.fits [6]
LFI_MASK_070-ps_2048_R1.00.fits [7]
Galactic plane masks
COM_MASK_gal-06_2048_R1.00.fits [8]
COM_MASK_gal-07_2048_R1.00.fits [9]

- Beam window functions
- Monte Carlo simulations
- binning scheme Media:Power_spectra_CTP_bin_tt.pdf.

File Names

LFI_PowerSpect_030_R1.10.fits [10]

LFI_PowerSpect_044_R1.10.fits [11]

LFI_PowerSpect_070_R1.10.fits [12]

Meta Data

The angular power spectra source list in each frequency is structured as a FITS binary table. The Fits extension is composed by the columns described below:

FITS header

Column Name	Data Type	Units	Description
L	Integer*4		ell parameter
TEMP_CL	Real*8	uK $^2_{CMB}$	C_l(temperature)
TEMP_CL_ERR	Real*8	uK $^2_{CMB}$	$C_l$error

Note.- in the comment keyword in the header, the galactic and point source maps used to generate the angular spectra are specified (LFI_MASK_030-ps_2048_R1.00.fits and COM_MASK_gal-06_2048_R1.00.fits in the example below). Note also that, due to an oversight, the mask description related to COM_MASK_gal-xxx is wrong and should refer to the galactic mask.

Below an example of the header.

```
XTENSION= 'BINTABLE'           /Written by IDL:  Sat Feb 16 00:44:22 2013
BITPIX  =                    8 /
NAXIS   =                    2 /Binary table
NAXIS1  =                   20 /Number of bytes per row
NAXIS2  =                  130 /Number of rows
PCOUNT  =                    0 /Random parameter count
GCOUNT  =                    1 /Group count
TFIELDS =                    3 /Number of columns
TFORM1  = '1J      '           /Integer*4 (long integer)
TTYPE1  = 'L       '           /
TFORM2  = '1D      '           /Real*8 (double precision)
TTYPE2  = 'TEMP_CL '           /
TFORM3  = '1D      '           /Real*8 (double precision)
TTYPE3  = 'TEMP_CL_ERR'        /
EXTNAME = 'POW-SPEC'           / Extension name
EXTVER  =                    1 /Extension version
DATE    = '2013-02-15'         /Creation date
TUNIT2  = 'uK_CMB^2'           /
TUNIT3  = 'uK_CMB^2'           /
FILENAME= 'LFI_PowerSpect_030_R1.00.fits' /
PROCVER = 'Dx9_delta'          /
COMMENT ---------------------------------------------
COMMENT     Original Inputs
COMMENT ---------------------------------------------
COMMENT TT_30GHz_maskCS0.60_PS30GHzdet_febecopWls
COMMENT Used Point source Mask LFI_MASK_030-ps_2048_R1.00.fits
COMMENT Used Point source Mask COM_MASK_gal-06_2048_R1.00.fits
COMMENT Used FebeCoP 30 GHz wls
END
```

Below an example of the header of two masks used as input: COM_MASK_gal-06_2048_R1.00.fits and LFI_MASK_030-ps_2048_R1.00.fits:

```
XTENSION= 'BINTABLE'           / binary table extension
BITPIX  =                    8 / 8-bit bytes
NAXIS   =                    2 / 2-dimensional binary table
NAXIS1  =                    4 / width of table in bytes
NAXIS2  =             50331648 / number of rows in table
PCOUNT  =                    0 / size of special data area
GCOUNT  =                    1 / one data group (required keyword)
TFIELDS =                    1 / number of fields in each row
TTYPE1  = 'Mask    '           / label for field   1
TFORM1  = 'E       '           / data format of field: 4-byte REAL
TUNIT1  = 'none    '           / physical unit of field
EXTNAME = '06-GalMask'
DATE    = '2013-02-16T11:07:42' / file creation date (YYYY-MM-DDThh:mm:ss UT)
CHECKSUM= 'NaGVNZGUNaGUNYGU'   / HDU checksum updated 2013-02-16T11:07:43
DATASUM = '2540860986'         / data unit checksum updated 2013-02-16T11:07:43
COMMENT
COMMENT *** Planck params ***
COMMENT
PIXTYPE = 'HEALPIX '           / HEALPIX pixelisation
ORDERING= 'NESTED  '           / Pixel ordering scheme, either RING or NESTED
NSIDE   =                 2048 / Resolution parameter for HEALPIX
FIRSTPIX=                    0 / First pixel # (0 based)
LASTPIX =             50331647 / Last pixel # (0 based)
INDXSCHM= 'IMPLICIT'           / Indexing: IMPLICIT or EXPLICIT
OBJECT  = 'FULLSKY '           / Sky coverage, either FULLSKY or PARTIAL
BAD_DATA=          -1.6375E+30
COORDSYS= 'GALACTIC'
FILENAME= 'COM_MASK_gal-06_2048_R1.00.fits'
COMMENT ---------------------------------------------------------------------
COMMENT Combined galactic mask 0.6 sky fraction
COMMENT Objects used:
COMMENT /sci_planck/lfi_dpc_test/ashdown/repository/masks/component_separation/d
COMMENT x9/combined_mask_0.60_sky_fraction.fits
COMMENT ---------------------------------------------------------------------
END
```

```
XTENSION= 'BINTABLE'           / binary table extension
BITPIX  =                    8 / 8-bit bytes
NAXIS   =                    2 / 2-dimensional binary table
NAXIS1  =                    4 / width of table in bytes
NAXIS2  =             50331648 / number of rows in table
```

```
PCOUNT  =                    0 / size of special data area
GCOUNT  =                    1 / one data group (required keyword)
TFIELDS =                    1 / number of fields in each row
TTYPE1  = 'Mask    '           / label for field   1
TFORM1  = 'E       '           / data format of field: 4-byte REAL
TUNIT1  = 'none    '           / physical unit of field
EXTNAME = '030-PSMask'
DATE    = '2013-02-16T11:03:20' / file creation date (YYYY-MM-DDThh:mm:ss UT)
CHECKSUM= 'fR7ThO7RfO7RfO7R'   / HDU checksum updated 2013-02-16T11:03:21
DATASUM = '3828742620'         / data unit checksum updated 2013-02-16T11:03:21
COMMENT
COMMENT *** Planck params ***
COMMENT
PIXTYPE = 'HEALPIX '           / HEALPIX pixelisation
ORDERING= 'NESTED  '           / Pixel ordering scheme, either RING or NESTED
NSIDE   =                 2048 / Resolution parameter for HEALPIX
FIRSTPIX=                    0 / First pixel # (0 based)
LASTPIX =             50331647 / Last pixel # (0 based)
INDXSCHM= 'IMPLICIT'           / Indexing: IMPLICIT or EXPLICIT
OBJECT  = 'FULLSKY '           / Sky coverage, either FULLSKY or PARTIAL
BAD_DATA=          -1.6375E+30
COORDSYS= 'GALACTIC'
FILENAME= 'LFI_MASK_030-ps_2048_R1.00.fits'
COMMENT ----------------------------------------------------------------------
COMMENT The radius of the holes is 3 times the sigma of the beam at the correspo
COMMENT nding frequency and sigma is FWHM/(2*sqrt(2ln2))
COMMENT FWHM at 30GHz used = 33.158 arcmin
COMMENT Objects used:
COMMENT /planck/sci_ops1/LFI_MAPs/DX9_Delta/MASKs/mask_ps_30GHz_beam33amin_nside
COMMENT 2048.00_DX9_nonblind_holesize3.fits
COMMENT ----------------------------------------------------------------------
END
```

References

<biblio force=false>

1. References

</biblio>

References

[1] http://prof.planck.fr/article141.html

[2] http://pla.esac.esa.int/pla/aio/product-action?MAP.MAP_ID=HFI_PowerSpect_Mask_2048_R1.10.fits

[3] http://pla.esac.esa.int/pla/aio/metadata-action?RESOURCE_CLASS=COSMOLOGY&SELECTED_FIELDS=COSMOLOGY.FILE_ID,COSMOLOGY.SIZE,COSMOLOGY_TYPE.NAME&COSMOLOGY_TYPE.NAME=Sky+Power+Spectra+and+Cov+Matrices&RELEASE.NAME=PR1&QUERY=%28COSMOLOGY.FILE_ID%20LIKE%20%27HFI%25%27%29&RETURN_TYPE=HTML

[4] http://healpix.sourceforge.net/

[5] http://pla.esac.esa.int/pla/aio/product-action?MAP.MAP_ID=LFI_MASK_030-ps_2048_R1.00.fits

[6] http://pla.esac.esa.int/pla/aio/product-action?MAP.MAP_ID=LFI_MASK_044-ps_2048_R1.00.fits

[7] http://pla.esac.esa.int/pla/aio/product-action?MAP.MAP_ID=LFI_MASK_070-ps_2048_R1.00.fits
[8] http://pla.esac.esa.int/pla/aio/product-action?MAP.MAP_ID=COM_MASK_gal-06_2048_R1.00.fits
[9] http://pla.esac.esa.int/pla/aio/product-action?MAP.MAP_ID=COM_MASK_gal-07_2048_R1.00.fits
[10] http://pla.esac.esa.int/pla/aio/product-action?COSMOLOGY.FILE_ID=LFI_PowerSpect_030_R1.10.fits
[11] http://pla.esac.esa.int/pla/aio/product-action?COSMOLOGY.FILE_ID=LFI_PowerSpect_044_R1.10.fits
[12] http://pla.esac.esa.int/pla/aio/product-action?COSMOLOGY.FILE_ID=LFI_PowerSpect_070_R1.10.fits

CMB and astrophysical component maps

Overview

This section describes the maps of astrophysical components produced from the Planck data. These products are derived from some or all of the nine frequency channel maps described above using different techniques and, in some cases, using other constraints from external data sets. Here we give a brief description of the product and how it is obtained, followed by a description of the FITS file containing the data and associated information. All the details can be found in #planck2013-p06.

CMB maps

CMB maps have been produced by the SMICA, NILC, and SEVEM pipelines. Of these, the SMICA product is considered the preferred one overall and is labelled *Main product* in the Planck Legacy Archive, while the other two are labeled as *Additional product*.

SMICA and NILC also produce *inpainted* maps, in which the Galactic Plane, some bright regions and masked point sources are replaced with a constrained CMB realization such that the whole map has the same statistical distribution as the observed CMB.

The results of each pipeline are distributed as a FITS file containing 4 extensions:

1. CMB maps and ancillary products (3 or 6 maps)
2. CMB-cleaned foreground maps from LFI (3 maps)
3. CMB-cleaned foreground maps from HFI (6 maps)
4. Effective beam of the CMB maps (1 vector)

For a complete description of the data structure, see the below; the content of the first extensions is illustrated and commented in the table below.

The maps (CMB, noise, masks) contained in the first extension

Col name	SMICA	NILC	SEVEM	Description / notes
1: I	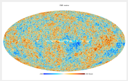	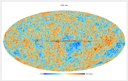	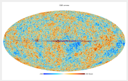	Raw CMB anisotropy map. These are the maps used in the component separation paper #planck2013-p06 Planck-2013-XII [1].
2: NOISE	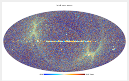	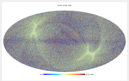	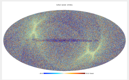	Noise map. Obtained by propagating the half-ring noise through the CMB cleaning pipelines.
3: VALMASK	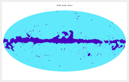	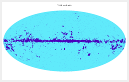	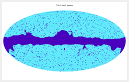	Confidence map. Pixels with an expected low level of foreground contamination. These maps are only indicative and obtained by different ad hoc methods. They cannot be used to rank the CMB maps.
4: I_MASK	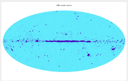	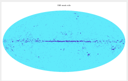	not applicable	Some areas are masked for the production of the raw CMB maps (for NILC: point sources from 44 GHz to 857 GHz; for SMICA: point sources from 30 GHz to 857 GHz, Galatic region and additional bright regions).

5: INP_CMB	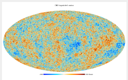	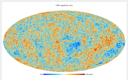	not applicable	Inpainted CMB map. The raw CMB maps with some regions (as indicated by INP_MASK) replaced by a constrained Gaussian realization. The inpainted SMICA map was used for PR.
6: INP_MASK	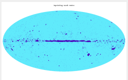	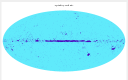	not applicable	Mask of the inpainted regions. For SMICA, this is identical to I_MASK. For NILC, it is not.

The component separation pipelines are described in the CMB and foreground separation section and also in Section 3 and Appendices A-D of #planck2013-p06 Planck-2013-XII [1] and references therein.

Product description

SMICA

Principle

SMICA produces a CMB map by linearly combining all Planck input channels (from 30 to 857 GHz) with weights which vary with the multipole. It includes multipoles up to $\ell = 4000$.

Resolution (effective beam)

The SMICA map has an effective beam window function of 5 arc-minutes truncated at $\ell = 4000$ **and deconvolved from the pixel window**. It means that, ideally, one would have $C_\ell(map) = C_\ell(sky) * B_\ell(5')^2$, where $C_\ell(map)$is the angular spectrum of the map, where $C_\ell(sky)$is the angular spectrum of the CMB and $B_\ell(5')$is a 5-arcminute Gaussian beam function. Note however that, by convention, the effective beam window function $B_\ell(fits)$provided in the FITS file does include a pixel window function. Therefore, it is equal to $B_\ell(fits) = B_\ell(5')/p_\ell(2048)$where $p_\ell(2048)$denotes the pixel window function for an Nside=2048 pixelization.

Confidence mask

A confidence mask is provided which excludes some parts of the Galactic plane, some very bright areas and the masked point sources. This mask provides a qualitative (and subjective) indication of the cleanliness of a pixel.

Masks and inpainting

The raw SMICA CMB map has valid pixels except at the location of masked areas: point sources, Galactic plane, some other bright regions. Those invalid pixels are indicated with the mask named 'I_MASK'. The raw SMICA map has been inpainted, producing the map named "INP_CMB". Inpainting consists in replacing some pixels (as indicated by the mask named INP_MASK) by the values of a constrained Gaussian realization which is computed to ensure good statistical properties of the whole map (technically, the inpainted pixels are a sample realisation drawn under the posterior distribution given the un-masked pixels.

NILC

Principle

The Needlet-ILC (hereafter NILC) CMB map is constructed from all Planck channels from 44 to 857 GHz and includes multipoles up to $\ell = 3200$. It is obtained by applying the Internal Linear Combination (ILC) technique in needlet space, that is, with combination weights which are allowed to vary over the sky and over the whole multipole range.

Resolution (effective beam)

As in the SMICA product except that there is no abrupt truncation at $\ell_{max} = 3200$but a smooth transition to $0$over the range $2700 \leq \ell \leq 3200$.

Confidence mask

A confidence mask is provided which excludes some parts of the Galactic plane, some very bright areas and the masked point sources. This mask provides a qualitative indication of the cleanliness of a pixel. The threshold is somewhat arbitrary.

Masks and inpainting

The raw NILC map has valid pixels except at the location of masked point sources. This is indicated with the mask named 'I_MASK'. The raw NILC map has been inpainted, producing the map named "INP_CMB". The inpainting consists in replacing some pixels (as indicated by the mask named INP_MASK) by the values of a constrained Gaussian realization which is computed to ensure good statistical properties of the whole map (technically, the inpainted pixels are a sample realisation drawn under the posterior distribution given the un-masked pixels.

SEVEM

The aim of SEVEM is to produce clean CMB maps at one or several frequencies by using a procedure based on template fitting. The templates are internal, i.e., they are constructed from Planck data, avoiding the need for external data sets, which usually complicates the analyses and may introduce inconsistencies. The method has been successfully applied to Planck simulations Leach et al., 2008 #leach2008 and to WMAP polarisation data Fernandez-Cobos et al., 2012 xx. In the cleaning process, no assumptions about the foregrounds or noise levels are needed, rendering the technique very robust.

Production process

SMICA

1) Pre-processing

All input maps undergo a pre-processing step to deal with point sources. The point sources with SNR > 5 in the PCCS catalogue are fitted in each input map. If the fit is successful, the fitted point source is removed from the map; otherwise it is masked and the hole is filled in by a simple diffusive process to ensure a smooth transition and mitigate spectral leakage. This is done at all frequencies but 545 and 857 GHz, here all point sources with SNR > 7.5 are masked and filled-in similarly.

2) Linear combination

The nine pre-processed Planck frequency channels from 30 to 857 GHzare harmonically transformed up to $\ell = 4000$and co-added with multipole-dependent weights as shown in the figure.

3) Post-processing

The areas masked in the pre-processing step are replaced by a constrained Gaussian realization.

Note: The visible power deficit in the raw CMB map around the galactic plane is due to the smooth fill-in of the masked areas in the input maps (the result of the pre-processing). It is not to be confused with the post-processing step of inpainting of the CMB map with a constrained Gaussian realization.

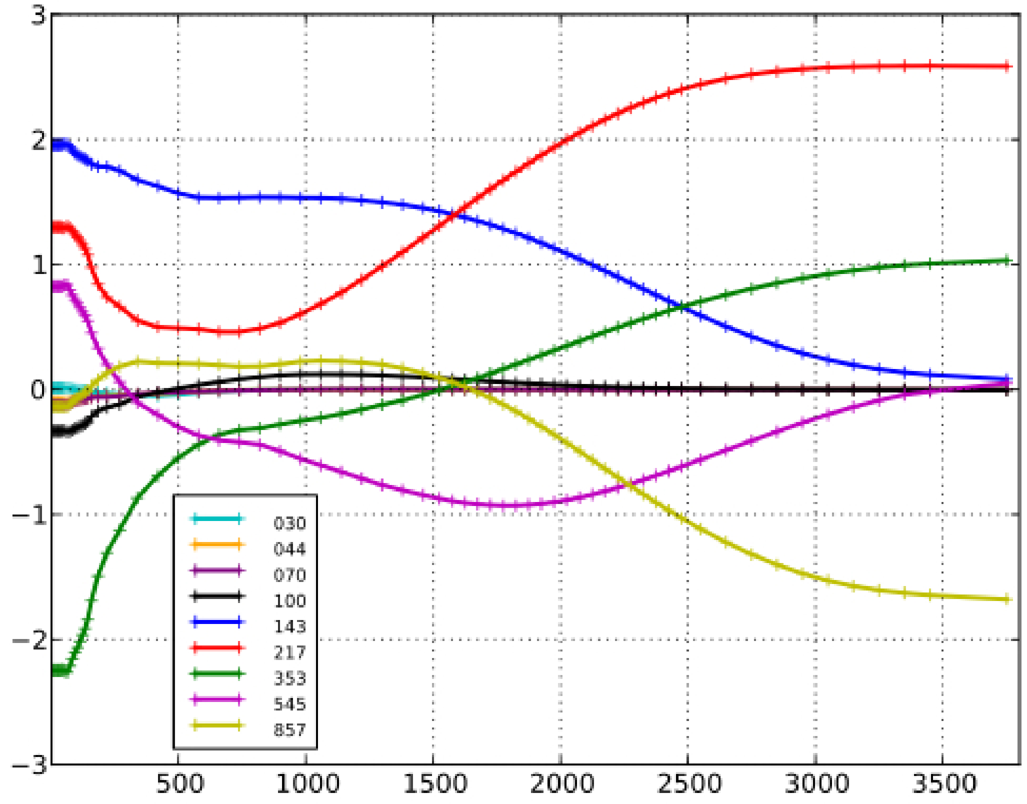

Weights given by SMICA to the input maps (after they are re-beamed to 5 arcmin and expressed in K), as a function of multipole.

NILC

1) Pre-processing

Same pre-processing as SMICA (except the 30 GHz channel is not used).

2) Linear combination

The pre-processed Planck frequency channels from 44 to 857 GHz are linearly combined with weights which depend on location on the sky and on the multipole range up to $\ell = 3200$. This is achieved using a needlet (redundant spherical wavelet) decomposition. For more details, see #planck2013-p06.

3) Post-processing

The areas masked in the pre-processing plus other bright regions step are replaced by a constrained Gaussian realization as in the SMICA post-processing step.

SEVEM

The templates are internal, i.e., they are constructed from Planck data, avoiding the need for external data sets, which usually complicates the analyses and may introduce inconsistencies. In the cleaning process, no assumptions about the foregrounds or noise levels are needed, rendering the technique very robust. The fitting can be done in real or wavelet space (using a fast wavelet adapted to the HEALPix pixelization; Casaponsa et al. 2011 #Casaponsa2011) to properly deal with incomplete sky coverage. By expediency, however, we fill in the small number of unobserved pixels at each channel with the mean value of its neighbouring pixels before applying SEVEM.

We construct our templates by subtracting two close Planck frequency channel maps, after first smoothing them to a common resolution to ensure that the CMB signal is properly removed. A linear combination of the templates $t_j$is then subtracted from (hitherto unused) map d to produce a clean CMB map at that frequency. This is done either in real or in wavelet space (i.e., scale by scale) at each position on the sky: where n_t is the number of templates. If the cleaning is performed in real space, the coefficients are obtained by minimising the variance of the clean map T_c outside a given mask. When working in wavelet space, the cleaning is done in the same way at each wavelet scale independently (i.e., the linear coefficients depend on the scale). Although we exclude very contaminated regions during the minimization, the subtraction is performed for all pixels and, therefore, the cleaned maps cover the full-sky (although we expect that foreground residuals are present in the excluded areas).

An additional level of flexibility can also be considered: the linear coefficients can be the same for all the sky, or several regions with different sets of coefficients can be considered. The regions are then combined in a smooth way, by weighting the pixels at the boundaries, to avoid discontinuities in the clean maps. Since the method is linear, we may easily propagate the noise properties to the final CMB map. Moreover, it is very fast and permits the generation of thousands of simulations to character- ize the statistical properties of the outputs, a critical need for many cosmological applications. The final CMB map retains the angular resolution of the original frequency map.

There are several possible configurations of SEVEM with regard to the number of frequency maps which are cleaned or the number of templates that are used in the fitting. Note that the production of clean maps at different frequencies is of great interest in order to test the robustness of the results. Therefore, to define the best strategy, one needs to find a compromise between the number of maps that can be cleaned independently and the number of templates that can be constructed.

In particular, we have cleaned the 143 GHz and 217 GHz maps using four templates constructed as the difference of the following Planck channels (smoothed to a common resolution): (30-44), (44-70), (545-353) and (857-545). For simplicity, the three maps have been cleaned in real space, since there was not a significant improvement when using wavelets (especially at high latitude). In order to take into account the different spectral behaviour of the foregrounds at low and high galactic latitudes, we have considered two independent regions of the sky, for which we have used a different set of coefficients. The first region corresponds to the 3 per cent brightest Galactic emission, whereas the second region is defined by the remaining 97 per cent of the sky. For the first region, the coefficients are actually estimated over the whole sky (we find that this is more optimal than perform the minimisation only on the 3 per cent brightest region, where the CMB emission is very sub-dominant) while for the second region, we exclude the 3 per cent brightest region of the sky, point sources detected at any frequency and those pixels which have not been observed at all channels. Our final CMB map has then been constructed by combining the 143 and 217 GHz maps by weighting the maps in harmonic space taking into account the noise level, the resolution and a rough estimation of the foreground residuals of each map (obtained from realistic simulations). This final map has a resolution corresponding to a Gaussian beam of fwhm=5 arcminutes.

Moreover, additional CMB clean maps (at frequencies between 44 and 353 GHz) have also been produced using different combinations of templates for some of the analyses carried out in #planck2013-p09 Planck-2013-XXIII [1] and #planck2013-p14 Planck-2013-XIX [2]. In particular, clean maps from 44 to 353 GHz have been used for the stacking analysis presented in #planck2013-p14, while frequencies from 70 to 217 GHz were used for consistency tests in #planck2013-p09.

The method has been successfully applied to Planck simulations #leach2008 and to WMAP polarisation data #Fernandez-Cobos2012.

Inputs

The input maps are the sky temperature maps described in the Sky temperature maps section. SMICA and SEVEM use all the maps between 30 and 857 GHz; NILC uses the ones between 44 and 857 GHz.

File names and structure

The FITS files corresponding to the three CMB products are the following:

- COM_CompMap_CMB-nilc_2048_R1.20.fits [3]
- COM_CompMap_CMB-sevem_2048_R1.11.fits [4]
- COM_CompMap_CMB-smica_2048_R1.20.fits [5]

The files contain a minimal primary extension with no data and four *BINTABLE* data extensions. Each column of the *BINTABLE* is a (Healpix) map; the column names and the most important keywords of each extension are described in the table below; for the remaining keywords, please see the FITS files directly.

CMB map file data structure

Ext. 1. EXTNAME = *COMP-MAP* (BINTABLE)			
Column Name	**Data Type**	**Units**	**Description**
I	Real*4	uK_cmb	CMB temperature map
NOISE	Real*4	uK_cmb	Estimated noise map (note 1)
VALMASK	Byte	none	Confidence mask (note 2)
I_MASK	Byte	none	Mask of regions over which CMB map is not built (Optional - see note 3)
INP_CMB	Real*4	uK_cmb	Inpainted CMB temperature map (Optional - see note 3)
INP_MASK	Byte	none	mask of inpainted pixels (Optional - see note 3)
Keyword	**Data Type**	**Value**	**Description**
AST-COMP	String	CMB	Astrophysical compoment name
PIXTYPE	String	HEALPIX	
COORDSYS	String	GALACTIC	Coordinate system
ORDERING	String	NESTED	Healpix ordering
NSIDE	Int	2048	Healpix Nside
METHOD	String	name	Cleaning method (SMICA/NILC/SEVEM)
Ext. 2. EXTNAME = *FGDS-LFI* (BINTABLE) - Note 4			
Column Name	**Data Type**	**Units**	**Description**
LFI_030	Real*4	K_cmb	30 GHz foregrounds
LFI_044	Real*4	K_cmb	44 GHz foregrounds
LFI_070	Real*4	K_cmb	70 GHz foregrounds
Keyword	**Data Type**	**Value**	**Description**
PIXTYPE	String	HEALPIX	
COORDSYS	String	GALACTIC	Coordinate system
ORDERING	String	NESTED	Healpix ordering
NSIDE	Int	1024	Healpix Nside
METHOD	String	name	Cleaning method (SMICA/NILC/SEVEM)
Ext. 3. EXTNAME = *FGDS-HFI* (BINTABLE) - Note 4			

Column Name	**Data Type**	**Units**	**Description**
HFI_100	Real*4	K_cmb	100 GHz foregrounds
HFI_143	Real*4	K_cmb	143 GHz foregrounds
HFI_217	Real*4	K_cmb	217 GHz foregrounds
HFI_353	Real*4	K_cmb	353 GHz foregrounds
HFI_545	Real*4	MJy/sr	545 GHz foregrounds
HFI_857	Real*4	MJy/sr	857 GHz foregrounds
Keyword	**Data Type**	**Value**	**Description**
PIXTYPE	String	HEALPIX	
COORDSYS	String	GALACTIC	Coordinate system
ORDERING	String	NESTED	Healpix ordering
NSIDE	Int	2048	Healpix Nside
METHOD	String	name	Cleaning method (SMICA/NILC/SEVEM)
Ext. 4. EXTNAME = *BEAM_WF* (BINTABLE)			
Column Name	**Data Type**	**Units**	**Description**
BEAM_WF	Real*4	none	The effective beam window function, including the pixel window function. See Note 5.
Keyword	**Data Type**	**Value**	**Description**
LMIN	Int	value	First multipole of beam WF
LMAX	Int	value	Lsst multipole of beam WF
METHOD	String	name	Cleaning method (SMICA/NILC/SEVEM)

Notes:

1. The half-ring half-difference (HRHD) map is made by passing the half-ring frequency maps independently through the component separation pipeline, then computing half their difference. It approximates a noise realisation, and gives an indication of the uncertainties due to instrumental noise in the corresponding CMB map.
2. The confidence mask indicates where the CMB map is considered valid.
3. This column is not present in the SEVEM product file.
4. The subtraction of the CMB from the sky maps in order to produce the foregrounds map is done after convolving the CMB map to the resolution of the given frequency.
5. The beam window function $B_\ell$given here includes the pixel window function $p_\ell$for the Nside=2048 pixelization. It means that, ideally, $C_\ell(map) = C_\ell(sky)\ B_\ell^2\ p_\ell^2$.

Cautionary notes

1. The half-ring CMB maps are produced by the pipelines with parameters/weights fixed to the values obtained from the full maps. Therefore the CMB HRHD maps do not capture all of the uncertainties due to foreground modelling on large angular scales.
2. The HRHD maps for the HFI frequency channels underestimate the noise power spectrum at high l by typically a few percent. This is caused by correlations induced in the pre-processing to remove cosmic ray hits. The CMB is mostly constrained by the HFI channels at high l, and so the CMB HRHD maps will inherit this deficiency in power.
3. The beam transfer functions do not account for uncertainties in the beams of the frequency channel maps.

Astrophysical foregrounds from parametric component separation

We describe diffuse foreground products for the Planck 2013 release. See Planck Component Separation paper #planck2013-p06 Planck-2013-XII [1] for a detailed description and astrophysical discussion of those.

Product description

Low frequency foreground component

The products below contain the result of the fitting for one foreground component at low frequencies in Planck bands,along with its spectral behavior parametrized by a power law spectral index. Amplitude and spectral indeces are evaluated at N$_\rm{side}$ 256 (see below in the production process), along with standard deviation from sampling and instrumental noise on both. An amplitude solution at N$_\rm{side}$=2048 is also given, along with standard deviation from sampling and instrumental noise as well as solutions on halfrings. The beam profile associated to this component is also provided as a secondary Extension in the N$_\rm{side}$ 2048 product.

Thermal dust

The products below contain the result of the fitting for one foreground component at high frequencies in Planck bands, along with its spectral behavior parametrized by temperature and emissivity. Amplitude, temperature and emissivity are evaluated at N$_\rm{side}$ 256 (see below in the production process), along with standard deviation from sampling and instrumental noise on all of them. An amplitude solution at N$_\rm{side}$=2048 is also given, along with standard deviation from sampling and instrumental noise as well as solutions on halfrings. The beam profile associated to this component is provided.

Sky mask

The delivered mask is defined as the sky region where the fitting procedure was conducted and the solutions presented here were obtained. It is made by masking a region where the Galactic emission is too intense to perform the fitting, plus the masking of brightest point sources.

Production process

CODE: COMMANDER-RULER. The code exploits a parametrization of CMB and main diffuse foreground observables. The naive resolution of input frequency channels is reduced to N$_\rm{side}$=256 first. Parameters related to the foreground scaling with frequency are estimated at that resolution by using Markov Chain Monte Carlo analysis using Gibbs sampling. The foreground parameters make the foreground mixing matrix which is applied to the data at full resolution in order to obtain the provided products at N$_\rm{side}$=2048. In the Planck Component Separation paper #planck2013-p06 Planck-2013-XII [1]additional material is discussed, specifically concerning the sky region where the solutions are reliable, in terms of chi2 maps.

Inputs

Nominal frequency maps at 30, 44, 70, 100, 143, 217, 353 GHz (LFI 30 GHz frequency maps [6], LFI 44 GHz frequency maps [7] and LFI 70 GHz frequency maps [8], HFI 100 GHz frequency maps [9], HFI 143 GHz frequency maps [10],HFI 217 GHz frequency maps [11] and HFI 353 GHz frequency maps [12]) and their II column corresponding to the noise covariance matrix. Halfrings at the same frequencies. Beam window functions as reported in the LFI and HFI RIMO.

Related products

None.

File names

- Low frequency component at N$_\rm{side}$ 256: COM_CompMap_Lfreqfor-commrul_0256_R1.00.fits [13]
- Low frequency component at N$_\rm{side}$ 2048: COM_CompMap_Lfreqfor-commrul_2048_R1.00.fits [14]
- Thermal dust at N$_\rm{side}$ 256: COM_CompMap_dust-commrul_0256_R1.00.fits [15]
- Thermal dust at N$_\rm{side}$ 2048: COM_CompMap_dust-commrul_2048_R1.00.fits [16]
- Mask: COM_CompMap_Mask-rulerminimal_2048_R1.00.fits [17]

Meta Data

Low frequency foreground component

Low frequency component at N$_\rm{side}$ 256

File name: COM_CompMap_Lfreqfor-commrul_0256_R1.00.fits

Name HDU -- COMP-MAP

The Fits extension is composed by the columns described below:

FITS header

Column Name	Data Type	Units	Description
I	Real*4	uK $_{CMB}$	Intensity
I_stdev	Real*4	uK $_{CMB}$	standard deviation of intensity
Beta	Real*4		effective spectral index
B_stdev	Real*4		standard deviation on the effective spectral index

Notes

Comment: The Intensity is normalized at 30 GHz

Comment: The intensity was estimated during mixing matrix estimation

Low frequency component at N$_\rm{side}$ 2048

File name: COM_CompMap_Lfreqfor-commrul_2048_R1.00.fits

Name HDU -- COMP-MAP

The Fits extension is composed by the columns described below:

FITS header

Column Name	Data Type	Units	Description
I	Real*8	uK ^{CMB}	Intensity
I_stdev	Real*8	uK ^{CMB}	standard deviation of intensity
I_hr1	Real*8	uK ^{CMB}	Intensity on half ring 1
I_hr2	Real*8	uK ^{CMB}	Intensity on half ring 2

Notes

Comment: The intensity was computed after mixing matrix application

Name HDU -- BeamWF

The Fits second extension is composed by the columns described below:

FITS header

Column Name	Data Type	Units	Description
BeamWF	Real*4		beam profile

Notes

Comment: Beam window function used in the Component separation process

Thermal dust

Thermal dust component at N$_\rm{side}$=256

File name: COM_CompMap_dust-commrul_0256_R1.00.fits

Name HDU -- COMP-MAP

The Fits extension is composed by the columns described below:

FITS header

Column Name	Data Type	Units	Description
I	Real*4	MJy/sr	Intensity
I_stdev	Real*4	MJy/sr	standard deviation of intensity
Em	Real*4		emissivity
Em_stdev	Real*4		standard deviation on emissivity
T	Real*4	uK ^{CMB}	temperature
T_stdev	Real*4	uK ^{CMB}	standard deviation on temerature

Notes

Comment: The intensity is normalized at 353 GHz

Thermal dust component at N$_\rm{side}$=2048

File name: COM_CompMap_dust-commrul_2048_R1.00.fits

Name HDU -- COMP-MAP

The Fits extension is composed by the columns described below:

FITS header

Column Name	Data Type	Units	Description
I	Real*8	MJy/sr	Intensity
I_stdev	Real*8	MJy/sr	standard deviation of intensity
I_hr1	Real*8	MJy/sr	Intensity on half ring 1
I_hr2	Real*8	MJy/sr	Intensity on half ring 2

Name HDU -- BeamWF

The Fits second extension is composed by the columns described below:

FITS header

Column Name	Data Type	Units	Description
BeamWF	Real*4		beam profile

Notes

Comment: Beam window function used in the Component separation process

Sky mask

File name: COM_CompMap_Mask-rulerminimal_2048.fits

Name HDU -- COMP-MASK

The Fits extension is composed by the columns described below:

FITS header

Column Name	Data Type	Units	Description
Mask	Real*4		Mask

Dust optical depth map and model

Thermal emission from interstellar dust is captured by Planck-HFI over the whole sky, at all frequencies from 100 to 857 GHz. This emission is well modelled by a modified black body in the far-infrared to millimeter range. It is produced by the biggest interstellar dust grain that are in thermal equilibrium with the radiation field from stars. The grains emission properties in the sub-millimeter are therefore directly linked to their absorption properties in the UV-visible range. By modelling the thermal dust emission in the sub-millimeter, a map of dust reddening in the visible can then be constructed.

Model of thermal dust emission

The model of the thermal dust emission is based on a modify black body fit to the data I_ν

$$I_\nu = A\, B_\nu(T)\, \nu^\beta$$

where B_nu(T) is the Planck function for dust equilibirum temperature T, A is the amplitude of the MBB and beta the dust spectral index. The dust optical depth at frequency nu is

$$\tau_\nu = I_\nu / B_\nu(T) = A\,\nu^\beta$$

The dust parameters provided are T, beta and τ_{353}. They were obtained by fitting the Planck data at 353, 545 and 857 GHz together with the IRAS (IRIS) 100 micron data. All maps (in Healpix Nside=2048 were smoothed to a common resolution of 5 arcmin. The CMB anisotropies, clearly visible at 353 GHz, were removed from all the HFI maps using the SMICA map. An offset was removed from each map to obtained a meaningful Galactic zero level, using a correlation with the LAB 21 cm data in diffuse areas of the sky ($N_{HI} < 2 \times 10^{20} cm^{-2}$). Because the dust emission is so well correlated between frequencies in the Rayleigh-Jeans part of the dust spectrum, the zero level of the 545 and 353 GHz were improved by correlating with the 857 GHz over a larger mask ($N_{HI} < 3 \times 10^{20} cm^{-2}$). Faint residual dipole structures, identified in the 353 and 545 GHz maps, were removed prior to the fit.

The MBB fit was performed using a chi-square minimization, assuming errors for each data point that include instrumental noise, calibration uncertainties (on both the dust emission and the CMB anisotropies) and uncertainties on the zero level. Because of the known degeneracy between $T$and βin the presence of noise, we produced a model of dust emission using data smoothed to 35 arcmin; at such resolution no systematic bias of the parameters is observed. The map of the spectral index βat 35 arcmin was than used to fit the data for $T$and τ_{353}at 5 arcmin.

The $E(B-V)$map

For the production of the $E(B-V)$map, we used Planck and IRAS data from which point sources in diffuse areas were removed to avoid contamination by galaxies. In the hypothesis of constant dust emission cross-section, the optical depth map $\tau_{353}$is proportional to dust column density. It can then be used to estimate E(B-V), also proportional to dust column density in the hypothesis of a constant differential absorption cross-section between the B and V bands. Given those assumptions, $E(B-V) = q\,\tau_{353}$.

To estimate the calibration factor q, we followed a method similar to #mortsell2013 based on SDSS reddening measurements ($E(g-r)$which corresponds closely to $E(B-V)$) of 77 429 Quasars #schneider2007. The interstellar HI column densities covered on the lines of sight of this sample ranges from $0.5$to $10 \times 10^{20}\, cm^{-2}$. Therefore this sample allows to estimate q in the diffuse ISM where dust properties are expected to vary less than in denser clouds where coagulation and grain growth might modify dust emission and absorption cross sections.

Dust optical depth products

The characteristics of the dust model maps are the following.

- Dust optical depth at 353 GHz : Nside=2048, fwhm=5 arcmin, no units
- Dust reddening E(B-V) : Nside=2048, fwhm=5 arcmin, units=magnitude, obtained with data from which point sources were removed.
- Dust temperature : Nside 2048, fwhm=5 arcmin, units=Kelvin
- Dust spectral index : Nside=2048, fwhm=35 arcmin, no units

Dust opacity file data structure

1. EXTNAME = 'COMP-MAP'			
Column Name	**Data Type**	**Units**	**Description**
TAU353	Real*4	none	The opacity at 353GHz
TAU353ERR	Real*4	none	Error in the opacity
EBV	Real*4	mag	E(B-V)
EBV_ERR	Real*4	mag	Error in E(B-V)
T_HF	Real*4	K	Temperature for the high frequency correction
T_HF_ERR	Real*4	K	Error on the temperature
BETAHF	Real*4	none	Beta for the high frequency correction
BETAHFERR	Real*4	none	Error on beta
Keyword	**Data Type**	**Value**	**Description**
AST-COMP	String	DUST-OPA	Astrophysical compoment name
PIXTYPE	String	HEALPIX	
COORDSYS	String	GALACTIC	Coordinate system
ORDERING	String	NESTED	Healpix ordering
NSIDE	Int	2048	Healpix Nside for LFI and HFI, respectively
FIRSTPIX	Int*4	0	First pixel number
LASTPIX	Int*4	50331647	Last pixel number, for LFI and HFI, respectively

CO emission maps

CO rotational transition line emission is present in all HFI bands but for the 143 GHz channel. It is especially significant in the 100, 217 and 353 GHz channels (due to the 115 (1-0), 230 (2-1) and 345 GHz (3-2) CO transitions). This emission comes essentially from the Galactic interstellar medium and is mainly located at low and intermediate Galactic latitudes. Three approaches (summarised below) have been used to extract CO velocity-integrated emission maps from HFI maps and to make three types of CO products. A full description of how these products were producedis given in #planck2013-p03a.

- Type 1 product: it is based on a single channel approach using the fact that each CO line has a slightly different transmission in each bolometer at a given frequency channel. These transmissions can be evaluated from bandpass measurements that were performed on the ground or empirically determined from the sky using existing ground-based CO surveys. From these, the J=1-0, J=2-1 and J=3-2 CO lines can be extracted independently. As this approach is based on individual bolometer maps of a single channel, the resulting Signal-to-Noise ratio (SNR) is relatively low. The benefit, however, is that these maps do not suffer from contamination from other HFI channels (as is the case for the other approaches) and are more reliable, especially in the Galactic Plane.
- Type 2 product: this product is obtained using a multi frequency approach. Three frequency channel maps are combined to extract the J=1-0 (using the 100, 143 and 353 GHz channels) and J=2-1 (using the 143, 217 and 353 GHz channels) CO maps. Because frequency channels are combined, the spectral behaviour of other foregrounds influences the result. The two type 2 CO maps produced in this way have a higher SNR than the type 1 maps at the cost of a larger possible residual contamination from other diffuse foregrounds.
- Type 3 product: using prior information on CO line ratios and a multi-frequency component separation method, we construct a combined CO emission map with the largest possible SNR. This type 3 product can be used as a sensitive finder chart for low-intensity diffuse CO emission over the whole sky.

The released Type 1 CO maps have been produced using the MILCA-b algorithm, Type 2 maps using a specific implementation of the Commander algorithm, and the Type 3 map using the full Commander-Ruler component separation pipeline (see above).

Characteristics of the released maps are the following. We provide Healpix maps with Nside=2048. For one transition, the CO velocity-integrated line signal map is given in K_RJ.km/s units. A conversion factor from this unit to the native unit of HFI maps (K_CMB) is provided in the header of the data files and in the RIMO. Four maps are given per transition and per type:

- The signal map
- The standard deviation map (same unit as the signal),
- A null test noise map (same unit as the signal) with similar statistical properties. It is made out of half the difference of half-ring maps.
- A mask map (0B or 1B) giving the regions (1B) where the CO measurement is not reliable because of some severe identified foreground contamination.

All products of a given type belong to a single file. Type 1 products have the native HFI resolution i.e. approximately 10, 5 and 5 arcminutes for the CO 1-0, 2-1, 3-2 transitions respectively. Type 2 products have a 15 arcminute resolution The Type 3 product has a 5.5 arcminute resolution.

Type-1 CO map file data structure

1. EXTNAME = 'COMP-MAP'			
Column Name	**Data Type**	**Units**	**Description**
I10	Real*4	K_RJ km/sec	The CO(1-0) intensity map
E10	Real*4	K_RJ km/sec	Uncertainty in the CO(1-0) intensity
N10	Real*4	K_RJ km/sec	Map built from the half-ring difference maps
M10	Byte	none	Region over which the CO(1-0) intensity is considered reliable
I21	Real*4	K_RJ km/sec	The CO(2-1) intensity map
E21	Real*4	K_RJ km/sec	Uncertainty in the CO(2-1) intensity
N21	Real*4	K_RJ km/sec	Map built from the half-ring difference maps
M21	Byte	none	Region over which the CO(2-1) intensity is considered reliable
I32	Real*4	K_RJ km/sec	The CO(3-2) intensity map
E32	Real*4	K_RJ km/sec	Uncertainty in the CO(3-2) intensity
N32	Real*4	K_RJ km/sec	Map built from the half-ring difference maps
M32	Byte	none	Region over which the CO(3-2) intensity is considered reliable
Keyword	**Data Type**	**Value**	**Description**
AST-COMP	string	CO-TYPE2	Astrophysical compoment name
PIXTYPE	String	HEALPIX	
COORDSYS	String	GALACTIC	Coordinate system
ORDERING	String	NESTED	Healpix ordering
NSIDE	Int	2048	Healpix Nside for LFI and HFI, respectively
FIRSTPIX	Int*4	0	First pixel number
LASTPIX	Int*4	50331647	Last pixel number, for LFI and HFI, respectively
CNV 1-0	Real*4	value	Factor to convert CO(1-0) intensity to Kcmb (units Kcmb/(Krj*km/s))
CNV 2-1	Real*4	value	Factor to convert CO(2-1) intensityto Kcmb (units Kcmb/(Krj*km/s))

CNV 3-2	Real*4	value	Factor to convert CO(3-2) intensityto Kcmb (units Kcmb/(Krj*km/s))

Type-2 CO map file data structure

1. EXTNAME = 'COMP-MAP'			
Column Name	**Data Type**	**Units**	**Description**
I10	Real*4	K_RJ km/sec	The CO(1-0) intensity map
E10	Real*4	K_RJ km/sec	Uncertainty in the CO(1-0) intensity
N10	Real*4	K_RJ km/sec	Map built from the half-ring difference maps
M10	Byte	none	Region over which the CO(1-0) intensity is considered reliable
I21	Real*4	K_RJ km/sec	The CO(2-1) intensity map
E21	Real*4	K_RJ km/sec	Uncertainty in the CO(2-1) intensity
N21	Real*4	K_RJ km/sec	Map built from the half-ring difference maps
M21	Byte	none	Region over which the CO(2-1) intensity is considered reliable
Keyword	**Data Type**	**Value**	**Description**
AST-COMP	String	CO-TYPE2	Astrophysical compoment name
PIXTYPE	String	HEALPIX	
COORDSYS	String	GALACTIC	Coordinate system
ORDERING	String	NESTED	Healpix ordering
NSIDE	Int	2048	Healpix Nside for LFI and HFI, respectively
FIRSTPIX	Int*4	0	First pixel number
LASTPIX	Int*4	50331647	Last pixel number, for LFI and HFI, respectively
CNV 1-0	Real*4	value	Factor to convert CO(1-0) intensity to Kcmb (units Kcmb/(Krj*km/s))
CNV 2-1	Real*4	value	Factor to convert CO(2-1) intensityto Kcmb (units Kcmb/(Krj*km/s))

Type-3 CO map file data structure

1. EXTNAME = 'COMP-MAP'			
Column Name	**Data Type**	**Units**	**Description**
INTEN	Real*4	K_RJ km/sec	The CO intensity map
ERR	Real*4	K_RJ km/sec	Uncertainty in the intensity
NUL	Real*4	K_RJ km/sec	Map built from the half-ring difference maps
MASK	Byte	none	Region over which the intensity is considered reliable
Keyword	**Data Type**	**Value**	**Description**
AST-COMP	String	CO-TYPE1	Astrophysical compoment name
PIXTYPE	String	HEALPIX	
COORDSYS	String	GALACTIC	Coordinate system
ORDERING	String	NESTED	Healpix ordering
NSIDE	Int	2048	Healpix Nside for LFI and HFI, respectively
FIRSTPIX	Int*4	0	First pixel number
LASTPIX	Int*4	50331647	Last pixel number, for LFI and HFI, respectively

CNV	Real*4	value	Factor to convert to Kcmb (units Kcmb/(Krj*km/s))

References

<biblio force=false>

1. References

</biblio>

References

[1] http://www.rssd.esa.int/doc_fetch.php?id=3168552&page=1

[2] http://www.rssd.esa.int/doc_fetch.php?id=3168406&page=1

[3] http://pla.esac.esa.int/pla/aio/product-action?MAP.MAP_ID=COM_CompMap_CMB-nilc_2048_R1.20.fits

[4] http://pla.esac.esa.int/pla/aio/product-action?MAP.MAP_ID=COM_CompMap_CMB-sevem_2048_R1.11.fits

[5] http://pla.esac.esa.int/pla/aio/product-action?MAP.MAP_ID=COM_CompMap_CMB-smica_2048_R1.20.fits

[6] http://pla.esac.esa.int/pla/aio/metadata-action?RESOURCE_CLASS=FREQUENCY_MAP&SELECTED_FIELDS=MAP.MAP_ID,MAP.SIZE,MAP_PERIOD.NAME,INSTRUMENT.NAME&INSTRUMENT.NAME=LFI&FREQUENCY.VALUE=30&MAP_PERIOD.NAME=Nominal&FREQUENCY_MAP.RING_HALF=&FREQUENCY_MAP.ZODI_CORR=&RELEASE.NAME=PR1&RETURN_TYPE=HTML

[7] http://pla.esac.esa.int/pla/aio/metadata-action?RESOURCE_CLASS=FREQUENCY_MAP&SELECTED_FIELDS=MAP.MAP_ID,MAP.SIZE,MAP_PERIOD.NAME,INSTRUMENT.NAME&INSTRUMENT.NAME=LFI&FREQUENCY.VALUE=44&MAP_PERIOD.NAME=Nominal&FREQUENCY_MAP.RING_HALF=&FREQUENCY_MAP.ZODI_CORR=&RELEASE.NAME=PR1&RETURN_TYPE=HTML

[8] http://pla.esac.esa.int/pla/aio/metadata-action?RESOURCE_CLASS=FREQUENCY_MAP&SELECTED_FIELDS=MAP.MAP_ID,MAP.SIZE,MAP_PERIOD.NAME,INSTRUMENT.NAME&INSTRUMENT.NAME=LFI&FREQUENCY.VALUE=70&MAP_PERIOD.NAME=Nominal&FREQUENCY_MAP.RING_HALF=&FREQUENCY_MAP.ZODI_CORR=&RELEASE.NAME=PR1&RETURN_TYPE=HTML

[9] http://pla.esac.esa.int/pla/aio/metadata-action?RESOURCE_CLASS=FREQUENCY_MAP&SELECTED_FIELDS=MAP.MAP_ID,MAP.SIZE,MAP_PERIOD.NAME,INSTRUMENT.NAME&INSTRUMENT.NAME=HFI&FREQUENCY.VALUE=100&MAP_PERIOD.NAME=Nominal&FREQUENCY_MAP.RING_HALF=&FREQUENCY_MAP.ZODI_CORR='false'&RELEASE.NAME=PR1&RETURN_TYPE=HTML

[10] http://pla.esac.esa.int/pla/aio/metadata-action?RESOURCE_CLASS=FREQUENCY_MAP&SELECTED_FIELDS=MAP.MAP_ID,MAP.SIZE,MAP_PERIOD.NAME,INSTRUMENT.NAME&INSTRUMENT.NAME=HFI&FREQUENCY.VALUE=143&MAP_PERIOD.NAME=Nominal&FREQUENCY_MAP.RING_HALF=&FREQUENCY_MAP.ZODI_CORR='false'&RELEASE.NAME=PR1&RETURN_TYPE=HTML

[11] http://pla.esac.esa.int/pla/aio/metadata-action?RESOURCE_CLASS=FREQUENCY_MAP&SELECTED_FIELDS=MAP.MAP_ID,MAP.SIZE,MAP_PERIOD.NAME,INSTRUMENT.NAME&INSTRUMENT.NAME=HFI&FREQUENCY.VALUE=217&MAP_PERIOD.NAME=Nominal&FREQUENCY_MAP.RING_HALF=&FREQUENCY_MAP.ZODI_CORR='false'&RELEASE.NAME=PR1&RETURN_TYPE=HTML

[12] http://pla.esac.esa.int/pla/aio/metadata-action?RESOURCE_CLASS=FREQUENCY_MAP&SELECTED_FIELDS=MAP.MAP_ID,MAP.SIZE,MAP_PERIOD.NAME,INSTRUMENT.NAME&INSTRUMENT.NAME=HFI&FREQUENCY.VALUE=353&MAP_PERIOD.NAME=Nominal&FREQUENCY_MAP.RING_HALF=&FREQUENCY_MAP.ZODI_CORR='false'&RELEASE.NAME=PR1&RETURN_TYPE=HTML

[13] http://pla.esac.esa.int/pla/aio/product-action?MAP.MAP_ID=COM_CompMap_Lfreqfor-commrul_0256_R1.00.fits

[14] http://pla.esac.esa.int/pla/aio/product-action?MAP.MAP_ID=COM_CompMap_Lfreqfor-commrul_2048_R1.00.fits

[15] http://pla.esac.esa.int/pla/aio/product-action?MAP.MAP_ID=COM_CompMap_dust-commrul_0256_R1.00.fits

[16] http://pla.esac.esa.int/pla/aio/product-action?MAP.MAP_ID=COM_CompMap_dust-commrul_2048_R1.00.fits

[17] http://pla.esac.esa.int/pla/aio/product-action?MAP.MAP_ID=COM_CompMap_Mask-rulerminimal_2048_R1.00.fits

CMB spectrum and likelihood code

General description

CMB spectra

The Planck best-fit CMB temperature power spectrum, shown in figure below, covers the wide range of multipoles $\ell = 2 - 2479$. Over the multipole range , the power spectrum is derived from a component-separation algorithm, Commander, applied to maps in the frequency range 30–353 GHz over 91% of the sky #planck2013-p06. The asymmetric error bars associated to this spectrum are the 68% confidence limits and include the uncertainties due to foreground subtraction. For multipoles greater than $\ell = 50$, instead, the spectrum is derived from the CamSpec likelihood #planck2013-p08 by optimally combining the spectra in the frequency range 100-217 GHz, and correcting them for unresolved foregrounds. Associated 1-sigma errors include beam and foreground uncertainties.

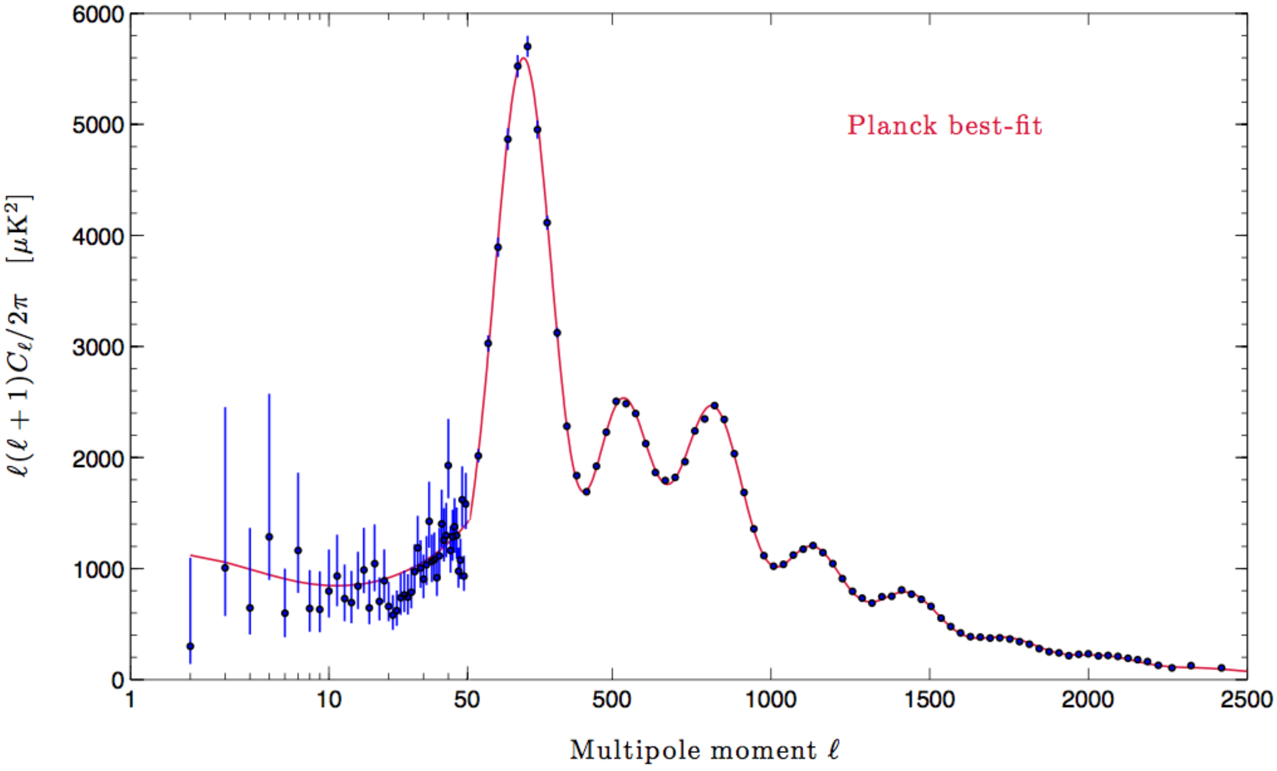

CMB spectrum. Logarithmic x-scale up to $\ell = 50$, linear at higher ℓ; all points with error bars. The red line is the Planck best-fit primordial power spectrum (cf Planck+WP+highL in Table 5 of #planck2013-p11).

Likelihood

The likelihood code and data allow to compute the likelihood of a model that predicts the CMB power spectra, lensing power spectrum and foreground and some instrumental parameters. The data file are built from the Planck mission results, as well as the some ancillary data from the wmap9 data release. The data file are in a specific internal format and can only be read by the code. The code consists in a c/f90 library, along with some optional tools in python. The code allows to read the data files, and provided model power spectra and nuisance parameters to compute the log likelihood of the model.

Detailed description of the installation and usage of the likelihood code and data is provided in the package.

The package includes 4 data packages. 3 for the CMB likelihoods and 1 for the lensing likelihood. All of the likelihood delivered are described full in the Power spectrum & Likelihood Paper #planck2013-p08 (for the CMB based likelihood) and in the Lensing Paper (for the lensing likelihood) #planck2013-p12.

The CMB full likelihood has been cut in 3 different part to allow using selectively different range of multipoles. It also reflects the fact that the mathematical approximation used for those different part are very different, as well as the underlying data. In details, we are distributing one low- ℓ Temperature only likelihood (commander), one low- ℓ Temperature and Polarisation likelihood (lowlike) and one higl- ℓ likelihood CAMspec.

The commander likelihood is covering the multipoles 2 to 49. It uses a semi-analytic method to sample the low- ℓ Temperature likelihood on an intermediate product of one of the component separated maps. The samples are used along with an analytical approximation of the likelihood posterior to do the likelihood computation in the code. See #planck2013-p08 section 8.1 for more details.

The lowlike likelihood is covering the multipole 2 to 32 for Temperature and Polarization data. Planck is not releasing any polarisation data in this release. We are using here the WMAP9 polarization map which are included in the data package. A temperature map is needed to perform the computation nevertheless, and we are using here the same commander map. The likelihood is computed using a map based approximation at low resolution and a master one at intermediate resolution, as in WMAP. The likelihood code actually calls a very slightly modified version of the WMAP9 code. This piece of the likelihood is essentially providing a prior on the optical depth and has almost no other impact on cosmological parameter estimation. As such it could be replaced by a simple prior, and user can decide to do so, which is one of the motivation to leave the three pieces of the CMB likelihood as different data packages. See #planck2013-p08 section 8.3 for more details.

The CAMspec likelihood is covering the multipoles 50 to 2500 for Temperature. The likelihood is computed using a quadratic approximation, including mode to mode correlations that have been precomputed on a fiducial model The likelihood uses data from the 100, 143 and 217Ghz channels. Doing so it must model the foreground in each of those frequency using a model described in the likelihood paper. Uncertainties on the relative calibration and on the beam transfer functions are included either as parametric models, or marginalized and integrated in the covariance matrix. Detailled description of the different nuisance parameter names and meaning is given below. Priors are included in the likelihood on the cib spectral index, relative calibration factors and beam error eigenmodes. See #planck2013-p08 section 2.1 for more details.

The lensing likelihood is covering the multipoles 40 to 400. It uses the result of the lensing reconstruction. It uses a quadratic approximation for the likelihood, with a covariance matrix including the marginalized contribution of the beam transfer function uncertainties, the diffuse point source correction uncertainties and the cosmological model uncertainty affecting the first order non-gaussian bias (N1). The correlation between Temperature and lensing one is not taken into account. Cosmological uncertainty effects on the normalization are dealt with using a first order renormalization procedure. This means that the code will need both the TT and $\phi\phi$ power spectrum up to ℓ =2048 to correctly perform the integrals needed for the renormalization. Nevertheless, the code will only produce an estimate based on the data between ℓ=40 to 400. See #planck2013-p12 section 6.1 for more details.

Production process

CMB spectra

The $\ell < 50$ part of the Planck power spectrum is derived from the Commander approach, which implements Bayesian component separation in pixel space, fitting a parametric model to the data by sampling the posterior distribution for the model parameters #planck2013-p06. The power spectrum at any multipole ℓ is given as the maximum probability point for the posterior C_ℓ distribution, marginalized over the other multipoles, and the error bars are 68% CL #planck2013-p08.

The ℓ > 50 part of the CMB temperature power spectrum has been derived by the CamSpec likelihood, a code that implements a pseudo-Cl based technique, extensively described in Sec. 2 and the Appendix of #planck2013-p08. Frequency spectra are computed as noise weighted averages of the cross-spectra between single detector and sets of detector maps. Mask and multipole range choices for each frequency spectrum are summarized in Table 4 of #planck2013-p08. The final power spectrum is an optimal combination of the 100, 143, 143x217 and 217 GHz spectra, corrected for the best-fit unresolved foregrounds and inter-frequency calibration factors, as derived from the full likelihood analysis (cf Planck+WP+highL in Table 5 of #planck2013-p11). A thorough description of the models of unresolved foregrounds is given in Sec. 3 of #planck2013-p08 and Sec. 4 of #planck2013-p11. The spectrum covariance matrix accounts for cosmic variance and noise contributions, together with unresolved foreground and beam uncertainties. Both spectrum and associated covariance matrix are given as uniformly weighted band averages in 74 bins.

Likelihood

The code is based upon some basic routine from the libpmc library in the cosmoPMC [1] code. It also uses some code from the WMAP9 likelihood [2] for the lowlike likelihood. It also includes codes from the ACT&SPT #dun2013,#Keis2011,#Reic2012 dun2013 [3], Keis2011 [4] Reic2012 [5] multifrequency likelihood that has been used by the planck collaboration in the Parameter paper. Data is not included and has to be downloaded here [6]. The other code has been specificly written for the Planck data.

Each of the likelihood file has been processed using a different and dedicated pipeline as described in the likelihood paper #planck2013-p08 (section 2 and 8) and in the lensing paper #planck2013-p12 (section 6.1). We refer the reader to those papers for full details.

The data is then encapsulated into the specific file format.

Each dataset comes with its own self check. Whenever the code is used to read a data file, a computation will be done against an included test spectrum/nuisance parameter, and the log-likelihood will be displayed along with the expected result. Difference of the order of 10 $^{-6}$or less are expected depending of the architecture.

Inputs

CMB spectra

Low-l spectrum ($\ell < 50$):

- frequency maps from 30–353 GHz;
- common mask #planck2013-p06;
- compact sources catalog.

High-l spectrum ($50 < \ell < 2500$):

- 100, 143, 143x217 and 217 GHz spectra and their covariance matrix (Sec. 2 in #planck2013-p08);
- best-fit foreground templates and inter-frequency calibration factors (Table 5 of #planck2013-p11);
- Beam transfer function uncertainties #planck2013-p03c;

Likelihood

commander : All Planck channels maps, compact source catalogs, common masks, beam transfer functions for all channels.

lowlike : WMAP9 likelihood data. Low-ell commander map.

CAMspec : 100,143 & 217Ghz detector and detests maps. 857GHz chanel Map. compact source catalog. Common masks (0,1 & 3). beam transfer function and error eigenmodes and covariance for 100,143 and 217Ghz detectors & detsets. Theoretical templates for the tSZ and kSZ contributions. Color corrections for the CIB emission for the 143Ghz and 217Ghz detectors & detsets. Fiducial CMB model (bootstrapped from WMAP7 best fit spectrum) estimated noise contribution from the half-ring maps for 100, 143 & 217Ghz.

lensing : the lensing map, beam error eigenmodes and covariance for the 143Ghz and 217Ghz chanel maps. Fiducial CMB model (from Planck cosmological parameter best fit).

File names and Meta data

CMB spectra

The CMB spectrum and its covariance matrix is distributed in a single FITS file named *COM_PowerSpect_CMB_R1.10.fits* which contains 3 extensions

LOW-ELL (BINTABLE)

with the low ell part of the spectrum, not binned, and for l=2-49. The table columns are

1. *ELL* (integer): multipole number
2. *D_ELL* (float): D_l as described below
3. *ERRUP* (float): the upward uncertainty
4. *ERRDOWN* (float): the downward uncertainty

HIGH-ELL (BINTABLE)

with the high-ell part of the spectrum, binned into 74 bins covering $\langle l \rangle = 47-2419$ in bins of width $l=31$ (with the exception of the last 4 bins that are wider). The table columns are as follows:

1. *ELL* (integer): mean multipole number of bin
2. *L_MIN* (integer): lowest multipole of bin
3. *L_MAX* (integer): highest multipole of bin
4. *D_ELL* (float): D_l as described below
5. *ERR* (float): the uncertainty

COV-MAT (IMAGE)

with the covariance matrix of the high-ell part of the spectrum in a 74x74 pixel image, i.e., covering the same bins as the *HIGH-ELL* table.

The spectra give $D_\ell = \ell(\ell+1)C_\ell / 2\pi$ in units of $\mu\, K^2$, and the covariance matrix is in units of $\mu\, K^4$. The spectra are shown in the figure below, in blue and red for the low- and high- ℓparts, respectively, and with the error bars for the high-ell part only in order to avoid confusion.

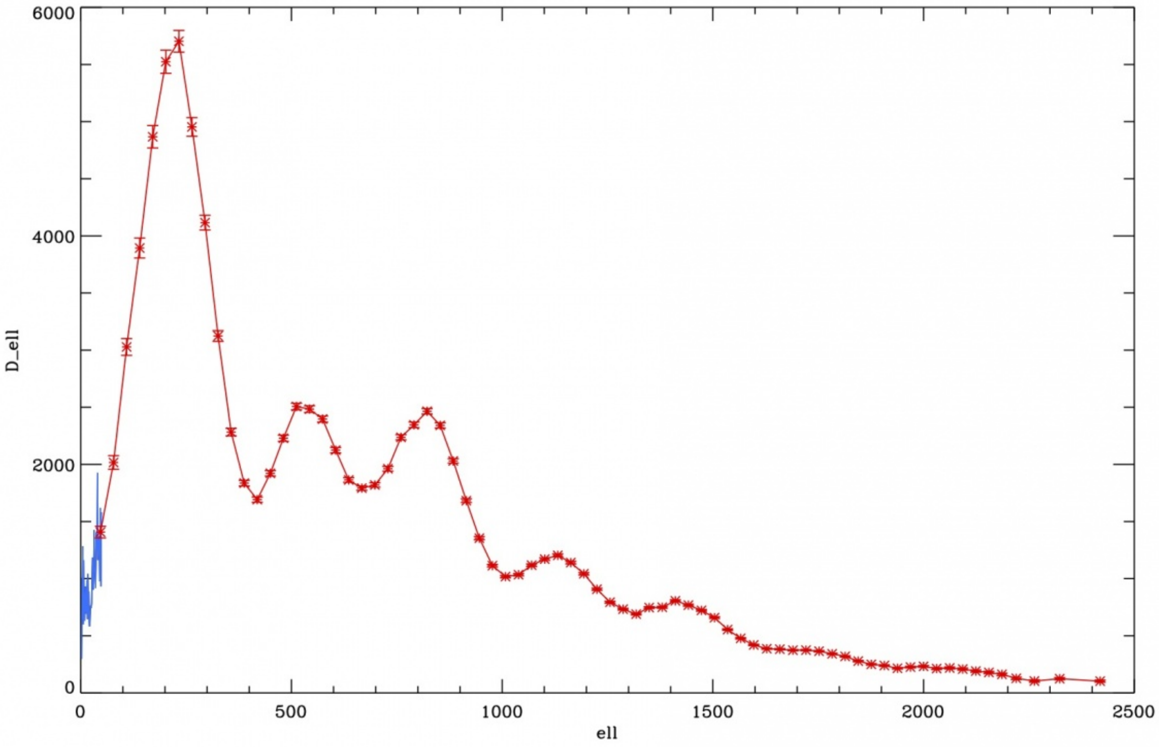

CMB spectrum. Linear x-scale; error bars only at high ℓ.

Likelihood

- source code:

```
* COM_Code_Likelihood-v1.0_R1.10.tar.gz [7] (C, f90 and python likelihood library and tools)
```

- data [8]

```
* COM_Data_Likelihood-commander_R1.10.tar.gz (low-ell TT likelihood)
* COM_Data_Likelihood-lowlike_R1.10.tar.gz (low-ell TE,EE,BB likelihood)
* COM_Data_Likelihood-CAMspec_R1.10.tar.gz (high-ell TT likelihood)
* COM_Data_Likelihood-lensing_R1.10.tar.gz (lensing likelihood)
```

Untar and unzip all files to recover the code and likelihood data. Each of the package comes with a README file describing the full package. Follow the instructions inclosed to build the code and use it. To compute the CMB likelihood one has to sum the log likelihood of each of the commander_v4.1_lm49.clik, lowlike_v222.clik and CAMspec_v6.2TN_2013_02_26.clik. To compute the CMB+lensing likelihood, one has to sum the log likelihood of all 4 files.

The CMB and lensing likelihood format are different. The CMB files have the termination .clik, the lensing one .clik_lensing. The lensing data being simpler (due to the less detailled modelling granted by the lower signal-noise) the file is a simple ascii file containing all the data along with comments describing it, and linking the different quantities to the lensing paper. The CMB file format is more complex and must accommodate different forms of data (maps, power spectrum, distribution samples, covariance matrices...). It consists into a tree structure containing the data. At each level of the tree structure a given directory can contain array data (in the form of fits files or ascii files for strings) and scalar data (joined in a single ascii file "_mdb"). Those files are not user modifiable and do not contain interesting meta data for the user.

Tools to manipulate those files are included in the code package as optional python tools. They are documented in the code package.

Retrieval from the Planck Legacy Archive

The Planck Legacy Archive can be accessed here:

http://www.sciops.esa.int/index.php?project=planck&page=Planck_Legacy_Archive

In order to retrieve the CMB spectra and likelihood files, one should select "Cosmology products" and look at the "CMB angular power spectra" and "Likelihood" sections. The files can be downloaded directly or through the "Shopping Basket".

References

<biblio force=false>

1. References

</biblio>

References

[1] http://arxiv.org/abs/1101.0950
[2] http://lambda.gsfc.nasa.gov/product/map/dr5/likelihood_get.cfm
[3] http://adsabs.harvard.edu/abs/2013arXiv1301.0776D
[4] http://adsabs.harvard.edu/abs/2011ApJ...743...28K
[5] http://adsabs.harvard.edu/abs/2012ApJ...755...70R
[6] http://lambda.gsfc.nasa.gov/product/act/act_fulllikelihood_get.cfm
[7] http://pla.esac.esa.int/pla/aio/product-action?COSMOLOGY.FILE_ID=COM_Code_Likelihood-v1.0_R1.10.tar.gz
[8] http://pla.esac.esa.int/pla/aio/metadata-action?RESOURCE_CLASS=COSMOLOGY&SELECTED_FIELDS=COSMOLOGY.FILE_ID,COSMOLOGY.SIZE&COSMOLOGY_TYPE.NAME=Likelihood&RELEASE.NAME=PR1&QUERY=%28COSMOLOGY.FILE_ID%20LIKE%20%27%25Data%25%27%29&RETURN_TYPE=HTML

Cosmological Parameters

Description

The cosmological parameter results explore a variety of cosmological models with combinations of Planck and other data. We provide results from MCMC exploration chains, as well as best fits, and sets of parameter tables. Definitions, conventions and reference are contained in #planck2013-p11.

Production process

Parameter chains are produced using CosmoMC, a sampling package available from [1]. This includes the sample analysis package GetDist, and the scripts for managing, analysing, and plotting results from the full grid or runs. Chain products provided here have had burn in removed. Some results with additional data are produced by importance sampling.

Note that the baseline model includes one massive neutrino (0.06eV). Grid outputs include WMAP 9 results for consistent assumptions.

Caveats and known issues

1. Confidence intervals are derived from the MCMC samples, and assume the input likelihoods are exactly correct, so there is no quantification for systematic errors other than via the covariance, foreground and beam error models assumed in the likelihood codes. We had some issues producing reliable results from the minimizer used to produce the best fits, so in some cases the quoted fits may be significantly improved. The chain outputs contain some parameters that are not used, for example the beam mode ranges for all but the first mode (the beam modes are marginalised over anlaytically internally to the likelihood).
2. Where determined from BBN consistency, the Y_P parameter uses an interpolation table from #Hamann2007sb based on the 2008 version of the Parthenope BBN code. More recent updates to the neutron lifetime suggest that the Y_P values reported in the tables may be in error by around 0.0005. This has a negligible impact on the predicted CMB power spectrum or any of the parameter results reported in this series of papers. However, the difference should be taken into account when comparing with BBN results reported in Sect. 6.4. of #planck2013-p11, which use an updated version for the neutron lifetime (and several other nuclear reaction rates that have negligible impact). Note also that the error on Y_P quoted in the tables here does not include theoretical errors in the BBN prediction.

Related products

Results of the parameter exploration runs should be reproducible using CosmoMC with the Planck likelihood code.

Parameter Tables

These list paramter constraints for each considered model and data combination separately

- PDF tables with 68% limits
- PDF tables with 95% limits

There are also summary comparison tables, showing how constraints for selected models vary with data used to constrain them:

- Comparison tables with 68% limits
- Comparison tables with 95% limits

Data combination tags used to label results are as follows (see #planck2013-p11 for full description and references):

Tag	Data
planck	high-L Planck temperature (CamSpec, 50 <= l <= 2500)
lowl	low-L: Planck temperature (2 <= l <= 49)
lensing	Planck lensing power spectrum reconstruction
lowLike	low-L WMAP 9 polarization (WP)
tauprior	A Gaussian prior on the optical depth, tau = 0.09 +- 0.013
BAO	Baryon oscillation data from DR7, DR9 and and 6DF
SNLS	Supernova data from the Supernova Legacy Survey
Union2	Supernova data from the Union compilation
HST	Hubble parameter constraint from HST (Riess et al)
WMAP	The full WMAP (temperature and polarization) 9 year data

Tags used to identify the model paramters that are varied are described in . Note that alpha1 results are not used in the parameter paper, and are separate from the isocurvature results in the inflation paper.

Parameter Chains

We provide the full chains and getdist outputs for our parameter results. The entire grid of results is available from as a 2.8GB compressed file:

- Full Grid Download [2]

You can also download key chains for the baseline LCDM model here:

- Planck+lensing [3]
- Planck+WP [4]
- Planck+WP+lensing [5]
- Planck+WP+highL [6]
- Planck+WP+highL+lensing [7]

The download contains a hierarchy of directories, with each separate chain in a separate directory. The structure for the directories is

base_AAA_BBB/XXX_YYY_.../

where AAA and BBB are any additional parameters that are varied in addition to the six parameters of the baseline model. XXX, YYY, etc encode the data combinations used. These follow the naming conventions described above under Parameter Tables. Each directory contains the main chains, 4-8 text files with one chain in each, and various other files all with names of the form

base_AAA_BBB_XXX_YYY.ext

where *ext* describes the type of file, and the possible values or *ext* are

Extension	Data
.txt	parameter chain file with burn in removed
.paramnames	File that describes the parameters included in the chains
.minimum	Best-fit parameter values, -log likelihoods and chi-square
.bestfit_cl	The best-fit temperature and polarization power spectra and lensing potential (see below)
.inputparams	Input parameters used when generating the chain
.minimum.inputparams	Input parameters used when generating the best fit
.ranges	prior ranges assumed for each parameter

In addition each directory contains any importanced sampled outputs with additional data. These have names of the form

base_AAA_BBB_XXX_YYY_post_ZZZ.ext

where ZZZ is the data likelihood that is added by importance sampling. Finally, each directory contains a *dist* subdirectory, containing results of chain analysis. File names follow the above convntions, with the following extensions

Extension	Data
.margestats	mean, variance and 68, 95 and 99% limits for each parameter (see below)
.likestats	parameters of best-fitting sample in the chain (generally different from the .minmum global best-fit)
.covmat	Covariance matrix for the MCMC parameters
.corr	Correlation matrix for the parameters
.converge	A summary of various convergence diagnostics

Python scripts for reading in chains and calculating new derived parameter constraints are available as part of CosmoMC, see the readme for details [8].

File formats

The file formats are standard March 2013 CosmoMC outputs. CosmoMC includes python scripts for generating tables, 1D, 2D and 3D plots using the provided data. The formats are summarised here:

Chain files

Each chain file is ASCII and contains one sample on each line. Each line is of the format

weight like param1 param2 param3 …

Here *weight* is the importance weight or multiplicity count, and *like* is the total -log Likelihood. *param1*,*param2*, etc are the parameter values for the sample, where the numbering is defined by the position in the accompanying.paramnames files.

Note that burn in has been removed from the cosmomc outputs, so full chains provided can be used for analysis. Importance sampled results (with *_post*) in the name have been thinned by a factor of 10 compared to the original chains, so the files are smaller, but this does not significantly affect the effective number of samples. Note that due to the way MCMC works, the samples in the chain outputs are not independent, but it is safe to use all the samples for estimating posterior averages.

.margestats files

Each row contains the marginalized constraint on individual parameters. The format is fairly self explanatory given the text description in the file, with each line of the form *parameter mean sddev lower1 upper1 limit1 lower2 upper2 limit2 lower3 upper3 limit3*

where sddev is the standard deviation, and the limits are 1: 68%, 2: 95%, 3: 99%. The limit tags specify whether a given limit is one tail, two tail or none (if no constraint within the assumed prior boundary).

.bestfit_cl files

They contain the best-fit theoretical power spectra (without foregrounds) for each model. The columns are: $l$, $D^{TT}_l$, $D^{TE}_l$, $D^{EE}_l$, $D^{BB}_l$, and $D^{dd}_l$, were $D_l \equiv l(l+1) C_l / (2\pi)$ in $\mu{\rm K}^2$. Also $D^{dd}_l= [l(l+1)]^2 C^{\phi\phi}_l/(2\pi)$ is the power spectrum of the lensing deflection angle, where $C^{\phi\phi}_l$ is the lensing potential power spectrum. For results not including the lensing likelihood, this is the prediction from linear theory; for lensing outputs this includes corrections due to non-linear structure growth. The $D_l$ are output to high $l$, but not actually computed above $l_{\rm max}=2500$ (Planck), $l_{\rm max}=4500$ (Planck+highL) or $l_{\rm max}=1500$ (WMAP), and $l$ values above these are fixed to a scaled fiducial template.

References

<biblio force=false>

1. References

</biblio>

References

[1] http://cosmologist.info/cosmomc

[2] http://pla.esac.esa.int/pla/aio/product-action?COSMOLOGY.FILE_ID=COM_CosmoParams_FullGrid_R1.10.tar.gz

[3] http://pla.esac.esa.int/pla/aio/product-action?COSMOLOGY.FILE_ID=COM_CosmoParams_base_planck_lowl_post_lensing_R1.10.tar.gz

[4] http://pla.esac.esa.int/pla/aio/product-action?COSMOLOGY.FILE_ID=COM_CosmoParams_base_planck_lowl_lowLike_R1.10.tar.gz

[5] http://pla.esac.esa.int/pla/aio/product-action?COSMOLOGY.FILE_ID=COM_CosmoParams_base_planck_lowl_lowLike_post_lensing_R1.10.tar.gz

[6] http://pla.esac.esa.int/pla/aio/product-action?COSMOLOGY.FILE_ID=COM_CosmoParams_base_planck_lowl_lowLike_highL_R1.10.tar.gz

[7] http://pla.esac.esa.int/pla/aio/product-action?COSMOLOGY.FILE_ID=COM_CosmoParams_base_planck_lowl_lowLike_highL_post_lensing_R1.10.tar.gz

[8] http://cosmologist.info/cosmomc/readme_planck.html

Additional maps

Overview

This section describes products that require special processing. Only one such product is available at this time; this section will be expanded with time as more products are added.

Lensing map

Description

Here we present the minimum-variance (MV) lens reconstruction which forms the basis for the main results of #planck2013-p12. This map is produced using a combination of the 143 and 217 GHz Planck maps on approximately 70% of the sky, and is the same map on which the Planck lensing likelihood is based.

We distribute:

PHIBAR

A (transfer-function convolved) map of the lensing potential, in NSIDE 2048 HEALPix RING format. It is obtained by convolving the lensing potential estimate $\hat{\phi}$ with the lensing response function $R_L^{\phi\phi}$. This map has been band-limited between multipoles $10 \le L \le 2048$.

MASK

This is a NSIDE = 2048 HEALPix map, containing the analysis mask used in the lens reconstruction. *Note*: the lensing map PHIBAR may take small but non-zero values inside the masked regions because it has been bandlimited.

RLPP

This column contains the response function $R_L^{\phi\phi}$.

NLPP

This column contains a sky-averaged estimate of the noise power spectrum of PHIBAR, $N_L^{\phi\phi}$. The noise is highly coloured. There is a dependence of the noise power spectrum on the local noise level of the map, discussed in Appendix A of #planck2013-p12. Note that the noise power spectrum estimate here is not sufficiently accurate for a power spectrum analysis.

Production process

The construction PHIBAR, RLPP and NLPP are described in detail in Sec. 2.1 of #planck2013-p12. The response function $R_L^{\phi\phi}$ here is analogous to the the beam transfer function in a CMB temperature or polarization map. We have chosen to distribute this transfer-function convolved map rather than the normalized lens reconstruction as it is a significantly more localized function of the CMB temperature map from which it is derived, and therefore more useful for cross-correlation studies.

Inputs

This product is built from the 143 and 217 GHz Planck frequency maps, with 857GHz projected out as a dust template. The analysis mask is constructed from a combination of thresholding in the 857GHz map (to remove the regions which are most contaminated by Galactic dust) and the Type2 CO map (to reduce contamination from CO lines at 217GHz). This is joined with a compact object mask synthesized from several Planck source catalogues, including the ERCSC, SZ and PCCS . The reconstruction was performed using the fiducial beam window functions B(l) from the HFI RIMO . Details of the procedure used to produce a lensing estimate from these inputs are given in

#planck2013-p12.

File names and format

A single file named

- *COM_CompMap_Lensing_2048_R1.10.fits* [1]

with two BINTABLE extensions containing the items described below.

For illustration, we show in the figures below the maps of the Wiener-filtered CMB lensing potential in Galactic coordinates using orthographic projection. The reconstruction was bandpass filtered to $L \in [10, 2048]$. Note that the lensing reconstruction, while highly statistically significant, is still noise dominated for every individual mode, and is at best $S/N \simeq 0.7$around $L = 30$.

FITS file structure

1. EXTNAME = *LENS-MAP*			
Column Name	**Data Type**	**Units**	**Description**
PHIBAR	Real*4	none	Map of the lensing potential estimate, convolved with RLPP
MASK	Int	none	Region over which the lensing potential is reconstructed
Keyword	**Data Type**	**Value**	**Description**
PIXTYPE	string	HEALPIX	
COORDSYS	string	GALACTIC	Coordinate system
ORDERING	string	NESTED	Healpix ordering
NSIDE	Int*4	2048	Healpix Nside
FIRSTPIX	Int*4	0	
LASTPIX	Int*4	50331647	
2. EXTNAME = *TransFun*			
Column Name	**Data Type**	**Units**	**Description**
RLPP	Real*4	none	Response function
NLPP	Real*4	none	Sky-averaged noise power spectrum estimate
Keyword	**Data Type**	**Value**	**Description**
L_MIN	Int*4	0	First multipole
L_MAX	Int*4	2048	Last multipole

References

<biblio force=false>

1. References

</biblio>

References

[1] http://pla.esac.esa.int/pla/aio/product-action?MAP.MAP_ID=COM_CompMap_Lensing_2048_R1.10.fits

Scientific data used to generate Planck products

This section was intentionally left empty. It will be filled in future releases of the PLA if specially processed external datasets are required in the production of Planck products.

Simulation data

This page is preliminary. It describes products that are not yet available and will be updated as necessary when these products are delivered.

Introduction

The 2013 Planck data release is supported by a comprehensive set of simulated maps, including both a fiducial realization of the sky as seen by Planck and 1000-realization Monte Carlo (MC) sets of CMB and noise simulations, collectively known as FFP6.

The simulation process consists of

- modeling the sky using pre-Planck data and generating an input sky map for each sky component for each detector that incorporates our best estimate of that detector's band-pass
- simulating each detector's observation of each input sky component, following the Planck scanning strategy and using our best estimates of the detector's beam and noise properties, and mapping the results.
- generating Monte Carlo realizations of the CMB and noise maps, again following the Planck scanning strategy and using our best estimates of the detector beams and noise properties respectively.

The first step is done by the *Planck Sky Model* (PSM), and the second and third by a suite of *Planck Simulation Tools* (PST). A brief description of these is given below.

The Planck Sky Model

The Planck Sky Model, a complete set data and code to simulate sky emission at millimeter-wave frequencies, is described in detail in the pre-launch PSM paper [1] (Delabrouille et al., arXiv/1207.3675).

The main simulations used to test and validate the Planck data analysis pipelines (and, in particular, component separation) makes use of simulations generated with version 1.7.7 of the PSM software. Sky emission comprises the following components: CMB, thermal dust, spinning dust, synchrotron, CO lines, free-free, thermal Sunyaev-Zel'dovich (SZ) effect (with first order relativistic corrections), kinetic SZ effect, radio and infrared sources, Cosmic Infrared Background (CIB).

The CMB is a based on adiabatic initial perturbations, with the following cosmological parameters:

- T_CMB = 2.725
- H = 0.684
- OMEGA_M = 0.292
- OMEGA_B = 0.04724
- OMEGA_NU = 0
- OMEGA_K = 0
- SIGMA_8 = 0.789
- N_S = 0.9732
- N_S_RUNNING = 0

- N_T = 0
- R = 0.0844
- TAU_REION = 0.085
- HE_FRACTION = 0.245
- N_MASSLESS_NU = 3.04
- N_MASSIVE_NU = 0
- W_DARK_ENERGY = -1
- K_PIVOT = 0.002
- SCALAR_AMPLITUDE = 2.441e-9

All other parameters are set to the default standard of the Jan 2012 version of CAMB. In addition, this simulated CMB contains non-Gaussian corrections of the local type, with an f_NL parameter of 20.4075.

The Galactic ISM emission comprises 5 major components: Thermal dust, spinning dust, synchrotron, CO lines, and free-free emission. We refer the reader to the PSM publication for details. For the simulations generated here, however, the thermal dust model has been modified in the following way: Instead of being based on the 100 micron map of Schlegel, Finkbeiner and Davis (SFD; 1998), the dust template uses an internal release of the 857 GHz Planck observed map itself, in which point sources have been subtracted, and which has been locally filtered to remove CIB fluctuations in the regions of lowest column density. A caveat is that while this reduces the level of CIB fluctuations in the dust map in some of the regions, in regions of moderate dust column density the CIB contamination is actually somewhat larger than in the SFD map (by reason of different emission laws for dust and CIB, and of the highr resolution of the Planck map).

The other emissions of the galactic ISM are simulated using the prescription described in the PSM paper. Synchrotron, Free-free and spinning dust emission are based on WMAP observations, as analyzed by Miville-Deschenes et al., 2008. Small scale fluctuations have been added to increase the variance on small scales and compensate the lower resolution of WMAP as compared to Planck (in particular HFI channels). The main limitation of these maps is the presence at high galactic latitude of fluctuations that may be imputable to WMAP noise. The presence of noise and of added Gaussian fluctuations on small scales may result in a few occasional pixels being negative (e.g. in the spinning dust maps). Low frequency foreground maps are also contaminated by some residuals of bright radio sources that have not been properly subtracted from the templates of diffuse emission.

The CO maps are simulated using the CO J=1-0 observations of Dame et al. (2001). The main limitations are limited sky coverage, lower resolution than that of Planck high frequency channels, line ratios (J=2-1)/(J=1-0) and (J=3-2)/(J=2-1) constant over the sky. The CO in the simulation is limited to the three lowest 12CO lines.

Galaxy clusters are generated on the basis of cluster number counts, following the Tinker et al. (2008) mass function, for the cosmological parameters listed above. Clusters are assumed perfectly spherical, isothermal, and are modeled using the universal pressure profile of Arnaud et al. (2010). Relativistic corrections following Itoh et al. (1998) are included to first order. The simulated kinetic SZ effect assumes no bulk flow, and a redshift-dependent average cluster velocity compatible with the linear growth of structures.

Point sources comprise radio sources (based on extrapolations across frequencies of radio observations between 800 MHz and 5 GHz) and infrared sources (based on extrapolations in frequencies of IRAS sources). One small caveat that should be mentioned is that because of the unevenness of the radio source surveys, the equatorial southern part of the sky has less faint radio sources than the northern part. Although all the missing sources are well below the Planck detection level, this induces a small variation of the total emission background over the sky. Check the individual faint point source emission maps if this is a potential problem for your applications. See also the PSM publication for details about the PSM point source simulations.

Finally, the far infrared background due to high redshift galaxies has been simulated using a procedure is based on the distribution of galaxies in shells of density contrast at various redshifts (Castex et al., PhD thesis; paper in preparation). This simulation has been modified by gradually substituting an uncorrelated extra term of CIB emission at low frequencies, artificially added in particular to decorrelate the CIB at frequencies below 217 GHz from the CIB above that frequency, to mimic the apparent decorrelation observed in the Planck Early Paper on CIB power spectrum.

While the PSM simulations described here provide a reasonably representative multi-component model of sky emission, the users are warned that it has been put together mostly on the basis of data sets and knowledge pre-existing the Planck observations themselves. While it is sophisticated enough to include variations of emission laws of major components of ISM emission, different emission laws for most sources, and a reasonably coherent global picture, it is not (and is not supposed to be) identical to the real sky emission. The users are warned to use these simulations with caution.

The Planck Simulation Tools

Since the full focal plane (FFP) simulations

- involve both HFI and LFI data
- include large, computationally challenging, MC realization sets

they cannot be generated using either DPC's single-instrument cluster-based pipeline. Instead the PST consists of three distinct tool chains, each designed to run on the largest available supercomputers, that are used to generate the fiducial sky realization, the CMB MC, and the noise MC respectively. FFP6 was primarily generated on the Hopper and Edison systems at NERSC [2], with some of the LFI noise MCs generated on the Louhi system at CSC [3].

While FFP6 is guaranteed to be internally self-consistent there are a number of differences with the real data that should be borne in mind, although all tests performed to date indicate that these are statistically insignificant:

- FFP6 includes our best measurements of the detector band-passes, main beams and noise power spectral densities - known issues include the absence of side-lobes and the use of a single, independent, noise spectrum per detector for the entire mission.
- FFP6 excludes all pre-processing residuals, assuming perfect calibration, transfer function deconvolution and deglitching.
- FFP6 uses the HFI pointing solution for the LFI frequencies, rather than the DPC's two focal plane model.
- FFP6 uses a different map-maker to HFI, and as a consequence implements very slightly different data cuts - primarily at ring boundaries - resulting in marginally different hit-maps.

Fiducial Sky

For each detector, fiducial sky time-ordered data are generated separately for each of its 10 PSM component maps and its strong point source catalogue using the LevelS software #reinecke2006 as follows:

- The detector's beam and PSM map are converted to spherical harmonics using *beam2alm* and *anafast* respectively.
- The beam-convolved map value is calculated over a 3-dimensional grid of sky locations and beam orientations using *conviqt*.
- The map-based time-ordered data are calculated sample-by-sample by interpolating over this grid using "multimod".
- The catalogue-based time-ordered data are calculated sample-by-sample by beam-convolving any point source laying within a given angular distance of the pointing at each sample time using *multimod*.

For each frequency, fiducial sky maps are generated for

- the total sky (including noise),
- the foreground sky (excluding CMB but including noise),
- the point source sky, and

- the noise alone

All maps are made using the *MADAM* destriping map-maker #[keihanen2010 interfaced with the *TOAST* data abstraction layer . In order to construct the total time-ordered data required by each map, for each detector *TOAST* reads the various component time-streams separately and sums then, and, where necessary, simulates and adds a noise realization time-stream on the fly.

HFI frequencies are mapped at *HEALPix* resolution nside=2048 using ring-length destriping baselines, while LFI frequencies are mapped at nside=1024 using 1s baselines.

CMB Monte Carlo

The CMB MC set is generated using *FEBeCoP* #mitra2010, which generates an effective beam for each pixel in a map at each frequency by accumulating the weights of all pixels within a fixed distance of that pixel, summed over all observations by all detectors at that frequency. It then applies this effective beam pixel-by-pixel to each of 1000 input CMB sky realizations.

Noise Monte Carlo

The noise MC set is generated just as the fiducial noise maps, using *MADAM/TOAST*. In order to avoid spurious correlations within and between the 1000 realizations, each stationary interval for each detector for each realization is generated from a distinct sub-sequence of a single statistically robust, extremely long period, pseudo-random number sequence.

Products delivered

This section was intentionally left blank; to be updated when the products are delivered.

References

<biblio force=false>

1. References

</biblio>

References

[1] http://adsabs.harvard.edu/abs/2012arXiv1207.3675D
[2] http://www.nersc.gov
[3] http://www.csc.fi/english

Software utilities

Software utilities

This chapter contains information about auxiliary software products extensively used by the two DPCs and available for download from the PLA.

Unit conversion and Color correction

Unit conversion and colour correction

The unit conversion and colour correction software (UC_CC) consists of a set of IDL procedures and functions that read the band transmission from the DPC RIMOs and perform the requested conversions. The package is delivered as a tarfile and contains a detailed instruction manual. The data and software file requirements are provided below along with basic use instructions and some simple examples. The full list of its contents is:

```
UC_CC_v102/get_hfibolo_list.pro
UC_CC_v102/hfi_co_correction.pro
UC_CC_v102/hfi_colour_correction.pro
UC_CC_v102/hfi_lfi_test_script.pro
UC_CC_v102/hfi_lfi_test_script_PLA_RIMO.pro
UC_CC_v102/hfi_read_avg_bandpass.pro
UC_CC_v102/hfi_read_bandpass.pro
UC_CC_v102/hfi_unit_conversion.pro
UC_CC_v102/lfi_read_avg_bandpass.pro
UC_CC_v102/lfi_read_bandpass.pro
UC_CC_v102/LFI_fastcc.pro
UC_CC_v102/LFI_fastcc_test.pro
UC_CC_v102/README.txt
UC_CC_v102/Instructions.pdf
```

The package is currently available on [[1]]

Relevant documentation

Please refer to the Spectral Response sections of the Explanatory Supplement (i.e. 2.2.1.2, 4.4.5, and 4.6), as well as the Spectral Response Paper #planck2013-p03d for details of the derivation of the detector spectra and band-average spectra included in the RIMO files, as well as additional details on the unit conversion and colour correction methodology, philosophy, and implementation. This section concentrates on the use of the provided UC_CC software itself, leaving the other sections to provide the basis for it.

Tarfile distribution package

This section provides a brief explanation of each file included in the UC_CC distribution.

1. `get_hfibolo_list.pro`: used to provide basic detector information (i.e. names) within subsequent routines.
2. `hfi_read_bandpass.pro`: a routine to get the desired detector level spectral transmission data (HFI) and output in a structure format used by the other routines.
3. `hfi_read_avg_bandpass.pro`: a routine to get the desired HFI band-average spectral transmission data and output in a structure format used by the other routines.
4. `hfi_unit_conversion.pro`: a routine that accepts spectral response information and outputs unit conversion coefficients.
5. `hfi_colour_correction.pro`: a routine that accepts spectral response information and outputs colour correction coefficients.
6. `hfi_co_correction.pro`: a routine that accepts spectral response information and outputs CO conversion coefficients.
7. `lfi_read_bandpass.pro`: a routine to get the desired detector level spectral transmission data (LFI) and output in a structure format used by the other routines.
8. `lfi_read_avg_bandpass.pro`: a routine to get the desired LFI band-average spectral transmission data and output in a structure format used by the other routines.
9. `hfi_lfi_test_script.pro`: a sample script providing examples of calling the various routines.
10. `hfi_lfi_test_script_PLA_RIMO.pro`: a sample script providing examples of calling the various routines using the PLA RIMO file (without detector-level spectra).
11. `LFI_fastcc.pro`: a routine to calculate LFI colour corrections using quadratic approximations (faster than integrating each time).
12. `LFI_fastcc_test.pro`: a sample script providing examples of calling the LFI_fastcc routine.
13. `README.txt`: a text file providing basic instructions and expected output for the hfi_lfi_test_script.pro file (basic introduction and precursor to this document).

Required input data

The UC_CC routines require access to the Planck spectral response data. This is nominally provided in the RIMO files included in the same location as this package. The ingestion routines are written in such a way as to accept updated RIMO files (provided the `.fits` header structure uses the same naming conventions as currently / previously implemented). For users with access to the HFI databases on magique3 (i.e. members of the HFI Core-team), the software is also able to access the spectral response data directly from the HFI IMO (see examples below for details). The software is written to allow use of the PLA RIMO file which includes only band-average spectra, as well as the full RIMO (with detector level spectra) which will be made available through the PLA in a future release.

A user may provide a unique model spectrum about which to generate colour correction coefficients specific to the model input (see §2.6.5), however this is not required for standard colour correction coefficients based on power-law spectral indices and/or modified blackbody spectra.

Required software packages

This software has been tested on IDL versions 6.4, 7.1, 8.0, 8.1, and 8.2. It requires use of the `mrdfits.pro` file, and related sub-routines, from *the IDL Astronomy User's Library* to read the RIMO `.fits` files. This library should be included with most IDL Healpix distributions, and is otherwise freely available online (http://idlastro.gsfc.nasa.gov/). The UC_CC routines will not work with the RIMO `.fits` files without routines from this library! The routines provided will work with either the full (internal) RIMO files containing detector level spectra, or the PLA (external) RIMO files with only frequency-band level spectra. To date the software has not been tested on the PLA RIMO files (this should change soon, and needs to prior to the data release).

Software initialization

No installation is required. It is recommended to add the UC_CC scripts to a directory within your IDL path, or add the UC_CC directory to your IDL path. As some of the UC_CC files contain multiple functions/procedures, it is also recommended to compile each of the UC_CC `.pro` files prior to running scripts using the respective routines; `get_hfibolo_list.pro` should be compiled before any of the other routines.

Software use

The following section outlines basic use of the UC_CC IDL scripts and provides examples.

Spectral input

The UC_CC routines accept individual detector and band-average spectra structures as input. The `hfi_read_bandpass.pro` and `hfi_read_avg_bandpass.pro` routines are used to obtain this data for HFI, and the `lfi_read_bandpass.pro` and `lfi_read_avg_bandpass.pro` routines are used to obtain this data for LFI. The spectra can be restored from either a RIMO file, or an IMO database (if access to such is available). The routines return the transmission spectra by default, but are also configured to return the spectral uncertainty and interpolation flag as additional output parameters. Here are some example IDL commands using these routines:

```
hfi_bp = hfi_read_bandpass(/RIMO, PATH_RIMO='/path/to/RIMO/file/', $

         NAME_RIMO='Name_of_RIMO_file.fits', FLG_INFO=flg, ER_INFO=er, /FLAG)
hfi_bp_withCO = hfi_read_bandpass(/RIMO, PATH_RIMO='/path/to/file', $

         NAME_RIMO='Name_of_RIMO_file.fits', FLG_INFO=flg_withCO, $

         ER_INFO=er_withCO, FLAG = 0)
hfi_avg = hfi_read_avg_bandpass(/RIMO, PATH_RIMO='/path/to/RIMO/file/', $

         NAME_RIMO='Name_of_RIMO_file.fits', FLG_INFO=flg_avg, ER_INFO=er_avg, /FLAG)
hfi_avg_withCO = hfi_read_avg_bandpass(/RIMO, PATH_RIMO='/path/to/file', $

         NAME_RIMO='Name_of_RIMO_file.fits', FLG_INFO=flg_avg_withCO, $

         ER_INFO=er_avg_withCO, FLAG = 0)
lfi_bp = lfi_read_bandpass(/RIMO, PATH_RIMO='/path/to/RIMO/file/', $

         NAME_RIMO='Name_of_LFI_RIMO_file.fits', ER_INFO=er)
lfi_avg = lfi_read_avg_bandpass(/RIMO, PATH_RIMO='/path/to/RIMO/file/', $

         NAME_RIMO='Name_of_LFI_RIMO_file.fits', ER_INFO=er_avg)
```

In the above examples, `hfi_bp`, `hfi_bp_withCO`, and `lfi_bp` represent IDL structures containing individual detector spectra. The variables `er` and `er_avg` containt the spectral uncertainty within a structure similar to that of the spectra. The `flg` and `flg_avg` structures contain the CO interpolation flag indiciating if a spectral data point is uniquely measured from the calibration data (i.e. `flg[i] = 0`), or interpolated (i.e. `flg[i] = 1`, see Ex. Supp. for more details). No such flag exists for LFI. If the `FLAG` keyword is set, flagged data points are removed from the spectral structures prior to being output; i.e. `FLAG=0` outputs all data and `FLAG=1` outputs only un-flagged data points, the default setting if FLAG is not input is the `FLAG=1` setting. With the `RIMO` keyword set, there must be a `RIMO.fits` file in the `PATH_RIMO` directory of the `NAME_RIMO` keyword value. The routines may also get the spectra from an IMO database (this requires the user to have access to an IMO data base with details available within the Planck collaboration).

The output of the ...read_bandpass.pro routines is an array of IDL structures. The other UC_CC routines are written in such a way as to accept these structures as input. The software has been modularized such that the subroutines within the scripts can accept input spectra in other formats. This level of use of the UC_CC routines is beyond this introduction, however. Those interested are directed to look through the original source code of the subroutines, paying particular attention to the subroutines without the hfi_ prefix within each script; these routines may be called externally. Further queries may be directed towards the authors (esp. Spencer).

The LFI RIMO files follow a different convention than that of HFI, so the ingestion routine also accounts for this. The LFI RIMO file frequency bins represent the bin start frequency rather than the bin centre frequency, and the convention is such that the transmission data need to be scaled by $\lambda^2$to be consistent with the HFI spectra. Both of these modifications are performed within the `lfi_read_bandpass` and `lfi_read_avg bandpass` routines, so their output structures are in the format expected by the remaining UC_CC routines.

The UC_CC routines follow HFI unit conversion and colour correction conventions, and have been developed primarily for use with HFI data processing. Functionality has also been included for the LFI spectra. The UC_CC routines LFI output has been verified against internal LFI coefficients for the combined case of K$_{\mathrm{CMB}}$to T$_{\mathrm{b}}$unit conversion and colour correction for spectral indices ranging from $-2$to $+4$. This validation confirmed that the UC_CC code treats the LFI spectra in the same way as in other LFI data processing, and thus all of the UC_CC LFI output is expected to conform with official LFI data processing.

UC_CC output

The UC_CC routines output conversion coefficients as arrays of IDL structures. This ensures that the detector name and coefficient are paired, and any additional information may also be provided, e.g. the CO rotational transition line in the case of a CO coefficient. It is important to note that the output for the 143-8 and 545-3 detector coefficients is intentionally set to -10^9in all cases. These two detectors have been excluded from HFI data processing due to their noise characteristics, and thus do not contribute to the band-average spectra or band-average coefficients. Ground measurements for these detectors do exist, and it is possible to determine these coefficients if needed, but they have been intentionally hidden from standard use.

Coefficient uncertainty estimate

An optional function of this software is to output an uncertainty for every unit conversion and colour correction coefficient determined. This requires spectral uncertainty as input (HFI only at present), and has uncertainty of other parameters as optional depending on the colour correction (e.g. CO radial velocity, dust temperature or emissivity, spectral index uncertainty, user-supplied spectral profile uncertainty (see §6.5), etc.). The GETERR keyword instructs the routines to calculate the coefficient uncertainty via NITER (another keyword) iterations of a Monte-Carlo uncertainty simulation. This requires the BP_ERR keyword to be set to the detector uncertainty (output from the hfi_read_bandpass routine), and/or the band-average spectral uncertainty to be set via the EABP (Error in Average Band-Pass) keyword (output from the hfi_read_avg_bandpass routine). Please refer to the test scripts for details on how these routine calls are performed. In principle it is possible to determine uncertainties for the LFI colour corrections, based on errors in the spectral index, dust temperature, etc. without spectral uncertainty; this is beyond the scope of this introduction and is left as an exercise (contact the authors for assistance if needed). The colour correction routine accepts various error keywords for use in the GETERR uncertainty estimate. These include ER_ALPHA, ER_TBD, ER_BETABD, ER_INU, associated with the ALPHA, TBD, BETABD, and INU input keywords. The default setting is zero to allow the uncertainty estimate to be strictly based on the spectral uncertainty. If any of the additional error keywords are set, then this additional uncertainty is combined with the spectral uncertainty in the simulation run. The defualt number of itereations is 2. Obviously this will not provide an accurate estimate, but not task processing time if accidentally set. The example routines use 100 iterations. Published uncertainty results typically use 10000 iterations (but this obviously takes longer to compute).

Unit conversion

The hfi_unit_conversion.pro routine will yield a structure of unit conversion coefficients for the provided spectral input, on a frequency channel and individual detector level for both LFI and HFI. It accepts an IDL structure containing individual detector spectra as input. It also accepts a band-average structure array as an additional keyword input, and outputs coefficients derived from the provided detector average spectrum. If this ABP optional keyword input is not provided, then the optional AVG_UC keyword output is not returned, and the main output returned by the function is set to zero (the individual bolometer coefficients are still returned via the keyword outputs).

```
hfi_100_uc = hfi_unit_conversion(BP_INFO=hfi_bp, '100',hfibolo_100_uc, $


         ABP=hfi_avg, AVG_UC=AVG_100_UC, CH_UC=ch_100_uc)
```

```
help, hfibolo_100_uc, /STRUCT ; Displays details of the structure contents.
uc_KCMB2MJy_100_1a = hfibolo_100_uc[0].KCMB2MJYSR
uc_KCMB2YSZ_100_2b = hfibolo_100_uc[3].KCMB2YSZ
uc_MJY2TB_100_avg = avg_100_uc.MJY2TB
lfi_44_uc = hfi_unit_conversion(BP_INFO=lfi_bp, '44', lfibolo_44_uc, $
```

```
         /lfi, ABP=lfi_avg, AVG_UC=AVG_44_UC)
```

In the above expressions, both the `hfi_100_uc` and `avg_100_uc` variables contain the coefficients determined using the band-average spectrum, and the `ch_100_uc` variable contains the average of the individual detector coefficients; these two variable sets may be similar but are not expected to be identical. The hfibolo_100_uc variable contains the individual detector values. The UC_CC unit conversion script accepts both LFI and HFI spectra in the format output by the corresponding read_..._bandpass routine. Details of the unit conversion equations are available in planck2013-p03d.

Colour correction

The colour correction routine works in much the same way as the unit conversion. It requires individual detector spectra as input, and band-average spectral input is optional, with the same caveats as above (§2.8). The colour correction routine has three distinct modes of operation. The first mode is a powerlaw spectral index where the output is a multiplicative coefficient for conversion *from* a spectral index of -1 *to* a user-supplied spectral index, α. The second is a modified blackbody where the conversion is *from* a -1spectral index *to* a Planck function of temperature, T, and emissivity $\propto \nu^{\beta}$(normalized by a $\nu_c^{\beta} B_{\nu}(\nu_c, T)$factor). The third is *from* a -1spectral index *to* a user supplied spectral profile. One example of this use is in the provision of colour correction coefficients for Mars, Jupiter, Saturn, Uranus, and Neptune where planet model spectra is provided as the user-specified spectral profile. Details of the colour correction equations are available in the Ex. Supp. An additional set of keywords have been added to the colour correction routines to provide the relevant effective frequency for a given spectral index, modified blackbody profile, or user-specified spectral profile. Examples of this use are included in the hfi_lfi_test_script.pro file. It is stressed that the use of effective frequencies is not within the official data processing philosophy of Planck; these outputs are provided strictly to allow comparison with other experiments that have adopted the effective frequency approach.

```
;    Determine a powerlaw colour correction for 100 GHz detectors.
hfi_100_cc = hfi_color_correction(BP_INFO=hfi_bp, '100', hfibolo_100_cc, $
    /POWERLAW, ALPHA=2.0, ABP=hfi_avg, AVG_CC=AVG_100_cc)
help, hfibolo_100_cc, /struct    ;    Print info about the detector output.
    ;    Determine a modified blackbody colour correction for Beta = 1.8 and T = 18 K.
hfi_545_cc = hfi_color_correction(BP_INFO=hfi_bp, '545', hfibolo_545_cc, /MODBLACKBODY, $
    TBD = 18d, BETABD = 1.8d, ABP=hfi_avg, CH_CC=CH_545_CC, AVG_CC=AVG_545_CC)
    print, hfibolo_545_cc.BOLONAME
    print, hfibolo_545_cc.CC
```

- Note that 545-3 is set to -10^9 as this detector is not included in flight data products due to excessive noise.

```
    ;    Try to use a user-input spectrum
nu = (hfi_avg[5].freq)    ;    in Hz
Inu = COS((hfi_avg[5].trans)) ;    some arb. profile
hfi_857_cc = hfi_color_correction(BP_INFO=hfi_bp, '857', nu, Inu, hfibolo_857_cc, $
    ABP=hfi_avg, CH_CC=CH_857_CC, AVG_CC=AVG_857_CC)
print, hfibolo_857_cc.BOLONAME
    print, hfibolo_857_cc.CC
```

```
    ;    Try to use another user-input spectrum
nu = (hfi_avg[5].freq)    ;    in Hz
Inu = LOG((hfi_avg[5].trans)) ;    some arb. profile
hfi_857_cc = hfi_color_correction(BP_INFO=hfi_bp, '857', nu, Inu, hfibolo_857_cc, $
    ABP=hfi_avg, CH_CC=CH_857_CC, AVG_CC=AVG_857_CC)
print, hfibolo_857_cc.BOLONAME
```

```
    print, hfibolo_857_cc.CC
```

The variable CH_CC represents the average of the individual detector coefficients. The AVG_CC keyword and the function return value are both the output variable for the colour correction based on the band-average spectrum (i.e. the spectra are averaged and single coefficients are determined, not the averaging of multiple coefficients). The hfibolo_... variable is the output for the individual detector coefficients. For the user specified spectral profile, i.e. nu and Inu provided by the user, the frequency sampling of nu and Inu must match that of the corresponding transmission spectra. This was demonstrated above by setting nu = (hfi_avg[5].freq) from the transmission structure array.

CO correction

The CO correction routine provides conversion for CO emission from units of K CMB to units of K km/s. The input and output formats are similar to the other UC_CC routines as described above. It is advised to use the `FLAG=0` setting in obtaining the detector and band-average spectra for the CO coefficients whereas it is recommended to use the `FLAG=1` or `/FLAG` setting for generation of any of the other coefficients (§2.6.1).

```
  ; Determine CO coefficients for 100 GHz detectors, COJ1-0 transition.
vrad = 0d ; radial velocity of 0 km/s.
    hfi_100_co = hfi_co_correction( BP_INFO=hfi_bp_withCO, ’100’, hfibolo_100_co, $
    hfibolo_100_13co, vrad=vrad, ABP=hfi_avg_withCO, AVG_CO=AVG_100_CO, $
    AVG_13CO=AVG_100_13CO, CH_CO=CH_100_CO, CH_13CO=CH_100_13CO, $
    BP_FLG=flg_withCO, FABP=flg_avg_withCO)

print, hfibolo_100_co.BOLONAME ; print the detector names
print, hfibolo_100_co.COLINE ; print the lower J value of the CO transition
print, hfibolo_100_co.CC ; print the CO coefficients
print, hfibolo_100_13co.CC ; print the 13CO coefficients

; Repeat the above while also getting an uncertainty estimate.
hfi_100_co_wEr = hfi_co_correction( BP_INFO=hfi_bp_withCO, ’100’, hfibolo_100_co_wEr, $
    hfibolo_100_13co_wEr, vrad=vrad, ABP=hfi_avg_withCO, AVG_CO=AVG_100_CO_wEr, $
    AVG_13CO=AVG_100_13CO_wEr, CH_CO=CH_100_CO_wEr, CH_13CO=CH_100_13CO_wEr, $
    BP_FLG=flg_withCO, FABP=flg_avg_withCO, BP_ERR=hfi_er_withCO, EABP=hfi_er_avg_withCO, $
    /GETERR, NITER=100)

print, hfibolo_100_co.BOLONAME ; print the detector names
print, hfibolo_100_co.COLINE ; print the lower J value of the CO transition
print, hfibolo_100_co.CC ; print the CO coefficients
print, hfibolo_100_co.ER ; print the CO coefficient uncertainties
print, hfibolo_100_13co.CC ; print the 13CO coefficients
print, hfibolo_100_13co.ER ; print the 13CO coefficient uncertainties

; Use a different vrad and get the coefficients for the 143 GHz detectors.
; You do not have to set the BP_FLG and FABP keywords, but the result is more accurate if you do.

vrad = -30d ; radial velocity of -30 km/s (towards viewer).
hfi_143_co = hfi_co_correction( BP_INFO=hfi_bp_withCO, ’143’, hfibolo_143_co, $
    hfibolo_143_13co, vrad=vrad, ABP=hfi_avg_withCO, AVG_CO=AVG_143_CO, $
    AVG_13CO=AVG_143_13CO, CH_CO=CH_143_CO, CH_13CO=CH_143_13CO)

print, hfibolo_143_co.BOLONAME ; print the detector names
print, hfibolo_143_co.COLINE ; There are two 143 GHz lines inc. (both coeffs. very small)
print, hfibolo_143_co.CC ; print the CO coefficients

; Use another vrad and get the coefficients for the 857 GHz detectors.
vrad = 60d ; radial velocity of 60 km/s (away from viewer).
hfi_857_co = hfi_co_correction( BP_INFO=hfi_bp_withCO, '857', hfibolo_857_co, $
    hfibolo_857_13co, vrad=vrad, ABP=hfi_avg_withCO, AVG_CO=AVG_857_CO, $
    AVG_13CO=AVG_857_13CO, CH_CO=CH_857_CO, CH_13CO=CH_857_13CO)

print, hfibolo_857_co.BOLONAME ; print the detector names
print, hfibolo_857_co.COLINE ; There are four 857 GHz lines
print, hfibolo_857_co.CC ; print the CO coefficients
```

Although it is possible to determine CO coefficients for all 9 of the lowest rotational transitions for each HFI channel, the UC_CC routine only outputs those within, or nearly within the relevant spectral band. The two out-of-band 143 GHz coefficients are included as a confirmation of the CO rejection within this band.

Nested correction

Combinations of the above coefficients may be used to obtain additional correction factors. A few illustrative examples are included below.

Colour correction from $\alpha = -2$to $\alpha = 4$

The colour correction from a spectral index of $-2$to $4$is done by first computing the conversion from both indices to -1, and then producing the correct ratio of the two.

```
    ;    Determine the -2 to -1 correction, and the 4 to -1 correction

alpha1 = -2d ;   the first  CC spectral index

alpha2 =  4d ;   the second CC spectral index

hfi_100_a1_cc = hfi_colour_correction(BP_INFO=hfi_bp, '100', hfibolo_100_a1_cc, $

    /POWERLAW, ALPHA=alpha1, ABP=hfi_avg, AVG_CC=AVG_100_a1_cc)

    ;    The above converts from -1 to alpha1

hfi_100_a2_cc = hfi_colour_correction(BP_INFO=hfi_bp, '100', hfibolo_100_a2_cc, $

    /POWERLAW, ALPHA=alpha2, ABP=hfi_avg, AVG_CC=AVG_100_a2_cc)

    ;    The above converts from -1 to alpha2

hfibolo_100_m2_to_4_cc = hfibolo_100_a1_cc    ;   Use this as a placeholder.
```

```
cc_m1_to_m2 = hfibolo_100_a1_cc.CC    ;  Coeffs. for -1 to -2

cc_m1_to_4  = hfibolo_100_a2_cc.CC    ;  Coeffs. for -1 to  4

cc_m2_to_4  = cc_m1_to_4/cc_m1_to_m2  ;  ratio the coeffs.

hfibolo_100_m2_to_4_cc.CC = cc_m2_to_4    ;  Set the structure values to the coeff. ratios.

print, cc_m1_to_m2    ;  the -1 -> -2 coeffs.

print, cc_m1_to_4     ;  the -1 ->  4 coeffs.

print, cc_m2_to_4     ;  the -2 ->  4 coeffs.
```

It is important to get the correct numerator and denominator when determining nested/combined unit conversion and colour correction ratios. Colour correction coefficients are from spectral index -1 *to* spectral index $\alpha$by definition. The units of the unit conversion coefficients should be clear. The IRAS convention implies a spectral index of -1, so the unit conversion coefficients yielding results in units of MJy/sr are expected to have an associated spectral index of -1.

Unit conversion / colour correction from K $\mathrm{CMB}$to $\alpha = 2$

In order to convert between units of K $\mathrm{CMB}$to MJy/sr with an effective spectral index of $\alpha = 2$requires both a unit conversion and a colour correction.

```
    ;    Determine the K_CMB to MJy/sr conversion (alpha=-1)

hfi_100_uc = hfi_unit_conversion(BP_INFO=hfi_bp, '100',hfibolo_100_uc, $

    ABP=hfi_avg, AVG_UC=AVG_100_UC)

uc_100_KCMB2MJy = hfibolo_100_uc.KCMB2MJYSR    ;    The UC Coeffs.

    ;    Determine the -1 to 2 colour correction.

hfi_100_cc = hfi_color_correction(BP_INFO=hfi_bp, '100', hfibolo_100_cc, $

    /POWERLAW, ALPHA=2.0, ABP=hfi_avg, AVG_CC=AVG_100_cc)

cc_100_m1_to_2 = hfibolo_100_cc.CC    ;    The CC coeffs.

uccc_100_Kcmb_to_2 = uc_100_KCMB2MJy*cc_100_m1_to_2    ;    Units are still MJy/sr/Kcmb

print, uccc_100_Kcmb_to_2    ;    Print the UC/CC Coeffs.
```

The above examples should demonstrate the basic idea. Users are welcome to experiment with various combinations of data conversion.

LFI quadratic (fast) colour correction

The IDL routine 'LFI_fastcc' provides a quick and easy method of calculating the colour corrections that should be applied to Planck LFI data depending on the source spectra. It uses quadratic fits of the form $cc=A + B\times\alpha + C\times\alpha^2 $ to the tabulated values in section 2 of #planck2013-p02b Planck-2013-V [4]. It does not have any external dependencies.

The routine can be called for the band averaged maps as

```
LFI_fastcc(freq,spectra)
```

where *freq* is one of 28.4, 44.1 or 70.4; or for individual RCA as

```
LFI_fastcc(70.4,spectra,detector=18)
```

(for the 70GHz RCA number 18).

Also included is the LFI_fastcc_test.pro script. This reproduces the tabulated values using the quadratic fits, and demonstrates that the values from the quadratic fit agree with those in the table to an accuracy of ~0.1%.

The conventions for the spectra and corrections are the same as in the paper, i.e. the measured values should be *multiplied* by the colour corrections to obtain the colour-corrected value.

Conclusions

The basic function and structure of the UC_CC routines has been described with command-line examples provided. Further details on the derivation of the equations used within the routines is found in the references cited above, i.e. #planck2013-p03d.

References

<biblio force=false>

1. References
2. References2

</biblio>

References

[1] http://externaltools.planck.fr

Survey and satellite data

Survey and satellite data

This chapter contains data related to the daily planning and operations of the mission as well as data describing the environment Planck was subjected to at L2.

Survey history

Pre-Programmed Pointing Lists

The Pre-Programmed Pointing Lists (PPL) are made by Planck Science Office from the Baseline Scanning Strategy with the help of the Software Planning and Performance Tool. They are sent to MOC/FD for use in making the Augmented Pre-Programmed Pointing Lists (APPL) used for commanding the spacecraft attitude.

The PPL file name is the following: YYYYMMDD_yyyymmdd_NNNN_X.PPL

with YYYYMMDD = start date of the valid span of the PPL file

yyyymmdd = end date of the valid span of the PPL file

NNNN = unique sequence number, in the range 0000 ≤ NNNN ≤ 9999, incrementing sequentially throughout the mission and uniquely identifying each new PPL file that is generated (i.e. no repeated numbers and no gaps in the sequence of PPLs) o 0000-8999 reserved for PSO o 9000-9999 reserved for attitude manoeuvres generated by MOC

X = type of PPL, as follows: o R = Routine (standard 4-week PPL) o C = Contingency (3-day replanning) o L = Long-Term PPL (LTPPL) o S = Special

PPLs contain the following information in ASCII columns:

- pointing reference number
- Ecliptic longitude
- Ecliptic latitude
- nominal start time for pointing
- earliest allowed start time
- latest allowed start time
- nominal dwell time
- observation type
- comments

PPLs can be found in the Planck Legacy Archive in the "Time-Ordered Information: Operational Files" section, ordered normally by periods of a month. A full list of the available files can be found here [1].

Detailed information about the PPL's can be found here: PPL ICD [2]

Augmented Pre-Programmed Pointing Lists

APPLs are made by MOC / Flight Dynamics using pointing information (PPLs) from the Planck Science Office.

The APPLs incorporate information about the Operational Days boundaries in order to fit pointings into each OD.

APPLs are grouped and summarized by MOC to form files called the APPL Summary Files or APS.

These are delivered in the Planck Legacy Archive in the "Time-Ordered Information: Operational Files" section, by Operational Day. A full list of the available files can be found here [3].

Detailed information about the APPL's can be found here: APPL Interface Control Document [4]

Attitude History Files

The pointing history of Planck is described in the Attitude History Files (AHF) sequence. All the AHF can be found in the Planck Legacy Archive, for three different methods of computation (AHF [5], DHF [6], GHF [7]).

The GHF are made using refined pointing information from the Fiber Optics Gyroscope.

Available information concerning the AHF can be found here: AHF Interface Control Document [8]

Focal plane geometry

The Spacecraft-Instrument Alignment Matrix (SIAM) contains all the geometry information for each detector of both instruments with respect to the main optical frame.

The last updated SIAM is provided in the Planck Legacy Archive in the "Time-Ordered Information: Operational Files" section and can also be downloaded here [9]

Information about the structure of the SIAM can be found here: SIAM ICD [10]

Example of SIAM information: for each detector the geometry data are provided:

100-1a 2012-05-21T12:20:33Z 2009-05-14T13:12:00Z

+6.0720828748030420D-02 -2.0182099307153797D-02 +9.9795073216251973D-01

+9.1870882469655513D-01 +3.9201126860886798D-01 -4.7971457225525649D-02

-3.9023976781054348D-01 +9.1973901088907972D-01 +4.2344721842881641D-02

100-1b 2012-05-21T12:20:33Z 2009-05-14T13:12:00Z

+6.0701704221756109D-02 -2.0112134059606067D-02 +9.9795330811022553D-01

+3.6930168885547898D-01 -9.2839700605522935D-01 -4.1173556516014474D-02

+9.2732495152080596D-01 +3.7104514713341125D-01 -4.8927835387228120D-02

143-1a 2012-05-21T12:20:33Z 2009-05-14T13:12:00Z

+1.0777605789673984D-01 -2.3428762574447454D-02 +9.9389909670371901D-01

+6.9845387670400361D-01 +7.1322499496182634D-01 -5.8926128999380371D-02

-7.0749311195331566D-01 +7.0054350303598756D-01 +9.3232488396908259D-02

143-1b 2012-05-21T12:20:33Z 2009-05-14T13:12:00Z

+1.0778382836227447D-01 -2.3451301846261791D-02 +9.9389772249728381D-01

+7.3378157679069944D-01 -6.7264740206943763D-01 -9.5446686960791699D-02

+6.7078107002667198D-01 +7.3959144730787174D-01 -5.5292378886437468D-02

217-1 2012-05-21T12:20:33Z 2009-05-14T13:12:00Z

+6.9536754016818220D-02 -1.6979192448348744D-02 +9.9743488352102772D-01

+1.1808481560694440D-03 +9.9985584312129827D-01 +1.6938080582827864D-02

-9.9757869135143240D-01 +0.0000000000000000D+00 +6.9546779663498287D-02

```
353-1 2012-05-21T12:20:33Z 2009-05-14T13:12:00Z
+8.7069162938225447D-02 -3.5549378340174860D-02 +9.9556777899089488D-01
+3.0972122976328201D-03 +9.9936792108793815D-01 +3.5414200207773784D-02
-9.9619745439406726D-01 -2.1175823681357513D-22 +8.7124232328209705D-02
143-5 2012-05-21T12:20:33Z 2009-05-14T13:12:00Z
+1.1717127774596003D-01 -1.9543330278624677D-02 +9.9291940756186214D-01
+2.2903544129261044D-03 +9.9980901088238894D-01 +1.9408658764649294D-02
-9.9310908058885550D-01 +1.0842021724855047D-19 +1.1719366045976087D-01
217-5a 2012-05-21T12:20:33Z 2009-05-14T13:12:00Z
+7.8306055032829461D-02 -2.0852430804578555D-02 +9.9671126103537944D-01
+6.8116502453463090D-01 +7.3113166028431409D-01 -3.8219166404281218D-02
-7.2793019658201552D-01 +6.8191764272486954D-01 +7.1455982567074930D-02
```

Orbit file

The orbit file is produced by the Flight Dynamics team at ESOC and contains the information of the Planck orbital history throughout the whole mission (since launch).

This product is available in the Planck Legacy Archive interface in the "Time-ordered information : Orbit file" section. Only one orbit file is delivered since it contains all the past information for the whole of the Planck mission.

The orbit file can be downloaded here [11].

Orbit events file

The orbit events file .LEV is produced by the Flight Dynamics team at ESOC and contains the information of the Planck orbit events throughout the whole mission (since launch).

This product is available in the Planck Legacy Archive interface in the "Time-ordered information : Orbit events file" section. Only one orbit events file is delivered since it contains all the past information for the whole of the Planck mission.

The orbit events file can be downloaded here [12].

Planck operational state history

The Planck Operational State History (POSH) provides an easily accessible summary of the status of the Planck spacecraft, throughout the course of its mission. It should be useful to scientists as a complement to the data they are analyzing.

Due to the type and quantity of data that describes the state of a satellite and its instruments, it is common for it to be spread over a large number of files and formats which may have to be retrieved from a large number of systems. In addition there are a significant number of potentially interesting occurrences during the mission which are not found in any one single repository; examples are mission milestones, definitions of operational days and anomalous events. The initial motivation for the creation of the POSH was to provide the state of the spacecraft and its instruments in an easily accessible way at any given time. States to be included were the operational phases and the operational status/mode of each of the major payload components. The intention being that this information could be used to assist not only in the operational work in monitoring the status of the survey but also as a data source that could be consulted whilst analyzing science data.

Two main record types are stored in the POSH:

EVENTS, consisting of occurrences during the mission that can be described by a start and end time (e.g. survey boundaries, anomalies, ODs, manoeuvres). The definition of an event is provided for operational purposes; it may or may not agree with the definition of an event for data analysis purposes (e.g. the boundaries of a survey may be defined in a different way in the pipeline).

HOUSE KEEPING (HK) SUMMARY which consists of some HK timelines with one data point per pointing period (e.g. temperatures, position in the sky, drift rates, sun angles). This data set contains a very compact operational summary of the mission (not an exhaustive list of HK).

The full dataset and accompanying documentation can be download here [13]

References

[1] http://pla.esac.esa.int/pla/aio/metadata-action?PAGE_SIZE=1500&PAGE=1&RESOURCE_CLASS=OPERATIONAL_FILE&SELECTED_FIELDS=OPERATIONAL_FILE.FILE_ID,OPERATIONAL_FILE.SIZE&OPERATIONAL_FILE_TYPE.NAME=PPL&RELEASE.NAME=PR1&RETURN_TYPE=HTML

[2] http://www.rssd.esa.int/llink/livelink/fetch/-60063/65211/65216/200039/2785625/PGS-ICD-017_Pre-programmed_Pointing_List_%5BPPL%5D.pdf?nodeid=2785628&vernum=-2

[3] http://pla.esac.esa.int/pla/aio/metadata-action?PAGE_SIZE=1500&PAGE=1&RESOURCE_CLASS=OPERATIONAL_FILE&SELECTED_FIELDS=OPERATIONAL_FILE.FILE_ID,OPERATIONAL_FILE.SIZE&OPERATIONAL_FILE_TYPE.NAME=APS&RELEASE.NAME=PR1&RETURN_TYPE=HTML

[4] http://www.rssd.esa.int/llink/livelink/fetch/-60063/65211/65216/200039/2785625/PGS-ICD-050_Augmented_Pre-programmed_Pointing_List_%5BAPPL%5D.pdf?nodeid=2865927&vernum=-2

[5] http://pla.esac.esa.int/pla/aio/metadata-action?PAGE_SIZE=1500&PAGE=1&RESOURCE_CLASS=OPERATIONAL_FILE&SELECTED_FIELDS=OPERATIONAL_FILE.FILE_ID,OPERATIONAL_FILE.SIZE&OPERATIONAL_FILE_TYPE.NAME=AHF&RELEASE.NAME=PR1&RETURN_TYPE=HTML

[6] http://pla.esac.esa.int/pla/aio/metadata-action?PAGE_SIZE=1500&PAGE=1&RESOURCE_CLASS=OPERATIONAL_FILE&SELECTED_FIELDS=OPERATIONAL_FILE.FILE_ID,OPERATIONAL_FILE.SIZE&OPERATIONAL_FILE_TYPE.NAME=DHF&RELEASE.NAME=PR1&RETURN_TYPE=HTML

[7] http://pla.esac.esa.int/pla/aio/metadata-action?PAGE_SIZE=1500&PAGE=1&RESOURCE_CLASS=OPERATIONAL_FILE&SELECTED_FIELDS=OPERATIONAL_FILE.FILE_ID,OPERATIONAL_FILE.SIZE&OPERATIONAL_FILE_TYPE.NAME=GHF&RELEASE.NAME=PR1&RETURN_TYPE=HTML

[8] http://www.rssd.esa.int/llink/livelink/fetch/-60063/65211/65216/200039/2785625/PGS-ICD-006_Attitude_History_File_%5BAHF%5D.pdf?nodeid=2808899&vernum=-2

[9] http://pla.esac.esa.int/pla/aio/metadata-action?PAGE_SIZE=1500&PAGE=1&RESOURCE_CLASS=OPERATIONAL_FILE&SELECTED_FIELDS=OPERATIONAL_FILE.FILE_ID,OPERATIONAL_FILE.SIZE&OPERATIONAL_FILE_TYPE.NAME=SIAM&RELEASE.NAME=PR1&RETURN_TYPE=HTML

[10] http://www.rssd.esa.int/llink/livelink/fetch/-60063/65211/65216/200039/2785625/PGS-ICD-039_Spacecraft_Instrument_Alignment_Matrix_%5BSIAM%5D.pdf?nodeid=2831007&vernum=-2

[11] http://pla.esac.esa.int/pla/aio/metadata-action?PAGE_SIZE=1500&PAGE=1&RESOURCE_CLASS=OPERATIONAL_FILE&SELECTED_FIELDS=OPERATIONAL_FILE.FILE_ID,OPERATIONAL_FILE.SIZE&OPERATIONAL_FILE_TYPE.NAME=ORB&RELEASE.NAME=PR1&RETURN_TYPE=HTML

[12] http://pla.esac.esa.int/pla/aio/metadata-action?PAGE_SIZE=1500&PAGE=1&RESOURCE_CLASS=OPERATIONAL_FILE&SELECTED_FIELDS=OPERATIONAL_FILE.FILE_ID,OPERATIONAL_FILE.SIZE&OPERATIONAL_FILE_TYPE.NAME=LEV&RELEASE.NAME=PR1&RETURN_TYPE=HTML

[13] http://pla.esac.esa.int/pla/aio/metadata-action?RESOURCE_CLASS=POSH&SELECTED_FIELDS=POSH.POSH_VERSION,POSH.FILE_ID,POSH.SIZE&RELEASE.NAME=PR1&RETURN_TYPE=HTML

Satellite history

This section was intentionally left empty. It will be filled in future releases of the PLA to accompany the Planck house keeping data.

SREM

Product description

The SREM data files contain calibrated data for the different energy and particle species channels available in the SREM. Each data file contains 24 hours of data - from midnight to midnight (note this is **not** an Operational Day) - with the date covered by the file easily identifiable through the file name.

Inputs

SREM calibrated data was produced from the SREM raw data acquired during the entire mission.

Related products

Data for the SREM on board other ESA missions can be retrieved from the Paul Scherrer Institut [1]

Data files

The files containing the SREM calibrated data will have a name of the form SREMPlanck_PACC_YYYYMMDD.fits where PACC stands for Processed ACCumulated data and YYYYMMDD is the date the data in the file was acquired.

The SREM processed data can be downloaded from the PLA interface: "Ancillary data" tab of the "Time-ordered information" section.

A list of the files available can be found here: SREM files [2]

Data format

Each file contains three binary table extensions named CDFFITS1,CDFFITS2 and CDFFITS3. The first extension contains the accumulated counts data, the second extension the labels to identify the data in the first extension and the third extension the total radiation dosis. The contents of each extension are as follows.

CDFFITS1

Column Name	Contents	Format	Unit
EPOCH	vector containing 1 string with UTC for center of accumulation interval in ISO format (YYYY-MM-DDTHH:MM:SS.MMMZ)	A24	NA
COUNTRATE	vector containing 15 elements (1 for each channel) with counts for accumulation period identified in the EPOCH column	E15.4	s^{-1}
ORBIT	position (x,y,z) of the SREM in the ECI frame. Distance from center fo the Earth is $R = \sqrt{(x^2 + y^2 + z^2)}$	E15.4	Km
ATTITUDE	Not in use	E15.4	-
PROT FITQUAL	Not in use	I1	NA

ODPF	Not in use.	E15.4	-
ODPFERR	Not in use	E15.4	-
ELEC FITQUAL	Not in use	I1	-
ODEF	Not in use	E15.4	-
ODEFERR	Not in use	E15.4	-
ANISOTROPY	Not in use	E15.4	-
TEMPERATURE	2 element vector containing temperature of the two detector heads at each EPOCH	E15.4	℃

CDFFITS2

Column Name	Contents	Format	Unit
EPOCH	this is a keyword	Km^2	

CDFFITS3

Column Name	Contents	Format	Unit
RADEPOCH	this is a keyword	A24	Km^2
RADFET	Value proportional to the absorbed dose on a diode mounted on the surface of SREM	E15.4	NA

Note: SREM calibrated data files where initially provided in the Common Data Format (cdf) format [3]. This has traditionally been the preferred data format for SREM on board previous ESA missions. However, as cdf is not widely used in the astrophysics community it was later agreed with the provider that fits files should also be provided. This meant taking the original cdf format and converting it to fits. The original cdf files can be retrieved from the SREM site [4] at the PSI.

References

[1] http://srem.web.psi.ch/cgi-bin/srem_data_sec.cgi

[2] http://pla.esac.esa.int/pla/aio/metadata-action?RESOURCE_CLASS=ANCILLARY_DATA&ANCILLARY_DATA.DATA_TYPE=SREM&RETURN_TYPE=HTML

[3] http://cdf.gsfc.nasa.gov/

[4] http://srem.web.psi.ch/html/srem_home.shtml

Appendix

Appendix

PLA quick start guide

Introduction

The Planck Legacy Archive (PLA) contains all public products originating from the Planck mission. A graphical user interface accessible from this page allows to list, display, inspect, select, and download these products.

The first public product present in the Planck Legacy Archive was the Early-Release Compact Source Catalogue (ERCSC) released in January 2011.

As of January 2013, the PLA contains all temperature maps per Planck frequency, as well as ancillary maps like Survey maps, detector maps, etc. It also contains the first public version of the Planck Catalogue of Compact Sources and information about the spacecraft, instrument and survey history, notably through all the operational files and the Planck Operations State History (POSH).

Purpose

The PLA will mainly serve the needs of professional astrophysicists wishing to carry out astronomical research, related to various astronomy fields as the Cosmic Microwave Background, extragalactic astronomy, Galactic interstellar medium, and Solar System studies, among others. In addition to these professional users, a number of others will be browsing the PLA, including members of the general public and members of the press. In both cases, they will be looking for general information on the Planck satellite and its scientific results, news about Planck, pictures and other public-relations material, among other things.

Contents

The Planck Legacy Archive contains the following classes of products as of January 2013:

- frequency maps at all nine frequencies of Planck (in temperature only)
- sky component maps per frequency per component
- various ancillary maps like survey maps, detector maps, detector set maps, etc
- the first version of the Planck Legacy Catalogue of Compact Sources
- the Early-Release Compact Source Catalogue (since January 11th, 2011)
- operational files for the first six surveys (approximately first three years of Planck routine operations): pointing lists (programmed and achieved), orbit information, data-quality reports, instrument health reports, etc)
- the Planck Operational State History (POSH) - the "state vector" of the Planck mission
- documents associated to the above products

In addition to these public products, the same archive has an internal part (Planck Internal Archive or PIA) containing products restricted to the Planck collaboration.

Software

The data browsing and retrieval from the PLA interface involves the following actions:

- there are several search panels or tabs (Maps, Catalogues, Time-Ordered Information, Documents...) which offer a set of filters to set the search criteria for the data queries
- after executing a query, a new result panel is automatically created with the result contents
- each result tab contains a list of the data which match the specified query. From this page several operations can be performed, depending on the type of data to be retrieved (e.g. display a set of sources, save result tables as XML or CSV, send them to another application, download the products, etc).

Some products require authentication (only those pertaining to the Planck Internal Archive, restricted to some people in the Planck Collaboration). The user must enter their username and password (Planck LDAP credentials) in the login window. If authorisation is granted, the status bar in the left bottom corner of the application window will be updated to the current user's ID and login time.

A general set of help pages is present on the Java interface. Please refer to these pages for further explanations on the software.

Access

The PLA main page can be accessed here [1].

The Java interface can also be directly launched from here [2].

Trouble shooting for the PLA Java client

To run the PLA your web browser must be Java compliant (Java version 1.5.x or higher is required for running the PLA), if not please install the latest Java following the instructions provided here [3].

In case of problem, and to make sure that you are using the latest version of our software, please clean your Java Web Start cache (see below) and run the application again. If the problem persists, please open a web browser (Internet Explorer, Mozilla Firefox, Safari, ...) and send us the output from this page [4] (which lists your configuration) along with the description of your problem. If the problem is related to data searching, it will be very helpful if you include the contents of your Log Console, which you'll find at the bottom of the ERCSC window, when you contact us (see Helpdesk section).

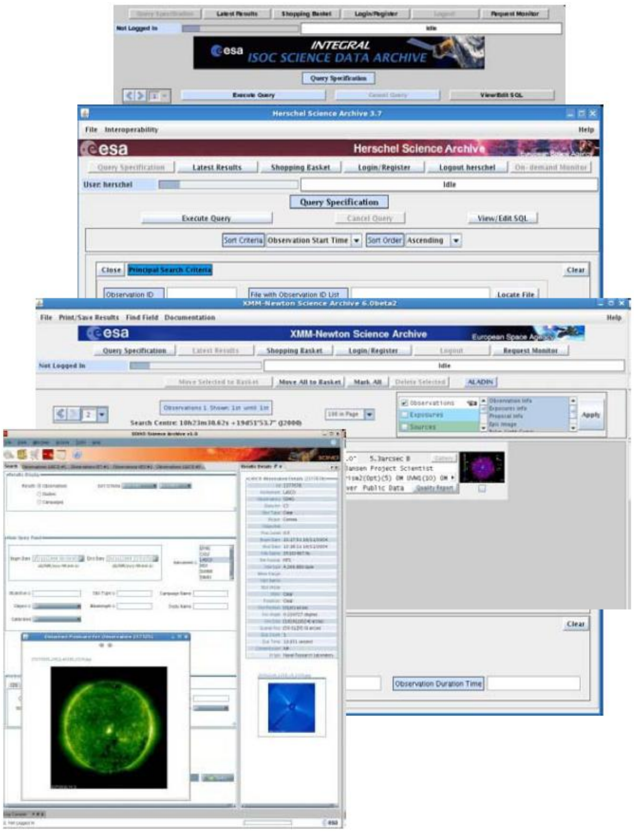

The Planck Legacy Archive Java interface is part of the general archiving effort developed by the Science Archives Team at ESAC

How to clean your Java Web Start cache on Windows systems:

- Click on the "Start" icon in the lower left hand corner of your screen, followed by clicking on the "Run" menu choice.
- In the run box, type "javaws -viewer" (w/o the quotes) and hit "Enter".
- Select all the entries and then click on the "Remove Selected Applications/Items/Entries" button/icon.

On Linux systems:

- Find out what version of Java you are running by and typing in "java -version" at the command line (w/o the quotes).
- Type in the command "$JAVA_HOME/jre/javaws/javaws" or "$JAVA_HOME/jre/javaws/javaws -viewer" on the command line if your Java version is 1.5 or 1.6 respectively.
- Select all the entries and then click on the "Remove Selected Applications/Items/Entries" button/icon.

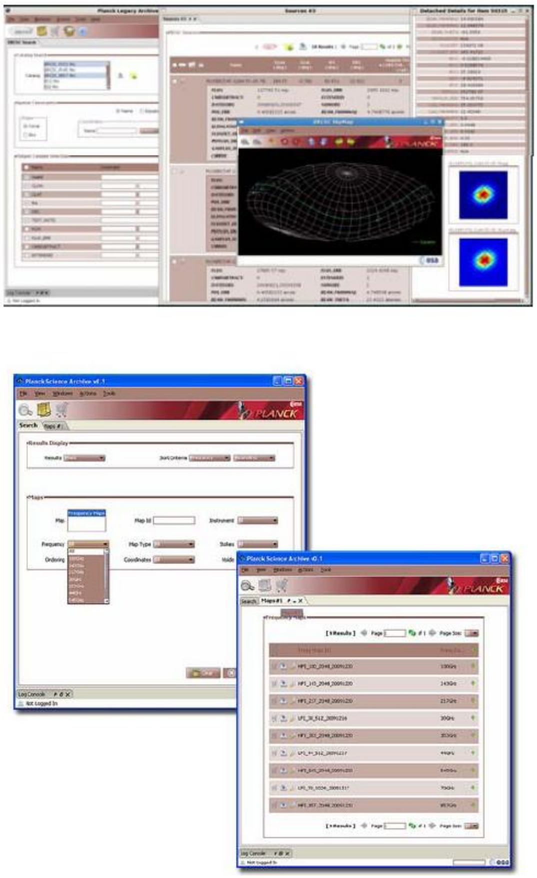

Illustration of the specific case of the Planck Legacy Archive interface

On Mac OS X systems:

- Find out what version of Java you are using by running "Applications/Utilities/Terminal" and typing in "java -version" at the command line (w/o the quotes).
- Type in the command "javaws" or "javaws -viewer" on the command line if your Java version is 1.5 or 1.6 respectively.
- Select all the entries and then click on the "Remove Selected Applications/Items/Entries" button/icon.

On Windows systems, in case of trouble with Java WebStart and Comodo Firewall:

- When trying to launch the archive interface, Java WebStart may return the error “splash recv failed”.
- Possible solution: Add Java WebStart to the list of authorized applications in the Comodo Firewall.

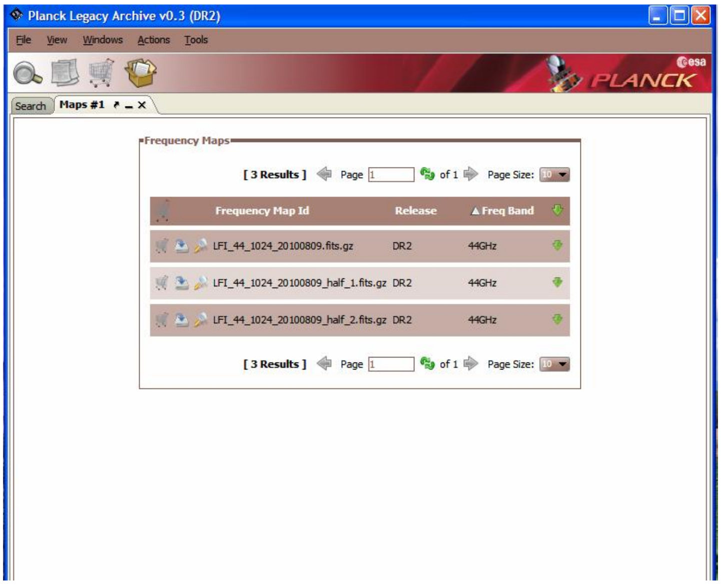

Frequency Map Id	Release	Freq Band
LFI_44_1024_20100809.fits.gz	DR2	44GHz
LFI_44_1024_20100809_half_1.fits.gz	DR2	44GHz
LFI_44_1024_20100809_half_2.fits.gz	DR2	44GHz

Illustration of the specific case of the Planck Legacy Archive interface

Planck Legacy Archive Helpdesk

The PLA Helpdesk consists of the three scientists of Planck Science Office. For some questions related to data products and instruments, the questions may be re-directed to data-processing or instrument specialists in science institutes of the Planck Ground Segment.

In order to send a request to the Helpdesk, please fill in the form at: [[5]]

("Submit a ticket")

References

[1] http://www.sciops.esa.int/index.php?page=Planck_Legacy_Archive&project=planck

[2] http://pla.esac.esa.int/pla/pla.jnlp

[3] http://www.java.com/en/download/manual.jsp

[4] http://www.java.com/en/download/testjava.jsp

[5] http://www.sciops.esa.int/helpdesk_pia

Glossary

- **4K lines**: EMI/EMC influence of the 4K cooler mechanical motion on the bolometer readout electronics.
- **calibration** [HFI meaning]: For a single detector, the absolute calibration is gain factor between the measured signal (watts absorbed by the detector) and the sky signal (in astrophysical units); can vary with time. For a set of detectors, the relative calibration is the difference in the calibration between detector pairs. The latter can be measured very accurately from the observations of the same source by different detectors, and is only slightly affected by the differences in the detector spectral responses, which are similar; the former requires observations of sources with well modeled spectral energy distributions or well known spectra, and requires that the detector's spectral bandpass also be well known.
- **calibration**: [LFI meaning]: absolute calibration refers to the 0th order calibration for each channel, 1 single number, while the relative calibration refers to the component of the calibration that varies pointing period by pointing period.
- **detector set** [HFI meaning]: a detector set (aka detset aka quad) is a combinaison of two pairs of Polarization Sensitive Bolometers pairs at the proper orientations. The lists of detsets is given in here.
- **DMC** : Data Management Component, the databases used at the HFI and LFI DPCs
- **effective beam** [HFI meaning]: the effective beam at the map level is the overall angular response to the sky in a map pixel, which results from the combined effect of the instrumental response, the scanning strategy and the data processing.
- **far sidelobe** [HFI meaning]: the response to the sky of a detector more than 5 degrees from the beam centroid.
- **half ring difference** : difference between the map built using the first half of each pointing period (typically 20 minutes of contiguous data) and the one built with the second half. This difference effectively removes the sky signal and most of the correlated noise, leaving only the noise components that have time scales of < ~ 20 min.
- **HPR** [HFI meaning]: HEALPix Rings are introduced to avoid any additional binning of the data. We choose a sky pixelization as a basis for this ring making (HEALPix, Górski et al. 2005). HPR are therefore partial sky maps produced via a projection onto the sky of each single pointing period separately.
- **IMO** [HFI meaning]: the HFI Instrument MOdel is a central repository containing the models (or a link to them) and sets of fixed parameters used in these models describing for example how photons are gathered and transformed into data. IMO is oriented toward the data reduction and data processing. IMO is also used to monitor the instrument health. IMO represents at any time the official knowledge of the instrument response. It is intended to represent its best current knowledge agreed on by the project and applicable to the data processing. IMO does not represent the knowledge of the instrument. It is a knowledge of its response, (e.g. how photons are gathered

and transformed into data). It is a simplified fraction of this knowledge directly useful to reduce the data. The IMO is restricted to the sole parameters used in the DPC. IMO does not contain timelines, nor maps, although it can provide links to calibration timelines (e.g. gain evolution) and calibration maps (e.g. beam maps). Models do not need to be unique (not a single model for a single process). Depending on the purpose for which they are used, they can be more or less sophisticated. (e.g. bolometer models, beam representations, very simplified for first assessment of pointing parameters, ...). IMO does not choose between them : it contains the parameters for each of them at the same time. See HFI RIMO.

- **jump** : sudden change of the baseline level inside a ring
- **main beam** [HFI meaning] Response to the sky within 23 arcminutes of the centroid of response.
- **near sidelobe** [HFI meaning] Response to the sky between 23 arcminutes and 5 degrees from the main beam centroid.
- **OD** : Operation Day definition is geometric visibility driven as it runs from the start of a DTCP (satellite Acquisition Of Signal) to the start of the next DTCP. Given the different ground stations and spacecraft will takes which station for how long, the OD duration varies but it is basically once a day.
- **optical beam** [HFI meaning] The response to the sky due to optics alone.
- **PBR** [HFI meaning]: Phase Bin Rings provide a compressed and higher signal-to-noise ratio rendition of the original Time Order Data
- **polarization leakage** [HFI meaning]: in general, systematic effects mix the I,Q,U signals. Given the amplitudes of the sky signals, leakage from temperature to polarisation can be dramatic for polarisation analysis.
- **ring** [HFI meaning]: at the HFI DPC level the ring is the time intervalle between two First Thurster Firings as defined in AHF description document [2]. It thus starts with a satellite slew and thus an unstable pointing period and continue with a satellite dwell and thus stable pointing period.
- **RIMO** [HFI meaning]: The RIMO, or Reduced Instrument Model is a FITS file containing selected instrument characteristics that are needed by users who work with the released data products.
- **sample** [HFI meaning]
- **scanning beam** [HFI meaning]: the scanning is defined as the beam measured from the response to a point source of the full optical and electronic system, after the filtering.
- **scanning beam** [LFI meaning]: the actual beam which couples the optics of the instrument with the scanning movement of the satellite (beam smearing). It can be measured from planet observations.
- **SOVT** : System Operation and Validation Test
- **spectral response** (or bandpass): steady state response of a detector system (i.e., detector and its electronics + horn + filter) as a function of frequency. It does not consider the temporal response and associated transfer function.
- **survey** [HFI meaning]: sky surveys (aka Scan #)are defined in terms of the direction of the satellite's spin axis. Survey periods are given here.
- **TOD** [HFI meaning]: Time-Ordered Data
- **TOD** [LFI meaning]: Time-Ordered Data, refers to calibrated data
- **TOI** [HFI meaning]: Time Ordered Information
- **TOI** [LFI meaning]: Time Ordered Information, refers to uncalibrated data
- **warm units** : JFET, Bellow, PAU et REU

List of acronyms

- **ACMS** : Attitude Control & Measurement Subsystem (AOCS)
- **ADC** : analog to digital converter
- **AHF** : Attitude History File
- **APID** : Application Program Identifier
- **APPL** : Augmented Preprogrammed Pointing List
- **BEM** : LFI warm electronics Back End Module
- **BEU** : LFI warm electronics Back End Unit
- **BTB** : Back To Back HFI horns
- **CDMS** : Command and Data Management System
- **CDMU** : Command and Data Management Unit
- **CMB** : Cosmic Microwave background
- **CoP** : Commissioning Phase
- **CPV** : Calibration and Performance Verification
- **CSL** : Centre Spatial de Liège
- **CTR** : Central Time Reference
- **CUC** : CCSDS Unsegmented Time Code
- **DAE** : LFI Data Acquisition Electronics
- **DCE** : Dilution Cooler Electronics
- **DDS** : MOC's Data Distribution System
- **DMC** : Data Management Component, the databases used at the HFI and LFI DPCs
- **DPC** : Data Processing Center
- **DPU** : Data Processing Unit
- **DQR** : Daily Quality Report
- **DTCP** : Daily Tele-Communication Period
- **EOL** : End Of Life
- **ERCSC** : Early Release Compact Source Catalog
- **ESA** : European Space Agency
- **ESOC** : European Space Operations Centre (Darmstadt)
- **ESTEC** : European Space TEchnology and Research Centre
- **FEM** : LFI cryogenic amplifying stage Front End Module
- **FEU** : LFI cryogenic amplifying stage Front End Unit
- **FH** : Feed Horn
- **FITS** : Flexible Image Transfer Specification
- **FOG** : Fiber Optic Gyroscope
- **FOV** : Field-Of-View
- **FPU** : Focal Plane Unit
- **FWHM** : Full-Width-at-Half-Maximum
- **HCM** : Angular momentum Control Mode
- **HEMT** : High Electron Mobility Transistor
- **HFI** : (Planck) High Frequency Instrument
- **HK** : House Keeping
- **HPFTS** : Herschel/Planck File Transfer System
- **HPMCS** : Herschel/Planck Mission Control System
- **HSK** : House-Keeping data

- **ICD** : Interface Control Document
- **ILS** : Instrument Line Shape
- **IMO** : Instrument MOdel
- **IOT** : Instrument Operation Team
- **JFET** : Junction Field Elect Transistor
- **LEOP** : Launch & Early Orbit Phase
- **LFER** : low frequency excess response
- **LFI** : (Planck) Low Frequency Instrument
- **LOBT** : Local On Board Time
- **LOS** : Line Of Sight
- **mission** [HFI meaning]
- **MOC** : [ESA's] Mission Operation Center [Darmstadt, Germany]
- **NEP** : Noise Equivalent Power
- **NET** : Noise Equivalent Temperature
- **OBT** : On-Board Time
- **OD** : Operational Day
- **OMT** : LFI Ortho Module Transducer
- **P/L** : Payload
- **PAU** : Pre_Amplification Unit
- **PBR** : phase binned ring
- **PI** : Principal Investigator
- **PIA** : Planck Internal Archive
- **PLA** : Planck Legacy Archive
- **PLM** : Payload Module
- **PO** : Physical Optics
- **POI** : Phase-Ordered Information (DMC group/object)
- **PPL** : Pre-programmed Pointing List
- **PPLM** : Planck Payload Module
- **PSM** : Planck Sky Model
- **PSO** : Planck Science Office
- **PTD** : Physical Theory of Diffraction
- **PUS** : Packet Utilisation Standard
- **RAA** : LFI Radiometer Array Assembly
- **RAF** : Raw Attitude history File
- **RCA** : LFI Radiometer Chain Assembly
- **REBA** : LFI Radiometer Electronics Box Assembly
- **REU** : Readout Electronic Unit
- **RFQM** : Radio Frequency Qualification Model
- **RIMO** : reduced IMO
- **ROI** : Ring-Ordered Information (DMC group/object)
- **rpm** : revolutions per minute
- **RSSD** : Research Space Science Division of ESA [ESTEC, Netherlands]
- **RTS** : random telegraphic signal
- **S/C** : Spacecraft
- **SAA** : Solar Aspect Angle
- **sample** [HFI meaning]
- **SCC** : Sorption Cooler Compressor assembly

- **SCS** : Sorption Cooler Subsystem (Planck)
- **SEV** : Sun Earth Vector
- **SGR** : Small Gap Recovery
- **SGS** : Science Ground Segment
- **SIAM** : Spacecraft Instrument Alignment Matrix
- **SLT** : System Level Test
- **SOVT** : System Operation and Validation Test
- **SPPT** : Survey Performance and Planning Tool
- **SPU** : Signal Processing Unit
- **SREM** : Space Radiation Environment Monitor
- **SRP** : Solar Radiation Pressure
- **SSCE** : Sun-SpaceCraft-Earth angle max= 15°
- **SSO** : Solar System Object
- **STR** : Star TRacker
- **SVM** : Service Module
- **SZ** : Sunyaev-Zel'dovich
- **TBC** : To be confirmed
- **TBD** : To be defined / determined
- **TC** : Tele-Command
- **THF** : Telecommand History File
- **TOD** [HFI meaning]: Time-Ordered Data
- **TOD** [LFI meaning]: Time-Ordered Data, refers to calibrated data
- **TOI** [HFI meaning]: Time Ordered Information
- **TOI** [LFI meaning]: Time Ordered Information, refers to uncalibrated data
- **ToS** : Time of Sample
- **TSA** : hermal Stabilization Assembly
- **UTC** : Universal Time Coordinate(d)
- **warm units** : JFET, Bellow, PAU et REU
- **WG** : LFI Waveguide
- **WHR** : Weekly Health Report

Article Sources and Contributors

Warning for readers of the pdf version *Source*: http://www.sciops.esa.int/wikiSI/planckpla/index.php?oldid=7530 *Contributors*: Lmendes

Changelog (pdf) *Source*: http://www.sciops.esa.int/wikiSI/planckpla/index.php?oldid=7574 *Contributors*: Lmendes

The Planck mission *Source*: http://www.sciops.esa.int/wikiSI/planckpla/index.php?oldid=7228 *Contributors*: Lmendes, Xdupac

The satellite *Source*: http://www.sciops.esa.int/wikiSI/planckpla/index.php?oldid=7371 *Contributors*: Lmendes, Rleonard

HFI design, qualification, and performance *Source*: http://www.sciops.esa.int/wikiSI/planckpla/index.php?oldid=7112 *Contributors*: Acoulais, Bcrill, Fpajot, Fpiacent, Jhaissin, Jlamarre, Kganga, Lmendes, Lspencer, Lvibert

HFI cryogenics *Source*: http://www.sciops.esa.int/wikiSI/planckpla/index.php?oldid=7114 *Contributors*: Acoulais, Fpajot, Jhaissin, Jlamarre, Lmendes, Lvibert

HFI cold optics *Source*: http://www.sciops.esa.int/wikiSI/planckpla/index.php?oldid=7560 *Contributors*: Acoulais, Fpajot, Jhaissin, Jlamarre, Lmendes, Lspencer, Lvibert

HFI detection chain *Source*: http://www.sciops.esa.int/wikiSI/planckpla/index.php?oldid=7116 *Contributors*: Acoulais, Jhaissin, Jlamarre, Lmendes, Lvibert, Splaszcz

HFI operations *Source*: http://www.sciops.esa.int/wikiSI/planckpla/index.php?oldid=7117 *Contributors*: Jhaissin, Lmendes, Lvibert

HFI performance summary *Source*: http://www.sciops.esa.int/wikiSI/planckpla/index.php?oldid=7271 *Contributors*: Jhaissin, Jlamarre, Lmendes, Lvibert

HFI instrument annexes *Source*: http://www.sciops.esa.int/wikiSI/planckpla/index.php?oldid=7119 *Contributors*: Lmendes, Lvibert

HFI optical efficiency *Source*: http://www.sciops.esa.int/wikiSI/planckpla/index.php?oldid=7120 *Contributors*: Lmendes, Lvibert

HFI reference bolometer *Source*: http://www.sciops.esa.int/wikiSI/planckpla/index.php?oldid=7121 *Contributors*: Lmendes, Lspencer, Lvibert

HFI detector feedhorn model parameters *Source*: http://www.sciops.esa.int/wikiSI/planckpla/index.php?oldid=7124 *Contributors*: Jhaissin, Lmendes, Lvibert

HFI CO response *Source*: http://www.sciops.esa.int/wikiSI/planckpla/index.php?oldid=7125 *Contributors*: Lmendes, Lvibert

HFI time response model *Source*: http://www.sciops.esa.int/wikiSI/planckpla/index.php?oldid=7126 *Contributors*: Jlamarre, Lmendes, Lvibert

HFI data compression *Source*: http://www.sciops.esa.int/wikiSI/planckpla/index.php?oldid=7127 *Contributors*: Lmendes, Lvibert

HFI operations timeline *Source*: http://www.sciops.esa.int/wikiSI/planckpla/index.php?oldid=7128 *Contributors*: Lmendes, Lvibert

LFI design, qualification and performance *Source*: http://www.sciops.esa.int/wikiSI/planckpla/index.php?oldid=7129 *Contributors*: Agregori, Lmendes

LFI design, qualification, and performance *Source*: http://www.sciops.esa.int/wikiSI/planckpla/index.php?oldid=7132 *Contributors*: Agregori, Gmorgant, Lmendes

LFI Annexes *Source*: http://www.sciops.esa.int/wikiSI/planckpla/index.php?oldid=7171 *Contributors*: Agregori, Lmendes

Ground Segment and Operations *Source*: http://www.sciops.esa.int/wikiSI/planckpla/index.php?oldid=7234 *Contributors*: Lmendes, Xdupac

Operational history *Source*: http://www.sciops.esa.int/wikiSI/planckpla/index.php?oldid=4236 *Contributors*: Lmendes, Rleonard

Survey scanning and performance *Source*: http://www.sciops.esa.int/wikiSI/planckpla/index.php?oldid=7240 *Contributors*: Lmendes, Xdupac

Thermal environment *Source*: http://www.sciops.esa.int/wikiSI/planckpla/index.php?oldid=4238 *Contributors*: Lmendes, Rleonard

Radiation environment *Source*: http://www.sciops.esa.int/wikiSI/planckpla/index.php?oldid=7368 *Contributors*: Lmendes

Pointing performance *Source*: http://www.sciops.esa.int/wikiSI/planckpla/index.php?oldid=7475 *Contributors*: Lmendes, Xdupac

Data flow overview *Source*: http://www.sciops.esa.int/wikiSI/planckpla/index.php?oldid=7092 *Contributors*: Lmendes, Rleonard

MOC data transfer and storage *Source*: http://www.sciops.esa.int/wikiSI/planckpla/index.php?oldid=7093 *Contributors*: Lmendes, Rleonard

The HFI DPC *Source*: http://www.sciops.esa.int/wikiSI/planckpla/index.php?oldid=7137 *Contributors*: Amoneti, Fbouchet, Fdesert, Jhaissin, Kganga, Lmendes, Lspencer, Lvibert

Pre-processing *Source*: http://www.sciops.esa.int/wikiSI/planckpla/index.php?oldid=7141 *Contributors*: Amoneti, Jhaissin, Lmendes, Lvibert

TOI processing *Source*: http://www.sciops.esa.int/wikiSI/planckpla/index.php?oldid=7142 *Contributors*: Acoulais, Amoneti, Crenault, Fdesert, Jhaissin, Jlamarre, Lmendes, Lsanselm, Lvibert

Detector pointing *Source*: http://www.sciops.esa.int/wikiSI/planckpla/index.php?oldid=7143 *Contributors*: Lmendes, Lvibert

Beams *Source*: http://www.sciops.esa.int/wikiSI/planckpla/index.php?oldid=7144 *Contributors*: Ajaffe, Lmendes, Lvibert

Map-making and photometric calibration *Source*: http://www.sciops.esa.int/wikiSI/planckpla/index.php?oldid=7145 *Contributors*: Amoneti, Fdesert, Kganga, Lmendes, Lvibert, Operdere, Xdupac

Spectral response *Source*: http://www.sciops.esa.int/wikiSI/planckpla/index.php?oldid=7146 *Contributors*: Amoneti, Lmendes, Lspencer

Internal overall validation *Source*: http://www.sciops.esa.int/wikiSI/planckpla/index.php?oldid=7147 *Contributors*: Acoulais, Fbouchet, Kganga, Lmendes, Lmontier, Lvibert, Stechene

Power spectra *Source*: http://www.sciops.esa.int/wikiSI/planckpla/index.php?oldid=7148 *Contributors*: Ehivon, Fbouchet, Lmendes, Lvibert

Summary of HFI data characteristics *Source*: http://www.sciops.esa.int/wikiSI/planckpla/index.php?oldid=7149 *Contributors*: Ajaffe, Lmendes, Lvibert

The LFI DPC *Source*: http://www.sciops.esa.int/wikiSI/planckpla/index.php?oldid=7154 *Contributors*: Agregori, Azacchei, Lmendes

Pre-processing *Source*: http://www.sciops.esa.int/wikiSI/planckpla/index.php?oldid=7153 *Contributors*: Agregori, Lmendes, Mfrailis

TOI processing *Source*: http://www.sciops.esa.int/wikiSI/planckpla/index.php?oldid=7155 *Contributors*: Agregori, Lmendes, Pleahy, Pmeinhol, Sgaleott

Detector pointing *Source*: http://www.sciops.esa.int/wikiSI/planckpla/index.php?oldid=7156 *Contributors*: Agregori, Lmendes, Sgaleott

Beams *Source*: http://www.sciops.esa.int/wikiSI/planckpla/index.php?oldid=7561 *Contributors*: Agregori, Fvilla, Grocha, Lmendes

Map-making LFI *Source*: http://www.sciops.esa.int/wikiSI/planckpla/index.php?oldid=7563 *Contributors*: Agregori, Assirvio, Azacchei, Ekeihane, Hkurkis, Jvalivii, Lmendes

Systematic effect uncertainties *Source*: http://www.sciops.esa.int/wikiSI/planckpla/index.php?oldid=7159 *Contributors*: Agregori, Lmendes

Internal overall validation *Source*: http://www.sciops.esa.int/wikiSI/planckpla/index.php?oldid=7160 *Contributors*: Agregori, Dmaino, Lmendes

Power spectra *Source*: http://www.sciops.esa.int/wikiSI/planckpla/index.php?oldid=7161 *Contributors*: Agregori, Lmendes

Summary of LFI data characteristics *Source*: http://www.sciops.esa.int/wikiSI/planckpla/index.php?oldid=7270 *Contributors*: Agregori, Lmendes

HFI/LFI joint data processing *Source*: http://www.sciops.esa.int/wikiSI/planckpla/index.php?oldid=7165 *Contributors*: Agregori, Amoneti, Fbouchet, Joagonza, Lmendes

Compact Source catalogues *Source*: http://www.sciops.esa.int/wikiSI/planckpla/index.php?oldid=7167 *Contributors*: Agregori, Joagonza, Lmendes, Mashdown

Astrophysical component separation *Source*: http://www.sciops.esa.int/wikiSI/planckpla/index.php?oldid=7223 *Contributors*: Agregori, Jcardoso, Lmendes, Lvibert, Mashdown

Mission products *Source*: http://www.sciops.esa.int/wikiSI/planckpla/index.php?oldid=7211 *Contributors*: Amoneti, Lmendes

Timelines *Source*: http://www.sciops.esa.int/wikiSI/planckpla/index.php?oldid=7381 *Contributors*: Amoneti, Lmendes

Sky temperature maps *Source*: http://www.sciops.esa.int/wikiSI/planckpla/index.php?oldid=7568 *Contributors*: Acoulais, Agregori, Amoneti, Assirvio, Azacchei, Crenault, Ekeihane, Fdesert, Jlamarre, Lmendes, Lvibert, Operdere, Xdupac

The instrument model *Source*: http://www.sciops.esa.int/wikiSI/planckpla/index.php?oldid=7264 *Contributors*: Agregori, Amoneti, Ehivon, Lmendes, Lspencer, Lvibert

Effective Beams *Source*: http://www.sciops.esa.int/wikiSI/planckpla/index.php?oldid=7204 *Contributors*: Agregori, Ajaffe, Amoneti, Grocha, Lmendes, Lvibert, Xdupac

Catalogues *Source*: http://www.sciops.esa.int/wikiSI/planckpla/index.php?oldid=7180 *Contributors*: Acoulais, Agregori, Amoneti, Joagonza, Lmendes, Lvibert, Mashdown, Xdupac

Sky temperature power spectra *Source*: http://www.sciops.esa.int/wikiSI/planckpla/index.php?oldid=7276 *Contributors*: Agregori, Amoneti, Ehivon, Fbouchet, Gpolenta, Lmendes

CMB and astrophysical component maps *Source*: http://www.sciops.esa.int/wikiSI/planckpla/index.php?oldid=7504 *Contributors*: Agregori, Amoneti, Lmendes, Lvibert

CMB spectrum and likelihood code *Source*: http://www.sciops.esa.int/wikiSI/planckpla/index.php?oldid=7287 *Contributors*: Agregori, Amoneti, Fbouchet, Kbenabed, Lmendes, Mfreschi, Mmigliac, Xdupac

Cosmological Parameters *Source*: http://www.sciops.esa.int/wikiSI/planckpla/index.php?oldid=7484 *Contributors*: Agregori, Alewis, Amoneti, Lmendes, Lvibert, Xdupac

Additional maps *Source*: http://www.sciops.esa.int/wikiSI/planckpla/index.php?oldid=7316 *Contributors*: Agregori, Amoneti, Dhanson, Lmendes

Scientific data used to generate Planck products *Source*: http://www.sciops.esa.int/wikiSI/planckpla/index.php?oldid=7382 *Contributors*: Lmendes

Simulation data *Source*: http://www.sciops.esa.int/wikiSI/planckpla/index.php?oldid=7384 *Contributors*: Agregori, Amoneti, Jborrill, Jdelabro, Lmendes

Software utilities *Source*: http://www.sciops.esa.int/wikiSI/planckpla/index.php?oldid=7209 *Contributors*: Amoneti, Lmendes, Lspencer, Mpeel, Xdupac

Unit conversion and Color correction *Source*: http://www.sciops.esa.int/wikiSI/planckpla/index.php?oldid=7208 *Contributors*: Acoulais, Amoneti, Lmendes, Lvibert

Survey and satellite data *Source*: http://www.sciops.esa.int/wikiSI/planckpla/index.php?oldid=7385 *Contributors*: Lmendes

Survey history *Source*: http://www.sciops.esa.int/wikiSI/planckpla/index.php?oldid=7345 *Contributors*: Lmendes, Rleonard, Xdupac

Satellite history *Source*: http://www.sciops.esa.int/wikiSI/planckpla/index.php?oldid=7387 *Contributors*: Lmendes, Xdupac

SREM *Source*: http://www.sciops.esa.int/wikiSI/planckpla/index.php?oldid=7541 *Contributors*: Lmendes, Xdupac

Appendix *Source*: http://www.sciops.esa.int/wikiSI/planckpla/index.php?oldid=7221 *Contributors*: Lmendes, Lspencer

Glossary *Source*: http://www.sciops.esa.int/wikiSI/planckpla/index.php?oldid=7200 *Contributors*: Agregori, Bcrill, Lmendes, Lvibert, Rleonard

List of acronyms *Source*: http://www.sciops.esa.int/wikiSI/planckpla/index.php?oldid=7378 *Contributors*: Agregori, Jhaissin, Lmendes, Lvibert, Xdupac

Image Sources, Licenses and Contributors

file:Planck_Logos.jpg *Source*: http://www.sciops.esa.int/wikiSI/planckpla/index.php?title=File:Planck_Logos.jpg *License*: unknown *Contributors*: Rleonard

file:PlanckMissionTimeline.JPG *Source*: http://www.sciops.esa.int/wikiSI/planckpla/index.php?title=File:PlanckMissionTimeline.JPG *License*: unknown *Contributors*: Xdupac

file:HerschelPlanckLaunch.jpg *Source*: http://www.sciops.esa.int/wikiSI/planckpla/index.php?title=File:HerschelPlanckLaunch.jpg *License*: unknown *Contributors*: Xdupac

file:PLANCK_HERSCHEL_LAUNCH.jpg *Source*: http://www.sciops.esa.int/wikiSI/planckpla/index.php?title=File:PLANCK_HERSCHEL_LAUNCH.jpg *License*: unknown *Contributors*: Xdupac

file:Cooldown.jpg *Source*: http://www.sciops.esa.int/wikiSI/planckpla/index.php?title=File:Cooldown.jpg *License*: unknown *Contributors*: Xdupac

File:381-Herschel_reflection_in_Primary_Reflector_H.jpg *Source*: http://www.sciops.esa.int/wikiSI/planckpla/index.php?title=File:381-Herschel_reflection_in_Primary_Reflector_H.jpg *License*: unknown *Contributors*: Rleonard

Image:HFI_horns.jpg *Source*: http://www.sciops.esa.int/wikiSI/planckpla/index.php?title=File:HFI_horns.jpg *License*: unknown *Contributors*: Lvibert

Image:HFI_2_4_1_JML_SignalFormation.png *Source*: http://www.sciops.esa.int/wikiSI/planckpla/index.php?title=File:HFI_2_4_1_JML_SignalFormation.png *License*: unknown *Contributors*: Acoulais

Image:HFI_2_4_1_overal_cryo.jpg *Source*: http://www.sciops.esa.int/wikiSI/planckpla/index.php?title=File:HFI_2_4_1_overal_cryo.jpg *License*: unknown *Contributors*: Fpajot

Image:HFI_2_4_1_JML_FeedHorns.png *Source*: http://www.sciops.esa.int/wikiSI/planckpla/index.php?title=File:HFI_2_4_1_JML_FeedHorns.png *License*: unknown *Contributors*: Acoulais

Image:HFI_2_4_1_JML_PowerDiff.png *Source*: http://www.sciops.esa.int/wikiSI/planckpla/index.php?title=File:HFI_2_4_1_JML_PowerDiff.png *License*: unknown *Contributors*: Acoulais

Image:HFI_2_4_1_JML_FarField.png *Source*: http://www.sciops.esa.int/wikiSI/planckpla/index.php?title=File:HFI_2_4_1_JML_FarField.png *License*: unknown *Contributors*: Acoulais

Image:HFI_2_4_1_JML_FarField2.png *Source*: http://www.sciops.esa.int/wikiSI/planckpla/index.php?title=File:HFI_2_4_1_JML_FarField2.png *License*: unknown *Contributors*: Acoulais

File:HFI_FilterPlots_100GHz.png *Source*: http://www.sciops.esa.int/wikiSI/planckpla/index.php?title=File:HFI_FilterPlots_100GHz.png *License*: unknown *Contributors*: Lspencer

File:HFI_FilterPlots_143GHz.png *Source*: http://www.sciops.esa.int/wikiSI/planckpla/index.php?title=File:HFI_FilterPlots_143GHz.png *License*: unknown *Contributors*: Lspencer

File:HFI_FilterPlots_217GHz.png *Source*: http://www.sciops.esa.int/wikiSI/planckpla/index.php?title=File:HFI_FilterPlots_217GHz.png *License*: unknown *Contributors*: Lspencer

File:HFI_FilterPlots_353GHz.png *Source*: http://www.sciops.esa.int/wikiSI/planckpla/index.php?title=File:HFI_FilterPlots_353GHz.png *License*: unknown *Contributors*: Lspencer

File:HFI_FilterPlots_545GHz.png *Source*: http://www.sciops.esa.int/wikiSI/planckpla/index.php?title=File:HFI_FilterPlots_545GHz.png *License*: unknown *Contributors*: Lspencer

File:HFI_FilterPlots_857GHz.png *Source*: http://www.sciops.esa.int/wikiSI/planckpla/index.php?title=File:HFI_FilterPlots_857GHz.png *License*: unknown *Contributors*: Lspencer

Image:OOBstitch_bc00_Prad_Apod5_v302_sm.png *Source*: http://www.sciops.esa.int/wikiSI/planckpla/index.php?title=File:OOBstitch_bc00_Prad_Apod5_v302_sm.png *License*: unknown *Contributors*: Lspencer

Image:COflags_v300_sm.png *Source*: http://www.sciops.esa.int/wikiSI/planckpla/index.php?title=File:COflags_v300_sm.png *License*: unknown *Contributors*: Lspencer

Image:COJ10_HFI100_SpecTrans_v300_Apod5_sm.png *Source*: http://www.sciops.esa.int/wikiSI/planckpla/index.php?title=File:COJ10_HFI100_SpecTrans_v300_Apod5_sm.png *License*: unknown *Contributors*: Lspencer

Image:HFI_2_4_1_FPiacentini_bolo1.png *Source*: http://www.sciops.esa.int/wikiSI/planckpla/index.php?title=File:HFI_2_4_1_FPiacentini_bolo1.png *License*: unknown *Contributors*: -

Image:HFI_2_4_1_FPiacentini_bolo2.png *Source*: http://www.sciops.esa.int/wikiSI/planckpla/index.php?title=File:HFI_2_4_1_FPiacentini_bolo2.png *License*: unknown *Contributors*: Acoulais

Image:HFI_2_4_1_FPiacentini_table1.png *Source*: http://www.sciops.esa.int/wikiSI/planckpla/index.php?title=File:HFI_2_4_1_FPiacentini_table1.png *License*: unknown *Contributors*: Acoulais

Image:HFI_2_4_1_FPiacentini_FocalPlaneGeo.png *Source*: http://www.sciops.esa.int/wikiSI/planckpla/index.php?title=File:HFI_2_4_1_FPiacentini_FocalPlaneGeo.png *License*: unknown *Contributors*: Acoulais

Image:HFI_2_4_1_FPiacentini_table2.jpeg *Source*: http://www.sciops.esa.int/wikiSI/planckpla/index.php?title=File:HFI_2_4_1_FPiacentini_table2.jpeg *License*: unknown *Contributors*: Acoulais

File:BREF_LowF_Apod5_avgSpec_SN_sm.png *Source*: http://www.sciops.esa.int/wikiSI/planckpla/index.php?title=File:BREF_LowF_Apod5_avgSpec_SN_sm.png *License*: unknown *Contributors*: Lspencer

File:BREF_HighF_Apod5_avgSpec_SN_sm.png *Source*: http://www.sciops.esa.int/wikiSI/planckpla/index.php?title=File:BREF_HighF_Apod5_avgSpec_SN_sm.png *License*: unknown *Contributors*: Lspencer

File:Bref_LowF_HighF_SN_sm.png *Source*: http://www.sciops.esa.int/wikiSI/planckpla/index.php?title=File:Bref_LowF_HighF_SN_sm.png *License*: unknown *Contributors*: Lspencer

File:BREF_LowF_Apod5_avgSpec_SN_100_sm.png *Source*: http://www.sciops.esa.int/wikiSI/planckpla/index.php?title=File:BREF_LowF_Apod5_avgSpec_SN_100_sm.png *License*: unknown *Contributors*: Lspencer

File:BREF_LowF_Apod5_avgSpec_SN_143_sm.png *Source*: http://www.sciops.esa.int/wikiSI/planckpla/index.php?title=File:BREF_LowF_Apod5_avgSpec_SN_143_sm.png *License*: unknown *Contributors*: Lspencer

File:BREF_LowF_Apod5_avgSpec_SN_217_sm.png *Source*: http://www.sciops.esa.int/wikiSI/planckpla/index.php?title=File:BREF_LowF_Apod5_avgSpec_SN_217_sm.png *License*: unknown *Contributors*: Lspencer

File:BREF_HighF_Apod5_avgSpec_SN_353_sm.png *Source*: http://www.sciops.esa.int/wikiSI/planckpla/index.php?title=File:BREF_HighF_Apod5_avgSpec_SN_353_sm.png *License*: unknown *Contributors*: Lspencer

File:BREF_HighF_Apod5_avgSpec_SN_545_sm.png *Source*: http://www.sciops.esa.int/wikiSI/planckpla/index.php?title=File:BREF_HighF_Apod5_avgSpec_SN_545_sm.png *License*: unknown *Contributors*: Lspencer

File:BREF_HighF_Apod5_avgSpec_SN_857_sm.png *Source*: http://www.sciops.esa.int/wikiSI/planckpla/index.php?title=File:BREF_HighF_Apod5_avgSpec_SN_857_sm.png *License*: unknown *Contributors*: Lspencer

Image:SNall_sm.png *Source*: http://www.sciops.esa.int/wikiSI/planckpla/index.php?title=File:SNall_sm.png *License*: unknown *Contributors*: Lspencer

Image:setting.png *Source*: http://www.sciops.esa.int/wikiSI/planckpla/index.php?title=File:Setting.png *License*: unknown *Contributors*: Splaszcz

Image:cl_DPU_217unlensed.png *Source*: http://www.sciops.esa.int/wikiSI/planckpla/index.php?title=File:Cl_DPU_217unlensed.png *License*: unknown *Contributors*: Splaszcz

File:lfi_instrument.jpg *Source*: http://www.sciops.esa.int/wikiSI/planckpla/index.php?title=File:Lfi_instrument.jpg *License*: unknown *Contributors*: Agregori

File:LFI_schema.jpg *Source*: http://www.sciops.esa.int/wikiSI/planckpla/index.php?title=File:LFI_schema.jpg *License*: unknown *Contributors*: Agregori

File:schema.jpg *Source*: http://www.sciops.esa.int/wikiSI/planckpla/index.php?title=File:Schema.jpg *License*: unknown *Contributors*: Agregori

File:rca_schematic.jpg *Source*: http://www.sciops.esa.int/wikiSI/planckpla/index.php?title=File:Rca_schematic.jpg *License*: unknown *Contributors*: Agregori

File:phase_switch_operation.jpg *Source*: http://www.sciops.esa.int/wikiSI/planckpla/index.php?title=File:Phase_switch_operation.jpg *License*: unknown *Contributors*: Agregori

File:FUNCT_tests_schedule_vs_K-eps-converted-to.jpg *Source*: http://www.sciops.esa.int/wikiSI/planckpla/index.php?title=File:FUNCT_tests_schedule_vs_K-eps-converted-to.jpg *License*: unknown *Contributors*: Agregori

File:SCS_CAD_Figure.jpg *Source*: http://www.sciops.esa.int/wikiSI/planckpla/index.php?title=File:SCS_CAD_Figure.jpg *License*: unknown *Contributors*: Gmorgant

File:TSA_LVHX2_mission.jpg *Source*: http://www.sciops.esa.int/wikiSI/planckpla/index.php?title=File:TSA_LVHX2_mission.jpg *License*: unknown *Contributors*: Gmorgant

File:fh1.jpg *Source*: http://www.sciops.esa.int/wikiSI/planckpla/index.php?title=File:Fh1.jpg *License*: unknown *Contributors*: Agregori

File:fh2.jpg *Source*: http://www.sciops.esa.int/wikiSI/planckpla/index.php?title=File:Fh2.jpg *License*: unknown *Contributors*: Agregori

File:omt.jpg *Source*: http://www.sciops.esa.int/wikiSI/planckpla/index.php?title=File:Omt.jpg *License*: unknown *Contributors*: Agregori

File:fem1.jpg *Source*: http://www.sciops.esa.int/wikiSI/planckpla/index.php?title=File:Fem1.jpg *License*: unknown *Contributors*: Agregori

File:fembem70.jpg *Source*: http://www.sciops.esa.int/wikiSI/planckpla/index.php?title=File:Fembem70.jpg *License*: unknown *Contributors*: Agregori

File:bem1.jpg *Source*: http://www.sciops.esa.int/wikiSI/planckpla/index.php?title=File:Bem1.jpg *License*: unknown *Contributors*: Agregori

File:bem2.jpg *Source*: http://www.sciops.esa.int/wikiSI/planckpla/index.php?title=File:Bem2.jpg *License*: unknown *Contributors*: Agregori

File:4krl.jpg *Source*: http://www.sciops.esa.int/wikiSI/planckpla/index.php?title=File:4krl.jpg *License*: unknown *Contributors*: Agregori

File:4kload.jpg *Source*: http://www.sciops.esa.int/wikiSI/planckpla/index.php?title=File:4kload.jpg *License*: unknown *Contributors*: Agregori

File:4krl_t.jpg *Source*: http://www.sciops.esa.int/wikiSI/planckpla/index.php?title=File:4krl_t.jpg *License*: unknown *Contributors*: Agregori

File:OBS.jpg *Source*: http://www.sciops.esa.int/wikiSI/planckpla/index.php?title=File:OBS.jpg *License*: unknown *Contributors*: Agregori

File:compression.jpg *Source*: http://www.sciops.esa.int/wikiSI/planckpla/index.php?title=File:Compression.jpg *License*: unknown *Contributors*: Agregori

File:compr1.jpg *Source*: http://www.sciops.esa.int/wikiSI/planckpla/index.php?title=File:Compr1.jpg *License*: unknown *Contributors*: Agregori

File:compr2.jpg *Source*: http://www.sciops.esa.int/wikiSI/planckpla/index.php?title=File:Compr2.jpg *License*: unknown *Contributors*: Agregori

File:LFI_OpsMode.jpg *Source*: http://www.sciops.esa.int/wikiSI/planckpla/index.php?title=File:LFI_OpsMode.jpg *License*: unknown *Contributors*: Agregori

File:LFIfreq.jpg *Source*: http://www.sciops.esa.int/wikiSI/planckpla/index.php?title=File:LFIfreq.jpg *License*: unknown *Contributors*: Agregori

File:Colorcorr.jpg *Source*: http://www.sciops.esa.int/wikiSI/planckpla/index.php?title=File:Colorcorr.jpg *License*: unknown *Contributors*: Agregori

File:band1.jpg *Source*: http://www.sciops.esa.int/wikiSI/planckpla/index.php?title=File:Band1.jpg *License*: unknown *Contributors*: Agregori

File:band2.jpg *Source*: http://www.sciops.esa.int/wikiSI/planckpla/index.php?title=File:Band2.jpg *License*: unknown *Contributors*: Agregori

File:stability.jpg *Source*: http://www.sciops.esa.int/wikiSI/planckpla/index.php?title=File:Stability.jpg *License*: unknown *Contributors*: Agregori

File:Sensor_position.jpg *Source*: http://www.sciops.esa.int/wikiSI/planckpla/index.php?title=File:Sensor_position.jpg *License*: unknown *Contributors*: Agregori

File:Din_t1.jpg *Source*: http://www.sciops.esa.int/wikiSI/planckpla/index.php?title=File:Din_t1.jpg *License*: unknown *Contributors*: Agregori

File:Susc_t.jpg *Source*: http://www.sciops.esa.int/wikiSI/planckpla/index.php?title=File:Susc_t.jpg *License*: unknown *Contributors*: Agregori

file:ESOC.jpg *Source*: http://www.sciops.esa.int/wikiSI/planckpla/index.php?title=File:ESOC.jpg *License*: unknown *Contributors*: Xdupac

file:ESAC_6.JPG *Source*: http://www.sciops.esa.int/wikiSI/planckpla/index.php?title=File:ESAC_6.JPG *License*: unknown *Contributors*: Xdupac

file:GS.jpg *Source*: http://www.sciops.esa.int/wikiSI/planckpla/index.php?title=File:GS.jpg *License*: unknown *Contributors*: Xdupac

file:GSPlanck.JPG *Source*: http://www.sciops.esa.int/wikiSI/planckpla/index.php?title=File:GSPlanck.JPG *License*: unknown *Contributors*: Xdupac

file:FocalPlane.png *Source*: http://www.sciops.esa.int/wikiSI/planckpla/index.php?title=File:FocalPlane.png *License*: unknown *Contributors*: Rleonard

File:ScannStrategy.png *Source*: http://www.sciops.esa.int/wikiSI/planckpla/index.php?title=File:ScannStrategy.png *License*: unknown *Contributors*: Xdupac

File:Cycloidal_scanning.JPG *Source*: http://www.sciops.esa.int/wikiSI/planckpla/index.php?title=File:Cycloidal_scanning.JPG *License*: unknown *Contributors*: Xdupac

File:Crab_Nebula.jpg *Source*: http://www.sciops.esa.int/wikiSI/planckpla/index.php?title=File:Crab_Nebula.jpg *License*: unknown *Contributors*: Xdupac

File:Mars.jpg *Source*: http://www.sciops.esa.int/wikiSI/planckpla/index.php?title=File:Mars.jpg *License*: unknown *Contributors*: Xdupac

File:PlanckMissionTimeline.JPG *Source*: http://www.sciops.esa.int/wikiSI/planckpla/index.php?title=File:PlanckMissionTimeline.JPG *License*: unknown *Contributors*: Xdupac

File:PointingPerformance2011.JPG *Source*: http://www.sciops.esa.int/wikiSI/planckpla/index.php?title=File:PointingPerformance2011.JPG *License*: unknown *Contributors*: Xdupac

file:PointingPerformance2011latitude.JPG *Source*: http://www.sciops.esa.int/wikiSI/planckpla/index.php?title=File:PointingPerformance2011latitude.JPG *License*: unknown *Contributors*: Xdupac

file:PointingPerformanceCorrelation.jpg *Source*: http://www.sciops.esa.int/wikiSI/planckpla/index.php?title=File:PointingPerformanceCorrelation.jpg *License*: unknown *Contributors*: Xdupac

File:GroundSegment.png *Source*: http://www.sciops.esa.int/wikiSI/planckpla/index.php?title=File:GroundSegment.png *License*: unknown *Contributors*: Rleonard

File:HFI_4_4_1_deltatos.png *Source*: http://www.sciops.esa.int/wikiSI/planckpla/index.php?title=File:HFI_4_4_1_deltatos.png *License*: unknown *Contributors*: Lvibert

File:HFI_4_4_1_deltatoszoom.png *Source*: http://www.sciops.esa.int/wikiSI/planckpla/index.php?title=File:HFI_4_4_1_deltatoszoom.png *License*: unknown *Contributors*: Lvibert

File:HFI_4_4_1_ringduration.png *Source*: http://www.sciops.esa.int/wikiSI/planckpla/index.php?title=File:HFI_4_4_1_ringduration.png *License*: unknown *Contributors*: Lvibert

File:HFI_4_4_1_OBTUTC.png *Source*: http://www.sciops.esa.int/wikiSI/planckpla/index.php?title=File:HFI_4_4_1_OBTUTC.png *License*: unknown *Contributors*: Lvibert

File:10_143_5_PBR_10800RING_LFER4_JC.jpg *Source*: http://www.sciops.esa.int/wikiSI/planckpla/index.php?title=File:10_143_5_PBR_10800RING_LFER4_JC.jpg *License*: unknown *Contributors*: Fdesert

File:10_143_5_rcircles_LFER4_JC.jpg *Source*: http://www.sciops.esa.int/wikiSI/planckpla/index.php?title=File:10_143_5_rcircles_LFER4_JC.jpg *License*: unknown *Contributors*: Fdesert

File:10_143_5_fft_LFER4_JC.jpg *Source*: http://www.sciops.esa.int/wikiSI/planckpla/index.php?title=File:10_143_5_fft_LFER4_JC.jpg *License*: unknown *Contributors*: Fdesert

File:14_545_1_PBR_10800RING_LFER4_JC.jpg *Source*: http://www.sciops.esa.int/wikiSI/planckpla/index.php?title=File:14_545_1_PBR_10800RING_LFER4_JC.jpg *License*: unknown *Contributors*: Fdesert

File:14_545_1_rcircles_LFER4_JC.jpg *Source*: http://www.sciops.esa.int/wikiSI/planckpla/index.php?title=File:14_545_1_rcircles_LFER4_JC.jpg *License*: unknown *Contributors*: Fdesert

File:14_545_1_fft_LFER4_JC.jpg *Source*: http://www.sciops.esa.int/wikiSI/planckpla/index.php?title=File:14_545_1_fft_LFER4_JC.jpg *License*: unknown *Contributors*: Fdesert

File:baseline.jpg *Source*: http://www.sciops.esa.int/wikiSI/planckpla/index.php?title=File:Baseline.jpg *License*: unknown *Contributors*: Fdesert

File:figIntermPaperGR.jpg *Source*: http://www.sciops.esa.int/wikiSI/planckpla/index.php?title=File:FigIntermPaperGR.jpg *License*: unknown *Contributors*: Fdesert

File:group10_143_5.jpg *Source*: http://www.sciops.esa.int/wikiSI/planckpla/index.php?title=File:Group10_143_5.jpg *License*: unknown *Contributors*: Fdesert

File:group14_545_1.jpg *Source*: http://www.sciops.esa.int/wikiSI/planckpla/index.php?title=File:Group14_545_1.jpg *License*: unknown *Contributors*: Fdesert

File:T90.jpg *Source*: http://www.sciops.esa.int/wikiSI/planckpla/index.php?title=File:T90.jpg *License*: unknown *Contributors*: Fdesert

File:10_143_5_4Klines.jpg *Source*: http://www.sciops.esa.int/wikiSI/planckpla/index.php?title=File:10_143_5_4Klines.jpg *License*: unknown *Contributors*: Fdesert

File:14_545_1_4Klines.jpg *Source*: http://www.sciops.esa.int/wikiSI/planckpla/index.php?title=File:14_545_1_4Klines.jpg *License*: unknown *Contributors*: Fdesert

File:spinfreq1.jpg *Source*: http://www.sciops.esa.int/wikiSI/planckpla/index.php?title=File:Spinfreq1.jpg *License*: unknown *Contributors*: Fdesert

File:jump_exe.png *Source*: http://www.sciops.esa.int/wikiSI/planckpla/index.php?title=File:Jump_exe.png *License*: unknown *Contributors*: Fdesert

File:10_143_5_smooth_Watt.jpg *Source*: http://www.sciops.esa.int/wikiSI/planckpla/index.php?title=File:10_143_5_smooth_Watt.jpg *License*: unknown *Contributors*: Fdesert

File:14_545_1_smooth_Watt.jpg *Source*: http://www.sciops.esa.int/wikiSI/planckpla/index.php?title=File:14_545_1_smooth_Watt.jpg *License*: unknown *Contributors*: Fdesert

File:stddev_group10_143_5.jpg *Source*: http://www.sciops.esa.int/wikiSI/planckpla/index.php?title=File:Stddev_group10_143_5.jpg *License*: unknown *Contributors*: Fdesert

File:stddev_group_14_545_1.jpg *Source*: http://www.sciops.esa.int/wikiSI/planckpla/index.php?title=File:Stddev_group_14_545_1.jpg *License*: unknown *Contributors*: Fdesert

File:23_353_TwoLevel.jpg *Source*: http://www.sciops.esa.int/wikiSI/planckpla/index.php?title=File:23_353_TwoLevel.jpg *License*: unknown *Contributors*: Fdesert

File:HFI_4_4_2_RTSexample13.jpg *Source*: http://www.sciops.esa.int/wikiSI/planckpla/index.php?title=File:HFI_4_4_2_RTSexample13.jpg *License*: unknown *Contributors*: Fdesert

File:HFInominal_IntegrationTime.jpg *Source*: http://www.sciops.esa.int/wikiSI/planckpla/index.php?title=File:HFInominal_IntegrationTime.jpg *License*: unknown *Contributors*: Fdesert

File:SSOflag_10_143_5J.png *Source*: http://www.sciops.esa.int/wikiSI/planckpla/index.php?title=File:SSOflag_10_143_5J.png *License*: unknown *Contributors*: Crenault

File:SSOflag_10_143_5S.png *Source*: http://www.sciops.esa.int/wikiSI/planckpla/index.php?title=File:SSOflag_10_143_5S.png *License*: unknown *Contributors*: Crenault

File:SSOflag_10_143_5M.png *Source*: http://www.sciops.esa.int/wikiSI/planckpla/index.php?title=File:SSOflag_10_143_5M.png *License*: unknown *Contributors*: Crenault

File:SSOflag_10_143_5a.png *Source*: http://www.sciops.esa.int/wikiSI/planckpla/index.php?title=File:SSOflag_10_143_5a.png *License*: unknown *Contributors*: Crenault

File:SSOflag_25_857_1J.png *Source*: http://www.sciops.esa.int/wikiSI/planckpla/index.php?title=File:SSOflag_25_857_1J.png *License*: unknown *Contributors*: Crenault

File:SSOflag_25_857_1S.png *Source*: http://www.sciops.esa.int/wikiSI/planckpla/index.php?title=File:SSOflag_25_857_1S.png *License*: unknown *Contributors*: Crenault

File:SSOflag_25_857_1M.png *Source*: http://www.sciops.esa.int/wikiSI/planckpla/index.php?title=File:SSOflag_25_857_1M.png *License*: unknown *Contributors*: Crenault

File:SSOflag_25_857_1a.png *Source*: http://www.sciops.esa.int/wikiSI/planckpla/index.php?title=File:SSOflag_25_857_1a.png *License*: unknown *Contributors*: Crenault

Image:FocalPlane.png *Source*: http://www.sciops.esa.int/wikiSI/planckpla/index.php?title=File:FocalPlane.png *License*: unknown *Contributors*: Rleonard

Image:map-cc-HFI_Spec_Bands_180mm.png *Source*: http://www.sciops.esa.int/wikiSI/planckpla/index.php?title=File:Map-cc-HFI_Spec_Bands_180mm.png *License*: unknown *Contributors*: Lspencer

File:CheckCCcutoff_v302_nuInu2RJ_100_GHz_bc100_avg.png *Source*: http://www.sciops.esa.int/wikiSI/planckpla/index.php?title=File:CheckCCcutoff_v302_nuInu2RJ_100_GHz_bc100_avg.png *License*: unknown *Contributors*: Lspencer

File:CheckCCcutoff_v302_nuInu2RJ_143_GHz_bc143_avg.png *Source*: http://www.sciops.esa.int/wikiSI/planckpla/index.php?title=File:CheckCCcutoff_v302_nuInu2RJ_143_GHz_bc143_avg.png *License*: unknown *Contributors*: Lspencer

File:CheckCCcutoff_v302_nuInu2RJ_217_GHz_bc217_avg.png *Source*: http://www.sciops.esa.int/wikiSI/planckpla/index.php?title=File:CheckCCcutoff_v302_nuInu2RJ_217_GHz_bc217_avg.png *License*: unknown *Contributors*: Lspencer

File:CheckCCcutoff_v302_nuInu2RJ_353_GHz_bc353_avg.png *Source*: http://www.sciops.esa.int/wikiSI/planckpla/index.php?title=File:CheckCCcutoff_v302_nuInu2RJ_353_GHz_bc353_avg.png *License*: unknown *Contributors*: Lspencer

File:CheckCCcutoff_v302_nuInu2RJ_545_GHz_bc545_avg.png *Source*: http://www.sciops.esa.int/wikiSI/planckpla/index.php?title=File:CheckCCcutoff_v302_nuInu2RJ_545_GHz_bc545_avg.png *License*: unknown *Contributors*: Lspencer

File:CheckCCcutoff_v302_nuInu2RJ_857_GHz_bc857_avg.png *Source*: http://www.sciops.esa.int/wikiSI/planckpla/index.php?title=File:CheckCCcutoff_v302_nuInu2RJ_857_GHz_bc857_avg.png *License*: unknown *Contributors*: Lspencer

File:100GHz_HitMapWeights_IMO_3_16_detilt_t2_ptcor6_Sfull_Plot_88mm.png *Source*: http://www.sciops.esa.int/wikiSI/planckpla/index.php?title=File:100GHz_HitMapWeights_IMO_3_16_detilt_t2_ptcor6_Sfull_Plot_88mm.png *License*: unknown *Contributors*: Lspencer

File:143GHz_HitMapWeights_IMO_3_16_detilt_t2_ptcor6_Sfull_Plot_88mm.png *Source*: http://www.sciops.esa.int/wikiSI/planckpla/index.php?title=File:143GHz_HitMapWeights_IMO_3_16_detilt_t2_ptcor6_Sfull_Plot_88mm.png *License*: unknown *Contributors*: Lspencer

File:217GHz_HitMapWeights_IMO_3_16_detilt_t2_ptcor6_Sfull_Plot_88mm.png *Source*: http://www.sciops.esa.int/wikiSI/planckpla/index.php?title=File:217GHz_HitMapWeights_IMO_3_16_detilt_t2_ptcor6_Sfull_Plot_88mm.png *License*: unknown *Contributors*: Lspencer

File:353GHz_HitMapWeights_IMO_3_16_detilt_t2_ptcor6_Sfull_Plot_88mm.png *Source*: http://www.sciops.esa.int/wikiSI/planckpla/index.php?title=File:353GHz_HitMapWeights_IMO_3_16_detilt_t2_ptcor6_Sfull_Plot_88mm.png *License*: unknown *Contributors*: Lspencer

File:545GHz_HitMapWeights_IMO_3_16_detilt_t2_ptcor6_Sfull_Plot_88mm.png *Source*: http://www.sciops.esa.int/wikiSI/planckpla/index.php?title=File:545GHz_HitMapWeights_IMO_3_16_detilt_t2_ptcor6_Sfull_Plot_88mm.png *License*: unknown *Contributors*: Lspencer

File:857GHz_HitMapWeights_IMO_3_16_detilt_t2_ptcor6_Sfull_Plot_88mm.png *Source*: http://www.sciops.esa.int/wikiSI/planckpla/index.php?title=File:857GHz_HitMapWeights_IMO_3_16_detilt_t2_ptcor6_Sfull_Plot_88mm.png *License*: unknown *Contributors*: Lspencer

File:DX9_Y3_consistency.png *Source*: http://www.sciops.esa.int/wikiSI/planckpla/index.php?title=File:DX9_Y3_consistency.png *License*: unknown *Contributors*: Stechene

Image:Glitch_PowerSPectra_Expla.png *Source*: http://www.sciops.esa.int/wikiSI/planckpla/index.php?title=File:Glitch_PowerSPectra_Expla.png *License*: unknown *Contributors*: Lmontier

File:A143.png *Source*: http://www.sciops.esa.int/wikiSI/planckpla/index.php?title=File:A143.png *License*: unknown *Contributors*: Ehivon

File:A217.png *Source*: http://www.sciops.esa.int/wikiSI/planckpla/index.php?title=File:A217.png *License*: unknown *Contributors*: Ehivon

File:PlanckFocalPlane.png *Source*: http://www.sciops.esa.int/wikiSI/planckpla/index.php?title=File:PlanckFocalPlane.png *License*: unknown *Contributors*: Grocha

File:slb_lfi_30_27_y_tricromia.png *Source*: http://www.sciops.esa.int/wikiSI/planckpla/index.php?title=File:Slb_lfi_30_27_y_tricromia.png *License*: unknown *Contributors*: Fvilla

File:Comparison_Cls_NMC_WNC_JN_WNCmean_removed_nominal_nomask.png *Source*: http://www.sciops.esa.int/wikiSI/planckpla/index.php?title=File:Comparison_Cls_NMC_WNC_JN_WNCmean_removed_nominal_nomask.png *License*: unknown *Contributors*: Jvalivii

File:Comparison_Cls_NMC_WNC_JN_WNCmean_removed_survey1_nomask.png *Source*: http://www.sciops.esa.int/wikiSI/planckpla/index.php?title=File:Comparison_Cls_NMC_WNC_JN_WNCmean_removed_survey1_nomask.png *License*: unknown *Contributors*: Jvalivii

File:Comparison_Cls_NMC_WNC_JN_WNCmean_removed_survey2_nomask.png *Source*: http://www.sciops.esa.int/wikiSI/planckpla/index.php?title=File:Comparison_Cls_NMC_WNC_JN_WNCmean_removed_survey2_nomask.png *License*: unknown *Contributors*: Jvalivii

File:LFI_4_5_5_4_madam_mask_1sec_DB10_1_noise_70GHz_all_DX9delta_nom_1024outmap.00000.gif *Source*: http://www.sciops.esa.int/wikiSI/planckpla/index.php?title=File:LFI_4_5_5_4_madam_mask_1sec_DB10_1_noise_70GHz_all_DX9delta_nom_1024outmap.00000.gif *License*: unknown *Contributors*: Hkurkis

File:LFI_4_5_5_4_madam_mask_1sec_DB10_1_white_70GHz_all_DX9delta_nom_1024binmap.00000.gif *Source*: http://www.sciops.esa.int/wikiSI/planckpla/index.php?title=File:LFI_4_5_5_4_madam_mask_1sec_DB10_1_white_70GHz_all_DX9delta_nom_1024binmap.00000.gif *License*: unknown *Contributors*: Hkurkis

File:LFI_4_5_5_4_madam_mask_1sec_DB10_1_rcnoise_70GHz_all_DX9delta_nom_1024map.00000.gif *Source*: http://www.sciops.esa.int/wikiSI/planckpla/index.php?title=File:LFI_4_5_5_4_madam_mask_1sec_DB10_1_rcnoise_70GHz_all_DX9delta_nom_1024map.00000.gif *License*: unknown *Contributors*: Hkurkis

File:Systematics.jpg *Source*: http://www.sciops.esa.int/wikiSI/planckpla/index.php?title=File:Systematics.jpg *License*: unknown *Contributors*: Agregori

File:Syst2.jpg *Source*: http://www.sciops.esa.int/wikiSI/planckpla/index.php?title=File:Syst2.jpg *License*: unknown *Contributors*: Agregori

File:syst_f1.jpg *Source*: http://www.sciops.esa.int/wikiSI/planckpla/index.php?title=File:Syst_f1.jpg *License*: unknown *Contributors*: Agregori

File:syst_f2.jpg *Source*: http://www.sciops.esa.int/wikiSI/planckpla/index.php?title=File:Syst_f2.jpg *License*: unknown *Contributors*: Agregori

File:cons1.jpg *Source*: http://www.sciops.esa.int/wikiSI/planckpla/index.php?title=File:Cons1.jpg *License*: unknown *Contributors*: Agregori

File:cons2.jpg *Source*: http://www.sciops.esa.int/wikiSI/planckpla/index.php?title=File:Cons2.jpg *License*: unknown *Contributors*: Agregori

File:cons3.jpg *Source*: http://www.sciops.esa.int/wikiSI/planckpla/index.php?title=File:Cons3.jpg *License*: unknown *Contributors*: Agregori

File:LFI_TTspectra_styleguide_final.jpg *Source*: http://www.sciops.esa.int/wikiSI/planckpla/index.php?title=File:LFI_TTspectra_styleguide_final.jpg *License*: unknown *Contributors*: Agregori

File:tab_perf2.jpg *Source*: http://www.sciops.esa.int/wikiSI/planckpla/index.php?title=File:Tab_perf2.jpg *License*: unknown *Contributors*: Agregori

File:smica.jpg *Source*: http://www.sciops.esa.int/wikiSI/planckpla/index.php?title=File:Smica.jpg *License*: unknown *Contributors*: Agregori

File: SkyMap30.png *Source*: http://www.sciops.esa.int/wikiSI/planckpla/index.php?title=File:SkyMap30.png *License*: unknown *Contributors*: Amoneti

File: SkyMap44.png *Source*: http://www.sciops.esa.int/wikiSI/planckpla/index.php?title=File:SkyMap44.png *License*: unknown *Contributors*: Amoneti

File: SkyMap70.png *Source*: http://www.sciops.esa.int/wikiSI/planckpla/index.php?title=File:SkyMap70.png *License*: unknown *Contributors*: Amoneti

File: SkyMap100.png *Source*: http://www.sciops.esa.int/wikiSI/planckpla/index.php?title=File:SkyMap100.png *License*: unknown *Contributors*: Amoneti

File: SkyMap143.png *Source*: http://www.sciops.esa.int/wikiSI/planckpla/index.php?title=File:SkyMap143.png *License*: unknown *Contributors*: Amoneti

File: SkyMap217.png *Source*: http://www.sciops.esa.int/wikiSI/planckpla/index.php?title=File:SkyMap217.png *License*: unknown *Contributors*: Amoneti

File: SkyMap353.png *Source*: http://www.sciops.esa.int/wikiSI/planckpla/index.php?title=File:SkyMap353.png *License*: unknown *Contributors*: Amoneti

File: SkyMap545.png *Source*: http://www.sciops.esa.int/wikiSI/planckpla/index.php?title=File:SkyMap545.png *License*: unknown *Contributors*: Amoneti

File: SkyMap857.png *Source*: http://www.sciops.esa.int/wikiSI/planckpla/index.php?title=File:SkyMap857.png *License*: unknown *Contributors*: Amoneti

File: ZodiRes100.png *Source*: http://www.sciops.esa.int/wikiSI/planckpla/index.php?title=File:ZodiRes100.png *License*: unknown *Contributors*: Amoneti

File: ZodiRes143.png *Source*: http://www.sciops.esa.int/wikiSI/planckpla/index.php?title=File:ZodiRes143.png *License*: unknown *Contributors*: Amoneti

File: ZodiRes217.png *Source*: http://www.sciops.esa.int/wikiSI/planckpla/index.php?title=File:ZodiRes217.png *License*: unknown *Contributors*: Amoneti

File: ZodiRes353.png *Source*: http://www.sciops.esa.int/wikiSI/planckpla/index.php?title=File:ZodiRes353.png *License*: unknown *Contributors*: Amoneti

File: ZodiRes545.png *Source*: http://www.sciops.esa.int/wikiSI/planckpla/index.php?title=File:ZodiRes545.png *License*: unknown *Contributors*: Amoneti

File: ZodiRes857.png *Source*: http://www.sciops.esa.int/wikiSI/planckpla/index.php?title=File:ZodiRes857.png *License*: unknown *Contributors*: Amoneti

File:30.png *Source*: http://www.sciops.esa.int/wikiSI/planckpla/index.php?title=File:30.png *License*: unknown *Contributors*: Grocha

File:ist_GB.png *Source*: http://www.sciops.esa.int/wikiSI/planckpla/index.php?title=File:Ist_GB.png *License*: unknown *Contributors*: Grocha

File:e_030_GB.png *Source*: http://www.sciops.esa.int/wikiSI/planckpla/index.php?title=File:E_030_GB.png *License*: unknown *Contributors*: Grocha

File:solidarc_030_GB.png *Source*: http://www.sciops.esa.int/wikiSI/planckpla/index.php?title=File:Solidarc_030_GB.png *License*: unknown *Contributors*: Agregori, Grocha

File:plot_dx9_LFI_GB_pix.png *Source*: http://www.sciops.esa.int/wikiSI/planckpla/index.php?title=File:Plot_dx9_LFI_GB_pix.png *License*: unknown *Contributors*: Grocha

File:mask_Cl.png *Source*: http://www.sciops.esa.int/wikiSI/planckpla/index.php?title=File:Mask_Cl.png *License*: unknown *Contributors*: Ehivon

File: CMB-smica.png *Source*: http://www.sciops.esa.int/wikiSI/planckpla/index.php?title=File:CMB-smica.png *License*: unknown *Contributors*: Amoneti

File: CMB-nilc.png *Source*: http://www.sciops.esa.int/wikiSI/planckpla/index.php?title=File:CMB-nilc.png *License*: unknown *Contributors*: Amoneti

File: CMB-sevem.png *Source*: http://www.sciops.esa.int/wikiSI/planckpla/index.php?title=File:CMB-sevem.png *License*: unknown *Contributors*: Amoneti

File: CMBnoise-nilc.png *Source*: http://www.sciops.esa.int/wikiSI/planckpla/index.php?title=File:CMBnoise-nilc.png *License*: unknown *Contributors*: Lmendes

File: CMBnoise-sevem.png *Source*: http://www.sciops.esa.int/wikiSI/planckpla/index.php?title=File:CMBnoise-sevem.png *License*: unknown *Contributors*: Lmendes

File: valmask-smica.png *Source*: http://www.sciops.esa.int/wikiSI/planckpla/index.php?title=File:Valmask-smica.png *License*: unknown *Contributors*: Lmendes

File: valmask-nilc.png *Source*: http://www.sciops.esa.int/wikiSI/planckpla/index.php?title=File:Valmask-nilc.png *License*: unknown *Contributors*: Lmendes

File: valmask-sevem.png *Source*: http://www.sciops.esa.int/wikiSI/planckpla/index.php?title=File:Valmask-sevem.png *License*: unknown *Contributors*: Lmendes

File: cmbmask-smica.png *Source*: http://www.sciops.esa.int/wikiSI/planckpla/index.php?title=File:Cmbmask-smica.png *License*: unknown *Contributors*: Lmendes

File: cmbmask-nilc.png *Source*: http://www.sciops.esa.int/wikiSI/planckpla/index.php?title=File:Cmbmask-nilc.png *License*: unknown *Contributors*: Lmendes

File: CMBinp-smica.png *Source*: http://www.sciops.esa.int/wikiSI/planckpla/index.php?title=File:CMBinp-smica.png *License*: unknown *Contributors*: Lmendes

File: CMBinp-nilc.png *Source*: http://www.sciops.esa.int/wikiSI/planckpla/index.php?title=File:CMBinp-nilc.png *License*: unknown *Contributors*: Lmendes

File: inpmask-smica.png *Source*: http://www.sciops.esa.int/wikiSI/planckpla/index.php?title=File:Inpmask-smica.png *License*: unknown *Contributors*: Lmendes

File: inpmask-nilc.png *Source*: http://www.sciops.esa.int/wikiSI/planckpla/index.php?title=File:Inpmask-nilc.png *License*: unknown *Contributors*: Lmendes

File: CMBnoise-smica.png *Source*: http://www.sciops.esa.int/wikiSI/planckpla/index.php?title=File:CMBnoise-smica.png *License*: unknown *Contributors*: Lmendes

File: mission_spectrum.png *Source*: http://www.sciops.esa.int/wikiSI/planckpla/index.php?title=File:Mission_spectrum.png *License*: unknown *Contributors*: Mmigliac

File: CMBspect.jpg *Source*: http://www.sciops.esa.int/wikiSI/planckpla/index.php?title=File:CMBspect.jpg *License*: unknown *Contributors*: Amoneti

file:Archives.JPG *Source*: http://www.sciops.esa.int/wikiSI/planckpla/index.php?title=File:Archives.JPG *License*: unknown *Contributors*: Xdupac

file:PLA.JPG *Source*: http://www.sciops.esa.int/wikiSI/planckpla/index.php?title=File:PLA.JPG *License*: unknown *Contributors*: Xdupac

file:PLAview.JPG *Source*: http://www.sciops.esa.int/wikiSI/planckpla/index.php?title=File:PLAview.JPG *License*: unknown *Contributors*: Xdupac